

NASA Technical Memorandum 4069  
Volume 1

**Microgravity Science and  
Applications Flight Programs,  
January–March 1987,  
Selected Papers**

*NASA Office of Space Science and Applications  
Washington, D.C.*



National Aeronautics  
and Space Administration

**Scientific and Technical  
Information Division**

**1988**

## CONTENTS

### VOLUME I

Foreword.....	vii
---------------	-----

#### MICROGRAVITY SCIENCE AND APPLICATIONS RESEARCH AREAS

##### Biotechnology

Human Blood Platelets at Microgravity.....	3
D.M. Surgenor	
Continuous Flow Electrophoresis System Experiments on Shuttle Flights	
STS-6 and STS-7.....	5
R.S. Snyder, P.H. Rhodes, and T.Y. Miller	
Preparative Electrophoresis for Space.....	27
P.H. Rhodes and R.S. Snyder	
Heterogeneity in the Growth Hormone Pituitary Gland "System" of Rats	
and Humans: Implications to Microgravity Based Research.....	47
W.C. Hymer, R. Grindeland, et al.	
Kidney Cell Electrophoresis in Space Flight: Rationale, Methods, Results	
and Flow Cytometry Applications.....	89
P. Todd, D.R. Morrison, et al.	
DeMixing Kinetics of Phase Separated Polymer Solutions in Microgravity.....	119
D.E. Brooks, S.B. Bamberger, et al.	
Hormone Purification by Isoelectric Focusing in Space.....	133
M. Bier	
Development of Immunoassays for Human Urokinase.....	147
M. Z. Atassi	
Hydrodynamic Effects on Cell Growth in Agitated Microcarrier Bioreactors.....	155
R.S. Cherry and E.T. Papoutsakis	
An Expert System Based Intelligent Control Scheme for Space Bioreactors.....	159
K-Y. San	
Shear Stress Induced Stimulation of Mammalian Cell Metabolism.....	163
L.V. McIntire, J.A. Fangos, and S.G. Eskin	
Biochemical Assays on Plasminogen Activators and Hormones	
from Kidney Sources.....	175
G.H. Barlow, M.L. Lewis, and D.R. Morrison	



Human Cell Culture in a Space Bioreactor.....	195
D.R. Morrison	
Cellular Effects of Microgravity.....	217
D.R. Morrison	
Antibody Enhancement of Free-Flow Electrophoresis.....	227
H.H.P. Cohly, D.R. Morrison and M.Z. Atassi	
The Stress Response System of Proteins: Implications for Bioreactor Scaleup.....	235
C.F. Goochee	
Protein Crystal Growth in a Microgravity Environment.....	249
C.E. Bugg	

### Electronic Materials

Growth of Mercuric Iodide (HgI <sub>2</sub> ) for Nuclear Radiation Detectors.....	269
L. van den Berg and W.F. Schneppe	
Crystal Growth and Transport Rates of the GeSe-Xenon System under Microgravity Conditions.....	287
H. Wiedemeier, S.B. Trivedi, et al.	
Modeling the Growth of Triglycine Sulfate Crystals in Spacelab 3.....	289
Yoo, H-D., Wilcox, W.R., and R.B. Lal	
A Comparative Study of the Influence of Buoyancy Driven Fluid Flow on GaAs Crystal Growth.....	337
J.A. Kafalas and A.H. Bellows	
Growth of GaAs Crystals from the Melt in a Partially Confined Configuration.....	349
H.C. Gatos	
Growth of Solid Solution Single Crystals.....	377
S.L. Lehoczky and F.R. Szofran	
Growth of Compound Semiconductor Alloys.....	391
A.L. Fripp, R.K. Crouch, et al.	

### Metals and Alloys

Isothermal Dendritic Growth - A Low Gravity Experiment.....	411
M.E. Glicksman, R.C. Hahn, et al.	
Isothermal Solidification in a Binary Alloy Melt.....	427
V. Laxmanan	
Casting and Solidification Technology (CSAT) - Directional Solidification Phenomena in a Model Metal at Reduced Gravity.....	459
M.H. McCay	

Dendritic Growth and Structure of Undercooled Nickel Based Alloys.....	469
M.C. Flemings and Y. Shiohara	
The Influences on Convection on Directional Solidification of Eutectic Bi/MnBi.....	485
D.J. Larson	
Pb-Sn Liquid Metal Diffusion.....	511
R.B. Pond and J.M. Winter	

## FOREWORD

The Microgravity Science and Applications Division is responsible for a major segment of NASA's research in space in the areas of basic and applied science dealing with materials and fluids and with fundamental studies in physics and chemistry in a low gravity environment. In the past, when the Shuttle was flying at regular intervals, the philosophy of the program was to fly several missions per year with hardware that was of high quality, but that did not contain subsystem redundancy. It was postulated that if the hardware failed, it could be fixed and reflown in a relatively short time at less expense than building in the redundant systems that are often required for unmanned satellites. In addition, since the microgravity disciplines constitute an emerging science which is still in a formative stage of development, it was believed that the program should be very broadly based in order to establish a data base of results that were applicable to several different areas of science and technology. As the Space Shuttle program matured, and especially after the Challenger disaster, it became clear that access to space would remain a rare commodity, and a resource that would be utilized only when absolutely essential to test a scientific hypothesis.

The implementation of this new philosophy required that the scientific goals of the present Microgravity Science and Applications flight program be reassessed and prioritized to assure that experiments of the highest quality would be flown. Other research efforts could be redefined and/or redirected to clarify the hypotheses to be tested in the space environment and to optimize the experimental approach, in order to most effectively use the limited flight opportunities. Dr. J. Robert Schrieffer was approached and graciously agreed to serve as chairman of a review committee to evaluate all of the research in the flight program and to make recommendations to the Director of the Microgravity Science and Applications Division as to the quality of the science contained in the program and improvements that could be made in some of the research efforts. The membership of the committee was selected by Dr. Schrieffer and consisted of an expert from each of the discipline areas funded by the MSAD. The following papers are a result of that review.

This office is deeply indebted to scientists who prepared the papers. Their efforts and sacrifices make possible the steps required to establish a program that will allow the United States to grasp this opportunity in an emerging area of science and to advance the U.S. as a world leader in new technologies. NASA and the MSAD sincerely appreciate the contributions of the review committee and thank them for their dedication to the completion of this task. The MSAD wishes to thank the Universities Space Research Association (USRA) and in particular Ms. Elizabeth Pentecost, Deputy Program Manager for the USRA Microgravity Science and Applications Program, for her efforts in the compilation and publication of this report.

## **BIOTECHNOLOGY**

Human Blood Platelets at Microgravity  
D. M. Surgenor

(Reprint, to be sent under separate cover)

**CONTINUOUS FLOW ELECTROPHORESIS SYSTEM EXPERIMENTS  
ON SHUTTLE FLIGHTS STS-6 AND STS-7**

Robert S. Snyder, Percy H. Rhodes, and Teresa Y. Miller  
Space Science Laboratory  
NASA Marshall Space Flight Center  
Huntsville, AL 35812

**ABSTRACT**

In 1978, McDonnell Douglas Astronautics Company (MDAC) began discussions with NASA on the opportunities to develop a space continuous flow electrophoresis system (CFES) that would incorporate specific modifications to their laboratory instruments to take advantage of weightlessness. A Joint Endeavor Agreement (JEA) that allocated certain flights on the Space Shuttle to MDAC in return for opportunities for NASA and interested scientists to do research in the MDAC laboratory and on their space instruments was made.

Under terms of the JEA, NASA was provided an opportunity to process two samples on STS-6. All experiment objectives and operational parameters, such as applied field, sample residence time in the field, and buffer composition had to accommodate the MDAC capabilities and NASA flight constraints. The NASA objectives were formulated so as to include investigation of the sample concentration effects reported by MDAC on STS-4. The specific objectives were (1) to use a model sample material at a high concentration to evaluate the continuous flow electrophoresis process in the MDSC CFES instrument and compare its separation resolution and sample throughput with related devices on Earth and (2) to expand our basic knowledge of the limitations imposed by fluid flows and particle concentration effects on the electrophoresis process by careful design and evaluation of the space experiment. Because the MDAC instrumentation did not include sample mixing facilities, cell separation procedures were precluded and after a variety of soluble materials were considered, hemoglobin and polysaccharide were selected as primary samples. The results from space show a large band spread of the high concentration of the single species

of hemoglobin that was principally due to the mismatch of electrical conductivity between the sample and buffer.

The seventh mission of the Space Shuttle carried two additional NASA experiments in the CFES instrument. The major objective was to evaluate the influence of the electrical properties of the sample constituents on the resolution of the continuous flow electrophoretic device. As expected, the polystyrene latex microspheres dispersed in a solution with three times the electrical conductivity of the curtain buffer separated with a significantly larger band spread than in the second experiment under matched conductivity conditions. The structure of the bands is also different between the samples and laboratory experiments have been conducted to further evaluate the phenomena affecting the electrophoresis. The analysis of both flight results is nearing completion and a qualitative explanation based upon the non-gravity dependent electrical conductivity mismatch is being developed.

## 1.0 Introduction

A series of electrophoresis experiments on Apollo [1], Apollo Soyuz Test Project (ASTP) [2], and Space Shuttle [3] have been carried out in space to show that disturbances due to buoyancy-induced thermal convection and sample sedimentation during the separation process are negligible in reduced gravity. The experiments to date have been small-scale demonstrations of specific principles that have increased our knowledge of electrokinetic and fluid dynamic phenomena and have supported our long range electrophoresis goals [4]. Simultaneously, the limitations of ground-based electrophoretic separators have been documented [5], and new concepts have been proposed for future experiments [6].

Several laboratory instruments have been constructed utilizing past developments in the design and operation of continuous flow electrophoretic separators by Strickler [7] and Hannig [8] combined with innovative developments in the field of fluids analysis by Saville [9] and Ostrach [10]. Building on these developments the McDonnell Douglas Astronautics Co. (MDSC) designed a continuous flow electrophoresis system that evolved from a detailed survey of the requirements for fractionation of biological materials.

In 1978, MDAC began discussions with NASA on the opportunities to develop a space continuous flow electrophoresis system (CFES) that would incorporate specific modifications to their laboratory instruments to take advantage of weightlessness. The first MDAC flight experiments with the CFES



on STS-4 in June 1982 fractionated a proprietary tissue culture medium and evaluated the effect of sample concentration using mixtures of rat and egg albumin. MDAC concluded that there was no loss of resolution at the higher concentrations processed in space. In addition, MDAC reported that the quantity of albumin that could be fractionated in the CFES in space was significantly higher (over 400 times) than the quantity that could be processed in their ground laboratory instrument during the same time interval. They proposed that these improvements originated from both instrument modifications and increased sample concentrations permitted by weightlessness.

Under the terms of the JEA, NASA was provided an opportunity to process two samples on STS-6 in April 1983 [11]. All experiment objectives and operational parameters, such as applied field, sample residence time in the field, and buffer composition had to accommodate the MDAC capabilities and NASA flight constraints. The NASA objectives were formulated so as to include validation of the sample concentration effects reported by MDAC on STS-4. The specific objectives were (1) to use a model sample material at a high concentration to evaluate the continuous flow electrophoresis process in the MDAC CFES instrument and compare its separation and sample throughput resolution with related devices on Earth and (2) to expand our basic knowledge of the limitations imposed by fluid flows and particle concentration effects on the electrophoresis process by careful design and evaluation of the space experiment. Hemoglobin and a polysaccharide were selected as primary samples for STS-6 by the Marshall Space Flight Center (MSFC).

The NASA experiments on STS-7 in June 1983 were intended to build upon the results obtained on STS-6 [12]. Because MDAC changed the curtain buffer on STS-7 from a barbital buffer (pH 8.3) to a propionate buffer (pH 5.2), it was not possible to perform a follow-up experiment using hemoglobin and polysaccharide as processed on STS-6. The change in pH would have resulted in both the hemoglobin and polysaccharide becoming positively charged and migrating toward the cathode. Polystyrene latex particles (PSL) were, therefore, chosen for separation on STS-7 since they are known to be negatively charged at pH 5.2 and are produced in a range of sizes with different surface charge groups and surface charge densities.

## **2.0 Materials and Methods**

### **2.1 Electrophoresis Instruments**

The internal dimensions of the space CFES (Figure 1) plexiglas separation (flow) chamber is 16 cm wide, 120 cm long, and 0.3 cm thick. A cooling jacket covers each broad chamber face with one electrode in each cooling chamber positioned diagonally across from each other to provide the electric field across the length of the chamber. The platinum electrodes are in contact with the separation chamber via slots cut into the chamber plates and are covered with a proprietary, porous membrane. The circulation of cooled electrolyte, from the bottom (flow entrance) of the chamber to the top through a serpentine passageway, establishes a uniform lateral temperature gradient and removes the bubbles formed at each electrode. Rectangular

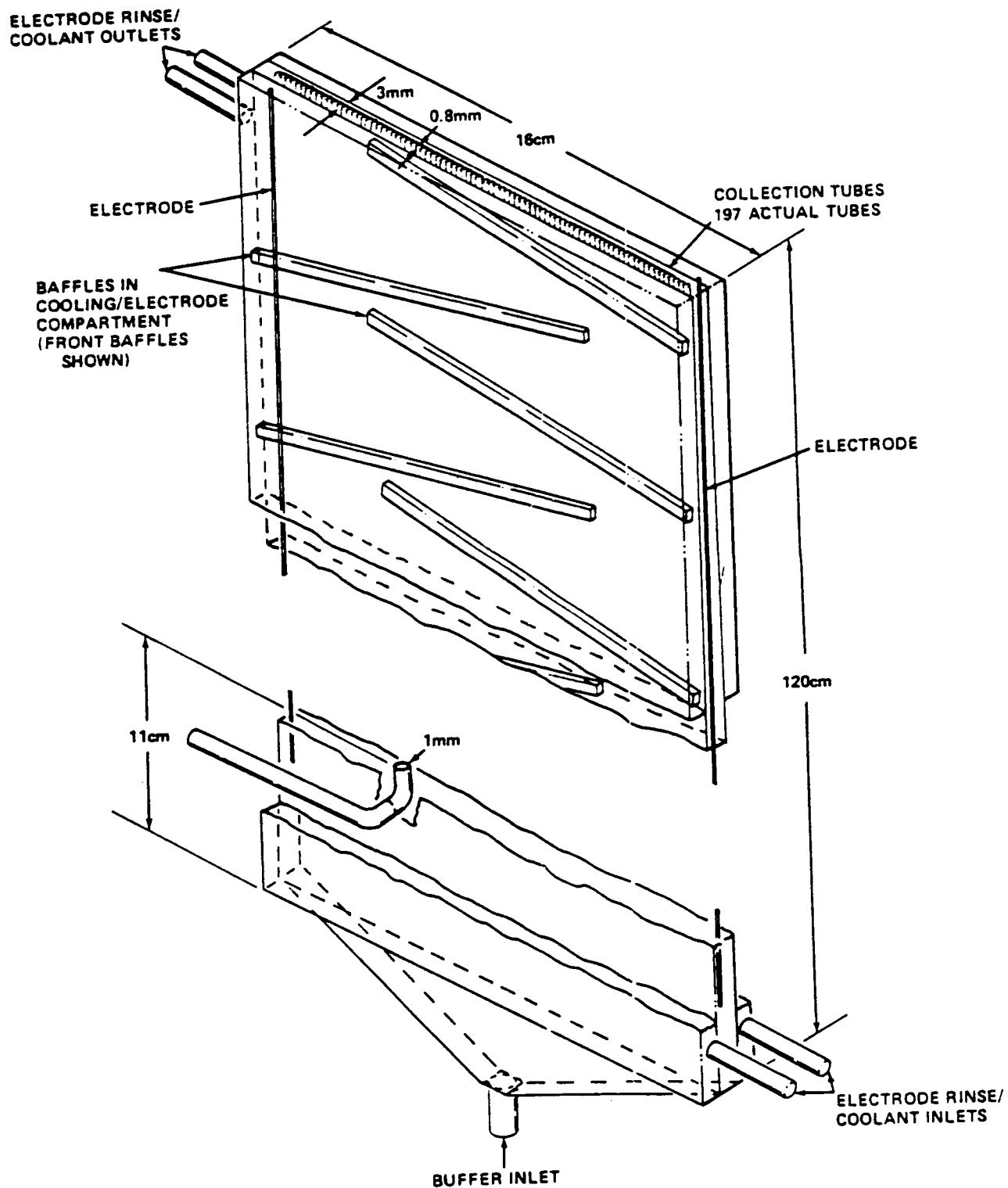


Figure 1 Continuous Flow Electrophoresis System (CFES)

struts used to form the coolant passage also provide some support to the thin, separation chamber plates. The sample enters the chamber through a thin-wall glass tube (0.1 cm inside diameter) located 11 cm from the curtain buffer entrance of the chamber. The buffer and separated sample fractions exit at the top of the chamber through a collection array of 197 Tygon tubes (0.068 cm inside diameter, 0.078 cm outside diameter) which span the width of the chamber.

## **2.2 Samples and Buffer for STS-6**

Hemoglobin was selected as the primary sample candidate based upon its: availability in large quantities as a single, molecular species; visibility for easy analysis; utility as an electrophoresis standard in laboratories; availability as variants with different electrophoretic mobilities; and stability in the cyanmethemoglobin form. Hemoglobin A (HbA) provided for ground and space use was prepared at the Centers for Disease Control (CDC). Selected from a single donor, the HbA was purified on an ion exchange column, converted to cyanmethemoglobin and concentrated to nearly 11%. The hemoglobin was sent to MSFC where it was then dialyzed against the flight buffer and stored for use in the planned experiments.

The second sample was one type of pneumococcal capsular polysaccharide (PCP) obtained from Lederle Laboratories, Pearl River, New York. PCP type 6 had a distinctly higher mobility than HbA with minimal variation and, although not colored, could be detected in low concentrations immunologically. The purity of

the PCP was determined by specific antibody tests. Since it is known that the PCP's have multiple repeating units of the basic saccharide chain, an attempt was made to obtain PCP with constant molecular weight using chromatography and laboratory continuous flow electrophoresis.

The buffer selected by MDAC for laboratory and flight experiments was 2 mM barbital consisting of 0.386 mg/ml sodium barbiturate, 0.070 mg/ml barbituric acid, and 50  $\mu$ g/ml gentamycin sulfate, pH 8.3 and electrical conductivity 160  $\mu$ mho/cm at 25 °C.

### **2.3 Samples and Buffer for STS-7**

Monodisperse polystyrene latex (PSL) particles less than 1.0  $\mu$ m in diameter were chosen to minimize sedimentation and eliminate any requirement for resuspending the sample during flight. Three particle sizes were ultimately chosen, and two of the particle populations were dyed to enhance photographic detail and aid in experimental analysis.

The latex particles with the highest mobility (nominal diameter of 0.56  $\mu$ m) were dyed red; the particles with the lowest mobility (nominal diameter 0.80  $\mu$ m) were dyed blue. The particles with intermediate mobility (nominal diameter 0.30  $\mu$ m) were not dyed. The latexes were then suspended in the curtain buffer containing Brij using a procedure of buffer exchange with filtration. Appropriate volumes of each latex were combined to yield equal concentrations for the final flight sample with the following properties: total latex concentration, 5.0%; pH, 5.6%; and conductivity,  $155 \pm 5$   $\mu$ mhos/cm. The

conductivity of a second sample of PSL was increased approximately three times that of the initial sample to  $455 \pm 5$  mhos/cm using 0.10 M NaCl, while maintaining a total latex concentration of 5.0% by weight.

The curtain buffer was prepared from a 100X stock solution of 225 mM sodium propionate, pH 5.2 by 100X dilution with distilled water to give a 225 mM solution of pH 5.0 and conductivity of  $140 \pm 5$   $\mu$ mhos. Laboratory tests were initially performed with a noionic surfactant, 0.05% w/v Brij 35 (polyoxyethylene lauryl ether 35) added to the sample and curtain buffer. Shortly before flight, however, it became necessary for MDAC to remove the Brij from the curtain buffer. Since the sample latex had been selected according to their separation in buffer with Brij, the flight samples included Brij in the suspension medium although Brij was excluded from the curtain buffer.

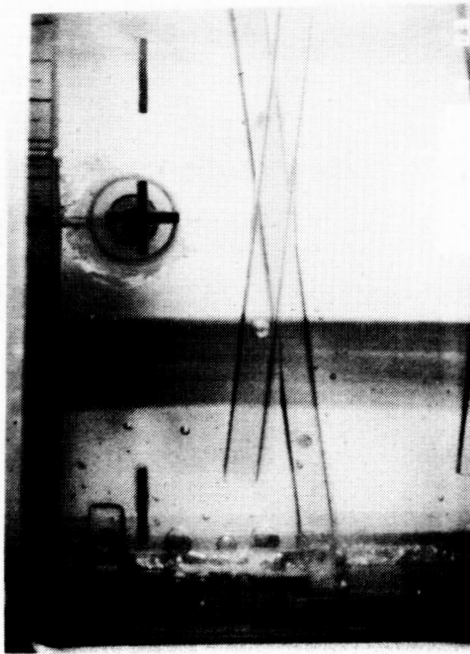
### **3.0 Space Electrophoresis-Experiments**

The two samples processed in the first NASA space experiment on CFES were (1) a high concentration of hemoglobin alone and (2) a mixture of polysaccharide and hemoglobin at a lower concentration. The band behavior obtained from processing the single species was used to define the performance of the space instrument. The low concentration mixture, 1.9% Hb and 0.5% PCP-6, although still higher than can be processed at high resolution on Earth would permit a comparison of the separations achieved before flight in the various laboratory units.

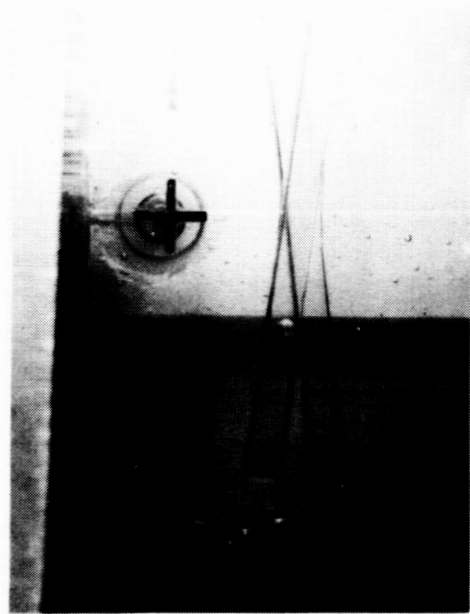
In orbit, the NASA hemoglobin sample of 8.7% concentration was processed first to establish the initial CFES performance. The hemoglobin experiments each started with an initial zero voltage segment. The sample band spread only slightly during its 8 minute passage through the chamber which can be attributed to diffusion. After the zero run, an electric field of  $25 \text{ V cm}^{-1}$  was applied for an interval of about 32 minutes in order to establish steady state conditions. Photographs of the electrophoresis runs were taken at sample insertion, midway up the chamber and at the collection end. A portion of the separated samples were also collected for later analysis.

Photographs of the high concentration HbA, taken at the same chamber region are shown in Figure 2 with the time in hours and minutes shown in the lower right hand corner of each picture. Figure 2a shows the zero voltage position of the sample stream. With the cathode on the left, the sample should proceed only toward the right to the anode when the electric field is applied. However, Figures 2b-2d were taken over a period of ten minutes and show that the band spreading is so extensive that some of the sample is in a retrograde migration. This condition could only exist if the sample spread in the chamber thickness past the electroosmotic stationary layer. Based on comparison of the photographs there appears to be a build up of sample near the walls as the more intense color of the later photograph seems to suggest.

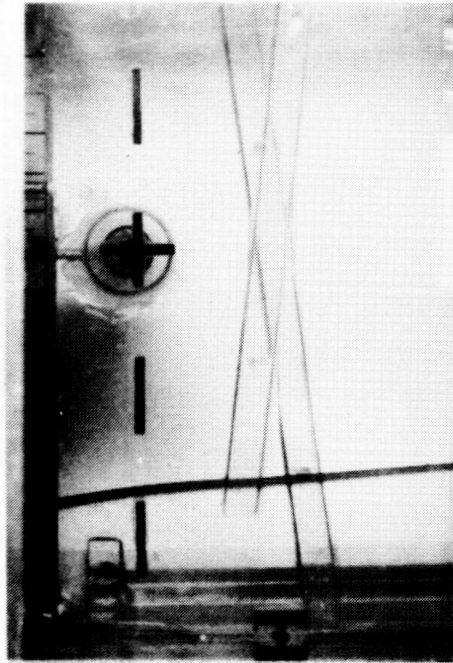
After completing half the MDAC proprietary samples, the second NASA preparation, the HbA and PCP mixture, was



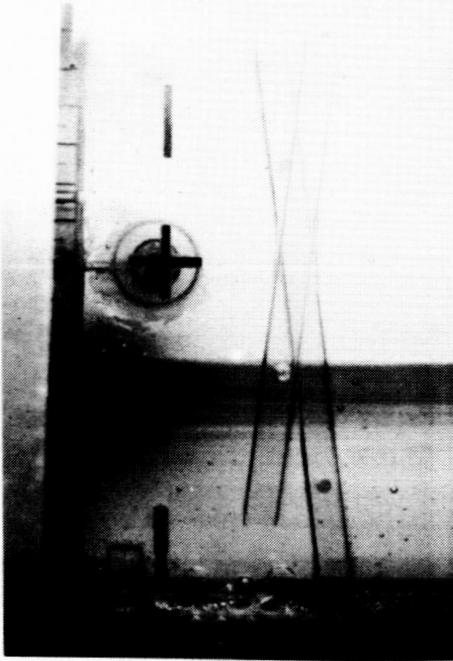
B. Deflection at 4 hours, 3 minutes



D. Deflection at 4 hours, 13 minutes



A. Zero Voltage



C. Deflection at 4 hours, 10 minutes

Figure 2 Photographs of the Collection of High Concentration  
Sample of Hemoglobin



processed. Although faint, the stream was more compact with little indication of spreading. The migration of the leading edge of the sample was roughly the same as in the previous experiment. However, there does not appear to be the large retrograde migration observed in the high concentration experiment.

In addition to the photographs just described, the sample was collected for the two experiments. The entire fluid output of the space chamber was collected, as noted previously, during the middle of each separation run in 197 small (1.5 ml) polypropylene pockets arranged in a steel tray. The trays containing the NASA samples were analyzed for hemoglobin and polysaccharide with the results shown in Figures 3 and 4.

Figure 3 shows a very broad single peak with some sample deflected toward the cathode side of the zero field location. However, this does not show the total amount of retrograde sample migration, since some of the sample near the walls clearly remained in the chamber. This is apparent by observing the color extending to the left (cathode) wall in Figure 2d.

Figure 4 shows a separation of the low concentration hemoglobin and polysaccharide. The separation, however, was not as distinct as obtained in the laboratory CFES or in the Desaga FF48 [11]. Also, none of the Earth-based laboratory experiments had sample appear on the cathode side of the zero field location. It is interesting to note that Figure 4 shows about the same amount of retarded and retrograde sample between tubes #28 and #55 as observed for the high concentration experiment in Figure 3.

MDAC CFES STS-6 EXP-1  
HEMOGLOBIN A (8.7%)

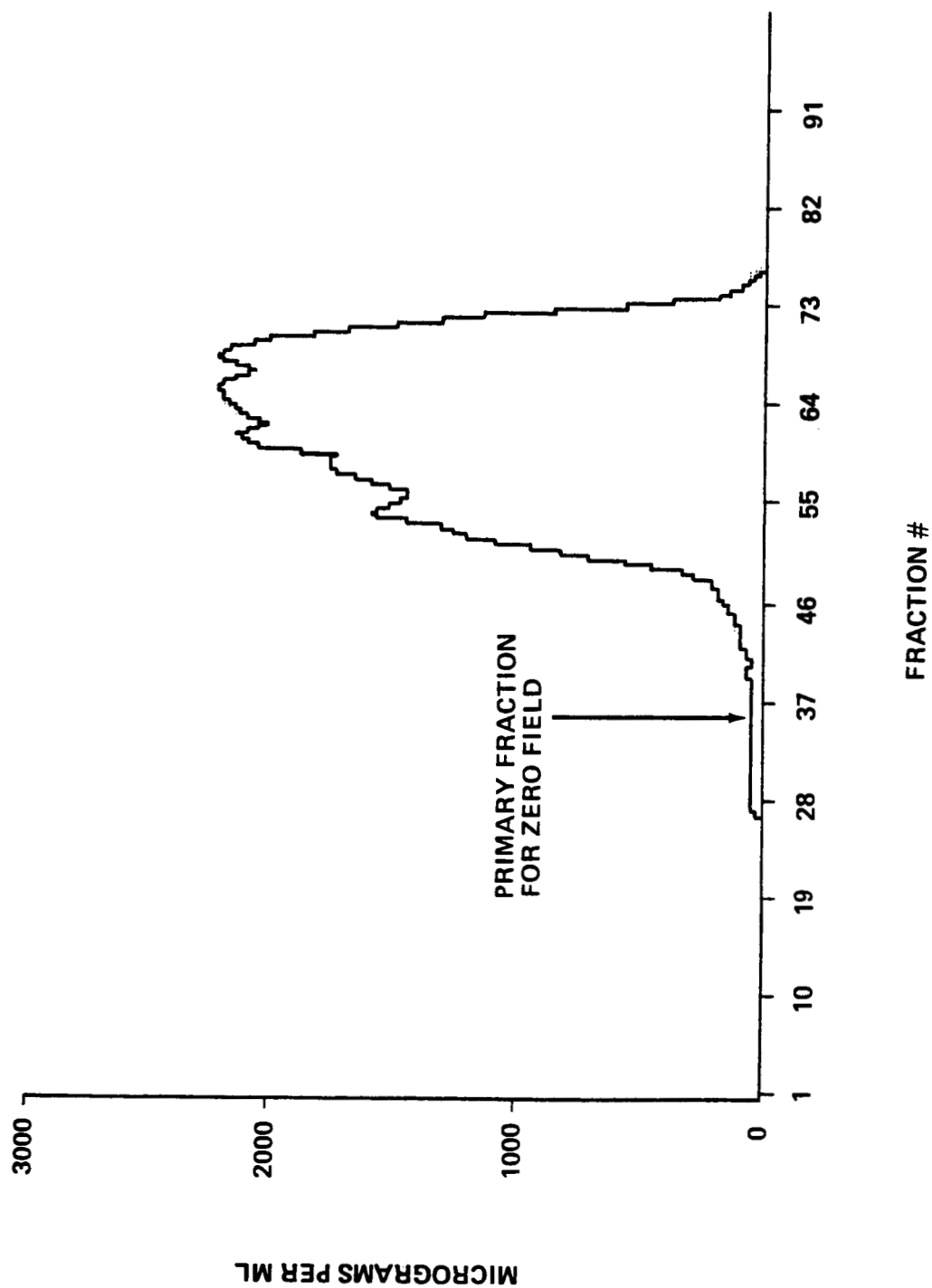


Figure 3 Band Spread of High Concentration Hemoglobin Sample

MDAC CFES STS-6 EXP-4  
 HEMOGLOBIN A (1.8%)  
 POLYSACCARIDE 6B (0.5%)

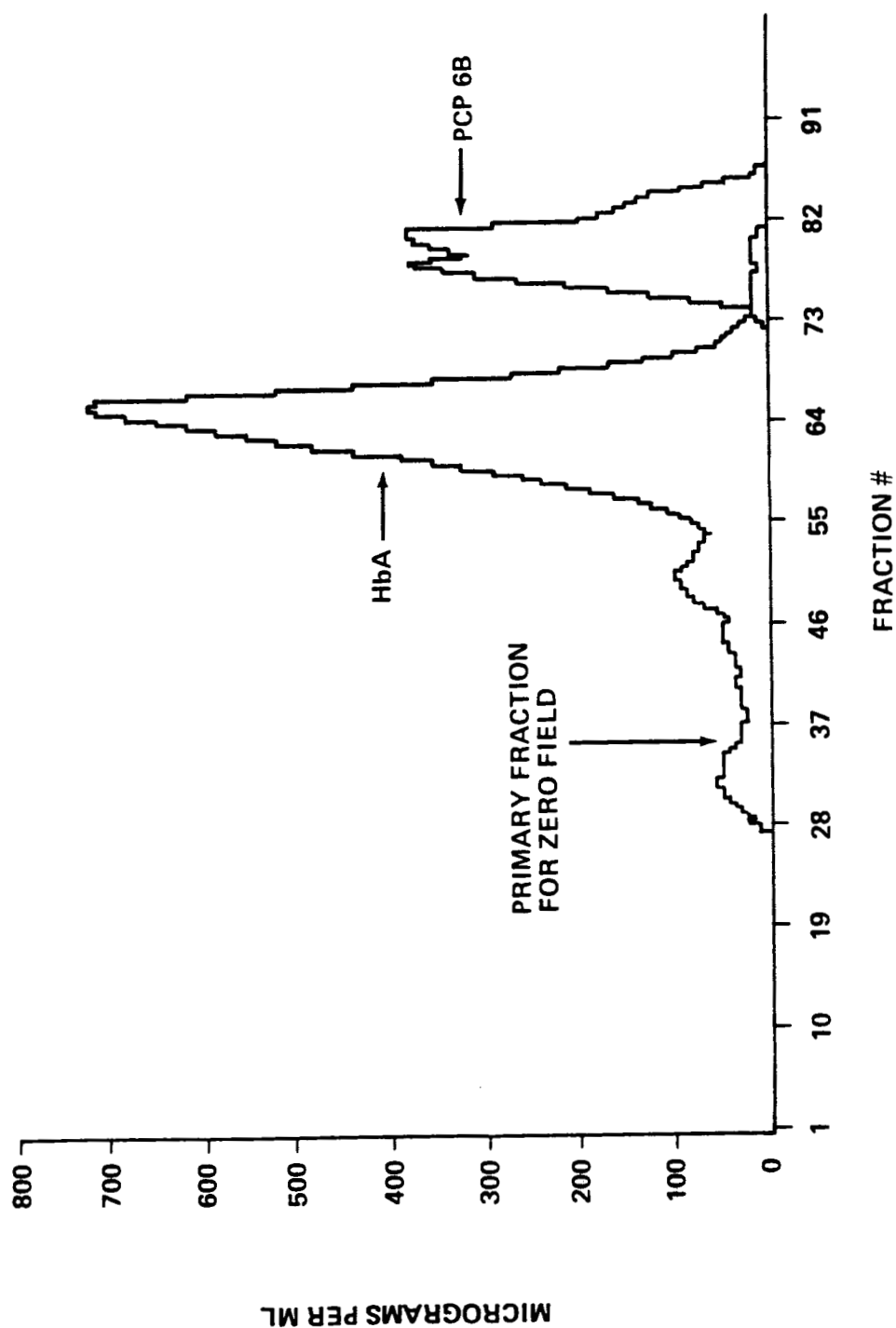


Figure 4 Band Spread of Low Concentration Hemoglobin and Polysaccharide Sample

The same procedures were followed with the polystyrene latex samples on the next flight, STS-7. The results of the earlier flight demonstrated considerable band broadening when the sample conductivity was approximately three times that of the curtain buffer. These results, as well as prior ground-based data, provided the justification for the design of the STS-7 experiment which evaluated the relationships between the sample and curtain buffer properties and the fractionation resolution.

Figure 5 shows a series of photographs of the unmatched sample conductivity (left side) and matched sample conductivity (right side). These photographs are of the separated latexes just before entering the collection tray at the top of the CFES. The band distortion and spreading of the PSL samples when the conductivities of the samples and curtain were not matched is evident from the photographs and was confirmed by analysis of the collected fractions (Figure 6).

#### **4.0 Discussion and Conclusion**

These two experiments in the MDAC CFES were intended to confirm two previous space observations: only electrophoresis and electroosmosis determined particle migration in an electric field during zone electrophoresis on Apollo 16 and electrophoresis was independent of sample concentration with albumin up to 20% on STS-4. Instead, these experiments showed that the previous conclusions were too simplistic.

First, the sample insertion disk used for the Apollo zone electrophoresis experiments is not a valid model for the sample

ORIGINAL PAGE  
BLACK AND WHITE PHOTOGRAPH

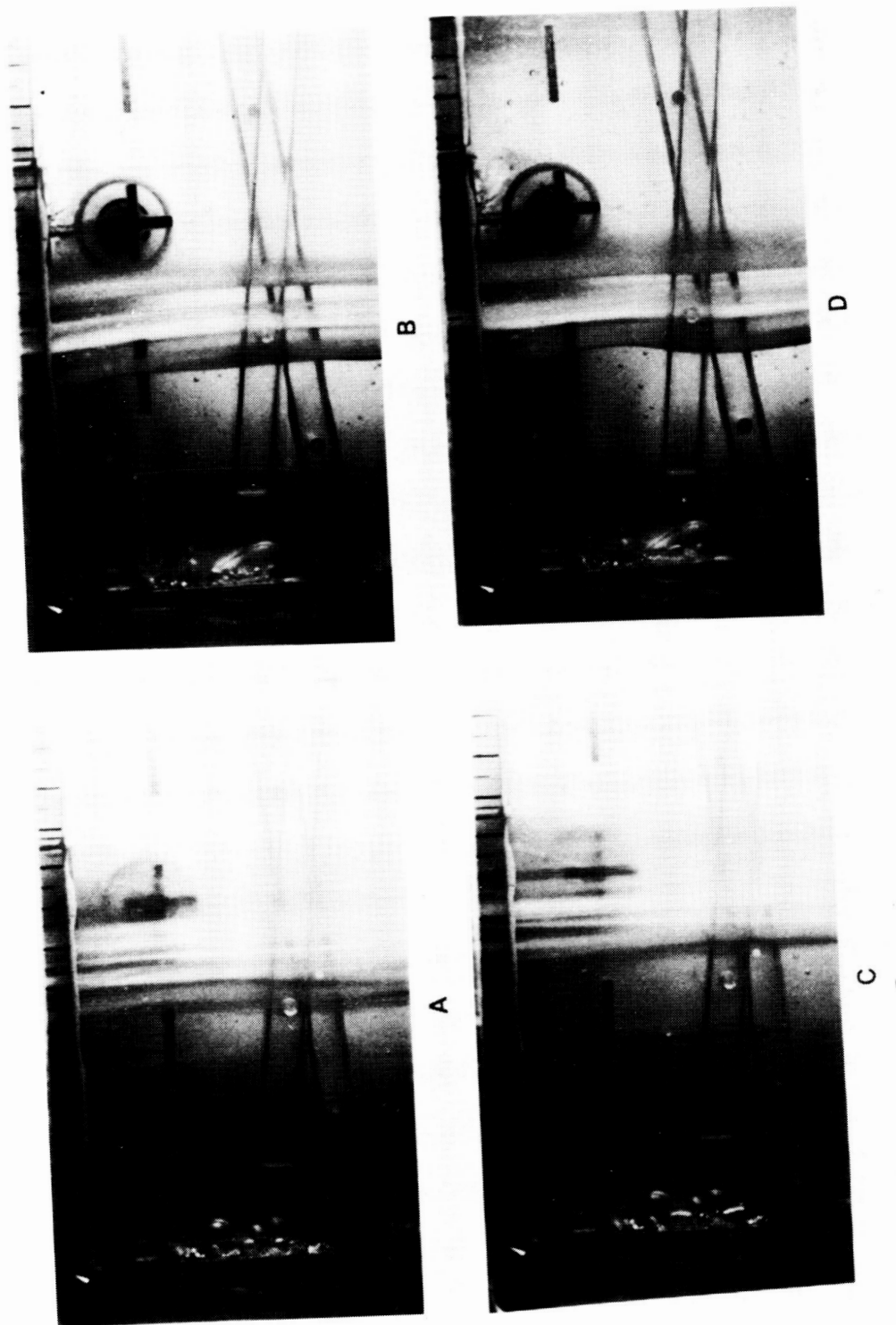


Figure 5 Photographs of Polystyrene Latex Samples With Unmatched Conductivity (A and C) and Matched Conductivity (B and D)

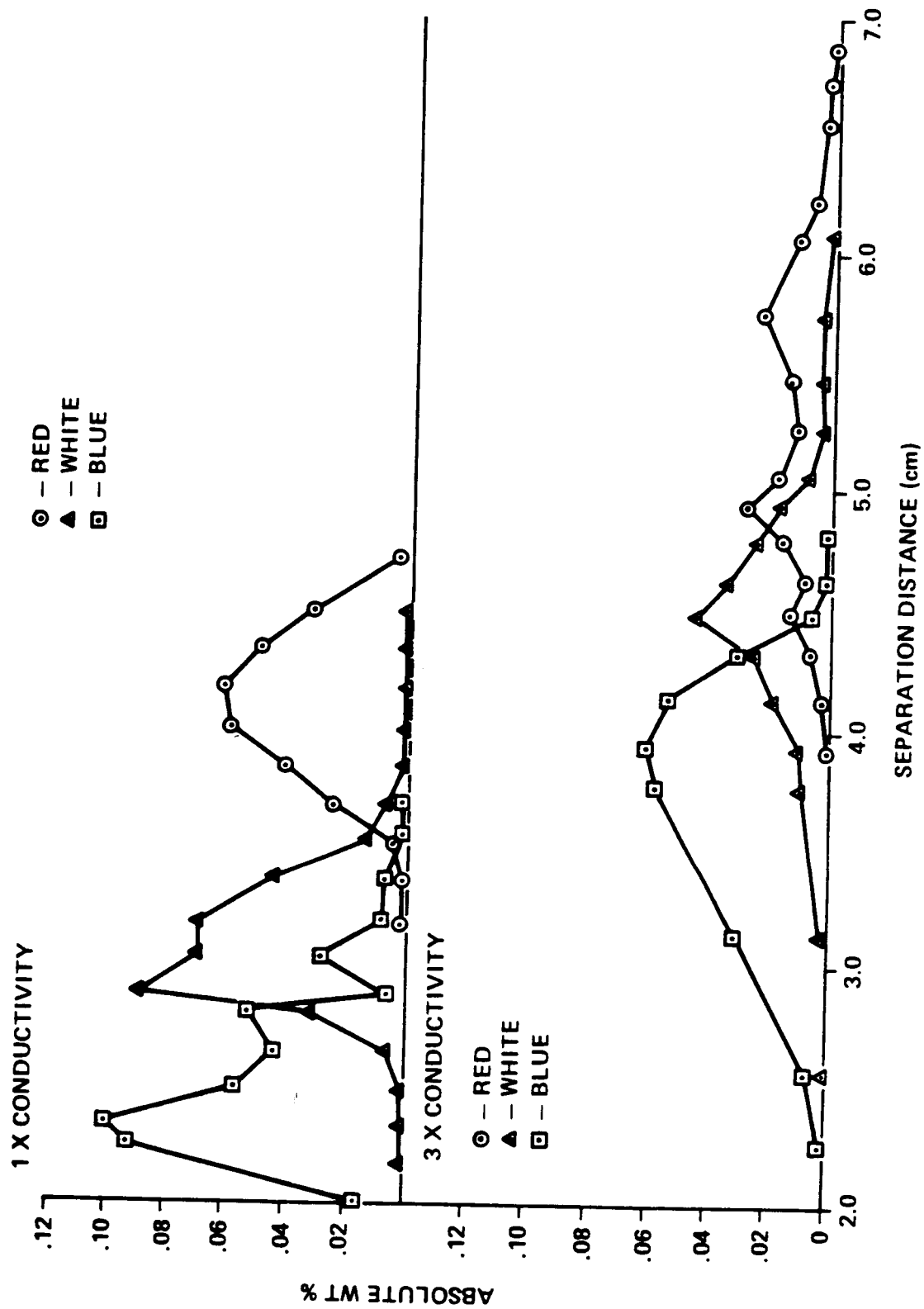


Figure 6 Band Spread of Polystyrene Latex Samples

filament configuration of continuous flow electrophoresis. Second, increasing the quantity of protein or latex particles added to the electrophoresis buffer to constitute the sample also proportionally changes the electrical properties of the sample and this has a significant impact on the subsequent electrophoresis of that sample by continuous flow electrophoresis.

The predisposition of the analysis made the interpretation of the two separate but complementary microgravity experiments more difficult. The hemoglobin samples were done first in space, but the pattern of the collected sample did not fit our model. Although the hemoglobin had a single electrophoretic mobility, this mobility could not be measured with precision in the barbital buffer. This made any estimate of electroosmosis subject to error and thus the band structure of the high concentration of hemoglobin was not understood.

During the past year, a more detailed analysis of the hemoglobin experiment has led to the following probable sequence of events. The 9% hemoglobin sample added to the 2 mM barbital buffer (pH 8.2) reduced the overall sample pH to 7.5. Since the pK of the barbituric ion is 7.8, less than half of those ions in the sample were ionized. As soon as the sample entered the chamber and the region of the electric field, the positive sodium ions had to carry most of the current so  $\text{Na}^+$  rapidly built up at the rear of the sample. This led to a hemoglobin sample with reduced conductivity in the front of the band and higher conductivity in the rear. The significance of this conductivity

distribution in causing the dispersion of the hemoglobin in space was not determined until after the polystyrene latex distributions in space were analyzed.

Electrophoretic mobilities of the polystyrene latex were measured in a microscope electrophoresis instrument for the next flight experiment but the sample bands still did not fit the anticipated distribution. The sample with higher conductivity showed the expected broader spread but an attempt to fit the shape of the sample distribution into the nested crescents formed by electroosmosis was only partially successful.

The resulting sample geometry may be the product of a phenomena first reported by Sir Geoffrey Taylor [13] describing the distortion which occurs when an electric field is applied to a conducting drop suspended in a liquid of lower conductivity. The elongation of the drop parallel to the field is analogous to the spread of the high conductivity polystyrene latex sample in the center-plane of the chamber when the electric field was applied. Ground-based experiments and a theoretical analysis of continuous flow electrophoresis based upon Taylor's framework now appears to confirm this analogy. The polystyrene latex apparently did not reach the vicinity of the chamber walls where electroosmosis would dominate. Instead, the sample was smeared by the conductivity mismatch with the surrounding electrophoresis buffer.

A plausible model of the hemoglobin sample can also be obtained from Taylor's drop analysis. Since a low conductivity drop in a higher conductivity liquid elongates perpendicular to



an applied electric field, the low conductivity front of the hemoglobin sample spread perpendicular to the field and approached the chamber walls where electroosmosis carried the hemoglobin toward the cathode. At the rear of the hemoglobin sample, the higher conductivity caused a sample spread in the chamber center-plane similar to the polystyrene latex. Thus, the collected hemoglobin distribution shows some sample spread by electroosmosis and a broad but uniform concentration of hemoglobin near the front of the electrophoresis pattern.

This qualitative model of the space experiments is an attempt to explain the observed results of past experiments. When CFES is operated again on the Shuttle it will be important to conduct additional experiments to test the sample distortion predicted by Taylor.

## REFERENCES

- [1] Snyder, R. S., R. N. Griffin, A. J. Johnson, H. Leidheiser, Jr., F. J. Micale, S. Ross, C. J. van Oss, and M. Bier, "Free Fluid Electrophoresis on Apollo 16," Sep. and Purif. Meth., 2(2), 259-282 (1973).
- [2] Allen, R. E., P. H. Rhodes, R. S. Snyder, G. H. Barlow, M. Bier, P. E. Bigazzi, C. J. van Oss, R. J. Knox, G.V.F. Seaman, F. J. Micale, and J. W. Vanderhoff, "Column Electrophoresis on the Apollo-Soyuz Test Project," Sep. and Purif. Meth., 6(1), 1-59 (1977).
- [3] Snyder, R. S., P. H. Rhodes, B. J. Herren, T. Y. Miller, G.V.F. Seaman, P. Todd, M. E. Kunze, and B. E. Sarnoff, "Analysis of Free Zone Electrophoresis of Fixed Erythrocytes Performed in Microgravity," Electrophoresis, 6, 3-9 (1985).
- [4] Snyder, R. S., "Separation Techniques," in Materials Sciences in Space - A Contribution to the Scientific Basis of Space Processing, eds., B. Feuerbacher, H. Hamacher, and R. J. Naumann (Springer-Verlag: Berlin), pp. 465-481 (1986).
- [5] Miller, T. Y., G. O. Williams, and R. S. Snyder, "Effect of Conductivity and Concentration on the Sample Stream in the Transverse Axis of a Continuous Flow Electrophoresis Chamber," Electrophoresis, 6, 377-381 (1985).
- [6] Rhodes, P. H. and R. S. Snyder, "Sample Band Spreading Phenomena in Ground and Space-Based Electrophoretic Separators," Electrophoresis, 7, 113-120 (1986).
- [7] Strickler, A., "Continuous Particle Electrophoresis: A New Analytical and Preparative Capability," Sep. Sci., 2(3), 335-355 (1967).
- [8] Hannig, K., "Separation of Cells and Particles by Continuous Free Flow Electrophoresis," Tech. Biochem. Biophys. Morphology, 1, 191-232 (1972).
- [9] Saville, D. A., "The Fluid Mechanics of Continuous Flow Electrophoresis," Physicochemical Hydrodynamics, 2, 832-912 (1978).
- [10] Ostrach, S., "Convection in Continuous Flow Electrophoresis," J. Chrom., 140, 187-197 (1977).
- [11] Snyder, R. S. et al., "Unexpected Electrophoretic Behavior of Macromolecular Sample on Space Shuttle Flight STS-6," in preparation (1987).

- [12] Snyder, R. S., P. H. Rhodes, T. Y. Miller, F. J. Micale, R. V. Mann, and G.V.F. Seaman, "Polystyrene Latex Separations by Continuous Flow Electrophoresis on the Space Shuttle," Separation Sci. and Tech., 22(1), 157-185 (1986).
- [13] Taylor, G. I., "Studies in Electrohydrodynamics in the Circulation produced in a Drop by an Electric Field, Proc. Roy. Soc.,. Sec. A, 291, 159 (1966).

## PREPARATIVE ELECTROPHORESIS FOR SPACE

Percy H. Rhodes and Robert S. Snyder  
Space Science Laboratory  
Marshall Space Flight Center  
Huntsville, AL 35812

## ABSTRACT

A basic premise of continuous flow electrophoresis is that removal of buoyancy-induced thermal convection caused by axial and lateral temperature gradients will result in ideal performance of these instruments in space. Although these gravity dependent phenomena disturb the rectilinear flow in the separation chamber when high voltage gradients and/or thick chambers are used, distortion of the injected sample stream due to electrohydrodynamic effects causes major broadening of the separated bands.

Although the electrophoresis separation process is simple in concept, flows local to the sample filament produced by the applied electric field have not been considered. These electrohydrodynamical flows, formulated by G. I. Taylor in 1965 for drops suspended in various liquids, distort the sample stream and limit the separation. In addition, electroosmosis and viscous flow, which are inherent in the continuous flow electrophoresis device, combine to further disturb the process. Electroosmosis causes a flow in the chamber cross section which directly distorts the sample stream, while viscous flow causes a parabolic profile to develop in the flow plane. This flow profile in turn distorts migration by causing a varying residence time across the thickness of the chamber. Thus, sample constituents at the center plane will be in the electric field a shorter time and hence move less than comparable constituents closer to the chamber wall.

A moving wall concept is being proposed for space which will eliminate and/or control all of the above-mentioned disturbances. The moving wall will entrain the fluid to move as a rigid body and hence produce a constant residence time for all sample distributed across the chamber thickness. By aligning the moving wall at an angle to the chamber axis, a component of the moving wall motion can be made to oppose and hence cancel the electroosmotic flow. In the absence of electrokinetic effects, i.e. electroosmosis, the electrohydrodynamical effect manifests itself as a ribbon, being either vertical (perpendicular to the electric field) or horizontal (aligned with the electric field) depending on the ratio of conductivity of the sample to that of the buffer. Therefore, by using low conductivity sample solutions to provide a vertical ribbon, the moving wall concept

should produce distortion-free separations.

The moving wall electrophoresis chamber can only be operated in space because there is no viscous flow in the chamber to stabilize against thermal convection. Laboratory prototype instruments have been built which confirm the sensitivity of their operation. These prototypes have also identified engineering problems such as liquid seals. However, the moving wall electrophoresis system is a concept designed for space which should permit preparative electrophoresis to attain its potential.

## Introduction

The major goal of the electrophoresis program at the Marshall Space Flight Center (MSFC) is to obtain high resolution separation of viable cells in space that is not attainable on Earth. Although the requirement for the separation and collection of viable cells is not as extensive as it was in the 1970's when cells were cultured principally for their protein production, purification of cells is still of interest for research. Continuous flow electrophoresis (CFE) remains the major technique which can fractionate viable unmodified biological cells in excess of  $10^8$  cells/hour. However, the resolution of separation for this technique is limited by inherent extraneous flows and sample/electric field interactions which have not been recognized or fully understood.

At the beginning of the NASA electrophoresis program it was proposed that electrophoresis of cells in free fluid in space should achieve an optimum separation because the main detractors to resolution, thermal convection and sedimentation, were removed.<sup>1</sup> This rationale was based on the fact that electrophoresis in porous gels had become the standard technique to separate and identify the various protein constituents in a complex mixture. Experiments in our laboratory established that the limiting pore size for agarose, an extremely large pore size gel, was  $0.5\text{ }\mu\text{m}$ .<sup>2</sup> The first experiments in the Apollo spacecraft in 1972 and Apollo-Soyuz Test Project in 1975 attempted "gel-

free" electrophoresis of latex particles and viable cells in cylindrical columns of buffer. Photographs showed bands of polystyrene latex distorted by electroosmosis<sup>3</sup> and separated cells that were too few in number to analyze for secreted products.<sup>4</sup> These experiments did show, however, that for free zone electrophoresis of particles in microgravity, only electrophoresis and electroosmosis determined the migration.

The pause in space flight between the Apollo and Space Shuttle and the encouraging results from the zone electrophoresis experiments led to the development of the Continuous Flow Electrophoresis System (CFES) by the McDonnell Douglas Astronautics Company (MDAC). Commercial continuous flow electrophoresis instruments are not efficient because of the major design requirement to compensate for gravity-induced convection and sedimentation. Their chambers are thin (typically 0.5 mm) to minimize temperature gradients and, consequently, sample input is restricted and detrimental wall effects (to be discussed later) are enhanced. McDonnell Douglas increased their flight electrophoresis chamber dimensions by a minimum factor of two over their ground-based chamber to increase the sample throughput; however, the ratio of chamber thickness to sample bore diameter remained 3:1 which is typical of some commercial instruments.

Recent experiments and analysis at MSFC indicate that electrohydrodynamic considerations are the major factors limiting

the resolution of separation in continuous flow electrophoresis. A new electrophoresis instrument has been designed to take advantage of both the reduced gravity environment and electrohydrodynamic (EHD) effects. In order to determine the effect of EHD on continuous flow electrophoresis and how this effect may be used to enhance CFE performance in space, sample stream distortion and its resulting degradation of performance must be understood.

Continuous Flow Electrophoresis (CFE) takes place within a flowing curtain of aqueous electrolyte contained in a long rectangular chamber of high aspect ratio as shown schematically in Figure 1. The narrow gap between the broad faces of the chamber confines the flow to a thin curtain. The sample is continuously injected into this curtain as a finely-drawn stream (filament) and fractionated under the influence of a lateral electric field produced by flanking electrodes. The fractionated sample bands are subsequently collected in a uniform array of collection ports situated along the exit end of the chamber. The no-slip condition at the chamber wall causes a parabolic profile to develop in the direction of buffer flow. In addition, a lateral flow, across the width of the chamber (perpendicular to buffer flow), called electroosmosis, exists when charged walls are present. These independent phenomena are inherent in the CFE process and they combine to produce crescent-shaped distortions, the curvature of which is determined by the flow that predominates,



# FLUID FLOW AND SAMPLE MIGRATION DURING CONTINUOUS FLOW ELECTROPHORESIS

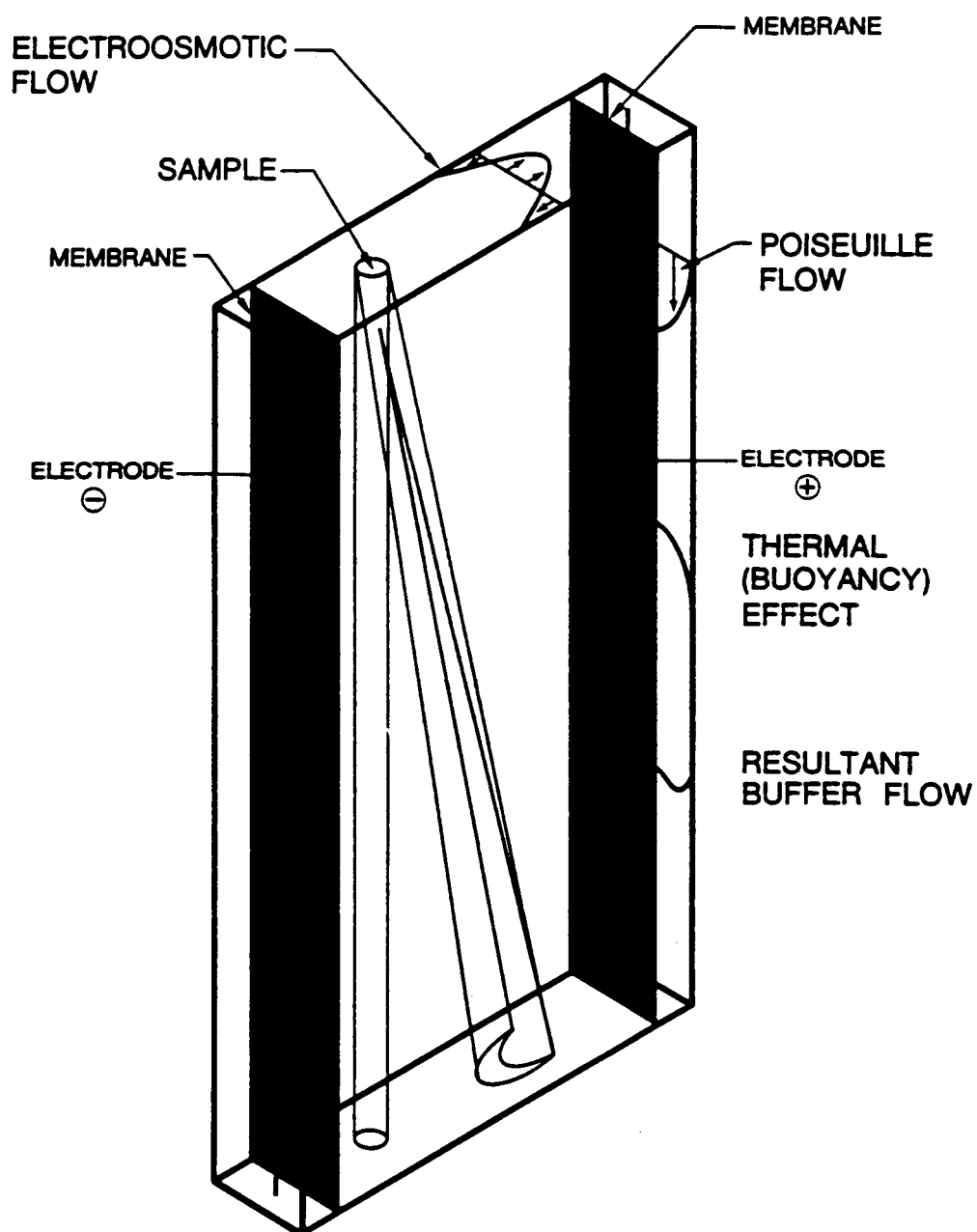


Figure 1. Schematic of typical CFE separation chamber.

either laminar flow or electroosmosis. This mechanism of sample stream distortion has always been thought to be a major cause of resolution degradation in CFE devices. The term "wall effects" has frequently been used to describe the phenomenon.

These "wall effects" were first noted and recorded by Strickler<sup>6</sup> in 1967 through the use of his cross-section illuminator. Figure 2 shows six different samples of varying electrophoretic mobility and their distorted bands. The crescents arising from viscous flow and electroosmosis influence the observed shapes in two ways. First, the no-slip condition at the chamber wall causes the parabolic profile to develop in the direction of buffer flow causing sample residence time to vary locally in the thickness of the chamber. Therefore, sample near the walls remains in the electric field longer than identical sample near the center plane and is deflected further by the electric field. This causes a crescent with the nose toward the negative electrode on the left. Electroosmosis acts to produce the opposite effect. Positive charges induced in the buffer at the wall as a result of its negatively charged surface causes the buffer at the wall to flow to the left toward the negative electrode and return to the right along the chamber center plane. This effect causes crescent formations with noses toward the positive electrode on the right. It is important to note that these are competing effects, so that one must either balance or eliminate them. Until recently, this so-called "wall effect" was

all that was known about sample filament distortion, i.e., it was not known what caused the sample to deviate from the center-plane and approach the wall. Although a correlation between sample stream spreading and sample conductivity was observed by Strickler<sup>7</sup>, no explanation of sample movement toward the walls was given. Therefore, sample stream spreading has primarily been considered sample migration away from the center plane region into marginal zones near the wall, with spreading of the band induced by combined action of viscous flow and electroosmosis.

It has been determined, however, that the actual initial sample stream distortion is an electrohydrodynamic effect whose shape is determined by ratios of dielectric constant and conductivity between the sample and buffer, and which has a magnitude proportional to the square of the voltage gradient. It is this distortion mechanism which moves the sample toward the walls and produces the spreading previously mentioned. However, under certain conditions the sample stream can also spread laterally and migrate toward the chamber center plane. This lateral mode of sample stream distortion could have a more adverse effect on resolution than the case of transverse sample migration.

## 2. ANALYSIS

The electrohydrodynamic relationships are developed along the lines of Taylor<sup>8</sup>. Taylor showed the elongation of a drop of one dielectric fluid in another depended on the ratios of the conductivity, viscosity and dielectric constant for the drop

and the surrounding fluid. He determined a discriminating function to predict whether the drop would become prolate or oblate.

His arguments can be used to calculate the distortion of a sample stream during electrophoresis. Consider a cylindrical fluid sample filament in a rectangular flow section. It is assumed that the Reynolds number is small so that it is permissible to use the linear (Stokes) equation of motion; and that the cylindrical sample stream is small compared to the thickness of the chamber. If a typical cross-section is analyzed, the sample will appear as a circle in an infinite expanse of buffer. Taking the subscripts of 1 for the sample and 2 for the buffer, the conductivities, dielectric constants and viscosities are  $\sigma_1$ ,  $k_1$  and  $\eta_1$ , respectively. The sample filament has a radius  $a$  and  $E$  is the uniform electrical field far from the filament. Note that the field is such that a negatively charged particle moves from left to right. Following the arguments of Taylor an expression for the surface stress can be derived:

$$C = \frac{E^2 K}{4\pi (R^2 + 1)^2} [S(R^2 + R + 1) - 3] \cos 2\theta$$

where:  $C$  = surface stress

$E$  = Electric field strength

$R$  = Ratio of Conductivity of Sample to that of Buffer

$K$  = Dielectric constant of buffer

$S$  = Ratio of dielectric constant of buffer to that of  
sample -  $K_2/K_1$

The term inside the brackets can be considered a discriminating factor since it determines the sign of the surface stress at a specific angle,  $\theta$ . The ratio of dielectric constants,  $S$ , will be near unity for experiments with dilute polystyrene latex samples in buffers made of the same constituents as the flowing curtain. When the conductivity of the sample equals that of the buffer,  $R = 1$ , and the surface stress is zero signifying an undistorted sample stream. When  $R$  is greater than one (high conductivity sample), the discriminating factor and surface stress is positive and the surface stress varies with  $\theta$  as shown in Figure 3. When a relatively low conductivity sample is used,  $R$  is less than one and the surface stress vectors shown in the Figure 3 are reversed.

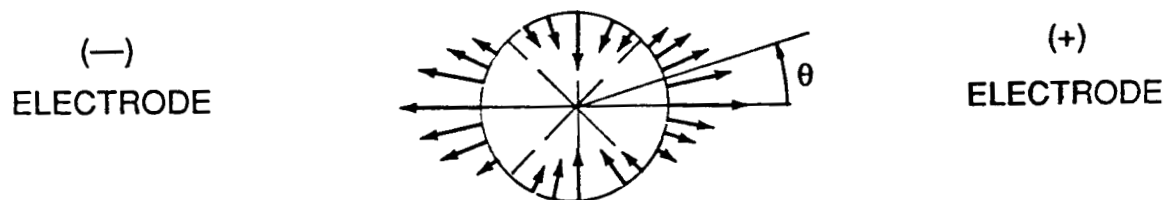


Fig. 3. Case of high conductivity sample showing surface stress acting on a cylindrical sample filament in an electric field.

The major difference between Taylor's case of the immiscible fluid drop and this case of the sample filament in a buffer solution is that no restoring force such as surface tension is present to limit the distortion of the sample filament. Therefore, it follows that the deformation will continue until a ribbon is formed. This ribbon formation is confirmed by the following experiments. Figure 4 shows a view of the buffer collection end of a horizontal electrophoresis chamber. A single species of white polystyrene latex was inserted into the input end of the chamber (not in view) and the thin cylindrical sample can be seen. The electric field is produced by electrodes that extend the length of the six-inch long chamber. Figure 5 shows an example of the low conductivity latex sample distorted into a vertical (transverse) ribbon in the high conductivity buffer. Figure 6 shows a horizontal (lateral) ribbon obtained when a high conductivity sample is inserted into a low conductivity curtain buffer. These distortions resulted from the application of a 400 Hz A.C. field. Since the equation for surface stress contains  $E^2$ , a steady component along with the varying component of 400 Hz can be expected. Of course, in this instance, only the steady component is evident and, thus, only the phenomena described by the analysis is observed. The use of an A.C. field also serves to eliminate all electrokinetic effects, i.e. viscous flow effects and electroosmosis, which otherwise mask the electrohydrodynamic phenomena.

THIS PAGE INTENTIONALLY LEFT BLANK

Since there is no practical way to exactly satisfy conditions with the discriminating function equal to unity, the distortions must then necessarily be controlled. Also, since it is apparent that none of these phenomena are gravity-related, then for any continuous flow device to operate efficiently in space, the candidate apparatus must control these effects.

#### Moving Wall Electrophoresis

The moving wall electrophoresis instrument disclosed in a previous publication<sup>9</sup> and patent<sup>10</sup> will theoretically take care of these distortions (Figure 7). The moving wall will entrain the buffer to flow as a rigid body, eliminating the parabolic profile and providing constant residence time for all sample in the chamber thickness. Also, by rotating the chamber axis at an angle to the direction of motion of the moving walls, a component of belt motion can be made to cancel the electroosmotic flow at the wall. Therefore, with the "wall effects" eliminated, sample suspensions of lower conductivity than the curtain buffer can be utilized to produce the vertical ribbon formation that focuses the sample filament. Since the apparatus will be operated in space, curtain buffers of higher ionic strengths can be used without producing the convective disturbances generated by equivalent voltage gradients at 1-g. This arrangement will not only give optimum resolution, but also will increase the throughput of the device by utilizing the entire thickness of the chamber.

To effect the elimination of electroosmosis, the two paral-



ORIGINAL PAGE  
BLACK AND WHITE PHOTOGRAPH

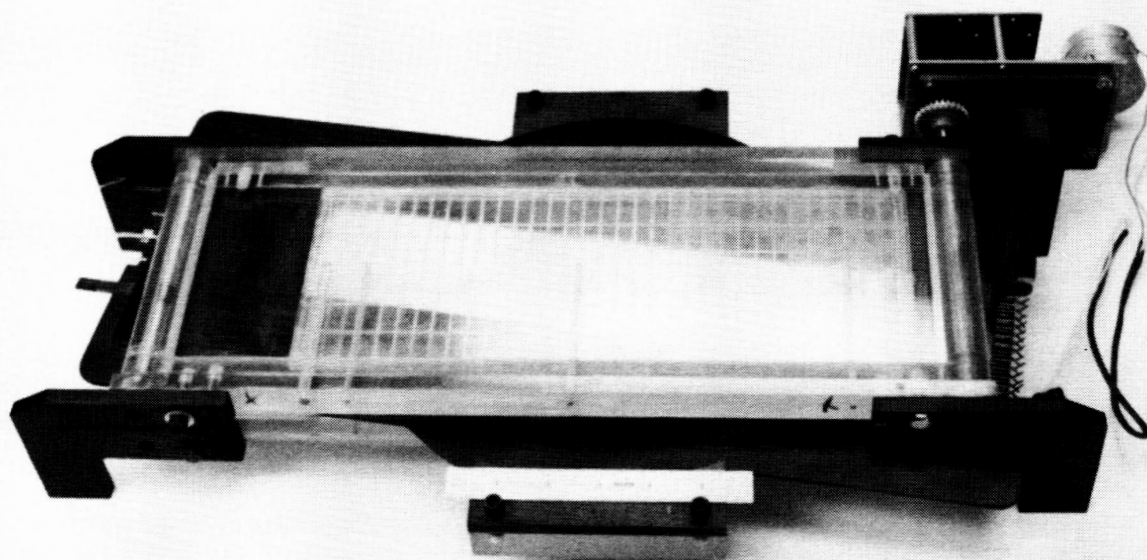


Figure 7. Moving wall chamber prototype.

1el flanking electrodes which bound the separation chamber are moved at a slight angle to the direction of belt motion. This produces a component of belt motion which can be used to compensate for the electroosmotic velocity. The natural wall charge will then determine the amount of electroosmosis present; also, using a material with a high zeta potential will minimize the affects of any contamination. The compensation is thus achieved mechanically through the use of a stepper motor which, in turn, is controlled by a computer. Thus, the output in the collection tubes can be monitored and the resulting potential information fed into the computer to give precise control of electroosmosis.

The three main subassemblies of the device are shown in Figure 8. The upper moving wall assembly contains a belt which is shown being transported from one roller and collected on another roller. The gear synchronizes the belt motion. Channels allow a slight vacuum to be applied to ensure close contact of the moving film to the subsurface. The schematic of the electrophoresis chamber shows a buffer insertion port, a sample insertion port, the two electrode channels, and the multi-tube collection array. Semi-circular protrusions fit into the guides of the lower moving wall assembly. This arrangement permits the electrophoresis chamber to rotate relative to the moving film belts in both the upper and lower assemblies. The lower assembly is similar to upper one and functions to transport the thin, polymeric film slowly from one roller to the other. The speeds

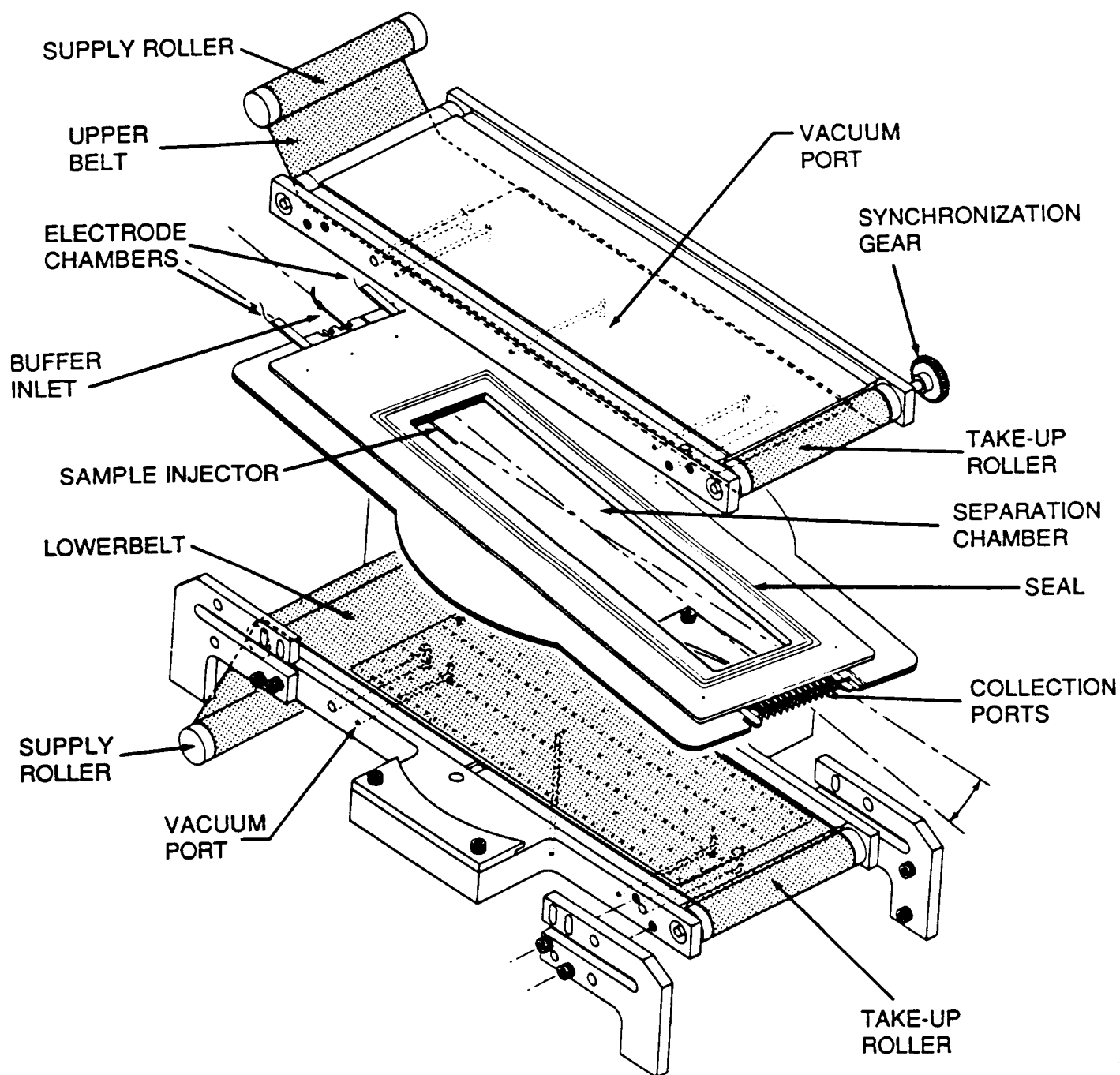


Figure 8. Schematic of moving wall electrophoresis.

of both belts are controlled precisely by the synchronization gear. The film is kept flat on the surface using the same method of vacuum application.

### Conclusion

It is clear from flight experiments using the MDAC CFES that the initial argument, the removal of thermal convection and sedimentation in space would result in optimized operation, is wrong. These same space experiments, recent literature reviews, and laboratory experiments have shown that electrohydrodynamic factors significantly degrade CFE in space as well as in 1-g. At present, only a device such as the moving wall electrophoresis system containing a high conductivity buffer with a large applied electric field can give high resolution separations in space. This device is designed exclusively for space and can only be operated there with optimum efficiency. Although the feasibility of this moving wall concept has not yet been established, it does not seem practical to fly devices which are defeated in space by the same phenomena that limit their efficiency on the ground.

## References

1. Bier, M., J.O.N. Hinckley, A.J.K. Smolka, and R. S. Snyder, "Role of Gravity in Preparative Electrophoresis," in The Proceedings of the Third Space Processing Symposium, 2, 729-755(1974).
2. Righetti, P.G., B.W. Brost, and R.S. Snyder, "On the Limiting Pore Size of Hydrophilic Gels for Electrophoresis and Isoelectric Focusing," J. Biochem. & Biophys. Meth., 4, 347-363(1981).
3. Snyder, R.S., et. al., "Free Fluid Electrophoresis on Apollo 16," Sep. and Purif. Meth., 2(2), 259-282(1973).
4. Allen, R.E., et. al., "Column Electrophoresis on the Apollo-Soyuz Test Project," Sep. and Purif. Meth., 6,(1), 1-59(1977).
5. Richman, D. W., "Electrophoresis Research Applications," AIAA Automation and Robotics Conference, Washington, DC, September 5, 1985.
6. Strickler, A., "Continuous Particle Electrophoresis: A New Analytical and Preparative Capability," Sep. Sci., 2(3), 335-355(1967).
7. Strickler, A., personal communication.
8. Taylor, G.I., "Studies in Electrohydrodynamics I. The Circulation Produced in a Drop by an Electric Field," Proc. Roy. Soc., A291, 159-167(1966).
9. Rhodes, P.H., "High Resolution Continuous Flow Electrophoresis in the Reduced Gravity Environment," Electrophoresis '81, Walter de Gruyter, Berlin, 919-932(1981).
10. Rhodes, P. H., U. S. Patent 4,358,3581 (1982).

HETEROGENEITY IN THE GROWTH HORMONE PITUITARY GLAND "SYSTEM"  
OF RATS AND HUMANS: IMPLICATIONS TO MICROGRAVITY BASED RESEARCH

W. C. Hymer<sup>+</sup>, R. Grindeland<sup>++</sup>, C. Hayes<sup>+</sup>,  
J. W. Lanham<sup>\*</sup>, C. Cleveland<sup>\*</sup>, P. Todd<sup>°</sup>, and D. Morrison<sup>\*\*</sup>

<sup>+</sup>Department of Molecular and Cell Biology  
The Pennsylvania State University  
University Park, PA 16802

<sup>++</sup>NASA Ames Research Center  
Moffett Field, CA

<sup>\*</sup>McDonnell Douglas Astronautics Co.  
St. Louis, MO

<sup>°</sup>University City Science Center  
Philadelphia, PA

<sup>\*\*</sup>Biomedical Application Branch  
Johnson Space Center, Houston, TX

## INTRODUCTION

Since its discovery over 50 years ago, growth hormone (GH) has attracted the attention of both clinical and basic researchers alike. The hormone accounts for 20% of the total protein contained in the anterior pituitary gland. Further, some 35-50% of the six different hormone producing cell types are committed specifically to the synthesis of GH. Milligram quantities of GH are present in the human pituitary gland whereas only microgram quantities of the five other peptide hormones are contained in this 500 mg, bean-shaped structure. Why should there be such a disproportionate amount of GH?

As the techniques to study cells and hormone molecules became more sensitive, it also became clear that heterogeneity was a landmark of pituitary GH. The picture that is emerging indicates that several variant forms of the hormone molecule exist within the gland as well as in the blood stream. New research also indicates that these variant forms possess unique biological activities. Finally, there is evidence to suggest that GH producing cells are also functionally heterogeneous. Our NASA sponsored research deals directly with these issues in both the human and rat pituitary gland. We believe that the large percentages of cells committed to GH production, taken together with the sizeable numbers of variant forms of GH, offer great flexibility to the "GH system". It is tempting to speculate that this flexibility helps the body meet the varied metabolic demands placed on it. Textbooks describe how GH increases muscle mass, increases breakdown of fat, decreases uptake of carbohydrate into cells and increases cell division. In light of these numerous activities, the recent claim that synthetic human GH "will soon be used to make short children taller and, possibly, help dieters lose fat and make aging people look young" (1) is therefore not surprising.

Spaceflight provides a unique environment which impacts the GH system on

several levels. First, GH controls muscle and bone metabolism, two tissues known to be negatively affected in flight. Second, cellular "life" as we know it has obviously evolved under the constant force of gravity. Evidence is beginning to accumulate that cell function, in the absence of gravity, is altered. Third, space bioprocessing takes advantage of the lack of convective forces in production of materials of medical relevance. Our NASA sponsored researches on GH touch on all three of these levels.

Before summarizing our experimental approaches and results, it is important to highlight the underlying theme of this work, viz. the importance of the assay system used to measure GH. Indeed, a dichotomy between bioassayable and immunoassayable GH was recognized over 10 years ago (2). While the cellular and molecular basis for this dichotomy remain unresolved, our efforts show that it unquestionably exists. Our progress is summarized below.

#### I. Separation of GH cells.

The pituitary gland is markedly heterogeneous with respect to cell type. Over the last 20 years we have developed several methods to purify and study GH cells. These cell separation methods are now briefly reviewed. Special emphasis is placed on the different GH assay methods used to evaluate the performance of these cells once they are isolated.

##### A. Cell Separation by Sedimentation.

Our laboratory was the first to apply the techniques of velocity sedimentation at unit gravity and density gradient centrifugation to pituitary tissue (see (3) (4) for reviews). An important outgrowth of these experiments was the observation that two subpopulations of somatotrophs (GH cells) could be routinely separated on the basis of their differences in density (5). Key differences in cell morphology and cell function of these subpopulations are briefly summarized in Table 1. It is important to note that all of the GH



secretion data in that original study were obtained using an established GH radioimmunoassay. Can the dichotomy between immunoassayable and bioassayable GH, described above, be attributed to differential release of GH forms from Type I vs. II somatotrophs? Many experiments were done to test this possibility and the data in Fig. 1 suggest that this is indeed the case (6). In this experimental series, GH released from type I vs. II cells into tissue culture medium was assayed by standard immunological (I) procedures or by the rat tibial line bioassay (B). This bioassay, originally described in 1949, is based on the action of GH to promote widening of the tibial epiphyseal cartilage plate of hypophysectomized rats after eight injections over four days. Quantitation is accomplished by ocular micrometry of stained growth plates. While the procedure suffers from lack of sensitivity (5 ug), it is the accepted bioassay for GH. The data in Fig. 1 establish that GH initially released from type II somatotrophs has a much higher B/I ratio than type I cells.

It can be argued that the "ultimate" bioassay one could use to test the activity of GH released from type I vs. II somatotrophs would be their reimplantation into animals deficient in GH (i.e. a hypophysectomized rat). As we had developed the methodology to do this unique type of implantation experiment at about the same time the data in Fig. 1 were being collected, the experiment was relatively straightforward. The implantation method itself involves encapsulation of cells (usually  $2.5 \times 10^5$  in  $1.8 \mu\text{l}$  of culture medium) in 10 mm long XM-50 Amicon hollow fibers. These fibers are composed of a polyvinylchloride-acrylonitrile copolymer and have an internal diameter of either 500 or 1100  $\mu\text{m}$ . Their unique feature is that the lumen of this fiber is lined with a thin membrane containing pores of well defined size, viz. 40A° ( $\pm 5\%$ ). By virtue of this pore size, only spherical molecules  $< 50,000$  daltons

can theoretically pass through the membrane. Since GH has a mass of 22 kd, hormone released from encapsulated cells could in theory pass through the hollow fiber and enter the animals blood stream to deliver GH to its ultimate biological target(s).

Shown in Fig. 2 are micrographs of the hollow fiber as well as the appearance of cells within the fiber prior to implantation. The results of an experiment designed to test the biological responses of GH released from Type I vs. II somatotrophs in this hollow fiber system is offered in Fig. 3. These data show that animals implanted with type II somatotrophs a) gained more body weight, b) had increased tibial epiphyseal width and c) had increased muscle weight. Since the relative percentage increases in muscle mass were greater than increases in total body weight, we conclude that lean body mass was stimulated by hormone released from type II cells. We have seen this kind of result in several additional experiments. Details on this unique application of the hollow fiber method are to be found in (7,8).

#### B. Separation of cells by light scatter

Cytoplasmic granulation constitutes a dominant feature of pituitary cells (Fig. 4). We reasoned that this feature might be used to advantage when scattering of laser light was used as the probe. This idea has been tested using an EPICS V cell sorter equipped with an argon ion laser tuned to the 488 nm line at 150 mW. We have been able to show that the back scatter signal produced from living cells (a complex function of diffractive, reflective and refractive components) was indeed related to the degree of cytoplasmic granulation. Shown in the top panel of Fig. 5 are the back scatter (PLS-X axis) and forward angle light scatter (FALS-Y axis) signals produced by the total mixture of living pituitary cell types viewed from different projections. Also shown in Fig. 5 are the light scatter ridges after

separation using the cell sort mode of the flow cytometer. Staining analysis revealed that a) 82% of the cells in region C were GH cells, b) 65-75% of the cells in region B were PRL cells and c) 80% of the cells in region A were either follicular cells, macrophages, or endothelial cells (9,10).

The flow cytometer has proven to be an extremely useful tool not only for the separation of different live pituitary cell types (as demonstrated by Fig. 5), but also in an analytical mode where the percentage distributions of fixed and stained pituitary cell types can be objectively determined with considerable statistical accuracy in a very few minutes (11).

We have not as yet had the opportunity to attempt to sort type I and type II somatotrophs using flow cytometry. However, the instrument is proving to be extremely useful for analyzing cells separated by other methods (see later).

#### C. Cell separation by electrophoresis.

Our early attempts to electrophoretically separate pituitary cells employed the density gradient electrophoresis method of Boltz and Todd (12). This method required insertion of cells at the bottom of an isotonic density gradient which consists of a 5.4-6.5% sucrose gradient (bottom to top) and 2.0-8.0% Ficoll gradient (top to bottom). Electrophoresis was in the upward direction. We obtained evidence that type II somatotrophs might have a different electrophoretic mobility from cells in the type I region (13). Cells in the somatotroph enriched fraction had lower electrophoretic mobilities than those cells recovered from the band I area. However, additional analytical procedures, viz microscopic electrophoresis using a Zeiss 'cytopherometer' and automated light scattering electrophoresis using a Pen Kem 3000 Automated Electrokinetic Analyzer were also tried. Neither of these two instruments was able to distinguish significant differences in electrophoretic mobilities between band I and band II cells. Pretreatment of the cells with secretory

agents also had no significant effects on this result (see 13 for additional details.)

In 1981 the issue of whether GH cells could be electrophoretically separated from other types of hormone producing cells was reinvestigated when the continuous flow electrophoretic separator, (CFES) designed and built by the McDonnell-Douglas Astronautics Corp., became available for our use. The interested reader is referred to the chapter by Todd et. al. in this volume for information regarding the description and operation of this device.

Early trials in 1981-82 involved pituitary cell separations utilizing a low conductivity triethanolamine-potassium acetate buffer, pH 7.25, 300 mOsm/liter in the CFES device at a flow rate of 20 ml/min. The results of these early trials were encouraging in that they showed that GH cells were among the most mobile and that GH cells after CFES produced hormone and released it into the culture medium. These results were published in (13) and are not reviewed here. A second, more extensive experimental series was recently completed and published (14). Analyses of cells in the different fractions included a) counting of GH and PRL containing cells to determine their percentage distributions b) measurement of intracellular hormone by immunoassay and c) cell culture to establish the secretory capability of cells after CFE. The results of four experiments, each utilizing glands from ~50 rats, are given in Fig. 6. With no current applied cells emerged from the chamber within two outlets (1.6 mm) of the inlet port. With current applied, all pituitary cells showed anodal migration, a majority being spread over 40-50 outlet tubes (Fig. 6 panels A,F,K,N). Intracellular GH levels were 4-8 times higher in more mobile fractions (Fig. 6, panels B,G,O). Further, 60-80% of the more mobile cells were identified as containing GH by immunocytochemistry (Fig. 6, panels, C,H and L). In one experiment, intracellular LH, FSH and TSH

were also measured and found to be localized in anodal fractions (Fig. 6 panels P,Q and R). Finally, in experiments 3 and 4, GH and PRL levels in culture medium after electrophoresis were measured by immunoassay. In general, hormone output reflected GH/PRL enrichments as estimated by RIA or immunocytochemistry; a result which attests to the fidelity of separation estimates as well as inferring cell viability after CFE. The issue of the biological vs. immunological activity of the GH released from cells separated by CFE was also studied in Exp. #4 of Fig. 6. The data, summarized in Fig. 7, establish that somatotrophs in the more anodal fractions release GH which is more bioactive than corresponding somatotrophs in the less mobile areas. On the basis of these assay results it is tempting to speculate that type II somatotrophs are more electrophoretically mobile than type I GH cells in the McDonnell Douglas device.

As discussed previously (section B) the potential of the flow cytometer in analyzing cells after CFES has only recently begun to be investigated. For illustrative purposes, the results of a preliminary experiment are offered in Figs. 8 and 9. The mobility profile of the total cell population is shown in Fig. 8 (top). Counting the stained cells in this experiment by flow cytometry showed that GH cells tended to be found in two regions [fractions 11-15 and 16-20; Fig. 8 (middle)] while PRL cells were also found in two regions, but they were of lower electrophoretic mobility [fractions 6-11 and 12-14; Fig. 8 (bottom)]. Results of two parameter analyses of GH-stained cells in fraction 5 vs. fraction 19 are given in Fig. 9. In this figure the log of the green fluorescence staining (LPGFL), which can be attributed specifically to GH cells, is shown on the X axis whereas the forward angle light scatter, attributed specifically to cell size, is shown on the Y axis. All of the "events" shown in Fig. 9 (29,999 for Fr. #5 and 14,338 for Fr. 19) can be

unequivocally attributed to cell signals since they were "gated" on red fluorescence signals generated using propidium iodine. The predominant difference between GH cells in Frs. 5 vs. 19 is that a majority of GH cells in Fr. 19 are large and well defined (area labeled by V) whereas small, less intensely stained GH cells are common to both fractions (identified by \*).

What bearing and relationships do the pituitary cell separations by CFES have on the issue of microgravity-based research? In light of the different densities of the various hormone-producing cell types, we were concerned that this parameter might contribute to the apparent electrophoretic separations actually achieved (especially those on the CFES device). However, the results of our microgravity experiment on board STS-8 in September 1983, (identified as Exp. #2 in Fig. 6), establish the general principle that we have seen consistently, viz--that a majority of the GH cells are more electrophoretically mobile than the PRL-containing cells. Therefore we feel confident in concluding that the net charge on the surface of most somatotrophs is significantly different from that of most PRL cells. This non-trivial result will be confirmed, optimized and considerably extended in a future microgravity based separation experiment (see later).

## II. Purification of human growth hormone (hGH).

In a well known textbook on Endocrinology one finds the following statements concerning GH in the human pituitary gland after death:

"Fortunately, the human pituitary is particularly rich in GH, and the somatotrophic granule resists autolytic dissolution after death. Despite the fact that radio-immunoassays suggest a much higher content, the yield of somatotropin with present extraction methods is between 8 and 16% of the dry weight of human pituitaries, equivalent

to 4-8 mg of hormone/gland. No significant changes in GH content with age are evident."

A number of years ago the National Pituitary Agency was established for the purposes of purifying hGH from post mortem glands and providing this material for clinical medicine. Over the years, many children of short stature benefited significantly from injections of the purified hormone. In fact, the National Pituitary Agency processed about 50,000 pituitaries a year, supplying the hGH from them to about 5000 children. Supply did not keep pace with demand. Quite recently this situation changed dramatically when the program responsible for purification of hGH was shut down when the deaths of three patients receiving hGH were attributed to a slow virus contaminating the hormone preparations (15). In the Fall of 1985 the Food and Drug Administration gave its approval for use of a genetically engineered version of hGH produced by Genentech. Patients are currently receiving this hGH at a cost of \$10,000/year for three injections/week.

In section I of this report we presented evidence that there were at least two forms of GH secreted from subpopulations of rat pituitary somatotrophs. One had a significantly higher bioactivity/immunoactivity ratio than the other. Our current research efforts with human pituitary GH are based on a similar idea, viz that a discrete form of hGH with high biopotency is contained within the human pituitary. Our goal is to purify this material. The different approaches which are being used are now briefly summarized.

Approach #1. Continuous Flow Electrophoresis (CFE) of human post mortem pituitary granules.

Shown in Fig. 10 is an electron micrograph of the appearance of human pituitary tissue eight hrs after death. The dominant feature of this tissue, as is evident from the figure, is that it is laden with hormone-containing

granules. We reasoned that CFE of suspensions containing such particles might be a useful approach to the isolation of hGH with high biopotency. The experiment involved a) preparation of homogenate of 11 hr post mortem tissue in isotonic sucrose, b) preparation of a crude granule fraction by centrifugation at 20,000 xg, c) washing of the pellet in CFES buffer, d) CFE separation (ET150), e) collection of material from CFE into 200 individual tubes containing alkali (to disrupt granules), f) radioimmunoassay of the solubilized material in each of the 200 tubes and finally g) pooling of tubes for assay of bioactive GH via the tibial line assay. Shown in Fig. 11 is the profile of immunoreactive hGH after continuous flow electrophoresis. Although each of 200 tubes were analyzed, only #'s 90-140 are shown since the others contained no detectable activity. Clearly, there is a sharp, symmetrical peak encompassed by tubes 100-109 which contain the bulk of the immunoactive hormone. The position where most of the bioactive hGH was recovered was clearly somewhat different (Fig. 12). While 75% of the bioactive hormone was recovered in tubes 88-113, the hormone in combined fraction #4 (tubes 114-200) was obviously enriched in bioactivity.

Approach #2. Fractionation of hGH contained in alkaline extracts of human post mortem pituitary by high performance liquid chromatography (HPLC).

On the basis of earlier findings by Ellis and Grindeland which suggested that bioactive rat GH might be of considerably higher apparent molecular weight than the well characterized monomeric 22 kD form, some experiments have been done using HPLC on alkaline extracts of human post mortem pituitary tissue. The results of one such experiment are given in Fig. 13. Shown in the top portion of this figure is the OD 214 nm of the general protein profile after HPLC. Approximate molecular weights of material eluting in the pooled fraction areas indicated are: fr. 1, void volume; fr. 2 >117kD; fr. 3, 40-117



kD; and fr. 4 <40kD. Shown in the lower portion of Fig. 13 are data listing the contents of protein, immunoassayable and bioassayable hormone in these fractions. In this experimental series, bioassayable GH was measured by the 3T3 cell adipogenic assay of Nixon and Green (16). The data confirm the earlier observations of Ellis and Grindeland in that there is a high molecular weight form of the hormone which is enriched in bioactivity.

Approach #3. Fractionation of hGH contained in alkaline extracts of human post mortem pituitary by HPLC and CFES.

Since CFES offered promise in the separation of a GH form in secretory granules with high B/I activity (Fig. 12) we reasoned that a combination of the HPLC and CFES techniques might prove interesting. Accordingly, an extract of post mortem pituitary gland was fractionated by HPLC. As before (Fig. 13) a high molecular weight fraction was obtained which had 23  $\mu$ g of bioactive hormone and 2.8  $\mu$ g of immunoactive hormone. This material was fractionated by CFES into 200 individual tubes and pooled on the basis of 15 tubes/assay fraction. Results concerning the distribution of biologically active hormone (3T3 assay) indicated the surprising result that ~50% of the bioactive hormone showed cathodal migration (Fig. 14). Although not shown on this figure, only 20% of the total immunoactive hormone was associated with material in combined fractions 1-5. A major peak of immunoactive hGH was associated with combined fraction 8. These results again show the good potential of the CFES device in the fractionation of hGH with high bioactivity.

Approach #4. Separation of bioactive human growth hormone by affinity chromatography.

The results of each of the three previous approaches offer evidence to support the hypothesis that there is a form of the hGH molecule, high in biological potency, which can be isolated from a majority of the immunoactive

form. If true, a more direct approach for the isolation of bioactive hGH would be affinity chromatography. In this procedure, the hGH antibody is covalently bound to a column support. On passing an unknown sample containing immunoreactive hormone through the column, the immunoactive form binds whereas the bioactive form passes through. Recovery of the immunoactive form from the column is accomplished by running a high salt solution through to displace bound hormone. Only preliminary results have been obtained thus far using this approach. They are shown in Fig. 15 and Fig. 16. When the hormone standard was run through the affinity column, 99% of the recovered immunoactive hGH bound to the column. As a result, the B/I activity ratio of the pass through material was 9.3 (Fig. 15). When a fresh alkaline extract of human pituitary gland tissue was run through this affinity column, 100% of the immunoactive hormone bound to the column while a small, but nonetheless detectable, amount of bioactive hormone passed through (Fig. 15). It is important to indicate that this material was devoid of immunological activity. [Why more bioactive hGH is recovered than was applied is unknown. However, it is a highly repeatable observation and many relate to removal of a natural inhibitor of this bioactive form on purification].

The efficacy of the affinity chromatographic approach to the isolation of hGH is also shown by the Western blots in Fig. 16. All of the bands seen in this figure are reactive against hGH antiserum and are, by definition hGH. Identification of materials in lanes 1-6 are as follows: Lane 1, unfractionated hormone standard; lane 2, hGH in hormone standard bound to affinity column; lane 3, hGH in hormone standard which passed through column; lane 4, hGH in fresh human pituitary extract; lane 5, hGH in human pituitary extract bound to column; lane 6, hGH in human pituitary extract which passed through the affinity column. We interpret the molecular weight estimations of

the stained GH molecules to reflect monomeric hGH (22kD); dimeric GH (~40kD) and trimeric aggregates (~60kD). Clearly, the efficacy of the column in removing these immunoactive forms of hGH is documented by the data in Fig. 15 and Fig. 16.

### III. Experiments previously done in microgravity.

Over the period of 1983-1985 our group has done three GH-related experiments on the Shuttle. A brief summary of the findings from each of these three experiments, together with their significance to the "GH system" as specifically related to microgravity, are presented in this section.

Experiment #1. The separation of rat pituitary GH cells from other hormone containing cell types was accomplished by CFES on the flight of STS-8. The data (Fig. 6, exp. 2) showed that GH cells have a surface charge which is different from prolactin cells, thereby indicating that differences in cell density could not explain the separations actually achieved on Earth.

While the microgravity experiment was generally successful, not all of its original objectives were met since cell recoveries from the CFES device were very low. This situation forced us to pool cells in order to have sufficient numbers to do those analyses shown in Fig. 6. Thus, we were unable to culture these separated cells for the purposes of determining whether high bioproducers were actually separated from the low bioproducers in microgravity. Considering the results of our second microgravity experiment (see below) there is some question as to how well the high bioproducers might actually function in space. The need to repeat the pituitary cell separation experiment in microgravity is critical to find out if the separated cells do retain their ability to produce bioactive GH.

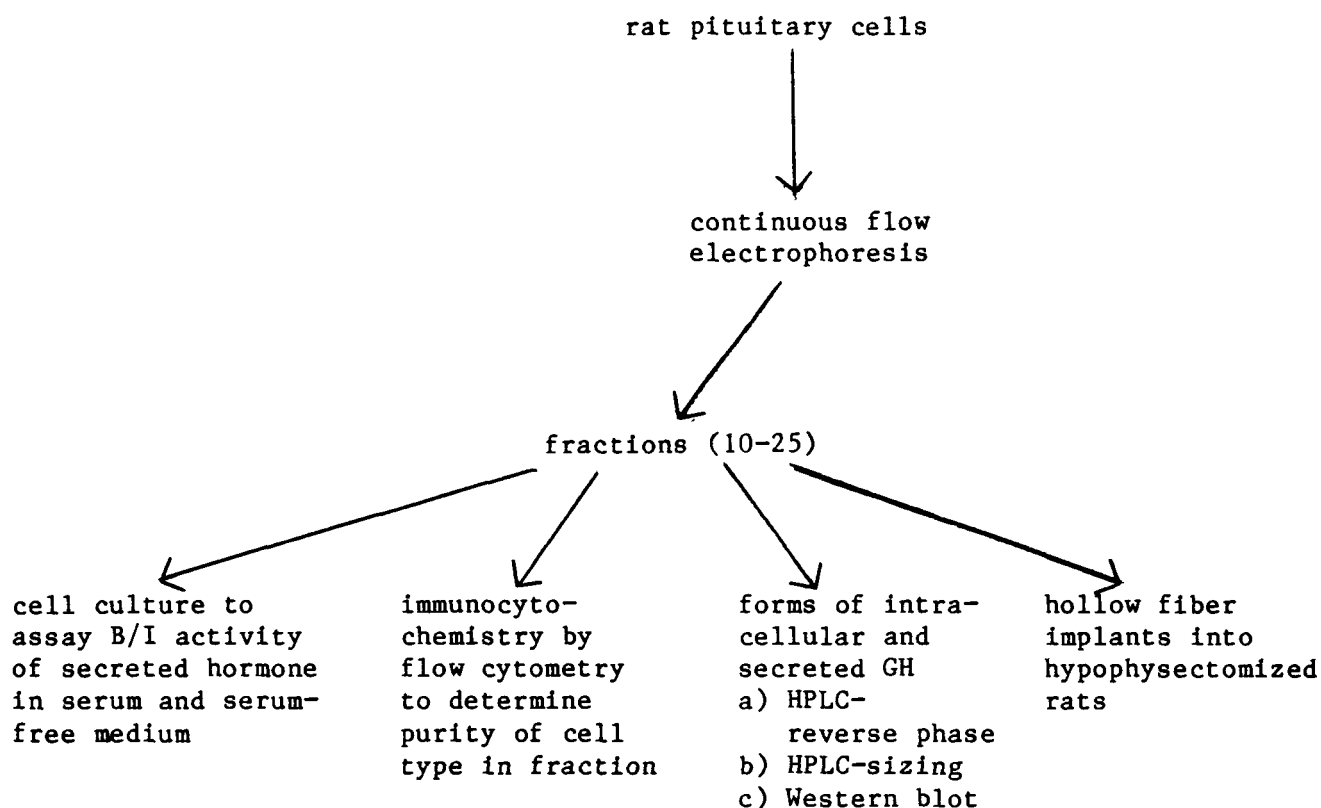
Experiment #2. A preliminary pituitary cell culture experiment was also done on the flight of STS-8. This experiment involved storage of dispersed pituitary cells in sealed tubes in middeck lockers maintained at 37°C. On recovery, the cells were washed and cultured for six days to evaluate the secretory capacity of prolactin (PRL) and GH producing cells. As shown in Table 2, the secretory activity of GH cells was severely compromised by exposure to microgravity, while that of PRL cells was not. Considered with the experiences of the Cogoli group with regard to the failure of microgravity exposed lymphocytes to respond to Con A (17) and alteration of varied cell functions recorded on the German D-1 mission in late 1985, the possibility that the lack of gravity has direct effects at the cellular level appears worthy of further study. In specific regard to GH, the issue assumes added importance in terms of the documented effects of this hormone on function of muscle and bone, two tissues known to be significantly affected by flight. Another pituitary cell culture experiment has been approved for flight and currently awaits remanifesting.

Experiment #3. Pituitary GH cells contained in glands of rats flown on SL-3 in April, 1985 were also studied by our group and shown to be defective in GH secretion. The results of this study (18) showed that release of both bioactive and immunoactive GH from isolated cells after flight was reduced by about 50% relative to appropriate ground based controls. On the other hand, PRL secretion was unaffected. In this regard, the SL-3 results and STS-8 results regarding a defect in GH release are internally consistent. Additional evidence suggested that a high molecular weight form of the GH molecule, enriched in bioactivity, was not released from the flight cells.

IV. Preparation for a future flight experiment: Aims, protocols, rationale, ground based research, potential problems.

A. The experimental protocol for aim #1 of our approved ground based research and flight experiment is given below. In essence this experiment involves the separation of different rat pituitary cell types by CFE.

#### AIM #1 Experimental Protocol



With this approach we should be able to obtain answers to such questions

as:

1. What is the degree of cell purification achieved by CFE under conditions where extensive cell pooling is not required (as it was on STS-8)?
2. What are the B/I activities of GH released from the electrophoretically separated cells?

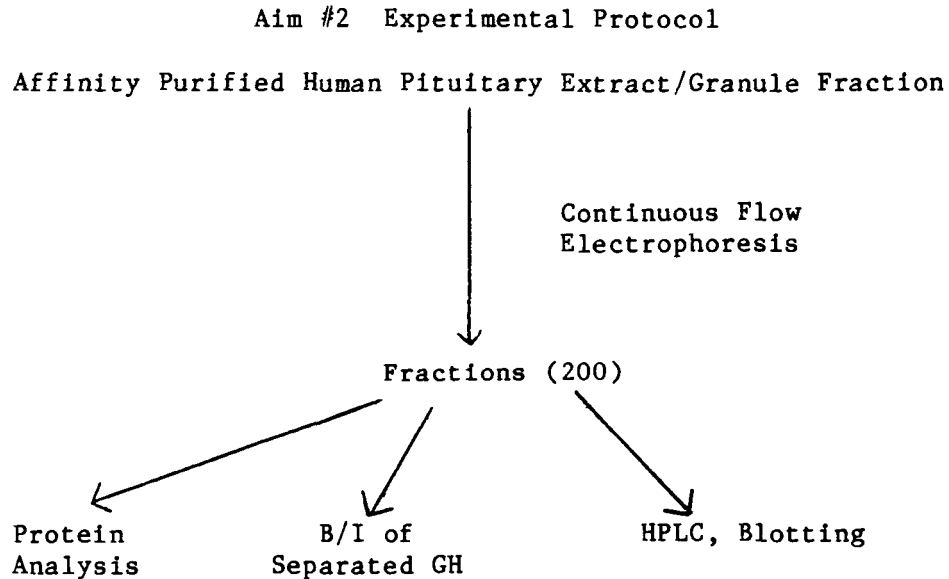
3. What are the molecular forms of the secreted GH?
4. Which electrophoretically purified population of GH cells is capable of reinitiating total body growth, increases in muscle mass, and increases in organ weights?
5. What effect does microgravity have on the answers to questions 1-4?

If we are correct in our suspicion that GH cells in microgravity experience a lesion in hormone secretion, a successful outcome to this experiment will not only helped to define the cellular and molecular basis of this lesion, but will also identify the specific GH cell subpopulation (in terms of its electrophoretic mobility) that is affected by microgravity.

#### GENERAL CONSIDERATION AND POTENTIAL PROBLEMS TO BE ADDRESSED IN THIS RESEARCH

It is obvious that the experimental conditions found to yield optimal results on Earth should be the ones actually used in the microgravity experiment. We believe that the cell holding conditions prior to electrophoresis should be made more compatible with the physiology of the actual cell system; (e.g. under ambient temperatures in proten containing buffers). Furthermore, the issue of the use of a CFES buffer system more compatible with excellent cell viability needs to be addressed. The actual CFES run of the cells should ideally be performed early on in the flight. The separated cells should be held in culture media so that the issue of GH secretion from cells in microgravity can be investigated. Finally, it is essential that the rats be killed at KSC in order to prepare cells under conditions where the possibility of picking up contamination during cell preparation is virtually eliminated. This procedure is done routinely in our laboratory with virtually 100% success.

B. The experimental protocol for aim #2 of our approved ground based research and flight experiment is given below. In essence, this experiment involves the separation, by CFES, of variant forms of the human growth hormone molecule contained in either secretory granules/or alkaline extracts of human post mortem pituitary tissue.



With this approach we should be able to answer the following:

1. Can the CFES device be utilized to purify a hGH form which is high in biological activity, but low in immunoactivity?
2. What are the molecular forms of the GH contained in these fractions?
3. Can the amount of hGH processed through CFES be significantly increased in microgravity?

Based on the experiences of McDonnell Douglas researchers with the CFES device in microgravity, we anticipate that "throughput" will be significantly

increased in microgravity. The electrophoretic separation of a biologically potent form of hGH would be of considerable interest to the pharmaceutical industry as well as to the medical community. Obviously, any findings from this experiment could serve as the basis for future work by the such groups.

GENERAL CONSIDERATIONS AND POTENTIAL PROBLEMS TO BE ADDRESSED IN THIS RESEARCH.

Since in aim #2 we are dealing with extract/subcellular particulate material, the sample for the actual microgravity experiment can be prepared in the PI's laboratory well ahead of the launch date and be stored in a frozen state until the time of electrophoresis. After the electrophoresis run, the 200 samples can be stored at 4°C until return to Earth.



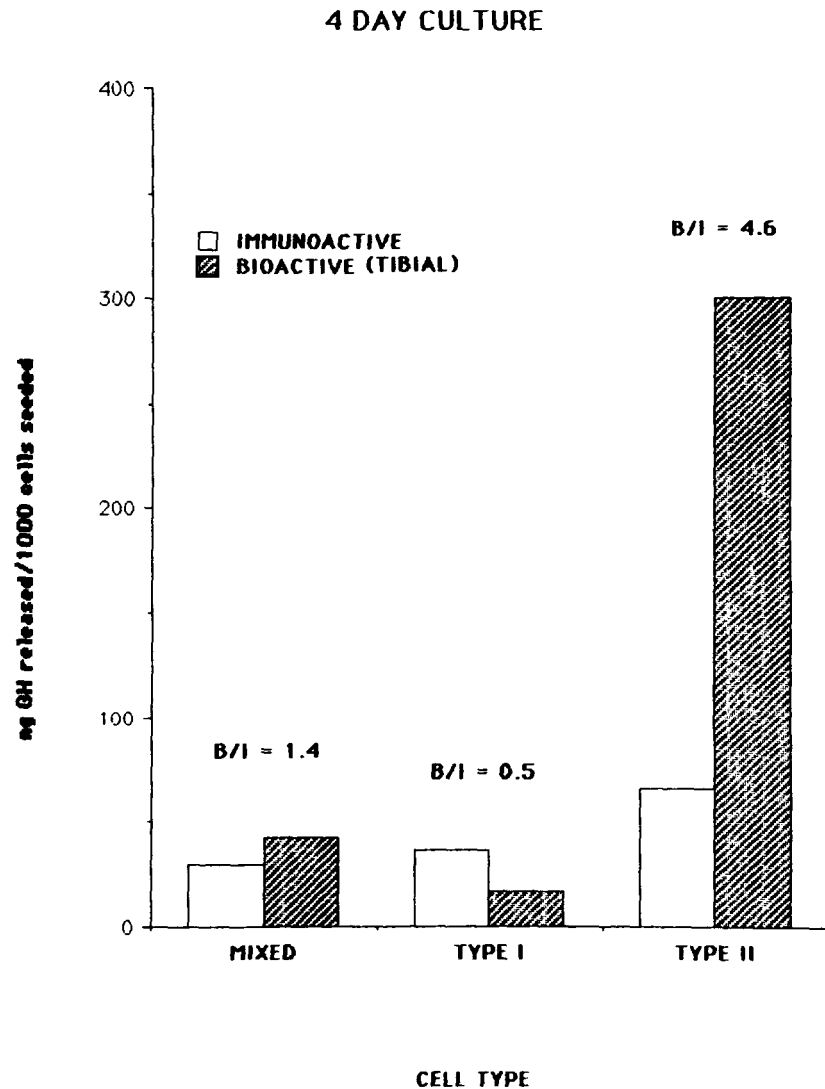


Fig. 1. Immunological and biological activities of growth hormone released from mixed, type I and type II somatotrophs over a four day culture period. Immunoassays were performed by RIA; bioassays by the tibial line assay in hypophysectomized rats. Culture medium was MEM + 5% calf serum and antibiotics.

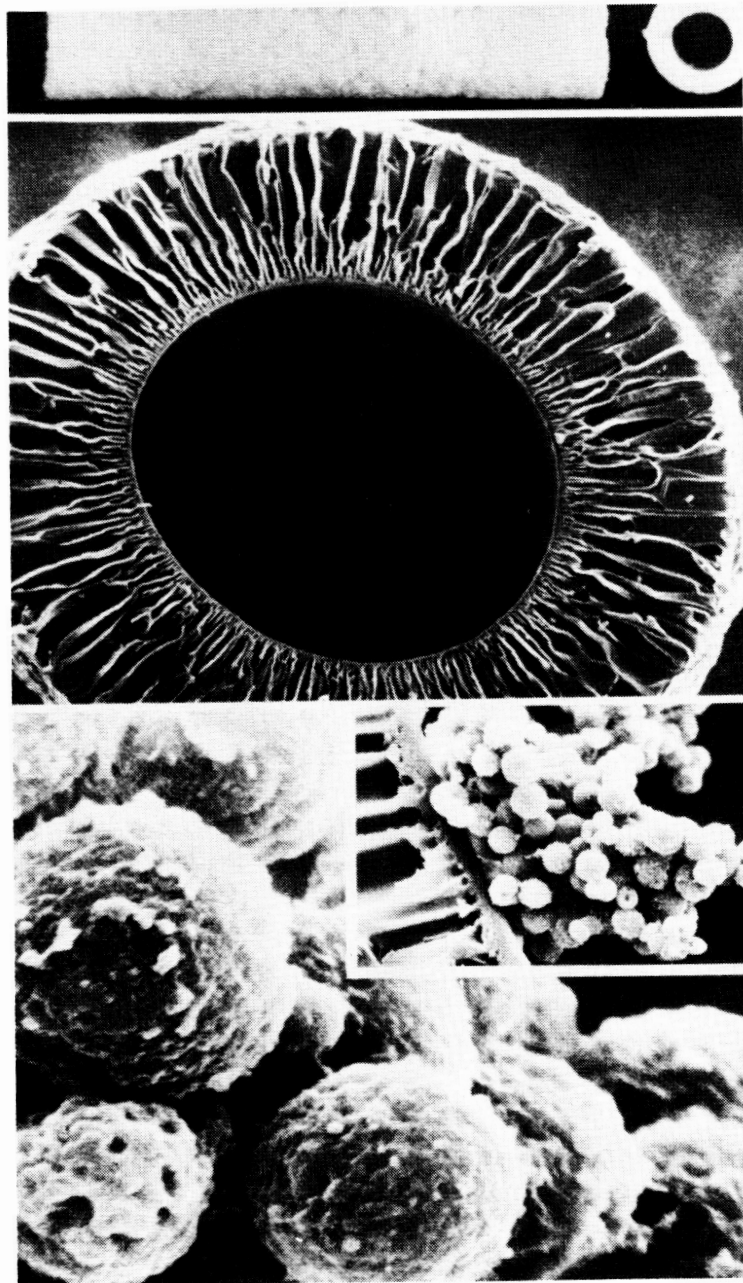


Fig. 2. (Top) Photomicrograph of 10 mm long XM-50 hollow fiber and in cross section. (Middle) Scanning electron micrograph showing lumen and fiber wall. (Bottom) Scanning micrograph of pituitary cells in hollow fiber.

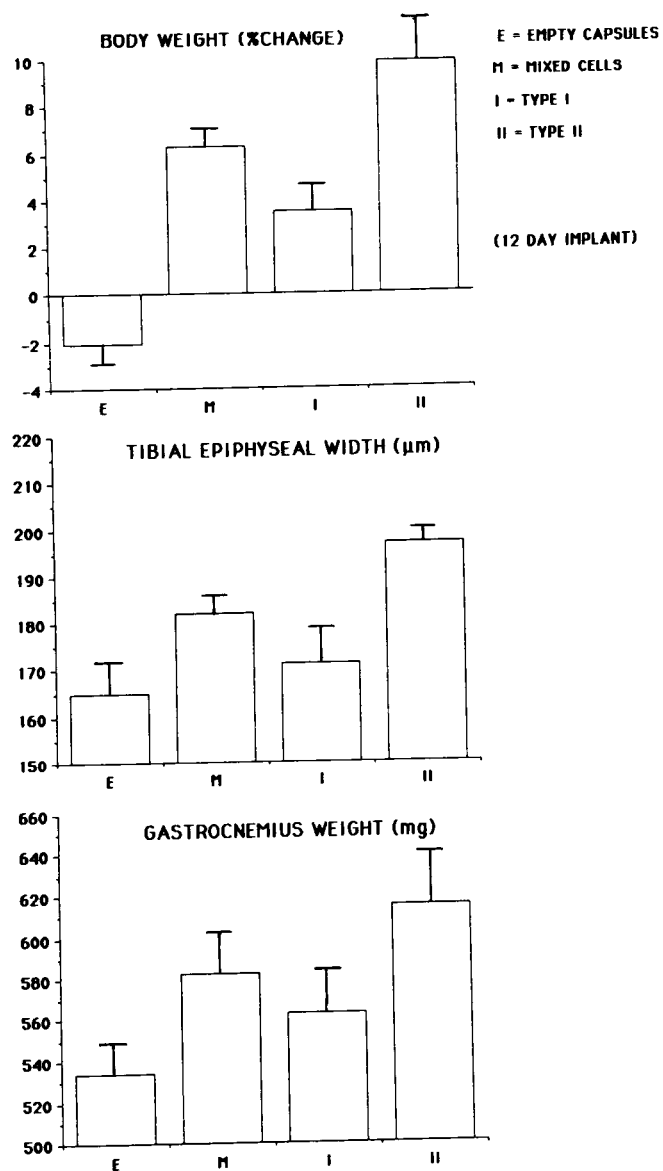


Fig. 3. Responses of hypophysectomized rats receiving hollow fibers containing nothing (empty, E); mixed (M); type I (I) or type II (II) somatotrophs 12 days post implantation.

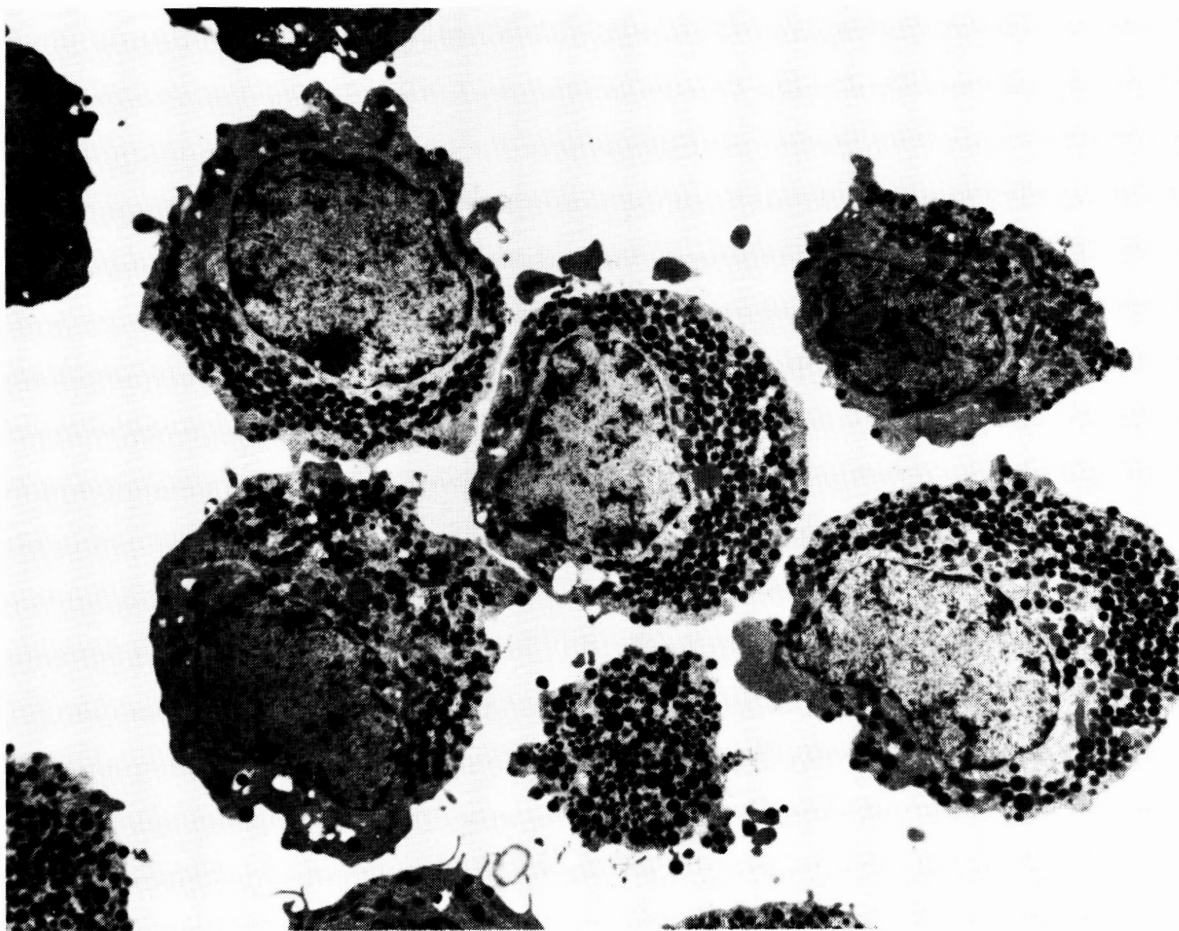


Fig. 4. Electron micrograph of freshly dispersed rat pituitary cells. Most of these cells are GH producers. Note the large numbers of cytoplasmic secretory granules which are known to contain GH.

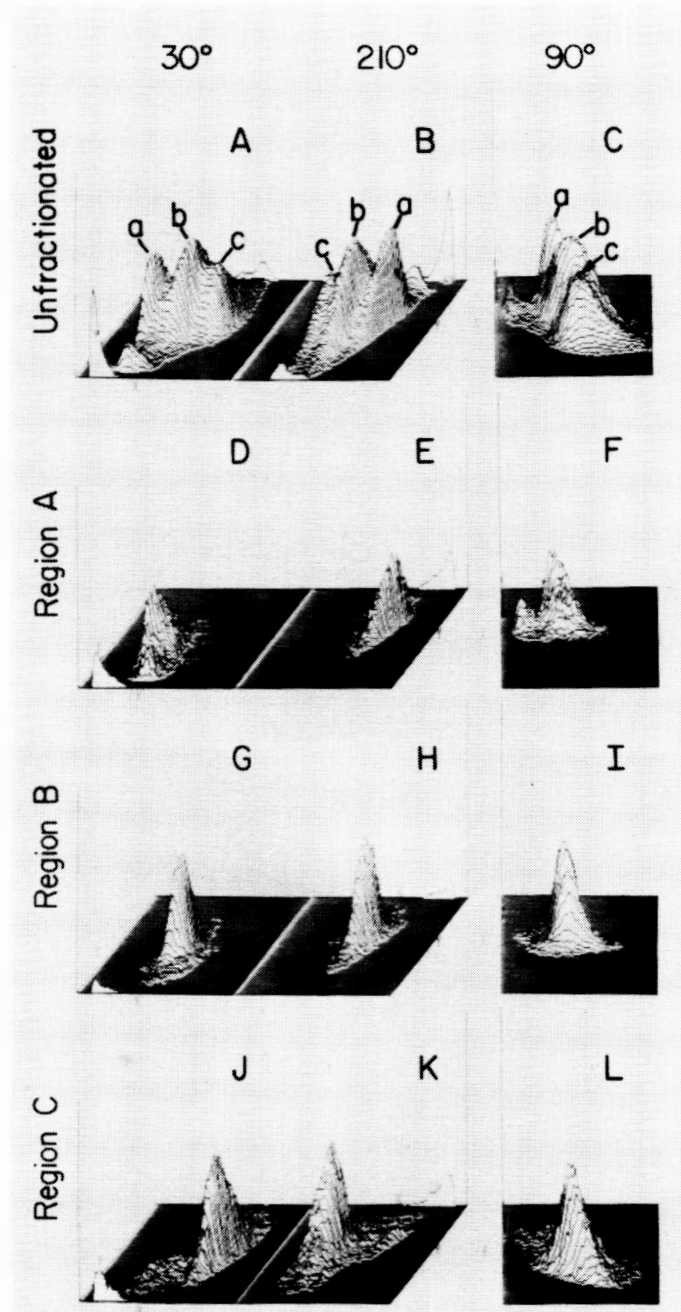


Fig. 5. Light scatter profiles of live pituitary cells before (A-C) and after (D-L) sorting. Cells from 46-day-old male rats were dissociated in the presence of dopamine ( $10^{-5}$  M) and analyzed for PLS (X-axis) and FALS (Y-axis). Note correspondence of the light scatter profiles of cells sorted from regions A (D-F,  $2 \times 10^4$  cells), B (G-I,  $5 \times 10^4$  cells), and C (J-L,  $4.3 \times 10^4$  cells) with the ridges marked a,b,c on the profiles generated from the unfractionated cells (A-C,  $7 \times 10^5$  cells).

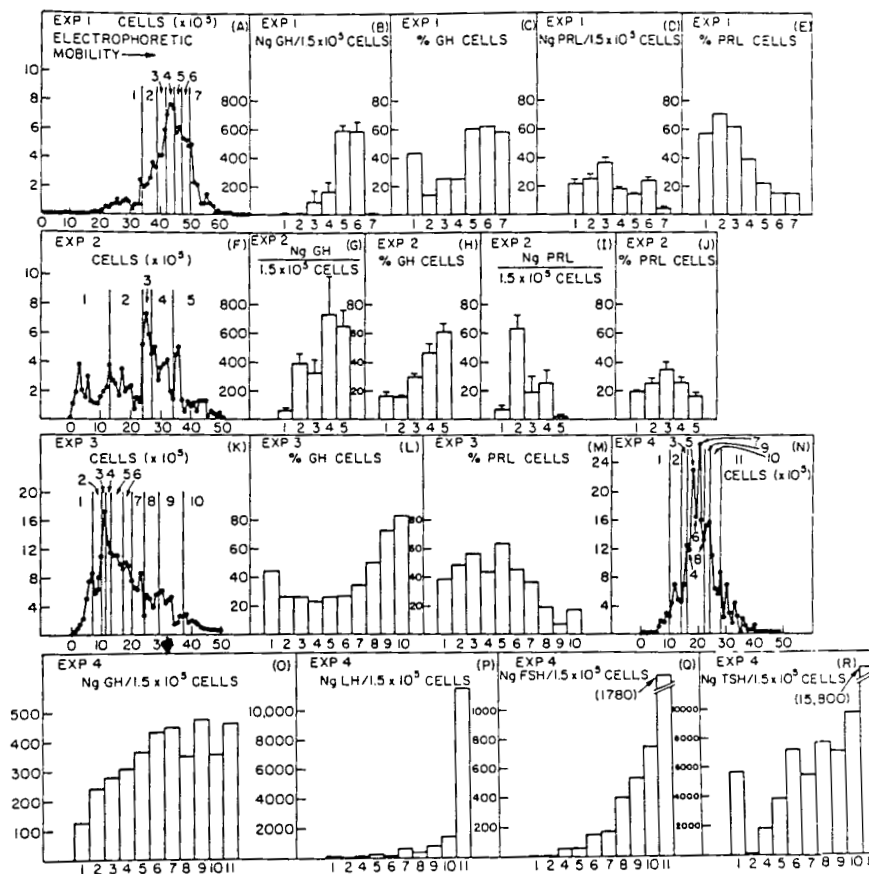


Fig. 6. Separation of rat pituitary cells by CFES. Mobility profiles of cells are shown in panels A,F,K and N. Intracellular GH and PRL contents of cells obtained from pooled areas shown were determined by immunoassay. Percentages of GH and PRL containing cell types in these fractions were determined by immunohistochemistry. Exp. #2 was done in microgravity. All runs were at ET 150 under conditions described in the text.

# RAT PITUITARY CELLS (6 DAY CULTURE)

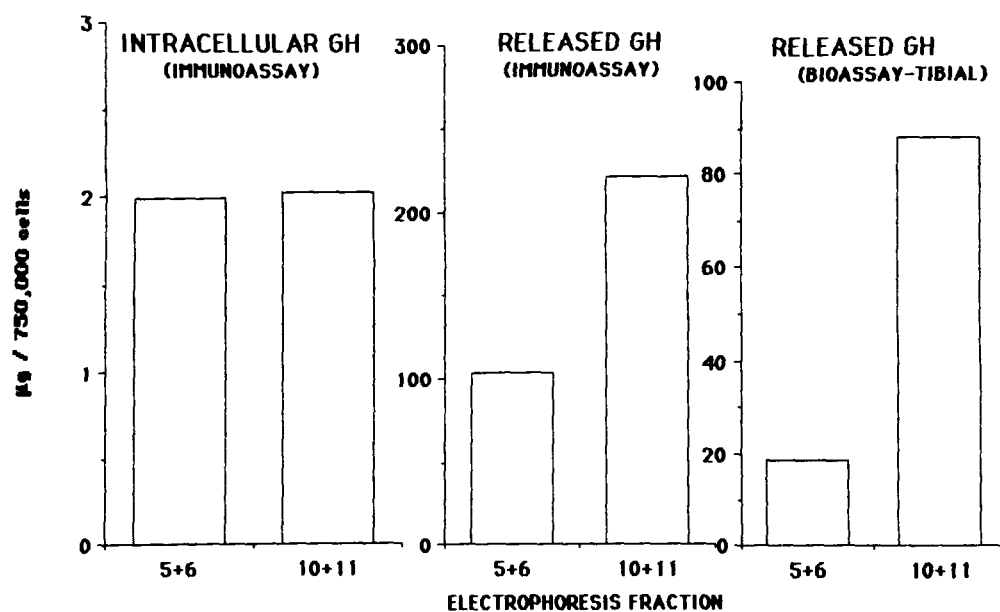


Fig. 7. GH released from GH cells separated by CFE. Cells in pooled electrophoresis fractions 5+6 and 10+11 (see Fig. 6, Exp. 4, panel 0) were cultured for six days and the GH released into the medium was assayed by RIA and tibial line bioassay. The intracellular contents of GH in cells in these pooled fractions prior to culture are shown in the left panel.

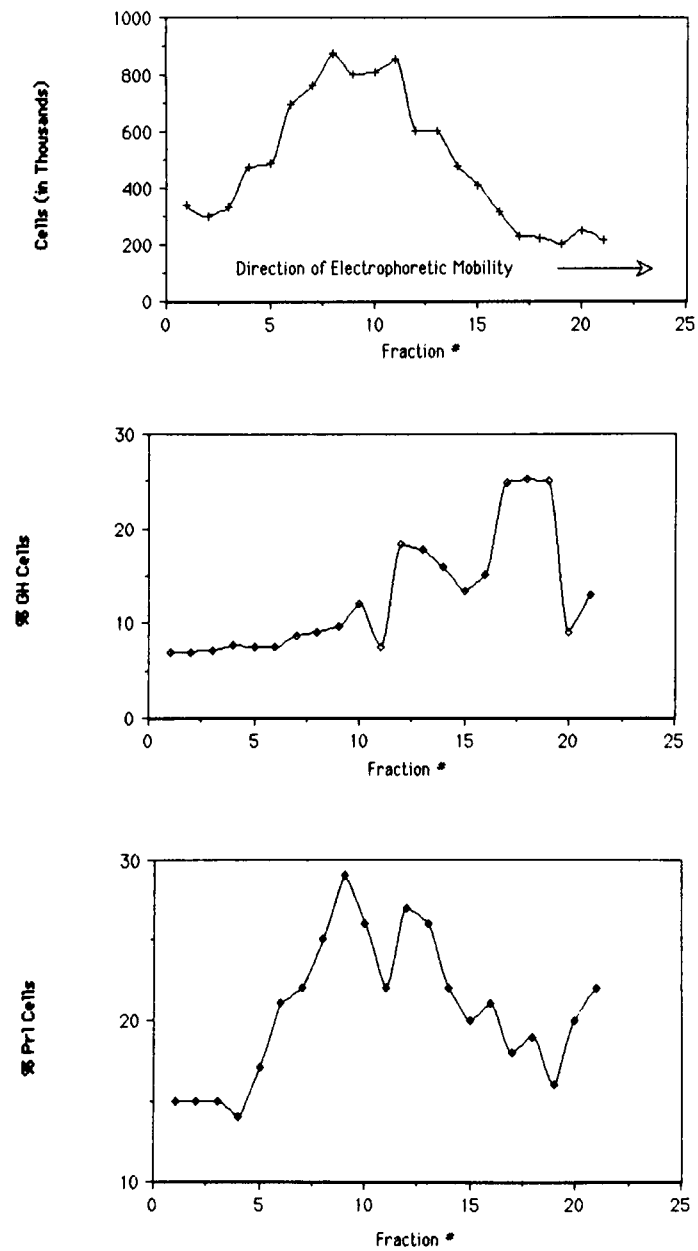


Fig. 8. Distributions of GH and PRL containing cells in fractions after CFES. These distributions were determined from counts of 30,000 cells/fraction, after staining with hormone specific antibody, by flow cytometry.



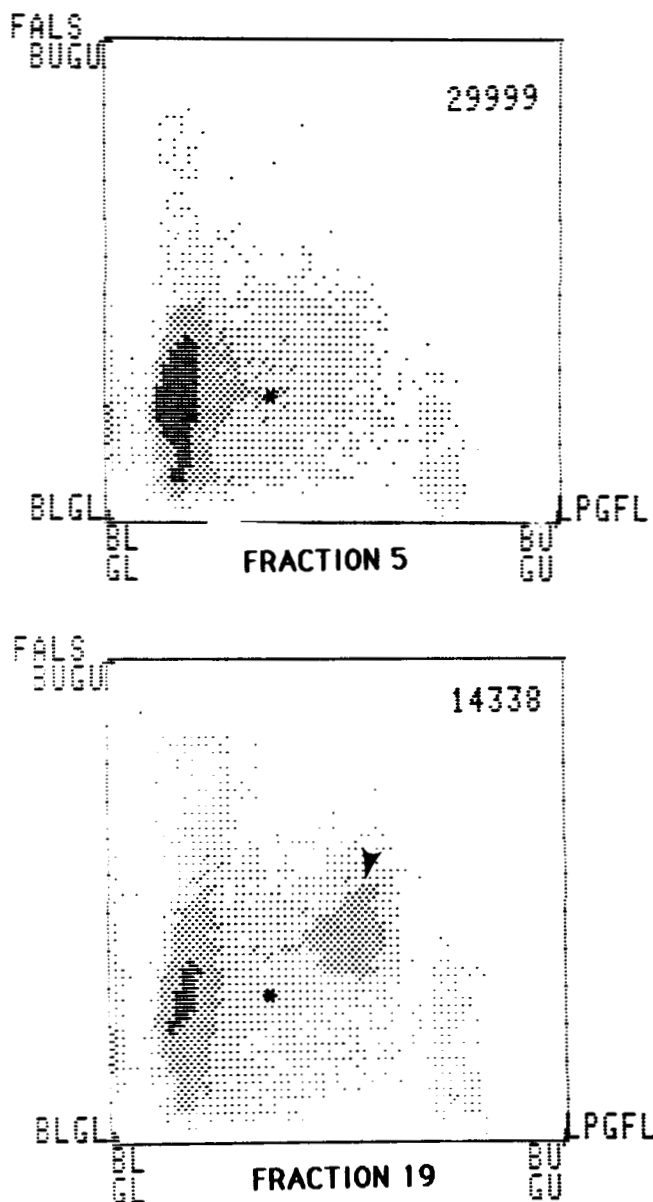


Fig. 9. Two parameter flow cytometric analysis of GH cells contained in Fr. 5 (top) and Fr. 19 (bottom) after the CFES trial shown in Fig. 8. The intensity of the green fluorescence (X axis) relates to the presence of GH cells, while the forward angle light scatter (FALS, Y axis) relates to the cell size. Numbers of cells counted are shown in upper right corner. The intensely stained GH cells in Fr. 19 (identified by ▼) are not present in fr. 5. However, some less intensely stained GH cells are seen in both fractions (\*).

ORIGINAL PAGE IS  
OF POOR QUALITY

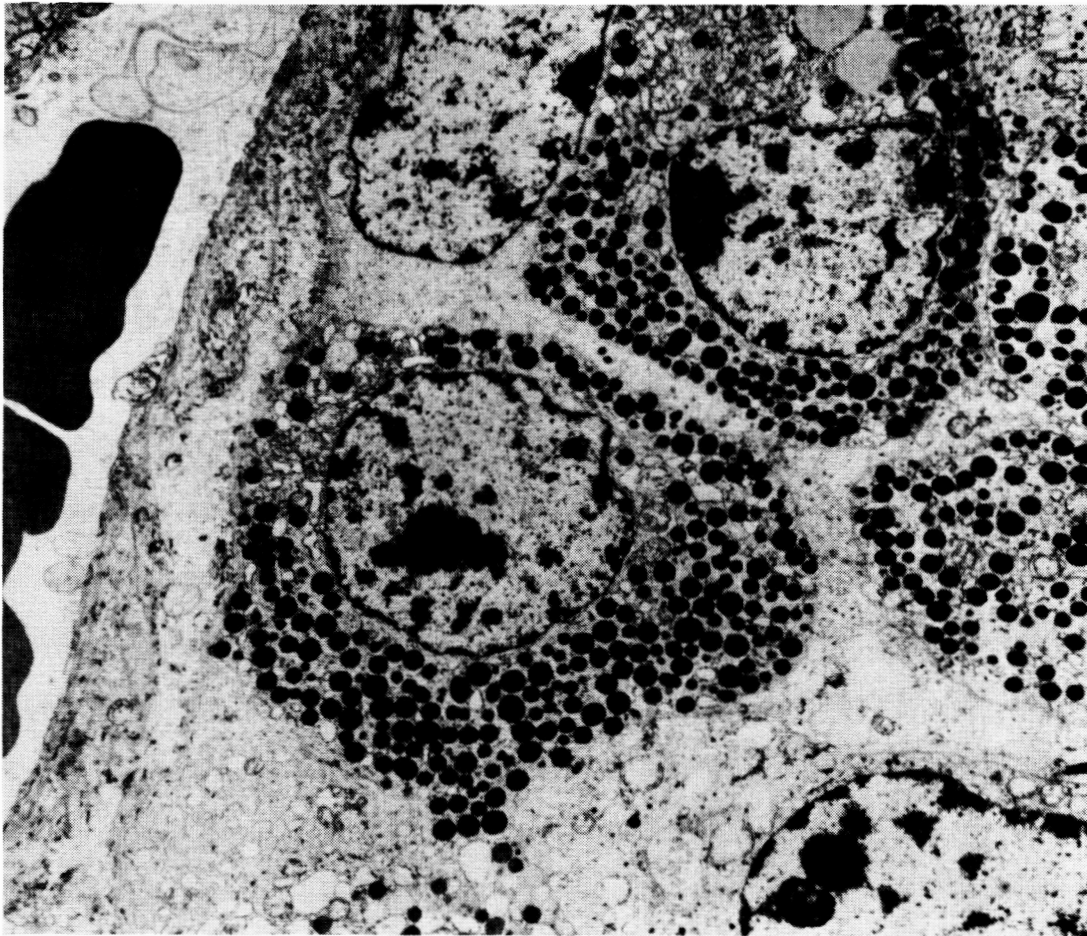


Fig. 10. Electron micrograph of a human post mortem pituitary gland 8 hrs. after death. Although general cell autolysis is evident, the GH-containing granules are intact.

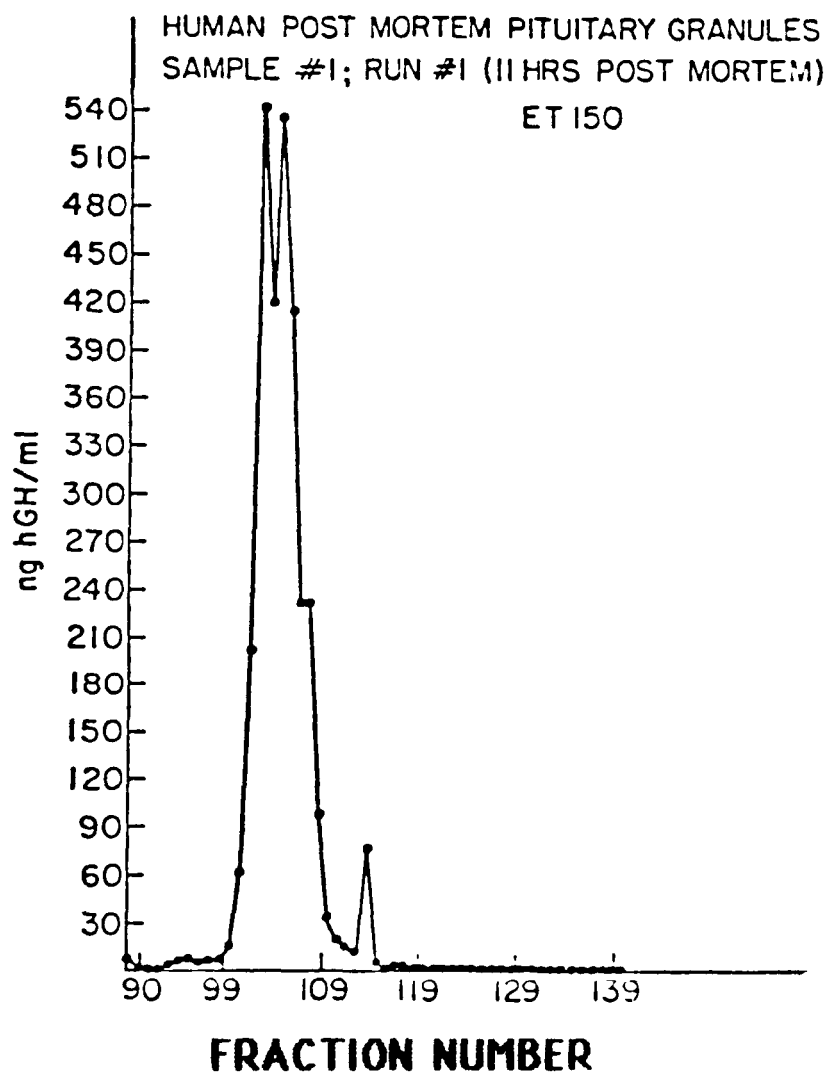


Fig. 11. Distribution profile of immunoactive human GH contained in CFE fractions after electrophoresis of a crude pellet (20,000 X g) containing granules. Although not shown on figure, tubes 1-89 and 141-200 were assayed and found not to contain GH.

# HUMAN POST MORTEM PITUITARY GRANULES (CFE)

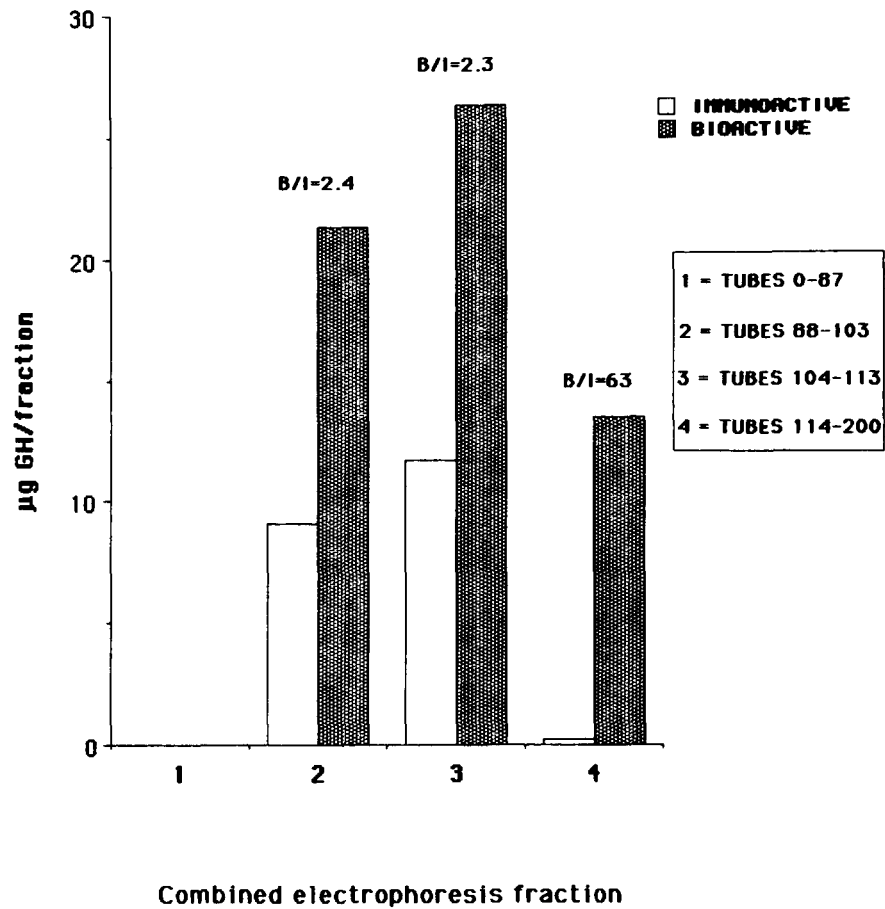


Fig. 12. Biological activities of hGH contained in granule fractions separated by CFES. The experiment depicted in Fig. 11 resulted in 200 tubes which were pooled into four areas shown in the insert. Hormone in these pooled fractions was measured by immunoassay and tibial line bioassay.

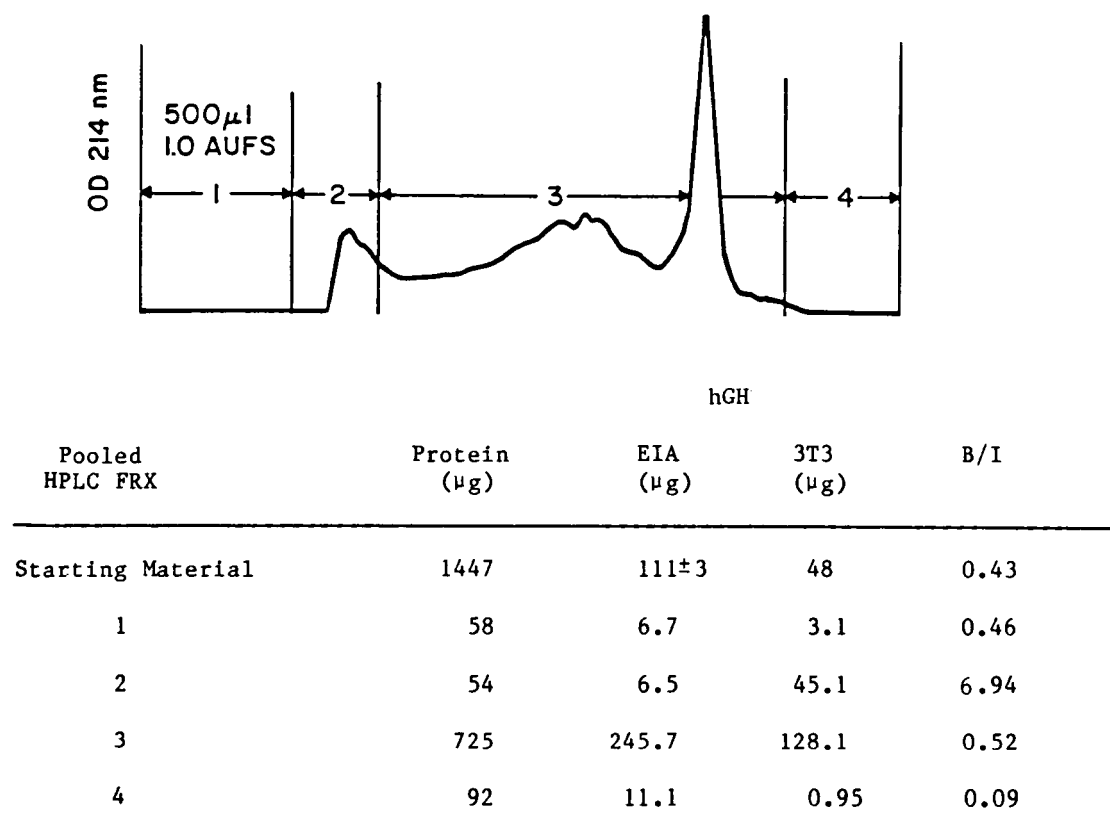


Fig. 13. Fractionation of an alkaline extract of a human pituitary gland by HPLC and immunological/biological activities of the hGH contained in pooled fractions eluting from the SW300 sizing column. The OD<sub>214</sub> profile (at a setting of 1.0 full scale deflection) is shown in the upper panel and the hormone activities of the pooled areas are shown in the table (bottom). Biological activity of the hGH was determined by 3T3 bioassay.

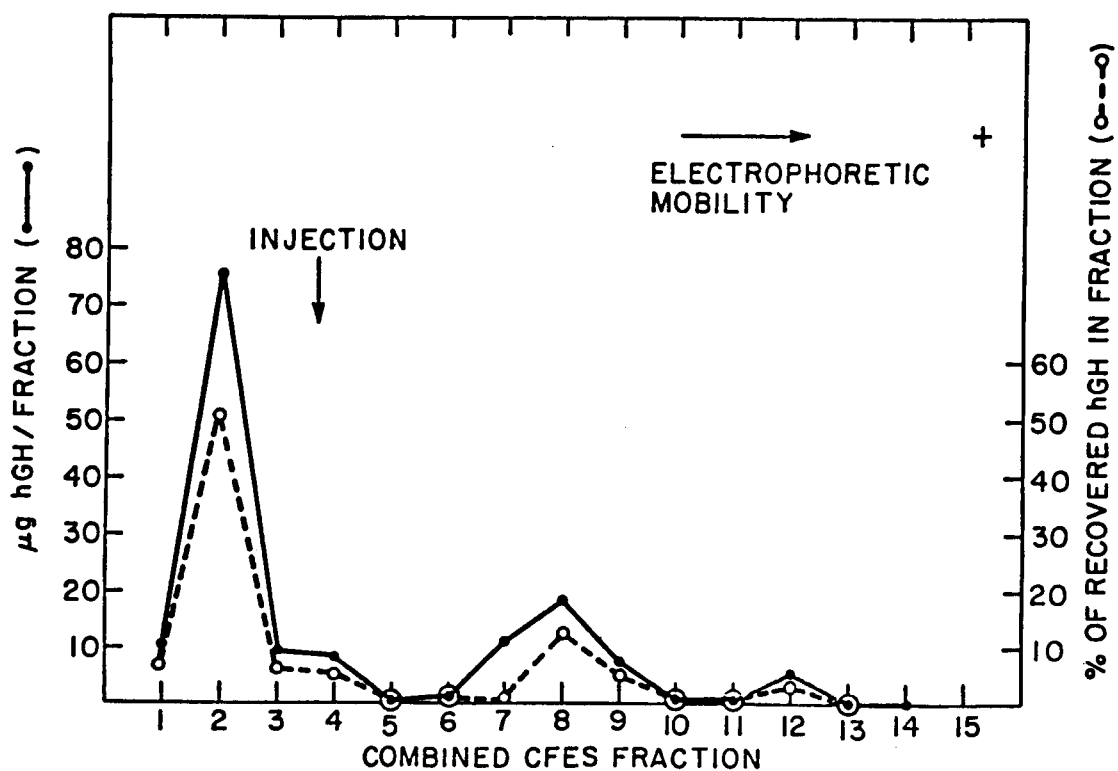


Fig. 14. CFES of human pituitary extract. Fr. #2 from an HPLC run (see Fig. 13) was applied to CFES and the resulting 200 tubes were pooled (15/fraction) prior to assay by 3T3 cell bioassay. Although not shown in the figure, only 20% of the total recovered immunoreactive hGH was associated with material in frs. 1-5.

# AFFINITY CHROMATOGRAPHY OF HUMAN GROWTH HORMONE

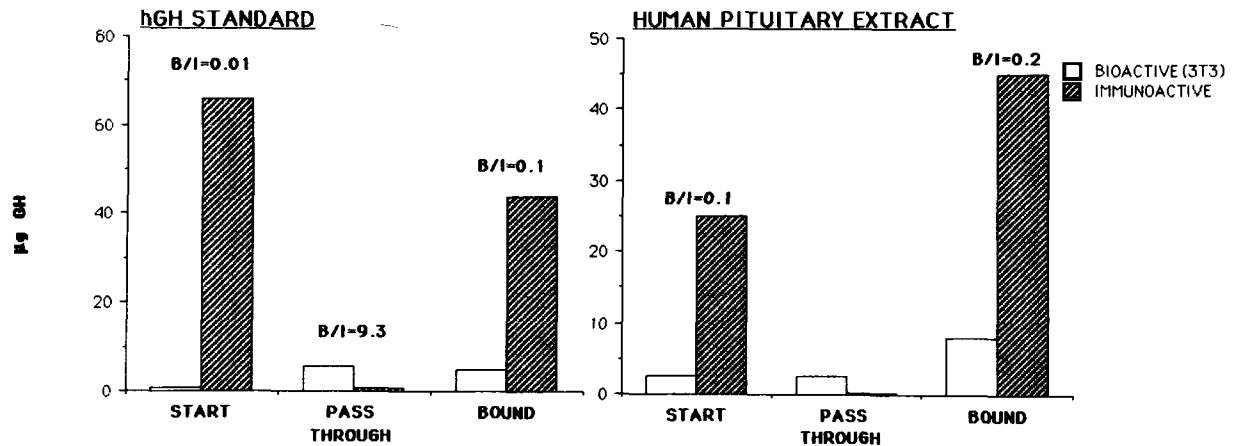


Fig. 15. Biological and immunological activities of hGH standard and a human pituitary extract before and after affinity chromatography. A highly potent hGH antiserum was covalently coupled to Pierce Reactigel (see text). Material bound to the column was removed by elution with 4M KSCN.

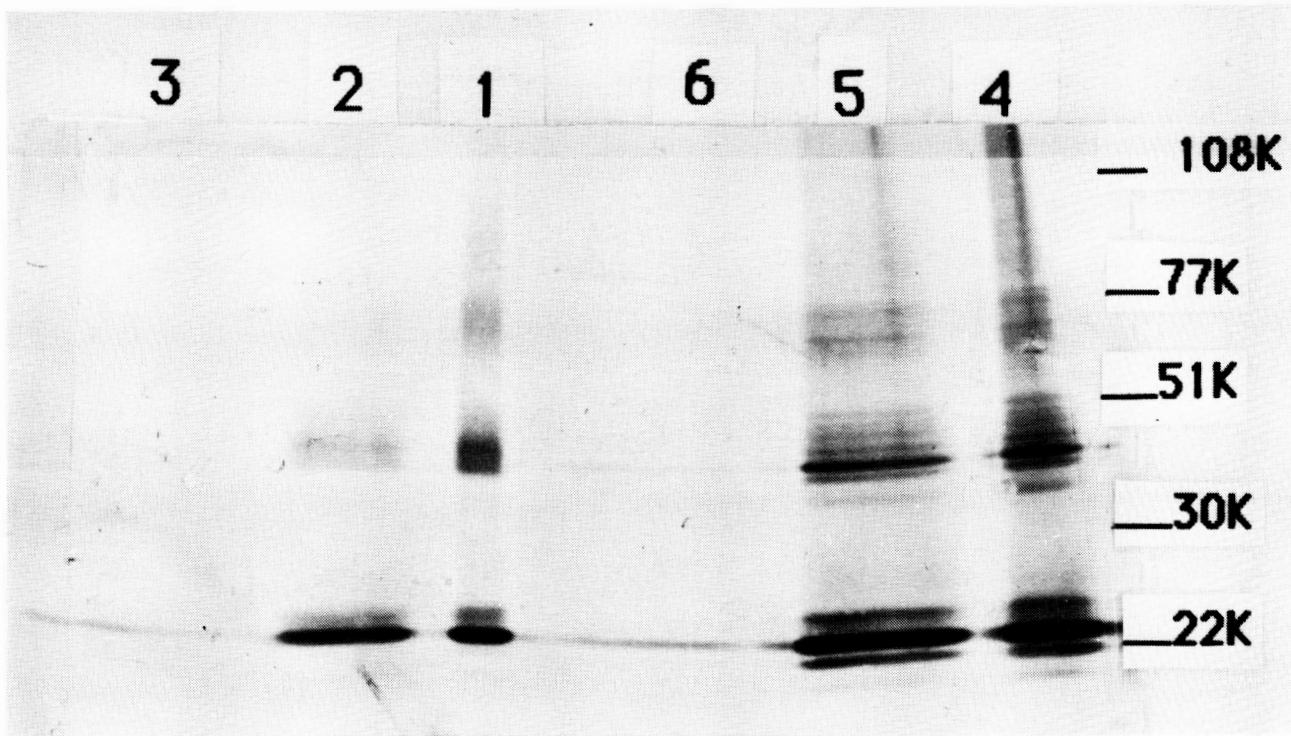


Fig. 16. Western blot SDS-PAGE profiles of hGH contained in hormone standard or in human pituitary extract before and after affinity chromatography. Lanes 1 and 4 show hGH in standard or fresh extract respectively. Lanes 2 and 5 show the appearance of hGH forms after elution from the column with KSCN. Note that virtually no hGH immunoactivity is present in the passthrough of either the hGH standard (lane 3) or pituitary extract (lane 6). Molecular weight markers show mobilities of known standards. See figure 15 for assay data.



TABLE 1  
COMPARISONS OF TWO TYPES OF SOMATOTROPHS

	<u>Type I</u>	<u>Type II</u>
Density (g/cm <sup>3</sup> )	1.050 - 1.068	1.071 - 1.086
Secretory Granules	Few	Many
Appearance (EM)	Abundant Regions of RER and Golgi Apparatus	Few Regions of RER and Golgi Apparatus
Db-cAMP ( $3 \times 10^{-3}$ M)	Stimulated Secretion	Stimulated Secretion
Somatostatin ( $10^{-7}$ M)	Inhibited Secretion	Inhibited Secretion
Thyroxine ( $10^{-6}$ M)	No Effect	Stimulated Secretion
Hydrocortisone ( $10^{-6}$ M)	Increased Cell GH	No Effect

---

Snyder, G., W. Hymer, and J. Snyder, ENDOCRINOLOGY 101:788, 1977.

TABLE 2

HORMONE RELEASE FROM CELLS ON EARTH  
AFTER 7 DAYS IN MICROGRAVITY\*

	$\mu$ G Hormone Released <sup>+</sup>		$\mu$ G Hormone Produced <sup>++</sup>	
	GH	PRL	GH	PRL
Earth	16.8	3.3	12.9	1.6
Space	0.8	5.0	0.2	4.9

\*Cells flown for 7 days on STS-8 in September 1983.

<sup>+</sup>6 day culture;  $1 \times 10^6$  cells in 5 ml  $\alpha$ MEM + 5% calf serum.

<sup>++</sup>Hormone produced = hormone released - intracellular hormone seeded

## REFERENCES

1. Kolata, G. "New Growth Industry in Human Growth Hormone?," Science, Vol. 234, October 3, 1986, pp. 22-24.
2. Ellis, S. and R. E. Grindeland, "Dichotomy Between Bioassayable and Immunoassayable Growth Hormone," Advances in Human Growth Hormone Research, Washington, D. C., U. S. Government Printing Office, DHEW Publication No. (NIH) 74-612, 1974, pp. 409-433.
3. Hymer, W. C. and J. Hatfield, "Purification of Cells from the Anterior Pituitary," in Methods in Enzymology, Coloureck and Kaplan, eds., Academic Press, Vol. 103, part h, ed., P. Conn, 1983, pp. 257-287.
4. Hymer, W. C. and J. M. Hatfield. 1984. Separation of cells from the rat anterior pituitary gland. In Cell Separation: Methods and Selected Applications, ed. T. G. Pretlow and T. Pretlow. Academic Press, Vol. 3, pp. 163-194.
5. Snyder, G., W. C. Hymer and J. Snyder. 1977. Functional heterogeneity in somatotrophs isolated from the rat anterior pituitary. Endocrinology 101:788-799.
6. Grindeland, R., W. C. Hymer, P. Lundgren and C. Edwards. Differential secretion of bioassayable growth hormone by two types of rat somatotrophs. The Physiologist, 25 (4), 1982, pp. 262.
7. Hymer, W. C., D. L. Wilbur, R. Page, E. Hibbard, R. C. Kelsey and J. M. Hatfield. Pituitary hollow fiber units in vivo and in vitro. Neuroendocrinology, 32, 1981, pp. 339-349.
8. Hymer, W. C., M. Angeline, M. Chu, R. Grindeland, J. Harkness, J. Hatfield, E. Hibbard, K. Kovacs, G. Mansur, A. Mastro, K. Motter, J. Parsons, C. Phelps, B. Ruskin, A. Signorella, W. Taylor, M. Thorner, G. Tindall and D. Wilbur. Hollow Fibers: Their applications to the study of mammalian cell function. Regulation of Target Cell Responsiveness, Vol. 1, (Eds. K. W. McKerns, A. Aakvaag, and V. Hansson) 1984, pp. 407-461 (plenum Publishing Corp.)
9. Hatfield, J. M. and W. C. Hymer. 1986. Flow cytometric analysis and sorting of live male rat anterior pituitary cell types by forward angle and perpendicular light scatter. Endocrinology. 119:2670-2682.
10. Hatfield, J. M. and W. C. Hymer. 1986. Flow cytometric analysis and sorting of live female rat anterior pituitary cell types by forward angle and perpendicular light scatter: Effect of 17 $\beta$ -Estradiol. Endocrinology. 119:2683-2694.
11. Hatfield, J. M. and W. C. Hymer. 1985. Flow cytometric immunofluorescence of rat anterior pituitary cells. Cytometry 6:137-142.
12. Boltz, R. C. and P. Todd. 1979. In Electrokinetic Separation Methods (Righetti, P. G., Van Oss, C. J. and Vanderhoff, J. W., eds.) 229-250, Elsevier/North-Holland Biomedical Press, Amsterdam.

13. Plank, L. D., W. C. Hymer, M. E. Kunze, G. M. Marks, J. W. Lanham and P. Todd, A study of cell electrophoresis as a means of purifying growth hormone secreting cells. J. Biochem. Biophys. Methods, 9, 1983, pp. 275-289.
14. Hymer, W. C., Grant H. Barlow, Steven J. Blaisdell, Carolyn Cleveland, Mary Ann Farrington, Mary Feldmeier, Richard Grindeland, J. Michael Hatfield, J. Wayne Lanham, Marian L. Lewis, Dennis R. Morrison, Barbara J. Olack, David W. Richman, James Rose, David W. Scharp, Robert S. Snyder, Carol A. Swanson, Paul Todd and William Wilfinger. 1987. Continuous Flow electrophoretic separation of proteins and cells from mammalian tissues. Cell Biophysics (in press).
15. Science "News and Comment" Vol. 228, June 7, 1985.
16. Nixon, T. and H. Green. "Contribution of Growth Hormone to Adipogenic Activity of Serum," Endocrinology, Vol. 114, 1984, pp 527-532.
17. Cogoli, A., A. Tschoop. and P. Fuchs-Bislin, "Cell Sensitivity to Gravity," Science, Vol. 225, 1984, pp. 228-230.
18. Grindeland, R., W. C. Hymer, M. Farrington, T. Fast, C. Hayes, K. Motter, L. Patil and M. Vasques. 1987. Changes in pituitary growth hormone cells prepared from rats flown on Space Lab 3. Am. J. Physiol. (in press).

Pooled HPLC FRX	Protein ( $\mu$ g)	hGH <sup>+</sup>		
		EIA ( $\mu$ g)	3T3 ( $\mu$ g)	B/I
Starting Material	1447	111 $\pm$ 3	48	0.43
1	58	6.7	3.1	0.46
2	54	6.5	45.1	6.94
3	725	245.7	128.1	0.52
4	92	11.1	0.95	0.09

TABLE 6  
Fractionation of hGH by affinity chromatography

Sample ( $\mu$ g)	Column <sup>+</sup> Fraction	Bioactive hGH ( $\mu$ g) <sup>+</sup>	Immuno- positive	B/I
Purified hGH standard	a) Unfractionated starting material	0.9	66	0.01
	b) Pass through	5.6	0.6	9.3
	c) Bound	4.8	44	0.1
Crude alkaline extract of human pituitary gland	a) Unfractionated starting material	2.5	25	0.1
	b) Pass through	2.6	0	-
	c) Bound	8.0	45	0.2

An IgG fraction of rabbit antiserum raised against hGH was coupled to Pierce activated imidazolyl-carbamaite (Fractogel). The starting material was prepared in 0.01 M PBS and the column run in this buffer. Bound material was eluted from the column with 4M KSCN.

TABLE 5

GH activity in crude granule fractions of human post mortem pituitary tissue after continuous flow electrophoresis<sup>+</sup>

Combined electrophoresis fraction	Tube number	GH/fraction (μg)		B/I
		Immunoactive	Bioactive	
1	0-87	0	0	0
2	88-103	9.1	21.4	2.4
3	104-113	11.7	26.4	2.3
4	114-200	0.2	13.5	62.8

<sup>+</sup>11 hr post mortem pituitary gland; See Fig. 8 for distribution of immunoactive GH in individual fractions from the DFE device.

<sup>++</sup>Determined by tibial line bioassay.

Table 4

Immunological and biological activities of GH released from cells into culture medium after CFE

Fractions <sup>+</sup>	Intracellular GH (immunoassay)	Released GH μg/750,000 cells	
	μg/750,000 cells	immunoassay <sup>++</sup>	bioassay
5+6	1.99	104	18.5
10+11	2.03	221	88

<sup>+</sup>See Fig. 4, exp. #4 for positions of cells migrating to these areas.

<sup>++</sup>5x10<sup>4</sup> cells/fraction cultured in 200 μl αMEM containing calf serum and antibiotics in 96 well plates (5 wells/fraction) at 37°C under 95% humidified air:5% CO<sub>2</sub> for eight days. GH in these media were then tested by RIA or by tibial line bioassay.

In summary, we have used the cell separation techniques of velocity sedimentation, flow cytometry and continuous flow electrophoresis to obtain enriched populations of GH cells. Since our ultimate goal is to isolate a GH cell subpopulation which releases GH molecules which are very high in biological activity (but relatively poor in immunological activity), it will be important to use a method which can effectively process large numbers of cells over a short time span. The techniques based on sedimentation are limited by cell-density overlaps and streaming. For example, pituitary FSH/LH cell types have identical densities to GH (type II) cells. While flow cytometry is useful in the analytical mode for objectively establishing cell purity, the numbers of cells which can be processed in the sort mode are so small as to make this approach ineffective in terms of our long term goals. We have shown that CFES can separate GH cells from other cell types on the basis of differences in surface charge. Importantly, the bioactive producers appear to be more electrophoretically mobile than the low producers. Current ground based CFES efforts are hampered by cell clumping in low ionic strength buffers and poor cell recoveries from the CFES device. It seems likely that future research will partially alleviate some of these problems. The already proven increased throughput of the CFES device in microgravity should provide the means to achieve our ultimate goal, viz. the large scale production of bioproducing cells so that isolation and characterization of this bioactive GH form can be realized.

KIDNEY CELL ELECTROPHORESIS IN SPACE FLIGHT:  
RATIONALE, METHODS, RESULTS AND FLOW CYTOMETRY  
APPLICATIONS

P. Todd<sup>+</sup>, D.R. Morrison<sup>++</sup>, G.H. Barlow<sup>0</sup>,  
M.L. Lewis<sup>\*</sup>, J.W. Lanham<sup>\*\*</sup>, C. Cleveland<sup>\*\*</sup>,  
K. Williams<sup>00</sup>, M.E. Kunze<sup>00</sup>, and C.L. Goolsby<sup>00</sup>

+ Bioprocessing and Pharmaceutical Research Center  
3401 Market Street  
Philadelphia, PA 19104

++ Biomedical Laboratories Branch  
Johnson Space Center  
Houston, TX

<sup>0</sup> Bioprocessing Research Center  
The University of Texas Health Science Center  
Houston, TX

\* Life Sciences Division  
Krug International, Inc.  
Houston, TX

\*\* Electrophoresis Operations in Space  
McDonnell Douglas Astronautics Co.  
St. Louis, MO

<sup>00</sup> Department of Molecular and Cell Biology  
The Pennsylvania State University  
University Park, PA



## SUMMARY INTRODUCTION

The human kidney performs an incredible number of different functions. There are individual cells responsible for the production of renin, erythropoietin, enzymes of vitamin D metabolism, plasminogen activators of at least 3 types, granulocyte conditioning factor, the maintenance of electrolyte balance, and the clearance of soluble wastes from the blood, to mention a few. The sharing of these functions among cells will take decades to fully characterize, and many of these functions, if they could be isolated, are also of commercial importance to biotechnology. For example, the kidney is perhaps the second most prolific tissue with respect to plasminogen activator production, while plasminogen activator is one of today's "hottest" biotechnology future market items (Kadouri and Bohak, 1985). The purpose of the research project was to develop the most effective means of purifying subpopulations of cultured human embryonic kidney (HEK) cells and produce living subpopulations for study. Originally primarily urokinase, a plasminogen activator found in urine, was the product goal. Since primary cultures of differentiating epithelioid cells are not immortal, adequate numbers of cells could not be purified by cloning or cell sorting. Historically, Barlow and Kolin showed some three major subpopulations by "continuous belt" electrophoresis in a magnetic field (Barlow et al., 1977). This finding was not pursued at the time of its discovery, but it was confirmed as an early goal in this project, and the original premise that electrophoretic subfractions would separate according to function was also confirmed. A series of ground-based electrophoretic and enzymologic studies led to an experiment on the Apollo-Soyuz mission in which evidence for urokinase-rich cell subpopulations was found. The first objective of the present project was to reproduce this result with adequate statistical data and superior technique but with the same apparatus. The "EEVT" experiment on STS-3 included two columns of fixed erythrocytes, which were photographed in flight. The remaining 6 tubes were dedicated to living kidney cells that had to be frozen for several weeks before and immediately after electrophoresis in space. Liquid nitrogen loss in a ground refrigeration unit destroyed all samples from this flight, and only photographic data from the fixed erythrocytes was usable (Snyder et al., 1985; Morrison and Lewis, 1983; Sarnoff, et al., 1983). Owing to the development of a Joint Endeavor Agreement with McDonnell Douglas Astronautics Co. NASA made time available on the Continuous Flow Electrophoresis System (CFES) aboard the space shuttle orbiters. Without the necessity of freezing cells and without worrying about the influence of particle sedimentation or zone convection it became possible and logical to separate cells by CFES in microgravity. This undertaking was suggested by the clear finding of a gravity-dependent component of pituitary cell separation in free fluid electrophoresis methods (Plank et al, 1983). Prior to the Challenger tragedy it was only possible to separate two samples of kidney cells, both on STS-8. Extensive reporting has been accomplished on these cells, but there are still numerous analytical results to be completed and published. The following text (1) introduces the subject, (2) describes the space-based electrophoresis apparatus and its testing, (3) reviews results of kidney cell electrophoresis, and (4) presents results in the application of flow cytometry to kidney cell electrophoresis in low gravity.

## WHY STUDY CELL ELECTROPHORESIS IN SPACE?

Any cell type with limited or no proliferative capabilities that is needed in pure form must be separated by a technique that provides adequate purity, adequate yield, adequate relationship to cell type, and adequate function after separation. Cell electrophoresis, high gradient magnetic filtration, two-phase partitioning, and affinity chromatography have been identified as such processes. All are in their infancy, and some processes may not yet have been discovered. The reasons for purifying suspended animal and plant cells are numerous, and the activity itself is amply justified by the demands for pure cell populations as objects of chemical research, living material for transplantation, and sources of uncontaminated bioproducts. These reasons include the anticipated needs of biochemists and biotechnologists in the 1990's.

### 1. Stokes heterogeneity of cells with similar charge and function

Cell parameters related to Stokes sedimentation, namely density and radius, are distributed values in any living cell population. These may or may not be related to cell function. For example, neutrophils and somatotrophs are extraordinarily dense owing to their densely packed granules of secretory proteins. Sedimentation helps separate such cells from others with which they are naturally mixed. Heterogeneity of sedimentation in a pure subpopulation interferes with purity and yield in most purification processes. Figure 1 is an indication of the heterogeneity of a population of human embryonic kidney cells with respect to diameter. Terminal sedimentation velocity increases with the square of the radius, so there could be an 8-fold difference in the sedimentation velocities of the most and least rapidly sedimenting cells. In populations with less size heterogeneity it has been shown that density differences also affect vertical electrophoretic migration (Plank et al., 1983) and probably horizontal electrophoretic migration in continuous flow electrophoresis (Todd, 1985), as indicated schematically in Fig. 2.

### 2. Ambiguity of electrophoretic migration

Given the above, in continuous flow electrophoresis cell type X could sediment into the same electrophoretic pathway as cell type Y, or vice versa, as shown in Fig. 2. Thus, two electrophoretic subpopulations would be collected as one, or an electrophoretically homogeneous population could be detected as widely distributed.

### 3. Discovery of new cell types

Extensive electrophoretic studies on pituitary cells (Plank et al., 1983; Hymer et al., 1987) and kidney cells (Todd et al., 1986) demonstrate that different cells in a tissue perform different secretory, synthetic, and metabolic functions despite morphological similarity. While these findings may seem amusing to histochemists, who routinely make similar discoveries, histochemistry will not reveal the subtle differences that have been discovered by cell purification, such as immunologically similar molecules with different biological function produced by separable, morphologically similar, cells (Hymer et al., 1987). Histochemistry cannot measure the molecular weights or determine gene sequences in such cells; cell purification has made it possible to do these. Owing to electrophoretic purification, we now know, for example, that two pituitary cell types make two types of growth hormone and that two electrophoretic subpopulations of kidney cells make urokinase molecules having different molecular weights.

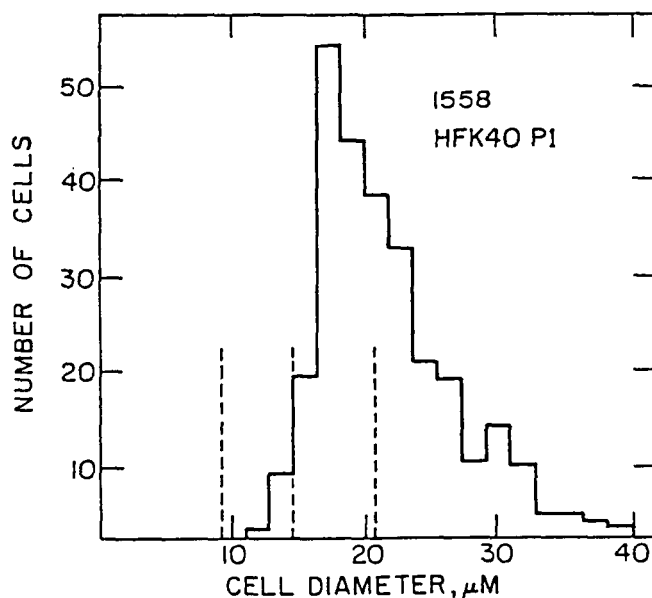


Figure 1. Histogram of microscopically determined sizes of passage-1 HEK cells. The three dashed lines indicate the calibration points based on the diameters of 9.5  $\mu\text{m}$ , 14.5  $\mu\text{m}$ , and 20.5  $\mu\text{m}$  spheres also determined microscopically.

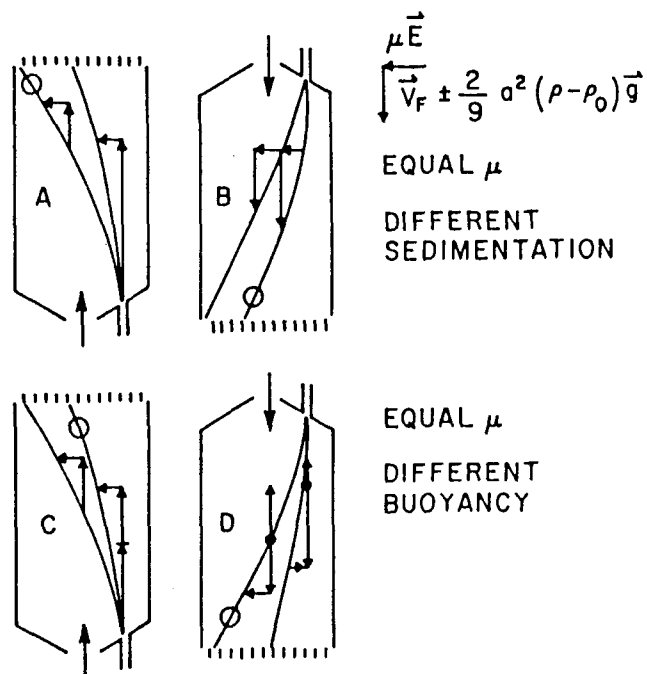


Figure 2. Effects of particle sedimentation on continuous flow electrophoresis of cells. In A and B the circles show the path of more rapidly sedimenting cells. In C and D the circles show the path of more buoyant cells. All cells are considered to have the same electrophoretic mobility.

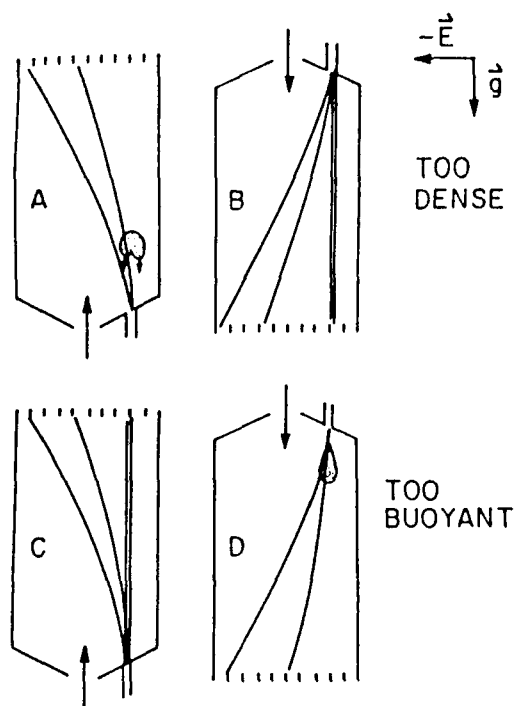


Figure 3. Sketch of the consequences of sample zones that are too dense or too buoyant in continuous flow electrophoresis. Sample flow is stopped or too fast, depending on relative densities of sample and carrier buffers.

#### 4. Rare cell types

A popular activity in flow cytometry is the detection of rare cell types--one in a million or so. Detection alone does not produce workable amounts of material. To perform any analysis or post-separation study requires adequate cell numbers. Consider that a biochemical measurement requires 1 million cells -- a typical lower limit. Obviously the starting population must be  $10^{12}$  cells. Passing these through a cell sorter at current maximum rates of 10,000/sec (depending on the complexity of sort logic) would yield the desired number of cells in 100 million seconds (or 3 years). A technique for accomplishing the same thing in a day would be useful, but ground based electrophoresis is not equal to this task owing to limited capacity and limited resolution. The erythropoietin gene is only an early example of a problem of this magnitude; its original isolation required a few years by other methods.

#### 5. Cells for transplantation

The treatment of congenital or chronic diseases by a single injection or implantation of cells has been a goal of several disease-specific research programs and projects. Many believe that cell therapy is safer than gene therapy. It is necessary to devise methods that prevent the transplantation of unwanted cells, such as graft-vs-host cells in bone marrow, alpha cells in pancreatic islets, or mammatrophs in pituitary. These specific examples have been addressed in ground-based CFES, which has produced adequate quantities of the appropriate cell types for research (Hymer et al., 1987). Whether or not ground based electrophoresis is equal to the same task for medical transplantation needs to be determined.

#### 6. The capacity problem

The previous two items point to the need for high capacity separation accompanied by adequate resolution. Cells in suspension have a very low diffusion coefficient, so they do not diffuse out of the zone in which they are injected into a free-fluid separator. Rapidly diffusing substances flow into the zone, and the zone sediments rapidly if the cell concentration is above a critical value (Mason, 1976). The effect of this phenomenon on CFES is described in Fig. 3. For most nucleated cells the critical concentration is below 10 million cells per ml (Boltz and Todd, 1978). It has been mentioned that for certain research purposes the capacity of ground-based CFES is adequate because the availability of cells is limiting (Hymer et al., 1987). However,

there will be cases in which it is not. Biochemical assays on single fractions without reculturing, in vivo implantation of single fractions, and mechanistic studies on isolated rare cell populations will require the separation, within a few hours, of larger pure cell populations have been heretofore available.

Thus, the ability to process more than 30 million cells per hour (current practice) will eventually be needed. In microgravity zone sedimentation is absent, and such capacity is feasible.

## 7. The resolution problem

In CFES samples are injected in a fine stream into a flowing buffer stream. The small distance between the walls causes laminar flow in a steep parabolic profile from front wall to back wall. Cells near the walls move more slowly and spend more time in the field and hence are swept anodally a greater distance than are their counterparts at the center of the stream. The ideal sample stream is one whose diameter is negligible compared to the chamber thickness; hence a thick chamber is desirable, but chamber thickness is fixed by the need to reject heat uniformly to the cooling jacket at the walls. The quantitative nature of this problem can be modeled by computer and studied in low gravity where buoyancy driven convective flow is absent and thicker chambers can be used. Stable operating ranges of CFES in microgravity have been explored by computer simulations, and 4 g/hr processing rate can be achieved in a 10.0 mm thick chamber (McCreight, 1977). A typical commercial chamber is 0.3 - 0.5 mm thick. The McDonnell Douglas Astronautics Co. chamber is 1.5 mm thick, and the space flight CFES has a 3.0 mm thick chamber. The study of thicker chambers is desirable, but the thermal stability of the sample also must be considered. Cells could withstand 10 min. at 41°C, for example, so a chamber thickness that maintains this temperature at useful currents could be studied in space. To date, modifications of sample stream diameter have been studied in space and on earth, and a 4-fold enhancement of resolution has been possible within the working constraints of the studies.

## 8. Current carrying capacity of the separands

Highly concentrated cells in very low conductivity fluid will themselves carry a substantial amount of current, thereby increasing the current passed through the sample zone relative to the carrier buffer if the buffer is of very low conductivity. In the case of cells, the influence of this phenomenon on resolution is not known, because adequate

concentrations must be achieved to study it. These concentrations can be achieved in low gravity space experiments.

The above several types of experiments and processes require heroic measures or long projects to perform. In most of these, low gravity offers a short-cut to early answers or unavailable products. Nevertheless, low gravity research excellence in this limited field depends on maintaining a relevant research capability that supports the progress of comparable ground-based technologies.

#### METHODS AND EVALUATION OF CONTINUOUS FLOW CELL ELECTROPHORESIS IN LOW GRAVITY

The paragraphs that follow are adapted from the major paper by Hymer et al., (1987). They describe, as concisely as possible, the physical methods used on Space Shuttle flights and the results of specific tests, including kidney cell separation experiments using the McDonnell Douglas CFES.

##### 1. The McDonnell Douglas Continuous Flow Electrophoresis Systems

In continuous flow electrophoresis (CFE), cells or molecules are separated from one another on the basis of their surface charge density. The instrument used to conduct the cell separations differs from other designs (Hannig et al., 1975) in thickness and width of the separation chamber, and in the method of cooling. It consists of a rectangular separation chamber sandwiched between two electrode chambers which are also cooling jackets (Snyder et al., 1985 Plank et al., 1983; Hymer et al., 1987; Rose and Richman, 1979) and are separated from the chamber at its edges by semipermeable membranes (Fig. 4A,C). A stable electric field is maintained by ion flow through the membranes. Carrier buffer (low conductivity triethanolamine-potassium acetate buffer, pH 7.25, 300 mOsm per liter for cells or barbital buffer for proteins) flows upward through the separation chamber at a rate of 20 ml/min. The electrode and separation chambers are differentially pumped. Computerized flow balancing tends to eliminate transverse flow and pressure gradients in the sample chamber, enhancing cell stream stability and reproducibility of results. Dimensions of both ground and space instruments are described in Fig. 4. Cells ( $\sim 10^6$ /ml) previously washed and suspended in carrier buffer are injected into the bottom of the chamber using an infusion pump (4 ml/hr). Cells are exposed to the electric field for 4 minutes before they exit the top of the flow chamber through 197 ports and are collected as "fractions". The separands migrate across the

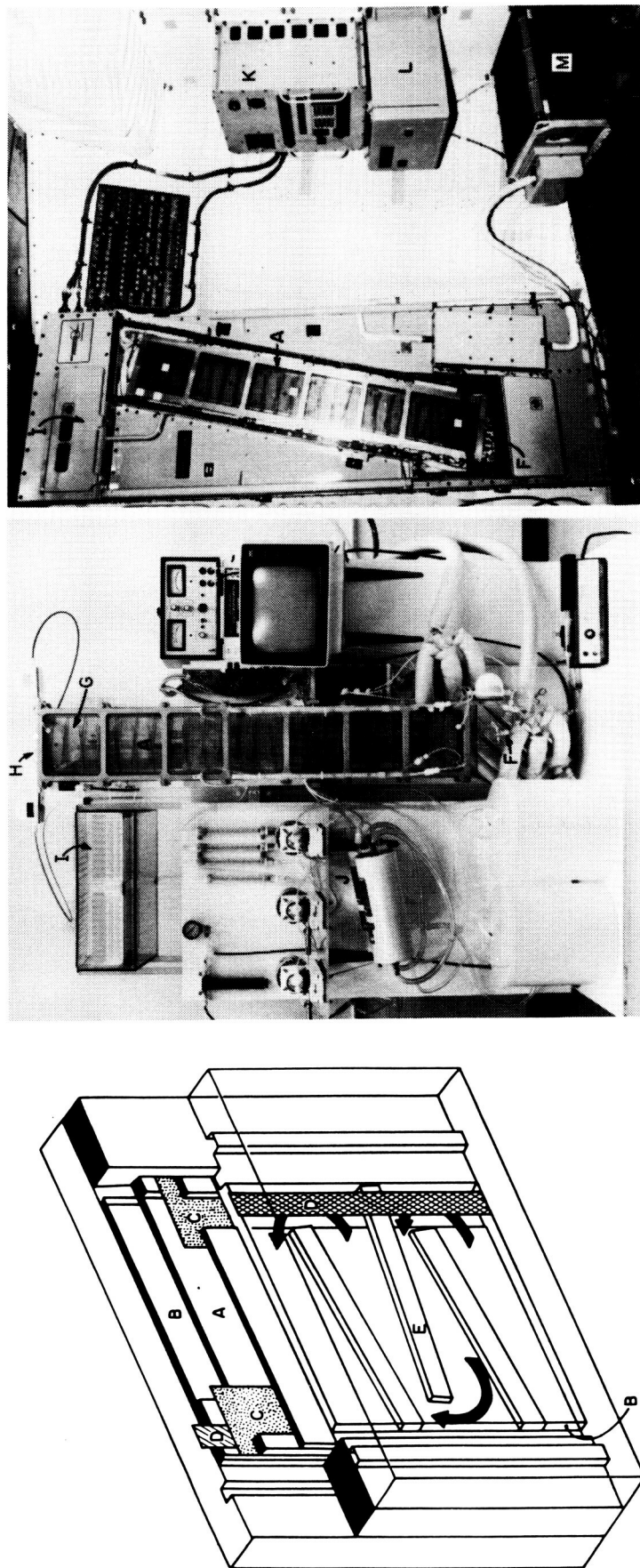


Figure 4. Continuous flow electrophoretic separators used in the laboratory and in space flight. Left: Diagram indicating how the separation chamber is surrounded by the coolant/electrode flow chambers. Center: Photograph of laboratory model. Right: Photograph of space flight unit installed on Shuttle Orbiter. The following components are labeled: (A) separation chamber, which is 0.15 cm thick and 6 cm wide in the laboratory model and 0.30 cm thick and 16 cm wide in the space flight unit and 120 cm long in both units; (B) front and back coolant/electrode chambers, through which electrode buffer (which also serves as coolant) is pumped in a serpentine path under computerized pressure control; (C) two semipermeable membranes which separate coolant/electrode chambers from sample chamber fluid while permitting free passage of ions for the maintenance of a stable electric field across the chamber; (D) a platinum ribbon electrode placed parallel to the semipermeable membrane in each of the two coolant/electrode chambers; (E) baffles which force serpentine flow of coolant/buffer fluid between the electrodes and membranes; (F) sample inlet; (G) flared region of the chamber of the laboratory model, to accommodate outlet tubes; (H) 197 sample outlets that permit fractions to exit through Tygon tubes at the top of the chamber; (I) thermostated fraction collection and storage area containing tubes (on the ground) or plastic bags (in space); (J) buffer pumping and cooling unit. In addition the space flight system consists of a separate computer module (K) for controlling separation commands, a sample storage module (L) for cooling up to six 20-ml samples and 6 trays having either fifty 15-ml fractions for cell separation or 197 fractions, 1.4 ml each, for protein collections; and a thermoelectric cooler (M).



separation chamber at different velocities depending on their net surface charge and viscous drag cross section and therefore leave the chamber through different outlet tubes. Lateral migration distance thus depends on the time,  $t$ , spent by the cells in the chamber, the applied field,  $E$ , and the cell surface charge density. The product is  $Et$ , expressed in volt-min-cm<sup>-1</sup>.

The CFE unit for space flight (Fig. 4) has been used for separations of various materials, including test proteins on Shuttle flight STS-4 and STS-6, particles on STS-7, and mammalian cells on Shuttle flight STS-8. The collection system was reduced to 40 tubes to accommodate a fraction volume of 13 ml required when living cells were collected. During operation in space the astronaut first removes a sample collection tray and syringe from a thermostated cabinet and places them into the fraction collection drawer and sample injection device, respectively. The electrophoresis process is initiated by a command at the computer keyboard. Sample enters the separation chamber, and fractions exit through tygon collection tubes ending with 20-gauge needles. At collection command, each of these needles penetrates a rubber septum covering the collection trays. The astronaut hears a signal to remove the sample collection tray and syringe, and the process can be repeated several times in one flight.

In space, temperature during storage prior to separation was 4°C; during separation temperatures were 6°C at chamber inlet, 12°C at outlet tubes and 16°C during collection. After collection, samples were maintained at 4°C. Samples processed in the ground chamber were collected into tubes at 4°C at the top of the unit. Temperatures within the chamber ranged from 6 to 8°C.

## 2. Test Protein Separations

Droplet sedimentation and convection currents caused by uneven Joule heating distort free-fluid electrophoretic separations. Since these gravity-dependent effects would theoretically play no role in the electrophoretic separations performed in microgravity, it should be possible to process samples containing greater concentrations of protein in space. This possibility was demonstrated by comparing laboratory and space flight separations.

A sample containing 0.1% rat serum albumin and 0.1% ovalbumin was electrophoresed at  $Et=110$ . A 4 tube peak-to-peak separation, with a 5 tube overlap between the two proteins, was routinely achieved. Whenever

the protein concentration was increased, the higher sample density resulted in decreased resolution. On Shuttle flight STS-4 a sample containing 12.5% rat serum albumin and 12.5% ovalbumin (25% protein w/v) was separated to the same 4-tube peak separation that was achieved on earth with 0.2% protein solution.

The diameter of the sample stream in the space-flight chamber was twice that of the laboratory chamber (see Fig. 4), so a four-fold increase in sample volume/unit time was realized. This plus the increased sample concentration (permitted by lack of zone sedimentation) resulted in 500-fold increased "throughput" achieved by performing the separation in microgravity.

### 3. Test particle experiments

The ability of CFE to separate particles on the basis of charge was confirmed in experiments designed by Dr. R. S. Snyder and co-workers (1986). Mixtures of test particles having known electrophoretic mobilities and different sizes were used. Polystyrene latex spheres having diameters (in  $\mu\text{m}$ ) of 0.56 (red), 0.30 (white) and 0.80 (blue) were synthesized by Interfacial Dynamics Co., Portland, OR (white particles), and Particle Technology, Inc., Bethlehem, PA (red and blue particles). These were separated from each other on Space Shuttle flight STS-7, prior to the use of living cells on STS-8, to test for separability, absence of sedimentation, particle band width, and effects of conductance discontinuities. Mobilities of the particles were  $3.5 \pm 0.2$  (red),  $2.4 \pm 0.2$  (white) and  $1.6 \pm 0.1$  (blue)  $\mu\text{m-cm-V}^{-1}\text{-s}^{-1}$  (Snyder et al., 1986).

## KIDNEY CELL ELECTROPHORESIS

### 1. Historical Introduction

Barlow's experiment (Barlow et al., 1977; Allen et al., 1977) on Apollo Soyuz in 1975 using a free-fluid column electrophoresis device showed that human kidney cells could be separated into 7 or 8 subfractions which are capable of producing high levels of plasminogen activators. Many difficulties were presented by freezing cells before flight and on orbit (after separation), then harvesting the cells postflight from the frozen ice column. Cell viability was low, and the small sample size and cell recovery methods precluded extensive study of the most interesting fractions. The corresponding technique on the ground, vertical density gradient electrophoresis, separates cells with satisfactory resolution (Platsoucas, 1983; Todd et al., 1981), but the

number of cells per fraction is not adequate to allow extensive studies of the highest producing subpopulations. The availability of the continuous flow electrophoresis system (CFES) in the middeck of the Space Shuttle offered much greater throughput at adequate resolution and eliminated the need for the freeze-thaw procedures used in the static column device. Ground-based separation of human embryonic kidney (HEK) cells using the CFES began in 1981 by a NASA/ university/ industry principal investigator team.

Early results showed that: 1) extensive qualification of the candidate cell lots was mandatory (Morrison and Lewis, 1983); 2) standard assays for target cell secretory function were often inadequate to distinguish among multiple subfractions (Lewis et al., 1984); and 3) HEK cells could be separated by CFES into more than 30 different fractions, all of which produced some level of plasminogen activators (Lewis et al., 1982). Prior to the first CFES separations of live cells on the Space Shuttle, research was performed to determine the effects of cell lot, harvesting and handling procedures, post-separation storage, and culture conditions on electrophoretic mobility (EPM) distribution and plasminogen activator production. Three different methods of analytical electrophoresis were used to characterize the EPM distribution of cultured HEK cells under a variety of conditions (Todd et al., 1986), and comparisons were made between density gradient electrophoresis (DGE) and CFES which confirmed the results of the first separation of HEK cells in space (Barlow et al., 1977; Allen et al., 1977). The following sections describe the most significant results of the first CFES separation of HEK cells under microgravity conditions on STS-8, the major compromises which occurred, and the subsequent research which has been done or is planned to prepare for future CFES flight experiments. Only the basic relationship between the EPM distribution and initial production of urokinase (u-PA) is discussed here. The details of the secretion of different PA's produced by the subpopulations following electrophoresis is described in the report by Barlow et al (1987) in this series.

## 2. Materials and Methods

Frozen suspensions of human kidney cells were obtained from MA Bioproducts (Rockville, MD, U.S.A.) and cultured in a serum supplemented medium according to previously published methods (Lewis et al., 1984). More than 35 cell lots were screened for viability, growth, karyotype, PA production, and morphology (Morrison and Lewis, 1983). For plasminogen production cells were plated into complete growth medium, allowed to multiply to confluence and changed to a serum-free PA production medium (UKPM) developed by Barlow et al., (1977a). The medium was harvested at

4 or 6 day intervals for 28 days, and the conditioned medium samples were frozen and analysed later for PA secretion rates. PA activity was determined by fibrin clot lysis, artificial substrate hydrolysis, or Enzyme Linked Immunosorbent (ELISA) assays according to methods previously published (Morrison and Lewis, 1983; Lewis et al., 1984; Morrison et al., 1984, 1984a). A detailed description of the culture and assay methods is found in the accompanying paper by Barlow et al (1987). For the Shuttle control and flight experiments the HEK cells (lot #8514) were grown on flasks, trypsinized and recultured on microcarrier beads. At 46 hours before separation (20 hours before STS-8 launch) the cells were trypsinized, harvested and suspended in a low ionic strength triethanolamine buffer containing 10% dialysed horse serum and antibiotics. Cells were stored in this buffer at 4°C until injection into the CFES, at which time they were mechanically redispersed and inserted as described in detail elsewhere (Morrison et al., 1984). Separations on STS-8 were performed at a field strength of 26 V/cm and a sample residence time of 12 minutes. Cells were injected at two different concentrations:  $2.6 \times 10^6$  cells/ml and  $8.0 \times 10^6$  cells/ml, whereas ground control experiments using a similar value of Et were conducted at concentrations of 2.5 and  $7.2 \times 10^6$  cells/ml. Each of 50 separated cell fractions was collected in 13 ml bags containing serum and stored at 4°C until return to Earth. Postflight the cells were recovered from the CFES collection tray, grown to 95% confluence in growth medium, then maintained on serum-free UKPM for up to 28 days. Supernatant medium was removed at 4-day intervals and frozen for PA analysis.

### 3. Results of STS-8 experiment and related research

The results confirmed that HEK cells are suitable test cells for microgravity separations. They are heterogeneous in EPM and function, predictable in growth and maintenance culture, stable in karyotype, and hardy enough to withstand the combined rigors of pre- and post-flight handling, the electrophoresis processing, and extended storage in the CFES buffer.

By using three methods of cell electrophoresis, the EPM distributions of early passage cultures of human embryonic kidney cells were determined in a variety of low ionic strength buffers of different chemical composition (Morrison and Lewis, 1983; Todd et al., 1986). HEK cells were found to be quite heterogeneous, having a broad range of EPM's and often distributions with multiple peaks. Electrophoretic heterogeneity, as measured by the coefficient of variation, was retained throughout several subcultures and in a variety

of buffers with various ionic strengths. Trypsin and EDTA, normally used to remove cells from the culture surface, had only a minor effect on the EPM distribution. In the CFES buffer (triethanolamine, ionic strength=0.0015 M) the mean EPM was found to be  $-1.47 \pm 0.27$   $\mu\text{m-cm/V-sec}$ ; however, after storage the mobility decreased to  $-1.28 \pm 0.26$   $\mu\text{m-cm/V-sec}$ . Thus storage in these low ionic strength buffers does not cause major changes in EPM or its CV. The role of cell cycle and size was also studied using density gradient electrophoresis (DGE), and no systematic relationship between either of these parameters and EPM was found (Todd et al., 1986).

Cell separation experiments using DGE (Todd et al., 1981, 1986) demonstrated that HEK cells could be separated into some 20 fractions with several major groups of cells producing high levels of u-PA. The highest secreting cells were found to have a characteristic EPM that was approximately 15 percent lower than that of the most mobile cells. In comparison, CFES separations showed a bandsread of 35 electrophoretic fractions, containing five or six major subpopulations, which produced high levels of u-PA (Morrison and Lewis, 1983; Lewis et al., 1982). In these studies the highest producing subpopulation typically had an EPM approximately 30 percent less than that of the most mobile cells. The relationship of these combined findings to those of microgravity experiments is detailed below (see Figure 8).

Replicated quantitative assays of the slowest and fastest electrophoretic fractions are seldom feasible, owing to limited cell numbers per fraction.<sup>6</sup> Attempts to increase sample input concentration greater than  $2.5 \times 10^6$  cells/ml in CFES ground-based experiments resulted in a reduction in the mean migration distance and in the bandsread of the distribution. This could be due to cell-to-cell interactions which have been shown to affect the EPM of cultured mammalian cells, but not erythrocytes (Todd and Hjertén, 1985).

In cell separations in microgravity, separated HEK cells were collected in 45 fractions from CFES experiments on STS-8, however, low cell numbers and viability in the most mobile cells resulted in only 36 cultured subpopulations. Figures 5a and 5b show the electrophoretic distributions of cells separated in the flight and control experiments. The mean migration distance of cells in the flight experiment was approximately 30 percent greater than that of the ground controls (see Figure 5a). The breadth and heterogeneity of the EPM distribution in the space experiments was also greater.

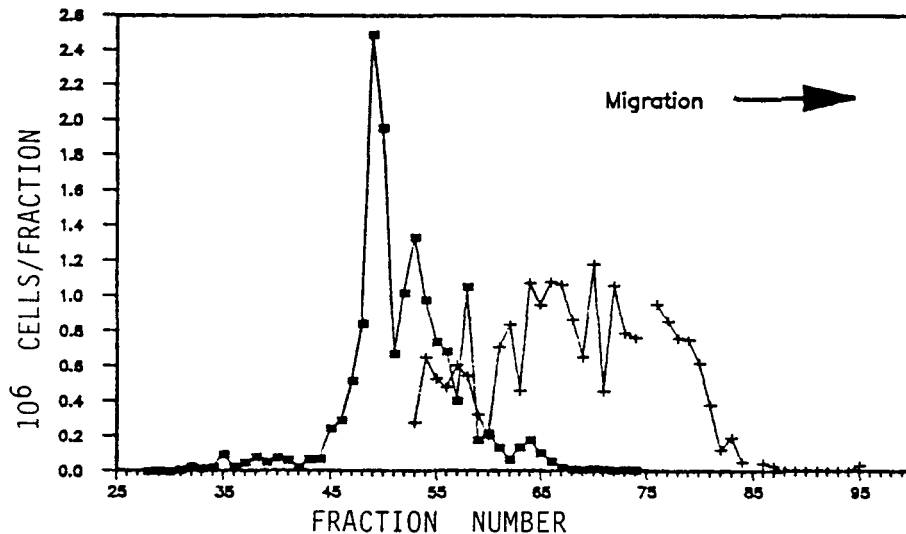


Figure 5a. Electrophoretic distribution of HEK cells separated by CFES in 1-g (squares) and micro-g (+). In micro-g the cells migrated farther, although the separation potential was similar. The mean migration in both flight experiments was 14 fractions closer to the anode than that of the ground controls. Input sample concentration was  $7.2 \times 10^6$  cells/ml for ground control Run 5c and  $8.0 \times 10^6$  cells/ml for Run 4, in flight. Migration is shown from left to right and fraction number is relative to sample inlet tube.

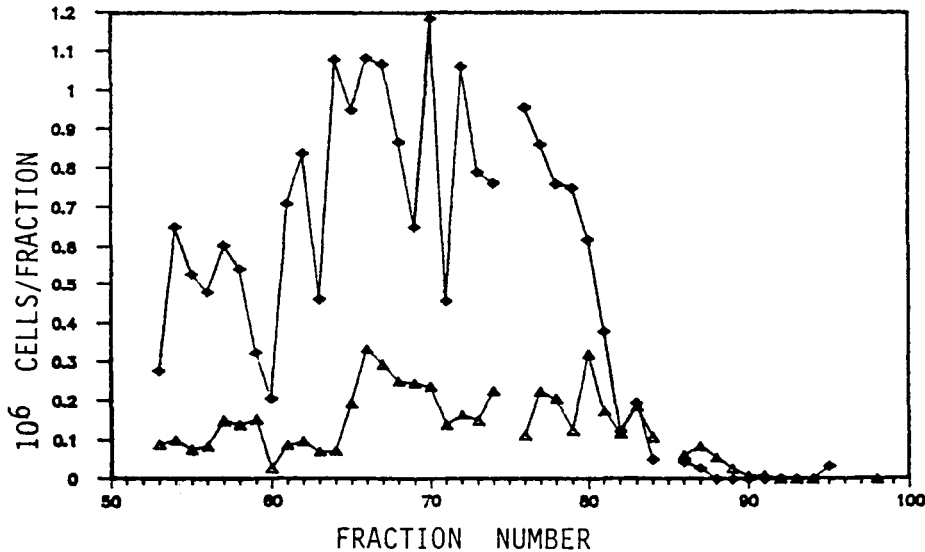


Figure 5b. Distributions of HEK cells from both CFES runs conducted in micro-g. Input cell concentration was  $2.6 \times 10^6$  cells/ml for Run 3 (triangles) and  $8.0 \times 10^6$  cells/ml for Run 4 (diamonds). Narrowing of the EPM distribution did not occur at cell concentration  $> 2.6 \times 10^6$  cells/ml as had been observed in ground-based CFES experiments.

Calculations indicated that six to eight of the lowest mobility fractions might not have been collected in the flight experiments due to preflight selection of the 50 sample outlets that were connected to the 50 bags in the sample trays. Figure 5b shows that the EPM patterns of the two flight experiments were similar. No reduction in mean migration distance or bandspread was noted at the higher input cell concentration (Run 4). Figure 6a shows the urokinase (u-PA) production rate of the ground control fractions as measured by the S-2444 chromogenic substrate assay. Most of the fractions in the upper 15 percent and lower 50 percent of the distribution produced low levels of u-PA. Several fractions in the upper 50 to 80 percent of the distribution produced high levels of u-PA. Figure 6b shows that the u-PA secretion from flight cells was considerably greater in the lowest 30 percent, and some productive fractions were found in the uppermost 20 percent of the electrophoretic distribution. In both the ground and flight distributions the highest producing subpopulation was found at approximately the same point in the distribution (86% of maximum migration distance). Secretion of other PA's and PA inhibitors also was found and is described in detail by Barlow et al., (1987, this volume).

Postflight analysis of the EPM distribution of individual fractions, collected in space and then subcultured on Earth, indicated that the progeny cells studied had mobilities that were related to the fractions from which they were collected. However, Figure 7 shows that the fraction studied with the lowest original mobility (Exp 1530) produced differentiated progeny cells which had a greater EPM (Morrison et al., 1984a). Summarized comparisons of the results of different methods of preparative electrophoresis, both in 1-g and in micro-g, show that the subpopulations of HEK cells that produce PA's at the greatest or higher than average rates have the same relative EPM's (Todd et al., 1986) (see Figure 8). Microscopic studies of cells cultured after separation showed a unique distribution of four morphological types which are believed to have different physiological functions (see next section: Figures 9 and 10).

#### 4. Discussion of procedures and results

Minor in-flight problems occurred during redispersion of the cells prior to injection into the CFES and with the automatic syringe drive mechanism, and fewer cells were processed in micro-g than planned. An apparent preflight microbial contamination of the CFES device could not be eliminated due to Shuttle turnaround operations that did not allow the CFES to be removed from the Challenger between STS-7 and STS-8. The contamination caused significant changes in the postflight procedures.

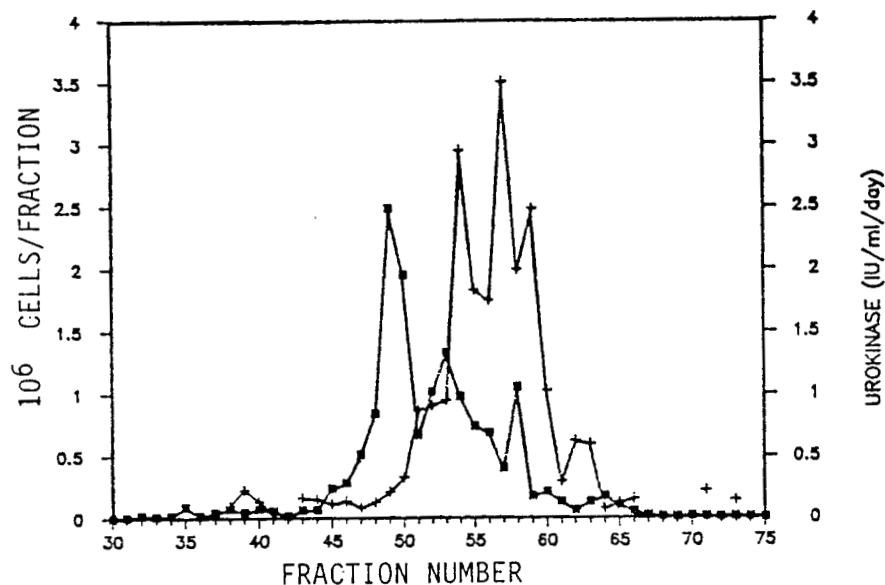


Figure 6a. Electrophoretic distributions of cell number (squares) and urokinase production as measured by S-2444 chromogenic substrate assay (+) following separation of HEK cells by CFES at 1-g, then cultured in 8-10 replicated cultures per fraction seeded at 3000 cells/cm<sup>2</sup>, grown to 95% confluence and changed to u-PA production medium. Most fractions in the lower half of the EPM distribution (Fractions 30-50) produced minimal levels of urokinase. Fraction number is relative to sample inlet tube. (Ground experiment 5c).

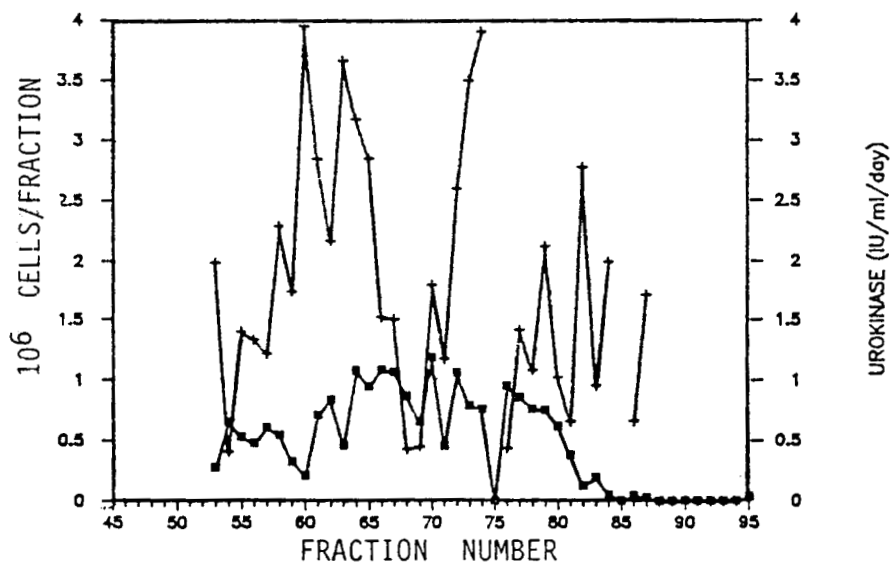


Figure 6b. Comparison of cell number (squares) and u-PA production (+) by HEK cells separated by CFES in microgravity. EPM distribution was broader than that of 1-g experiment (Figure 6a). Most fractions in lower mobility range (fractions 53-66) were high producers of u-PA as compared with ground control experiment (Figure 6a). (Flight experiment 4).



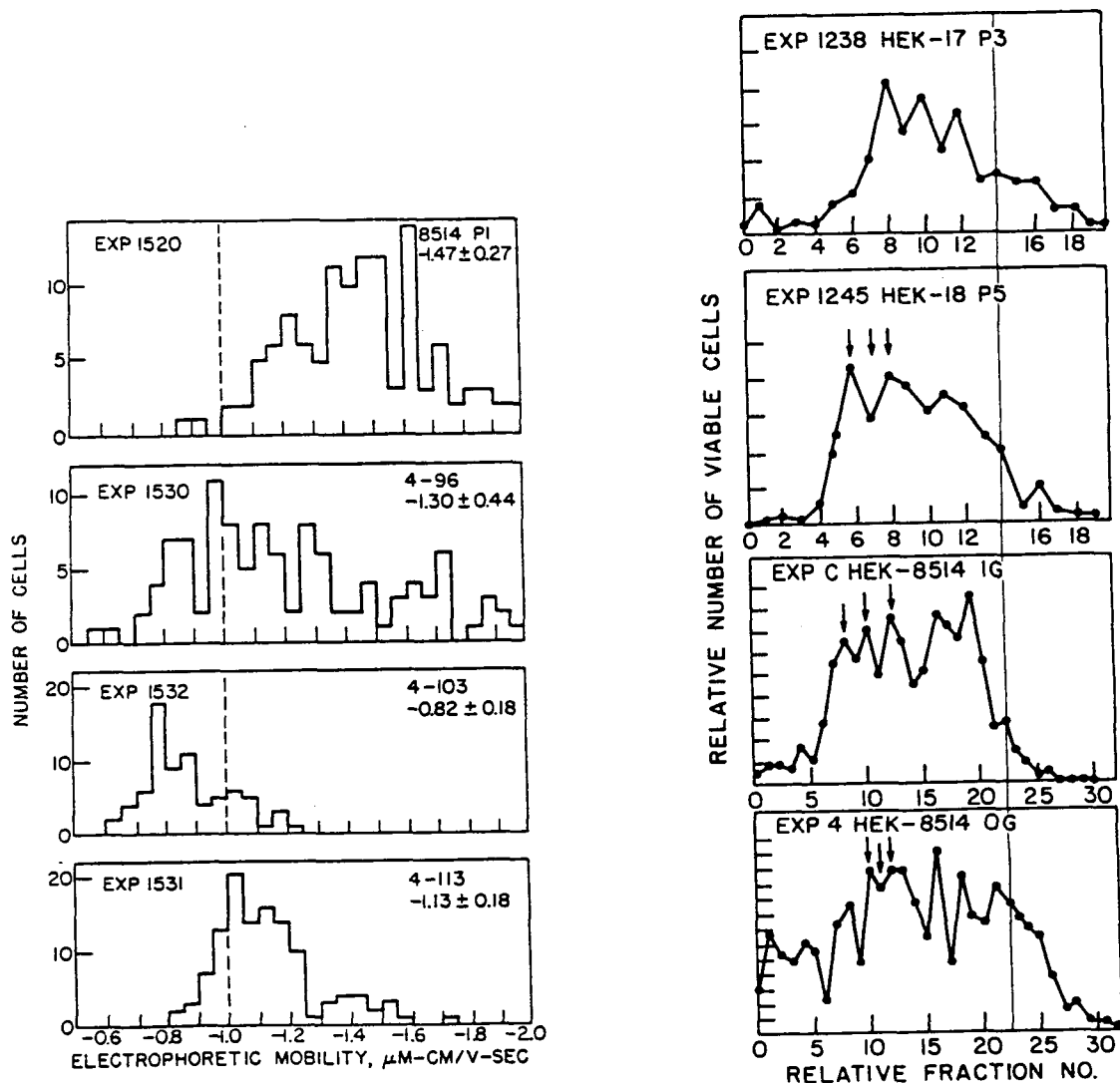


Figure 7. (Left) Electrophoretic mobility (EPM) distributions of starting mixture (top) and 3 fractions of human embryonic kidney cells (strain HEK-8514) separated by Continuous Flow Electrophoresis in microgravity and subsequently grown in cell culture. Original EPM is linearly related to fraction number (96, 103, and 113 in this case). The low EPM fraction (number 96) yielded higher-EPM progeny cells (from Morrison et al., 1984a).

Figure 8. (Right) Electrophoresis profiles of three kidney cell strains, separated by three different methods of preparative cell electrophoresis. The relative number of viable cells is plotted against electrophoretic fraction, renumbered, and scaled so that direct comparisons are possible. The cell strain number is indicated on each panel. The data in the top two panels were obtained from density-gradient electrophoresis experiments, and the lower two panels are data from continuous-flow electrophoresis experiments. Experiment 4 (in the bottom panel) was performed on Space Shuttle Flight STS-8. The solid, vertical line marks the fraction which, in every case, gave rise to cells with the highest level of plasminogen activator production, while downward arrows indicate fractions with above-average production (from Todd et al., 1986).

The bacteria were resistant to antibiotics which HEK cells can tolerate, and this contamination eventually resulted in the loss of 25 percent of the HEK flight samples.

## FLOW CYTOMETRY APPLICATIONS IN THE ANALYSIS OF CFES FRACTIONS

### 1. Cell subpopulations in human embryonic kidney cultures

Flow cytometry was applied to the analysis of fractions of electrophoretic cells that produce PA's. As there are five morphological subpopulations identifiable in cultures of HEK cells (domed, fenestrated, large and small epithelioid, and fibroblastoid cells), shown as sketched in Figure 9, different types of cells should exhibit different light scatter properties. Unseparated and electrophoretically separated kidney cells were therefore analysed on the EPICS V cell sorter (Coulter Electronics, Hialeah, FL) to attempt to characterize the light scattering signatures of the various morphological types and to attempt to relate morphology to enzyme production.

### 2. Materials and Methods

HEK cells were separated by microgravity electrophoresis on space shuttle flight STS-8 (Morrison et al., 1984, 1984a). Counts of viable cells were made on each sample. The cells were then plated for propagation in culture. After allowing time for attachment and flattening, the medium was replaced with urokinase production medium (UKPM), and after several days the amount of urokinase per sample was determined. Several fractions were further propagated, and the per cent of each morphological cell type was determined by phase contrast microscopy by counting at least 200 cells in each fraction.

HEK cells obtained from MA Bioproducts were put into a single cell suspension using 0.05% trypsin and 0.37% EDTA in saline A and were analysed on the EPICS V cell sorter. Two-parameter 488 nm light scatter distributions were obtained (forward angle light scatter and 90° integrated light scatter pulse) as well as 90° pulse-width "time-of-flight" for cell sizing (Leary, et al., 1978). Two-parameter distributions combining these measurements were obtained of HEK cell subpopulations that had been purified by microgravity electrophoresis and subsequently propagated in culture.

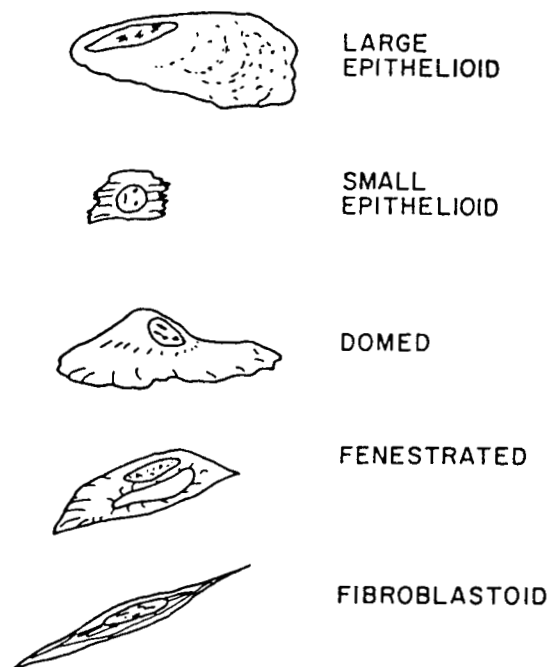


Figure 9. Sketches of the 5 major identifiable cell types found in early-passage human embryonic kidney cell cultures.

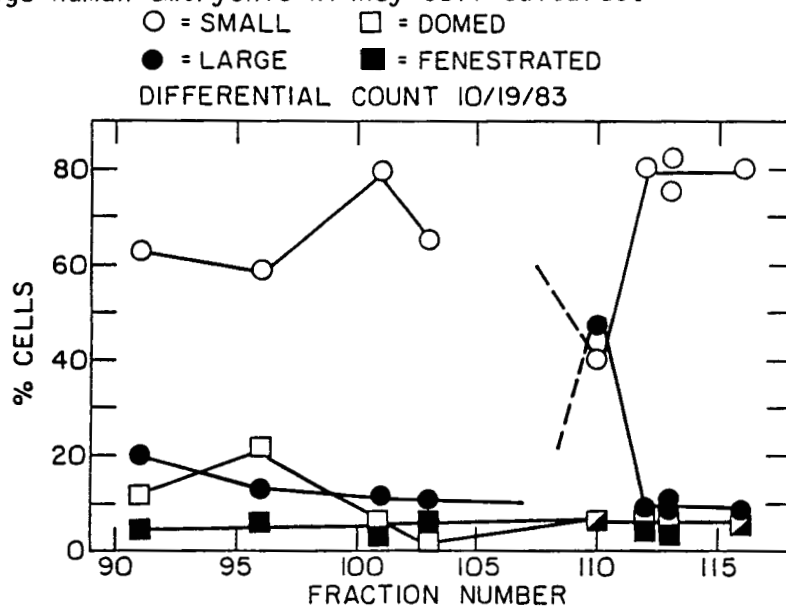


Figure 10. Electrophoretic distribution of the 4 morphological types of cultured HEK cells retrieved from STS-8 separation experiment. Cultures consisted of progeny of cells one passage after retrieval.

Flow cytometry can be used to identify plasminogen activator containing cells by using a fluorescent staining method for cells that contain plasminogen activators, especially urokinase. The general approach to this problem was similar to that used by Dolbeare and Vanderlaan (1979). First a simple staining technique was tested in which a fluorogenic substrate was mixed with cells and the cells were analyzed by fluorescence flow cytometry. The kidney cell strain which was designated "1593", and which was found to be high in cells producing PA's, was tested. Cells were maintained either on complete culture medium or urokinase production medium (UKPM) (Barlow et al., 1977a). Cells were suspended by trypsinization and exposed briefly to the fluorogenic substrate CBZ-gly-gly-arg-MNA. Cleavage of the basic arginyl amide bond releases 4-methoxy-2-naphthylamine, which can be stimulated to fluoresce by the 488 nm light from the argon ion laser of the EPICS V cell sorter. Fluorescent light was detected through a 590 nm band pass filter.

### 3. Results

The first passage progeny of cells obtained from fractions 91, 96, 101, 103, 110, 112, 113, and 116 of flight experiment 4 were counted according to morphological type at various times after retrieval. The distributions of the four principal morphological types among these fractions is shown in Figure 10.

The size measuring capability of the EPICS V sorter, which is a pulse-height-independent measure of pulse width using the unintegrated  $90^\circ$  light scatter signal ("time of flight") was calibrated with different sizes of microspheres, and a resolution of 0.45  $\mu\text{m}/\text{channel}$  was obtained, as shown in Figure 11. Microscopic measurements of HEK cells were also performed using 9.5, 14.5 and 20.5  $\mu\text{m}$  microspheres as standards. The size distribution is shown in Figure 1, where it is seen that the majority of these passage-1 HEK cells are between 15 and 25  $\mu\text{m}$  in diameter. Size was used as a correlated parameter with light scatter intensity in Figures 12-14.

The integrated  $90^\circ$  light scatter signal intensity reflects the internal structure of the cell, including granulation (Goolsby, 1985), nuclear size (Brunsting and Mullaney, 1972), and shape (Latimer et al., 1978). Granular cells should scatter more light at  $90^\circ$  than non-granular cells. Forward angle light scatter (2.5-19 degrees) is a measure of size and refractive index in live cells (Leary, Notter and Todd, 1978; Goolsby, 1984). Cells with a high refractive index have reduced forward angle light intensity.

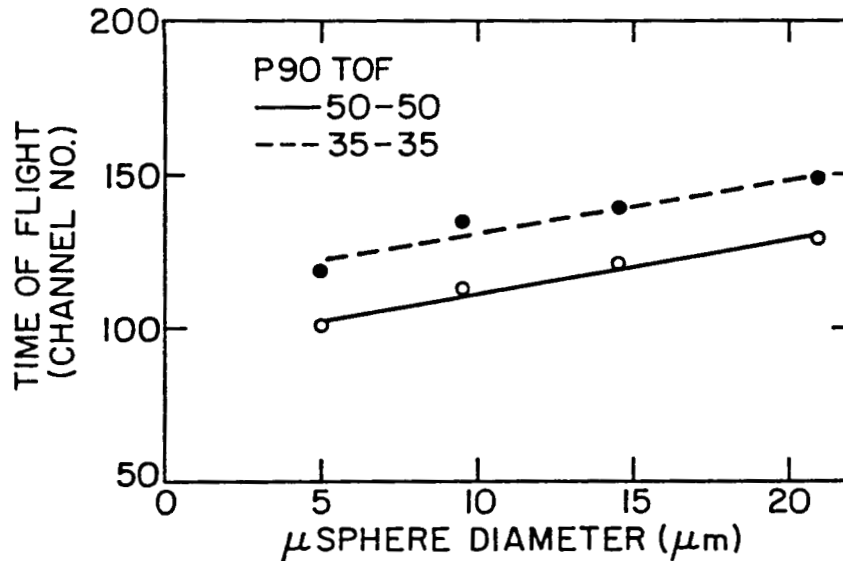


Figure 11. Calibration curve for pulse-height-independent time-of-flight sizing using 5, 10, 15, and 20  $\mu\text{m}$  spheres. Pulse width measurements were made at 50% (solid line) and 35% (dashed line) of the peak height of the raw (unintegrated)  $90^\circ$  ( $70-110^\circ$ ) light scatter signal.

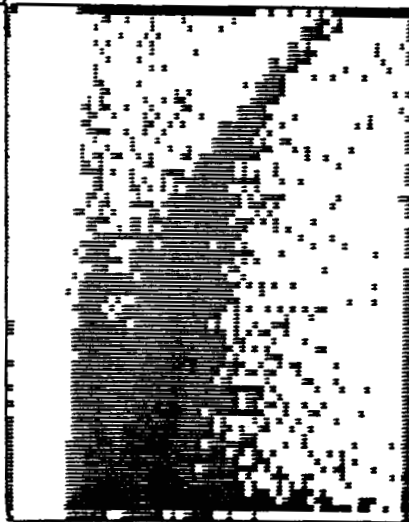
P90TF-I90LS  
898

25000

P90TF-I90LS  
1946

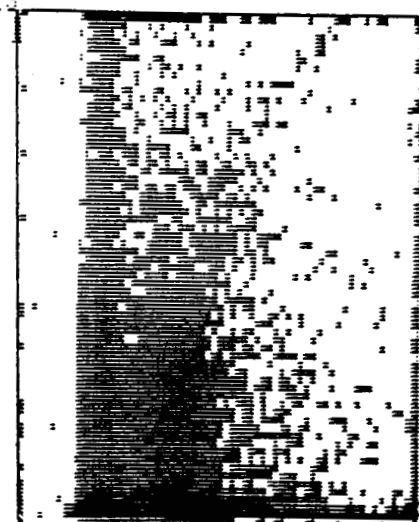
25000

I90LS



P90TF

I90LS



P90TF

Figure 12. Two examples of raw histograms from the EPICS V cell sorter. Four two-parameter light scatter distributions were obtained on each fraction available after the Shuttle flight. These are scattergrams of integrated  $90^\circ$  light scatter signals (ordinate) vs of time-of-flight cell diameter (abscissa) for two of the separated fractions from the STS-8 experiment. Darker areas indicate higher cell counts.

ORIGINAL PAGE IS  
OF POOR QUALITY

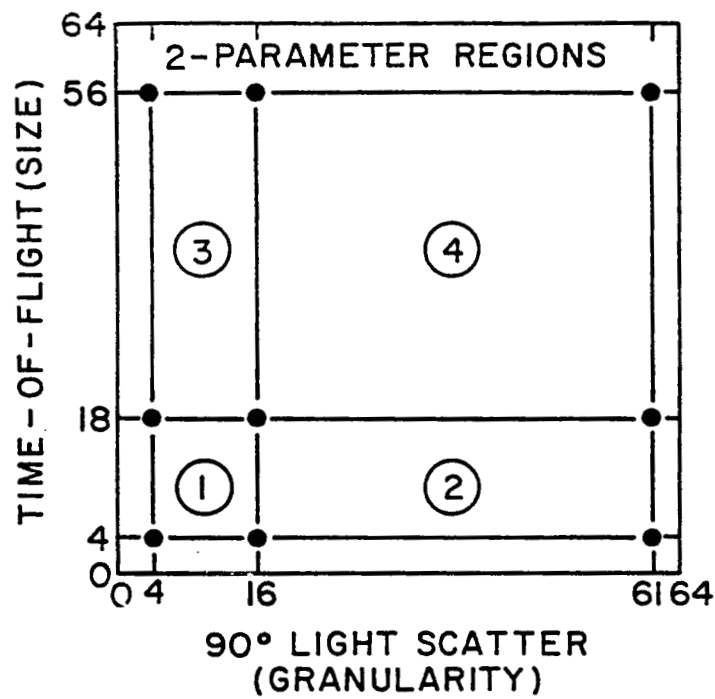


Figure 13. A diagram of the method of analysis of the histograms of the type shown in Figure 12. Each two-parameter histogram was divided into four regions, and the percentages of cells falling into each region was determined. Note inversion of axes relative to Figure 12 (region 3 cells lie along the abscissa in Figure 12).

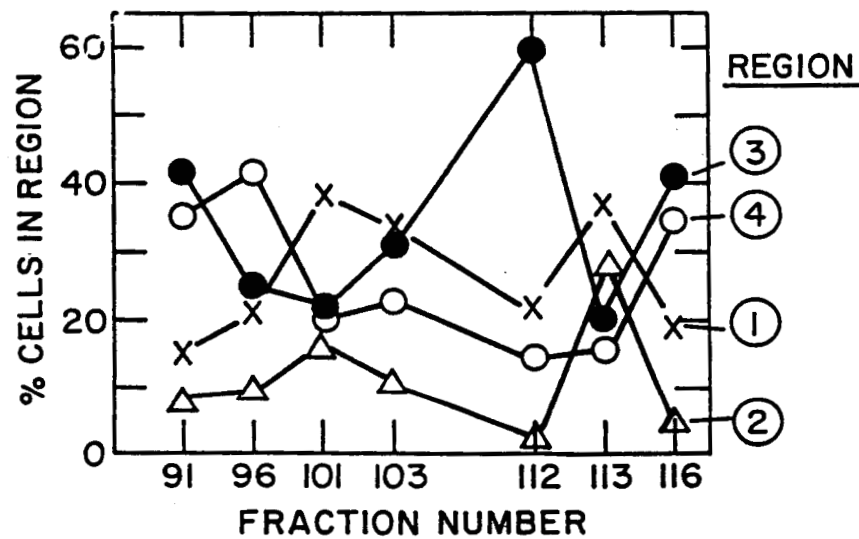


Figure 14. Percentages of cells from each electrophoretic fraction falling into each of the 2-parameter regions defined in Figure 13. Region 1 contained debris and was therefore eliminated from further analysis.

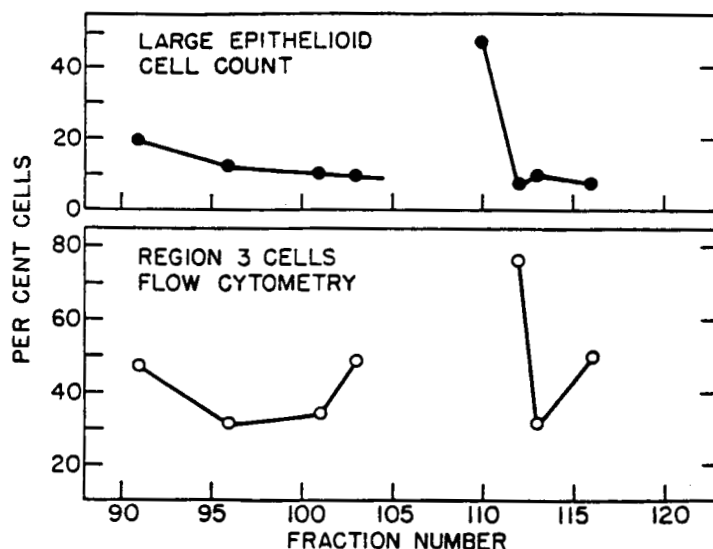


Figure 15. Comparison of morphological and flow cytometric light scatter analyses of cells separated on Space Shuttle flight STS-8. Percentage of large epithelioid cells as determined microscopically from cells in culture is given on the upper graph, and the percentage of cells in Region 3 (see Figures 13 and 14) determined by flow cytometry is given on the lower graph. Large size and low granularity are consistent with appearance of large epithelioid cells. Highest plasminogen activator activity was found in fraction 110, which corresponds to fraction 73 of Figure 6b.

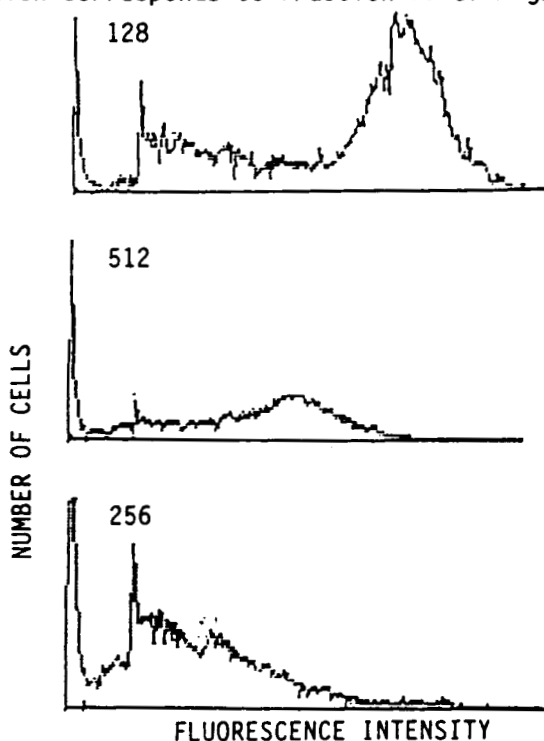


Figure 16. Fluorescence intensity distributions of cultured human embryonic kidney cells "1593" at the 5th passage stained with CBZ-gly-gly-arg-4-methoxy-2-naphthylamide after cultivation in microcarrier medium "MM1" plus 10% fetal bovine serum (TOP distribution) or 3 days after transfer to serum-free production medium "UKPM" (MIDDLE distribution) compared to unstained cells (BOTTOM distribution).

Single cell suspensions of the above-mentioned electrophoretic fractions were analyzed on the EPICS V cell sorter. Two-parameter distributions of integrated  $90^0$  light scatter vs time-of-flight, integrated  $90^0$  light scatter vs forward angle light scatter, and integrated  $90^0$  light scatter vs peak  $90^0$  light scatter were acquired. Two examples of these distributions are shown in Figure 12. Each distribution was divided into four regions (Figure 13), and the percentage of cells in each region was determined for each fraction (Figure 14).

A selected portion of these results, is compared with and the morphological observations are shown in the 2 graphs of Figure 15. Large size and low granularity correlated with a high frequency of large epithelioid cells, as expected, and a high frequency of epithelioid cells correlates with high total plasminogen activator production (Figures 6 and 8).

When cells were stained for plasminogen activator content by the fluorogenic substrate method the resulting fluorescence distributions revealed subpopulations of stained and unstained cells. Incubation in UKPM actually decreased cell fluorescence (possibly due to such cells having already secreted their PA), and unstained cells had the same fluorescence distribution (roughly) as the low intensity population in stained cells. These findings are illustrated by the three fluorescence distributions given in Figure 16.

#### 4. Conclusions

Results of flow cytometric light scattering experiments with prepurified cultured human kidney cells indicate that subpopulations of living cells that were high in plasminogen activator also contained the highest percentage of cells with large size and low  $90^0$  light scatter intensity and that these cells corresponded to the large epithelioid population.

By staining cells with a fluorescent substrate, it has been shown, in preliminary experiments, that plasminogen activator is synthesized and retained by cells multiplying in growth medium and released by cells transferred to serum-free production medium.

#### CONCLUSIONS AND FUTURE RESEARCH

Cultures of human embryonic kidney cells consistently contain an electrophoretically separable subpopulation of cells that produce high levels of urokinase and have an EPM about 85% as high as that of the most



mobile HEK cells. This subpopulation is rich in large epithelioid cells that have relatively little internal structure. When resolution and throughput are adequate free-fluid electrophoresis can be used to isolate a broad band of low mobility cells which also produces high levels of PA's.

In the course of performing this research we have discovered that all electrophoretic subpopulations of cultured human embryonic kidney cells produce some plasminogen activators and that separate subpopulations produce high quantities of different types of PA's. This information and the development of sensitive assays for this project have provided new insights into cell secretion mechanisms related to fibrinolysis. These advances would probably not have been made without the NASA program to explore fundamental questions of free-fluid electrophoresis in space and McDonnell Douglas Astronautics Co.'s Joint Endeavor Agreement with NASA.

The results of STS-8 demonstrated some advantages of cell separations in microgravity; however, the experiments must be repeated under optimized conditions and with the use of refined assay techniques to determine the full potential of CFES for live cell separations. Enough viable cells in each subpopulation must be returned for the functional assays to be able to identify the important fractions, which then can be subcultured for continued studies. Postflight research will determine the factors that affect the relationship between cell surface charge in an electrophoresis buffer and subsequent secretory function in a complex medium following growth and maintenance under various culture conditions.

The current and planned research is focused on preparations for the next CFES flight opportunity and on improvements in micro-g experiment conditions and sample storage. Ground control studies include quality control of flight cell lots, optimization of CFES buffers, improvements in pre- and post-separation storage conditions, testing effects of chemical disinfectants used in the CFES, and cell tolerance to antibiotics required for microbial contamination control. Post-separation growth and function studies are used to determine cell viability ranges and the typical retention of target cell function following storage and successive subcultures. This work is being conducted in collaboration with the Biochemical Assays of Kidney Cells and Bioseparations (CFES) research project at the Bioprocessing Research Center at Houston (Barlow et al, 1987, this volume) and at Johnson Space Center.

## ACKNOWLEDGEMENTS

The dedicated participation of the technical staffs of the four organizations that hosted this research is gratefully acknowledged. The careful attention given to the experiments on orbit by the STS-8 crew members was a vital component of the success of this research. Although the participants are too numerous to mention individually, the additional leadership provided by Prof. W. C. Hymer and the completion of the manuscript through the efforts of Ms. T. Thompson are particularly noteworthy. Gratitude is extended to the management and leadership of McDonnell Douglas Astronautics Co. for the use of the CFES and buffers on orbit and on the ground through a Joint Endeavor Agreement with the U. S. National Aeronautics and Space Administration, which supported this work financially through contracts NAS 9-15583, NAS 9-16389, NAS 9-16550, and NSA 9-17440.

## REFERENCES

- Allen, R.E., P.H. Rhodes, R.S. Snyder, G.H. Barlow, M. Bier, P.E. Bigazzi, C.J. van Oss, R.J. Knox, G.V.F. Seaman, F.J. Micale, and J.W. Vanderhoff. Column electrophoresis on the Apollo-soyuz Test Project. *Sep. Purif. Meth.*, 1-59 (1977).
- Barlow, G.H., S.L. Lazer, A. Rueter, and R. Allen. Electrophoretic separation of human kidney cells at zero gravity. In D.R. Morrison, Ed. *Bioprocessing in Space*, NASA TM X-58191, Lyndon B. Johnson Space Center, January 1977, pp. 125-142.
- Barlow, G.H., A. Rueter, and I. Tribby. Biosynthesis of plasminogen activator by tissue culture technique. *Vascular Surg.* 11, 406-412 (1977a).
- Barlow, G.H., M.L. Lewis, and D.R. Morrison. Biochemical assays on plasminogen activators and hormones from kidney sources. This document (1987).
- Boltz, R.C. and P. Todd. Density gradient electrophoresis of cells in a vertical column. In *Electrokinetic Separation Methods* (Eds. P.G. Righetti, C.J. van Oss, and J. Vanderhoff) Elsevier/North-Holland Biomedical Press, Amsterdam, 1978, pp. 229-250.
- Brunsting, A. and P.F. Mullaney. Light scattering from coated spheres: model for biological cells. *Appl. Opt.* 11, 675-680, 1972.
- Dolbeare, F.A and M. Vanderlaan. A fluorescent assay of proteinases in cultured mammalian cells. *J. Histochem. Cytochem.* 27, 1493-1495 (1979).

Goolsby, C.L. Application of light-scattering theory to flow cytometry of stained cells. M.S. dissertation, The Pennsylvania State University, University Park, PA, 1984.

Goolsby, C.L. Theory and applications of light scattering by cells in flow cytometry. Ph.D. Thesis. The Pennsylvania State University, University Park, PA, 1985.

Hannig, K., H. Wirth, B. Neyer, and K. Zeiller. Free-Flow electrophoresis I. Theoretical and experimental investigations of the influence of mechanical and electrokinetic variables on the efficiency of the method. Hoppe-Szeilyers Z. Physiol. Chem. 356, 1209-1223 (1975).

Hymer, W.C., G.H. Barlow, C. Cleveland, M. Farrington, R.E. Grindeland, J.M. Hatfield, M.E. Kunze, J.W. Lanham, M.L. Lewis, D.R. Morrison, N. Olack, D. Richman, J. Rose, D. Scharp, R.S. Snyder, P. Todd, and W. Wilfinger. Continuous flow electrophoretic separation of proteins and cells from mammalian tissues. Cell Biophysics 10, 000-000 (1987). (In Press).

Kadouri, A. and Z. Bohak. Production of plasminogen activator by cells in culture. Adv. Biotechnol. Processes 5, 275-299 (1985).

Latimer, P., A. Brunsting, B.E. Pyle, and C. Moore. Effects of asphericity on single particle scattering. Appl. Opt. 17, 3152-3158 (1978).

Leary, J.F., M.F.D. Notter, and P. Todd. Laser flow cytophotometric immunoperoxidase detection of herpes simplex virus type 2 antigens in infected cultured human cells. J. Histochem. Cytochem. 25, 1249-1257 (1976).

Leary, J.F., P. Todd, J.C.S. Wood, and J. H. Jett. Laser flow cytophotometric light scatter and fluorescence pulse width and pulse rise-time sizing of mammalian cells. J. Histochem. Cytochem. 27, 315-320 (1979).

Lewis, M.L., G.H. Barlow, D.R. Morrison, D.S. Nachtwey, and D.L. Fessler. Plasminogen activator produced by sub-populations of human embryonic kidney cells separated by continuous flow electrophoresis. In Progress in Fibrinolysis 6, Churchill Livingstone, Edinburgh 1982, Chapter 33.

Lewis, M.L., D.R. Morrison, B.J. Mieszkuc, and D.L. Fessler. Problems in bioassay of products from cultured HEK cells: Plasminogen activators, In Advances in Experimental Medicine and Biology, Eukaryotic Cell Culture Basic and Applications, Ed. R.T. Acton and J.D. Lynn, Plenum Press, New York, 1984, pp. 241-250.

Mason, D.W. A diffusion driven instability in systems that separate particles by velocity sedimentation. *Biophys. J.* 16, 407-416 (1976).

McCreight, L.R. Electrophoresis for biological production. In Bioprocessing in Space, Ed. D.R. Morrison, NASA TMX-58191 (1977), pp.143-158.

Morrison, D.R., and M. L. Lewis. Electrophoresis tests on STS-3 and ground control experiments: A basis for future biological sample selections. 33rd International Astronautical Federation Congress. International Astronautical Federation, 1983, Paper No. 82-152.

Morrison, D.R., G. H. Barlow, C. Cleveland, R. Grindeland, W.C, Hymer, M. E. Kunze, J. W. Lanham, M. L. Lewis, B. E. Sarnoff, P. Todd, and W. Wilfinger. Electrophoretic separation of kidney and pituitary cells on STS-8. *Adv. Space Res.* 4(5), 67-76 (1984).

Morrison, D.R., M. L. Lewis, C. Cleveland, M. E. Kunze, J. W. Lanham, B. E. Sarnoff, and P. Todd. Properties of electrophoretic fractions of human embryonic kidney cells separated on Space Shuttle flight STS-8. *Adv. Space Res.* 4(5), 77-79 (1984a).

Plank, L.D., W. C. Hymer, M. E. Kunze, G. M. Marks, J. W. Lanham and P. Todd. A study of cell electrophoresis as a means of purifying growth hormone secreting cells. *J. Biochem. Biophys. Meth.* 8, 275-289 (1983).

Platsoucas, C.D. Separation of cells by preparative density gradient electrophoresis. In Cell Separation Methods and Selected Applications, Vol. 2, Ed. T.G. Pretlow II and T.P. Pretlow, Academic Press, NY, 1983, pp. 145-182.

Rose, A.L., and D.W. Richman. U.S. Patent No. 4,310,408 (1979).

Sarnoff, B.E., M. E. Kunze, and P. Todd. Electrophoretic purification of cells in space: Evaluation of results from STS-3. *Adv. Astronaut. Sci.* 53, 139-148 (1983).

Sharpless, T.K., M. Bartholdi, M.R. Melamed. Size and refractive index dependence of simple forward angle scattering measurements in a flow system using sharply focused illumination. *J Histochem. Cytochem* 25, 845, (1977).

Snyder, R.S., P. H. Rhodes, B. J. Herren, T. Y. Miller, G. V. F. Seaman, P. Todd, M. E. Kunze, and B. E. Sarnoff. Analysis of free zone electrophoresis of fixed erythrocytes performed in microgravity. *Electrophoresis* 6, 3-9 (1985).

Snyder, R.S., P.H. Rhodes, T.Y. Miller, F.J. Micale, R.V. Mann, and G.V.F. Seaman. Polystyrene latex separations by continuous flow electrophoresis on the space shuttle. *Sep. Sci. Technol.* 21, 157-185 (1986).

Todd, P. Microgravity cell electrophoresis experiments on the space shuttle: a 1984 overview. In *Cell Electrophoresis*, Eds. W. Schütt and H. Klinkmann, Walter de Gruyter & Co., Berlin, 1985, pp. 4-19.

Todd, P. Applications of free flow electrophoresis in orbital space flight. In *Electrophoresis '86*, Ed. M. J. Dunn, VCH Verlagsgesellschaft, Weinheim, 1986, pp. 3-12.

Todd, P. and S. Hjertén. Free zone electrophoresis of animal cells. I. Experiments on cell-cell interactions. In *Cell Electrophoresis*, Ed. W. Schütt and H. Klinkman, Walter de Gruyter & Co., Berlin, 1985, pp. 23-31.

Todd, P., W.C. Hymer, L.D. Plank, G.M. Marks, M. Hershey, V. Giranda, M.E. Kunze, and J.R. Mehrishi. Separation of functioning mammalian cells by density gradient electrophoresis. In *Electrophoresis '81*, Ed. R.C. Allen and P. Arnaud, Walter De Grueter Press, NY, 1981, pp. 871-882.

Todd, P., M.E. Kunze, K. Williams, D.R. Morrison, M.L. Lewis, and G.H. Barlow. Morphology of human embryonic kidney cells in culture after space flight. *Physicologist* 28 (supplement 6), 183-184 (1985).

Todd, P., L. D. Plank, M. E. Kunze, M. L. Lewis, D. R. Morrison, G. H. Barlow, J. W. Lanham, and C. Cleveland. Electrophoretic separation and analysis of living cells from solid tissues by several methods. Human embryonic kidney cell cultures as a model. *J. Chromatogr.* 364, 11-24 (1986).

DEMIXING KINETICS OF PHASE SEPARATED POLYMER SOLUTIONS  
IN MICROGRAVITY

D E Brooks

S B Bamberger

J M Harris

Depts of Pathology  
and Chemistry  
University of B.C.  
Vancouver, Canada

Dept of Neurology  
Oregon Health  
Sciences University  
Portland OR, USA

Dept of Chemistry  
University of  
Alabama  
Huntsville AL, USA

J Van Alstine & R S Snyder

Space Sciences Laboratory  
Marshall Space Flight Center AL, USA

# ABSTRACT

Phase-separated solutions of two neutral polymers in buffer provide a useful and versatile medium for the partition separation of biological cells. However, the efficiency of such separations is orders of magnitude lower than the thermodynamic limit. To test the hypothesis that this inefficiency is at least partially due to the convection and sedimentation that occur during the gravity-driven demixing that follows introduction of cells to the systems, we have begun a series of experiments aimed at performing cell partition in a low  $g$  environment. We have studied demixing of isopycnic three polymer-solvent systems, performed experiments on KC-135 aircraft and completed one shuttle mid-deck experiment. Analysis of the results of these experiments and comparisons with the predictions of scaling relations for the dependence of phase domain size on time, derived for a number of possible demixing mechanisms, are presented.

# INTRODUCTION

When two neutral polymers such as dextran and poly(ethylene glycol) (PEG) are mixed at constant temperature in aqueous solution above a set of critical concentrations two phases are formed. These have proven useful as partition media for the separation of a wide variety of biological macromolecules, organelles and cells (1,2). If the species to be separated are larger than a few hundred angstroms in diameter the distributions take place between one of the bulk phases and the interface between them, rather than between the two bulk phases as occurs with molecular partition. This is possible because the interfacial tension between the phases is extremely low (typically  $\leq 10 \mu\text{N/m}$ ), resulting in relatively weak adsorption of particulates in the interface.

Our principle interest in the present context is in the separation of cells. In this case it is clear that the partition behavior, i. e. the fraction of a population which is adsorbed at the interface as opposed to being suspended in one of the bulk phases, is determined by the surface properties of the cells and the manner in which these properties determine the interaction

between the cell and the two phases. To a major degree this interaction can be tailored through choice of the constituents of the two phase system. For instance, including certain salts such as phosphates or citrates in the mixtures produces a type of Donnan potential difference between the bulk phases which provides an electrostatic contribution to the free energy of adsorption of the cell at the interface (3). Hence, separations based on surface charge differences can be achieved. Similarly ligands, such as antibodies, which exhibit a high affinity for a surface feature on the cell subpopulation of interest can be modified by coupling one of the phase polymers to them and be included in the system. The polymer-modified ligands will then exhibit a strong preference for the phase in which that polymer is concentrated. Hence their binding to the targeted cells will result in that subpopulation partitioning into the phase in which the modified ligand accumulates, leaving, in optimal circumstances, the remaining cells adsorbed at the phase boundary (4,5).

The above picture implies that the free energy of adsorption, i.e., the decrease in free energy which occurs when the cell adsorbs at the interface between the two phases,  $\Delta G^\circ$ , should be the only characteristic of the system which determines the partition behavior. If thermodynamic equilibrium prevails the partition coefficient, K, (defined as the ratio of the number of cells free in the bulk phase to the number adsorbed at the interface) should be determined only by the free energy of adsorption and the temperature. Quantitatively, K should be given by the Boltzmann expression:

$$K = \exp [-\Delta G^\circ / kT] \quad (1)$$

where k is Boltzmann's constant and T is the absolute temperature. This equation predicts that in order to observe values of K in the range that is useful experimentally, (0.2 to 5, say)  $\Delta G^\circ$  must be within a factor of  $\pm 2$  of kT.

The above prediction has been tested (4,5). Without going into details, it is possible to calculate  $\Delta G^\circ$  if the equilibrium contact angle formed between the surface of a cell and the interface between the phases can be measured for a representative population of cells adsorbed at the phase boundary. By varying features such as the Donnan potential between the phases, the interfacial tension and the concentration of polymer-derivatized affinity ligand it is possible to vary the contact angle, and hence  $\Delta G^\circ$ , over a wide range. The partition coefficients are measured independently for each set of conditions and the predictions of the Boltzmann expression tested. The remarkable result is that K depends approximately exponentially on  $\Delta G^\circ$ , as predicted, but the apparent value of kT is several orders of magnitude greater than the actual value. This, along with other results discussed in (4), demonstrates that partition is a stochastic process but its characteristic energy is much larger than thermal energies. Put another way, a random selection of the cells which, on the basis of their adsorption free energy would be expected to be found at the interface following a distribution experiment, have been removed from that location and released into the bulk phase by forces which are not thermal in origin.

The forces responsible for removing cells from the interface have not been identified. We hypothesize, however, that they result from the complex hydrodynamic environment to which adsorbed cells are exposed as the cells are mixed with the phase system and the resulting emulsion allowed to settle and demix. The two bulk phases, which differ in density, collect at the bottom and top of the container chiefly via strong convective streams which in turn

set up secondary flows, creating a chaotic environment which produces relatively strong, unsteady shear forces. In addition, following the convection, sedimentation and flotation of phase droplets with cells adsorbed to their surfaces also occurs. At any stage in the demixing, then, fluid shear forces are present which may be responsible for the removal of cells from the phase boundary to which they are adsorbed. The goal of our program of space experiments, therefore, is to study partition in the absence of appreciable convection and sedimentation and to see how closely the partition process approaches thermodynamic behavior under these conditions.

## PHASE DEMIXING EXPERIMENTS

One obvious problem with the above approach is the possibility that in the absence of significant gravitational forces the two phase systems, once emulsified, may not demix in an acceptable length of time. This seemed to be a very real possibility before we began our experiments since Otto and Lacy (6) had reported that oil and water emulsions were extremely stable in a reduced gravity environment, showing no sign of demixing over a period of many hours. As a first step towards performing partitioning experiments in space, therefore, we have begun to study the demixing of mixed two phase polymer systems in the absence of appreciable gravitational effects.

Our work in this area to date has been of three types: studies on the demixing of an isopycnic two phase system containing three polymers in water; short term low g experiments on KC-135 aircraft and a single shuttle mid-deck experiment flown in April, 1985. In all three cases the experimental approach has been simply to mix the systems manually and to observe and photograph them as they demix with time.

### Experimental

The polymers were obtained from Pharmacia (dextran; Ficoll) and Union Carbide (PEG, Sentry Grade). Their approximate molecular weights are given in Table 1 where the compositions of the systems studied along with some of their physical properties are listed. The methods for making up and characterizing the phase systems are fully described in Chapter 3 of reference 2. Typical phase diagrams for the systems used are given in (1).

### Results of Ground Experimentation

The first systems examined were the isopycnic mixtures of dextran, Ficoll and PEG. While these systems are rather viscous and not generally useful for cell partitioning work they did prove to adequately model the behavior of dextran/PEG systems in microgravity. Demixing of these systems occurred over a period of approximately 10 min following mechanical mixing at constant temperature. Microscopically, domains of each phase could be detected 2 s after mixing. As the domains grew, reducing the area of interface, they formed three dimensional bicontinuous structures which eventually evolved into a central, dextran-rich phase surrounded by the Ficoll/PEG-rich phase. The latter phase spreads on the poly(methyl methacrylate) chamber wall when both phases are exposed to the plastic. Characteristic photographs taken over the first four minutes of demixing are shown in Fig. 1.



Table 1

Composition (% w/w) (DEX/PEG/FIC)	Salt	Dextran Type	Viscosity (cP)		Interfacial Tension (uN/m)	Density (g/ml)		Tie Line Length (% w/w)
			Top	Bottom		Top	Bottom	
(5/3.5/0) <sup>a</sup>	I	T500	3.36	24.6	5.24	1.0263	1.0563	9.41
(5/4/0) <sup>a</sup>	I	T500	3.41	32.1	10.54	1.0281	1.0566	10.97
(6/4/0) <sup>a</sup>	I	T500	3.76	44.3	19.22	1.0286	1.0545	11.59
(8/4/0) <sup>a</sup>	I	T500	4.38	69.1	34.71	1.0239	1.0697	14.11
(7/5/0) <sup>a,b</sup>	II	T40	4.96	12.2	6.00	1.0277	1.0578	11.69
(5.5/0.67/9.5) <sup>c,d</sup>	III	T500	39.6	19.4	3.9	1.072	1.072	ND <sup>e</sup>
(7/0.29/12) <sup>a,c,d</sup>	III	T500	ND	ND	16	1.085	1.085	ND

Composition and physical properties of phase systems with equal volumes of each phase containing the polymers dextran (DEX), poly(ethylene glycol) MW 8000 (PEG) and Ficoll 400 (FIC), (MW ~ 400,000). Salt concentrations: 109 mM  $\text{Na}_2\text{HPO}_4$ , 35 mM  $\text{NaH}_2\text{PO}_4$ , pH 7.2 (I); 150 mM NaCl, 7.3 mM  $\text{Na}_2\text{HPO}_4$ , 2.3 mM  $\text{NaH}_2\text{PO}_4$ , pH 7.2 (II); 84.6 mM  $\text{Na}_2\text{HPO}_4$ , 25.4 mM  $\text{NaH}_2\text{PO}_4$ , pH 7.5 (III).<sup>4</sup> All dextran fractions have  $M_w \sim 500,000$  except the (7/5/0) system which contains a fraction with  $M_w \sim 40,000$ .

a System flown during Space Shuttle flight 51-D.

b System flown on KC-135 aircraft.

c Isopycnic system at 1 g.

d The phase properties of the isopycnic systems are listed as follows: the Ficoll-rich phase in "Top" column, the dextran-rich phase in "Bottom" column.

e ND: not determined.

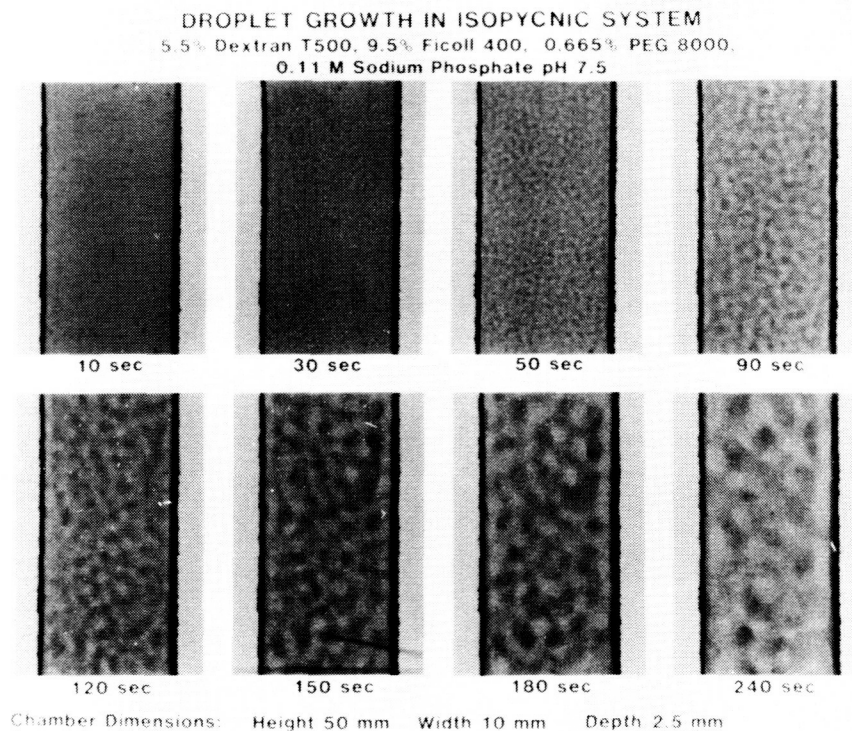


Figure 1. Growth of phase domains during the first 4 min of demixing of the (5.5/.67/9.5) isopycnic system described in Table 1.

To provide a measure of the rate of demixing, an estimate of the projected areas of the domains of each phase was made as a function of time after mixing. Slides taken at each time were projected, the outlines of connected domains traced and the area of each domain estimated following manual digitization. An example of the result at each stage is illustrated in Fig. 2 where the distribution of the drop areas measured is also given. The mean area at each time was used to calculate the radius of a circle of equivalent area to provide a characteristic linear dimension. The data, presented as a log-log plot, is shown in Fig. 3. The slope of this plot provides the power law coefficient which can be used to characterize the demixing rate.

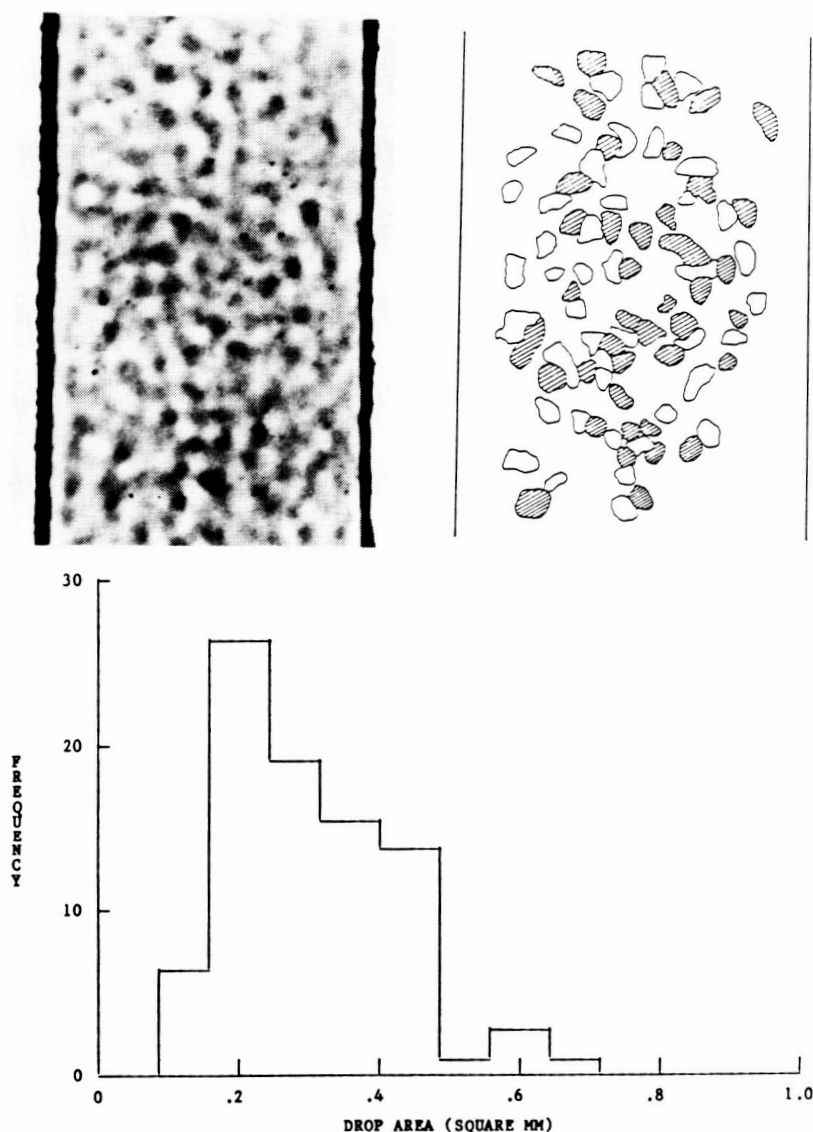


Figure 2. Isopycnic system (5.5/.67/9.5) 90 s after mixing, showing tracing of domains and frequency histogram of areas.

#### Results of Flight Experiments

An indication of the behavior to be expected with systems of use in cell partitioning was obtained by observing the early stages (first 20 s) of

demixing of dextran/PEG systems on KC-135 aircraft undergoing parabolic flight profiles. Qualitatively similar results to those seen with the isopycnic systems were obtained. The results were quite consistent from experiment to experiment, as shown by the overlapping of the data from three parabolas included in Fig. 3. The system illustrated in Fig. 3 demixed more rapidly than the isopycnic systems studied, perhaps because of the lower viscosities of the phases (Table 1).

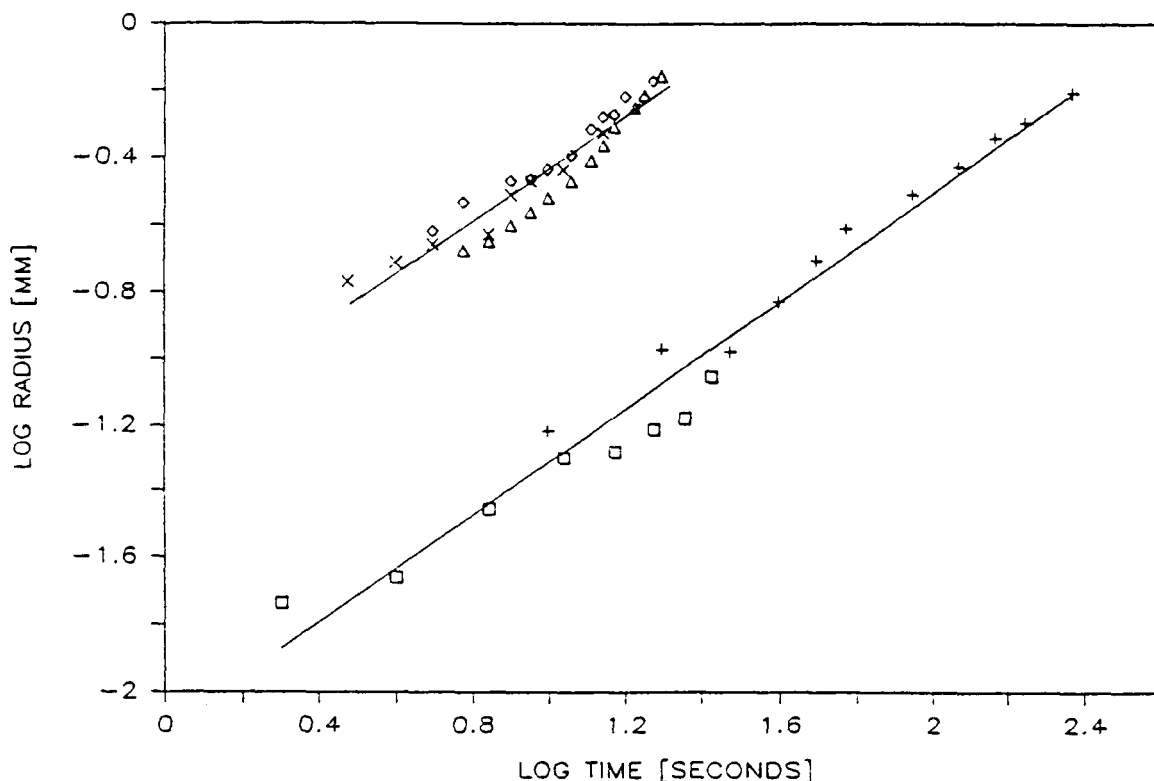


Figure 3. Log-log plot of characteristic length vs time for three KC-135 experiments on the (7/5/0) system (upper) and for the (5.5/.67/9.5) isopycnic system at 1 x g.

In April, 1985 on mission 51-D experiment PPE-1 was performed in which the time course of demixing was observed and photographed for a series of dextran/PEG systems as well as for one of the isopycnic mixtures, included as a control. The systems were contained in a small plastic box (10 x 13 x 3 cm) containing 15 transparent chambers (1.5 x 1.8 x 1.0 cm), each of which contained a stainless steel mixing ball as well as a two phase mixture. At the beginning of the experiment the box was shaken manually, the action of the steel balls being sufficient to emulsify each sample. The box was then taped to a fluorescent light box and photographed at appropriate times over a period of 110 min to record the evolution of the demixing. The time at which each exposure was made was printed directly on the film by the data back of the camera.

The control experiments performed on the ground are illustrated in Fig.4. The contents of the ten chambers illustrated are given below, using the designations defined in the legend to Table 1; the final fraction in the

description of each sample indicates the ratio of PEG-rich to dextran-rich phase volume. First row, left to right: (8/4/0)I, 2/3; (8/4/0)I, 3/2; (7/0.29/12)III, 1/1; (7/5/0)II, 1/1 and (7/5/0)II, 1/1. Second row, left to right: (8/4/0)I, 1/1; (6/4/0)I, 1/1; (5/4/0)I, 1/1; (5/3.5/0)I, 1/1 and (5/4/0)I, 1/1. All phase systems contained 0.05 mg/ml Trypan Blue (which accumulates in the PEG-rich phase) except the last chamber in each row which contained glutaraldehyde-fixed human erythrocytes.

Representative photographs taken from the space experiment are shown in Fig. 5. Qualitatively, comparison with the control experiment shows that in all cases demixing occurred more rapidly on the ground than in space. However, the systems (5/3.5/0; 5/4/0; 7/0.29/12) characterized by values of interfacial tension and viscosities typical of those useful for cell partitioning on earth demixed with a time course consistent with the requirements. Systems comprised of higher polymer concentrations, with larger differences in concentration between the phases (6/4/0; 8/4/0), were much slower to demix. The phase volume ratio also had a strong effect on the demixing rate in the (8/4/0) system. Interestingly, the chamber with the 1/1 mixture did not demix as soon as did that containing the lower amount of PEG-rich phase. In the sample in which this ratio was reversed, no visible demixing occurred over the time course of the experiment.

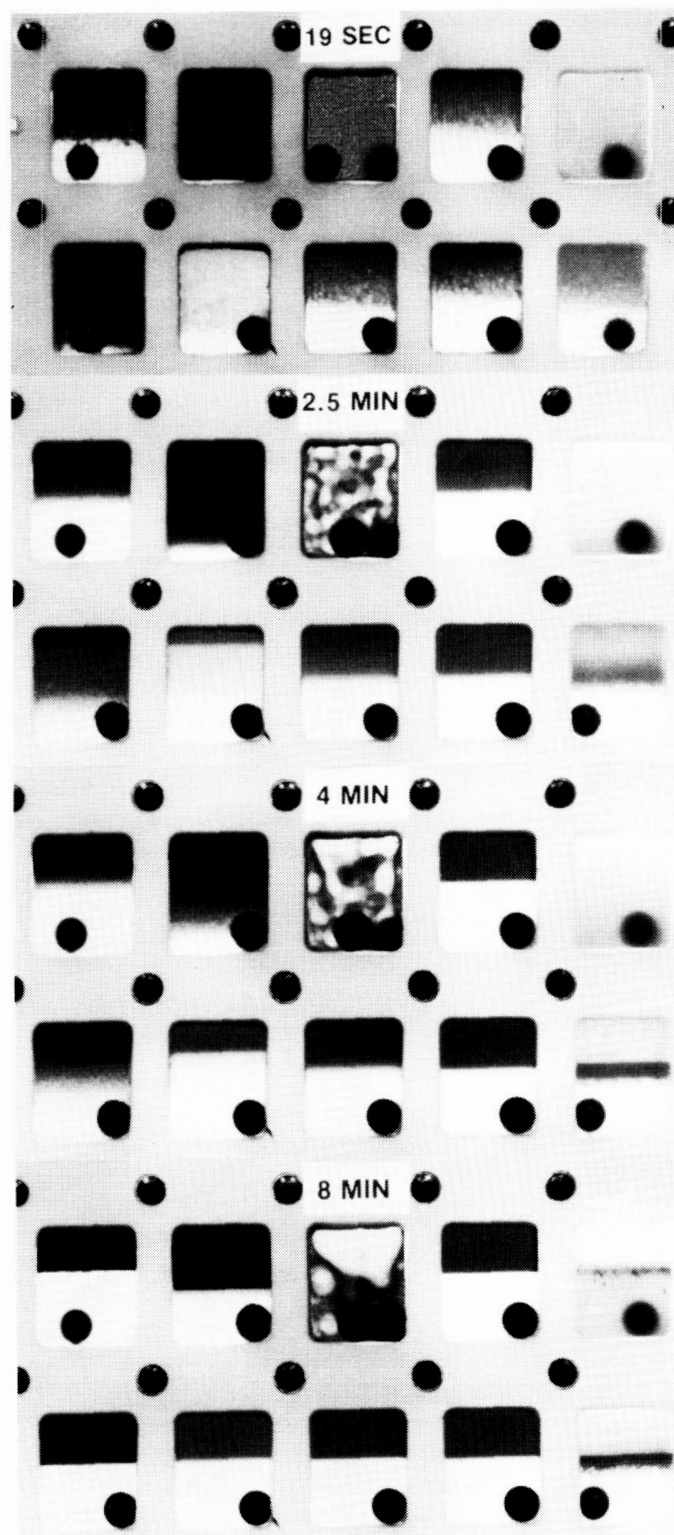


Figure 4. Control 1 x g demixing experiment for PPE-1; see text for description of the systems.

ORIGINAL PAGE IS  
OF POOR QUALITY

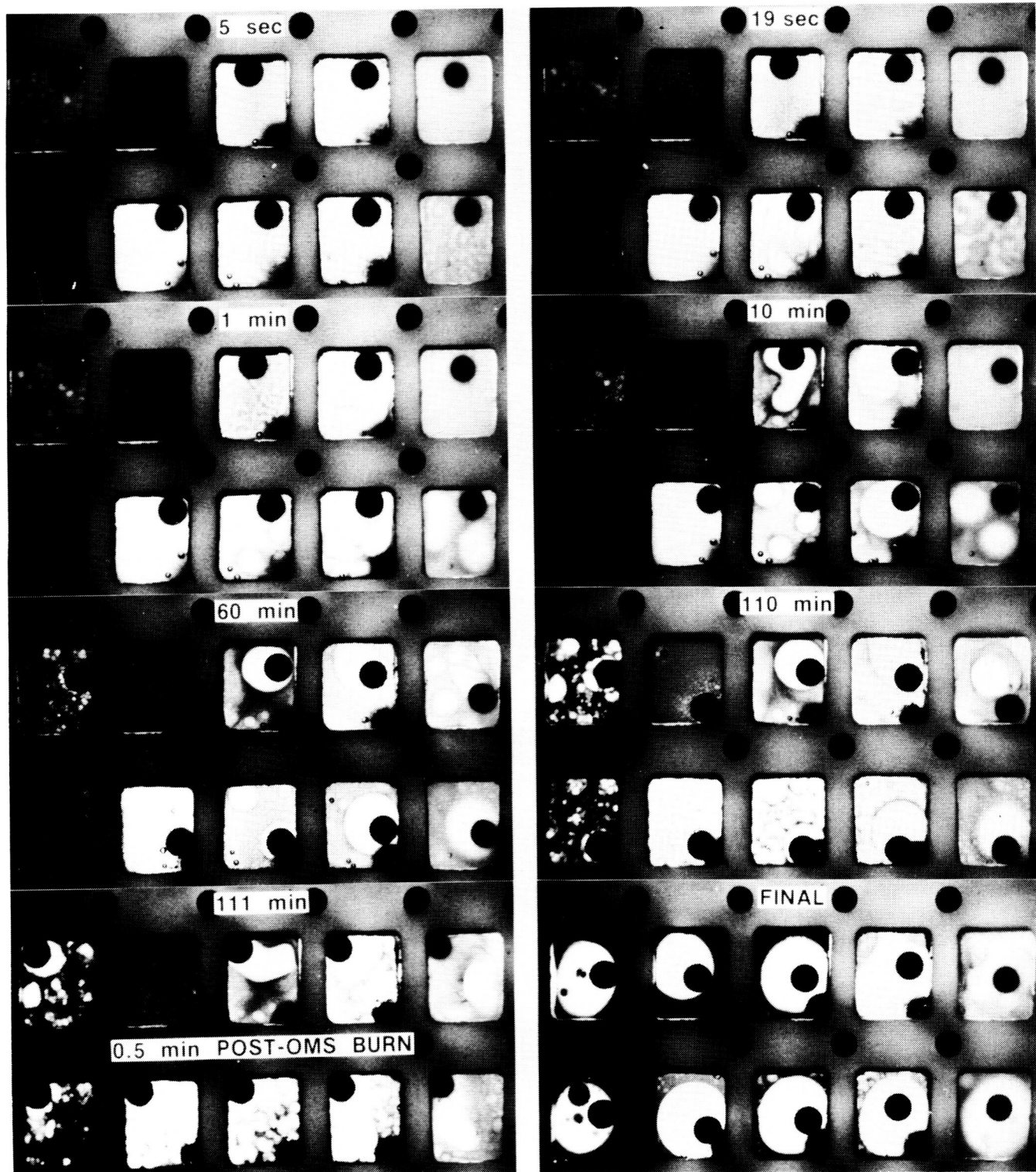


Figure 5. Photographs from PPE-1 experiment carried out on STS 51-D taken at times after mixing indicated; see text.

The disposition of the localized phases was as expected based on the spreading of the PEG-rich phase on the chamber wall. That is, in every sample, after six days in orbit, before the systems were mixed (the photograph marked FINAL in Fig. 5) the PEG-rich phase was located adjacent to the chamber walls with the dextran-rich phase displaced into an "egg yolk" in the interior of the chamber. The steel mixing balls, on which the dextran-rich phase spread, were found within that phase in every case.

The presence of particulates (fixed erythrocytes) had no effect on the demixing rate in one case (5/4/0) but appeared to reduce the rate in the other system (7/5/0). This experiment needs to be repeated; the reason for the observed behavior is not clear at present.

The final noteworthy feature of the PPE-1 experiment is the apparent shift in chemical equilibrium which became evident about 15 to 20 min after shaking. Under laboratory conditions, once the phases demix they remain stable and of constant composition indefinitely. The PPE-1 photographs clearly show a change in composition of the localized, PEG-rich phases from 30 min onwards, seen as a further decomposition of the fairly uniform dark regions into mottled areas of demixing. We have never observed a phenomenon like this on the ground unless a change in the experimental conditions, such as dilution or concentration through evaporation or a temperature shift occurred. In any of these cases the shift in equilibrium results in a change in composition of each of the phases, presumably in the present instance by the mechanism of spinodal decomposition since the systems flown lie well within the binodal. It seems very probable that the secondary decomposition observed in the PPE-1 experiment was due to a temperature increase. It was found after the flight that the surface of the light box increased in temperature by 9°C in 30 min, the likely source of the temperature change. For this reason the kinetic analysis discussed below was carried out where possible on data generated from photographs taken during the first ten minutes of the experiment.

## DISCUSSION

It is clear from the above results that the polymer phase systems demix much more rapidly in microgravity than did the oil/water mixtures flown by others (6), in spite of the fact that the latter systems were characterized by interfacial tensions orders of magnitude larger than those typical of the systems studied here. The observed demixing rates are, in most cases, quite compatible with the times over which cells retain viability and separation experiments can be run (1,2). However, in all cases, demixing in a one g environment occurred much more rapidly than was observed in the sensible absence of gravitational effects. Even without the effects of a density difference the localized phases were relatively stable in microgravity as shown in the 111 min panel in Fig. 5. This frame shows the appearance of the samples following a sudden acceleration produced by the orbital maneuvering system. Even though all the mixing balls have clearly been shifted the systems have not mixed appreciably.

At present the factors that control the demixing rate in microgravity are not clear. Preferential wetting of the container walls does not seem to have a significant effect on the kinetics until the characteristic dimension of the localized phases approaches that of the container. That is, the demixing appears to occur uniformly throughout the sample until the process is well advanced (Fig. 1). As the demixing nears completion, however, the disposition of the localized phases is determined by which of the two phases



spreads over the container wall, the non-spreading one (in our case the dextran-rich phase) then being forced into the center of the chamber. We have not yet studied systems in which wall wetting with an intermediate contact angle occurs.

As would be expected, the phase volume ratio had a strong effect on the demixing, the most rapid separation resulting when the phase which did not spread on the chamber wall was in the majority. When the ratio was reversed, no demixing was observed over the time course of the experiment (although demixing evidently did occur eventually as shown by the last frame in Fig. 5). The 1:1 combination demixed with an intermediate time course.

Although it is clear that the demixing rate will depend in some way on the viscosities of the phases and the interfacial tension between them the present experiments do not allow any conclusions to be drawn regarding the form of that dependence. It is obvious from our results that systems containing higher concentrations of polymers demix more slowly than those closer to the critical concentrations required for phase separation. However, both the interfacial tension and the phase viscosities increase strongly as the total polymer concentrations are increased so the individual effects of each of these parameters cannot yet be determined.

To obtain a more quantitative assessment of the demixing process, suitable photographs taken on PPE-1 were analyzed as described above for the isopycnic system and for the KC-135 experiments. The results are given in Table 2. It

Table 2

System (See Table 1)	Power Law Parameters $\log r = A + B \log t$			Exponential Parameters $r = r_0 \exp(\beta t)$		
	A	B	r.c.	$r_0$	$\beta$	r.c.
<u>Isopycnic 1xg</u>						
(5.5/69/9.5)	-2.11	0.80	0.985	0.052	0.014	0.757
(7/.29/12)	-1.23	0.55	0.970	0.188	0.010	0.928
<u>KC-135</u>						
(7/5/0)	-1.22	0.78	0.954	0.148	0.081	0.968
<u>Shuttle</u>						
(7/.29/12)	-1.31	0.61	0.967	0.30	0.069	0.940
(7/5/0)	-0.89	0.66	0.989	0.37	0.041	0.941
(5/3.5/0)	-0.78	0.51	0.917	0.33	0.041	0.983
(6/4/0)	-4.76	1.21	0.948	0.089	0.020	0.986
(8/4/0) 1/1	-3.5	0.79	0.857	0.083	0.00022	0.894
(8/4/0) 2/3	-1.31	0.26	0.987	0.20	0.00017	0.937
(5/4/0) $\Delta T$	-18.0	4.74	0.976	0.0069	0.00078	0.976

Note: Linear dimensions given in mm; data points leading to best fit parameters had an average standard deviation of  $\pm 17\%$ ; r.c. = linear regression coefficient. For the system designated as (5/4/0)  $\Delta T$  the parameters were derived from the secondary decomposition of the system after the temperature had probably risen (see text).

should be noted that the temperature was probably not constant during the period covered by the photographs analyzed for the 5/4/0, 6/4/0 and 8/4/0 systems, as mentioned above.

Referring to Fig. 3, it is seen that the data obtained over the 20 s available on KC-135 flights is a reasonable predictor of the behavior up to times at least ten-fold longer. Hence, such experiments can be useful in examining some of the fundamental determinants of the demixing rate in the systems of interest here. The large difference in the initial size of the domains between the two types of experiments may relate to the difficulty in mixing the systems thoroughly under the conditions prevailing in the KC-135 experiment.

The mechanisms by which the polymer phases demix are of direct interest to our cell partition work, as explained in the Introduction. Evidently there has been little work done in this area. Baird (7) has calculated characteristic times for the demixing of two phase systems of the type used here assuming the coarsening of the emulsion takes place by the mechanism of Ostwald ripening. This is the process whereby diffusion of solute takes place out of small drops and into large ones until all the dispersed phase is centralized in a single drop. His result indicates demixing times of the order of years for our systems, however, so this mechanism is clearly not the dominant one.

If it is assumed that the composition of the phases is unaffected by the emulsification process and that only the interfacial area and curvature is affected, then it seems likely, given the high volume concentration of each phase present, that coalescence between domains will occur during the demixing process. Whether or not this would be the only mechanism responsible for the localization of the phases is not clear since it is conceivable that extended bicontinuous structures could be formed which would then reduce their interfacial area spontaneously, causing localization of the phases. Such structures are observed macroscopically in isopycnic systems in the latter stages of demixing (not shown). The photographs we have analyzed to date do not provide a definitive answer to this question due to the depth of focus of the camera and the high concentration of interface present early in the process.

If coalescence is the dominant process responsible for demixing, the observations on the dependence of demixing on the volume ratio can be rationalized. When the phase which spreads on the chamber wall is in the minority the concentration of drops of the non-spreading phase in the interior of the chamber will be high, increasing the probability of collision and coalescence. When the ratio is reversed, however, the dispersed, non-spreading phase will be at a much lower concentration, reducing the frequency of coalescence events, consistent with the results observed for the 8/4/0 system.

If coalescence between dispersed drops of the phases is responsible for the observed demixing rates, the question arises regarding what processes determine the rate at which the coalescence events take place. We have derived some approximate scaling relations which describe cases in which collisions which lead to drop coalescence are induced by drop diffusion, by externally imposed shear (such as might be present as a residual from the mixing process) and by shear produced by the local fluid disturbance generated by coalescence of two drops (unpublished). In the drop diffusion case the length scale characteristic of the average drop size,  $r$ , depends on



the time after mixing,  $t$ , according to:

$$r \propto t^{1/3}$$

This dependence is also found for Ostwald ripening. If coalescence is produced by externally applied shear:

$$r \propto \exp[\beta t]$$

If the shear produced locally by the coalescence of two drops is responsible for inducing further collisions:

$$r \propto t$$

The analysis summarized in Table 2 does not provide a definitive answer as to which of the above relations best fits the data. However, if the systems most likely to have been photographed at constant temperature are considered it is seen that demixing in four of the six (the three isopycnic experiments and the 7/5/0 system) is best described by a power law and that in these cases the power lies between 0.55 and 0.80, approaching the value of 1.0 predicted for the coalescence-induced shear case. In the other two systems the exponential fit appears marginally better, supporting the imposed shear interpretation. Obviously, further experimentation is required but the results to date seem consistent with the idea that coalescence is an important part of the mechanism by which phase separated polymer systems demix in the absence of gravitational effects.

#### ACKNOWLEDGEMENTS

This work was supported by contracts from the Microgravity Sciences and Applications Division of NASA. JVA is a Visiting Scientist of the Universities Space Research Association.

#### REFERENCES

1. Albertsson P-A 1986, Partition of Cell Particles and Macromolecules, Third edition, New York, Wiley-Interscience.
2. Walter H, Brooks D E & Fisher D 1986, Partitioning in Aqueous Two Phase Systems. Theory, Methods, Uses and Applications in Biotechnology, Orlando, Academic Press.
3. Brooks D E et al 1984, Electrostatic and electrokinetic potentials in two polymer aqueous phase systems, J Colloid and Interface Sci. 102, 1-15.
4. Brooks D E et al 1984, Rationale for two phase polymer system microgravity separation experiments, Proc. Fifth European Symp on Materials Science Under Microgravity, Schloss Elmau, 5-7 November 1984, ESA SP-222, 315-318.
5. Sharp K A & Brooks D E 1987, In preparation.

6. Lacy L L & Otto G H 1975, The stability of liquid dispersions in low gravity, Proc. AIAA-IAGU Conf. on Scientific Expts. of Skylab, AIAA Paper 74-1242, Marshall Space Flight Center, Alabama, November, 1974.
7. Baird, J K 1984, Application of the theory of Ostwald ripening to microgravity experiments, Proc. Fifth European Symp on Materials Science Under Microgravity, Schloss Elmau, 5-7 November 1984, ESA SP-222, 319-324.

MICROGRAVITY SCIENCE REVIEW  
February 10-12, 1987

ABSTRACT

NASA CONTRACT NAS8-32950

HORMONE PURIFICATION BY ISOELECTRIC FOCUSING IN SPACE

M. Bier, P.I.  
Center for Separation Science  
University of Arizona  
Tucson, AZ 85721

The objective of our program is the definition and development of optimal methods for electrophoretic separations in microgravity. Our approach is based on a triad consisting of ground based experiments, mathematical modeling and experiments in microgravity. Our methodology differs radically from that of McDonnell Douglas, who base their continuous flow electrophoresis apparatus on so-called zone electrophoresis, while our approach is based on isoelectric focusing.

Zone electrophoresis is a rate process, where separation is achieved in uniform buffers on the basis of differences in electrophoretic mobilities. It is an inherently low resolution method, mainly applicable to separation of cells and cell organelles. In contrast, isoelectric focusing is an equilibrium process, components separating according to their isoelectric points. A pH gradient is necessary, usually also established electrophoretically. Focusing has gained high favor for protein analysis because of its exquisite resolution. Our basic objective is to adapt this technique for large scale protein separation.

Optimization and modeling of continuous flow electrophoresis mainly concern the hydrodynamics of the flow process, including gravity dependent fluid convection due to density gradients and gravity-independent electroosmosis. A background of uniform non-interacting buffer system is generally assumed. Because of the role of gravity in inducing natural convection, the potential benefits of operation in microgravity can be easily assessed.

Optimization of focusing requires a rather different and more complex model describing the molecular transport processes involved in electrophoresis of interacting systems. Our mathematical model represents the first generalized theory of electrophoresis and has been extensively used for computer simulations.

Three different focusing instruments were designed, embodying novel principles of fluid stabilization. Thus, some of the fluid dynamics problems of continuous flow electrophoresis could be avoided. Fluid stabilization has been achieved by (1) flow streamlining by means of membrane elements in combination with rapid fluid recycling; (2) apparatus rotation in combination with said membrane elements; and (3) shear stress induced by rapid recycling through a narrow gap channel.

One of our major unknowns was the assessment of electroosmosis in presence of pH gradients. Experimentally, all ground-based methods suppressing gravity effects also seem to suppress electroosmosis. Microgravity provides a unique opportunity to decouple these two effects, which was the objective of our last space experiment (February 1984). While at first puzzling, the results of the space experiment have led us to the development of a much more comprehensive understanding of electroosmosis.

We now see the classical explanation of electroosmosis with nicely symmetrical laminar flow patterns as only an idealized limited case, restricted to systems of uniform composition at low Reynolds numbers and low electric power. Any departure from these conditions results in a far more complex set of fluid instabilities. This realization has greatly facilitated the design of our latest ground-based prototype instrument. In general, we have directed our space experiments to sharply focused scientific questions, rather than generalized separation instruments.

## INTRODUCTION

This space experiment has been rendered possible only through close collaboration with several technicians, scientists and administrators from NASA at Marshall. Unfortunately, time does not permit me to acknowledge all of them, but I must single out Dr. Robert S. Snyder, our science collaborator in this as in all previous space experiments and Mr. Vaughn H. Yost, our program coordinator.

Space electrophoresis was one of the earliest components of NASA's endeavor to develop the basis for a technologic utilization of microgravity. This identification of electrophoresis as possibly benefiting from operations in microgravity was eminently correct. The whole development of electrophoretic methodology has been affected, whether consciously or unconsciously, by the need to neutralize the buoyancy resulting from density gradients. Density gradients, of course, are not always destructive, but can also be utilized constructively as a stabilizing mechanism, as in the original Tiselius electrophoresis apparatus. Gravity can even be utilized as part of the driving force, as in electrodecantation and electrophoresis-convection.

Personally, I was privileged to be part of the NASA effort virtually since its inception. Most of my earlier professional life had been dedicated to preparative electrophoresis, in particular to forced-flow electrophoresis - a variant of electrodecantation. Thus, I was particularly sensitive to the gravity issue. Nevertheless, I had conceptual problems with the efforts to develop zone electrophoresis in space, rather than the more sophisticated techniques of isoelectric focusing and isotachopheresis. A brief explanation of these three variants of electrophoresis is in order.

Zone electrophoresis separates components according to differences in their electrophoretic mobility. It requires a uniform buffer in which the sample is the only discontinuity. It is a rate process, where sample zones broaden with time due to diffusion and sample/buffer interactions without achieving steady state. Because of its inherently low resolution, it is rarely used for protein separations.

Isoelectric focusing separates components according to their isoelectric point. It requires buffers capable of forming a stable pH gradient, established by the electric field. A self-sharpening stationary steady state is achieved irrespective of the starting conditions. It is a high resolution method, widely used for protein and peptide analysis and separations.

Isotachopheresis is a process in which the sample constituents are sorted according to relative net mobilities between a leading and a terminating electrolyte. A steady state is achieved, all sample zones migrating at the same velocity, with contiguous self-sharpening boundaries. While mainly used for the analysis of small molecular weight ions, it offers intriguing possibilities for preparative applications.

## RESEARCH APPROACH

The choice between zone electrophoresis and isoelectric focusing will depend to a large degree on the ultimate purpose of the space facility. Zone electrophoresis offers better control of the ionic composition of the buffer and is compatible with separation of living cells. Isoelectric focusing is a more drastic method, where some cells may not survive the treatment. Thus, for cells, zone electrophoresis is the method of choice, while for proteins isoelectric focusing is often preferable.

Our emphasis on isoelectric focusing was predicated by our value judgment that protein and peptide separation presents a more pressing need than cell separations. Mainly, the relation between function and charge is not as clearly established for cells as for proteins. Our emphasis was to a large degree validated by the explosive growth and development of genetic engineering in the last 5 years. This has imposed entirely new demands on separation science. It has also rendered possible the production in recombinant systems of many products which were hitherto derivable only from tissue culture of natural cells. In fact, cloning has replaced the need for cell separations for production purposes.

Furthermore, there may be at present a surfeit of work in continuous flow zone electrophoresis, with independent programs in United States, Soviet Russia, Japan, Germany and France. Some may involve duplication of effort. We believe we are the only group seriously dedicated to the alternate approaches of isoelectric focusing and isotachophoresis in space processing.

The engineering profession has given relatively little attention to electrophoresis, which was largely the province of biochemists. Thus, at the onset of our work there was only a superficial understanding of zone electrophoresis, isoelectric focusing and isotachophoresis. They were treated as separate processes and discussed in models of limited scope. Yet, it was obvious that they are but different aspects of the same process and that they could be described by a single set of equations.

Thus, to advance the understanding of electrophoresis, one of our first efforts was the development of the first general mathematical model based on the fundamentals of the flux due to electromigration and diffusion, conservation of mass and charge, electroneutrality, and solvent/solute interactions due to ionic dissociation equilibria. A computer simulation program has been developed which predicts the behavior of most electrophoretic systems, which are seen to differ only in terms of initial and boundary conditions.

Experimentally, the recycling isoelectric focusing apparatus (RIEF) was constructed, based on a novel recycling principle. Advantage is taken of the fact that in focusing the final steady state is independent of the initial state. Flow stabilization has been achieved by inserting an array of screen elements into the focusing chamber. The fluid dynamics of this apparatus is entirely different from that of the conventional continuous flow zone electrophoresis instrument.

The screen elements, actually nylon monofilament screens of 1 micron porosity, coupled to rapid recirculation, have solved not only the major

problem of gravity driven convection but have also apparently abolished wall electroosmosis. On the other hand, the RIEF has certainly not solved all the problems of effective isoelectric focusing. Thus, there was a strong incentive to develop a focusing apparatus embodying the thin film principle of fluid stabilization employed in the continuous flow zone electrophoresis instruments. The major unknown for the design and optimization of such an apparatus was the role of electroosmosis in isoelectric focusing.

## ELECTROOSMOSIS

Classical hydrodynamic treatment of electroosmosis in closed round tubes predicts the development of an axially symmetric laminar recirculation flow pattern with a parabolic flow velocity distribution across the tube. This has been repeatedly verified experimentally through microscope electrophoresis. This involves visual measurement of the migrating velocity of particles in a d.c. electric field at different radial distances of the tube. The velocities describe a parabola, the true mobility of the particle being determined at the so-called stationary level. In flat rather than round cells, the same parabolic profile is observed, though the stationary level is presumed to be located at a somewhat different depth.

In the above measurements, the apparatus is typically filled with a homogeneous buffer, with the electrodes sufficiently far removed from the observation point to preclude changes in electrolyte concentration or composition. Thus, it is also assumed that the electric charge at the walls of the tube is uniform, this so-called zeta potential giving rise to electroosmosis.

Unfortunately, in focusing, the pH gradients affects not only the mobility of the particle but also the zeta potential of the walls of the vessel as well as the local electric field. Thus, microscope electrophoresis cannot yield information on the extent and role of electroosmosis in isoelectric focusing. In fact, all ground-based methods of isoelectric focusing require the abolition of natural convection due to gravity and thus seem also to abolish electroosmosis.

## MICROGRAVITY APPARATUS

Microgravity seemed to offer a unique opportunity to decouple gravity driven convection from the electrically driven electroosmosis. An apparatus has been designed for the middeck lockers, incorporating 8 focusing cells, an autonomous power supply and a camera for the recording of the focusing process. Three proteins were to be separated by focusing, HbA and HbC, two genetic variants of human hemoglobin, with isoelectric points at pH 7.0 and 7.35, and human albumin, isoelectric point 4.8. The albumin was stained blue with Bromphenol Blue and the hemoglobins saturated with carbon monoxide for increased stability.

Several constraints had to be observed: cooling of the cells was not practical, thus focusing at low power input had to be adopted. A novel non-gassing electrode system had to be developed, including a palladium electrode for hydrogen adsorption and a palladium-silver half-cell for oxygen adsorption. Two-week stability of the proteins had to be assured,

requiring the addition of bacteriostatic and fungicide agents, as well as pH adjustment. The effect of the long incubation on the palladium electrodes required a great deal of attention.

All features of the space experiment were studied extensively using a ground-based simulator of microgravity. This incorporated a mechanism for rotation of the cell assemblies around their horizontal axis. The continuous change of the direction of the gravity vector is known to permit a degree of convective stabilization.

A number of other variants were to be tested:

Conventional focusing utilizes carrier ampholytes specifically synthesized to generate stable pH gradients. Best known is Ampholine, a product of LKB of Bromma, Sweden. Because such carrier ampholytes are of unspecifiable chemical composition, we have dedicated a great part of our simulation studies to the development of suitable focusing buffers using simple electrolytes of known chemical composition. While Ampholines create a near linear pH gradient, several three component mixture can be utilized to create sharp step-gradients, which will resolve the albumin from the hemoglobins. Because of their sharper concentration gradients they are also likely to exhibit greater convective disturbances. Thus, we decided to test both buffering systems in space.

NASA had developed quite effective anti-electroosmosis coatings, but these were never tested in a focusing arrangement. Thus, the space experiment represented an opportunity to evaluate their effectiveness, though questions regarding coating survival during prolonged incubation in Ampholine were unresolved.

As final design, focusing chambers were tubes, 4.5 cm in length, with an internal diameter of 0.625 cm. Two basic designs were utilized: either a single glass tube of the requisite length, or a series of 14 concentric glass rings, each 0.32 cm in length, for the same total length. These rings could be assembled in three modalities, with monofilament screens, mylar constrictors with an opening of half the internal diameter of the glass rings, or mylar spacers of same internal diameter as the glass rings. All assemblies were housed in plexiglass blocks containing the requisite accessories and assuring leak-proof storage.

The rationale for the screens is their effectiveness for flow stabilization in the RIEF apparatus. They also proved effective in the rotating microgravity simulator. Thus, the cell with screens was most likely to result in good focusing.

The mylar constrictors were used as a test of the hypothesis that disruption of the smooth bore tube with protruding partitions may decrease electroosmosis. This proved to be the case in the microgravity simulator and has been also extensively studied through computer simulation.

The third configuration with mylar spacers of same internal diameter as the glass rings was included as a control for the effects of slicing the glass tube into individual rings.



The final assembly of the eight focusing cells were as follows:

Ampholine-filled:

Cell 1: Single glass tube, uncoated.

Cell 2: Single glass tube, anti-electroosmosis coated.

Cell 3: Rings, separated by non-constricting mylar spacers.

Cell 4: Rings, separated by nylon monofilament screens.

Cell 5: Rings, separated by constricting mylar spacers.

3-component buffer system:

Cell 6: Single glass tube, uncoated

Cell 7: Single glass tube, anti-electroosmosis coated.

Cell 8: Rings, separated by constricting mylar spacers.

All cells were to be focused at 75 volts dc, generated by a set of batteries. The space module had provisions to display the current through each cell. Focusing results in a gradual decrease of conductivity of the solution, thus the solid state ammeters were to give quantitative indication of the progress of focusing. Typically, in good focusing, such as in polyacrylamide gels, the current falls to about 10% of starting value.

Our laboratory has designed and constructed all the cells and furnished to NASA at Marshall, a bread-board arrangement of the final assembly. Marshall has constructed the flight instrument and provided all the requisite testing. Dr. Robert Snyder of Marshall has provided the anti-electroosmosis coating to selected cells and has been our most valuable collaborator throughout the experiment.

#### PREFLIGHT GROUND BASED TESTING

Preflight testing first required the development of the rotating microgravity simulator. After its satisfactory operation was established, it was also necessary to specify the conditions for the flight. This involved:

1. Development of the two solutions, Ampholine and buffer, offering complete focusing within the operational parameters of the space apparatus (90 minutes at 75 volts), consonant with stability of the proteins during prolonged incubation at room temperature.

2. Conditioning of the palladium electrodes to provide non-gasing service during the entire focusing period. This proved to be a particularly difficult problem.

3. Filling of the individual cells with complete exclusion of air bubbles.

All eight cell configurations were repeatedly tested in the rotator, with results as follows:

As expected, best separation was achieved in the apparatus if filled with a polyacrylamide gel. Not only were all three proteins, albumin, HbA and HbC clearly separated, but there were also visible two smaller bands of other hemoglobin variants. This separation was our standard of comparison.

The cells with the nylon screens showed good separation of albumin from the hemoglobins, essentially each protein occupying one glass ring. The two hemoglobins were not separated.

Second best separations were obtained in the cells with the mylar constrictors. While much more diffuse than in the cells with the nylon screens, separate zones of hemoglobins and albumins were routinely obtainable.

No useful separations were seen in unpartitioned glass tubes due to obvious convective mixing. Antiosmotic coating had no noticeable effect and the buffer solution and Ampholine gave comparable results.

Thus, the space experiment was so designed as to offer the possibility of improved separation at all levels of ground-based performance, as none of the ground-based tests showed the resolution of the polyacrylamide gel.

#### COMPUTER MODELING OF ELECTROOSMOSIS IN SEGMENTED CELLS

In cooperation with Prof. Saville of Princeton University, a model was constructed predicting the electroosmotic fluid flow with partitions of various geometries. This model has been extensively exercised and has predicted a gain in decreased electroosmosis at constant power. The constrictors obviously cause local recirculating eddies and break up the global recirculation characteristic of plain tubes. The model assumed constant composition and zeta potential as their variation in isoelectric focusing is unknown. The predicted improvement by the model was fully supported by experimental results, but was relatively modest. Unfortunately, the basic problem of the characteristics of electroosmosis in isoelectric focusing remained unsolved.

#### SPACE RESULTS

The apparatus performed in space as designed, giving us an excellent record of the migration of the colored proteins. Thirty photographs at 2 min. intervals were taken during the first 60 minutes, followed by 10 photographs at 3 min. intervals.

The focusing is best represented by the plots of the changes of measured currents with time. As expected, fastest decrease in current was seen in the cell with nylon screens, followed by the two cells with mylar constrictors. The results, however, were not noticeably better than those obtainable in the microgravity simulator. To the contrary, while hemoglobin was well focused in the screen cell, the albumin was much less well focused than routinely obtainable on the ground. The reason for this is not clear and may have been incidental. Resolution of HbA and HbC was not seen. Thus, while we did not obtain the expected improvement, the partitioned cells did not reveal any unexpected results.

Quite to the contrary, the focusing in the four cells with unpartitioned glass tubes exhibited a completely unexpected behavior. For the first 20 minutes, there was a rapid decrease in current, reflecting good focusing. Shortly thereafter, all four cells (2 with Ampholine and 2 with the 3-component buffer) showed a sudden reversal of the focusing process as

seen from a steadily increasing current. Moreover, the photographic record indicated a coincidental sudden appearance of rapid internal flow - taking the shape of a protruding finger. Considering the 3-component mixture, the reversal occurred between 20 and 22 minutes of focusing in the uncoated cell and 2 minutes later in the coated cell. This delay is a rather good evidence that this disturbance was not due to an external shock to the apparatus, but was caused by internal factors.

#### POSTFLIGHT ANALYSIS

Two elements of the flight experiment appeared most disturbing: (1) the rapid rate of growth of the protruding 'finger'. The rate was of the order of cm/min, which appeared too fast for electroosmosis; (2) the fact that the mixing, first signaled by the appearance of the finger, continued unabated for the next 70 minutes. Thus, the current through all four cells gradually reached or even exceeded the initial current at the start of the focusing.

Careful review of preflight data failed to reveal similar results. Moreover, despite intense efforts, it proved to be impossible to duplicate either of the two phenomena in a variety of operational modes, whether in the rotating microgravity simulator or stationary operation. It became evident, however, that decreasing the diameter of the tubes improved the focusing process. Thus, with glass tubes of .23 cm diameter or smaller, good focusing was obtained even in unpartitioned tubes, provided rotation is maintained.

In fact, electroosmosis may not have been the only driving force for the convection observed in space. It is certain that the nature of the flow changed in space after approximately 20 minutes of focusing. Protein focusing results in formation of sharp gradients of conductivity as well as of the dielectric constant of the solution. It is well known (e.g., J.R. Melcher and G.I. Taylor, Ann. Rev. Fluid Mech. 1,111,1969) that electric fields can induce electrohydrodynamic body forces due to gradients of the dielectric constant of the medium. This has been observed, however, only in mixtures of immiscible solvents, not in aqueous systems without interfaces.

We are presently evaluating experimentally and through computation this possibility. Experimentally, the effect differs from electroosmosis in two important respects: (1) it is proportional to the square of the imposed electric field, and (2) AC or DC fields are equally effective, provided the gradient is first generated through DC currents. If verified, it would demonstrate a new electrokinetic phenomenon, not previously associated with electrophoresis. It could conveniently account for the observed delay in the onset of turbulence in space, as having been necessary for the formation of the gradient.

This points out the importance of the microgravity experiment which was the first to reveal this effect. We know as yet very little about its scaling when critical dimensions are larger than those used in microscope electrophoresis.

We must assume, however, that the global, well ordered and laminar fluid behavior described in usual textbooks is but a limiting case. Drawing a

parallel between laminar and turbulent pressure driven flows, we can also postulate a turbulent phase of electrokinetically driven flows, whether due to electroosmosis or electrohydrodynamics. Turbulence will be facilitated by several factors: inhomogeneity of composition, large critical dimensions and high electrical field.

To test our hypothesis a series of other cell geometries were prepared for the next space flight, which was supposed to take place in March 1986. The unfortunate Challenger disaster has imposed an unavoidable delay.

#### POSITIVE FALL-OUT OF THE SPACE EXPERIMENT

As a result of the effectiveness of the microgravity simulator, a new apparatus for ground-based preparative focusing was developed. Dubbed ROTOFOR, it comprises a cylindrical body divided into twenty subcompartments by a parallel array of nylon screen elements. The total capacity of the apparatus is 40 ml. Joule heat is dissipated through a central cold-finger. The resolution is comparable to that obtainable in the RIEF apparatus, but the priming volume is significantly smaller. The patent for the apparatus has been assigned to the University of Arizona and licensed to BIO-RAD of Richmond, Ca.

A second ground-based apparatus has been also completed, this achieving remarkable fluid stability as a result of rapid recirculation of process fluid through a narrow channel between two parallel plates. It is essentially an adaptation of continuous flow zone electrophoresis apparatus to the recycling principle of focusing.

This apparatus is of considerable theoretical interest: it has clearly demonstrated the existence of laminar as well as turbulent electrokinetic flows. At any given recycling rate there appears to be a sharp threshold of electric potential above which the flow becomes turbulent. The shear induced by the rapid flow is essential for fluid stabilization: the higher the shear the higher the threshold. At a high recycling rate and high voltage, the interruption of the flow causes a near explosive outbreak of turbulence.

From a practical point of view, this new apparatus has an advantage over the RIEF and the ROTOFOR since it lacks the screen elements. These are subject to fouling from precipitating proteins. Thus, the new apparatus, referred to as Recycling Free Flow Focusing (RF3) is more tolerant of precipitation and can also be used for the focusing of particulate matter, such as chloroplasts.

#### FUTURE DIRECTIONS

As a result of the space experiment, two new ground-based instruments have been developed. A far better insight into electrokinetic phenomena has been gained. It remains to be seen if computer modeling will be helpful to predict the change-over from laminar to turbulent flows. Qualitative observations predict that much better focusing will be obtained in space with cells of smaller critical dimensions.

We expect to be scheduled for a second space experiment, where a variety

of new cell configurations will be tested. We will also test whether the presence of proteins is necessary for the onset of turbulence. This is likely, as we know that focused proteins are characterized by much sharper gradients than protein-free zones. We are quite convinced that turbulence is initiated by the presence of these heterogeneities, but microgravity may provide the ultimate proof.

We believe that our results have significant consequence not only for focusing but also for continuous flow zone electrophoresis. Mainly, we have demonstrated that high shear is an effective means for flow stabilization. One of the benefits of space operation is presumed to be the possibility of increasing chamber depth by eliminating gravitational convection. The benefits appear now less clear, as this will decrease shear and may actually destabilize flow.

Primarily, however, we believe that we are still rather far from having truly optimized electrophoresis instruments for either ground-based or space operation. While several of our instruments are quite usable in ground based operation, none of them achieve anywhere near the protein resolution of analytical gels. This is the ultimate objective. We would be less than forthright if we would claim to know how to achieve it, but we are committed to pursue it.

Microgravity related publications under the sponsorship of NASA

79. R.S. Snyder, M. Bier, R.N. Griffin, A.J. Johnson, H. Leideiser, Jr., F.J. Micale, S. Ross and C.J. van Oss: "Free Fluid Particle Electrophoresis on Apollo 16", Separation and Purification Methods, 2, 259-282 (1973).
80. M. Bier and R.S. Snyder: "Electrophoresis in Space at Zero Gravity," 12th AIAA Aerospace Sciences Meeting, Washington, D.C., AIAA Paper 74-210 (74A18854), February 1, 1974.
81. M. Bier, J.O.N. Hinckley, A.J.K. Smolka, R.S. Snyder, et al: "Role of Gravity in Preparative Electrophoresis," in 'The Proceedings of the Third Space Processing Symposium', Vol 2, pp. 729-755, NASA, N74-5, 1974.
82. M. Bier, J.O.N. Hinckley and A.J.K. Smolka: "Potential Use of Isotachophoresis in Space", in 'Protides Biological Fluids, XXII Colloquium' (H. Peeters, ed.) pp. 673-678, Pergamon Press, New York, 1975.
84. M. Bier: "Potential Contribution of the Space Program to the Advancement of Electrophoresis and its Biomedical Application", in 'Future Space Programs 1975', Committee on Science and Technology, U.S. House of Representatives, U.S. Government Printing Office No. 052-070-02891-2, September, 1975.
85. M. Bier, A.J.K. Smolka, A. Kopwillem and S. Ostrach: "Preparative Electrophoresis at Zero Gravity", J. Colloid Interface Science 55, 197-207, 1976.
87. R.E. Allen, G.H. Barlow, M. Bier, et al.: "Electrophoresis Technology, Experiment MA-011", in 'Apollo Soyuz Test Project, Summary Science Report', Vol. 1, NASA SP-412, 1977, pp. 307-334.
88. G.V.F. Seaman, R.E. Allen, G.N. Barlow and M. Bier: "Detailed Results of Apollo-Soyuz Test Project Experiment MA-011", in 'Proceedings European Space Association's Second European Symposium on Materials Sciences in Space', ESA Special Publication No. 114, 1976.
90. M. Bier: "Bioprocessing: Prospects for Space Electrophoresis," '1976 NASA Colloquium on Bioprocessing in Space', Houston, TX, March 1976, NASA-TM-X-58191.
93. J.O. Kessler, and M. Bier: "Gravitational Dynamics of Biosystems: Some Speculations", in 'Materials Sciences in Space with Applications to Space Processing Progress' (L. Steg, ed.), Astronautics and Aeronautics, Vol. 52, pp 125-149, American Institute of Aeronautics and Astronautics, New York, 1977.
94. M. Bier: "Electrophoresis" *ibid*, pp. 41-55, 1977.
97. M. Bier: "Reassessment of Space Electrophoresis" in 'COSPAR: Space Research', Volume XVIII (M.J. Rycroft and A.C. Stickland, Editors), pp. 537-540, Pergamon Press, New York, 1978.

## Microgravity related publications (continued)

98. M. Bier, and R.E. Lindberg: "Space Electrophoresis - Status and Potentials," AIAA 16th Aerospace Sciences Meeting, Huntsville, AL, January 1978, AIAA Paper 78-224.
99. N. Egen, G. Twitty, and M. Bier: "Recycling Isoelectric Focusing with Computer Controlled Data Acquisition System", New Orleans, La., AIAA 17th Aerospace Sciences Meeting, 1979, Paper No. 79-0405.
100. M. Bier and N. Egen: "Large Scale Recycling Isoelectric Focusing", in 'Electrofocusing' (Haglund, Westerfeld and Ball, eds.) pp. 35-48, Elsevier North Holland, Inc., New York, 1979.
104. M. Bier: "Space Bioprocessing - Status and Potentials", in 'Future Space Programs, Hearings Before the Committee on Science and Technology, U.S. House of Representatives, January 24-26, 1978', U.S. Government Printing Office, 1978, pp. 299-315.
105. M. Bier, et al.: "New Developments in Isoelectric Focusing", in 'Peptides, Structure and Biological Function' (E. Gross and J. Meienhofer, eds.) pp. 79-89, Pierce Chem. Co., Rockford, IL, 1979.
106. O.A. Palusinski, T.T. Allgyer, R.A. Mosher, M. Bier and D.A. Saville: "Mathematical Modeling and Computer Simulation of Isoelectric Focusing with Electrochemically Defined Ampholytes", Biophys. Chem. 13, 193-202, 1981.
108. O.A. Palusinski M. Bier and D.A. Saville: "Mathematical Model for Transient Isoelectric Focusing of Simple Ampholytes", Biophys. Chem., 14, 389-397, 1981.
109. R.A. Mosher, O.A. Palusinski and M. Bier: "Theoretical Studies in Isoelectric Focusing", in 'Materials Processing in the Reduced Gravity Environment of Space' (G.E. Rindone, ed.), Elsevier, pp. 255-260, 1982.
110. M. Bier, N.B. Egen, R.A. Mosher and G.E. Twitty: "Isoelectric Focusing in Space": ibid, pp. 261-266, 1982.
114. M. Bier, O.A. Palusinski, R.A. Mosher, A. Graham and D.A. Saville: "A Unified Mathematical Theory of Electrofocusing Processes", in 'Electrophoresis '82', (D. Stathakos, ed), Walter de Gruyter, Berlin, 1983.
116. M. Bier, O.A. Palusinski, R.A. Mosher and D.A. Saville: "Electrophoresis: Mathematical Modeling and Computer Simulation", Science, 219, 1281-1287, 1983.
117. M. Bier, R.A. Mosher, W. Thormann and A. Graham: "Isoelectric Focusing in Stable Pre-Formed pH Gradients", to be published in Electrophoresis '83, by Walter de Gruyter, Berlin.
118. N.B. Egen, W. Thormann, G.E. Twitty and M. Bier: "A New Preparative Isoelectric Focusing Apparatus", ibid.

Patents Obtained or Pending under NASA sponsorship

6. M. Bier: "Electrophoretic Fractional Elution Apparatus Employing a Rotational Seal Fraction Collector", U.S. Patent 4,040,940, August 9, 1977. Assigned to U. S. Government.
7. M. Bier: "Isoelectric Focusing Method and Apparatus", U. S. Patent 4,204,924, May 27, 1980. Assigned to the University of Arizona and licensed to Ionics, Inc., Watertown, Massachusetts.
8. M. Bier: "Isoelectric Focusing Apparatus", U. S. Patent 4,362,612, December 7, 1982. Assigned to University Patents, Inc. and licensed to Ionics, Inc., Watertown Massachusetts.
11. M. Bier: "Rotationally Stabilized Isoelectric Focusing Apparatus". Assigned to the University of Arizona and licensed to Bio Rad Laboratories, Richmond, California, patent pending.



## Development of Immunoassays for Human Urokinase

M. Zouhair Atassi

Department of Biochemistry, Baylor College of Medicine, Houston, Texas 77030

## ABSTRACT

The purpose of this work, is to develop radioimmune assays (RIA) and enzyme-linked immune assays for measurement of pro-urokinase and the two active forms of the enzyme. Polyclonal and monoclonal antibodies, with desired specificities against preselected synthetic regions of urokinase (UK), were obtained by immunization with the respective synthetic peptides and used to develop RIA for zymogen and the two activated forms of UK.

## INTRODUCTION

Continuous flow electrophoresis in microgravity has been employed in the separation of kidney cells into subgroups (1). It is necessary, however, to determine whether the separated cells retain function. Kidney-cell subgroups produce various amounts of UK. Presently, the assay for UK depends on the measurement of enzymic activity. This method is not very sensitive and it is an unreliable indicator of the amount of secreted UK because of the production of enzyme inhibitors by the cells. Furthermore, the method is unable to detect the zymogen, which is the initial synthetic product. The zymogen is synthesized as a single chain protein composed of 411 amino acid residues (2-4). This single chain zymogen has no enzymatic activity. Activation of the zymogen involves cleavage of the peptide bond Lys-158-Ile-159 and the loss of Lys-158, to produce a two-chain high molecular weight active UK (3,4). In this active enzyme, the A chain (residues 1-157) is linked to the B chain (residues 159-411) by a disulfide bond between Cys-148 and Cys-279 (3,4). Cleavage of the bond between Lys-135 and Lys-136 removes the segment 1-135 and gives a low molecular weight active enzyme (5,6) in which peptide 136-157 (A1 chain) is linked to the B chain by the above disulfide bond. Production by kidney-cell subgroups of normal, or even high, levels of UK cannot be measured when little or none of the zymogen undergoes activation.

In order to better monitor kidney cell separation and obtain a sound correlation with viability and activity of the various cell groups, a very precise method for measurement of all of the forms of urokinase (i.e. zymogen and the two active forms) is needed. The purpose of this work is to develop radioimmune assays (RIA) and enzyme-linked immune assays for measurement of the three forms of the enzyme. These assays depend on the preparation of polyclonal and monoclonal antibodies with specificities directed against preselected regions of UK. These preselected regions are made synthetically and the synthetic peptides are used as immunogens to obtain antibodies of the desired specificities (7-9). These antibodies will be used to develop RIA and ELISA assays for zymogen and activated UK.

It should be noted that development of these assays for UK will have a useful clinical spin-off. The enzyme is secreted by human carcinomas, especially in the lung, prostate, breast and colon cancers (10-13). By developing a sensitive assay for UK, it will be possible to detect these cancers early, even before a solid tumor becomes visible. Early detection will be extremely useful for design of therapy.

---

Abbreviations: UK, urokinase; RIA, radioimmune assay; BSA, bovine serum albumin; PBS, 0.15 M NaCl in 0.01 M sodium phosphate buffer, pH 7.2

## METHODS

### Preparation of peptides and peptide conjugates

Peptides were used as immunogens for the preparation of antibodies that possess pre-determined specificities. The locations of these regions within the UK polypeptide chain are shown in Table 1. These peptides were (or are being) synthesized, purified and analyzed by previously published procedures (7-9). Synthetic peptides were coupled to exhaustively succinylated (Su) derivatives of BSA, or hen lysozyme or to the native proteins after activation of the carrier carboxyl groups by conversion to the *p*-nitrophenyl-ester groups (14). The extent of coupling was determined by amino acid analysis of acid hydrolysates of the peptide-protein conjugates.

### Antisera against peptides

Antibodies against the synthetic peptides were raised in mice by two methods (a) Immunization by peptide-protein conjugates: Mice were injected and boosted with the peptide-SuBSA conjugate (50  $\mu$ g per mouse) as an emulsion in complete Freund's adjuvant in the footpads and subcutaneously in the neck. Serial bleedings from 10 days prior, up to 230 days after, the first injection will be collected and studied separately. (b) Immunization with free peptide: In view of the finding (7) that small synthetic peptides (6 residues or larger), when immunized in their free form in complete Freund's adjuvant, will stimulate an *in vivo* antibody response, peptides were injected into mice in their free form (i.e. without coupling to carrier). Each animal received peptide (25-50  $\mu$ g per mouse) as an emulsion in complete Freund's adjuvant distributed into three sites as above. The animals were boosted with similar doses 3 weeks after the first injection and thereafter monthly. Serial bleedings from 10 days before, up to 200 days after, the initial injection were studied separately.

### Preparation of monoclonal antibodies of preselected specificities

The recent discovery (7) that synthetic peptides will evoke antibody formation when used as immunogens in their *free* form (i.e. without coupling to a carrier) has been exploited in this laboratory to prepare monoclonal antibodies with preselected submolecular binding specificities to desired protein regions (15). Peptides representing antigenic sites as well as synthetic peptides representing surface regions that are not antigenic when the whole molecule is used as an immunogen have been shown to produce antisera and subsequently monoclonal antibodies of preselected specificities (16,17).

Mice were immunized as above with a given synthetic peptide (25-50  $\mu$ g) in complete Freund's adjuvant and boosted and test-bled at 3 week intervals until high antibody titer was obtained in the test sera. Somatic cell fusions, hybridoma selection, limiting dilution cloning and subcloning, and hybrid cell expansion were performed as described by Schmitz *et al.* (15). Expanded subclones were also injected into BALB/cByJ mice (2 x 10<sup>6</sup> cells/1.0 ml fresh tissue culture media) that had been primed with pristane (Sigma Chemical Co., St. Louis, MO). Ascites fluid were collected, clarified and stored frozen at -20°C until screened for the presence of hybridoma antibodies.

### Radiolabelling of proteins

Immune IgG preparations or protein A were radiolabelled with <sup>125</sup>I (Amersham Corp., Arlington Heights, IL) using the chloramine-T method (18). Unbound <sup>125</sup>I was separated from the radiolabelled sample by gel filtration on Sephadex G-25 (Pharmacia Fine Chemicals, Piscataway, NJ). Protein-associated <sup>125</sup>I was assayed by precipitation with 10% (v/v) trichloroacetic acid.



#### Screening for antibody binding by plate assay

Polyvinylchloride protein assay plates (Costar, Cambridge, MD) were incubated for 3 hours at 37°C with excess (1.5 µg in 50 µg of PBS/well) test and control antigens, washed extensively with PBS, and blocked with 1% BSA in PBS (100 µl/well) for 1 hr at 37°C to prevent non-specific binding of subsequent reagents. After washing, the plates were used for binding antibody.

Sera, culture supernatants and clarified ascites fluids were screened for anti-UK antibodies using a solid phase RIA described by Sakata and Atassi (19) as modified by Schmitz et al. (15). This assay was also used to determine antibody binding specificities to peptides. Briefly, RIA plates that had been coated with the appropriate test antigens (various forms of UK or peptide conjugates) were incubated for 3 hours at 37°C with an antibody preparation (50 µl/well) appropriately prediluted in PBS-BSA so as to maximize specific binding. The plates were subsequently washed with PBS and amplified with excess (1:1000 dilution of the stock reagent in PBS-BSA) rabbit anti-mouse IgG + IgM antisera (Litton Bionetics, Kensington, MS) for 2 hrs at 37°C. After washing, the plates were developed with excess ( $2.0 \times 10^5$  cpm in 50 µl PBS-BSA/well)  $^{125}\text{I}$ -labelled protein A for 2 hrs at room temperature, washed, and then separated into individual wells that are counted in a gamma counter (Beckman Instruments, Inc., Irvine, CA). Results are corrected for nonspecific (0.1-2%) binding detected in control wells not coated with test antigen but blocked with BSA.

When peptide-SuBSA conjugates are the immunizing antigens then antibody responses were analyzed by peptide-lysozyme (not succinyl lysozyme) conjugates since lysozyme and SuBSA do not cross-react immunochemically. Correction for non-specific binding is derived from binding to lysozyme control. When the free peptides were the antigens then antibodies were analyzed on peptide-SuBSA conjugates and employing lysozyme and SuBSA as controls.

#### RESULTS AND DISCUSSION

##### Antibodies that react specifically with the zymogen and the active form that has an A chain (residues 1-157) and a B chain (residues 159-411)

These will be antibodies that react specifically with the region 1-135 of the A chain. Certain regions of the molecule were selected for synthesis on the basis of the prediction that they have a high probability to be on the surface. In order for an antibody to bind to a protein, the regions it recognizes must be on the surface of the protein (20-22). However, since these predictive methods are not entirely reliable, several areas (peptides 1-8, Table 1) were selected for synthesis in order to improve our chances of success (i.e. obtaining anti-peptide antibodies that will react with the whole molecule). These peptides have all been synthesized, purified and characterized and are now being immunized into mice in order to prepare polyclonal and monoclonal antibodies that possess the desired specificities.

##### Antibodies that distinguish the zymogen from the active forms

The conversion of the zymogen to the active enzyme, involves scission at Lysine-158. We have synthesized a peptide centered around Lysine-158, fanning out three residues in each direction (peptide 9, Table 1). Also another peptide was made, elongating four and five residues on the two sides of Lys-158 (peptide 10, Table 1). These peptides were used as immunogens. Antibodies against the intact peptide will be expected to react only with the zymogen (in which the bond 158-159 is intact) and not with the active forms (in which this bond cleaved and Lys-158 is lost).

After injection of the peptides into outbred mice, and fusion of their spleen cells, 17 monoclonal antibodies were selected for their specificity to one of the peptides (154-163). Table 2 shows the results of this screening. These monoclonals were tested for binding to the different forms of UK by the western blot method. The nitrocellulose paper was incubated with cell culture supernatants followed by <sup>125</sup>I-labelled rabbit anti-mouse IgG. Three of the monoclonals showed specific binding to single chain UK. The clones involved are now being expanded and the monoclonal antibodies purified for further characterization and testing.

Table 2. Titer of monoclonal antibodies prepared by immunization with peptides 153-162 and 154-163.

Clone No.	Antibodies bound ( cpm) by		
	BSA-Urokinase Peptide	BSA-Nonsense peptide	BSA Only Blank
A3-E5-A7	71,813	803	901
A3-E5-B8	47,816	1,321	876
A3-E5-G10	58,503	1,454	1,311
A3-E5-H12	85,240	1,138	1,158
A3-E5-B3	59,674	871	821
A3-E5-D1	36,729	934	877
C2-A4-H4	7,633	1,855	928
C2-A4-F10	40,659	3,053	1,448
C2-A4-F11	91,196	6,987	1,726
D4-A5-E7	4,962	1,393	1,430
D4-C1-A5	25,631	1,579	1,355
D4-C1-G4	90,645	3,419	1,497
D4-C6-A4	72,303	1,101	1,045
D4-C6-AB	43,309	946	2,171
D4-C6-E12	82,320	1,405	1,055
D4-C6-F7	68,513	1,280	868
D4-C6-G12	43,013	1,109	781

note: group A; mice were immunized with free peptide 153-162  
group C; mice were immunized with free peptide 154-163  
group D; mice were immunized with BSA-conjugated peptide 154-163

#### Antibodies specific for the B chain

These will constitute general purpose antibodies that react with all forms of the enzyme. Several areas (peptides 11-17, Table 1) were selected from the B chain on the basis that they would have a high probability of being on the surface. These peptides have been (or are being) synthesized, purified and characterized. Polyclonal and monoclonal antibodies against these peptides should react with the immunizing peptides and with all forms of urokinase.

As part of this work, we have also carried out studies designed to determine optimum culture conditions, for kidney cells in bioreactor and also to find the nutrient requirements after electrophoretic separation of these cells. It is also necessary to determine whether the cells require any specific nutrients after flight experiments relative to earth-based duplicate cultures of the same cells. Depletion of certain nutrients would indicate the need for appropriate modifications in culture media composition for better support of cell growth and proliferation in future experiments.

## OTHER STUDIES

Using high pressure liquid chromatography (HPLC) and amino acid analysis, we have analyzed 164 samples of culture media that were supplied to us by JSC. The results have been delivered to NASA (JSC) and a computer analysis of the data is now being carried out by NASA scientists.

## ACKNOWLEDGEMENTS

This work is supported by NASA (Contract No. NAS 9-17403).

## REFERENCES

1. Todd, P., Kunze, M.E., Williams, K., Morrison, D.R., Lewis, M.L. and Barlow, G.H. (1985) Physiologist **28**, 6 Suppl. S183-184.
2. Steffens, G.J., Guenzler, W.A., Otting, F., Frankus, E. and Flohe, L. (1982); Hoppe-Seyler's Z. Physiol. Chem. **363**, 1043-1058.
3. Verde, P., Stoppelli, M.P., Galeffi, P., DiNocera, P.P. and Blasi, F. (1984); PNAS USA **81**, 4727-4731.
4. Riccio, A., Grimaldi, G., Verde, P., Sebastio, P., Boast, S. and Blasi, F. (1985); Nucl. Acids Res. **13**, 2759-2771.
5. Kasai, S., Arimura, H., Nishida, M. and Suyama, T. (1985); Cell Struc. and Function. **10**, 151-159.
6. Pennica, D., Holmes, W.S., Kohr, W.J., Harkins, R.N., Vohar, G.A. et al., (1983) Nature **301**, 214-221.
7. Young, C.R. and Atassi, M.Z. (1982) Immunol. Commun. **11**, 9-16.
8. Young, C.R., Schmitz, H.E. and Atassi, M.Z. (1983) Mol. Immunol. **20**, 567-570.
9. Atassi, M.Z. (1986) Methods Enzymol. **121**, 69-95.
10. Ossowski, L., and Reich, E. (1983); Cell **35**, 611-619.
11. Belin, D., Godeau, F. and Vassalli, J.D. (1984), EMBO Journal **3**, 1901-1906.
12. Harvey, S., Minowada, J., Takita, H., Kover, L., and Markus, G. (1982); J. Biol. Chem. **257**, 5645-5651.
13. Wun, T.C., Ossowski, L., and Reich, E. (1983); J. Biol. Chem. **257**, 7262-7268.
14. Atassi, M.Z., Kazim, A.L. and Sakata, S. (1981) Biochim. Biophys. Acta **670**, 300-302.
15. Schmitz, H.E., Atassi, H. and Atassi, M.Z. (1982) Mol. Immunol. **19**, 1699-1702.
16. Schmitz, H.E., Atassi, H. and Atassi, M.Z. (1983) Mol. Immunol. **20**, 719-726.
17. Schmitz, H.E., Atassi, H. and Atassi, M.Z. (1983) Immunol. Commun. **12**, 161-175.
18. Hunter, W.M. and Greenwood, F.C. (1962) Nature **194**, 495-496.

19. Sakata, S. and Atassi, M.Z. (1981) Mol. Immunol. 18, 961-967.
20. Atassi, M.Z. (1975) Immunochemistry 12, 423-438.
21. Atassi, M.Z. (1978) Immunochemistry 15, 909-936.
22. Atassi, M.Z. (1984) Europ. J. Biochem. 145, 1-20

## Hydrodynamic Effects on Cell Growth in Agitated Microcarrier Bioreactors

Robert S. Cherry and E. Terry Papoutsakis  
Chemical Engineering Department  
Rice University, Houston, Texas

### Abstract

The net growth rate of bovine embryonic kidney cells in a microcarrier bioreactor is the result of a variable death rate imposed on a cell culture trying to grow at a constant intrinsic growth rate. The death rate is a function of the agitation conditions in the system, and increases at higher agitation because of increasingly energetic interactions of the cell-covered microcarriers with turbulent eddies in the fluid. At very low agitation rates bead-bead bridging becomes important; the large clumps formed by bridging can interact with larger eddies than single beads, leading to a higher death rate at low agitation. The growth and death rates have been correlated with a dimensionless eddy number which compares eddy forces to the buoyant force on the bead.

### Introduction and Approach

The negative effect of excessive agitation on cells in culture is well known and has in the past been ascribed to vaguely defined "shear". Because the microgravity of space may allow the use of less agitation, there may be some operating improvement for a bioreactor in space. More importantly however, the study of cellular physiological differences between one g and microgravity requires that the agitation effects in each environment be known and quantified to eliminate them as uncontrolled variables. This project seeks to identify and describe quantitatively the mechanisms of cell damage in a stirred microcarrier bioreactor.

Because a microcarrier bioreactor is a complex turbulent two-phase (beads and liquid) system, a detailed analytical solution for all the forces imposed on the bead is not possible. We have tackled this problem by analyzing simplified models of potentially damaging bead-system interactions: bead-impeller collisions, bead behavior in a boundary layer, and interaction of the beads with turbulent fluid eddies [1]. The specific mechanisms of cell damage that are potentially significant based on the amount of shear stress or energy transmitted to the cell are bead-impeller collisions, bead-bead collisions, and direct bead-fluid eddy interactions. For each of these we derived a mathematical parameter which characterizes how much of that mechanism is occurring.

To test these ideas experimentally, we grew bovine embryonic kidney cells (analogous to NASA's human embryonic kidney cells but more readily available) on Cytodex 3 microcarriers in a well-controlled 1 liter stirred reactor [2]. Agitator geometry, speed, and diameter, bead diameter and medium viscosity and total volume were varied in different experiments, and the growth rate of the cells under each set of conditions was measured. In addition, the growth medium was replaced with a serum-free medium after some runs to measure the rate of decrease in the number of cells under non-growing conditions with specific agitation conditions. This gave us death rate information.



## Results and Discussion

Plotting our data against the various parameters for each potential damage mechanism showed that the eddy number gave the best and most consistent correlations. Figure 1 shows that the first order death rate of cells can be correlated with the log of the eddy number, a dimensionless number which compares the forces from turbulent eddies to the force a bead feels due to its buoyancy. Higher eddy numbers imply greater turbulent fluid forces, and the death rate increases correspondingly. Figure 2 shows growth rate data also correlates although there is a maximum in the curve. Above an eddy number of about 1, the trend decreases with the same slope as the death rate curve, which was an independent measurement. This implies that the decreased net growth rate is caused by an increase in the death rate acting on a population of cells trying to grow at some constant intrinsic rate.

At eddy numbers below about 1.0, the decrease in growth rate is apparently due to an increase in the amount of bridging in the system (Figure 3). Bridging causes cell death because the larger clumps formed by bridging can interact with more and larger eddies than can single beads, hence can suffer more damage. This result can also be shown mathematically with our derivations of the eddy number and the linear regressions of data.

The plan for future work in this area is to investigate more thoroughly the effect of such variables as volume fraction of beads in the system, other impeller configurations, and a broader range of medium viscosities. Now that the range of damage mechanisms to consider has been narrowed, a more detailed theoretical analysis of the fluid mechanics actually occurring is feasible. In addition, experiments measuring the death rate of cells in a well defined environment such as in a viscometer are planned. The goal of this work is to better and more accurately understand the interaction between a cell on a bead and its fluid environment.

This work was performed under NASA grant NAS 9-17403.

## References

1. Cherry, R. S. and E. T. Papoutsakis, *Bioproc. Eng.*, **1**, 29 (1986)
2. Cherry, R. S. and E. T. Papoutsakis, submitted to *Biotechnol. Bioeng.*, (1987)

FIGURE 1.

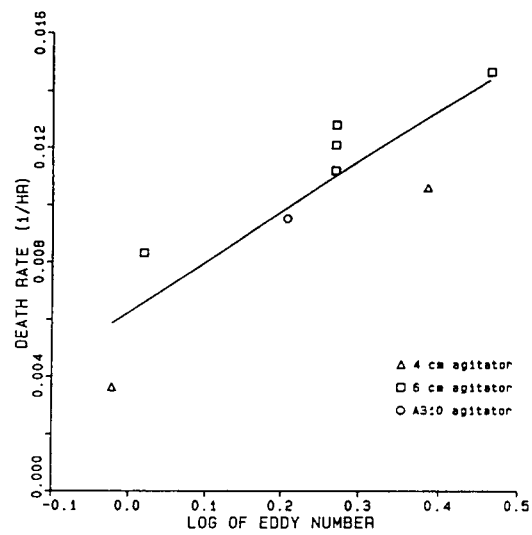


FIGURE 2.

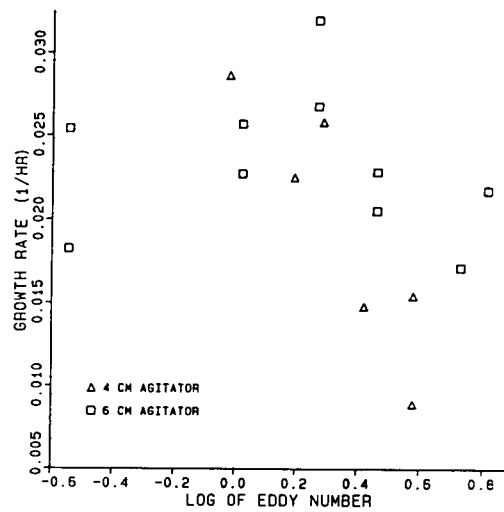
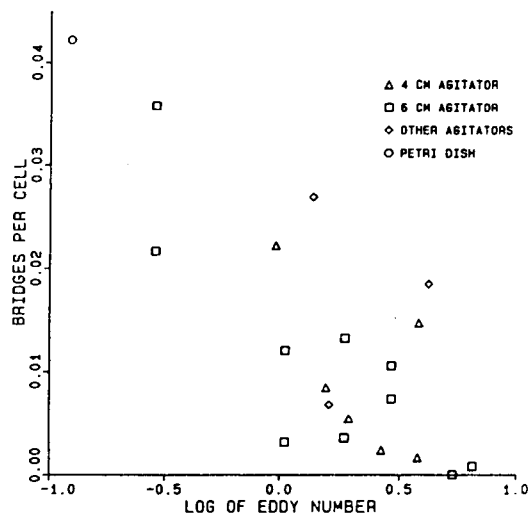


FIGURE 3.



## An Expert System Based Intelligent Control Scheme for Space Bioreactors

Ka-Yiu San  
Chemical Engineering Department  
Rice University, Houston, Texas

### Abstract

An expert system based intelligent control scheme is being developed for the effective control and full automation of bioreactor systems in space. The scheme developed will have the capability to capture information from various resources including heuristic information from process researchers and operators. The knowledge base of the expert system should contain enough expertise to perform on-line system identification and thus be able to adapt the controllers accordingly with minimal human supervision.

### Introduction and Approach

Mammalian tissue cells are very sensitive to small changes in their growth environment (pH, temperature, nutrient and byproduct concentrations) and thus require precise regulation on reactor parameters. However, the design and implementation of meaningful control strategies are often hindered by the lack of detailed knowledge about the system dynamics (growth kinetics of the tissue cells as an example) and the lack of availability of proper sensors. It is further complicated by the possibility of variations in process characteristics and parameters during the course of operation, such as change in the yield factor of the cells, the number of viable cells and their metabolic activities, etc. Under such situation, the proper tuning of a conventional proportional-integral-derivative controller can become an insurmountable task. This will, in most cases, result in poor reactor performance and possibly may lead to reactor failure. The above scenario clearly dictates the need for the development of a more sophisticated control scheme which is capable : 1) of providing proper control action despite changes in system dynamics, 2) of synthesizing meaningful and effective control strategies under highly uncertain environment, and 3) of integrating heuristic information into existing control algorithms to improve controller performance.

A novel controller design approach is being developed based on the observation that significant improvement in process performance can be achieved by implementing available ad hoc procedures. Most of these ad hoc procedures are in the form of rules that are the results of accumulated experiences and knowledge of the researchers or operators. These rules of thumb are frequently known as heuristics. Unfortunately, existing controller design approaches do not allow easy integration of this type of knowledge representation. We are presently developing an **expert system** which, in our believe, are best suited for the capturing and the utilization of this knowledge to improve controller performance. Expert systems are applications of the new and evolving techniques of Artificial Intelligence. It is a computer program that contains factual, as well as experimental, intuitive, uncertain, and judgemental knowledge. With this knowledge, the program reasons and infers new information to solve problems that are not amenable to algorithmic solutions. In general, an expert system contains three components: a knowledge base, a reasoning mechanism and a control mechanism.

The source of information that are being incorporated into the knowledge base of our expert system includes: 1) existing mathematical process models, 2) operators' and

researchers' experiences, 3) experimental data-base, and 4) up-to-date knowledge in cell biology and biochemistry of the process including metabolic pathways, proven or speculative kinetic mechanisms and so on (see figure attached). Furthermore, this knowledge base will be updated by the incoming process measurements. It is through the use of this powerful knowledge base that a meaningful control strategy will be synthesized and implemented.

In summary, the expert system developed herein will contain enough knowledge and expertise that it is capable of performing the tasks of system identification and process controller design with minimal human supervision. In addition, the final version of this control scheme will be a highly intelligent machine which is capable of learning by extracting information from the incoming measurements of the process variables and thus is capable of updating its reasoning pattern in response to changes in process behavior. This is the type of bioreactor control which has the best probability of success for long-term space bioprocessing applications.

## **Results and Discussion**

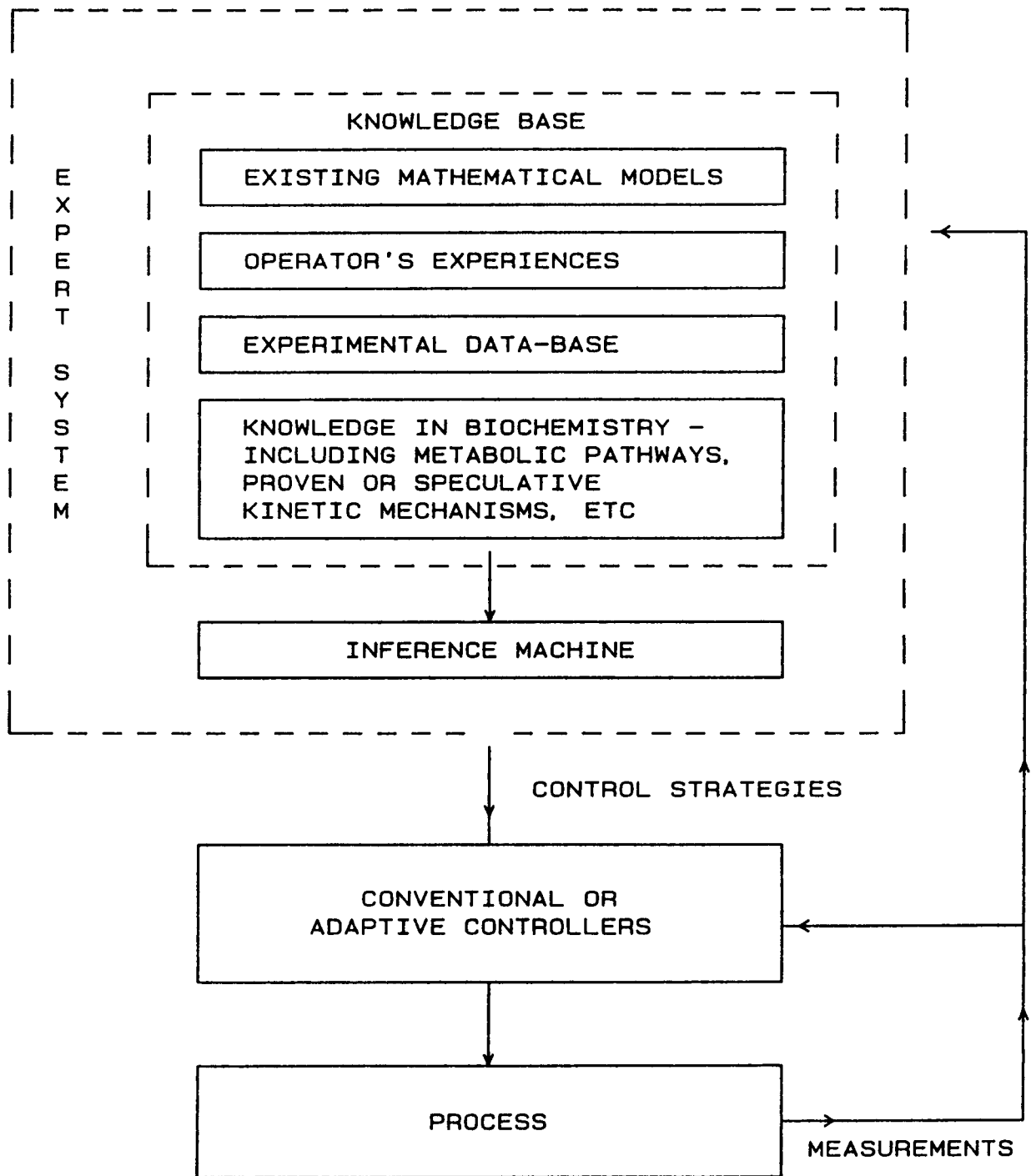
A study aiming at the investigation of the impact of the addition of an expert system to a conventional controller has been performed. Of particular interest is the feasibility of integrating ad hoc heuristic information to the overall control scheme. The control of pH value in a neutralization tank with inlets of different buffering capacities is chosen as a sample system. The set-up of this system is schematically shown in Fig. 1. The reactor pH is controlled by a PID controller which adjusts the flow rate of acid into the tank. Disturbances are introduced by changing the inlet composition according to table 1. The closed loop responses of the reactor pH with two fixed gain controllers tuned for different buffer content and an expert system consulting controller are shown in Fig. 2. The knowledge base of the expert system contains the necessary heuristic information about the process. Table 3 shows the square of the derivations of reactor pH from its set-point for each of the period as well as the total sum. Result from this study can be summarized as follows: 1) In the presence of system dynamic variation, a fixed gain controller may be either too tightly or too loosely tuned which results either in controller instability (middle curve of Fig. 2) or sluggish response (middle part of upper curve), and 2) An expert system based controller is capable of predicting the reactor buffer content and thus is able to select the correct controller setting. This results in a far better controller performance.

In conclusion, results from our studies demonstrate the feasibility as well as the potential of using an expert system to capture heuristic information to improve controller performance. We believe that this approach is capable to provide a fully automated environment with minimal human supervision which is critical for long-term space bioprocessing applications.

The plan for future work in this area is 1) to finish the development of such an expert system, 2) to perform a series of experiments to generate the required knowledge base as well as experiences about the process.

## **References and Acknowledgement**

1. Cardello R. and K.-Y. San, Proceedings of 1987 American Control Conference, June 10-12, Minnesota, to appear.
2. Cardello R. and K.-Y. San, submitted to Biotechnol. Bioeng., (1987)



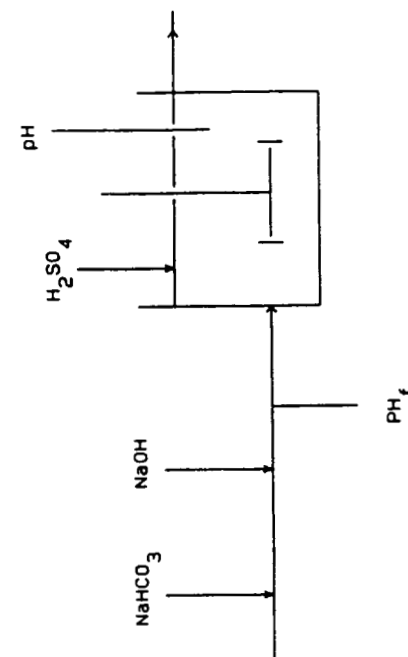
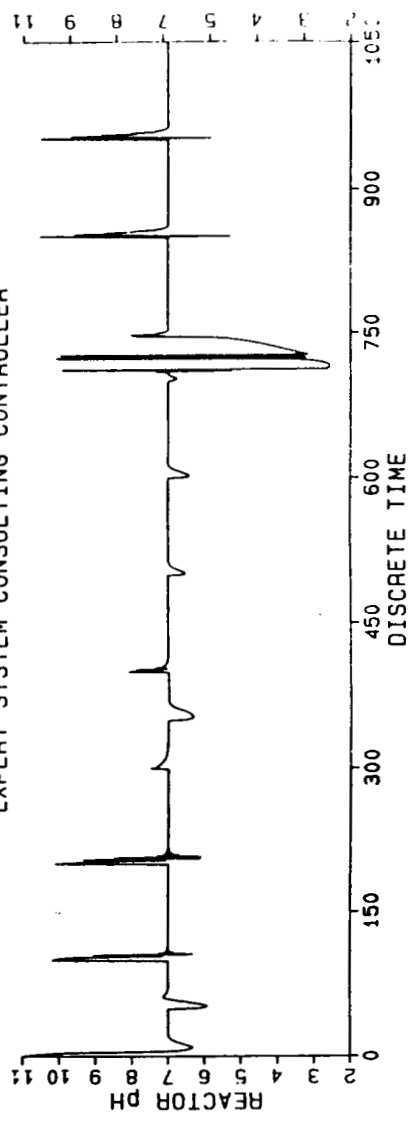
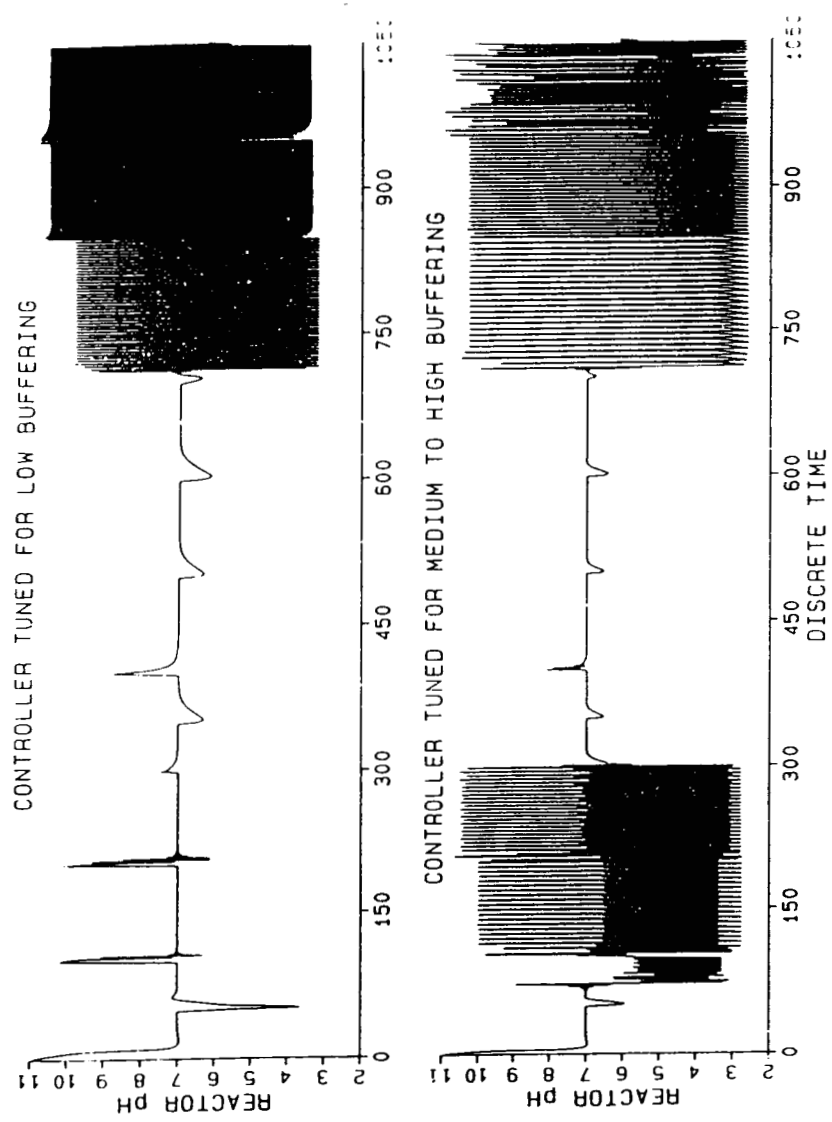


Fig. 4 Schematic of the Neutralization Tank

TIME	NaOH CONCENTRATION	NaHCO <sub>3</sub> CONCENTRATION	FEED pH
0	0.008	0.008	10.908
50	0.002	0.001	11.042
100	0.005	0.001	11.701
200	0.008	0.001	11.904
300	0.008	0.008	11.509
350	0.008	0.008	10.908
400	0.009	0.008	11.509
500	0.008	0.008	10.908
600	0.002	0.008	9.780
700	0.002	0.0	11.301
850	0.004	0.0	11.602
950	0.006	0.0	11.779

TABLE 1. FEED CONCENTRATION PROFILES

TIME	CONTROLLER TUNED FOR HIGH BUFFER CONTENT	CONTROLLER TUNED FOR LOW BUFFER CONTENT	EXPERT SYSTEM TUNED CONTROLLER
0	47.9	100.3	50.4
50	220.8	38.6	38.6
100	590.3	38.6	38.6
200	1130.4	30.0	30.2
300	19.3	0.6	0.6
350	1.0	4.6	3.9
400	2.2	10.3	2.2
500	1.0	4.6	1.0
600	1.8	8.0	1.8
750	2094.0	1529.3	406.9
850	1338.2	1284.7	29.6
950	1346.0	1280.3	29.6
TOTAL	7392.9	4348.5	600.2

TABLE 2. MEAN SQUARED ERROR FOR VARIOUS CONTROLLERS.

## SHEAR STRESS INDUCED STIMULATION OF MAMMALIAN CELL METABOLISM

L. V. McIntire, J. A. Frangos, and S. G. Eskin\*

Biomedical Engineering Laboratory  
Department of Chemical Engineering  
Rice University  
Houston, Texas 77251

\*Department of Surgery  
Baylor College of Medicine  
Houston, Texas 77030

**Abstract**

A flow apparatus has been developed for the study of the metabolic response of anchorage-dependent cells to a wide range of steady and pulsatile shear stresses under well-controlled conditions. Human umbilical vein endothelial cell monolayers were subjected to steady shear stresses of up to  $24 \text{ dynes/cm}^2$ , and the production of prostacyclin was determined. The onset of flow led to a burst in prostacyclin production which decayed to a long-term steady state rate (SSR). The SSR of cells exposed to flow was greater than the basal release level, and increased linearly with increasing shear stress. This study demonstrates that shear stress in certain ranges may not be detrimental to mammalian cell metabolism. In fact, throughout the range of shear stresses studied, metabolite production is maximized by maximizing shear stress.

**Introduction and Approach**

One of the major challenges to the scale-up of mammalian cell culture is often stated to be the detrimental effects of shear stress on cell viability. However, mammalian cells exhibit a wide range of shear sensitivity with respect to the stress level required to cause overt lysis and death. Some recent evidence suggests, that at lower levels, shear stress may have beneficial effects on cellular metabolism (1) and possibly viability. Since cells in most bioreactor configurations will invariably be subjected to some degree of fluid mechanical stresses, a clear understanding of the effects of shear stress on cellular metabolism will be required for optimal design and operation of mammalian cell reactors. This problem may be best approached by studying cell metabolism under conditions of well-characterized shear stress. To this end, we have developed a flow apparatus capable of subjecting cultured anchorage-dependent cells to a wide range of steady and pulsatile shear stresses for long time periods.

The cells used in this study are primary human umbilical vein endothelial cells. Endothelial cells form a multifunctional lining of the intimal surface of blood vessels. This lining is continuously subjected to both steady and oscillatory fluid shear stresses, resulting from the flow of blood in the circulation. Since they are the only anchorage-dependent cells that are normally physiologically exposed to shear stress, they may provide a useful model for cells in a bioreactor.

## SHEAR STRESS INDUCED STIMULATION OF MAMMALIAN CELL METABOLISM

One function of endothelial cells that appears to be modulated by shear stress is the metabolism of arachidonic acid (1, 2). Arachidonic acid is an essential polyunsaturated fatty acid stored in its esterified form in the cell membrane phospholipids. It is liberated from phospholipids by the action of a phospholipase (Figure 1). In umbilical vein endothelial cells, the major metabolite of arachidonic acid is prostaglandin I<sub>2</sub> (PGI<sub>2</sub>) or prostacyclin, which is produced by the cyclooxygenase pathway (Figure 1). Prostacyclin is a strong vasodilator and the most potent endogenously generated inhibitor of platelet aggregation. It has important biological activities in nanomolar concentrations.

Previously, we had demonstrated that shear stresses of 10 dynes/cm<sup>2</sup> stimulate the production of prostacyclin in cultured endothelial cells (1). Oscillatory shear stress (one Hertz) with the same mean value enhanced the production rate even further. In the present study, the flow apparatus we have developed for the study of the response of cultured anchorage-dependent cells to fluid shear stress is described in detail. In addition, the earlier data (1) are extended to demonstrate the effects of a wide range of steady shear stress on the production of prostacyclin by primary human umbilical vein endothelial cells.

Human umbilical vein endothelial cells were harvested from umbilical cords by means of culture procedures adapted from Gimbrone (3). For removal of the endothelial cells, the veins were cannulated, rinsed with 100 ml of phosphate-buffered saline (PBS; Gibco, Grand Island, NY), filled with 0.03% collagenase enzyme (Cooper Biomedical, Malvern, PA) in Medium 199 (Gibco, Grand Island, NY), and incubated for 30 minutes at room temperature. After incubation, the enzyme solution was flushed through the vessel with 100 ml of PBS, and the effluent was collected and centrifuged at 650 x g for 10 minutes. The cell pellet was resuspended in Medium 199 supplemented with 20% fetal bovine serum (Hyclone, Logan, UT), 200 U/ml penicillin, 200 µg/ml streptomycin (Gibco, Chagrin Falls, OH), and 300 µg/ml glutamine (Gibco). The cell suspension was plated onto glass slides (75 x 38 mm; Fisher Scientific, Pittsburgh, PA). The glass slides were pretreated with 0.5M NaOH for two to three hours and rinsed with distilled water, thereby enhancing cell adhesion by conferring a charge on the glass surface. Two slides were seeded per cord ( $5.0 \times 10^4$  to  $1.0 \times 10^5$  cells per slide). Cultures became confluent after three or four days and flow loop experiments were run three days after the cultures reached confluency.

The apparatus consists of two reservoirs, situated one above the other, with a parallel-plate flow chamber positioned between them (Figure 2). Flow is driven through the chamber by the hydrostatic pressure head created by the vertical distance between the upper and lower reservoirs. The pressure head is maintained constant by continuous pumping of culture medium from the lower to upper reservoirs at rates in excess of that flowing through the chamber. The excess drains down the glass overflow manifold (O.D. 19mm, Pyrex, Corning Glass Works, Corning, NY), which also serves to facilitate gas exchange with the medium. The upper and lower reservoirs are blown of glass, while the interconnecting tubing consists of Teflon PFE (O.D. 0.125 in., Cole Parmer, Chicago, IL), except for the section through the roller pump which is silicone (Masterflex, Cole Parmer, Chicago, IL). Silicone



## SHEAR STRESS INDUCED STIMULATION OF MAMMALIAN CELL METABOLISM

collars join the reservoirs to the manifold and tubing. The relatively inert and gas impermeable teflon tubing prevents water and gas loss and minimizes adsorption of cell metabolites.

The flow chamber consists of a machine-milled polycarbonate plate, a rectangular Silastic (size 0.020 in., Dow Corning, Midland, MI) gasket, and the glass slide with the attached endothelial cell monolayer (Figure 3). These were held together by a vacuum maintained at the periphery of the slide, forming a channel of parallel-plate geometry. The use of vacuum insured an uniform channel depth. The depth of the channel formed was normally 220  $\mu\text{m}$ , and the area of cells exposed to shear was 16  $\text{cm}^2$ . For studies of cell metabolism, it is usually important to minimize loop fluid volume and maximize cell surface area. The polycarbonate plate has two manifolds through which medium enters and exists the channel. The entry port is larger than the exit port and serves as a bubble trap. A valve opposite the entry port allows for the removal of the bubbles.

All loop parts are washed in Haemo-sol (Baltimore, MD), rinsed in deionized water, and oven-dried, then autoclaved. The loop parts are allowed to cool, assembled under a laminar flow hood, and reautoclaved. Medium is added to the top reservoir (10 - 20 ml), filling the bottom reservoir as well, and flooding the chamber. Then the slide with the cultured cells is inverted over the flooded chamber, and clamped. Care must be taken to avoid entrapment of air bubbles in flow channel.

During an experiment, the circuit components are placed in a 37°C air curtain incubator system and the reservoirs are connected to a gassing system that maintains a humidified atmosphere of 95% air and 5%  $\text{CO}_2$ .

The wall shear stress on the cell monolayer in the flow chamber may be calculated using the momentum balance for a Newtonian fluid and assuming parallel-plate geometry:

$$\tau = \frac{6Q\mu}{bh^2} \quad (1)$$

where

$Q$  = flow rate  $\text{cm}^3/\text{sec}$

$\mu$  = viscosity, about 0.01 dyne-sec/ $\text{cm}^2$

$h$  = channel height, 0.022 cm

$b$  = slit width, 2.5 cm

$\tau$  = wall shear stress, dynes/ $\text{cm}^2$

The mean residence time of medium in the flow chamber and the tubing between reservoirs for the experiments performed ranged from 5-30 seconds. Therefore, in time course studies of metabolite production, sampling from the lower reservoir contributes a temporal error of the order of less than one minute.

# SHEAR STRESS INDUCED STIMULATION OF MAMMALIAN CELL METABOLISM

The flow rate was controlled by adjusting the relative distance between the two reservoirs by changing the length of the overflow manifold tubing. The flow rates were monitored by an electromagnetic flow probe (Zepeda Instruments, Seattle, WA). The Reynolds number of the flow through the chamber is given by:

$$\begin{aligned} \text{Re} &= \frac{U h \rho}{\mu} \\ &= \frac{Q \rho}{\mu b} \end{aligned} \quad (2)$$

where  $U$  is the characteristic or mean average flow velocity,  $\rho$  is the density of the medium, and  $\mu$  is the viscosity of the medium. Combining equations (1) and (2),

$$\text{Re} = \tau \left( \frac{h^2 \rho}{6 \mu^2} \right) \quad (3)$$

The value of the quantity in the parenthesis for the apparatus is 0.807. For the range of shear stresses used in the present study, the Reynolds number varied from 0 to 20, indicating that fluid flow through the chamber was laminar. Because of the large aspect ratio ( $b/h$ ) and low Reynolds number found in the flow chamber, the above equation is valid for nearly all of the monolayer surface except very near the lateral edges of the flow chamber.

Schlichting (4) gives an estimate of the entry length ( $\ell$ ) for plane Poiseuille flow as:

$$\ell = .04 (h) \text{Re} \quad (4)$$

For our maximum Reynolds number of 20 and a channel height of .022 cm, the entry length is approximately .018 cm. Since the channel length was 6.4 cm, the entry length was negligible for these experiments.

In the present study, cell monolayers were subjected to shear stress for seven to eight hours. Samples were withdrawn every 5 to 30 minutes, and the flow circuit was simultaneously replenished with fresh medium to maintain a constant circulating volume of 20 ml. Sample and replenishing volumes were both 1 ml. At the end of each experiment, the monolayers were photographed and cells were harvested and counted with a hemocytometer to determine the total count. Cells were harvested enzymatically by treating the attached cells with trypsin-EDTA (1 mg/ml porcine trypsin, 0.2 mg/ml EDTA without  $\text{Ca}^{2+}$  and  $\text{Mg}^{2+}$ ; Gibco, Grand Island, NY) for three to five minutes, centrifuging the cell suspension at  $650 \times g$  for 10 minutes, and resuspending the pellet in  $\text{Ca}^{2+}$ - and  $\text{Mg}^{2+}$ -free Hanks balanced salt solution (Irvine Scientific, Santa Ana, CA). Viability was determined by the ability of cells to exclude trypan blue dye (Gibco, Grand Island, NY). The viable count was used to normalize the prostacyclin production rates with respect to cell number. To eliminate variations due to individual donors and monolayer age, replicate cultures were used. Here, cell monolayers were grown from cells seeded at identical density from the same pool of donor cords and utilized concurrently. Cell monolayers were exposed to steady shear

## SHEAR STRESS INDUCED STIMULATION OF MAMMALIAN CELL METABOLISM

stresses of 6, 16, and 24 dynes/cm<sup>2</sup> and sampling was done simultaneously. This covers the range of physiological interest for time average wall shear stresses in arterial vessels. In experiments designed to control for the flow chamber conditions, cell monolayers were perfused by a syringe pump at a near-zero shear stress (0.016 dynes/cm<sup>2</sup>). The outflow medium was collected for several hours to determine the basal release rate.

Prostacyclin production in the experiments was assayed in samples by measuring levels of immunoreactivity to the stable nonenzymatic breakdown product of prostacyclin, 6-keto-prostaglandin F<sub>1α</sub> (Figure 1). Before assaying, the samples were incubated at 37°C for half to one hour, to ensure hydrolysis of all prostacyclin to 6-keto-prostaglandin F<sub>1α</sub>. The assay sensitivity was 5 pg/0.1 ml, and cross-reactivity of the antibody with other culture media components and prostaglandins was negligible.

The radioimmunoassay buffer used for dilutions of antibody and tracer, and for the charcoal suspension, consisted of 0.05 M Tris-HCl, pH 7.5, and 0.1% gelatin (Sigma Chemical Co., St. Louis, MO). The solution was heated slightly to dissolve the gelatin. The radioimmunoassay was performed by incubating 0.1 ml of 6-keto-prostaglandin F<sub>1α</sub> standards (Sigma Chemical Co. St. Louis, MO) or samples with 0.2 ml of diluted antibody and 0.1 ml of <sup>3</sup>H-labelled 6-keto-prostaglandin F<sub>1α</sub> (10,000 cpm) (New England Nuclear, Boston, MA), in polypropylene tubes (Sarstedt, W. Germany) and vortexing. The standard curve was constructed from standards ranging in concentration from 5 pg/0.1 ml to 500 pg/0.1 ml, which were diluted in radioimmunoassay buffer. The efficiency of adsorption of free antigen by charcoal was determined by the blank tubes, which contained 0.1 ml tracer and 0.3 ml buffer. Each standard and sample was run in triplicate. Quality control was monitored by placing known standards (100 pg/0.1 ml) of 6-keto-PGF<sub>1α</sub> at intermediate points amongst the samples to be assayed. The incubation was carried out at 4°C for 16 hours. Separation of the bound and free antigen was achieved using gamma-globulin-coated charcoal. The charcoal suspension was prepared by dissolving 1 gm of bovine gamma-globulin (Sigma Chemical Co., St. Louis, MO) and 3 gm of Norit A charcoal (Sigma Chemical Co., St. Louis, MO) in 100 ml of radioimmunoassay buffer. The supernatant obtained after centrifugation was counted in a liquid scintillation counter, in the presence of 10 ml liquid scintillation fluid (Hydrofluor, National Diagnostics).

Cumulative production of prostacyclin was determined by performing a mass balance over the flow loop, taking into account samples withdrawn and medium replenished. By means of a Marquardt nonlinear regression analysis utilizing the statistical software package SAS, measurements of cumulative production of prostacyclin were fitted to a four-parameter equation:

$$P_c = A + B.(1 - \exp(-T/C)) + D.T \quad (5)$$

where  $P_c$  is the cumulative production of prostacyclin,  $T$  is time, and  $A$ ,  $B$ ,  $C$ , and  $D$  are the parameters to be determined. By taking the time

## SHEAR STRESS INDUCED STIMULATION OF MAMMALIAN CELL METABOLISM

derivative of Equation (5), a smooth expression for the rate of production (P) as a function of time is obtained:

$$P = B/C \exp (-T/C) + D \quad (6)$$

The parameters calculated by the regression analysis are related to the kinetics of the rate of production. The parameter D represents the steady-state or long-term production rate (SSR), and C was a time constant for the rapidity of decay of the initial burst in production of prostacyclin. Furthermore, given the length of the sampling interval, the peak production rate can be expressed as the rate of production at time zero ( $B/C + D$ ).

### Results and Discussion

Cell monolayers perfused at a near-zero shear stress of 0.016 dynes/cm<sup>2</sup> produced  $11 \pm 0.5$  pg PGI<sub>2</sub>/10<sup>6</sup> cells/min (n=3). This production rate of prostacyclin is essentially the same as that seen for tissue culture (no flow) controls of human umbilical vein endothelial cells. Figure 4 depicts the cumulative production and production rate of a typical set of experiments where replicate endothelial cell monolayers were exposed to shear stresses of 6, 16, and 24 dynes/cm<sup>2</sup>. The onset of flow led to a sudden increase in production of prostacyclin which decreased to a constant or steady state rate (SSR) within several minutes (Figure 4). The SSR increased with increasing shear stress (Table 1). The SSR of cells subjected to 24 dynes/cm<sup>2</sup> were significantly greater than the SSR of cells subjected to 6 dynes/cm<sup>2</sup> ( $p < 0.01$ ; two-tailed t-test). All values of the SSR are greatly different from the tissue culture (low or no flow) controls. In Figure 5, SSR is plotted as a function of the steady shear stress imposed. The SSR/stress response is essentially linear in this range of shear stress, with a slope of 4.9 pg/10<sup>6</sup> cells/min/dyne/cm<sup>2</sup> (corr = 0.93). It should be noted that this range of shear stresses covers the time average estimates of shear stresses normally seen in the human vascular system.

Both the peak production rate ( $B/C + D$ ) and the time constant for decay of the initial burst of PGI<sub>2</sub> production (C) were not significantly affected by the magnitude of steady shear stress exposure over the range studied (up to 24 dynes/cm<sup>2</sup>). This is shown graphically in Figure 4.

The flow apparatus described above provides a simple and inexpensive method for exposing anchorage-dependent cells to uniform wall shear stress, and has several advantages over other devices used to evaluate the effect of mechanical stress on cell function. Flow through the chamber is laminar and well characterized (5), and allows for in situ superposition of pulsatile flow. Furthermore, the flow chamber can be mounted on an inverted microscope, allowing for continuous visualization using video microscopy.

The flow system is well-suited for analysis of the effects of shear stress on the metabolism of attached cells. This system has been used

## SHEAR STRESS INDUCED STIMULATION OF MAMMALIAN CELL METABOLISM

to subject endothelial cells to shear for times in excess of five days. The excellent cell-to-volume ratio ( $10^6$  cells/10 ml) facilitates the study of the production of metabolites by cells. Furthermore, sampling of the medium is possible without cessation or disturbance to the flow in the cell-lined parallel plate flow chamber. Since most of the apparatus is assembled of glass and teflon, there is no loss of medium due to permeation through the tubing or evaporation. This avoids problems associated with changes in the osmotic balance of the medium.

Several groups have studied shear stress effects on cultured endothelial cells using a modified cone-and-plate viscometer (6, 7). Such an apparatus gives nearly uniform shear fields when operated at moderate to low speeds. These devices can be adapted to allow continuous microscopic monitoring, though this is not easy. The disadvantages of the cone-and-plate device as currently operated are that it has a smaller cell-to-volume ratio, does not permit continuous sampling of the cell incubating medium, and has significant tissue culture medium evaporation which requires continuous infusion of fresh medium for purposes of adjusting the osmolarity.

Others (8) have used flow loop devices qualitatively similar to the one described herein. However, the fluid volumes necessary to operate these apparatus are typically of the order of 100 ml, and the surface area of cells exposed to defined shear in the flow chambers has been approximately  $1 \text{ cm}^2$ . The low cell-to-volume ratio make these devices inadequate for use in most metabolic studies, since many metabolites of interest are produced at very low rates, yet have extremely important biological effects.

The data demonstrate that physiological levels of steady shear stress and the onset of shear stress dramatically stimulate prostacyclin production in cultured human endothelial cells. While step increases in shear stress led to a burst in production that leveled off within several minutes, shear stress itself exerted a sustained stimulation which lasted several hours (the duration of the experiments). This longer term stimulation of prostacyclin production rate varied linearly with increasing shear stress. Previously, we have shown that the degree of stimulation of production is a function of the pulsatility of the wall shear stress as well as its mean value (1).

The ability of cells to respond to external stimuli involves the transduction of a signal across the cell plasma membrane. One such external stimulus appears to be fluid shear stress.

Shear stress and the time-variance in shear stress presumably act on cells by perturbing the cell cytoskeleton and its membrane morphology. Time-varying or fluctuating shear stress, such as pulsatile shear and step-changes in shear, probably perturb the anchorage-dependent cell as a whole, causing membrane perturbations at the points of attachment to the cytoskeleton and the substratum. On the other hand, steady shear stress may act by amplifying the natural thermal or Brownian fluttering or rippling of the membrane (9). This fluttering has been observed in red blood cell membranes and phospholipid bilayers (9). Our earlier work (1) has shown that pulsatile stress (1 Hertz, amplitude 20% of the

## SHEAR STRESS INDUCED STIMULATION OF MAMMALIAN CELL METABOLISM

mean) can lead to significantly greater production rates of PGI<sub>2</sub> when compared to steady stress exposure at the same mean value.

Previously, it has been demonstrated that shear-induced production of prostacyclin may be blocked by ibuprofen (1). This would indicate that the point of action of stress stimulation is at the cyclooxygenation of arachidonic acid or in preceding steps. Since it is generally believed that arachidonic acid metabolism is rate-limited by its intracellular availability (10), it is possible that shear stress acts by increasing the rate of liberation of arachidonic acid. Active secretion of prostacyclin is not likely since there are no preformed intracellular stores of prostaglandins (11).

There are several possible mechanisms by which shear stress-induced membrane perturbations could mimic a hormone/receptor interaction to stimulate cell metabolism intracellularly. Shear stress may induce increased phospholipase C activity, caused by translocation of the enzyme, increased substrate (arachidonic acid) pool availability to phospholipase C (particularly from that stored in phosphoinositols) due to shear-induced membrane movements or changes in membrane fluidity, direct activation of calcium-activated phospholipase A<sub>2</sub> by increased calcium ion permeability, or most probably a combination of these mechanisms.

Levels of shear stress in the range of 5 - 20 dynes/cm<sup>2</sup> can be seen in mammalian cell bioreactor environments (12). Release of various arachidonic acid metabolites stimulated by this stress exposure can greatly modify reactor performance. It has been shown that cell-cell communication via arachidonic acid metabolites can alter cell function, leading to degranulation and aggregation in a shear field (13). The endothelial cells used in this study are unusual for tissue cells in that they normally do live in an environment which includes fluid mechanical force exposure. Because of this, the results presented above may be limited to this cell type, and extrapolation of these findings to the metabolic response of other mammalian cells to shear stress exposure should be done with care.

Hollis and co-workers (14, 15) have observed in both in vivo and in vitro studies that shear stress stimulates increased histamine forming capacity in bovine aortic endothelial cells. If shear stress stimulates protein synthesis, there may be possible applications in mammalian cell bioreactor design. Giard and co-workers (16) observed that human fibroblasts secrete up to 30 fold greater amounts of interferon when maintained on microcarriers in spinner flasks compared to cells in roller bottles. Since the shear stresses that cells are exposed to in the spinner flasks are much higher than those in roller bottles, the increased production may be attributable to shear stress-induced stimulation of interferon synthesis.

By choosing an appropriate reactor configuration, cells may be subjected to moderate shear stresses that would stimulate synthesis of proteins, yet not cause cell detachment and subsequent loss of viability. In fact, the strength of adhesion to the substrate, in and of itself, may be increased if cells are subjected to shear stress.

## SHEAR STRESS INDUCED STIMULATION OF MAMMALIAN CELL METABOLISM

Preliminary studies on endothelial cells subjected to shear in serum-free medium suggested that sheared cells exhibit increased strength of attachment and viability compared to control cultures (our laboratory, unpublished observations). Studies of these phenomena should include investigation of the effects of shear stress on the synthesis and release of adhesive proteins such as fibronectin and collagen.

### References and Acknowledgment

- 1 J.A. Frangos, S.G. Eskin, L.V. McIntire, and C.L. Ives: *Science*, 227, 1477 (1985).
- 2 E.F. Grabowski, E.A. Jaffe and B.B. Weksler: *J. Lab. Clin. Med.*, 105, 36 (1985).
- 3 M.A. Gimbrone Jr.: *Prog. Haemostas. Thromb.*, 3, 1 (1976).
- 4 H. Schlichting: *Boundary Layer Theory* (McGraw-Hill, New York, 1968), p. 178.
- 5 L.V. McIntire and S.G. Eskin: *White Cell Mechanics: Basic Science and Clinical Aspects* (Alan R. Liss, New York, 1984), H. Meiselman (ed.), pp. 209 - 219.
- 6 S.R. Bussolari and C.F. Dewey Jr.: *Rev. Sci. Instrum.* 53, 1951 (1982).
- 7 A. Van Grandelle, G.S. Worthen, D. Ellsi, M.M. Mathias, R.C. Murphy, R.J. Strife and N.F. Voelkel: *J. Appl. Physiol.* 57, 388 (1984).
- 8 M.J. Levesque and R.M. Nerem: *J. Biomech. Engr.* 107, 341 (1985).
- 9 M.B. Schneider, J.T. Jenkins and W.W. Webb: *Biophys. J.* 45, 891 (1984).
- 10 R.F. Irvine: *Biochem. J.* 204, 3 (1982).
- 11 M.A. Palmer, P.J. Piper and J.R. Vane: *Brit. J. Pharmac.* 49, 226 (1973).
- 12 R.S. Cherry and E.T. Papoutsakis: *Bioproc. Eng.* 1, 29 (1986).
- 13 B.G. Rhee and L.V. McIntire: *Chem. Engr. Comm.* 47, 147 (1986).
- 14 L.A. Rosen, T.M. Hollis and M.G. Sharma: *Exp. Mol. Path.* 20, 329 (1974).
- 15 J.M. DeForrest and T.M. Hollis: *Am. J. Physiol.* 234, H701 (1978).
- 16 D.J. Giard, D.H. Loeb, W.G. Thilly, D.I.C. Wang and D.W. Levine: *Biotech. Bioeng.* 21, 433 (1979).

This work was partially supported by Grants HL 18672 and HL17437 from the National Institutes of Health and Grants NAS9-17403 and NAG 9-207 from the National Aeronautics and Space Administration.

# SHEAR STRESS INDUCED STIMULATION OF MAMMALIAN CELL METABOLISM

**Table 1: Effect of Steady Shear Stress on the Steady-State Production Rate of Replicate Cell Monolayers**

Experiment	Shear Stress		
	6 dynes/cm <sup>2</sup> *	16 dynes/cm <sup>2</sup>	24 dynes/cm <sup>2</sup>
1	40	118	134
2	66	88	127
3	71	85	120
Mean $\pm$ S.D.	59 $\pm$ 16*	97 $\pm$ 18	127 $\pm$ 7*

\* p < 0.01; two-tailed t-test

Production rates are given as pg PGI<sub>2</sub>/10<sup>6</sup> cells/min. Note the very low flow or tissue culture production rate of PGI<sub>2</sub> was 11 pg/10<sup>6</sup> cells/min.

## Figure Legends

Figure 1: Arachidonic acid cascade via the cyclooxygenase pathway. Arachidonic acid is liberated from cell membrane phospholipids via the action of a phospholipase. This is metabolized by a series of enzymes (complex) to the unstable endoperoxide PGH<sub>2</sub>. In umbilical vein endothelial cells, the major pathway from PGH<sub>2</sub> is to PGI<sub>2</sub> via prostacyclin synthetase. PGI<sub>2</sub> is unstable and in buffers at pH 7.4 is hydrolyzed to 6-keto-PGF<sub>1 $\alpha$</sub>  with a half life of approximately 3 minutes.

Figure 2: Drawing of small volume flow loop. (1) upper reservoir, (2) lower reservoir, (3) overflow manifold, (4) filtered humidified 95% air + 5% CO<sub>2</sub> input, (5) gas outlet, (6) flow chamber, (7) gasket, (8) slide with cell monolayer, (9) microscope objective, (10) vacuum, (11) sampling port, (12) roller pump, (13) PFA teflon tubing, (14) constant pressure head, and (15) flow probe.

Figure 3: Parallel plate flow chamber. The polycarbonate plate, the gasket (G), and the glass slide (H) with the attached cells are held together by a vacuum (C), forming a channel of parallel plate geometry. Medium enters at entry port (A), through slit (E), into the channel, and exits through slit (F), and exit port (B). Entry port (A) also serves as a trap for bubbles, which can be removed through valve (D).

Figure 4: Effect of steady shear stress on prostacyclin production - representative set of experiments. Replicate cell monolayers were exposed to shear stresses of 6, 16, and 24 dynes/cm<sup>2</sup>. (A) The cumulative production of prostacyclin; (B) The production rate, computed as the derivative of the fitted curves in (A).

Figure 5: Effect of steady shear stress on prostacyclin production. The steady state production rates plotted against steady shear stress. The values 6, 16, 24 dynes/cm<sup>2</sup> represent averaged values of 3 replicate sets of experiments (Table 1). The values for 0.016 and 10 dynes/cm<sup>2</sup> were obtained from data presented elsewhere (1). Errors represent the SEM.



# SHEAR STRESS INDUCED STIMULATION OF MAMMALIAN CELL METABOLISM

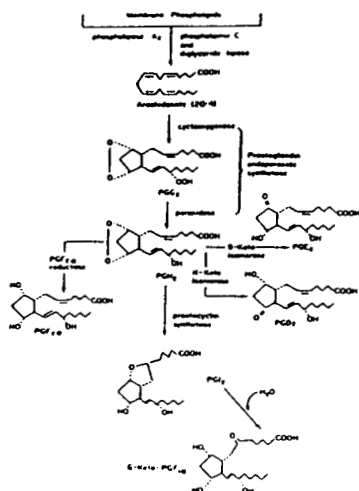


Figure 1

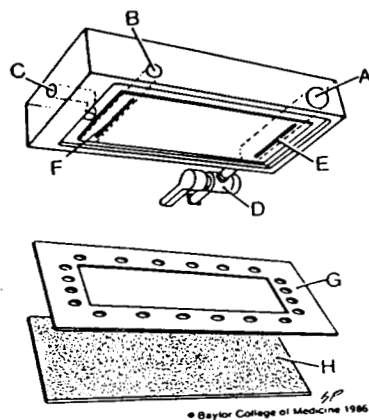


Figure 3

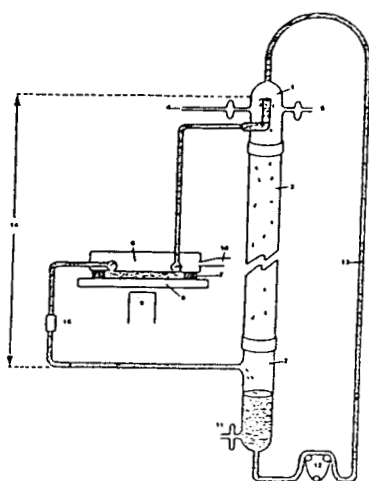


Figure 2

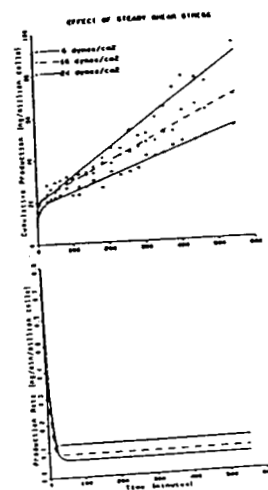


Figure 4

ORIGINAL PAGE IS  
OF POOR QUALITY

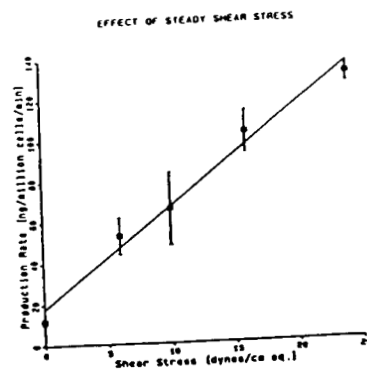


Figure 5

BIOCHEMICAL ASSAYS ON PLASMINOGEN ACTIVATORS  
AND  
HORMONES FROM KIDNEY SOURCES

GRANT H BARLOW, MARIAN L LEWIS, AND DENNIS R MORRISON

Bioprocessing Research Center, University of Texas Health  
Science Center at Houston, KRUG International, Technology Life  
Science Division, Houston, And NASA-Johnson Space Center, Houston

Ever since Williams (1) first described the plasminogen activator from human urine and Sobel (2) named it urokinase (UK) and the vascular activator was described by Aoki (3) the activator system in man has become more complex. What at first appeared to be single well defined proteins have now been shown to exist in multiple molecular forms. UK can exist as a single or two chain molecule (4) and as a fully active degraded two chain form (5), or a degraded single chain form (6). Vascular activator, which is now more widely known as tissue plasminogen activator (t-PA), can also exist as a single or two chain molecule (7) and has been reported to also have a degraded form (8). In any normal system the presence of many different molecular forms is highly possible and based on the potential for different responses in different assays can lead to a very complex problem with interpretation (9).

Determination of activity levels can be further complicated by inhibitors to the activator as well as to plasmin, the end product of the enzymatic activity of the activators. The use of amidolytic and esterolytic

assays that measure the enzyme activity directly can give a very different response than those assays which are of the indirect nature requiring the measurement of the enzyme plasmin, the results of the activation of plasminogen by the activator.

These investigations were established for the purpose of analyzing the conditioned media from human embryonic kidney cell subpopulations separated in space by electrophoresis. This data is based on the experiments performed on STS-8 on the Continuous Flow Electrophoresis System (CFES), developed by McDonnell-Douglas Astronautics Co. The primary biological activity that was analyzed was plasminogen activator activity, but some assays for erythropoietin and human granulocyte colony stimulating activity were also performed.

The cell preparation prior to separation and the subsequent culturing of the sub-fractions were not part of these investigations and were accomplished at the Johnson Space Center.

## ASSAYS

FIBRIN PLATE LYSIS ASSAY (FPL): The standard assay described by Brakkman (10) and modified by the addition of plasminogen (11) was adapted as follows. In 15 X 100 mm disposable petri plates the following materials were added: 10 ml of 7.5 mg/ml plasminogen free bovine fibrinogen (Miles Laboratories, Naperville, IL) in a 0.1 mol/l TRIS-HCl pH 8.0 buffer, 75 mg of human lys-plasminogen (American Diagnostica), and 4 IU plasminogen free

bovine thrombin (Miles Laboratories) in a 0.02 mol/l  $\text{CaCl}_2$  + 0.15 mol/l NaCl solution. To the clots, 20  $\mu\text{l}$  volumes of the conditioned medium sample at four serial two-fold dilutions were applied to each plate. After 18 hours at ambient temperature, the lysis zone diameters were read using a Transidyne General (Ann Arbor, MI) calibrating viewer (model 2743).

MICRO-CLOT LYSIS ASSAY (MCLA): This assay, developed in our laboratory was described by Lewis *et al.* (12) and utilizes 96 well flat bottom micro-well plates. The reaction mixture in the wells consisted of a fibrinogen solution containing plasminogen, thrombin, and the conditioned medium sample of PA standard. The optical density of the clots in each well was arbitrarily monitored at 405 nm at 5 minute intervals using an EIA automated microplate reader (Bio-Tek Instruments, Winoeski, VT, model EL310). The reader was connected via a serial interface to an Apple IIe computer. The computer received the data and determined the time at which the clots were half lysed, the assay endpoint, by use of software developed on the Apple IIe for this assay. As with the FPL assay, the activity for each sample was derived by comparison to the IRP-UK.

AMIDOLYTIC ASSAY (S-2444): The amidolytic assay using the synthetic substrate Pyro-Glu-Gly-Arg-pNA (S2444, KabiVitrum, Sweden) was essentially that described by Claeson *et al.* (13). For activation of latent PA in the conditioned medium, samples were incubated for 30 minutes at 37°C with human plasmin (American Diagnostica) at a final concentration of 2.3  $\mu\text{g/ml}$  of sample volume. Activation was stopped by the addition of aprotinin (Trasylol, FBA Pharmaceuticals, New York, NY) at 10 KIU/ml in a TRIS-NaCl-HCl buffer at pH 8.8. S-2444 was then added to this solution in

the wells of microtiter plates and the plates were incubated an additional 4 hours at 37°C. The absorbance was read at 405 nm using a Litton Bionetics (Charleston, SC) model LB130 microplate reader. The direct assay plates (without plasmin incubation) were handled in the same manner except that instead of addition of plasmin, an equivalent volume of the TRIS-NaCl-HCl buffer was added to samples.

TISSUE PLASMINOGEN ACTIVATOR (t-PA): The materials and methods for the t-PA assay were contained within the IMUBIND t-PA ELISA kit from American Diagnostica (14). The assay was modified using medium containing human serum albumen as a diluent. The flat bottom microwell plates (Immulon 2, Dynatech Laboratories, Alexandria, VA) plates were read at 490 nm on the EL310 autoreader.

PLASMIN INHIBITORS: To determine presence of plasmin inhibitors in the conditioned medium, samples were incubated with a known excess of human lys-plasmin. Residual plasmin activity was measured by the chromogenic substrate H-D-Val-Leu-Lys-pNA (S-2252, KabiVitrum, Sweden) at 405 nm (15) using the LB130 reader. Results are expressed as percent reduction in plasmin activity in the conditioned medium samples from the cultured cells compared to the unconditioned medium.

SODIUM DODECYL SULFATE POLYACRYLAMIDE ELECTROPHORESIS, (SDS PAGE), AND ZYMOGRAPHY: SDSPAGE electrophoresis to determine the molecular weight of the enzyme was performed as described by Laemmli (16). The resultant gels were analyzed for functional activity by development of a zymograph by the method of Tissot (17) involving a fibrin overlay.

ERYTHROPOIETIN: This assay was performed using a commercially available ELISA kit purchased from JCL Clinical Research Corp. (Knoxville, Tenn.). The analyses were performed as described in the methods brochure supplied with the kit.

HUMAN GRANULOCYTE COLONY STIMULATING ACTIVITY: This assay was performed using mouse marrow cells at a concentration of 75000 cells/ml. as described by Dipersio et al (18).

## RESULTS

Figure 1 shows the results on the conditioned media from the subpopulations by two assay for plasminogen activator activity, the fibrin plate lysis assay and the direct assay using the chromogenic substrate S-2444. As can be seen there is a large discrepancy between the activity levels as measured by these two different assays.

Figure 2 shows the results comparing the S-2444 direct with the S-2444 activated. These results show that much of the samples are in the single chain zymogen form and when activated with plasmin to the two chain form show a substantial increase in activity.

Figure 3A shows a comparison of the micro clot lysis assay with the fibrin plate lysis assay. As can be seen there is good correlation between the two assays except in the subpopulation region from fraction 9 thru 15. In Figure 3B these same fractions were analyzed for the presence of plasmin inhibitor and the fractions in the range 9-15 show significant

anti-plasmin activity. Thus the presence of anti plasmin in these fractions appear to be the cause for the discrepancy between the two different assays. The FPL assay appears to be independent of the presence of inhibitor while the MCLA assay is depended on the presence of such an inhibitor.

Figure 4 shows the entire set of data on the subfractions by the different assays. The results obtained are very dependent on the assay that is performed and points out dramatically the need to use a battery of assays to define the plasminogen activator profile of a sample from the conditioned media of cells in culture.

Figure 5A shows a typical fibrinogram on selected subpopulation samples. These fractions all show the presence of only species at 54,000 daltons, but do not distinguish between single and two chain forms. Figures 5B and 5C show the same gel on fibrinograms in which the fibrin overlay has been treated with specific antibody for u-PA to t-PA and allows one to determine the species present

While the majority of the analyses were to study the distribution of plasminogen activator(s), we did perform assays for two other biological activities associated with embryonic kidney cells in culture. The ELISA assay for erythropoietin showed areas of positive response but they were at a very low level. However, on triplicate determinations on the growth medium from run 4 there were consistent indications of a positive response in some subpopulations, these positive subpopulations showed levels of about 10 milli-immunological units per milliliter when compared with the standard. The assay kit as determined by our standard curve is insensitive to levels

below the 10 milliunits we detected. The mouse marrow assay for granulocyte colony stimulating activity was run on the growth media from both runs 3 and 4 and in both cases the results were negative.

## DISCUSSION

The major conclusion that can be reached by this work is that a battery of assays are required to completely define the plasminogen activator profile of a conditioned media from cell culture. Each type of assay measures different parts of the mixture and are influenced by different parameters. Table 1 expresses the functional role of each assay and gives an indication of which combination of assays are required to answer specific questions. With this type of information it is possible by combinations of assays with mathematical analysis to pinpoint a specific component of the system. This problem can sometimes be simplified by first analyzing the samples by SDSPAGE and zymography with the specific antibodies to detect the different molecular forms and different molecular species present.

It was disappointing that the assays for human granulocyte colony stimulating activity were negative and that the assays for erythropoietin were at best marginal in the response that was obtained. Since ground based experiments have shown that embryonic kidney cells produce both of these biological activities when grown in culture, the lack of detectable activity in the space experiments must be due to the mechanics involved in the treatment of the cells and/or cultures.



## REFERENCES

1. Williams J R B 1951 The fibrinolytic activity of urine. British J. Exp. Path. 32:530-537
2. Sobel G W, Mohler S R, Jones N W, Dowdy A B C, Guest M M 1952 Urokinase: an activator of plasma profibrinolysin extracted from urine. Am J Physiol 171:768- 769
3. Aoki N, von Kaulla K N 1971 The extraction of vascular plasminogen activator from human cadavers and a description of some of its properties. Amer. J. Clin. Path 55:171-179
4. Wun T-C, Ossowski L, Reich E 1982 A proenzyme form of human urokinase. J. Biol Chem 257:7262-7268
5. White W F, Barlow, G H, Mozen M M 1966 The isolation and characterization of plasminogen activators (urokinase) from human urine. Biochem 5:2160=2169
6. Stump D C, Lijnen H R, Collen, D 1986 Purification and characterization of a novel low molecular weight form of single chain urokinase-type plasminogen activator. J Biol Chem 261:17120-17126
7. Wallen P, Ranby M, Bergsdorf N, Kok P 1981 Purification and characterization of tissue plasminogen activator: on the occurrence of two

different forms and their enzymtic properties. In: Davidson J F et al. (eds), Progress in Fibrinolysis, Churchill Livingstone, Edinburgh, UK, 16-23

8. Heussen C, Dowdle E B 1980 Electrophoretic analysis of plasminogen activators in polyacrylamide gels containing sodium dodecyl sulfate and polymerized substrates. Anal. Biochem 102:196-202

9. Lewis M L, Morrison D R, Mieszkuk B J, Fessler D L 1984 Problems in the bioassay of products from HEK cells: Plasminogen activator. In: Acton R T et al (eds), Eukaryotic Cell Cultures, (Advances in Experimental medicine and Biology; Vol 172), Plenum Press, New York, 241-267

10. Brakkman K 1967 Fibrinolysis: a standardized fibrin plate method and a fibrinolytic assay of plasminogen. Scheltema and Holkema Publishing Amsterdam

11. Marsh N A, Gaffney P J 1977 The rapid fibrin plate- a method for plasminogen activator assay. Thromb Haem 38:541-551

12. Lewis M L, Nachtwey D S, Damron K L, Swank P R 1985 Development of a micro clot lysis assay for urokinase. Thromb Haem 54 102, Abstract P606.

13. Claeson G, Aurell L, Friberger P, Gustavsson S, Karlsson G 1978 Designing of peptide substrates. Different approaches exemplified by new chromogenic substrates for kallilreins and urokinase. Haemostasis 1:62-68

14. Bergsdorf N, Nilsson T, Wallen P 1983 An enzyme linked immuno-sorbent assay for determination of tissue plasminogen activator, Thromb Haem 50:740-744

15. Teger-Nilsson A C, Friberger P, Gyzander E 1977 Determination of a new rapid plasmin inhibitor in human blood by means of a plasmin specific tripeptide substrate. Scand J Clin Lab Inves 37:403-409

16. Laemmli U K 1970 Cleavage of structural proteins during assembly of the head of bacteriophage T4. Nature 227:680-685

17. Tissot J D, Schneider P, Hauert J, Ruegg M, Kruithof E K O, Bachmann F 1982 Isolation from human plasma of a plasminogen activator identical to urinary high molecular weight urokinase. J. Clin Invest. 70:1320-1323

18. Diersio, J F, Brennan J K, Lichtman M A, Abboud C N, Kirkpatrick F H, The fractionation characterization and subcellular localization of colony stimulating activities by the human monocyte-like cell line GCT. Blood 56:717-727

**TABLE 1.**

**1. FIBRIN PLATE LYSIS**

Diffusion based  
Not affected by many inhibitors  
Molecular weight dependent  
Zymogen partially seen

**2. MICRO CLOT LYSIS**

Modification of classic tube lysis method  
Measures uPA and tPA together all molecular weights  
Zymogen partially seen  
Inhibitors are functional

**3. CHROMOGENIC = DIRECT ASSAY WITH S-2444**

Sees both forms of uPA  
Zymogen not seen  
tPA most likely not seen  
Only activator inhibitors measured

**4. CHROMOGENIC = ACTIVATED ASSAY WITH S-2444**

Sees all forms of uPA including zymogen  
tPA not seen  
Inhibitor same as S-2444

**5. PLASMINOGEN ACTIVATION MEASURE PLASMIN BY CHROMOGENIC WITH S2251**

Sees both forms UK  
Zymogen partially seen  
tPA not seen (modify by adding fibrin monomer)  
Sees inhibitor

**6. SDS PAGE WITH ZYMOGRAPHY**

Shows all molecular weights for uPA-tPA  
Qualitative, not quantitative  
Does not differentiate zymogen

**FIGURE 1.**

Plasminogen activator activity in conditioned medium from human kidney (HK) cell subpopulations as detected by amidolytic S-2444 (○) and fibrin plate lysis (△) assays.

**COMPARISON OF FIBRIN PLATE AND CHROMOGENIC ASSAYS**

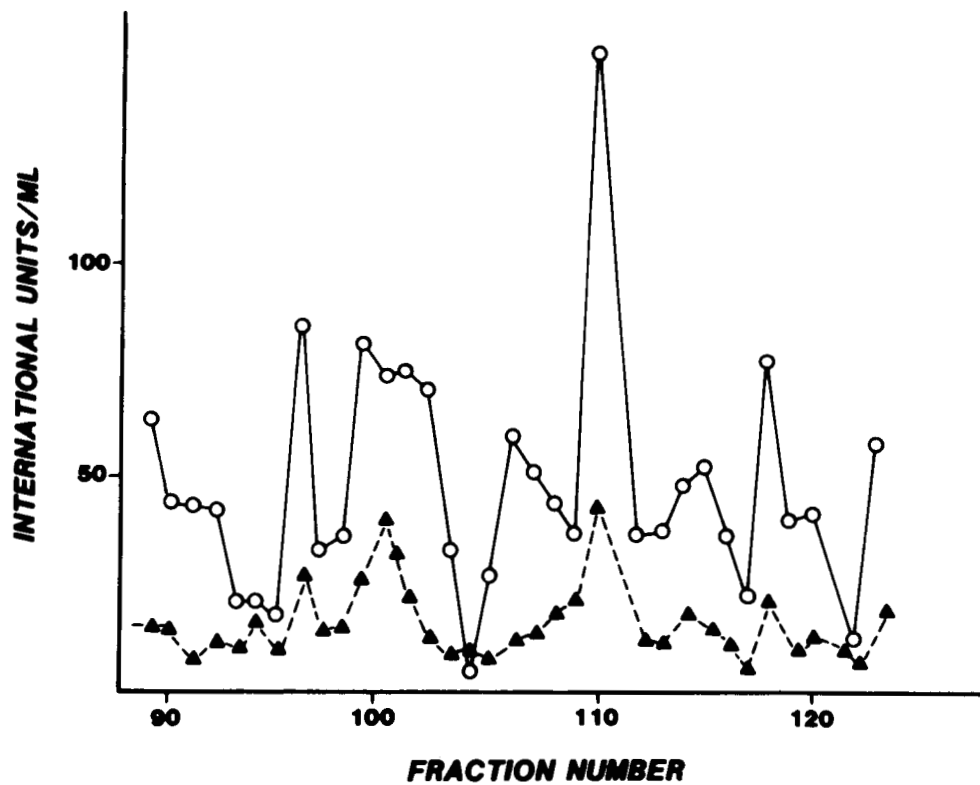


**FIGURE 2.**

Amidolytic activity detected after incubation of conditioned medium samples with plasmin for 30 minutes (activated,  $\Delta$ ) compared to activity of the same samples not incubated with plasmin (direct,  $\square$ ).

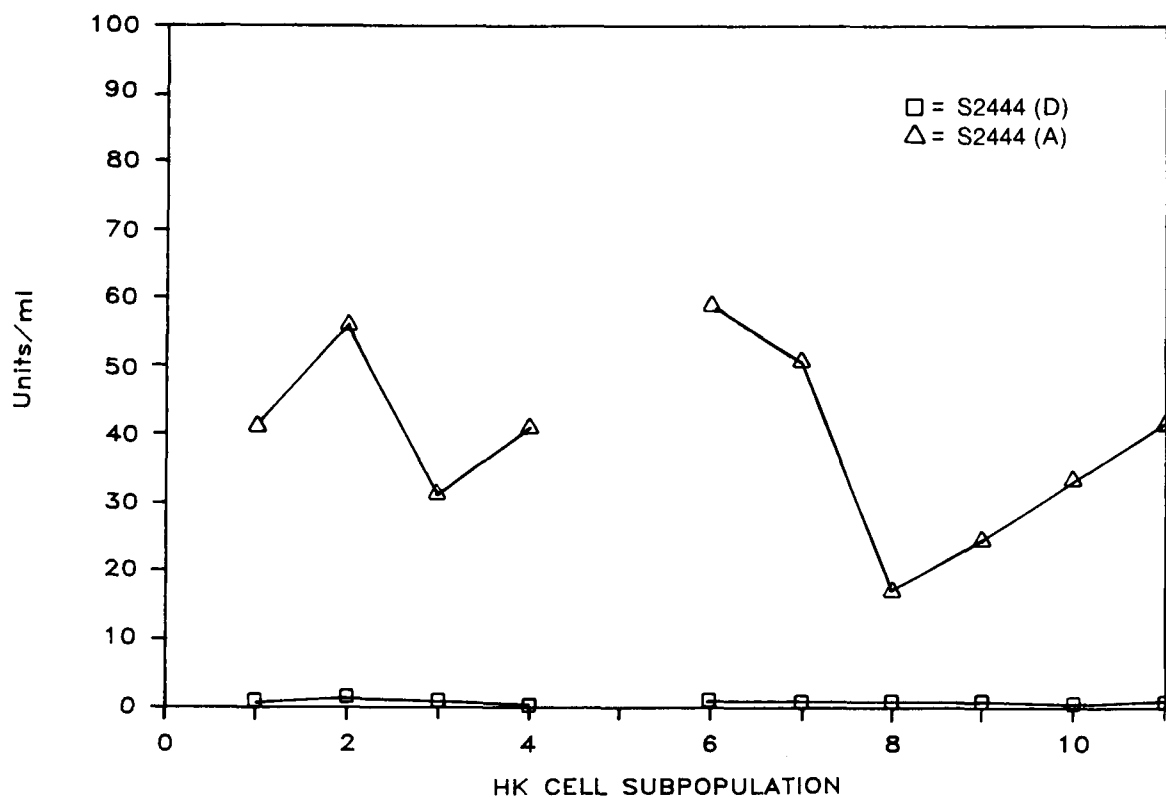


**FIGURE 3A.**

Comparison of the fibrin plate (+) and micro-clot lysis assays ( $\square$ ) for detecting fibrinolytic activity in conditioned medium from HK cell subpopulations. Both assays showed comparable activity except for the subpopulations in the range of 9-15.

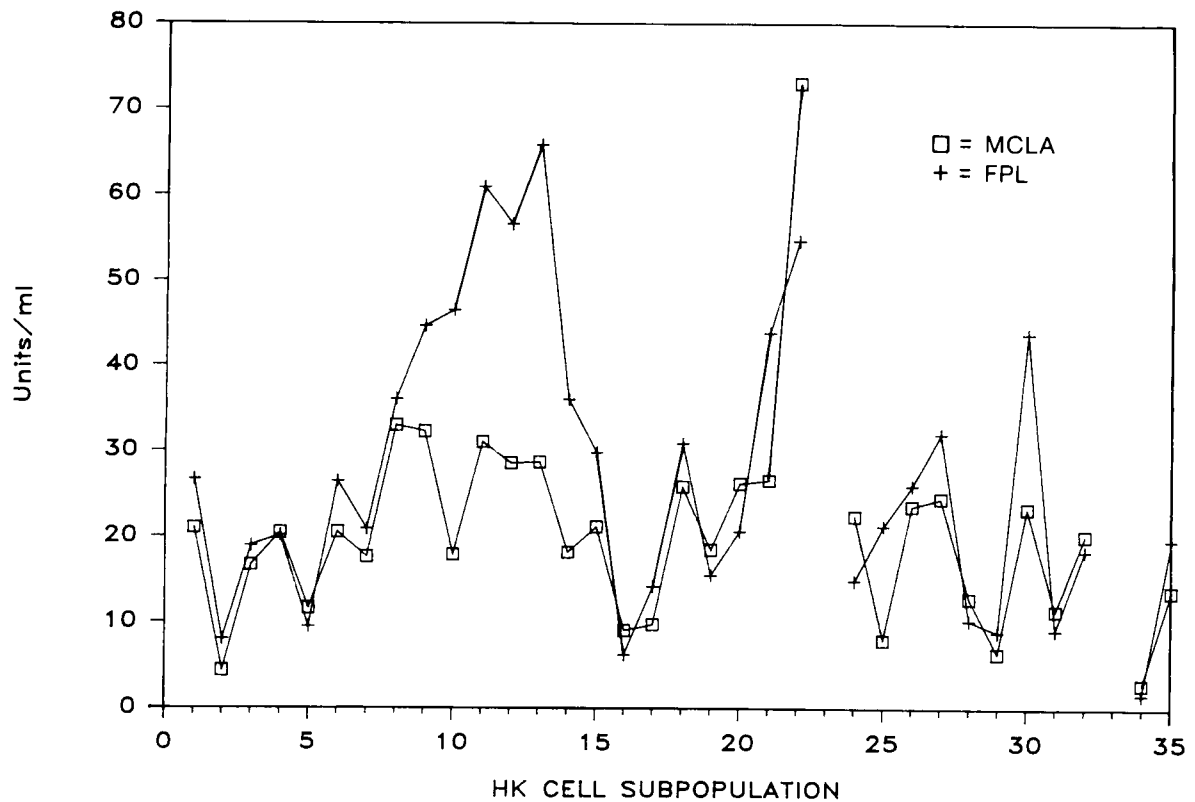
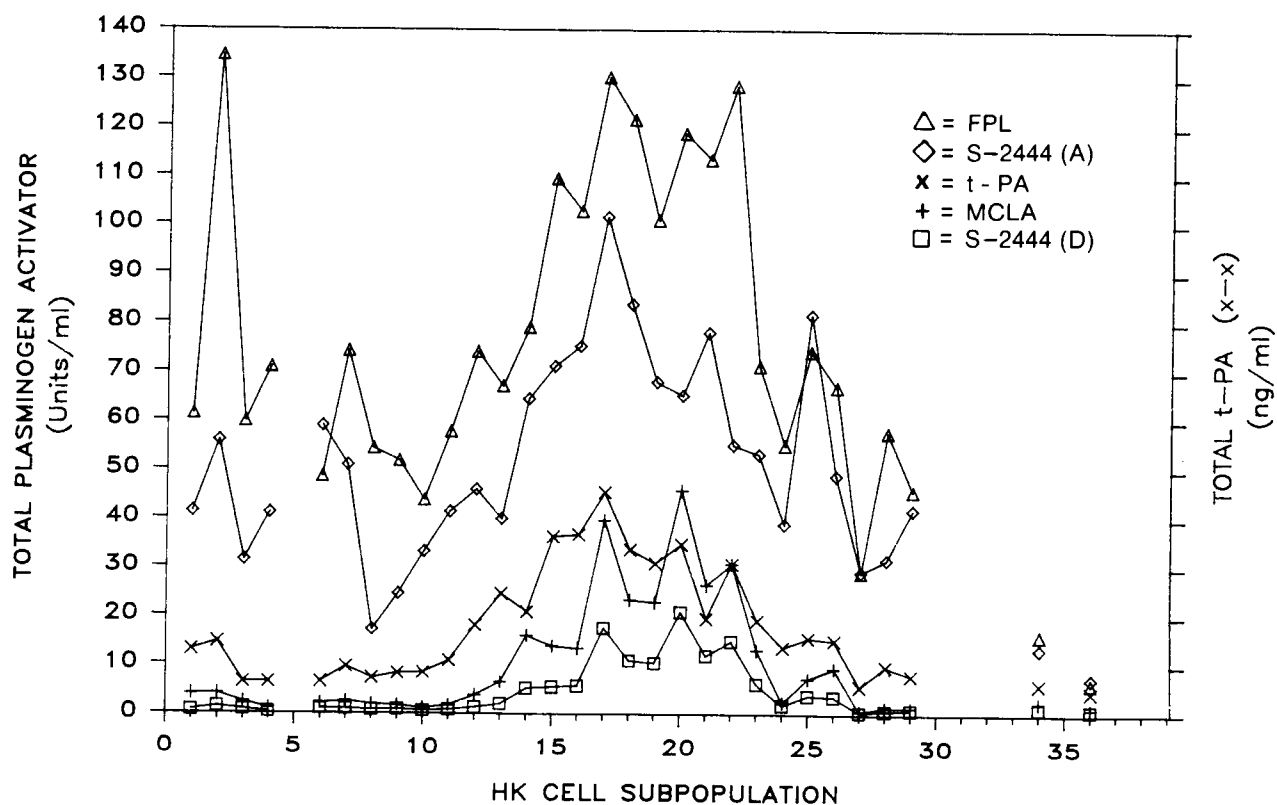


FIGURE 3B.

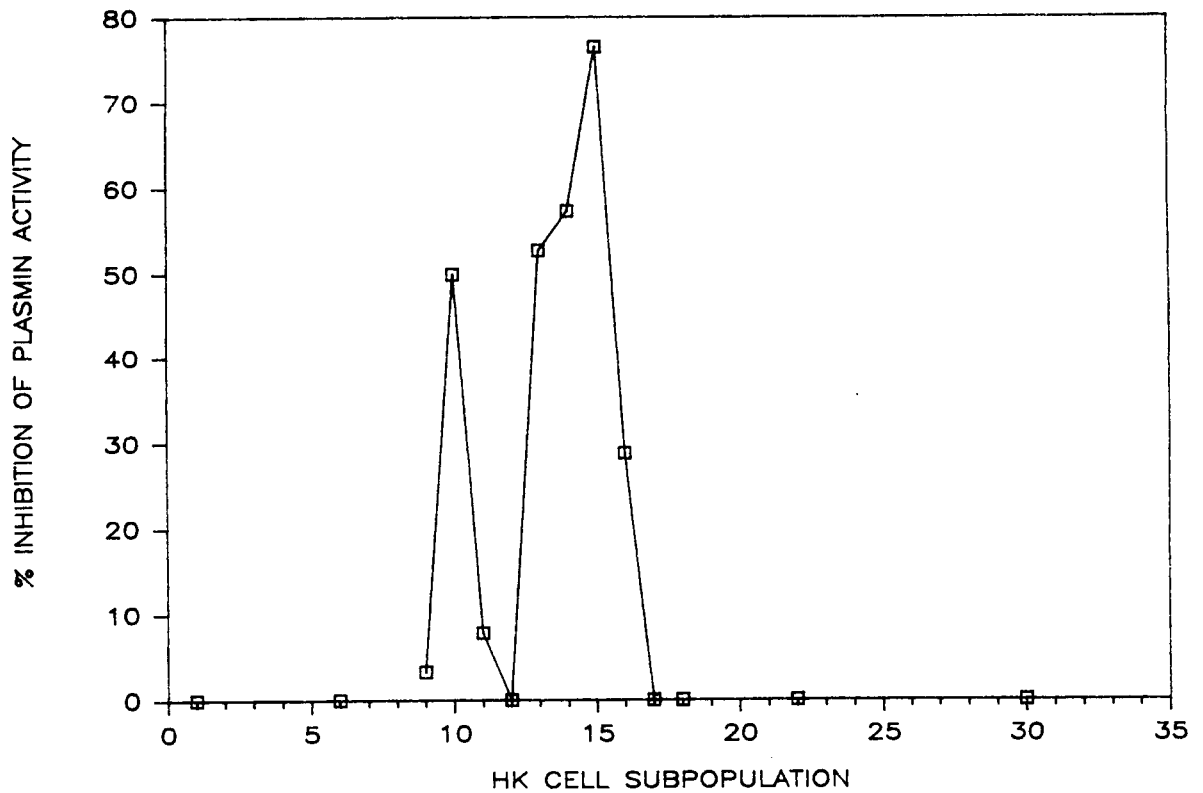
Presence of plasmin inhibitor in conditioned medium as detected by the chromogenic S-2251 ( $\square$ ). Residual plasmin activity after addition of excess lys-plasmin to the samples is expressed as a percent of activity in unconditioned medium.





**FIGURE 4.**

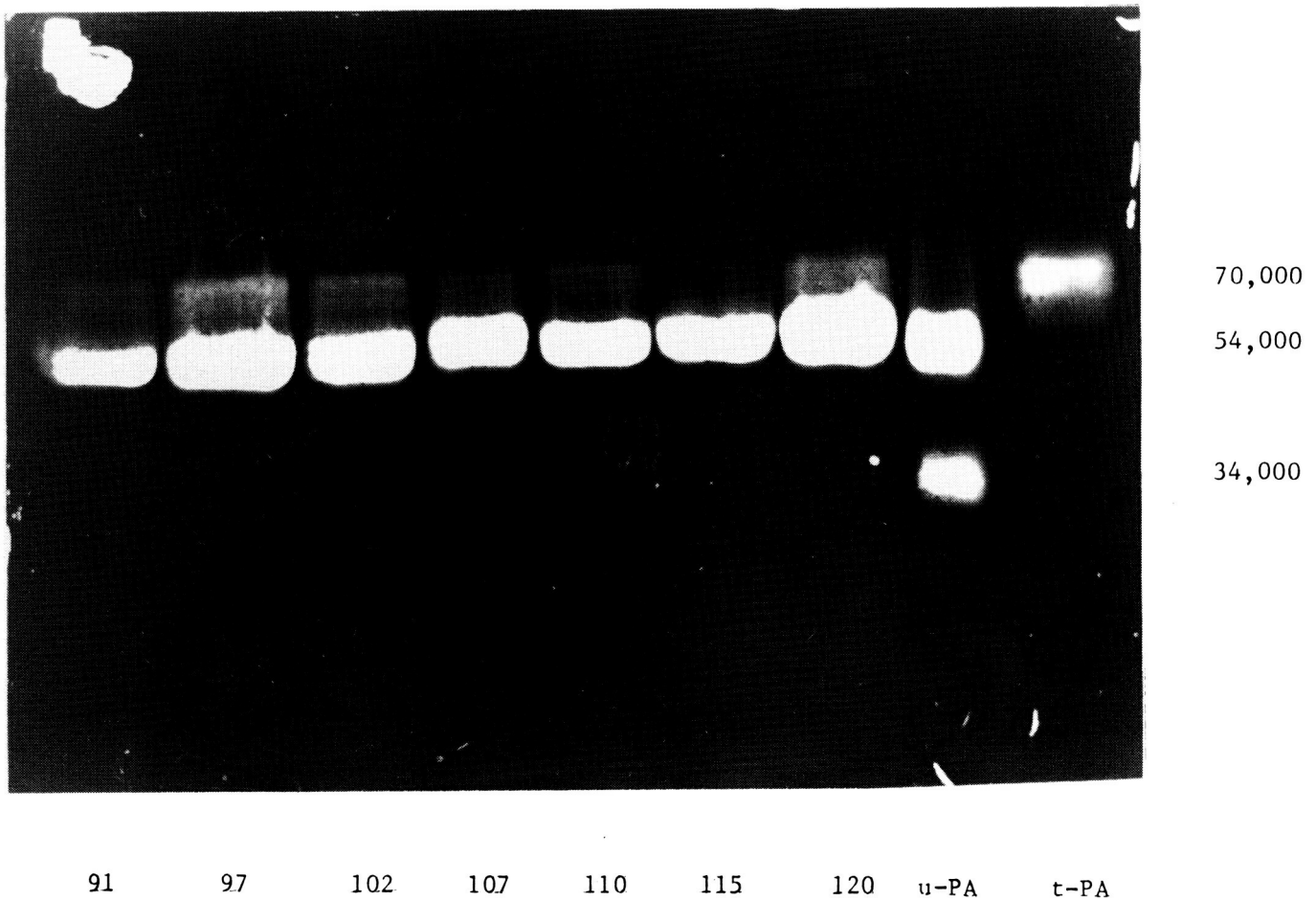
Plasminogen activators detected by a battery of five assays. These plots show the presence of active u-PA, (micro-clot lysis (+), S-2444 direct (□), and fibrin plate lysis (△) assays), scu-PA (difference between S2444 direct (□) and S-2444 activated (◇), and total t-PA in ng/ml enzyme linked immunosorbent assay) (x).



ORIGINAL PAGE IS  
OF POOR QUALITY

FIGURE 5A.

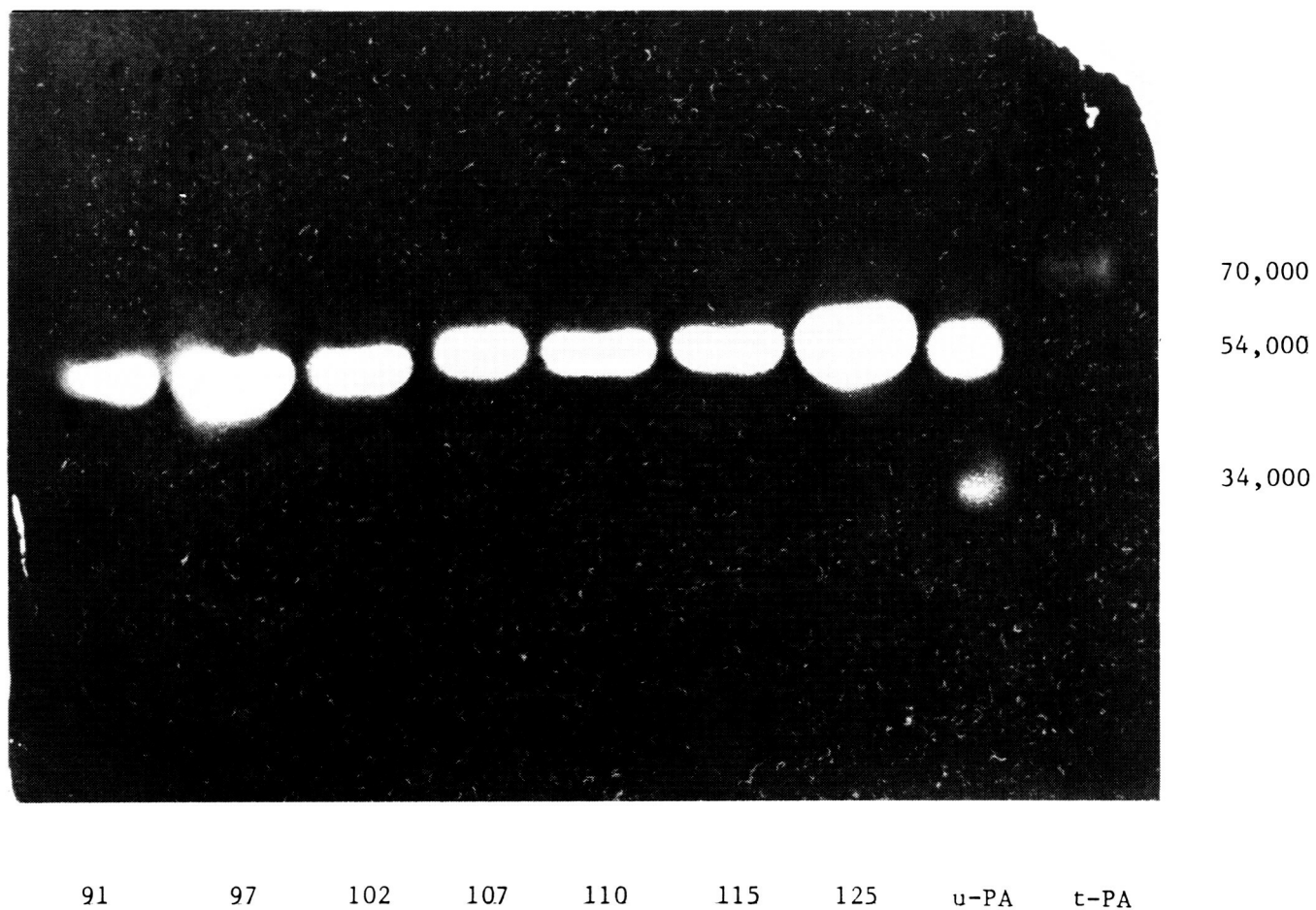
Fibrinogram from SDS PAGE gel on selected conditioned media samples from human embryonic kidney subpopulations.



ORIGINAL PAGE IS  
OF POOR QUALITY

**FIGURE 5B.**

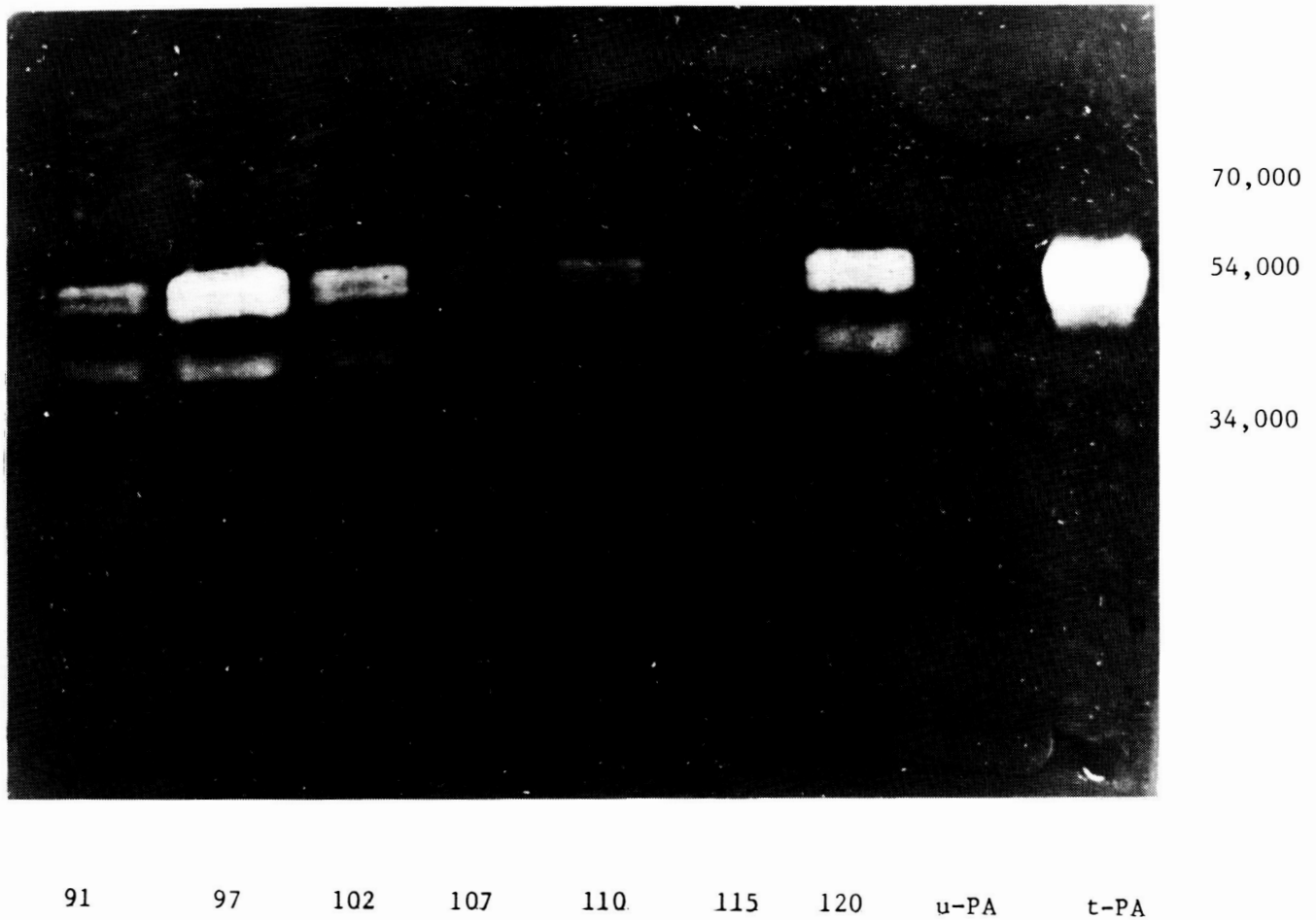
Fibrinogram from same SDS PAGE gel, overlay contains urokinase antibody.



ORIGINAL PAGE IS  
OF POOR QUALITY

**FIGURE 5C.**

Fibrinogram from same SDS PAGE gel, overlay contains tissue plasminogen activator antibody.



SPACE BIOREACTOR

Dennis R. Morrison, Ph.D.

NASA Johnson Space Center  
Houston, TexasAbstract

Microgravity offers new ways of handling fluids, gases, and growing mammalian cells in efficient suspension cultures. Some conceptual designs for a zero-g fermentor were developed as early as 1969. In 1976 bioreactor engineers designed another system using a cylindrical reactor vessel in which the cells and medium are slowly mixed. The reaction chamber is interchangeable and can be used for several types of cell cultures. NASA has methodically developed unique suspension type cell and recovery apparatus culture systems for bioprocess technology experiments and production of biological products in microgravity. The first Space Bioreactor has been designed for microprocessor control, no gaseous headspace, circulation and resupply of culture medium, and slow mixing in very low shear regimes. Various ground-based bioreactors are being used to test reactor vessel design, on-line sensors, effects of shear, nutrient supply, and waste removal from continuous culture of human cells attached to microcarriers. The small (500 ml) Bioreactor is being constructed for flight experiments in the Shuttle Middeck to verify systems operation under microgravity conditions and to measure the efficiencies of mass transport, gas transfer, oxygen consumption and control of low shear stress on cells.

Introduction

For several decades, many important pharmaceuticals and other biological products have been obtained from large scale culture of microbial cells. However, the mass cultivation of mammalian cells is much more difficult because of their delicate nature and their stringent environment requirements (1). In fact, contemporary culture technology is often inadequate in attempts to provide the proper conditions for optimum human cell growth and cell secretions. During the past 10 years the need for major technological improvements in human cell culture has increased because of the expanding demand for human cell products, such as hormones, enzymes, interferon, etc. to be used as pharmaceuticals.

Increased demand for large numbers of cells for virus and cancer research has also added impetus to develop practical systems for large scale culture of mammalian cells. Some improvements have been made, however, large scale culture systems still have major problems which make human cell culture very difficult and often uneconomical (2).

A great deal of excitement has resulted from the recent success in the genetic reprogramming of bacterial cells to produce human cell products such as growth hormones, human insulin, and interferon. However, the genetic

engineering of very complicated molecules is still several years from commercial practicality. Products are still contaminated with bacterial proteins and DNA fragments producing problems with allergenic or immune reactions to the preparation. To date only growth hormone, obtained from genetically engineered cells, has been approved by the Food and Drug Administration. Another limitation is the inability, so far, to genetically code for any glycosylated proteins. Certain human cell products which may not be practically produced by genetic engineering remain good candidates for production by culture of human cells whenever the technological problems are solved. Many diseases involving neoplasms, blood clots, hypertension, anemia, emphysema, growth disorders and others are now considered treatable with pharmaceuticals derived from cell culture if only the technology can be improved to make large scale cultures practical (3,4).

In the NASA bioprocessing laboratories at the Johnson Space Center we have evaluated several of the conventional and more recent methods for culturing human cells. Our studies involved: 1) the definition of the environmental conditions that must be controlled to insure successful growth and maintenance of human cells under microgravity conditions, 2) the recovery of cultured cells and cell products for postflight research, 3) the initial isolation or first step in down-stream processing which may be used as a feeder step to the purification of products by Continuous Flow Electrophoresis (CFE) or Recirculating Isoelectric Focusing (RIEF), and 4) the design features which must be included to maintain precise control of culture conditions under microgravity conditions (5).

In order to design proper control systems it was essential that we obtain performance data on various component elements of the culture apparatus. Special emphasis was placed on designs for fluid handling, temperature distribution, gas/liquid phase separation, etc., under microgravity conditions. We approached these problems by first identifying physical phenomena and operational principles of suspension culture which are gravity dependent. Then scientific workshops were held to determine which phenomena may be altered in microgravity to produce significant advantages or disadvantages in the culture process (6,7). It became apparent that many physical and biophysical interactions within cell culture systems are poorly understood. Several areas appeared to need additional research to better understand the importance of particular physical interactions which occur in suspension culture systems (see Table 1).

TABLE 1. CELL CULTURE RELATED RESEARCH AREAS (DATA IS NEEDED BOTH TO IMPROVE CULTURE TECHNOLOGY ON EARTH)

---

Microgravity Related Research Needed:

---

Upper limits of shear stress on cells  
 Minimum shear required for adequate mixing and mass transport  
 Details of required microenvironment surrounding the cell  
 Effects of shear on gas transport and cell membranes  
 Alterations (if any) of transport when bubbles don't coalesce  
 Mass transport in the absence of thermal convective mixing  
 Causes for attachment dependence and cell energy diverted to this behavior

---

## Evaluations of Earth-based Cell Culture Systems

Classic industrial and research methods of growing human cells have been limited to systems which grow and maintain cells in a monolayer. This is largely due to the anchorage dependence of mammalian cells. It appears that virtually all normal human cells must be firmly attached to some suitable surface before they will grow, multiply, and eventually secrete any products. Attempts to grow large numbers of cells in the inside surface of roller bottles (8) and multi-plate propagators (9) has permitted moderate scale mammalian cell cultures.

Some additional success has been achieved from growth cells attached to spiral wound membranes and to the inner surface of hollow-fiber dialysis bundles, in which nutrients can be supplied through the permeable membrane from media circulated on the opposite side of the membrane or hollow fiber (10). However, these techniques are still greatly restricted by poor surface-to-volume (culture medium) ratios. Some of the major problems associated with monolayer cultures; namely, 1) growth in only two dimensions (surface area), 2) cell proliferation limited by depletion of oxygen and nutrients, 3) difficulties with media circulation and volume to cell number ratios, 4) cell/product recovery, and 5) contamination control are more readily solved by using suspension culture. Unfortunately, almost all human cells of pharmaceutical interest grow quite poorly in modern suspension culture systems. Even when suspension culture of mammalian cells is accomplished on a small scale the maximum density of cells varies between  $5 \times 10^5$  to  $3 \times 10^6$  cells per  $\text{cm}^3$ . This concentration is orders of magnitude less than the number achieved in microbial cultures. Since the amount of product formed under proper physiological conditions, is directly proportional to the number of the cells, high cell concentrations are critical to successful commercial cultures.

In addition, the necessity to maintain the cells in a rather dilute nutrient media allows sedimentation to occur easily which in turn requires stringent mixing. Often the cells cannot tolerate the severe shear forces caused by even the best designed agitation systems. Prolific cells growth is also limited by the oxygen supply. Sparging of air is usually the best method to supply oxygen, however, the bubbles rise and coalesce so quickly that dissolution of oxygen is often incomplete during the bubbles' brief residence in the culture media. Vigorous bubbling of air causes high shear rates and too often produces uncontrolled foaming. Foaming in turn carries cells up out of the suspension where they dry out and die. Toxic waste products, cell fragments, and autolysis enzymes then fall back into the media where they poison the culture. Surfactants can be used to reduce foaming, however, their application is limited because they themselves are deleterious to living cells.

In an attempt to overcome the surface to volume disadvantages small (150-180 micron) Sephadex or DEAE cellulose beads were developed as microcarriers for cultured cells (11,12). Cells are allowed to attach to the surface of the bead then the beads are suspended in the culture vessel. This technique helped solve the attachment dependence problems of human cell culture, however, the particular surface of the bead must generally be custom designed to the requirements of the specific cell to be grown. Sometimes the surface

coating also acts as a repository for accumulation of cell waste products which in turn limits cell longevity.

We have compared several of the new cell culture technologies with the well established monolayer culture systems using several types of mammalian cells. This experience gave insight into selected features of each technique which may be combined into a suspension culture system for mammalian cells. We also have tested all of the commercial microcarrier beads (Cytodex, Superbeads, etc.) now on the market, however, sedimentation is still a problem especially after the cells are attached to the beads. Foaming problems from sparging of oxygen also remain. Often the mechanical mixing required to keep the beads suspended is so severe that cells are damaged and dislodged from the bead surface by high shear or bead-to-bead collisions.

Comparisons of commercially available microcarrier beads and discussions in cell culture workshops indicate that there may be many reasons to study cell culture technology under conditions of microgravity (6,7). The elimination of gravity dependent sedimentation of cells and bubble buoyancy may provide new insight into careful control of culture environments. Gentle mixing to insure adequate mass transport could be achieved while maintaining precise control of local temperature, pH, dissolved oxygen, shear, nutrient mixing, etc. in a manner heretofore not possible in Earth based laboratories. Figure 1 is a list of studies and workshops conducted by the Johnson Space Center to identify research topics and experiments which are needed to support the development of a suspension type Space Bioreactor to be used for precision controlled cell culture studies in microgravity.

#### Related Space Experiments and Cell Culture Systems

Studies of potential advantages of suspension cell culture technology in micro-G will only be valid if any direct effect of this environment on cell function is well understood. Early experiments with cells growing under weightlessness indicated that the cell density of S. typhimurium was significantly higher than the one obtained in the ground control experiment (13). The most noteworthy of several interpretations include the random distribution of cells in the culture liquid resulting in enhanced efficiency of nutrient transfer into, and waste transport from, the cells. There also could have been some improvement in the oxygen supply due to differences in gas-liquid mixing. Only one well controlled experiment has been carried out in growth of human WI-38 cells during the Skylab mission (14). Normal growth was observed along with normal mitotic index and subcellular structure. There was a small change in glucose utilization, however. This was considered inconclusive by the investigators.

Experiments on Spacelab 1 showed over a 95% reduction in the ability of human lymphocytes to respond to ConA mitogen (15). A change in glucose consumption was also noted but not considered significant until experiments could be repeated with an on-board one-G control. Other experiments showed an increase in proliferation of Hela cells, chicken embryo fibroblasts and mitogen stimulated lymphocytes of up to 30% due to hypergravity of 10-G while glucose utilization rate was unchanged from one-G (16). Experiments on Shuttle missions 7 and 8 were performed to determine the attachment efficiency of normal human kidney cells to collagen-coated microcarrier beads.



It was expected that the attachment rate would be reduced after mixing in microgravity, since the only opportunity would be random collisions while the cells and beads floated free in the culture medium. However, the results showed a significant increase in attachment for the flight samples vs. the ground control experiment (17). Within 3 hours, the cell attachment (based on the average number of single cells per bead) was 50% greater in microgravity than on Earth. Once attached, both the flight and ground control cells grew at the same rate during the first 25 hours. Cell-to-cell attachment was also greater among the cells free-floating in weightlessness. Future experiments are planned to give greater insight into the attachment mechanisms. However, practical implications include the possibility of seeding microcarrier cultures in microgravity and the knowledge that cells could reattach to microcarrier if they come off the bead surface in slowly mixed space bioreactors.

### Considerations for Culture of Mammalian Cells in Microgravity

The basic approach of NASA scientists to determine what factors must be included in the design of detailed cell culture experiments was to have industrial bioreactor experts study the merits of suspension cell culture systems and their applications in space. The definitive study (18) was performed by Drs. Nyiri and Toth at Fermentation Design, Inc. in 1976. They recommended a perfusion reactor system with an external, cell free, medium circulation loop to provide resupply of oxygen, nutrients, and scavaging of waste products using hollow fiber dialysis type membrane systems. The studies specified that the development of a dedicated microprocessor control system was essential to the proper operation and data acquisition required during space flight. Further, they evaluated the commercial potential of such a system and identified several hormones and cell secretory products as valuable enough to warrant the extra costs of production in space.

Figure 2 summarizes the general approach taken by the NASA Bioprocessing program in the development of the first Space Bioreactor.

Based on the interest generated by these studies and the results of a 1976 Colloquium on Bioprocessing in Space (19) a formal proposal to develop a Space Bioreactor flight unit was approved by NASA in 1978. Thereafter, several workshops were held with researchers to define experiments and typical science requirements for the design engineers. Major conclusions of the cell culture workshops identified several areas wherein the absence of gravity dependent phenomena in the culture environment could provide unique insight into certain cell functions and interactions between the cell and its micro-environment. Figure 3 shows the various areas where scientists believed that cell culture in micro-G could provide new information on the basic biodynamics of mammalian cells.

The objectives of the demonstration flight experiments are shown on Figure 4. Growth of normal human cells was selected because they are anchorage dependent and extremely fragile. Therefore these cells are very difficult to grow on Earth in suspension culture systems. In space potential advantages of lack of sedimentation and bubble buoyancy could enable operations with very gentle mixing and minimum turbulence to reduce shear effects on the cells. The basic objective also included exploration of product harvesting

techniques and principles of basic cell culture operation under microgravity conditions.

NASA and academic scientists then began a research program to study the specific gravity related problems which affected traditional and new cell culture techniques involving biosynthesis of cell secretory products. Research reactors were developed at two institutions and differences in gravity effects on the process technology of culturing cells which grow freely in suspension were contrasted with problems related to the anchorage dependent cells. Figure 5 shows these steps and the basic consideration for the initial design of the Space Bioreactor. Figure 6 illustrates more details of the systems development and biological systems (enzymes of cells) used to test the efficiencies of the prototype devices throughout three phases of development. As refinements were made, sensors added and mixing techniques tested various industrial process control systems were tested. Cultures were maintained for up to 14 days with L1210 cells, however, commercial process control systems were found to be inadequate to maintain the precise control required by human cells.

#### Space Bioreactor Development

In recent months the Bioreactor Test Unit (BTU) been designed and fabricated to be accommodated in a volume equivalent to two or three middeck lockers on the Shuttle. Current concepts call for an early flight test of the basic unit and sensor systems to verify operations with fast enzyme reactions before a major flight experiment is conducted with live kidney cells. Designs are also considering accommodations in the Spacelab racks or special middeck experiment racks.

The basic functional requirements for culturing human cells on microcarrier beads for 7 to 10 days on orbit are shown in Figure 7. Unique considerations include no gaseous headspace in the reaction vessel, sensors in the medium circulation loop (to eliminate turbulence in the reactor vessel) and flow/pressure controls to maintain pressures at or below 20 psia (to eliminate effects of pressure on cell functions). Practical considerations are also included based on our experience with limited access to biological experiments in the middeck while the Shuttle is on the launchpad.

Design and operational requirements for major components of the system are listed in Figure 8. The culture vessel design is based on an adaptation of two innovations by industrial researchers. We decided to use our own version of a spin filter type culture system originally designed by Thayer at Arthur D. Little Co. (20). This allows continuous removal of cell-free medium from the reactor vessel. We also decided to separate the mixing and spinning filter functions by using separate magnetic drives which allows independent control needed for very slow stirring during the flight portion of the experiment. The vessel volume was limited to 500 ml. because of the difficulty in maintaining a large supply of human epithelial kidney cells from the same lot to reduce inter-experimental variations. The target shear range for on-orbit operations was determined previously by researchers at Rice University in flow chamber studies of shear effects on kidney cells which secrete urokinase (21). The cell number to medium ratios must be kept within 125% of the most effective static cultures to insure that the cells will be able to condition

the medium for maximum viability and product secretions. The mixing device chosen was based on a recent design by Feder & Tolbert at Monsanto Co. (22) using flexible spiral vanes which helped to minimize turbulence and bead to impellor collision damage. Our designs call for a co-axial arrangement of the flexible vanes and the spin filter with special designs to allow high spin rates on the filter needed for high flow rates (80 - 100 ml./min.) of medium withdrawal from the reactor vessel. This unique design is complemented by provisions for alternating backwash routes using the medium return flow to keep the spin filter from clogging.

Process control considerations include a custom microprocessor control system to control the bioreactor to set point values, automatically log sensor data and provide minimum interface with the flightcrew. Our requirements include the capability to interface the process controller with a small personal computer (via RS-232) which in turn can operate off-line to perform statistical analysis of data, and prediction of adverse trend interception of alert or alarm set points. The capability to update the process controller with software commands from the "supervisory computer" has also been designed into the system.

The flow diagram of the reactor vessel, fluid loop, oxygenator and the protein concentration sideloop is illustrated in Figure 9. Detailed designs will be considered in later papers by Cross & Bowie, however, special mention should be made for position of the sensor blocks which allows calculations of cell metabolism from the difference in DO<sub>2</sub> and CO<sub>2</sub> levels in the input and the outflow from the reaction vessel. Provisions have been made to add concentrated culture medium, acid or base for pH control, dialysis type hollow fiber refeed system (which also can act as a repository for accumulating metabolic wastes). A microgravity bubble trap has also been included to remove any bubbles formed by gas dissolution during temperature or pressure changes and to trap any gas bubbles which may be injected into the medium circulation loop should the oxygenator membrane develop a leak during the flight. The function of the high molecular weight filter loop is to remove serum proteins from growth medium before changeout to maintenance medium when cells are confluent and to periodically (every 3 or 4 days) concentrate a sample of the circulating medium for product assays.

### Planned Flight Tests

The initial flight test requirements for the first two missions are shown in Figure 10. The selection of human kidney cells is based on some eight years of in-house experience with those epithelial cells which produce urokinase, one of the few pharmaceuticals approved for production from normal human cells grown in mass culture. Also our laboratories have extensive experience with detailed methods to screen cell lots to insure that they are normal, healthy, and hardy enough to withstand the rigors of space flight experiments. These cells have also been flown in space several times by our research group involved in separation of kidney cells in space by free-fluid electrophoresis techniques.

Several concepts for science objectives of planned early flight tests of the Space Bioreactor are listed in Figure 11. The major emphasis is on culture in environmental regimes which are impossible in one-G. These include cells

maintained in a very low shear field provided by slow gentle mixing which is possible in microgravity. Another tantalizing area is the culture of cells in the liquid phase of a controlled foam or bubbly culture medium comprised of oxygen bubbles which have no bouyancy nor do the coalesce readily in microgravity. Other suggested experiments involve studies of artificial oxygen carrier emulsions and specific cell physiology under quiescent culture conditions in space. More details are provided in the Appendix A, the Draft of the Space Bioreactor Science Requirements Document which was handed out for reference at this meeting.

Finally, it should be obvious that experiments involving human cell cultures and suspension bioreactors will provide basic engineering data on the design considerations required for most apparatus to culture cells in the absence of gravity. Once these principles are understood cell culture systems can be developed to provide live cells on orbit for cell biology and other types of bioprocessing related studies in microgravity. Should the expected advantages of micro-G be great enough it is possible that a Space Bioreactor could become the feeder facility in a multi-step bioprocessing system, wherein the cell products would be harvested from the bioreactor and fed to a Continuous Flow Electrophoresis System or other product purification device which can isolate pure pharmaceuticals direct from concentrated culture medium. Already the second phase of this type of bioprocess in space has been demonstrated by commercial CFES purifications on STS-4,6,7,8 and other flights. Such a multi-step bioprocess is a good candidate for commercially orientated research on the U.S. Space Station.

## REFERENCES

1. Feder, J. and Tolbert, W. R., "Large - Scale Cultivation of Mammalian Cells", *Scientific Amer.* 248:36-43, 1983.
2. Tolbert, W. R. et al, "An Analysis of Factors Limiting Commercial Utilization of Bioprocesses Involving Non-conventional Organisms", Workshop on Bioprocess Scale-up, Battelle-Columbus, Ohio, 1983.
3. Morrison, Dennis R., "Cell Culture in Microgravity As A Source of Commercial Products, presented at the AIAA Annual Conference, St. Louis, Mo., Jan. 1981.
4. Glacken, M. W., Fleischaker, R. J. and Sinsky, A. J., "Mammalian Cell Culture: Engineering Principles and Scale-up", *Trends in Biotechnology* Vol. 1:102-108, 1983.
5. Morrison, Dennis R., "Cell Culture Research in Space", in NASA Symposium on Gravity and the Cell, Ames Research Center, Moffett Field, CA. Mar 20-21, 1975.
6. A. D. Little, Inc., "Feasibility Study for the Manufacture of Zero-Gravity Pharmaceuticals, Immunobiological and Viral Agents", Final Report NASA-CR-120424, August 29, 1974.
7. Thayer, P. and Broome, M. G., "Cell Culture Biosynthesis in Space", Final Report, NASA Contract NAS9-15322, 1978.
8. Kruse, P. F. Jr., and Patterson, M. K. Jr., eds. *Tissue Culture: Methods and Applications*, Academic Press, New York, 1973.
9. Weiss, R. E. and Schleicher, J. B., *Biotechnol. Bioeng.* 10:601-615, 1968.
10. Knazek, R. A., et al., *Science* 178:65-67, 1972.
11. Van Wezel, A.L., *Nature (London)* 216:64-66, 1967.
12. Levine, D. W. et al., "Microcarrier Cell Culture: New Method for Research Scale Application", *Somatic Cell Genetics* 3:149-155, 1977.
13. Mattoni, R. H.T., "Spaceflight Effects and Gamma Radiation Interaction on Growth and Induction of Lysogenic Bacteria," *Bioscience* 18:602-608, 1963.
14. Montgomery, P. O. 'B. et al., "The Response of Single Human Cells to Microgravity," *In Vitro* 14:165-173, 1978.
15. Cogoli, A., Tschopp, A., and Fuchs-Bislin, P. "Cell Sensitivity to Gravity" *Science* 225:228-230, 1983.
16. Tschopp, A. and Cogoli, A., "Hypergravity promotes cell proliferation," *Experientia* 39:1323-1329 (Basel), 1983.

17. Tschopp, A., Cogoli, A., Lewis, M. L. and Morrison, D. R., "Bioprocessing in Space: Human Cells Attach to Beads in Microgravity", J. Biotech. 1:287-293, 1984.
18. Nyiri, L. K. and Toth, G. M., "Space Biosynthesis Systems", Final Report of NASA Contract NAS9-14961, 1976.
19. Nyiri, L. K., "Some Questions of Space Bioengineering" in Morrison, D. R., ed. Proceedings of the Colloquium on Bioprocessing in Space, March 1976 NASA Technical Memorandum NASA TM X-58191, Jan. 1977 avail. NTIS.
20. Thayer, P., Arthur D. Little Co., Acorn Park, Cambridge, MA.
21. Stathopoulos, N. A. and Helms, J. D., "Shear Stress Effects on Human Kidney Cells In Vitro", Biotechnol. & Bioeng. 27:1021-1026, 1985.

BIOREACTOR STUDIES

- 1976-77 "Space Biosynthesis Systems" - Contract NAS9-14961 by Fermentation Design Inc., Bethlehem, PA. Investigator: L.K. Nyiri, Ph.D. and G.M. Toth, Ph.D.
- 1977 Proposal to develop experiments for multipurpose Space Bioreactor System. Proposal #770056, NASA A.O. No. AO-77-3, L.K. Nyiri, Ph.D. and Marvi Charles, Ph.D..
- 1978-79 "Development of a Space Bioprocessing System for Cell Culture". Contract NAS9-15619, Lehigh University, Bethlehem, PA. Marvin Charles, Ph.D. and L.K. Nyiri, Ph.D.
- 1979 "Cell Culture Biosynthesis". Contract NAS9-15322, A.D. Little Co., Cambridge, MA. Phil Thayer, Ph.D. and M.G. Broone, Ph.D.
- Jan. 1978 M.I.T. Workshop on "The Feasibility of Cell Culture Systems for Space Experiments". Proceeding summarized by A.D. Little, Inc. - Final Report NAS9-15322.
- June 1979 Salk Institute Workshop on "Microgravity Cell Culture Systems". Proceedings summarized by A.D. Little, Inc. - Final Report NAS9-15322.
- Jan. 1982 JSC/Conference on "Fluid Mechanical Aspects of Cell Culture", Rice University. Summary Report by Mike Reynolds, Ph.D.
- 1982 "A Microprocessor Interface for the Space Bioreactor System", conducted by Robert A. Snyder, Ph.D., (NRC Postdoc).
- Aug. 1985 JSC/ Workshop on "Space Bioreactor Science". A joint NASA, Academic and Industrial workshop on the development of a space bioreactor and potential flight experiments. Proceedings published in JSC Document No. 22264, edited by D. R. Morrison, Ph.D., Aug. 1986.

Figure 2

SPACE BIOREACTOR

APPROACH

- o CONCEPTUAL STUDIES BY ACADEMIC INSTITUTIONS AND INDUSTRY STARTED IN 1976
- o CELL CULTURE SCIENCE CONFERENCES - MIT, SALK INSTITUTE, JSC
- o INDUSTRIAL CONSULTATION WITH: MONSANTO CORP.; STANFORD RESEARCH INSTITUTE; MDAC-ST. LOUIS; BIOCHEM TECHNOLOGIES; FERMENTATION DESIGN, INC.; K. C. BIOLOGICALS; BIOREACTOR, INC.; TISSUE CULTURE ASSOCIATION; ALTON JONES CELL SCIENCE CENTER; ARTHUR D. LITTLE CO.
- o ACADEMIC MEETINGS WITH: MIT, PRINCETON UNIVERSITY, UNIVERSITY OF ROCHESTER, UNIVERSITY OF MISSISSIPPI, STANFORD UNIVERSITY, RICE UNIVERSITY, UNIVERSITY OF HOUSTON, WASHINGTON SCHOOL OF MEDICINE
- o JSC HAS ACCUMULATED 8 YEARS' EXPERIENCE WITH CELL CULTURES AND 4 YEARS' EXPERIENCE WITH BIOREACTOR BREADBOARD SYSTEM
- o JSC WILL DEVELOP TWO SPACE BIOREACTOR LABORATORY TEST UNITS WHICH WILL CONFIRM DESIGN REQUIREMENTS FOR FLIGHT UNITS AND CAN BE USED FOR HARDWARE VERIFICATION FLIGHT TESTS (DSO'S)



Figure 3

## BIODYNAMICS

### MICRO-G ENVIRONMENT RESEARCH ON:

- SHEAR STRESS ON CELLS
- ANCHORAGE DEPENDENCE - CELL ATTACHMENT
- GAS TRANSFER / GAS - LIQUID FOAMS
- NUTRIENT / WASTE DIFFUSION
- INTERCELLULAR TRANSPORT
- GROWTH
- BIOENERGETICS
- PRODUCT SECRETIONS

Figure 4

## SPACE BIOREACTOR

### OBJECTIVES

- o DEVELOP AND TEST PROTOTYPE SYSTEM FOR CONTROLLED GROWTH OF MAMMALIAN CELLS IN MICROGRAVITY
- o DEMONSTRATE ADVANTAGES
  - LACK OF SEDIMENTATION
  - LACK OF BUBBLE BOUYANCY
  - UNCONVENTIONAL CONTROLLED MIXING AT SLOW SPEEDS TO KEEP SHEAR AT MINIMUM
  - CULTURE OF EXTREMELY FRAGILE CELLS
  - PRECISE CONTROL OF GAS/LIQUID TRANSPORT, NUTRIENTS, AND WASTE
  - EVALUATE NEW METHODS OF O<sub>2</sub> CONTROL
- o DEVELOP CONTINUOUS CULTURE METHODS AND PRODUCT HARVESTING TECHNIQUES
- o PROVIDE A BASIC CELL CULTURE AND MAINTENANCE FACILITY FOR SUPPORT OF CELL BIOLOGY EXPERIMENTS (SHUTTLE, SPACELAB, AND SPACE STATION)
- o PROVIDE A TESTBED CAPABILITY TO EXPLORE OTHER TYPES OF CELL CULTURE INCLUDING HYBRIDOMA CULTURES, YEAST FERMENTATION, ETC.

Figure 5

BIOSYNTHESIS

GRAVITY PROBLEMS IDENTIFIED  
COMPARISON OF CULTURE TECHNIQUES

- MONOLAYER/MULTIPLATE
- HOLLOW FIBER
- SPIN FILTER SUSPENSION
- MICROCARRIERS

DEVELOPMENT OF RESEARCH BIOREACTOR

- SUSPENSION CULTURES - L1210
  - HYBRIDOMA
- ATTACHED HUMAN CELLS - KIDNEY

DEVELOPMENT OF SPACE BIOREACTOR

- SPIN FILTER/MICROCARRIERS
- NO HEADSPACE
- MICRO-G FLUID HANDLING

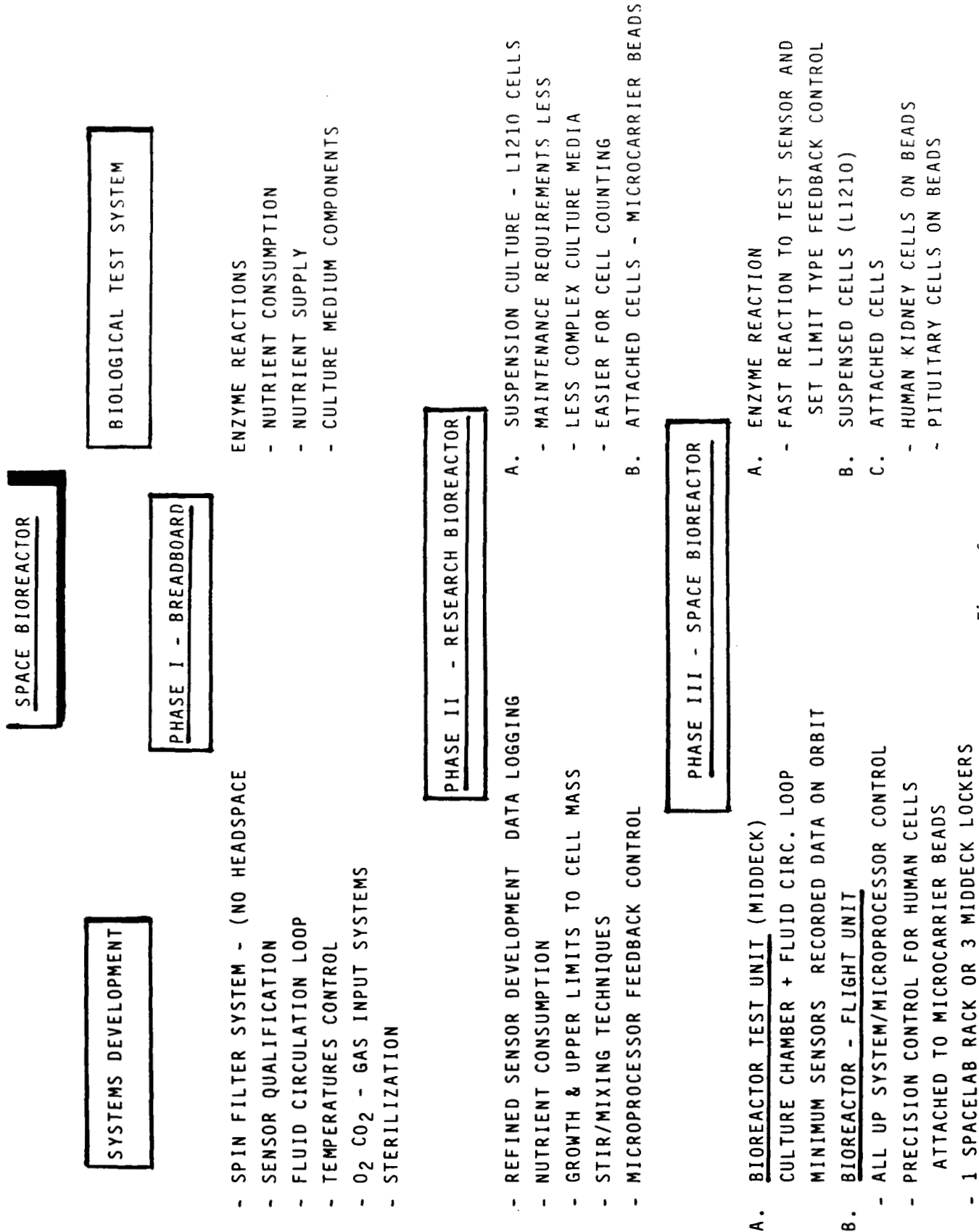


Figure 6

Figure 7

BIOREACTOR

BASIC FUNCTIONAL REQUIREMENTS

SYSTEM REQUIREMENTS

BASIC DESIGN - CELLS ON MICROCARRIERS

NO HEADSPACE IN REACTOR VESSEL

CELL/BEAD FREE MEDIA CIRCULATION LOOP

- OXYGENATION
- RE-SUPPLY NUTRIENTS
- REMOVE TOXIC WASTE
- PRODUCT REMOVAL
- IN-LINE SENSORS

AUTOCLAVE ENTIRE CORE BIOREACTOR

PRESSURE ON CELLS <-- 5 PSI

SYSTEM PRESSURE - UP TO 15 PSI

CORE BIOREACTOR LOADED AT KSC/INSTALLED AT L-10 HOURS

SELF-SUFFICIENT PROCESS CONTROLLER - STANDARD OPERATIONS AND ALARMS

SEPARATE SUPERVISORY COMPUTER

TARGET CORE BIOREACTOR - 2 LOCKERS

PROCESS CONTROLLER/SUPPORT ELECTRONICS - 1-2 LOCKERS

Figure 8

MAJOR COMPONENT REQUIREMENTS

REACTOR VESSEL

- SEPARATE DEVICES FOR SPIN FILTER AND MIXING
  - 500 ML CULTURE VOLUME
  - MINIMUM INTERNAL COMPONENTS
  - CONTROL MAXIMUM SHEAR 10-40 DYNES/CM<sup>2</sup>
- APPROACH - BASIC TEST VESSEL - SPIN FILTER (MUST BE KEPT CLEAN)
- MARINE IMPELLOR VS. SPIRAL VANES
  - ALTERNATING BACKWASH METHODS

PROCESS CONTROLLER

- ONBOARD CPU/OPERATING SYSTEM
- LOG ALL DATA - 12-24 HOURS
- MINIMUM TREND PROJECTIONS
- INTERFACE (RS-232) WITH SUPERVISORY COMPUTER
- MINIMUM CREW INTERACTIONS
- UPDATE WITH SOFTWARE COMMANDS

APPROACH - TEST COMMERCIAL SYSTEMS - NONE ADEQUATE

- BUILD CUSTOM SYSTEM
- BUY MDAC ECCM

SUPERVISORY COMPUTER

- OFF-LINE DATA ANALYSIS
- COMPLICATED TREND PROJECTIONS
- GRAPHICS

APPROACH - IBM-AT (GROUND ) AND LAP COMPUTER FOR FLIGHT

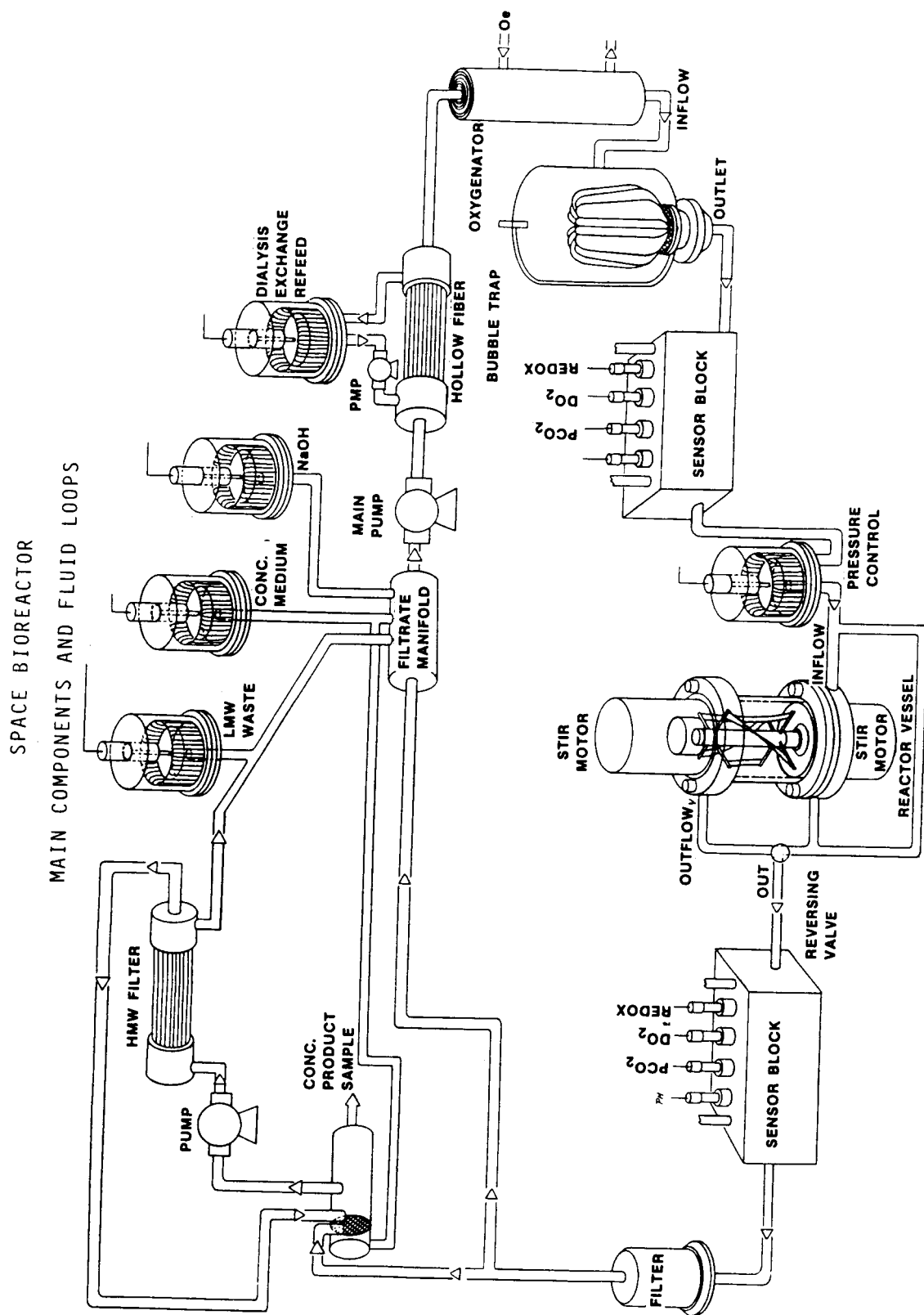


FIGURE 9

Figure 10

BIOREACTOR TEST REQUIREMENTS

- FIRST FLIGHT TEST
- NO CELLS
  - MINIMUM CONTAMINATION CONTROL
  - TEST - FLUID SYSTEM
    - MIXING
    - SENSORS
    - HMW FILTER SYSTEM

- SECOND FLIGHT TEST
- CULTURE FEASIBILITY DEMONSTRATION
  - 7-8 DAY MISSION
  - KIDNEY CELLS ON MICROCARRIERS
  - GROW ON BEADS BEFORE FLIGHT (GROWTH MEDIUM)
  - MAINTAIN CELLS ON UKPM (SERUM FREE)
  - EXERCISE HMW FILTER ON 4-DAY INTERVALS
  - REPLENISH MEDIUM WITH NEW MEDIUM OR DIALYSIS REFEEED

- LATER FLIGHTS
- GROW CELLS ON MICROCARRIERS, THEN SWITCH TO SERUM-FREE MEDIUM
  - OTHER REACTION VESSELS - HYBRIDOMAS
    - FERMENTATION (YEAST)



EXPERIMENTS WITH HUMAN CELLS (ATTACHED TO MICROCARRIERS)

A. EFFECTS OF SHEAR STRESS

- LOW SHEAR 10-40 DYNES/CM<sup>2</sup>
- TARGET EXACT SHEAR RANGE TO STIMULATE UK SECRETIONS
- DIRECT MEASURE OF METABOLISM - FLUROMEASURE SYSTEM

B. CULTURE IN A CONTROLLED FOAM IN THE ABSENCE OF BOUYANCY

- CREATE STABLE FOAM OF O<sub>2</sub> BUBBLES IN CULTURE MEDIUM
- GROW CELLS IN LIQUID PHASE
- PROVIDE CONTINUAL & INTERMEDIATE ACCESS TO O<sub>2</sub> SUPPLY WITHOUT CELLS EVER BEING EXPOSED TO GAS PHASE
- COMPLETELY AVOID USE OF ANTI-FOAMING AGENTS

C. USE OF FLUOROCARBON OXYGEN CARRIERS IN ABSENCE OF DENSITY-DRIVEN SEPARATION

- USE OF PERFLUORINATED CARBON SOLVENTS (S.G. 1.87)
- MAINTAIN A LONG-TERM STABLE DISPERSION TO CARRY O<sub>2</sub> FROM OXYGENATOR TO THE CELLS IN REACTOR VESSEL
- EXPLORE USE OF SERUM IN MEDIA WHERE FOAMING WILL NOT BE PRESENT AS IN EARTH BASED SYSTEMS

OTHER EXPERIMENTS TO DETERMINE DIRECT CELLULAR EFFECTS

- ALTERATIONS OF CELL PHYSIOLOGY OR MORPHOLOGY
- CELL SECRETIONS IN MICROGRAVITY - GH, UK
- CELLULAR EFFECTS OF MAGNETIC FIELDS IN ABSENCE OF GRAVITY
- ALTERATIONS IN CYTOSKELETON, CELL MOTILITY

## CELLULAR EFFECTS OF MICROGRAVITY

Dennis R. Morrison, Ph.D.  
NASA - Johnson Space Center

In the 1960's Soviet and U.S. investigators studied a variety of biological specimens on unmanned space vehicles. Most of these simple experiments reported normal growth and function, however, a few isolated results indicated increased growth in procaryotic cells (Taylor, 1974-review). Experiments with E. coli K-12 (lambda) phage on over 20 Soviet flights, beginning with Vostok series, showed an increased phage induction in lysogenic bacteria, which was correlated with mission duration (Parfenov and Lukin, 1973). The role of microgravity, however, was partially obscured by contribution of galactic radiation and some evidence that launch vibrations followed by increased radiation may increase the mutation rate (Zhukov-Verezhnikov et al., 1965). Flight experiments on Biosatellite II indicated that the cell density of Salmonella typhimurium cultures were greater than control cultures on Earth (Mattoni, 1968). During the 1970's a number of microbial studies were conducted to sort out the relative effects of microgravity and increased radiation exposure during orbital flight (Taylor, 1977). Since then only a few cell biology experiments with insect, mammalian and plant cells have been flown (Taylor, 1986). Figure 1 summarizes the significant results (excluding plant cell effects) indicating direct effects of microgravity on cells in vitro.

Only a few experiments have been performed on eucaryotic cells. These were confined to small holding chambers maintained at constant temperatures permitting only basic observations on orbit and occasional sample fixation for post flight analyses. No experiments have yet been possible in a carefully controlled perfusion bioreactor wherein nutrients can be constantly replenished and waste

products removed to avoid toxic levels.

Although Skylab experiments with WI-38 lung fibroblasts indicated that subcellular structure and growth was unchanged some indication of increased glucose utilization was observed( Montgomery, 1974). The notable lack of major effects and theoretical predictions that subcellular organelles would not be subject to sedimentation or other gravitational effects resulted in dramatic narrowing of focus for U.S. cell biology flight experiments. From 1975 to 1981 current theories held that cell function and intracellular physiology would be unaffected by exposure to microgravity.

Recent findings, however, clearly demonstrate that cell functions are significantly altered by micro-G. French experiments on Salyut-6 & 7 with Paramecium tetraurelia showed clearly an increase in cell proliferation rates and cell volume after just 60 hours of spaceflight (Planel, 1981 & Tixador, 1984) Hungarian-Soviet experiments on human lymphocytes showed that in vitro cultures exposed to several interferon inducers on orbit caused the release of 4-8x more alpha-interferon than ground controls( Talas et al, 1983). In contrast lymphocytes from cosmonauts do not respond to interferon inducers after spaceflight as they did preflight. Also in vivo Gamma-interferon production in rats on Spacelab-3 was severely inhibited (Gould et al, 1985). Swiss experiments on Spacelab-1 showed that Concanavalin A mitogen stimulation of lymphocytes in vitro was reduced by 97% in microgravity (Cogoli et al, 1984) in contrast to a 30% increase in mitogen response at 10-g's (Tschopp and Cogoli, 1983). Dramatic reduction in mitogen response was also confirmed on the D-1 Spacelab mission as described below. Observations from STS-8 and definitive results from Spacelab-3 showed that in vitro mammalian pituitary cells did not release normal amounts of growth hormone during flight, Moreover, the growth hormone secretions from pituitary cells taken from the flight animals and transplanted postflight into hypophysectomized animals did not stimulate growth of long bones as did control

cells (Hymer et al, 1985). In contrast prolactin secretions from those cells appeared unaltered by the spaceflight. In vitro experiments on STS-7 and STS-8 determined the efficiency of human kidney cells attachment to collagen coated microcarrier beads (Tschopp et al, 1984). It was expected that attachment would be less after mixing in micro-g since opportunities would be limited by random collisions. However, results showed a significant increase in attachment within the first three hours (Morrison and Lewis, 1986). Once cells were attached, both the flight cells and the ground control cultures appeared to grow at the same rate, at least for the first 25 hours.

The most dramatic results have just recently come from the Spacelab D-1 mission, wherein the Biorack experiments studied the effects of micro-G on the structure, proliferation, differentiation and functions of some nine different procaryotic and eucaryotic cells (See Figure 2). For the first time inflight experiments were performed at both micro-g and 1-G and the results were compared to ground controls. Figure 3 summarizes the results (Mesland et al., 1986) which indicate significant effects of spaceflight on cell growth, development and function. These include evidence for increased resistance of E. coli to an antibiotic and increased proliferation rate and greater cell mass of B. subtilis cultures. Also transfer of DNA during conjugation of bacterial cells was 2-3x greater in microgravity. Cell proliferation of Paramecium sp. was increased 4x, cell volume was increased and intracellular calcium was decreased which confirmed earlier results from experiments on Salyut flights. The in vitro mitogenic response of human lymphocytes to Con A showed a 90% decrease under microgravity conditions, whereas the inflight 1-G control cultures showed a 60% loss of response compared to ground controls.

In general, these experiments clearly showed significant alterations of cell proliferation, differentiation, and embryonic development (insect cells).

These results have already created a renewed interest in cellular effects of microgravity which may provide new insight into some human physiologic responses to prolonged spaceflight. They also indicate that space biotechnology process studies need to include effects of microgravity on the specimens to properly assess the potential advantages and trade-offs for a particular biological application.

Future flight experiments will require more sophisticated culture facilities. Experiments with fragile mammalian cells will require a capability for growth and maintenance of a large number of cells in a precision controlled culture environment. Figure 4 illustrates a typical growth curve for kidney cells grown on microcarrier beads. Attachment and proliferation requires a complex culture medium usually supplemented with serum. All sera contain a variety of known and unknown "growth factors" in addition to a large complement of different serum proteins and hormones (Taub, 1982), some of which are inhibitors of cell secretions (Verheijen, 1986). During log growth nutrient consumption is varied and often rapid for certain critical molecules. Waste product accumulation also can be quite rapid. Often cell secretion of important hormones and other proteins is depressed or absent during this phase. Once adequate packing density or confluence is reached growth and metabolic rates become slower. Then culture medium can usually be switched to a more simple, defined formula which can be designed to encourage cells secretions into the medium.

The indicators for improved cultures under better controlled local environmental conditions are different for growth phases and cells maintained at confluence. During proliferation the main indicators which can be quantitated are attachment, viability, and replication rate. However, in stable maintenance culture one can measure cell survival, cell turnover, respiration and metabolic rates, specific nutrient depletion rates, changes from aerobic to anerobic metabolism, and rates of product secretion. The first microgravity experiments in a

suspension-type Space Bioreactor are likely to be designed for separate studies of cells cultured either under proliferation conditions or under maintenance conditions specific for confluent cells with target secretory functions. Later flight experiments can be accommodated which look at the entire sequence of cell culture in a continuous operation where medium changeout can be accomplished via a dedicated microprocessor control system.

Some initial flight experiments have been proposed and concepts for other bioprocess experiments have been defined (See Figure 4). Various versions of the first Space Bioreactor also can be used to maintain cells under strict environmental conditions to support some of the more elaborate cell biology flight experiments. Typical experiment requirements are already being incorporated into the basic design of the first flight prototype.

#### REFERENCES CITED

- Cogoli, A., Tschopp, A. and Fuchs-Bislin, P. 1984. Cell sensitivity to gravity. *Science* 225: 228-230.
- Gould, C. L., Williams, J. A., Mandel, A. D., and Sonnenfeld, G., 1985. Effect of flight in mission SL-3 on interferon gamma production by rats, In Press, *The Physiologist*.
- Hymer, W. C., et al., 1985. Microgravity associated changes in pituitary growth hormone (GH) cells prepared from rats flown on Spacelab 3, *The Physiologist* 28: (No.6,Suppl.) 197-198.
- Mattoni, T. H. T., 1968. Spaceflight effects and gamma radiation interaction on growth and induction of lysogenic bacteria. *Bioscience* 18: 602.
- Mesland, D. A. M. et al., 1986. ESA Biorack Experiments. Preliminary science results obtained on the German Spacelab D-1 mission, ESA Document # TB/DM/DC/6397 March 10, 1986, European Space Agency, Paris 75738.
- Montgomery, P. O'B., et al., 1978. The response of single human cells to zero-gravity. *In Vitro* 14: 165-173.
- Morrison, D. R. and Lewis, M. L., 1986. Transport, harvest and attachment of kidney cells on microcarriers in micro-G. Proceedings of the Second Annual meeting of the American Society for Gravitational and Space Biology, October 1-3, Charlottesville, Va.

- Parfenov, G. P. and Lukin, A. A., 1973. Results and prospects of microbial studies in outer space, *Space Life Sciences* 4: 160-179.
- Planel, H. R., et al. 1981. Space flight effects on *Paramecium tetraurelia* flown aboard Salyut-6 in the Cytos I and Cytos M experiments. *Adv. Space Research* 1: 95-100.
- Talas, M., et al., 1983. Results of the space experiment program "Interferon" I. Production of interferon in vitro by human lymphocytes aboard space laboratory Salyut-6 ("Interferon I") and influence of space flight on lymphocyte functions of cosmonauts ("Interferon III"). *Acta Microbiologica Hungarica* 30: 53-61.
- Taub, M. 1982. Hormones control the growth and function of cultured kidney cells in: *Growth of Cells in Hormonally Defined Media*, eds. G. H. Sato, A. B. Pardee and D. A. Sirbasku, Cold Springs Harbor Conferences on Cell Proliferation, Vol. 9, Cold Springs Harbor, New York, pp. 581-592.
- Taylor, G. R., 1974. Space Microbiology. *Annu. Rev. Microbiol.* 28: 121-137.
- Taylor, G. R., 1977. Cell biology experiments conducted in space. *Bioscience* 27: 102-108.
- Taylor, G. R. 1986. Cell anomalies associated with spaceflight conditions. in: *Proceedings of the Fourth International Symposium on Immunobiology of Proteins and Peptides*, Dec. 1-4, 1986, Las Vegas, in press.
- Tixador, R., Richoilley, G., Gasset, G., and Planel, H., 1984. Effects of gravity and cosmic rays on cell proliferation in *Paramecium tetraurelia*. *Adv. Space Res.* 10: 91-95.
- Tschopp, A. and Cogoli, A. 1983. Hypergravity promotes cell proliferation. *Experientia* 39: 1323-1329.
- Tschopp, A., Cogoli, A., Lewis, M. L. and Morrison, D. R., 1984. Bioprocessing in space: Human cells attach to beads in microgravity. *J. Biotech.* 1: 287-293.
- Verheijen, J. H., 1986. Assay of plasminogen activators and their inhibitors. Eighth International Congress on Fibrinolysis: Workshop on Fibrinolysis, Vienna, Austria, August 24-25th.
- Zhukov-Verezhnikov, N. N., et al., 1965. Results of microbiological and cytological investigation conducted during the flights of "Vostok" type vehicles. *Probl. Space Biol.* 4: 252-259.

# CELLULAR EFFECTS OF MICROGRAVITY

<u>MISSION</u>	<u>CELLS</u>	<u>RESULTS</u>
BIOSATELLITE	<u>Salmonella typhimurium</u>	growth increased
Salyut-6	<u>Proteus vulgaris</u>	growth increased
Voskhod 3	<u>E. coli lambda phage</u>	induction increased (20 flights
Skylab-3	<u>WI-38 lung fibroblasts</u>	normal growth ( glucose inc.)
Salyut-6,7	<u>Paramecium tetraurelia</u>	growth rate & size increased
Salyut-6	<u>Lymphocytes (in vitro)</u>	interferon production incr. 4X
STS-8, SL-3	<u>Pituitary cells</u>	growth hormone secretion decr. normal prolactin secretion
SPACELAB-1	<u>Human lymphocytes (in vitro)</u>	mitogenic response decreased 97%
STS-8	<u>Embryonic kidney cells</u>	attachment increased 40 - 80%
D-1 SPACELAB	<u>procaryotic &amp; eucaryotic cells</u> ( 9 types )	changes in cell proliferation and cell differentiation

FIGURE 1



SUBJECT OF INVESTIGATION						
EXPERIMENT	INVESTIGATOR	FUNCTION			EFFECT OF	ORGANISM
		PROLIFERATION	STRUCTURE	INTERACTION		
48 F	M. BOUTEILLE	●				PLASMA CELLS
30 F	G. PERBAL	●	●			LENTIL SEEDS
21 F	H. PLANEL	●	●			PARAMECIUM
28 D	H.D. Mennigmann	●	●	●		BACTERIA
58 F	R. TIXADOR	●	●			BACTERIA
33 CH	A. COGOLI	●	●			LYMPHOCYTES
16 D	V. SOBICK	●			MICRO GRAVITY	SLIME MOLD
32 CH	A. COGOLI	●	●			HUMAN BLOOD
7 I	O. CIFERRI		●			BACTERIA
52 NL	G.A. UBBELS		●	●		AMPHIBIAN EGGS
16 E	R. MARCO			●		FRUIT FLY EGGS
16 D	H. BÜCKER			●		STICK INSECT EGGS
19 D	H. BÜCKER			●	RADIATION	NONE
27 D	D. MERGENHAGEN		●		ORBIT	GREEN ALGAE

FIG. 2 - BIORACK EXPERIMENTS FOR THE D-1 MISSION

10-22-1970 507

FIG. 2 - BIORACK EXPERIMENTS FOR THE D-1 MISSION

From Mesland et al , 1986

# RESULTS OF D-1 SPACELAB MISSION

(Nov. 1985)

## ORGANISM

## MICRO-G EFFECTS

### D. melanogaster

no. of embryos layed was 240% more than 1-G(Earth) and 25% more than inflight control (1-G)  
no. of developed embryos was only 10-15% that of 1-G (Earth & inflight) decrease in life-span of males , but not females

### E. coli

increased resistance to Colistin (antibiotic) 2 mg/l. vs 1 mg/l. at 1-G

### E. coli

DNA transfer at conjugation was 2-3X higher  
transduction and transformation same as 1-G

### B. subtilis

growth started earlier, final biomass greater, sporulation was less

### Physarum sp.

increased velocity of protoplasmic streaming, periodicity unchanged

### Paramecium tetraurelia

cell proliferation increased 4X (confirmed Salyut-6 & 7 results)  
cell volume increased and intracellular Ca was decreased

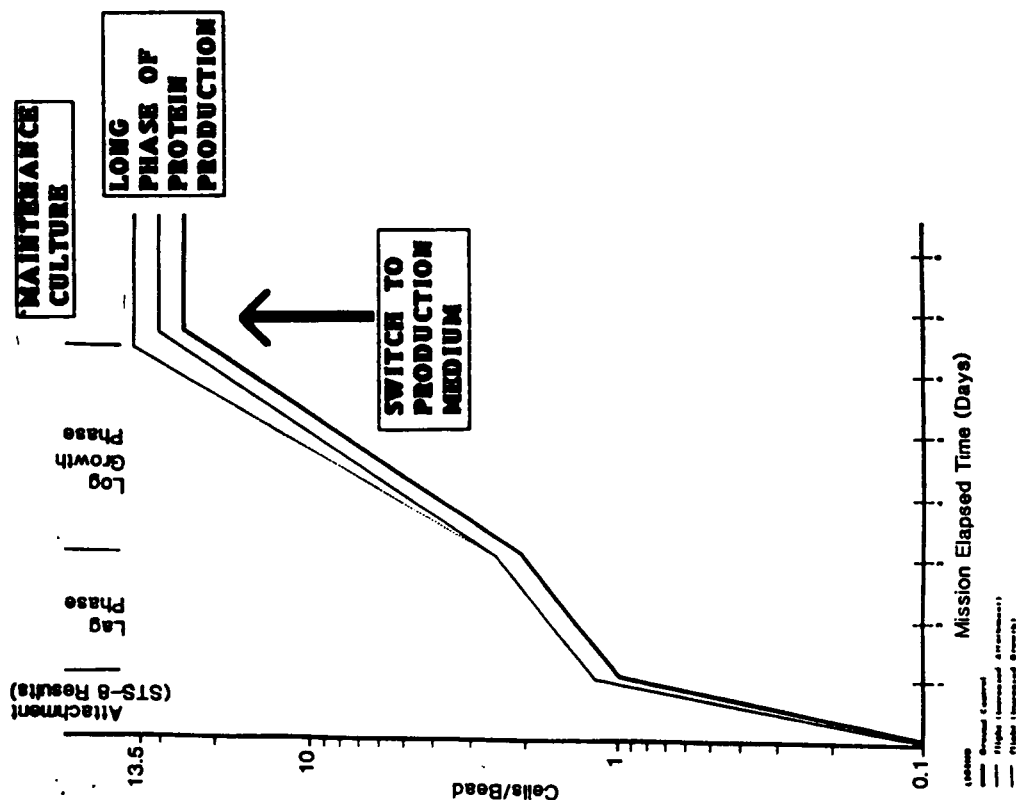
### lymphocytes (human)

confirmed that ConA mitogenic response was decreased by more than 90%  
60% decrease in 1-G inflight control vs. 30% increase at 10-G's

plasma cell hybridomas - ultrastructure, RNA synthesis, normal growth after return to Earth

FIGURE 3

## TYPICAL HUMAN CELL CULTURES



## BIOREACTOR FLIGHT PROPOSALS

### IN PREPARATION

- 1) KIDNEY CELL GROWTH- JSC IN HOUSE
  - INCREASED ATTACHMENT
  - HIGH DENSITY
- 2) LOW SHEAR EFFECTS- JSC, RICE, U.H.
  - CELL METABOLISM
  - CELL STRESS
  - PRODUCT FORMATION

### OTHER PROPOSALS EXPECTED

- GROWTH OF PLANT PROTOPLASTS
- KRIKORIAN (S.U.N.Y.), SCHELD
- CULTURE IN BUBBLY MEDIA
- DUCKLER (U.H.)
- FRAGILE HYBRIDOMAS
- LEY (LOVELACE MED.)
- YEAST FERMENTATION
- PETERSON (JPL)
- BIOSYNTHESIS OF CELLULOSE
- BROWN (U.T.)

Fig. 4

## ANTIBODY ENHANCEMENT OF FREE-FLOW ELECTROPHORESIS

H.H.P.Cohly, Ph.D., D.R. Morrison, Ph.D., M.Z. Atassi, Ph.D.

NASA-Johnson Space Center, Houston TX And Department of Biochemistry, Baylor college of medicine, Houston TX.

## Summary

The objective of this research is to develop specific T cell clones and antibodies (Abs) to study the efficiency of purifying closely associated T cells using Continuous Flow Electrophoresis System (CFES). Enhanced separation is accomplished by tagging cells first with Abs directed against the antigenic determinants on the cell surface and then with Abs against the Fc portion of the first Ab. This second Ab protrudes sufficiently beyond the cell membrane and glycocalyx to become the major overall cell-surface potential determinant and thus causes a reduction of electrophoretic mobility (EPM). This project has been divided into three phases. Phase one included development of specific T cell clones and separation of these specific clones. Phase two extends these principles to the separation of T cells from spleen cells and immunized lymph node cells. Phase three applies this double antibody technique to the separation of T cytotoxic (Tc) cells from bone marrow.

## Background

## Analytical Microelectrophoresis

Microelectrophoresis has been used to quantitate the effect of Ab treatment on the EPM of three populations of cells viz. mouse intestinal epithelial cells (IEC), human mononuclear cells (HMNC) and human erythrocytes (7, 8, 12). Comparison of EPM distributions of IEC and HMNC has shown that single Ab treatment caused no change in EPM while double Ab treatment caused considerable reduction. EPM of human erythrocytes has shown that for blood group A1 and N determinants associated with glycocalyx, a single Ab was sufficient to cause reduction while second Ab was needed for cell membrane-associated determinants (Rh blood group) (8, 10). Furthermore, the use of a cationized second Ab resulted in a higher reduction in EPM in a system where the antigen is presumably in the membrane. Single Ab treatment for membrane-associated antigens did not reduce the EPM. It has been proposed that the first Ab is unable to project beyond the glycocalyx of the cell and therefore does not cause a significant decrease in negative charge. However, the addition of second Ab allows the positive charges to extend beyond the glycocalyx resulting in an effective reduction in the normal net negative charge which causes the retardation of cell mobility. This hypothesis is illustrated in Fig. 1. It suggests that a single Ab suffices to affect EPM when the antigen is in the glycocalyx while second Ab is required for effective reduction in EPM when the antigen is in the cell membrane (Fig. 2).

## Preparative free-fluid electrophoresis

Studies using heavy water gradient electrophoresis have used the double Ab procedure to separate and purify intraepithelial lymphocytes (IEL) and spleen T

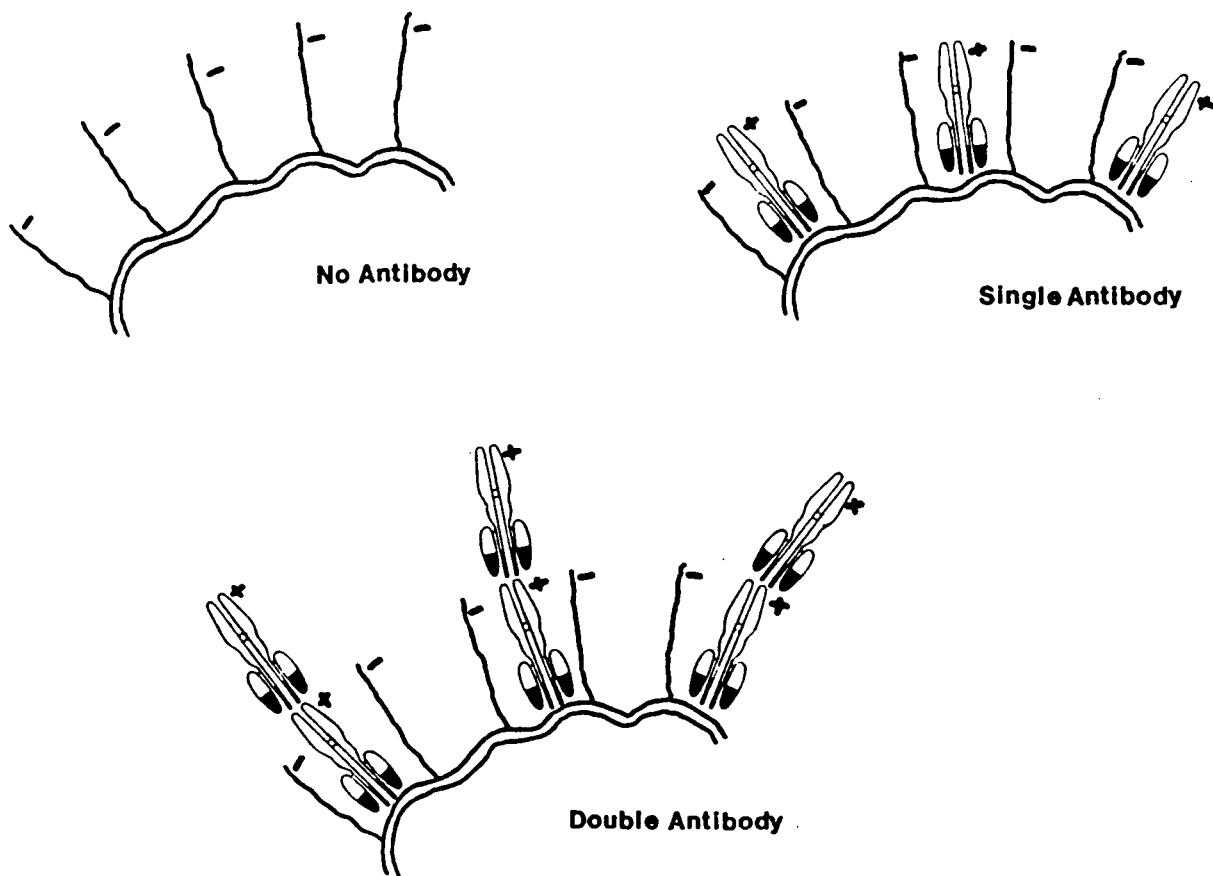
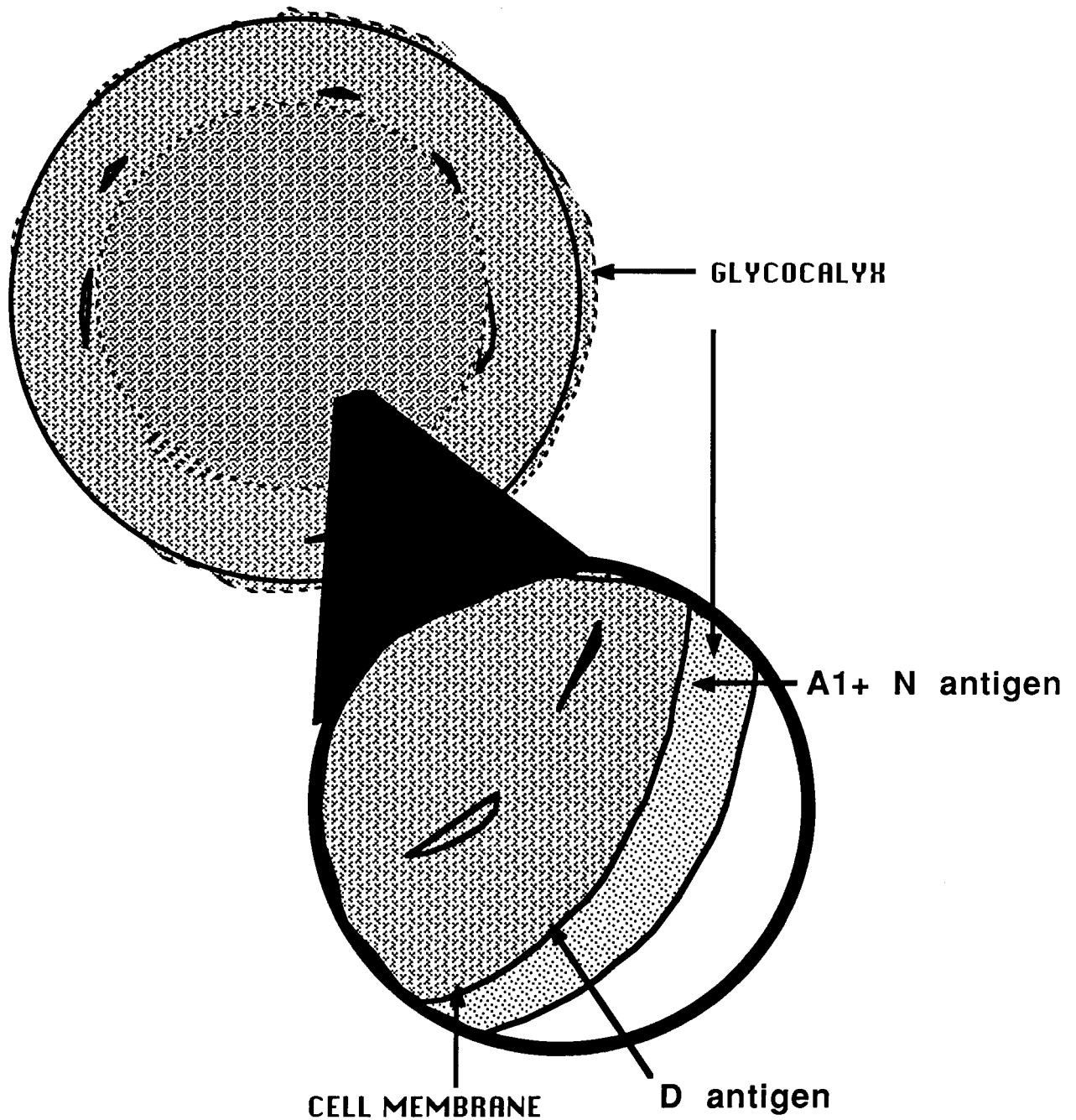


Fig. 1. Schematic representation of the effect of double Ab treatment on the effective charge of cells. A is a cell with its negatively charged glycoprotein strands sticking out. B is a cell which has Ab sticking on to the cell surface where the height of the Ab is similar to the height of the glycoprotein strands. C is a cell where the second Ab is sitting on top of the first Ab and extends beyond the glycocalyx. Only in the last case an effective decrease in EPM occurs.

**FIG. 2**  
**LOCATION OF BLOOD GROUP ANTIGENS**  
**ON A**  
**HUMAN RED BLOOD CELL**



cells (6, 7, 8). IEL from mouse small intestine, which have a 10% epithelial cell contamination after percoll separation, can be further purified by incubating with rabbit IgG (to rat intestinal brush border) followed by incubation with goat IgG to rabbit IgG. This double Ab incubation caused a reduction of EPM of tagged cells sufficient to achieve an electrophoretic fraction virtually devoid of contaminating epithelial cells. In another application T cells were separated from a mixture of Ficoll/Hypaque purified spleen cells by incubating cells with goat anti-mouse total immunoglobulins and then with rabbit anti-goat IgG. With no Ab treatment the fastest moving fraction of T cells had 20% B cell contamination while after double Ab treatment only 2% B cell contamination was found.

One of the main problems encountered in discontinuous heavy water gradient preparative electrophoresis is the small number of cells obtained from the most purified fraction. This restricted analysis of different fractions to phenotyping by cell surface immunofluorescence in lieu of testing their biological activity. This problem may be resolved by using the CFES which offers an increased throughput and resolution for separation of cells without thermoconvection-stabilizing additives.

### Approach

Previous methods of cell separation like preparative electrophoresis are limited since the sensitivity of double Ab technique is difficult to quantify by a biological assay. To explore the practical limits of double Ab and CFES a very well characterized model cell system was needed. The rationale was to generate two T cell clones which could differentiate between closely associated antigens. Sperm Whale Myoglobin (SWMb) and Apo-SWMb were selected as the antigens because they only differ in tertiary structure. The EPM of SWMb and Apo-SWMb clones will then be determined. If these two clones do not cross react and have unique EPMS they can be mixed and re-separated on CFES. If there is inadequate difference between the EPM distribution then Ab to known SWMb determinants can be used to increase the separation of SWMb and Apo-SWMb clones. After separation the fractions are tested for their biological activity using proliferative response assay (11). The understanding gained from the model system can then be used to project or predict how useful the double Ab technique will be for other selected target cells.

Phase one included generation of specific T cell clones to different antigenic sites on SWMb or Apo-SWMb. SWMb has five well characterized antigenic sites recognized by antibodies. Site 1 consists of residues 16-21, Site 2 consists of residues 56-62, Site 3 consists of 94-99, Site 4 consists of residues 113-119 and site 5 of residues 146-151 (1, 2). Very little is known about the molecular parameters involved in the T cell responses to protein antigens. This was mainly due to the inability to prepare specific T cells to well defined protein determinants. T cell cloning has now made it possible to prepare clones to well defined antigenic sites (3, 4, 9). Initial screening for T cell specificity is done with the whole SWMb and the peptide specificity must be determined after second limiting dilution. The specificity of the clones is determined by screening their proliferative response against a pannel of overlapping peptides encompassing the entire SWMb. Six regions of SWMb specifically antigenic to T cells (T sites) were found by a comprehensive synthetic strategy to stimulate SWMb-primed lymph node cells (1, 2, 5, 6, 7). The T sites are localized within the residues 10-22, 46-63, 69-80, 87-100, 107-120 and 137-151 (4, 13).

## Experimental Results

Before attempting to generate target clones proliferative assay was performed on Apo-SWMB and SWMB primed lymph node cells which were challenged by synthetic overlapping peptides encompassing the entire SWMB chain. In three separate experiments the response of SJL lymph node cells to Apo-SWMB was always higher than SWMB regardless of whether SWMB or Apo-SWMB was injected. This interesting finding needs to be verified further as it questions current theories about the mechanisms of antigen processing (5).

### SWMB clones

After 3 passages T cells specific for SWMB were cloned by serial dilution and 3 clones were obtained viz, A5B8, C2F5 and A2G12. The results of proliferative assay to test the specificity of these clones are shown in Table 2.

Table 2: Proliferative response of SWMB clones to whole SWMB and Apo-SWMB

	Antigen	Optimum dose	Net cpm
A5B8	SWMB	100 ug/ml	15,782
	Apo-SWMB	12 ug/ml	95,734
C2F5	SWMB	6 ug/ml	151,131
	Apo-SWMB	25 ug/ml	187,151
A2G12	SWMB	100 ug/ml	44,629
	Apo-SWMB	25 ug/ml	43,573

### Apo-SWMB clones

After first passage T cells specific for Apo-SWMB were cloned by serial dilution. The clones obtained were B4B6, D5A12 and B5C1. These cells are now in the process of being cloned for the second time by serial dilution.

Table 3: Proliferative response of Apo-SWMB clones to SWMB and Apo-SWMB

	Antigen	Optimum Dose	Net cpm
B4B6	SWMB	100 ug/ml	16,650
	Apo-SWMB	25 ug/ml	11,781
D5A12	SWMB	12 ug/ml	4,214
	Apo-SWMB	12 ug/ml	5,928
B5C1	SWMB	6 ug/ml	48,140
	Apo-SWMB	50 ug/ml	48,152

As indicated in Table 2 A5B8 SWMB clone has a higher response to Apo-SWMB than SWMB and in Table 3 the proliferative response of Apo-SWMB clones is similar.



## Future Work

The next phase will apply the double Ab technique to enhance the separation of spleen T and B cells. After separation, different fractions will be tested for their phenotypic determinants and mitogenic responses to concanavalin A and lipopolysaccharide. The mitogenic response is still a very crude indicator for the purity of T cells or B cells therefore the next step will be to separate T cells from lymph node cells of immunized mice using double Ab and then test their functional activity by a proliferative assay.

Phase three involves the removal of Tc cells from bone marrow then treatment by Ab tagging followed by free-fluid electrophoresis. The procedure would involve the employment of a battery of Abs specific for Tc to determine if single Ab or double Ab treatment is required to remove Tc cells. This approach could have great clinical significance e.g. "purging" of Tc cells from bone marrow for patient therapy and transplantation. Bone marrow transplants would require elimination of only Tc cells (which cause the immune rejection of bone marrow) followed by injection of all remaining cells back into the host.

## Conclusions

To date the effect of double Ab treatment to alter the net surface charge of living cells has been documented by analytical electrophoresis. This technique also has been used to purify spleen T and intestinal IEL population by preparative electrophoresis using a heavy water gradient. To better define the extent to which this technique can be applied to different target cells a model T clone system is being developed. Apo-SWMB and SWMB are two almost identical proteins for which specific clones have been generated. These clones will be studied for antigen processing and cell separation on ACE 710 and CFES. Other cell systems proposed to be separated are T cells from spleen, and lymph nodes and Tc from bone marrow. The CFES will be evaluated for efficiency in separating these target cells to determine if standard technique or double Ab enhancement will be sufficient to accomplish the desired cell separation. If not, this data will be used to develop proposals for flight experiments to use CFES in microgravity where the CFES resolution and throughput are enhanced.

## Experimental Procedures

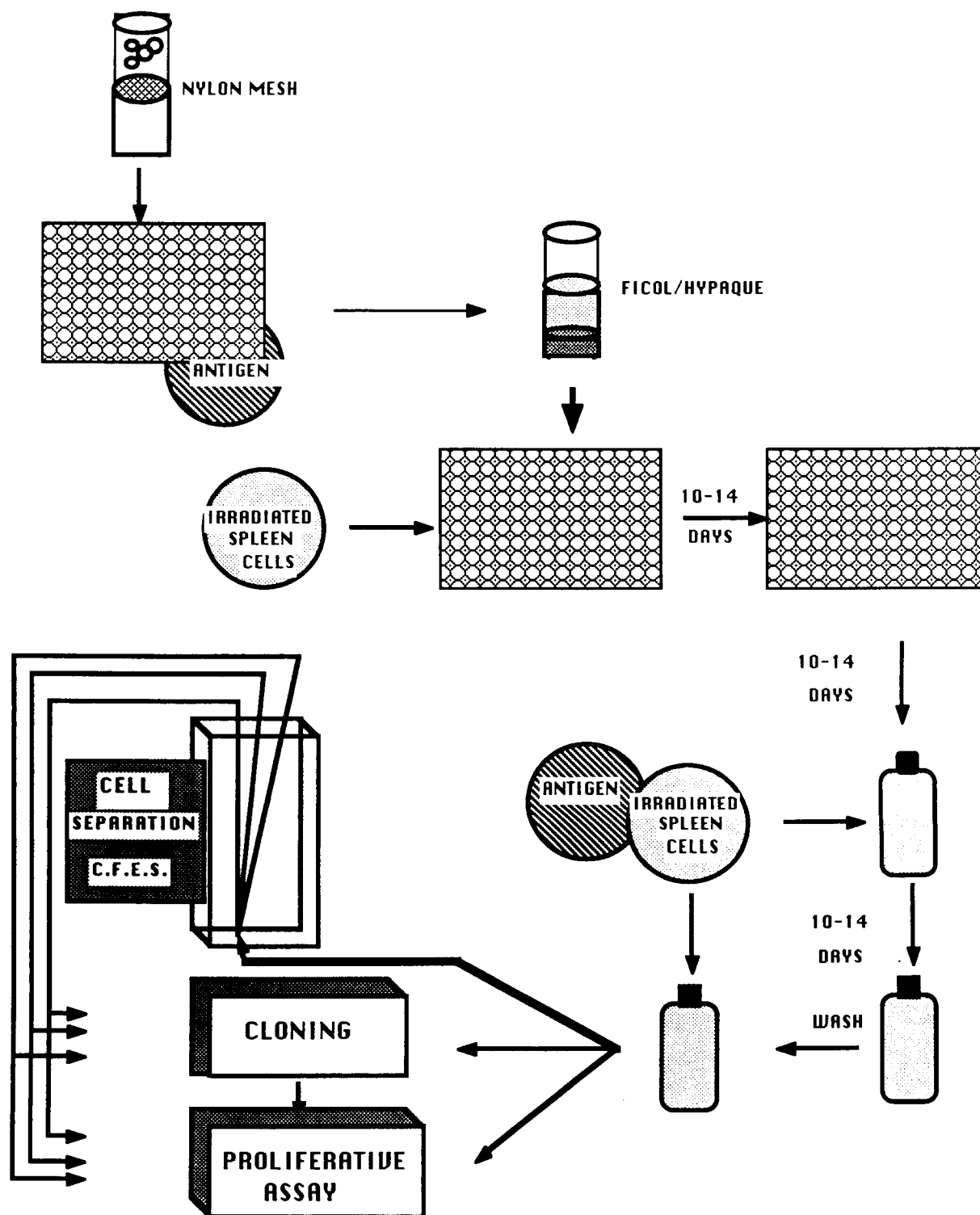
### Proliferative Assay

SJL mice were immunized subcutaneously at the base of the tail with 10 ug/mouse of major component (No 10) of Sperm Whale Myoglobin (SWMB) emulsified in Freund's complete adjuvant containing Mycobacterium Tuberculosis, strain H37Ra (Difco, Detroit, MI). Seven days after immunization, the inguinal and periaortic lymph node cells were harvested and the proliferative activity assessed. In a typical assay, lymph node cells suspended in RPMI-1640 containing 1% normal mouse serum were challenged, in triplicate, with various concentrations of antigens and mitogens in 96-well tissue culture plates. After 3 days the cultures were pulsed (18 hrs) with 1 uCi (3H) thymidine and then harvested onto a glass fiber filters for counting by liquid scintillation.

### Long term T cell culture

The basic approach to obtain and process long term T cell culture is indicated in Fig. 3. Cultured T cells will be separated on CFES, cloned and tested for

**FIG. 3**  
**LONG TERM T CELL CULTURE**



their specificity by proliferative assay. Furthermore, long term T cell culture will be cloned separately and their specificity tested by proliferative assay. Clones specific to SWMb long term T cell cultures were prepared as follows. SWMb primed lymph node cells were suspended in RPMI 1640 supplemented with 10% fetal bovine serum. The cells (2ml/well) were cultured for 4 days in 24-well flat bottom tissue culture treated polystyrene plates with antigen, harvested and then separated on ficoll-hypaque. The cell were recultured with filler cells (X-irradiated, 3300 R, syngeneic spleen cells) in 16 mm wells. Fourteen days later, fluorescein diacetate positive cells were restimulated with the appropriate antigen and filler cells. At 10-12 day intervals, antigen reactive cells were harvested, combined with additional filler cells and restimulated with antigen. T cell clones from protein specific bulk culture were isolated by limiting dilution at a frequency of 1, 0.5 and 0.25 cell/well. The clones were maintained by repeated passage with antigen, filler cells and serum. Specificity of the T cells was determined by their proliferative response. Long term culture of T cells were cocultured with antigens and mitogens in RPMI supplemented with 10% serum. Filler cells were added for macrophage source and the cells were cultured for 3 days and then pulsed with 1 uCi (3H) thymidine as described above.

#### Preparation and purification of synthetic peptides.

The synthetic peptides were based on the known primary structure of SWMb. The peptides were prepared by solid phase synthesis (11). The primary structure of the SWMb synthetic overlapping peptides was synthesized. Except for the carboxy-terminal peptide 141-153, the peptides are uniform in length (17 residues) and overlap adjacent peptides by 5 amino acids. SWMb sites 1, 2, 3 and 4 which were extended by an additional 5-6 residues (i.e. a total of 13 residues) also were synthesized.

#### References

- 1) Atassi, M.Z. (1980) *Mol. Cell Biochem.* 32, 21-44.
- 2) Atassi, M.Z. (1984) *Eur. J. Biochem.* 145, 1-20.
- 3) Bixler, G.S. and Atassi, M.Z. (1983) *Immunol. Comm.* 12, 593-603.
- 4) Bixler, G.S. and Atassi M.Z. (1984) *J. Immunogen.* 11, 339-353.
- 5) Bixler, G.S. and Atassi, M.Z. (1985) *Eur. J. Immunol.* 15, 917-922.
- 6) Bronson, P.M. and van Oss, C.J. (1979) *Prep. Bioch.* 9, 61-70.
- 7) Cohly H.H.P., Soroka C.J., Albin B., Weiser M.M. and van Oss C.J. (1986) *Fed. Proc.* 45: 733.
- 8) Cohly H.H.P., van Oss C.J., Albin B. and Morrison D. (1986) *ACS* 42: 15.
- 9) Infante, A.J., Atassi M.Z. and Fathman, C.G. (1981) *J. Exp. Med.* 154, 1342-1356.
- 10) Lorusso D.J. and Green, F.A. (1980) In "A seminar on antigens on blood cells and body fluids" (*Amer. Assoc. Blood Banks, Washington*) 226-235.
- 11) Merrifield, R.B. (1963) *J. Am. Chem. Soc.* 85, 2145-2154.
- 12) van Oss, C.J., Fike, R.M., Good, R.J. and Reining, J.M. (1974) *Anal. Biochem.* 60, 242-251.
- 13) Yoshioka, M., Bixler, G.S. and Atassi, M.Z. (1983) *Mol. Immunol.* 20, 1133-1137.

THE STRESS RESPONSE SYSTEM OF PROTEINS:  
IMPLICATIONS FOR BIOREACTOR SCALEUP

by Charles F. Goochee, Assistant Professor, Department of Chemical Engineering, University of Houston, Houston, TX 77004

**Abstract**

Animal cells face a variety of environmental stresses in large-scale bioreactors, including periodic variations in shear stress and dissolved oxygen concentration. We have embarked on a major research effort to develop diagnostic techniques for identifying the particular sources of environmental stresses for animal cells in a given bioreactor configuration, and to understand the mechanisms by which cells cope with such stresses. The individual concentrations and synthesis rates of hundreds of intracellular proteins are affected by the extracellular environment (e.g. medium composition, dissolved oxygen concentration, pH, and level of surface shear stress). We are currently developing techniques for quantifying the synthesis rates and concentrations of the intracellular proteins which are most sensitive to environmental stress. Previous research has demonstrated that a particular set of "stress response proteins" are synthesized by mammalian cells in response to temperature fluctuations, dissolved oxygen deprivation, and glucose deprivation. Recently, we have demonstrated that exposure of human kidney cells to high shear stress results in expression of a completely distinct set of intracellular proteins.

This research can be expected to have a significant impact on research at NASA, and on the developing U.S. biotechnology industry. The techniques developed in this project can be utilized to assess the sources of environmental stress in any bioreactor configuration for any type of animal cell. The techniques will therefore be of significant diagnostic value in the design and operation of animal cell bioreactors. In addition, an increased understanding of the response of cells to environmental stress can be expected to ultimately lead to genetic modifications which will lead to improved growth characteristics of animal cells in large-scale culture. We are currently collaborating with Cetus Corporation to assess these industrial implications.

## Introduction

There are several potential sources of stress for cells grown in suspension culture. A sudden change of environment may occur upon inoculation. High levels of shear may exist in the vicinity of an impeller. Significant hydrostatic pressure variation may exist between the top and bottom of the fermentor. Significant gradients in dissolved oxygen, pH and other environmental variables may exist in the culture vessel due to a combination of the finite circulation time in the vessel and the metabolic activities of the cells (e.g. consumption of oxygen, and production of acid or base). It will be particularly difficult to maintain a homogeneous growth environment for cells in large-scale, high-density or viscous cell cultures. As a consequence of this environmental heterogeneity, microbial, plant and animal cells will inevitably face a variety of environmental transients as they circulate in a culture vessel.

There are limits to the amount of environmental stress (e.g. periodic shear stress or variation in dissolved oxygen concentration) which can be readily accommodated by a particular cell type. Techniques for assessing these limits at the bench scale would be of obvious value in the design and scale-up of bioreactors and in the selection of host cell systems for large-scale production.

An understanding at the molecular level of the intracellular mechanisms by which cells respond to environmental stress would be even more valuable. With this knowledge one could begin to experiment with genetic modifications to improve the growth characteristics of the host system in large-scale culture.

We have embarked on a major research effort to understand the ability of cells to respond to environmental stress. In the first section of this report the scientific background of this research program will be presented. This will be followed by a brief statement of our research objectives and presentation of preliminary results. This report will conclude with a summary of the expected benefits of this research program.

## The Stress Response System of Proteins

Recent developments have provided a framework for the examination of the response of

cells to environmental transients. It has been recognized that all cell types, from bacterial to plant and mammalian cells, possess a network of proteins which are expressed in response to environmental stress (Schlesinger et al., 1982; Neidardt et al., 1984; Atkinson and Walden, 1985). The expression of these proteins, variously known as the "stress response proteins" or the "heat shock proteins", was first observed in response to sudden environmental temperature changes. It is now clear that there are numerous inducers of the stress response proteins, including changes in dissolved oxygen concentration, exposure to ethanol or amino acid analogues, stimulation with serum and infection by adenovirus 5 or simian virus 40 (summarized by Anathan et al., 1986 and Wu et al., 1986).

The stress response proteins appear to play a role in protecting cells from damage in adverse situations. In general, it has been observed that pretreatment of cells to elicit synthesis of the stress proteins results in protection of those cells from subsequent severe stress. For example, pretreatment of cells with ethanol or hypoxia results in increased thermotolerance. (Li and Werb, 1982). The specific roles of the stress response proteins are an area of current investigation. Recently, it has been noted that brief severe heat shock blocks the processing (i.e. removal) of intervening sequences in mRNA. The stress response proteins act to counteract this effect (Yost and Lindquist, 1986). The stress response genes are conspicuously free of introns, permitting synthesis of the stress response proteins under otherwise restrictive conditions.

The stress response proteins are by definition those intracellular proteins whose rates of synthesis increase following sudden environmental change. Eighteen major stress response proteins have been identified in *E. coli*. The number of major stress response proteins identified to date in insect and mammalian cells is on the order of eight to ten. Major stress response proteins with molecular weights of approximately 70 and 85 kDa have been noted in all species so far examined.

The 70 and 85 kDa stress response proteins have been highly conserved in evolution. Antibodies raised against the 70 and 85 kDa stress response protein from chicken cells cross-react with the equivalent proteins in yeast, *Drosophila*, corn, mouse and human cells (Kelley and Schlesinger, 1982). Recently, it was noted that the amino acid sequence of the human 70 kDa protein is 75 to 80% homologous to both the yeast and *Drosophila* 70 kDa stress response proteins and 55.5% homologous to the equivalent protein from *E. coli* (Voellmy et al., 1985).

intracellular proteins which triggers the transcription of the stress response genes. In this regard ubiquitin would play a regulatory role in the stress response system somewhat analogous to the role of cyclic AMP in the catabolite repression system. The existence of a unique promotor sequence upstream of the stress response genes suggests the existence of a specialized transcription factor, analogous to the catabolite gene-activator (CAP) protein of the catabolite repression system. Munro and Pelham have postulated that this transcription factor is a constant candidate for ubiquitin attachment. The transcription factor is proposed to be inactive in its "ubiquitinated" form and active only when it is "non-ubiquitinated". Therefore, when the level of free ubiquitin falls following an increase in abnormal protein, the transcription factor is active and the stress response genes are transcribed. Recently, it has been noted that ubiquitin is, itself, a stress response protein (Bond and Schlesinger, 1985).

The recent identification of multiple promotor sites for the stress response genes (Wu et al., 1986) raises the possibility that multiple mechanisms may exist which trigger expression of one or more of the stress response genes.

### **Research Objectives**

Our initial technical efforts are now focussed on the implementation of two-dimensional electrophoresis technology (O'Farrell gel electrophoresis) for analysis of the synthesis rates of intracellular proteins. A computerized, image analysis system is used for the quantitative analysis of autoradiographs produced using this technology. The utilization of 2D-PAGE for the qualitative and quantitative analysis of intracellular protein synthesis has been extensively examined over the past decade (O'Farrell, 1975; Anderson and Anderson, 1977; Cellis and Bravo, 1984). The development of computerized, image analysis systems has markedly enhanced the analysis of autoradiographic images produced by 2D-PAGE (Garrels, 1979; Miller et al., 1984) and other techniques (Goochee et al., 1980).

As an additional analytical tool, an immunoassay based on the important 70,000 MW "heat shock" protein (Welch and Feramisco, 1984) is being developed in conjunction with Dr. William Welch (Cold Spring Harbor Laboratory) and the University of Texas (Dr. Lynne Rutzky). The concentration of this protein appears to be a particularly clear indicator of the magnitude of the stress response in mammalian cells. The concentration of this protein is very low in unstressed cells. Following imposition of temperature stress, the rate of synthesis of this protein has been noted to increase 100-fold. The 70-kDa stress response protein has been

The regulatory mechanism for the production of the stress response proteins has also been conserved to a remarkable degree throughout evolution. The gene for the *Drosophila* 70 kDa stress response protein, including its native promotor region, is expressed in a normal, temperature-regulated fashion in frog, mouse and monkey cells (see references in Voellmy et al., 1985).

The wide spectrum of stimuli which promote the coordinated expression of this system of proteins suggest that the stress response is a "global regulatory response", comparable to the catabolite repression system and bacterial SOS and stringent response systems. A unique, common promotor sequence (upstream of the normal, eukaryotic TATA box) has recently been identified for the eukaryotic stress response genes (Pelham, 1982). More recent data suggest that there may be additional, alternative promotor sites upstream of the TATA box which respond to different stimuli (e.g. one promotor sequence related to temperature shock, and another related to serum stimulation) (Wu et al., 1986).

What is the specific mechanism which couples a sudden environmental change to the enhanced transcription of the stress response genes? Several hypotheses have been presented in the past few years to explain this coupling. The most compelling current hypothesis is that the stress response is triggered by the accumulation of abnormal or misfolded protein within the cell. Goff and Goldberg (1985) noted that the synthesis of large amounts of misfolded, human tissue plasminogen activator in *E. coli* led to the induction of the stress response system. Recently, it has been demonstrated that injection of denatured bovine serum albumin or bovine beta-lactoglobulin into *Xenopus laevis* (frog) oocytes led to the induction of the stress response system, while the injection of the native bovine proteins did not lead to induction (Ananthan et al., 1986). A reexamination of all of the other known inducers of the stress response suggests that most of these agents (i.e. temperature change, ethanol, etc.) could also be expected to result in the accumulation of denatured or damaged proteins within the cell.

A very specific hypothesis has recently emerged to explain how a sudden accumulation of abnormal intracellular protein could result in the expression of the stress response proteins (Munro and Pelham, 1985). In eukaryotic cells, aberrant proteins are recognized and tagged for proteolysis by the "ubiquitin-dependent degradation system" (i.e. the ubiquitin system). Ubiquitin is a 76-amino acid protein which is covalently attached to the N-terminal and/or lysine residues of proteins marked for degradation. It has been postulated that it is the decline in free ubiquitin concentration within the cell following an increase in abnormal



extremely conserved throughout evolution. This suggests that an antibody raised to the particular 70-kDa protein of one mammalian cell type can be utilized as a quantitative assay for the comparable protein in other mammalian, as well as for eukaryotic microorganisms, insect cells and plant cells.

Our initial research efforts will focus on mammalian and insect cell cultures, where the most significant industrial scale-up problems are perceived to exist. Two model mammalian cell culture systems are now under consideration: primary human embryonic kidney cells and mouse hybridomas (provided by Cetus Corporation). Insect cell culture scale-up studies are currently being initiated in collaboration with Max Summers of Texas A&M University.

Following the refinement of identification and quantification techniques we will examine several important questions with respect to the response of cells to stress:

1. Assessment of the effects of different types of environmental stress on intracellular protein synthesis. Temperature and dissolved oxygen transients have been clearly identified as inducers of the "stress response" system of proteins in most eukaryotic cell types which have been examined. The effects of pH and hydrostatic pressure transients and shear stress have not been examined. Our preliminary results indicate that sudden exposure to environmental shear leads to synthesis of a unique set of intracellular proteins (discussed below).
2. Assessment of the relationship between the duration and magnitude of a particular stress and the magnitude of the intracellular response. Previous studies of the stress response have focussed on rather large step changes in environmental variables (e.g. temperature step changes of 10 °C). We will examine the effect of smaller step, pulse and periodic environmental changes on intracellular protein synthesis. These are the types of environmental stress most likely to be experienced in mammalian cell bioreactors.
3. Assessment of the relationship between environmental stress and cell growth and product formation. This issue has not been directly addressed in the literature. It is our hypothesis that cell growth and the formation of protein products will be significantly curtailed during the stress response due to the preferred transcription and translation of the stress response protein mRNA.
4. Assessment of differences between alternative mammalian and insect cell host systems with respect to their ability to cope with environmental stress. One of the major issues in scale-up

is the capacity of the host cell to cope with environmental stress. It is our hypothesis that this capacity relates directly to the intracellular regulation of the stress response system of proteins.

## Preliminary Results

Preliminary experiments have been conducted to assess the potential of the approach which we have outlined above. Primary human embryonic kidney (HEK) cells were subjected to sudden changes in either temperature or shear stress, and the resulting patterns of intracellular protein synthesis were compared with the pattern for unstressed HEK cells. The results are presented in figures 1, 2 and 3. Cells were labelled for two hours with [S-35] methionine and were then separated by 2D-PAGE technology. Proteins were separated in the vertical dimension on the basis of molecular weight and in the horizontal dimension on the basis of isoelectric point. In figure 1, the pattern of protein synthesis is presented for the unstressed control cells.

The response of HEK cells to a sudden temperature increase from 37 °C to 42 °C is illustrated in figure 2. The synthesis rates of many intracellular proteins are observed to remain constant or decline, while the synthesis rates of at least eleven intracellular proteins are noted to increase dramatically. These "heat-shock/stress response" proteins are indicated by arrows in figure 2. Of particular note is the dramatic increase in protein synthesis of several proteins in the vicinity of molecular weight 70,000. These proteins represent the well-characterized 70-kDa family of stress response proteins.

The response of primary HEK cells to a sudden change in the level of hydrodynamic stress was next examined. This was accomplished in collaboration with Dennis Morrison and Errol Kalmez at Johnson Space Center (Houston). HEK cells were subjected for two hours to 12 dynes per square centimeter of shear stress in a laminar flow chamber, and were then labelled for two hours as previously described. The response of these cells to this sudden increase in shear is illustrated in figure 3. A dramatic increase in the synthesis of at least fifteen intracellular proteins is observed. A comparison of figures 2 and 3 reveals that the responses of cells to temperature and shear transients are substantially different. Of particular note, is the absence of increased synthesis of the 70kDa stress response proteins in figure 3.

The preliminary results for the response of HEK cells to shear stress are intriguing. It has been widely hypothesized that the "heat shock" system of proteins represents the fundamental

intracellular stress response mechanism. But, these proteins were not expressed by HEK cells in response to a sudden increase in environmental shear stress (figure 3). Evidently, the response of cells to environmental stress is more complex than might have previously been imagined. The precise identities of the intracellular proteins which experienced increased synthesis as a result of environmental shear are not known at this time. One of these proteins has a molecular weight and isoelectric point characteristic of the cytoskeletal protein tubulin. Increased synthesis of cytoskeletal proteins in response to environmental stress would not be surprising.

### **Expected Benefits**

This research can be expected to have a significant impact on research at NASA, and on the developing U.S. biotechnology industry. This methodology developed in this project will represent a valuable diagnostic tool in the analysis of large-scale bioreactors. The preliminary results illustrate the potential of 2D-PAGE to discriminate between different sources of environmental stress for a single cell type. Ultimately, it will be possible to discern the specific source(s) of stress for mammalian cells in any bioreactor configuration based on analysis of the profile of intracellular protein synthesis. The measurement of substantial stress for cells in a particular reactor assembly will provide justification for design changes which could be expected to lead to improvements in cell growth and product formation.

It is quite possible that the methodology developed in this study will also have an impact on the bench-scale evaluation of host systems for large-scale culture. One of the major issues in the scale-up of genetically-engineered mammalian cells is the capacity of the host cell to cope with environmental stress. The techniques developed in this study will permit rapid, side-by-side, bench-scale comparisons of alternative host systems in response to imposed environmental stress of the type which will be encountered in large-scale bioreactors. A comparison of the resulting profiles of intracellular protein synthesis may provide guidance in the selection of the best candidates for scale-up.

General guidelines will be developed with regard to the levels of environmental shear, pH, dissolved oxygen, hydrostatic pressure, and temperature stress which can be accommodated by mammalian cells in large-scale culture. These data will prove valuable in the subsequent design of mammalian cell bioreactors.

Finally, this research project can be expected to lead to an increased understanding of the mechanisms by which mammalian cells respond to environmental stress. This can be expected to ultimately suggest genetic modifications to improve the growth characteristics of mammalian cell systems in large-scale culture.

### Bibliography

Anathan, J., Goldberg, A.L. and Voellmy, R., "Abnormal Proteins Serve as Eukaryotic Stress Signals and Trigger Activation of Heat Shock Genes", *Science*, 232, 522(1986).

Anderson, L. and Anderson, N.G., "High Resolution Two-Dimensional Electrophoresis of Human Plasma Proteins", *Proc. Nat. Acad. Sci.*, 74, p. 5421-5425, (1977).

Atkinson, B.G. and Walden, D.B., editors, Changes in Eukaryotic Gene Expression in Response to Environmental Stress, Academic Press, New York, 1985.

Bond., U. and Schlesinger, M.J., "Ubiquitin is a Heat Shock Protein in Chicken Embryo Fibroblasts", *Molecular and Cellular Biology*, 5, p 949-956, (1985).

Celis, J.E. and Bravo, R., (editors), Two-Dimensional Gel Electrophoresis of Proteins: Methods and Applications, Academic Press, New York, 1984.

Garrels, J.I., "Two-dimensional Gel Electrophoresis and Computer Analysis of Proteins Synthesized by Clonal Cell Lines", *J. Biol. Chem.*, 254, p. 7961-7977, (1979).

Goff., S.A and Goldberg, A.L., "Production of Abnormal Proteins in *E. coli* Stimulates Transcription of *lon* and Other Heat Shock Genes", *Cell*, 41, p. 587-595, (1985).

Neidhardt F.C., VanBogelen, R.A. and Vaughn, V., "The Genetics and Regulation of Heat-Shock Proteins", *Ann. Rev. Genetics*, 18, p. 295-329, (1984).

Goochee, C., Rasband, W, and Sokoloff, L., "Computerized Densitometry and Color Coding of [ $^{14}\text{C}$ ]Deoxyglucose Autoradiographs", *Annals of Neurology*, 7, p. 359-370, (1980).

Kelley, P.M. and Schlesinger, M.J., "Antibodies to Two Major Chicken Heat Shock Proteins

Cross-react with Similar Proteins in Widely Divergent Species", *Mol. Cell. Biol.*, 2, p. 267-274, (1982).

Li, G.C. and Werb, Z., "Correlation Between Synthesis of Heat Shock Proteins and Development of Thermotolerance in Chinese Hamster Fibroblasts", *Proc. Nat. Acad. Sci.*, 79, p. 3218-3222, (1982).

Miller, M.J., Olson, A.D., and Thorgeirsson, S.S., "Computer Analysis of Two-Dimensional Gels: Automatic Matching", *Electrophoresis*, 5, p. 297-303, (1984).

Munro, S. and Pelham, H., "What Turns On Heat Shock Genes?", *Nature*, 317, p. 477-478, (1985).

O'Farrell, P.H., "High Resolution Two-Dimensional Electrophoresis of Proteins", *J. Biol. Chem.*, 250, p. 4007-4021, (1975)

Pelham, H.R.B., Cell, "A Regulatory Upstream Promoter Element in the *Drosophila* HSP 70 Heat-Shock Gene", 30, p. 517-528, (1982).

Schlesinger, M.J., Ashburner, M. and Tissieres, A., editors, Heat Shock from Bacteria to Man, Cold Spring Harbor Laboratory, 1982

Subjeck, J.R. and Shyy, T.-T., "Stress Protein Systems of Mammalian Cells", *Am. J. Physiol.*, 250, p. C1-C17, (1986).

Voellmy, R., Ahmed, A., Schiller, P., Bromley, P., and Rungger, D., "Isolation and Functional Analysis of a Human 70,000-Dalton Heat Shock Protein Gene Segment", *Proc. Nat. Acad. Sci.*, 82, p. 4949-4953, (1985).

Welch, W.J., Garrels, J.I., Thomas, G.P., Lin, J.J.-C., and Feramisco, J.R., "Biochemical Characterization of the Mammalian Stress Proteins and Identification of Two Stress Proteins as Glucose- and  $\text{Ca}^{+2}$ -Ionophore-regulated Proteins", *J. Biol. Chem.*, 258, p. 7102-7111, (1983).

Welch, W.J. and Feramisco, J.R., "Nuclear and Nucleolar Localization of the 72,000-Dalton Heat Shock Protein in Heat-shocked Mammalian Cells", *J. Biol. Chem.*, 259, p. 4501-4513,

(1984).

Wu., B.J., Kingston, R.E. and Morimoto, R.I., "Human HSP70 Promotor Contains at Least Two Distinct Regulatory Domains", Proc .Nat. Acad. Sci., 83, p. 629-633, (1986).

Yost, H.J and Lindquist, S., "RNA Splicing is Interrupted by Heat Shock and is Rescued by Heat Shock Protein Synthesis", Cell, 45, p. 185-193, (1986).

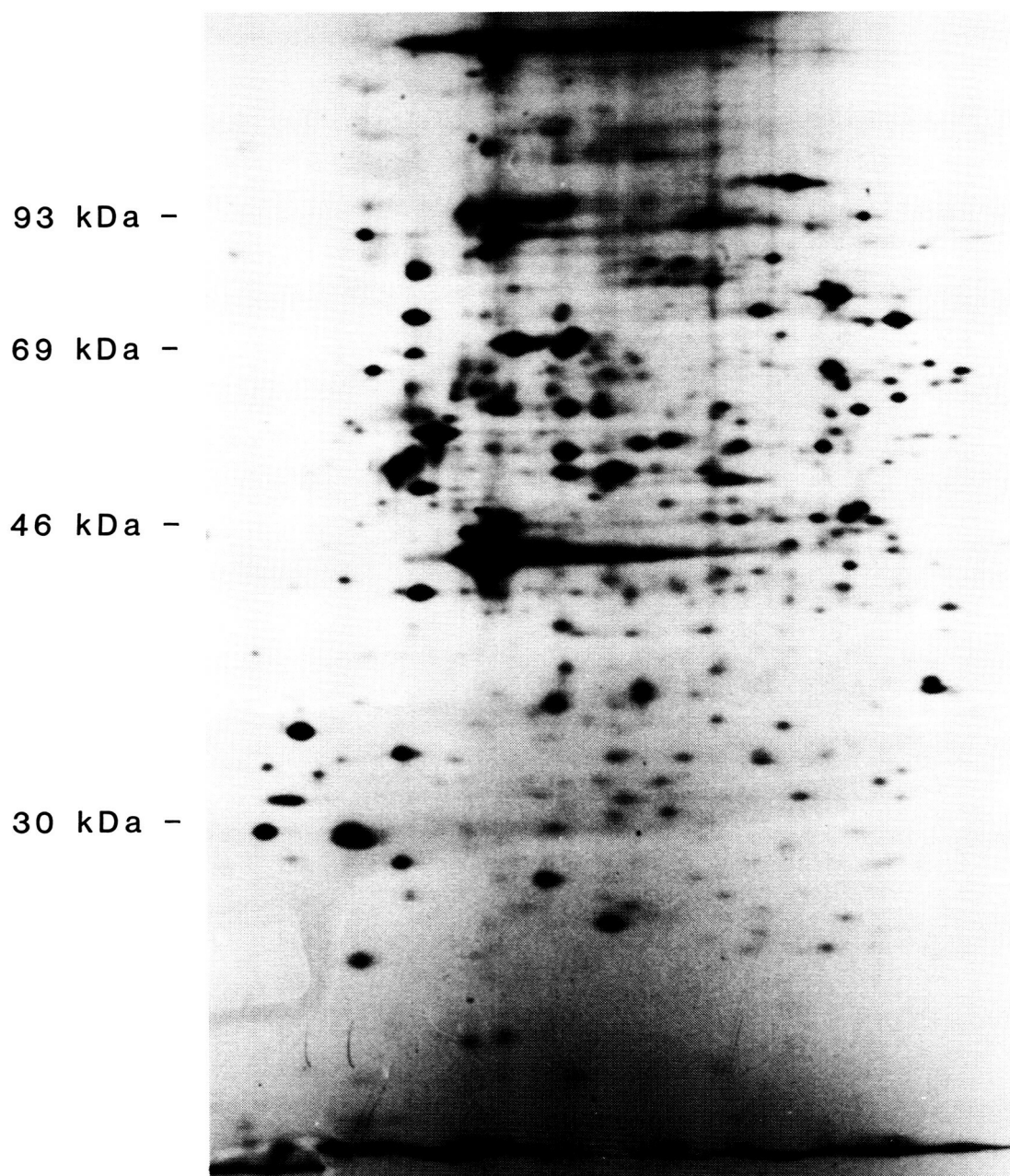


**Figure 1. Unstressed Control.** Primary HEK cells were labelled for two hours with [S-35] methionine and were then separated by 2D-PAGE technology. Proteins were separated in the vertical dimension on the basis of molecular weight (the location of molecular weight standards is indicated in the figure) and in the horizontal dimension on the basis of isoelectric point (pH 5 to 7 from left to right).

93 kDa -  
69 kDa -  
46 kDa -  
30 kDa -



**Figure 2. Response of Cells to Temperature Stress.** HEK cells were subjected to a sudden temperature increase from 37 °C to 42 °C. Cells were labelled for two hours with [S-35] methionine, and were then separated by 2D-PAGE technology under conditions identical to the control cells in figure 1. The locations of proteins whose synthesis rates increase significantly are indicated by arrows. Of particular note is the dramatic increase in protein synthesis of several proteins in the vicinity of molecular weight 70,000. These proteins represent the well-characterized 70-kDa family of heat shock proteins.



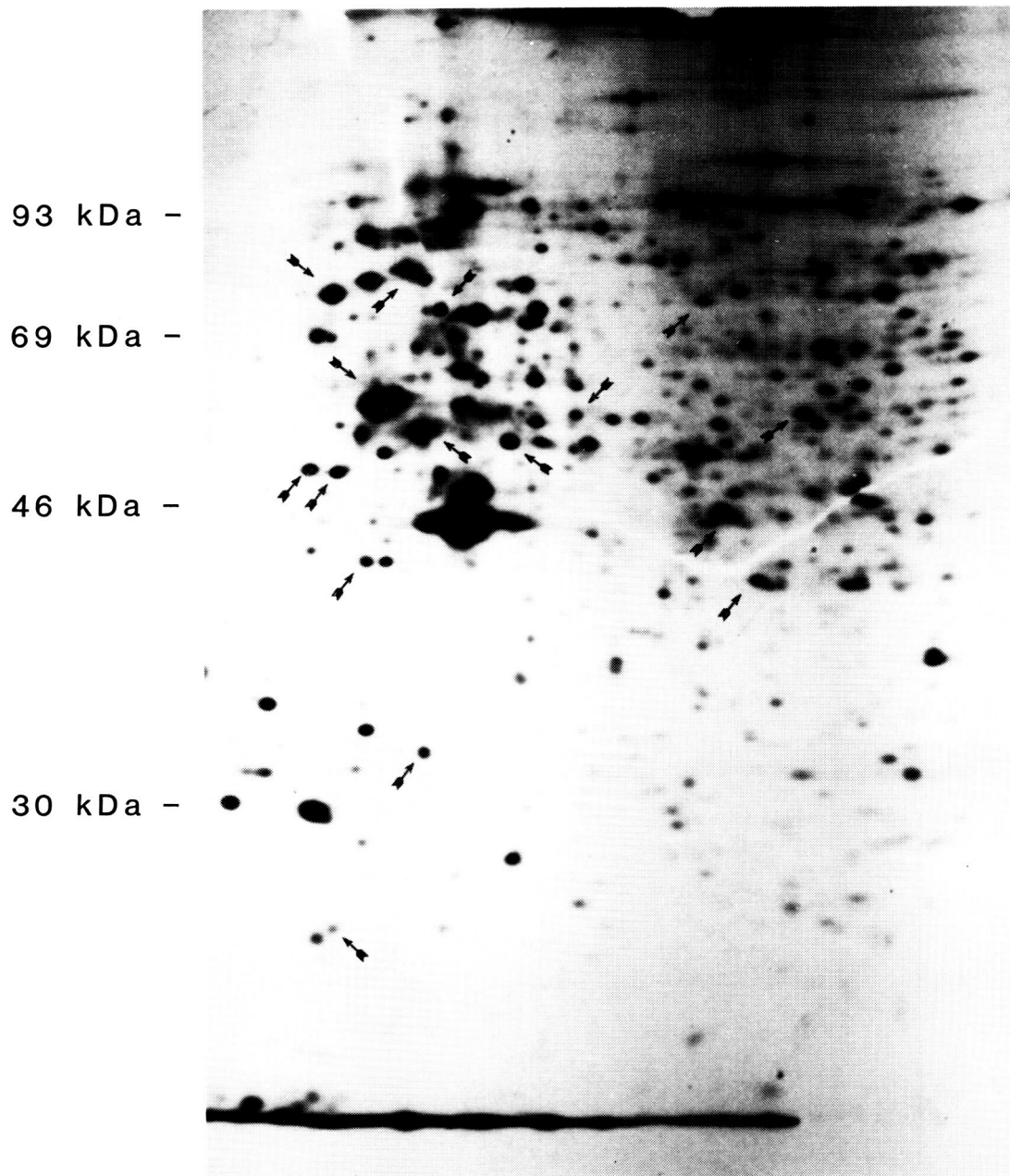


**Figure 3. Response of Cells to Shear Stress.** HEK cells were exposed to a sudden increase in the level of hydrodynamic stress was next examined. HEK cells were subjected for two hours to 12 dynes per square centimeter of shear stress in a laminar flow chamber. The cells were then labelled for two hours with [S-35] methionine and were separated by 2D-PAGE technology under conditions identical to the control cells in figure 1. The locations of proteins whose synthesis rates increase significantly (in comparison with the unstressed cells of figure 1) are indicated by arrows. Of particular note, is the absence of increased synthesis of the 70kDa stress response proteins.

**PROTEIN CRYSTAL GROWTH IN A MICROGRAVITY ENVIRONMENT**

**Nasa Contract Number:** NAS8-36611

**Principal Investigator:** Charles E. Bugg

**Co-Investigators:** See attached list

**Note:** This report is based primarily on the contents of two recent publications describing the background and results of the space shuttle experiments:

1. Charles E. Bugg  
"The Future of Protein Crystal Growth", Journal of Crystal Growth 76 (1986) 535-544.
2. Lawrence J. DeLucas, F. L. Suddath, Robert Snyder, Robert Naumann, M. Beth Broom, Marc Pusey, Vaughn Yost, Blair Herren, Daniel Carter, Bill Nelson, Edward J. Meehan, A. McPherson and C. E. Bugg  
"Preliminary Investigations of Protein Crystal Growth Using the Space Shuttle", Journal of Crystal Growth 76 (1986) 681-693.

**I. Introduction**

Crystallography is a powerful method for determining the three-dimensional structures of complicated biological molecules. Crystallographic studies of proteins and nucleic acids have played key roles in establishing the structural foundations of molecular biology and biochemistry, and for revealing structure/function relationships that are of major importance in understanding how other

macromolecules operate in biological systems. More recently, crystallographic studies of biological macromolecules have become of considerable interest to the pharmaceutical, biotechnology and chemical industries, as promising tools in protein engineering, drug design, and other applications to biological systems.

The elaborate information that can be learned from the three-dimensional structure of a protein is useful in a variety of ways. From the basic biological viewpoint, this information underlies our current understanding of the mechanisms by which enzymes, receptors, hormones, etc. function in biological systems. Within the pharmaceutical industry, protein structure information can be helpful in the development of novel drugs. Since many pharmaceutical agents exercise their activity by interacting with proteins, knowledge of the three-dimensional structure of a target protein can be used to design compounds that selectively bind to protein sites and thereby inhibit the activities of the protein (1-5). Several major pharmaceutical companies have now established protein crystallography groups to pursue this approach of rational drug design.

Another highly promising application of protein crystallography is in protein engineering (6-15). Readily available techniques of molecular biology permit investigators to specifically alter protein molecules by site-directed mutagenesis. In general, the most promising approaches to protein engineering depend upon detailed structural information about the proteins of interest. Although the techniques that are involved in protein engineering are under intense development at this stage, it is generally accepted that these methods will prove to be of tremendous practical value for the design of modified enzymes, and for the development of proteins that have carefully engineered physical and biological properties. There is likely to be a continued expansion of interest in applications of site-directed mutagenesis, and several protein crystallography groups in academic institutions and in biotechnology-oriented companies are expanding their programs in order to exploit the potential of this technology.

An additional use of protein crystallography is in the design of synthetic vaccines (16-19). Several recent studies have indicated that effective vaccines might be made from synthetic peptides that are representative of protein segments found on the surfaces of target proteins. Protein crystallography provides one of the most effective techniques for locating those peptides.

Because of the widespread fundamental and practical importance of knowing the structures of biological materials, the overall interest in protein crystallography has increased greatly during the past few years. At the present time, protein crystallography really has no substitute: It is the only general technique available for elucidating the precise atomic arrangements within complicated biological molecules. Other techniques, such as two-dimensional NMR spectroscopy, are likely to become more and more useful during the next few years, but it is unlikely that any of these techniques will be competitive with X-ray crystallography in the near future for routinely determining three-dimensional structures of large proteins and other complicated biological macromolecules. Unfortunately, protein crystallography has the unique requirement that relatively large, high-quality single crystals must be obtained before a structural study can be pursued. Therefore, protein crystal growth has become a topic of considerable importance.

Unfortunately, all of the major steps that are involved in determining a protein structure by crystallographic techniques are subject to a number of experimental difficulties. Most of the proteins that have been studied during the past three decades required many years of intense effort before the complete three-dimensional structure was known. Consequently, until recently, there was limited interest in using protein crystallography as a general tool in biological research, and protein crystallography programs were limited to a few laboratories, primarily in academic institutions.

Several recent advances in the technologies required for protein crystallographic studies have made it much easier to determine the crystal structure of a protein or other macromolecule:

(1) Recombinant DNA techniques have made it possible to obtain proteins that would have been impossible to isolate in sufficient quantities for X-ray diffraction studies several years ago (6-13).

(2) Synchrotron radiation sources, which provide X-ray beams with intensities that are several orders of magnitude greater than those available from laboratory sources, permit data sets to be collected rapidly, and from relatively few crystals (22-27). Synchrotrons also offer the capability of selecting specific wavelengths, and this capability might eventually prove to be of value in eliminating the need for heavy-atom derivatives in some specific cases (26).

(3) Electronic area detector systems have been developed, and are now available commercially from several different vendors. These two-dimensional detector systems permit data to be measured much faster than was possible with the single-counter detector systems that have been widely used in the past (28, 29).

(4) Recent applications of anomalous dispersion measurements have permitted protein structures to be determined without the addition of heavy-atom derivatives (30-32). Intense efforts are in progress in a number of laboratories to develop direct methods for determining protein phases, which are analogous to the powerful statistical techniques that have essentially eliminated the need for heavy-atoms in "small molecule" crystallography (33-39).

(5) Computer graphics methods have revolutionized techniques that are used to construct protein models from electron density maps (40, 41). Computer graphics techniques have also made it possible to understand and to interpret structures with ease (41, 42), and the widespread use of computer graphics in the pharmaceutical, chemical and biotechnology industries has served to further stimulate interest in applications of protein crystallography.

(6) A variety of approaches and software systems have been developed for refining protein structures, once an initial model is constructed from the electron density maps (43-46). Refinements are now being pursued routinely to high resolutions, and the increasing availability of super computers will make refinements of large proteins relatively routine (47).

It is noteworthy that the major advances in protein crystallography involve those experimental steps that are of importance after suitable crystals have been obtained. For the most part, the general procedures that are used for growing protein crystals have not changed appreciably during the past few years. Most protein crystals are still grown by brute-force, trial-and-error methods, which require investigations of large numbers of experimental conditions in hopes of finding the combination that produces usable crystals. However, once good crystals of a particular protein have been obtained, the crystallography often moves along at a rapid rate.

## **2. Current problems in protein crystal growth**

Nearly any protein crystallographer would immediately point to protein crystal growth as being the major bottleneck in the further widespread development in this field. Despite intensive efforts, a number of interesting proteins have never been crystallized. Many proteins and other biological macromolecules may yield small micro-crystals readily, but it can then take several years of tedious trial-and-error experimentation before these micro-crystals can be induced to grow large enough for a complete structural analysis. Even when large crystals are obtained, the crystals of essentially all biological macromolecules diffract very poorly, due to various types of internal disorder within these crystals.

Most protein crystallography laboratories could cite structural studies that have been delayed for years by problems with protein crystal growth. For example, the relative importance of the difficulties encountered with growing crystals that are

suitable for complete structural studies can be seen from our experiences in Birmingham with the enzyme human purine nucleoside phosphorylase (PNP), which is a trimeric protein with a molecular weight of about 97,000. We began our efforts to crystallize PNP in 1975, using enzyme isolated from several different sources. These efforts continued until 1981, when the first usable crystals of human PNP were grown (48). At the present time (early 1987), we have complete data sets collected for about one dozen substrate, substrate analog, and inhibitor complexes of PNP; we have refined the structure at 3.2 Å resolution (49); and we are well along with the 2.7 Å refinement of the structure. We had the benefit of most modern developments in protein crystallography, including map modification techniques, synchrotron data, molecular graphics for constructing and interpreting models, and automated refinement by restrained least-squares. The main point behind this history is that it took about twice as long to get usable crystals as it did to do the rest of the crystallography. Once we had suitable crystals, the project advanced fairly rapidly. Clearly, crystal growth was the major obstacle in the development of this research project. Even the best crystals that we now have are not highly ordered, which causes problems in efforts to refine the structure of the protein.

### **3. Microgravity applications to protein crystal growth studies**

One interesting new development in protein crystal growth involves studies of crystal growth under the microgravity conditions that are available in space. Crystal growth has been of considerable interest to NASA and to other space-oriented researchers for a number of years (66), and various fundamental studies of crystal growth in space are in progress. The major motivation behind undertaking these space experiments is to examine the effects that density-driven convective flow has on crystal growth. In the absence of gravity, these density-driven convective flow effects are eliminated, thus permitting the role of convection on crystal growth

to be examined directly. In addition to the possibility of suppressing convective flow effects, microgravity conditions may also serve to minimize sedimentation, which can interfere with uniform growth of protein crystals. Another potential advantage of microgravity is the option of doing containerless crystal growth. Contacts with vessel walls can lead to heterogeneous nucleation. In the absence of gravity, it is possible to form stable spherical droplets of crystallizing materials, which may be suspended by acoustical levitation, air streams or other methods. It is also possible to form relatively large, stable droplets of aqueous solutions by simply extruding the solutions from a pipette or a syringe; thus protein crystals might be grown in relatively large droplets adhering to syringe tips, without the extensive wall effects that generally accompany crystallization experiments on earth.

Several projects to study protein crystal growth in space are now in progress (50-54). In addition, investigators at the Marshall Space Flight Center and other researchers supported by NASA, who have considerable background experience in fluid mechanics and crystal growth theory, are now turning their attention and diverse disciplines to fundamental investigations of protein crystal growth. Although it is not clear at this stage if microgravity conditions will prove of general importance in significantly enhancing the growth of protein crystals, the space experiments should make it possible to control parameters that would be difficult or impossible to control on earth. Thus these space experiments should prove useful in better understanding the principles, and the limiting factors in protein crystal growth.

### **NASA-sponsored space shuttle experiments in protein crystal growth**

The space shuttle experiments have been described in considerable detail in the literature (53,54).

One of the most widely used methods of crystallizing proteins on earth involves the slow precipitation of protein from droplets of solution by vapor pressure equilibration against a solution containing a higher concentration of the



precipitating agent. The "hanging-drop method" is a common version of this general technique. Most protein crystallography laboratories have extensive experience with vapor-diffusion crystallization methods, and a large percentage of the protein crystals described in recent publications have been obtained by these methods.

In order to evaluate the possible effects of microgravity on protein crystal growth, it will be necessary to investigate a range of different types of proteins that have been well-characterized in ground-based studies. Many of the proteins that are being extensively studied in crystallography laboratories around the world are only available in milligram quantities. Vapor diffusion techniques are particularly suitable for crystallization experiments involving small quantities of protein and can be used for most types of biological materials. Therefore, we focused our initial experiments on development of a microgravity-adapted version of the popular hanging-drop method.

Prototype flight hardware for growing protein crystals by vapor-diffusion methods was developed, tested, and improved through a series of four shuttle flights in 1985 and 1986 (STS-51D, STS-51F, STS-61B and STS-61C). These experiments were performed in the middeck area of the shuttle. Although the prototype hardware was expected to be useful for testing concepts and developing the basic techniques for protein crystal growth in space, it was clear that it would be of limited value for performing systematic experiments in protein crystal growth, since relatively few samples could be included and important variables such as temperature could not be controlled.

The shuttle experiments were especially useful for optimizing the major variables in vapor diffusion protein crystal growth. We performed various experiments related to drop stability and found that large droplets (30-80  $\mu$ l) are stable on blunt syringe tips even when maneuvering rockets were fired while in orbit. Polypropylene syringes with flared tips, and blunt end glass syringe tips in several different diameters, with and without various types of coatings, have now been used successfully for retaining droplets of protein solutions. Although protein

crystals have been grown in droplets as large as 80  $\mu$ l, the experiments to date indicate that smaller droplets will assure complete equilibration during the limited period (3-6 days) available for protein crystal growth on space shuttle missions. In the most recent set of shuttle experiments (on STS-61C), 30 and 40  $\mu$ l droplets were used with good results. Ground-based and flight experiments also have provided qualitative information about equilibration rates within the vapor diffusion chambers. These studies have suggested that equilibration rates are significantly slower under microgravity conditions, presumably because of suppressed convection effects. The vapor equilibration chambers have now been designed to accelerate these equilibration rates. In addition, a reliable technique for seeding droplets of protein solutions within the vapor diffusion apparatus has been developed, and has been used to grow crystals of human C-reactive protein.

During the most recent shuttle experiments on STS-61C, crystals were grown of all proteins that were tested, including hen egg white lysozyme, human serum albumin, human C-reactive protein, bacterial purine nucleoside phosphorylase, concanavalin, and concanavalin B. That particular shuttle mission was prematurely shortened, and the protein crystal growth experiments were deactivated during the third day of the flight. Although many of the protein solutions had not completely equilibrated during that period of time, relatively large X-ray quality crystals were obtained for all of the proteins except lysozyme.

Comprehensive studies of the effects of microgravity on protein crystal growth will be made on future shuttle flights, using equipment based on the prototype system that was flown on STS-61C. Although quantitative conclusions about protein crystal growth cannot be made at this stage, there are several interesting qualitative observations that have been made during these preliminary shuttle experiments.

It appears that the elimination of density-driven sedimentation can affect crystal morphology. The best example of this is concanavalin, which grew crystals that were dispersed through the droplets in space. Nearly all the space-grown concanavalin

crystals appear to have formed from separate nucleation sites, resulting in uniform morphologies. On the other hand, canavalin crystals grown by this method on earth generally form as fused aggregates at the bottom of the droplets. In the case of human C-reactive protein, an entirely new crystal form, which had not previously been identified in ground-based crystal growth experiments, was obtained from shuttle experiments. Crystallization of C-reactive protein has been studied extensively over the past eight years in Birmingham and only one crystal form, with space group  $P4_122$  (or  $P4_322$ ) has been obtained in these experiments. A new crystal form was first observed for C-reactive protein from experiments on STS-61B, and copious quantities of this crystal form were obtained on STS-61C. The space group for the new crystal form is  $P4_222$ , and it diffracts to an appreciably higher resolution than the original crystal form. The new crystal form has now been obtained in ground-based experiments using the shuttle hardware, so it may be influenced by altered equilibration rates or other experimental conditions that are hardware dependent. It is not yet clear how microgravity affects the distribution of these two crystal forms of human C-reactive protein.

It is not yet clear if the internal order or diffraction resolutions of space-grown protein crystals are significantly different from that of crystals grown on earth. It will be necessary to do detailed comparisons involving large numbers of crystals grown under well-controlled conditions on earth and in space, before the potential effects of microgravity on protein crystal quality can be evaluated.

### Summary

Protein crystal growth is a major experimental problem and is the bottleneck in widespread applications of protein crystallography. Research efforts now being pursued and sponsored by NASA are making fundamental contributions to our understanding of the science of protein crystal growth. Microgravity environments offer the possibility of performing new types of experiments that may produce a better understanding of protein crystal growth processes and may permit growth environments that are more favorable for obtaining high-quality protein crystals.

A series of protein crystal growth experiments using the space shuttle has been initiated. The first phase of these experiments has been focused on the development of micro-methods for protein crystal growth by vapor diffusion techniques, using a space version of the hanging-drop method. The preliminary space experiments have been used to evolve prototype hardware that will form the basis for a more advanced system that can be used to evaluate effects of gravity on protein crystal growth.

### References

1. P. J. Goodford, *J. Med. Chem.* 27 (1984) 555.
2. T. Blundell, B. L. Sibanda and L. Pearl. *Nature* 304 (1983) 273.
3. R. A. Johanson and J. Henkin, *J. Biol. Chem.* 260 (1985) 1465.
4. T. Wilson and A. Klausner, *Biotechnology* (June 1984) 511.
5. W. Goddard, *Science* 227 (1985) 917.
6. K. P. Nambiar, J. Stackhouse, D. M. Stauffer, W. D. Kennedy, J. K. Eldredge and S. A. Benner, *Science* 223 (1984) 1299.
7. E. T. Kaiser and D. S. Lawrence, *Science* 226 (1984) 505.
8. L. J. Perry and R. Wetzel, *Science* 226 (1984) 555.
9. A. R. Fersht, J.-P. Shi, J. Knill-Jones, D. M. Lowe, A. J. Wilkinson, D. M. Blow, P. Brick, P. Carter, M. M. Y. Waye and G. Winter, *Nature* 314 (1985) 235.
10. C. S. Craik, C. Largman, T. Fletcher, S. Roczniak, P. J. Barr, R. Fletterick and W. J. Rutter, *Science* 228 (1985) 291.
11. J. Galloway, *Nature* 314 (1985) 228.
12. R. P. Wharton and M. Ptashne, *Nature* 316 (1985) 601.

13. D. A. Estell, T. P. Graycar and J. A. Wells, *J. Biol. Chem.* 260 (1985) 6518.
14. T. H. Maugh, *Science* 223 (1984) 269.
15. T. N. C. Wells and A. R. Fersht, *Nature* 316 (1985) 656.
16. E. Westhof, D. Altschuh, D. Moras, A. C. Bloomer, A. Mondragon, A. Klug and M. H. V. Van Regenmortel, *Nature* 311 (1984) 123.
17. R. J. P. Williams and G. R. Moore, *Trends Biochem. Sci.* 10 (1985) 96.
18. J. L. Marx, *Science* 226 (1984) 819.
19. J. A. Berzofsky, *Science* 229 (1985) 932.
20. T. L. Blundell and L. M. Johnson, *Protein Crystallography* (Academic Press, New York, 1976).
21. A. A. Kossiakoff, *Ann. Rev. Biochem.* 54 (1985) 1195.
22. T. J. Greenhough and J. R. Helliwell, *Progr. Biophys. Mol. Biol.* 41 (1983) 67.
23. H. D. Bartunik, P. N. Clout and B. Robrahn, *J. Appl. Cryst.* 14 (1981) 134.
24. R. Usha, J. E. Johnson, D. Moras, J. C. Thierry, R. Fourme and R. Kahn, *J. Appl. Cryst.* 17 (1984) 147.
25. K. S. Wilson, E. A. Stura, D. L. Wild, R. J. Todd, D. J. Stuart, Y. S. Babu, J. A. Jenkins, T. S. Standing, L. N. Johnson, R. Fourme, R. Kahn, A. Gadget, K. S. Bartels and H. D. Bartunik, *J. Appl. Cryst.* 16 (1983) 28.
26. U. W. Arndt, T. J. Greenhough, J. R. Helliwell, J. A. K. Howards, S. A. Rule and A. W. Thompson, *Nature* 298 (1982) 835.
27. K. Moffat, D. Szebenyi and D. Bilderback, *Science* 223 (1984) 1423.
28. R. Hamlin, C. Cork, A. Howard, C. Nielson, W. Vernon, D. Matthews, N. G. H. Xuong and V. Perez-Mendez, *J. Appl. Cryst.* 14 (1981) 85.
29. S. C. Harrison, *Nature* 309 (1984) 408.

30. W. A. Hendrickson and M. Teeter, *Nature* 290 (1981) 107.
31. W. E. Furey, A. H. Robbins, L. L. Clancy, D. R. Winge, B. C. Wang and C. D. Stout, *Science* 231 (1986) 704.
32. J. L. Smith, W. A. Hendrickson and A. W. Addison, *Nature* 303 (1983) 86.
33. H. Hauptman, S. Potter, C. Weeks, J. Karle, R. Srinivasan, S. Parthasarathy and G. N. Watson, *Acta Cryst.* A38 (1982) 289.
34. H. Hauptman, S. Potter and C. M. Weeks, *Acta Cryst.* A38 (1982) 294.
35. M. M. Woolfson, *Acta Cryst.* A40 (1984) 32.
36. J. Karle, *Acta Cryst.* A40 (1984) 1.
37. J. Karle, *Acta Cryst.* A40 (1984) 4.
38. J. Karle, *Acta Cryst.* A40 (1984) 526.
39. G. Bricogne, *Acta Cryst.* A40 (1984) 410.
40. A. Jones, *J. Appl. Cryst.* 11 (1978) 268.
41. A. J. Morffew and D. S. Moss, *Acta Cryst.* A39 (1983) 196.
42. P. A. Bash, N. Pattabiraman, C. Huang, T. E. Ferrin and R. Langridge, *Science* 222 (1983) 1325.
43. J. H. Konnert and W. A. Hendrickson, *Acta Cryst.* A36 (1980) 344.
44. J. L. Sussman and A. D. Podjarny, *Acta Cryst.* B39 (1983) 495.
45. A. G. W. Leslie, *Acta Cryst.* A40 (1984) 451.
46. O. Herzberg and J. L. Sussman, *J. Appl. Cryst.* 16 (1983) 144.
47. A. M. Silva and M. G. Rossmann, *Acta Cryst.*, in press.
48. W. J. Cook, S. E. Ealick, C. E. Bugg, J. D. Stoeckler and R. E. Parks, Jr., *J. Biol. Chem.* 256 (1981) 4079.

49. S. E. Ealick, T. Greenhough, Y. Babu, D. Carter, W. J. Cook, C. E. Bugg, S. Rule, J. Habash, J. Helliwell, J. Stoeckler, S. Chen and R. E. Parks, Jr., *Annals New York Academy Scis.*, 451 (1986) 311-312.
50. G. E. Rindone, Ed., *Materials Processing in the Reduced Gravity Environment of Space* (North-Holland, New York, 1982).
51. W. Littke and C. John, *Science* 225 (1984) 203.
52. P. Todd, *Biotechnology* 3 (1985) 786.
53. C. E. Bugg, in *Proc. Pharm Tech Conf. '85* (Aster, Springfield, OR, 1985) pp. 22-26.
54. L. DeLucas, F. L. Suddath, R. Snyder, R. Naumann, M. B. Broom, M. Pusey, V. Yost, B. Herren, D. Carter, B. Nelson, E. J. Meehan, A. McPherson and C. E. Bugg, *J. Crystal Growth* 76 (1986) 681.

Co-Investigators and Industrial Guest Investigators on the NASA-sponsored Project  
"Protein Crystal Growth in a Microgravity Environment"

- (1) E. L. Amma, Department of Chemistry, University of South Carolina, Columbia, South Carolina 29208, (803) 777-5263
- (2) Arthur Arnone, Department of Biochemistry, College of Medicine, The University of Iowa, Iowa City, Iowa 52242, (319) 353-6072
- (3) James K. Baird, Department of Chemistry, University of Alabama in Huntsville, Huntsville, Alabama 35899, (205) 895-6441
- (4) Beth Broom, ES-73 Space Science Laboratory, Marshall Space Flight Center, Huntsville, Alabama 35812, (205) 544-7805
- (5) Dan Carter, ES-73, George C. Marshall Space Flight Center, Huntsville, Alabama 35812, (205) 544-5492
- (6) Connie Chidester, The Upjohn Company, Kalamazoo, Michigan 49001, (616) 385-7624
- (7) Don Clifford, McDonnell Douglas Astronautics Company - St. Louis Division, Box 516, St. Louis, Missouri 63166, (314) 232- 2896
- (8) Larry J. DeLucas, School of Optometry, University of Alabama at Birmingham, Birmingham, Alabama 35294, (205) 934-3802
- (9) David J. Duchamp, The Upjohn Company, Kalamazoo, Michigan 49001, (616) 385-7766
- (10) Drake S. Eggleston, Smith Kline & French Laboratories, 1500 Spring Garden Street, P. O. Box 7929, Philadelphia, Pennsylvania 19101, (215) 751-4000
- (11) Howard M. Einspahr, The Upjohn Company, Kalamazoo, Michigan 49001, (616) 385-5492
- (12) William W. Fowles, ES-74, George C. Marshall Space Flight Center, MSFC, Alabama 35812, (205) 544-7813
- (13) Donald O. Frazier, ES-74, George C. Marshall Space Flight Center, MSFC, Alabama 35812, (205) 544-7825
- (14) Russell G. Greig, Department of Tumor Biology, Smith Kline & French Laboratories, 1500 Spring Garden Street, P. O. Box 7929, Philadelphia, Pennsylvania 19101, (215) 751-4000
- (15) Blair Herren, ES-73, George C. Marshall Space Flight Center, Huntsville, Alabama 35812, 544-7817
- (16) Jim Hogle, Scripps Clinic and Research Foundation, La Jolla, California 92037, (619) 455-9100



- (17) **Thomas A. Krenitsky**, Head, Department of Experimental Therapy, Burroughs-Wellcome Company, 3030 Cornwallis Road, Research Triangle Park, North Carolina 27709, (919) 541-9090
- (18) **Roger L. Kroes**, ES-74, George C. Marshall Space Flight Center, MSFC, Alabama 35812, (205) 544-7770
- (19) **W. Graeme Laver**, The John Curtin School of Medical Research, The Australian National University, G.P.O. Box 334, Canberra A.C.T. 2601, Australia, 49 2550
- (20) **Mitchell Lewis**, Department of Molecular Genetics, Smith Kline & French Laboratories, 1500 Spring Garden Street, P. O. Box 7929, Philadelphia, Pennsylvania 19101, (215) 276-5034
- (21) **Ponzy Lu**, Department of Chemistry, University of Pennsylvania, Philadelphia, Pennsylvania 19104, (215) 898-4863
- (22) **Alexander McPherson**, Department of Biochemistry, University of California at Riverside, Riverside, California 92521, (714) 787-5391
- (23) **Edward J. Meehan**, Department of Chemistry, University of Alabama in Huntsville, Huntsville, Alabama 35899, (205) 895-6188
- (24) **T. J. Nagabhushan**, Presidential Fellow - Vice President, Medicinal and Protein Chemical Research, Schering Corporation, 60 Orange Street, Bloomfield, New Jersey 07003
- (25) **Robert J. Naumann**, ES-71, George C. Marshall Space Flight Center, MSFC, Alabama 35812, (205) 544-7755
- (26) **Manuel Navia**, Merck Institute for Therapeutic Research, Rahway, New Jersey 07065, (201) 574-7256
- (27) **Edward C. Olson**, Manager, Physical & Analytical Chemistry Research, The Upjohn Company, Kalamazoo, Michigan 49001, (616) 385-7185
- (28) **Marc Pusey**, ES-73, George C. Marshall Space Flight Center, MSFC, Alabama 35812, (205) 544-7805
- (29) **David W. Richman**, McDonnell Douglas Astronautics Company - St. Louis Division, P. O. Box 516, St. Louis, Missouri 63166, (314) 232-6967
- (30) **William H. Riley**, The Dow Chemical Company, Central Research, Biotechnology Lab, 1701 Building, M. E. Pruitt Research Center, Midland, Michigan 48674, (517) 636-5243
- (31) **James T. Rose**, McDonnell Douglas Astronautics Company - St. Louis Division, P. O. Box 516, St. Louis, Missouri 63166, (314) 232-5485
- (32) **John M. Rosenberg**, University of Pittsburgh, Department of Biological Sciences, Pittsburgh, Pennsylvania 15260, (412) 624-4636

- (33) F. R. Salemme, DuPont de Nemours & Company, Central Research & Development Department, Experimental Station, Wilmington, Delaware 19898, (302) 772-1877
- (34) Paul B. Sigler, Department of Biophysics & Theoretical Biology, University of Chicago, CLSC, 920 E. 58th Street, Chicago, Illinois 60637, (312) 962-1086
- (35) Robert S. Snyder, ES-73, George C. Marshall Space Flight Center, MSFC, Alabama 35812, (205) 544-7805
- (36) F. L. Suddath, School of Chemistry, Georgia Institute of Technology, Atlanta, Georgia 30332, (404) 894-4028
- (37) Amy L. Swain, Department of Chemistry, University of South Carolina, Columbia, South Carolina 29208, (803) 777-5263
- (38) P. Trotta, Schering Corporation, 60 Orange Street, Bloomfield, New Jersey 07003, (201) 429-4000
- (39) Ada Yonath, Department of Structural Chemistry, The Weizmann Institute of Science, 76100 Rehovot, Israel, (08) 4821111
- (40) Vaughn Yost, SA-23, George C. Marshall Space Flight Center, MSFC, Alabama 35812, (205) 544-1998
- (41) Donald Voet, Department of Chemistry, University of Pennsylvania, Philadelphia, Pennsylvania 19104, (215) 898-6457
- (42) Keith Ward, Laboratory for the Structure of Matter, Code 6030, Naval Research Laboratory, Washington, D. C. 20375, (202) 767-2735
- (43) Keith D. Watenpaugh, The Upjohn Company, Kalamazoo, Michigan 49001, (616) 385-5481
- (44) Ian Wilson, Scripps Clinic and Research Foundation, LaJolla, California 92037, (619) 455-9706
- (45) William Witherow, ES-74, George C. Marshall Space Flight Center, MSFC, Alabama 35812, (205) 544-7811

## **ELECTRONIC MATERIALS**

**PRECEDING PAGE BLANK NOT FILMED**

GROWTH OF MERCURIC IODIDE ( $\text{HgI}_2$ ) FOR NUCLEAR RADIATION DETECTORS

L. van den Berg and W. F. Schnepple

EG&G Energy Measurements  
Santa Barbara Operations  
130 Robin Hill Road  
Goleta, California 93117, USA

February 6, 1987

## 1. INTRODUCTION

Mercuric Iodide is a material used for the fabrication of the sensing element in solid state x-ray and gamma ray detecting instruments. The advantage of the use of mercuric iodide in such instrumentation is that the systems are able to operate at room temperature, compared with systems based on germanium and silicon which need cooling to liquid nitrogen temperature.

The proper operation of the devices is determined to a large degree by the density of structural defects in the single crystalline material used in the sensing elements. Since there were strong indications that the quality of the material was degraded by the effects of gravity during the growth process (mechanical slippage and irregular convection) a research and engineering program was initiated to grow one or more crystals of mercuric iodide in the reduced gravity environment of space. A special furnace assembly was designed which could be accommodated in a Spacelab rack, and at the same time made it possible to use the same growth procedures and controls used when growing a crystal on the ground.

The space crystal, after the flight, was subjected to the same evaluation methods used for earth-grown crystals, so that comparisons could be made.

## 2. PREPARATORY GROUND-BASED RESEARCH

It is usually easy to suggest in general terms the possible benefits of an experiment in the reduced gravity of space flight. More effort is required to document with experimental results that the damaging effects of gravity on the structural quality of a crystal are indeed certain or at least highly probable.

Crystals of mercuric iodide are grown by physical vapor transport in a closed, evacuated ampoule. This means that mercuric iodide molecules sublime from a clump of heated source material and travel as vapor to the growing crystal. The transport in normal gravity is partially by diffusion and partially by convection, and as long as these transport mechanisms are constant with time, no negative effect on the crystal quality is expected to exist. Problems will arise when the convection transport becomes irregular with time, because the surface of the growing crystal will then be exposed to varying supersaturations of mercuric iodide vapor and growth irregularities will result. In the absence of gravity, transport will be exclusively by regular diffusion flow.

No technique has been developed at this point to measure in detail existing convection currents on the ground, and the only way to obtain information about the effects of the convection currents on the structural quality is by actually doing the experiment.

A different situation exists with respect to the statement that the crystal will slip by the force of its own weight, and thereby increase the density of defects. To obtain quantitative data concerning this effect the dislocation structure and the critical resolved shear stress (CRSS) of the crystalline material was studied in cooperation with a group at the University of California in Santa Barbara. This work has been reported in References 1 and 2. The results of the measurements indicated that, expressed on a macroscopic scale, a crystal of approximately  $1 \text{ cm}^3$  can be subject to slippage

perpendicular to the c-direction under the effect of its own weight when it is at the growth temperature. Figure 1 shows a series of yield strength measurements at different temperatures. The curves indicate how the CRSS of a sample changes with temperature and that no irregular hardening effects take place during the test. It should also be realized that the samples used for these measurements may already have been strain-hardened by the cutting and polishing process required to shape the samples.

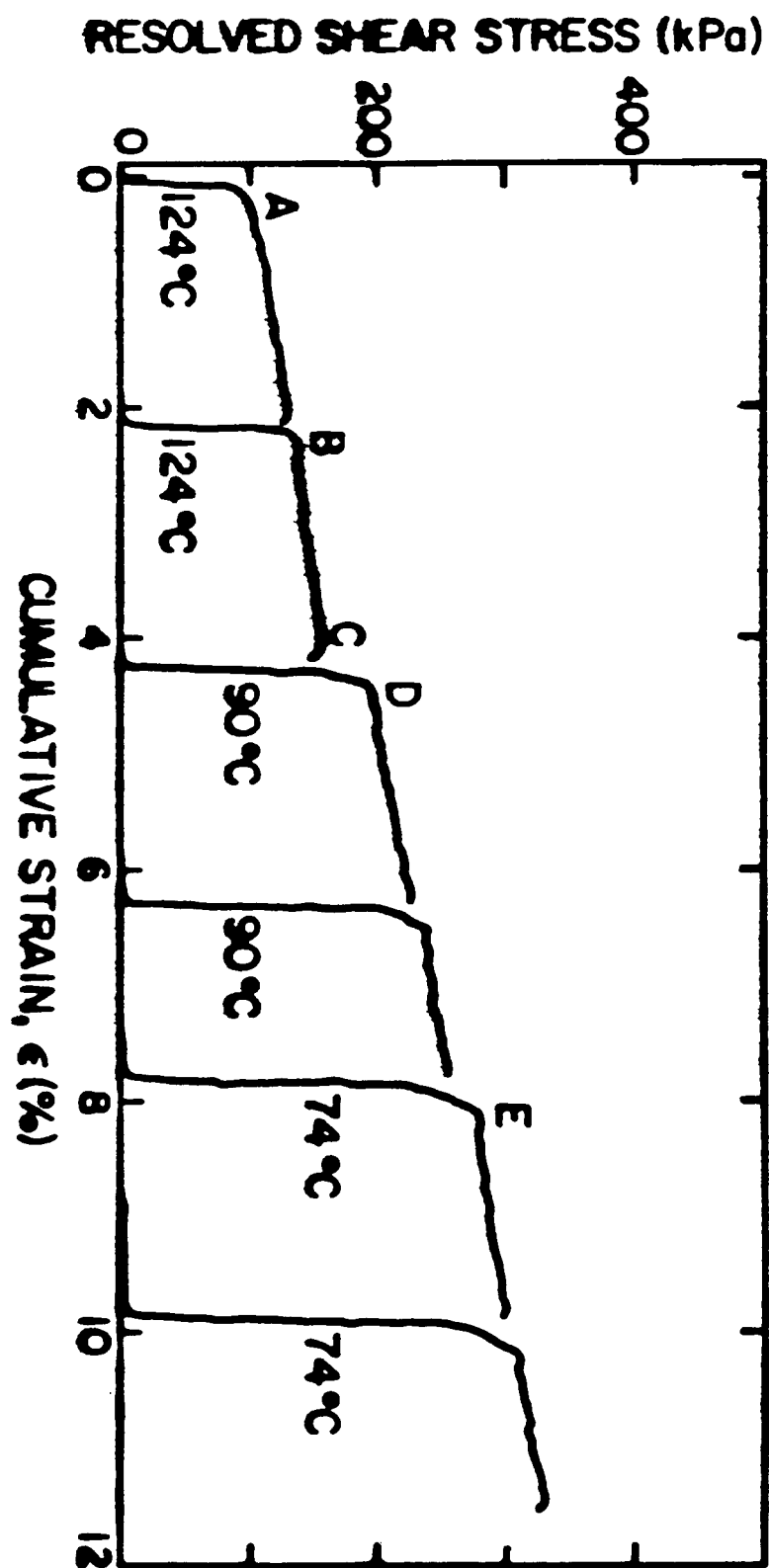


Fig. 1



### 3. CRYSTAL GROWTH

#### Furnace and Growth Ampoule Development

To accommodate the Spacelab III facilities, a special furnace has been designed which reflects the basic elements of the usual ground-based furnaces (Ref. 3). A sketch of this prototype furnace is shown in Figure 2.

The crystal growing ampoule, located in the center of the furnace, has a cylindrical shape. The bottom surface of the ampoule is indented so that internally it forms a pedestal on which the crystal grows. The indentation fits over a metal support tube, inside of which a Peltier cooler is installed to provide cooling to the growing crystal.

The thermal profile around the ampoule necessary for crystal growth is provided by two independently controlled heating coils. The lower part of the ampoule is heated by means of a circular coil which is covered with a metal heat equalization ring. A helically wound vertical coil provides basically an equally distributed amount of heat along the vertical walls of the ampoule. The combined heat inputs create a temperature profile which has a minimum at approximately half the height of the ampoule. At this level the crystal growth source material accumulates when the center of the pedestal is not cooled by the cold sting. Nucleation and crystal growth can be initiated by a combination of a reduction in the ampoule bottom temperature and activation of the Peltier cooler.

On the tope of the helical coil a reflective shield is installed to minimize heat losses. This furnace assembly is covered with a bell jar of high optical quality, so that the growing crystal can be observed through a microscope.

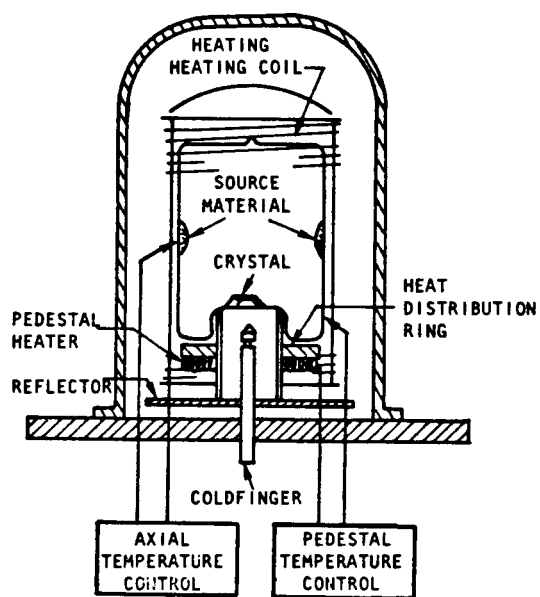


Fig. 2

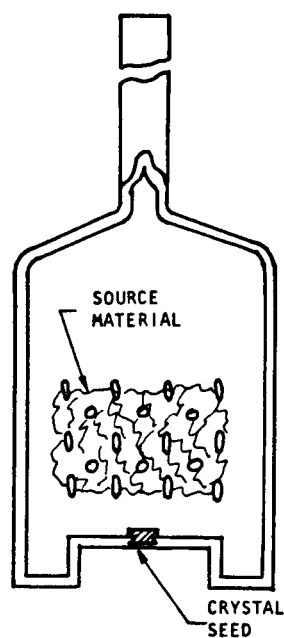


Fig. 3

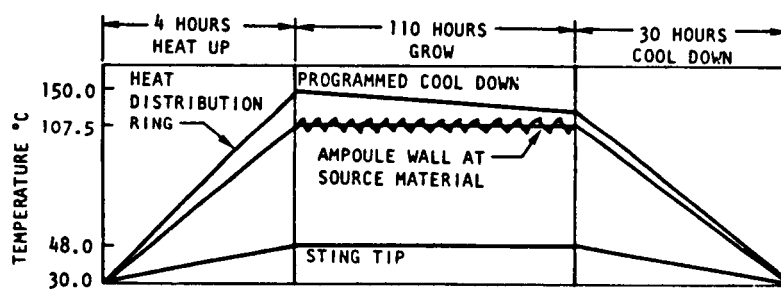


Fig. 4

The temperature profile along the walls of the ampoule used to grow the crystals on the ground is created by a combination of radiation and convection effects. During an experiment in the Spacelab, the driving force for convection in the air between the bell jar and ampoule will be reduced. In addition, the furnace assembly will assume different orientations with respect to the prevalent acceleration vector. In order to evaluate the effects of changed gravity conditions a series of experimental simulations was performed whereby the space between the bell jar and ampoule was evacuated and the whole furnace assembly was positioned upside down. These experiments showed that the heat supply around the top of the ampoule is not sufficient when there is not a continuous convective supply of hot air from the lower part of the furnace which collects in the upper part of the bell jar and keeps the top of the ampoule hot. This problem was corrected by installation of a lamellar heater on the inside surface of the reflecting dome (not shown in Figure 2). The power input to this heater is slaved to the power controls for the helical heating coil.

The normally used ground-based growth ampoules have smooth walls and a flat pedestal. In the initial phase of the crystal growth procedures, the poly-crystalline charge is evaporated from the bottom of the ampoule to the minimum temperature zone on the vertical wall, and subsequently a seed is nucleated by reducing the pedestal temperature and activating the Peltier cooler. In order to maximize the crystal growth time in space it was decided to perform these activities on the ground before the flight. The resulting ampoules with source and seed in place were subjected to vibration tests, simulating take-off and re-entry vibrations, to ascertain the adherence of source and seed to the glass surface. Both the grown seed and parts of the source material started to come loose at certain critical vibration intensities. The ampoule design was therefore modified to incorporate glass fingers on the part of the inside wall where the source is located and a dovetail cavity in the pedestal to anchor the seed (see Figure 3). The ampoule is positioned in the furnace with the section with glass fingers at the rear. The resistance of the furnace windings has been adjusted in that area so that an asymmetric cold region is created for the source material to collect. The seed is nucleated inside the dovetail cavity and is grown until it completely fills and extends somewhat beyond the cavity. The ampoules prepared in this way are again subjected to qualification testing before flight.

The growth sequence is fully automated and consists of three essential parts: heat-up, growth and cool-down (see Figure 4). During the heat-up phase the temperatures at the different control points in the furnace (source, heat distribution ring, cooling sting) are increased in a controlled way to values which are optimal for growth. The growth phase is then started by gradually decreasing the pedestal temperature, primarily by reducing the heat input to the base heater. During the growth phase it is possible, when necessary, to oscillate the temperature of the source material so that periodic growing and etching of the crystal occurs to obtain more stable crystal growth and to avoid spurious nucleation. This is a technique usually employed during the early stages of the growth of mercuric iodide crystals (Ref. 4 and 5).

When the source material has almost been depleted or when the experiment time has elapsed, the system is gradually cooled down to ambient temperature and is returned to its storage container for re-entry.

#### 4. SPACE EXPERIMENT

Notwithstanding the efforts made to predetermine the proper growth conditions on the ground (elimination of convection around the ampoule by evacuation of the space between the ampoule and the bell jar), the temperatures again had to be adjusted to obtain crystal growth in space. This accounts for the fact that during the first 14 hours in space no growth was observed. The temperature difference between the source and the pedestal had to be increased by  $1.6^{\circ}\text{C}$  to initiate growth.

As growth continued, it became clear that much higher temperature gradients could be applied than is usually done on the ground, without disturbing the stability of the crystal surfaces or without causing any new nucleation. Using the higher temperature gradients it was therefore possible to obtain higher growth rates by diffusion transport alone than is usually seen on the ground with both diffusion and convection transport, as shown in Figure 5.

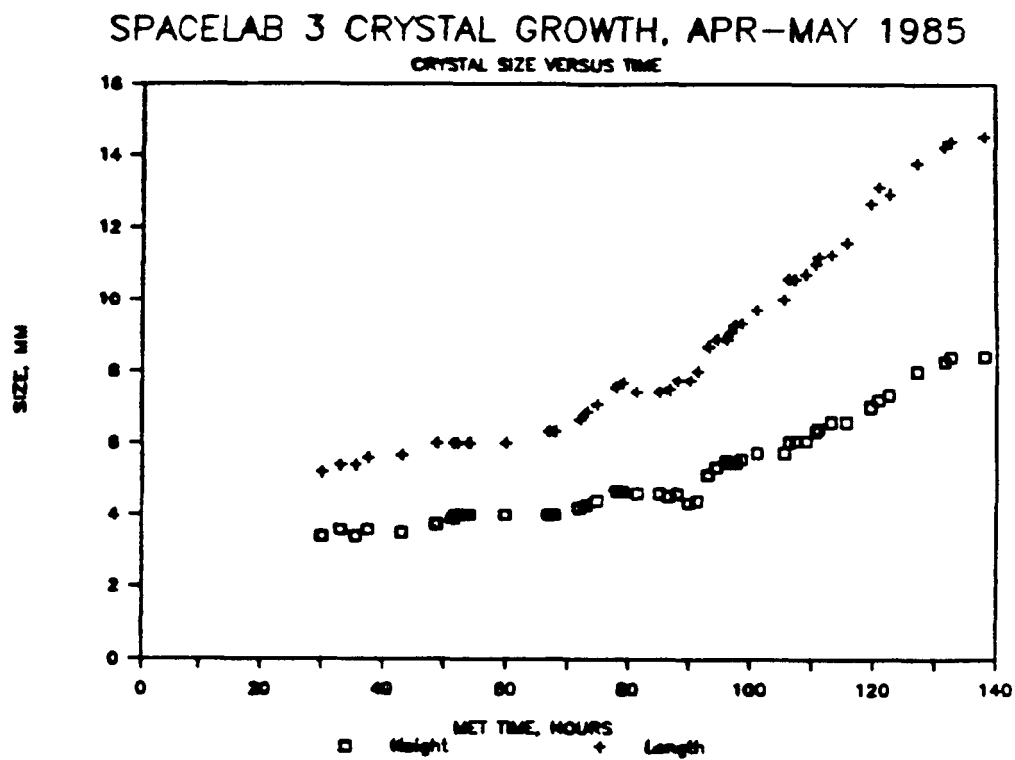
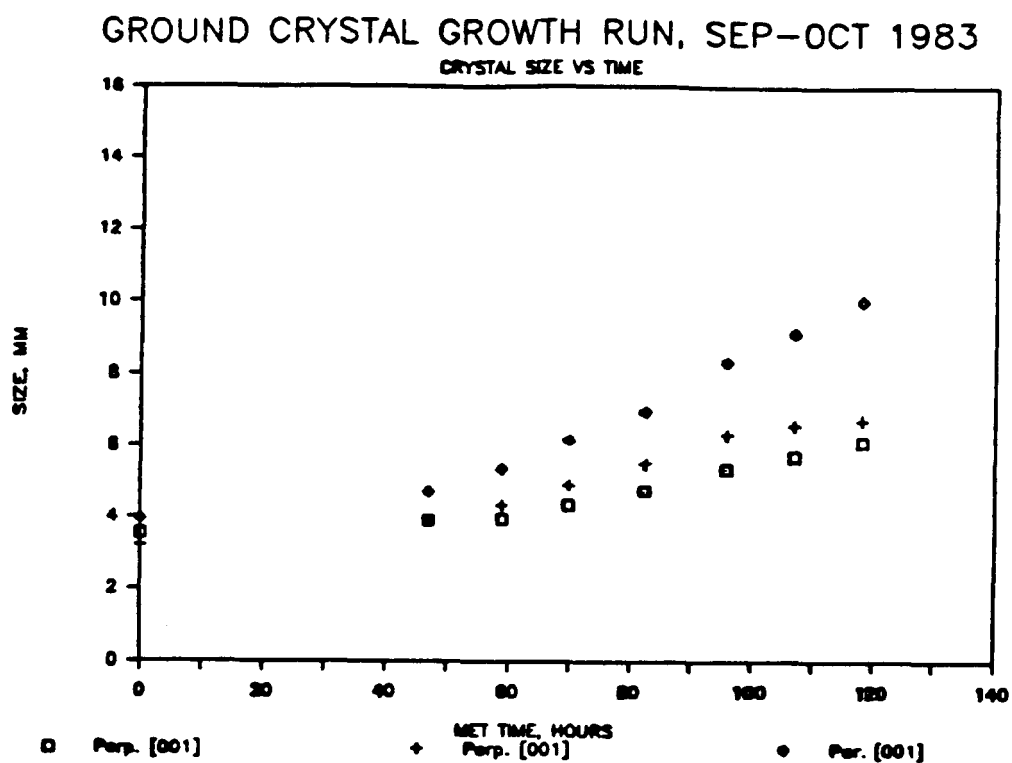


Fig. 5

ORIGINAL PAGE IS  
OF POOR QUALITY

## 5. CRYSTAL ANALYSIS

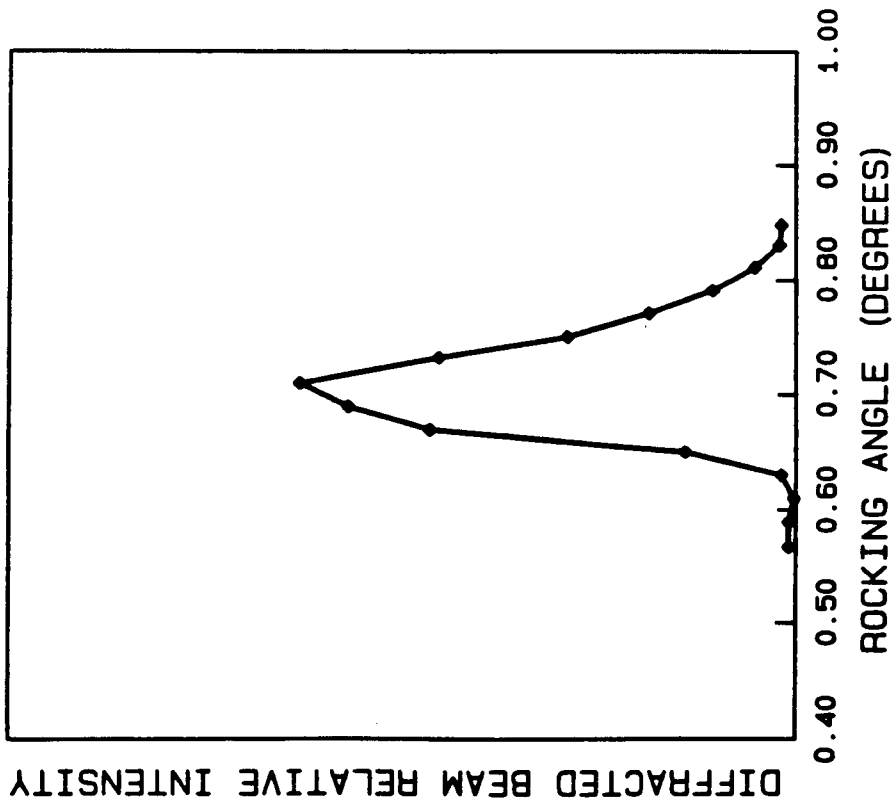
### Gamma Ray Rocking Curves

Since mercuric iodide is selected for radiation measurements because of its high absorption, it is impossible to use regular x-rays to do transmission measurements on pieces thicker than a few hundred  $\mu\text{m}$ . To evaluate the structural quality of a crystal approximately 1 cm thick it is necessary to use higher energy gamma rays emitted by artificial sources. The advantage of these kind of sources is that the radiation emitted by them is highly monochromatic, so that the diffraction peaks have a Gaussian shape.

Rocking curve measurements on the space crystal have been performed at the University of Missouri Research Reactor in Columbia, Missouri, where high intensity isotope sources can be produced and the equipment to do this type of measurements is available (Ref. 6). The results are shown in Figures 6a and 6b. The rocking curve of an earth-grown crystal shows several peaks, indicating that the crystal really consists of three sections at slight angles with respect to each other. The rocking curve of the space crystal on the other hand shows only the one peak expected of a single crystal without major grain boundaries. The space crystal however shows signs of internal strain as evidenced by the width and asymmetrical shape of the peak.

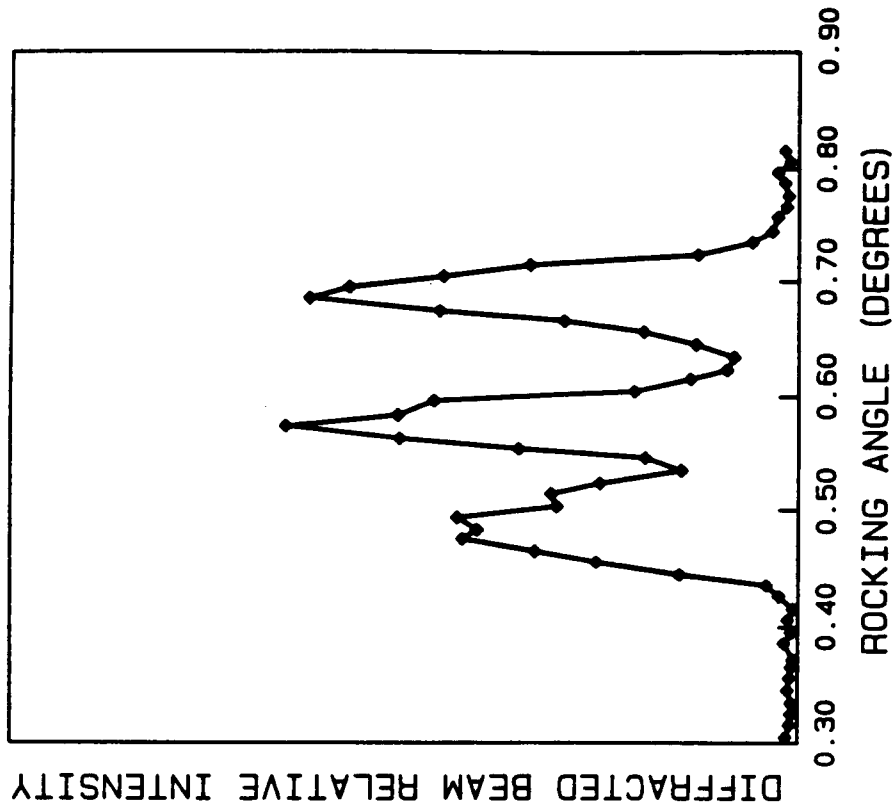
### Electronic Measurements

The operation of radiation detectors is critically dependent on the transport properties of the electronic charge carriers created by the incident radiation. A good measure of the quality of the material is therefore provided by the values of the electron and hole mobilities and lifetimes (trapping times). Because of the high resistivity of the material these values can most adequately be determined by evaluation of the nuclear spectral response of a detector structure as a function of applied bias. Details of this procedure have been described in the literature (Ref. 7).



GAMMA DIFFRACTION ROCKING CURVE  
FOR THE SL-3 CRYSTAL

Fig. 6a



GAMMA DIFFRACTION ROCKING CURVE  
FOR AN EARTH GROWN CRYSTAL

Fig. 6b



The data obtained for detectors made from the space crystal and the maximum values found for ground-based detectors are as follows:

	$\frac{\mu_e}{(\text{cm}^2/\text{Vsec})}$	$\frac{\mu_h}{(\text{cm}^2/\text{Vsec})}$	$\frac{\mu_e \tau_e}{(10^{-4} \text{cm}^2/\text{V})}$	$\frac{\mu_h \tau_h}{(10^{-6} \text{cm}^2/\text{V})}$
Ground-based Crystals (max.)	125	4.2	20	6.2
Space Crystal	250	10.7	21	42

One can see that the electronic properties of the space crystal are significantly improved over ground-based crystals, especially with respect to the holes, which is the most critical factor for detector operation. When considering these results it should be realized that the maximum values quoted for the ground-based crystals are for different detectors and are not found together in one single detector.

## SUMMARY AND CONCLUSIONS

The experiment to grow a crystal of mercuric iodide in space performed exceptionally well, so that the stated experimental objectives were fulfilled. That the experiment was successful the very first time around is, in our opinion, for a large part due to the extensive pre-flight ground-based research and operational experiments.

The space growth conditions showed that the stability of the crystal surfaces is much higher than on the ground where convection is present. As a result the temperature gradient in the furnace could be increased so that the growth rate with diffusion transport alone was still larger than on the ground.

The structural quality of the space crystals, as measured by gamma ray rocking curves, is superior to ground-based crystals. As a result, the electronic transport properties of the material were significantly improved.

## ACKNOWLEDGMENTS

The investigators want to acknowledge the technical and programmatic support of the NASA Spacelab Payload Project Office. Especially the efforts by Messrs. R. Ruff and R. Porter have been critical to the success of this experiment.

### References

1. T. W. James and F. Milstein, J. Mat. Sci. 16 (1981) 1167.
2. F. Milstein, et al., Nucl. Inst. Meth. 213 (1983) 65.
3. W. F. Schnepple, et al., J. of Spacecraft and Rockets 16 (1979) 144.
4. M. Schieber, et al., J. of Crystal Growth 33 (1976) 125.
5. L. van den Berg, et al., J. of Crystal Growth 42 (1977) 160.
6. W. B. Yelon, et al., J. Appl. Physics 52 (1986) 4604.
7. A. J. Dabrowski, Advances in X-ray Analysis 29, edited by John C. Russ, Charles S. Barrett, and Donald I. Leyden (Plenum Publishing Corporation, 1982) 185.

## FUTURE ACTIVITIES

THE VAPER CRYSTAL GROWTH (VCG) EXPERIMENT IS PRESENTLY SCHEDULED TO BE REFLOWN ON THE IML-1 MISSION. THE PURPOSE OF THE IML-1 EXPERIMENT IS PRIMARILY TO REPEAT THE SPACELAB 3 EXPERIMENT SO THAT BETTER STATISTICS ABOUT THE QUALITY OF SPACE-GROWN CRYSTALS AND THE PERFORMANCE OF THE EQUIPMENT WILL BE AVAILABLE. USING THE EXPERIENCE GAINED IN SPACELAB 3, IT WILL BE POSSIBLE TO MAKE THE GROWTH PROCEDURE MORE EFFICIENT BY STARTING ACTUAL GROWTH SOONER. IN ADDITION, SOME NEW ASPECTS OF THE CRYSTAL GROWTH PROCEDURE WHICH ARE ALREADY BEING USED ON THE GROUND WILL BE INCORPORATED IN THE FLIGHT PROCEDURES.

Crystal Growth and Transport Rates of the GeSe-Xenon System under Microgravity  
Conditions, H. Wiedemeier, S.B. Trivedi, et al.

(Reprint, to be sent under separate cover)

## MODELLING THE GROWTH OF TRIGLYCINE SULPHATE CRYSTALS IN SPACELAB 3

HAK-DO YOO\* and WILLIAM R. WILCOX

Department of Chemical Engineering and Center for Advanced Materials  
Processing, Clarkson University, Potsdam, NY 13676, USA

RAVINDRA LAL

Department of Physics, Alabama A &amp; M University, Normal, AL 35762, USA

JAMES D. TROLINGER

Spectron Development Laboratories, Inc., Costa Mesa, CA 92626, USA

## ABSTRACT

Two triglycine sulphate crystals were grown from an aqueous solution in Spacelab 3 aboard a Space Shuttle. Using a diffusion coefficient of  $2 \times 10^{-5} \text{ cm}^2/\text{s}$ , a computer simulation gave reasonable agreement between experimental and theoretical crystal sizes and interferometric lines in the solution near the growing crystal. This diffusion coefficient is larger than most measured values, possibly due to fluctuating accelerations on the order of  $10^{-3} \text{ g}$  (Earth's gravity). The average acceleration was estimated to be less than  $10^{-6} \text{ g}$ . At this level buoyancy-driven convection is predicted to add approximately 20% to the steady-state growth rate. Only very slight distortion of the interferometric lines was observed at the end of a 33 hour run. It is suggested that the time to reach steady state convective transport may be inversely proportional to  $g$  at low  $g$ , so that the full effect of convection was not realized in these experiments.

\* Present address: Samsung Advanced Institute of Technology, Kihung-Eup, Kyungki-Do, South Korea.

## 1. Introduction

In May of 1985 a layer of triglycine sulphate (TGS) was grown from aqueous solutions onto two seed crystals in Spacelab 3 aboard a Space Shuttle.

The objectives of the experiment were to determine how crystal growth from solution progresses in a nearly convection-free environment, the influence of low g growth on crystal properties, and the extent of buoyancy-driven convection in the small fluctuating accelerations that are present in the Shuttle.

In the absence of convection, crystal growth from solutions will rapidly become slower as the adjacent solution is depleted of solute, unless the growth temperature is lowered to compensate. However if the temperature is lowered too fast the growth rate will reach the level at which solvent inclusions are formed (1). In order to estimate the optimal temperature program prior to the Spacelab 3 mission, a one dimensional spherical computer model was developed and used with a diffusion coefficient  $D$  of  $5 \times 10^{-5} \text{ cm}^2/\text{s}$  in the solution (2,3). Later the computations were repeated with  $D = 1 \times 10^{-5} \text{ cm}^2/\text{s}$  using both the spherical model and a newly developed two-dimensional cylindrical model (4). It was estimated that only about 10% of the supersaturation of the bulk solution is required to drive the interface kinetics; i.e. the growth is 90% diffusion-controlled.

Here we report on a comparison of the computations using the cylindrical model and the experiments. Estimates are made of the buoyancy-driven convection that occurred and its development with time.

PRECEDING PAGE BLANK NOT FILMED



## 2. Spacelab 3 experiments

The growth experiments were performed in the Fluid Experiment System (FES) designed and constructed by TRW Systems in Redondo Beach, California, with final debugging by NASA's Marshall Space Flight Center (MSFC) in Huntsville, Alabama. Based on the original concept of Lal, the growth cell in the FES was designed so that a seed crystal is cemented onto a controlled temperature rod (sting) (5,6). An optical system provided real time schlieren video, transmission holograms and reflection holograms of the entire interior of the cell (7,8).

Quantum Technology of Sanford, Florida provided 3.4 mm thick (001) cylindrical seeds for the two growth runs. For Cell 2 the seed was 15 mm in diameter and for Cell 3 10 mm diameter. In each cell the seed was covered by a polymer diaphragm cap to prevent the solution from contacting the seed prematurely. The cell was filled with a TGS solution of concentration equivalent to saturation at 45 C (9). During storage of the cell at room temperature TGS crystallized throughout the cell. In Spacelab 3 the cell was slowly heated to 70 C and held at that temperature for several hours to redissolve this material. A pump provided circulation. The temperature was reduced to 46.5 C for Cell 2 and 46 C for Cell 3, the circulating pump turned off, and the cap withdrawn from the seed crystal. The cap in Cell 2 had leaked and spurious crystals were seen upon cap removal. Several of these later grew around the periphery of the crystal, while one floated in the solution.

At cap withdrawal the solution temperature was above its saturation temperature so that dissolution was expected. The schlieren video confirmed

that dissolution was taking place as planned. After 30 minutes for Cell 2 and 40.8 minutes for Cell 3, the sting temperature and the cell wall temperature were slowly reduced. Dissolution continued for some time before the schlieren showed the beginning of growth. Figures 1 to 3 show the temperature vs. time data. Note that during the Cell 2 experiment the ground crew called for a temperature increase because they feared the growth rate was becoming too large.

During growth, accelerometers in FES measured accelerations as high as 0.1 of Earth's gravity (g), with average fluctuations of  $10^{-3}$  g and a maximum in the power spectrum at 17 Hz. The average DC acceleration level was approximately  $10^{-6}$  g.

After growth the cap was replaced over the crystal. The sting was withdrawn from the cell and excess solution blotted off with soft tissue. Later the crystal was pried from the sting, measured and photographed (Figures 4 and 5). While crystal properties will be reported in detail elsewhere (27), it is noteworthy that the boundaries between the seed crystals and the space-grown layers could not be seen using optical microscopy. (Earth-grown crystals typically form inclusions at this boundary, with dislocations emerging from the inclusions into material grown on top of them. (e.g. Ref. 10)) Presumably this is a reflection of the very slow transition from dissolution to growth that occurs under diffusion-controlled conditions. The top surface of both crystals was concave, indicating more rapid vertical growth around the periphery. Around the edge (001) and (010) facets formed. From one edge of the Cell 2 crystal a thin transparent sheet had grown over almost the entire surface. Such a feature has never been observed on Earth, possibly because such a thin sheet would be bent or broken due to gravity.

Holograms were developed and converted into views of the growth cell and interferograms of the solution, both parallel and perpendicular to the sting. Typical interferograms of Cell 3 are given in Figures 6 to 8. The interferograms from Cell 2 are badly distorted because of the perturbation of the concentration field by growth of the spurious crystals. If cylindrical symmetry is assumed the interferograms can be converted to refractive index maps (and vice versa), permitting the comparison of theory and experiment described later.

The side views of Cell 2 permitted R. Naumann at MSFC to measure the size and movement rate of the floating spurious crystal. Use of Stokes law with the viscosity of the solution and the densities of solution and crystal (9) yielded an acceleration level of  $4 \times 10^{-7}$  g (8). This must be regarded as a lower limit because movement of the crystal parallel to the line of view was not determined. Furthermore the solution was considered to be stationary, whereas some buoyancy-driven convection may have been present. Stokes law assumes that the solid object is spherical and that the solution is of uniform density, while the actual crystal was not spherical and the solution near the crystal had a lower density because it was depleted in solute due to growth.

### 3. Mathematical model

Details of the mathematical model, including all of the FORTRAN computer programs, are given in Reference (4). Figure 9 shows the geometry used for the numerical model of diffusion and heat conduction during growth. Heat and mass transfer due to buoyancy-driven convection were ignored. (The consequences of this are discussed later.)

Cylindrical symmetry was assumed. While the sting and the seed are cylindrical, the cell walls constitute a 10 X 10 X 10 cm cube. In addition a temperature sensor runs parallel to the sting and a vacuum line attaches to the sting, as can be seen in Figure 8. Nevertheless a cylindrical model is a reasonable approximation because the refractive index field in the solution is determined almost entirely by the concentration field, and this varies markedly only near the crystal.

Because the partial molar volume of TGS is different in the crystal and in the solution, the growth generates a gentle flow of solution toward the crystal. This flow carries both heat and mass. However examination of the terms in the transport differential equations revealed that this flow contributes only about 0.2% to the mass transfer rate and 0.001% to the heat transfer. Consequently these contributions were ignored. If we assume constant properties in the solution this leads to the differential equation for mass transfer:

$$D \left[ \frac{1}{r} \frac{\partial}{\partial r} \left( r \frac{\partial C}{\partial r} \right) + \frac{\partial^2 C}{\partial z^2} \right] = \frac{\partial C}{\partial t} \quad (1)$$

and for heat transfer:

$$k \left[ \frac{1}{r} \frac{\partial}{\partial r} \left( r \frac{\partial T}{\partial r} \right) + \frac{\partial^2 T}{\partial z^2} \right] = \rho c_p \frac{\partial T}{\partial t} \quad (2)$$

where the symbols are defined in the Table of Nomenclature. The temperatures at the wall and sting tip were taken to be prescribed functions of time (Figures 1 to 3). Heat flux balances and continuity of temperature were used at each phase boundary. The normal concentration gradient at sting, cap and wall surfaces was set equal to zero because of the absence of diffusion

through these boundaries. Along the cylindrical axis ( $r = 0$ ) the radial concentration and temperature gradients were set to zero because of symmetry. L'Hopital's theorem was applied to eliminate the singularity in the convective terms at  $r = 0$ .

The heat transfer and mass transfer are independent of one another except at the surface of the crystal, where they are coupled by the relations for interface kinetics:

$$V_c = K(T_e - T_i) \quad (3)$$

and solubility:

$$C_i = 0.237 \exp(-1679/T_e) \text{ mol/cm}^3 \quad (4)$$

The interface kinetics constant  $K$  was derived from the data of References (10,11), i.e. for a (001) face a growth rate of 1 mm/day for an interfacial undercooling of 1 K and 2.4 mm/day for a (010) face. Since the top face in the flight experiments was (001),  $K = 1 \text{ mm/day.K}$  was used for that face. For the side surface and for dissolution on the top surface equilibrium was assumed, i.e. infinite  $K$  so that  $T_i = T_e$ .

The relationship between the concentration gradient at the crystal surface and the growth rate were found from a material balance taking into account the Stefan or crystallization flow (12) and the absence of solvent (water) in the crystal:

$$V_c = \frac{D(\nabla C)_i}{C_c(1-C_i\bar{V})} \quad (5)$$

The crystallization flow gives rise to the term  $C_i \bar{V}$ , which equals the volume fraction of solute at the crystal surface (approximately 0.2 in these experiments). It is negligible only if the solubility of a salt is negligible, which is most definitely not true for TGS.

The foregoing set of equations were solved using the Multiple Alternating Direction Implicit (MADI) finite difference method (13). It is a modification of the Alternating Direction Implicit (ADI) method in which new values of concentration (or temperature) are calculated for each row by implicit methods using values in adjacent rows from the preceding time step (14). In the next time step of an ADI computation, new values in each column are calculated using values in adjacent columns from the preceding time step. In MADI the new value at a point is taken as the average of values calculated from adjacent rows and from adjacent columns. MADI allows larger time increments to be used than ADI with the same accuracy, thereby reducing the computation time required.

A time increment of 10 s was used for the temperature calculations and 20 s for the concentration calculations. For isothermal dissolution a negligible difference was found for a time step ranging from 0.5 s to 30 s for concentration computations.

Because the concentration gradient was expected to be largest near the crystal, a finer mesh was used there as shown in Figure 10. Because of the assumed axisymmetry, only one-half of the cell needed to be solved.

During growth the crystal surface moves relative to the cell, so that it is generally between mesh points. In order to track the top crystal surface

and the conditions there, the following operations were performed at each time step. First the interfacial temperature  $T_i$  was found by interpolating between temperatures at adjacent mesh points in the crystal and the solution. This left three unknowns in Equations 3, 4 and 5;  $C_i$ ,  $V_c$  and  $T_e$  (assuming that the interfacial concentration gradient can readily be calculated once  $C_i$  is known). After eliminating  $V_c$  by setting Equations 3 and 5 equal to one another and substituting for  $C_i$  from Equation 4, the combination was solved for  $T_e$  by successive approximations. Knowing  $T_e$ ,  $C_i$  was calculated from Equation 4 and  $V_c$  from Equation 3.

For the top surface during dissolution and for the side crystal surface during both dissolution and growth  $K$  was taken as infinite, and so  $T_e = T_i$ ,  $C_i$  was calculated from Equation 4, and  $V_c$  from Equation 5.

In the computation of concentration and temperature fields the crystal was maintained in a cylindrical shape by determining new interfacial positions for the entire top surface using the growth rate computed for the midpoint between the center and the periphery. For the side surface the growth rate halfway down was used. This procedure amounts to ignoring the effect of the deviation from cylindrical shape on the heat and mass transfer, resulting in a slight underestimation of the growth rate at the periphery (top corner). In comparing theory and experiment the crystal shape vs. time was computed from the calculated growth rate at each mesh point.

#### 4. Comparison of experiment and theory

Initial comparison of theory and experiment were made for Cell 3 because of the problems with the Cell 2 experiment (cap leakage during storage,

spurious crystals, and crystal sheet grown above top surface of seed). Figure 11 shows a comparison of the size of the actual crystal received on Earth with computed sizes for  $D = 1, 2$  and  $3 \times 10^{-5} \text{ cm}^2/\text{s}$ . The best fit with crystal thickness (height) was for  $D = 2 \times 10^{-5} \text{ cm}^2/\text{s}$ , and so this value was used for subsequent computations. Note that theory and experiment both produced a concave top surface, i.e. the growth rate was higher at the periphery. Likewise the growth on the side of the crystal was several times larger than on the center of the top face.

Figure 12 shows isoconcentration lines for Cell 3 at the end of the 40.83 minute isothermal dissolution period. The solute concentration is highest at the crystal surface. As the temperatures of the wall and the sting are slowly decreased, dissolution continues for a considerable time, albeit at a continually declining rate. Eventually growth begins and the solute concentration at the crystal surface declines. This leads to a maximum in concentration some distance away from the crystal in the solution, as shown in Figure 13. Figure 14 shows the iso-concentration lines at the end of the run. Note that there is no significant change in concentration at the cap, the cell walls or even the side of the sting. Thus the original assumption of cylindrical symmetry is reasonable.

As the temperature of the wall and the sting tip are reduced after the initial isothermal dissolution period, heat flows from the solution to these surfaces, resulting in a maximum of temperature in the center of the cell as shown in Figure 15. This maximum persists for some time after the end of ramping down the temperature, until eventually the solution is again isothermal.



Using the data of Reference (9) we computed refractive index maps from the temperature and concentration data. The variation in concentration has a much larger effect on refractive index than does the variation in temperature.

Thus the refractive index lines look much like the isoconcentration lines. Figure 16 shows a refractive index map at the end of the isothermal dissolution, where only concentration varies in the cell. Figure 17 shows refractive index during the programmed cooldown period, at a time showing a maximum in concentration and temperature in the middle of the cell. For long times where the solution is again isothermal, the refractive index maps look exactly like the concentration maps.

Interferograms were calculated from the refractive index field in order to compare with those obtained from the Spacelab 3 holograms (see Figures 6 to 8). Since the laser beam came in the side of the cell parallel to the top crystal surface, it was necessary to compute the optical pathlength<sup>l</sup> in that direction (y) at every position using:

$$l = \int n \, dy \quad (6)$$

Bright interference lines pass through points at which the optical pathlength has changed by an integral number of wavelengths of the helium-neon laser (0.633 microns). Dark lines occur between the bright lines at half-integral wavelength changes in optical pathlength. Results are given in Figures 18 and 19 (for clarity, every other fringe is deleted in Figure 19). Comparison of the experimental results in Figure 6 with the calculated results in Figure 18 for the same time give perfect agreement in the number of fringes above the top crystal surface and the number intersecting the top crystal surface. At the time represented in Figures 7 and 19, the number of fringes along the top

surface of the crystal is the same from experiment and computation. Moving straight sideways from the top surface the number of fringes from the edge of the crystal to a point directly above the edge of the sting insulator is 48 from the computations and 46 from experiment.

Finally Figure 20 shows computed and experimental crystal shapes resulting from the Cell 2 experiment. In this case the amount of growth on the side of the crystal is about the same from experiment and computation, while the computed growth on the top face is over twice as much. In view of the crystal sheet that grew over the top surface, less growth is not surprising because the sheet would have prevented diffusion from the bulk of the solution. In addition there is considerable uncertainty in the initial position of the crystal because of the cap leakage. Because of the presence of spurious crystals during cap retraction it is probable that solution had leaked in about the time the cell was filled, causing crystals to nucleate and grow during the long storage at room temperature. The seed crystal must have grown a little thicker at the same time. During the 70 C dissolution period in Spacelab 3 both the spurious crystals and the seed crystal would have dissolved, with the total dissolution exceeding the amount that had crystallized during storage. Upon cooling to 46.5 C regrowth and possibly nucleation would have occurred.

## 5. Convection

While the accelerations in orbiting spacecraft are small, they are not zero, as indicated in Section 2 above. Because the density of the solution was not constant during the Spacelab 3 FES experiments, some buoyancy-driven

convection was to be expected. We need to separate the effects of acceleration into those due to fluctuations and those arising from the much smaller steady background. We first consider fluctuating effects and compare expectations with experimental results.

As we show shortly, the time constant for fluid mechanics is on the order of 1 to 100 minutes in an FES cell. Since the fluctuating components of acceleration had much shorter periods than this, one would not expect any direct evidence of convection such as rapid shifts in the schlieren pattern. Indeed rapid shifts in schlieren were not observed and observable shifts in interferograms were not detected even after 1 day of growth. (Double exposure holograms did sometimes reveal local changes in a few seconds.) It is conceivable that a fluctuating acceleration could cause minute movements of solution sufficient to influence mass transfer, which is very sensitive to convection for liquids. Evidence for this might be found in the diffusion coefficient required to bring experiment and convection-free theory into agreement. If such an effective diffusion coefficient exceeds independently measured values, we might conclude that convection affected the mass transfer.

As noted earlier, the effective diffusion coefficient found for these experiments is  $2 \times 10^{-5} \text{ cm}^2/\text{s}$ . This value equals the average found by Reddy using a porous diaphragm technique for temperatures ranging from 25 to 45 C and concentrations up to 1.2 molar (15). However the scatter in the data was on the order of +/- 100%. Using a similar technique Kroes and Reiss obtained for very dilute solutions a value of  $1.3 \times 10^{-5} \text{ cm}^2/\text{s}$  at 45 C (9). Using a

refractometric technique Novotny, Moravec and Solc obtained  $0.7 \times 10^{-5} \text{ cm}^2/\text{s}$  for a saturated TGS solution at 45 C. While the foregoing indicates that fluctuating acceleration may increase mass transfer rates, the evidence is weak. A computer simulation would be most helpful, but a supercomputer is needed for a full three-dimensional time-dependent coupled fluid mechanics / mass transfer solution.

The steady background acceleration, on the order of  $10^{-6} \text{ g}$ , is expected to generate convection after some period of time (as discussed later). We can use existing correlations (16-21) to estimate the steady state contribution of this convection to the growth rate. (These correlations are for buoyancy-driven natural convection about spheres (16), cylinders (17, 21) and vertical flat plates (18-20) with low Grashof number.) The ratio of the contribution of convection to the growth rate to that for diffusion is given by:

$$\frac{V_{\text{conv}}}{V_{\text{diff}}} = \frac{Sh_{\text{conv}} \Delta C}{d(\nabla C)_i} \quad (7)$$

where  $Sh_{\text{conv}}$  is the contribution of convection to the Sherwood number from a correlation. The concentration difference  $\Delta C$  between solution at the crystal surface and far from it is taken to be  $0.057 \text{ mmol/cm}^3$ , the crystal diameter 1.5 cm, and the interfacial concentration gradient  $0.44 \text{ mmol/cm}^4$ . Using the properties given in the Table of Nomenclature for TGS solutions we calculate a value of 0.14 for the Grashof number  $Gr$  at  $10^{-6} \text{ g}$  and 650 for the Schmidt number  $Sc$ . From Equation (7) and the correlations we estimate a convective contribution to the growth rate ranging from 13 to 22% of the diffusive contribution.

The steady state fluid velocity due to convection is on the order of (22):

$$V = \nu Gr/d \quad (8)$$

for a Grashof number much less than unity, and

$$V = \nu Gr^{1/2}/d \quad (9)$$

for a Grashof number much greater than unity. With the values given above ( $Gr = 0.14$ ) we use Equation (8) to estimate  $V = 4.5$  cm/hr, which is sufficiently large that it should have been obvious in both the schlieren pattern and the inteferograms for Cell 3. The fact that distortion was not observed until very late in this run indicates that steady state convection was not obtained. We must ask ourselves how long it takes to reach steady state natural convection at low acceleration levels.

Three-dimensional time-dependent convection computations were carried out using the discrete element method (23). Unfortunately computer requirements were extremely heavy so only short periods of real time could be simulated. In order to isolate initial transient diffusion effects from transient convection effects, diffusion was allowed to proceed for 46 hours in the absence of convection for a concentration difference of 0.057 mmol/cc between the top crystal surface and the bulk solution. Figure 21 shows the maximum solution velocity in Cell 2 after turning on an acceleration of  $10^{-4}$  g ( $Gr = 14$ ). If the velocity continued to increase at the same rate, it would take 0.36 hours to reach the steady state velocity of 0.032 cm/s estimated from Equation (9). However in practice the rate of velocity increase with time

would diminish, so that more than 0.36 hours would be required to reach steady state. The question is, how much time would be required at  $10^{-6}$  g? If the concentration field is not influenced by convection, which is not likely to be true for large  $Sc$ , the hydrodynamic transient time is independent of  $g$  level. However for the coupled mass transfer and fluid mechanics that occurs in natural convection, this may not be true.

In the literature we located three boundary layer theoretical treatments (good for large  $Gr$ ) of transient natural convection from a vertical flat plate (24-26). All of these treatments agree on the  $Gr$  dependence of the transient time, but only one (24) examined the  $Sc$  dependence. The time required to reach steady state after turning on a temperature or concentration difference is approximately (24):

$$t = 5.24(0.95 + Sc)^{1/2} Gr^{-1/2} x^2 / \nu \quad (10)$$

from which we calculate 1.69 hours for the Cell 2 conditions examined above with an acceleration of  $10^{-4}$  g and 16.9 hours at  $10^{-6}$  g. However for low  $Gr$ , as we have for  $10^{-6}$  g, it is likely that the  $1/g$  dependence of transient time is greater than the one-half power. Since the  $g$  dependence of velocity goes from  $1/2$  power to 1 as  $Gr$  becomes small (Equations 8 and 9), it is likely that the same thing happens for transient time. If we assume a time dependence of  $1/g$ , then we estimate a transient time of 169 hours to achieve steady state conditions. This is far longer than the length of the Spacelab 3 experiment! But is this reasonable?

## 6. Transients

In order to gain some theoretical guidance on the various transient times, we turn to the governing partial differential equations. The Navier-Stokes equation for hydrodynamics with the usual Boussinesq approximation is:

$$\frac{\partial \mathbf{V}}{\partial t} + \mathbf{V} \cdot \nabla \mathbf{V} = \nu \nabla^2 \mathbf{V} - \beta g \Delta C \quad (11)$$

The mass transfer equation with convection is:

$$\frac{\partial C}{\partial t} = D \nabla^2 C - \mathbf{V} \cdot \nabla C \quad (12)$$

The convective heat transfer equation for low velocity flows is:

$$\rho c_p \frac{\partial T}{\partial t} = k \nabla^2 T - \rho c_p \mathbf{V} \cdot \nabla T \quad (13)$$

We non-dimensionalize these PDE by dividing all lengths by a characteristic length  $L$ , all concentrations by a characteristic concentration difference  $\Delta C$ , all temperatures by a characteristic temperature difference  $\Delta T$ , all velocities by a reference velocity  $V_r$ , and all times by a reference time  $t_r$ . Thus the above equations become:

$$\frac{L^3 V_r}{\nu^2 t_r} \frac{\partial \mathbf{v}}{\partial \tau} + \frac{L^2 V_r^2}{\nu^2} \mathbf{v} \cdot \nabla \mathbf{v} = \frac{L V_r}{\nu} \nabla^2 \mathbf{v} - Gr \quad (14)$$

where  $\mathbf{v} = \mathbf{V}/V_r$  is the dimensionless velocity. The first term in this equation is for acceleration, the second for inertia, the third for viscous effects, and the third comes from buoyancy and drives the convection. Similarly the

dimensionless mass transfer equation is:

$$\frac{L^2}{t_r D} \frac{\partial \phi}{\partial \tau} = \nabla^2 \phi - \frac{v_r L}{D} \mathbf{v} \cdot \nabla \phi \quad (15)$$

The first term is the transient term, the second the diffusive transport term and the third the convective transport term. The dimensionless heat transfer equation is.

$$\frac{L^2 \rho c_p}{t_r k} \frac{\partial \psi}{\partial \tau} = \nabla^2 \psi - \frac{v_r L \rho c_p}{k} \mathbf{v} \cdot \nabla \psi \quad (16)$$

All of the pre-differential expressions and all of the differentials in the above equations are dimensionless. The non-dimensionalising parameters must be chosen such that every differential in the PDEs is of order one. Thus a logical choice for  $L$  is the crystal diameter, for  $\Delta C$  the difference in solution concentration between the crystal surface and the cell wall, and for  $\Delta T$  the difference in temperature between the sting and the cell wall. The reference velocity is on the order of the maximum velocity in the system and the reference time is on the order of the transient time. The maximum velocity and the transient time are what we want to estimate.

If acceleration is zero,  $Gr = 0$ . Noting that viscous decay damps convection in the absence of a driving force, we set the acceleration term equal to the viscous term to obtain the following estimate for the transient time due to fluid mechanics alone:

$$(t_r)_{\text{fluid}} = L^2/\nu \quad (17)$$



For a characteristic length of 1 cm and a kinematic viscosity of  $0.013 \text{ cm}^2/\text{s}$ , Equation 17 gives a transient time of 77 seconds.

In the absence of convection the convective transport terms in the heat and mass transfer PDEs are zero and the pre-differential expressions in them must be of order one. Thus the transient times for diffusion and conduction are:

$$(t_r)_{\text{diff}} = L^2/D \quad (18)$$

$$(t_r)_{\text{cond}} = L^2 \rho c_p / k \quad (19)$$

From these we estimate a transient diffusion time of 14 hours and a transient conduction time of 19 minutes for our experiments.

For large  $Gr$ , the viscous term in the momentum Equation 14 is negligible compared to the inertial term. Thus the pre-differential expression in the inertial term must equal the buoyancy term, from which:

$$V_r = Gr^{1/2} \nu / L \quad (20)$$

This is the same as reported in the literature (22). In the mass transfer equation 15, convective effects are fully established when the transient term is about equal to the convection term. Equating the pre-differentials and substituting equation 20 we obtain:

$$(t_r)_{\text{comb}} = \frac{L}{V_r} = \frac{L^2}{\nu Gr^{1/2}} \propto \frac{1}{g^{1/2}} \quad (21)$$

which is the same functional dependence on  $g$  as reported in the literature for large  $Gr$  (24-26). (Implicit in the foregoing is the assumption that density differences arise entirely from concentration differences, which is a good approximation in crystal growth from solution.)

For small  $Gr$ , the inertial term in equation 14 is negligible compared to the viscous term. Equating the pre-differential expression in the viscous term to buoyancy we obtain:

$$V_r = Gr \nu / L \quad (22)$$

which is the same as given in the literature (22). Substituting this into the mass transfer equation and equating transient and convective pre-differentials we obtain:

$$(t_r)_{\text{comb}} = \frac{L}{V_r} = \frac{L^2}{\nu Gr} \propto \frac{1}{g} \quad (23)$$

## 7. Summary

Both experiments and theory indicate that the time required to reach steady state in buoyancy-driven mass transfer increases as the average acceleration level decreases. The same might be true for heat transfer controlled free convection, as is common in solidification. Thus some experiments performed in space may terminate before the convection reaches

steady state levels. Transient computer simulations are needed to confirm these predictions.

The experiments indicate that fluctuating accelerations may significantly enhance mass transport rates, even when global convection is not generated. Transient three dimensional computer simulations are needed to confirm this result.

The lack of vigorous convection in a space environment makes it easy to achieve a gentle transition from dissolution to growth so that solvent inclusions are not formed between the seed and the grown layers. Experiments on earth have shown that closure of such inclusions tends to result in dislocations which propagate through subsequently grown materials and degrade properties. It may be that this will permit us to grow crystals from solution in space superior to what is possible on earth. More flight experiments are needed to adequately test this possibility.

#### Acknowledgements

This research was supported by NASA Contract NAS8-32945 and by Clarkson University. The Principal Investigator for this program was Ravindra Lal and the Co-Investigator was Roger L. Kroes at NASA's Marshall Space Flight Center. The flight experiments were performed by Lodewijk van den Berg and Don Lind. We are grateful to the many dedicated persons at TRW Systems and NASA MSFC who helped with hardware development and operation, and especially Rudy Ruff for his continual assistance during the planning and execution of the flight experiment. Arsev Eraslan recommended the MADI computational technique and provided the discrete element program used to simulate three-dimensional convection.

## References

- (1) W.R. Wilcox, J. Crystal Growth 65 (1983) 133.
- (2) L.C. Liu, W.R. Wilcox, R. Kroes and R. Lal, p. 389 in Materials Processing in the Reduced Gravity Environment of Space, ed. G. Rindone (Elsevier, 1982).
- (3) L.C. Liu, M.S. Thesis, Clarkson University, 1981.
- (4) H.D. Yoo, Ph.D. Thesis, Clarkson University, 1986.
- (5) R.B. Lal, M.D. Aggarwal, R.L. Kroes and W.R. Wilcox, Phys. Stat. Solidi 80 (1983) 547.
- (6) R.B. Lal, R.L. Kroes and W.R. Wilcox, p. 399 in Materials Processing in the Reduced Gravity Environment of Space, ed. G. Rindone (Elsevier, 1982).
- (7) R.B. Owen and R.L. Kroes, Optics News 11 (1985) No. 7.
- (8) R.B. Owen, R.L. Kroes and W.K. Witherow, Optics Letters 11 (1986) 407.
- (9) R.L. Kroes and D. Reiss, J. Crystal Growth 69 (1984) 414.
- (10) F. Moravec and J. Novotny, Kristall und Technik 7 (1972) 891.
- (11) J. Novotny, F. Moravec and Z. Solc, Czech. J. Phys. B23 (1973) 261.
- (12) W.R. Wilcox, J. Crystal Growth 12 (1972) 93.
- (13) A.H. Eraslan, Numerical Analysis and Computer Methods, University Tennessee Space Institute (Tullahoma, 1969).
- (14) D.W. Peaceman and H.H. Rachford, J. Soc. Ind. Appl. Math. 3 (1955) 28.
- (15) B.S. Reddy, M.S. Thesis, Clarkson University (1984).
- (16) W.G. Mathern, A.J. Madden, Jr., and E.L. Piret, Ind. Eng. Chem. 49 (1957) 961.

- (17) J.J. Mahony, Proc. Roy. Soc. A238 (1956) 412.
- (18) F.J. Suriano and K.T. Yang, Int. J. Heat Mass Transfer 11 (1968) 473.
- (19) S.W. Churchill and H. Ozoe, Trans. ASME 95C (1973) 540.
- (20) F. Geoola and A.R.H. Cornish, Int. J. Heat Mass Transfer 25 (1982) 1677.
- (21) Y.T. Shee and S.N. Singh, Natural Convection, American Society of Mechanical Engineers (1981).
- (22) S. Ostrach, Ann. Rev. Fluid Mech. 14 (1982) 313.
- (23) A. Eraslan, W.L. Lin and R.D. Sharp, FLOWER: A computer code for simulating three-dimensional flow, temperature, and salinity conditions in rivers, estuaries and coastal regions, NUREG/CR-3172, ORNL/TM-8401, Oak Ridge National Laboratory, Oak Ridge, Tennessee (1983).
- (24) R. Siegel, Trans. ASME 80 (1958) 347.
- (25) R.J. Goldstein and D.G. Briggs, J. Heat Transfer 86 (1964) 490.
- (26) G.D. Callahan and W.J. Marner, Int. J. Heat Mass Transfer 19 (1976) 165.

# Nomenclature

(Properties used in computations are given in parentheses)

C	-	Concentration of TGS in solution ( $\text{mol/cm}^3$ )
$\Delta C$	-	Difference in solution concentration at crystal surface and in bulk solution ( $\text{mol/cm}^3$ )
$C_c$	-	TGS concentration in crystal ( $\rho_c/M$ ) ( $5.23 \times 10^{-3} \text{ mol/cm}^3$ )
$C_i$	-	Solution concentration at crystal surface
$c_p$	-	Heat capacity - of solution ( $5 \times 10^3 \text{ J/kg.K}$ )
	-	- of crystal ( $1.5 \times 10^3 \text{ J/kg.K}$ )
	-	- of Teflon ( $1.26 \times 10^3 \text{ J/kg.K}$ )
	-	- of Dow Corning 732 RTV adhesive ( $1.46 \times 10^3 \text{ J/kg.K}$ )
D	-	TGS diffusion coefficient in solution ( $2 \times 10^{-5} \text{ cm}^2/\text{s}$ )
d	-	Diameter of crystal (1 and 1.5 cm)
Gr	-	Grashof number for mass transfer, $g_a \beta d^3 \Delta C / \nu^2$
g	-	Earth's gravitational acceleration ( $9.8 \text{ m/s}^2$ )
$g_a$	-	Acceleration ( $\text{m/s}^2$ )
K	-	Interface kinetics constant ( $1.16 \times 10^{-8} \text{ m/s.K}$ for (001) TGS)
k	-	Thermal conductivity - of solution ( $0.5 \text{ J/m.k.s}$ )
	-	- of crystal ( $0.68 \text{ J/m.k.s}$ )
	-	- of Teflon ( $0.41 \text{ J/m.k.s}$ )
	-	- of cement ( $0.19 \text{ J/m.k.s}$ )
L	-	Characteristic length (d or half of cell width)(m)
$l$	-	Optical path length (m)
M	-	Molecular weight (323 g/mol for TGS)
n	-	Refractive index
Sc	-	Schmidt number of solution, $\nu/D$ (650)
r	-	Radial position (m)
$Sh_{\text{conv}}$	-	Sherwood number due to convective mass transfer
T	-	Temperature (K)
$T_e$	-	Equilibrium temperature corresponding to solubility (K)

$T_i$	-	Temperature at crystal surface (K)
$\Delta T$	-	Temperature difference (K)
$t$	-	Time since retraction of cap (s)
$t_r$	-	Characteristic transient time (s)
$\bar{V}$	-	Partial molar volume (181 cm <sup>3</sup> /mol)
$V$	-	Velocity (m/s)
$V_c$	-	Crystal growth rate (m/s)
$V_r$	-	Reference velocity (m/s)
$v$	-	$V/V_r$ , Dimensionless velocity
$z$	-	Axial position (m)
$\beta$	-	Concentration densification coefficient of solution, $(-\partial\rho/\partial C)_T/\rho$ (0.46 cm <sup>3</sup> /mol)
$\nabla$	-	Gradient (m <sup>-1</sup> )
$\phi$	-	$(C - C_i)/\Delta C$ , Dimensionless concentration
$\nu$	-	Kinematic viscosity of solution (0.013 cm <sup>2</sup> /s)
$\psi$	-	$(T - T_i)/\Delta T$ , Dimensionless temperature
$\rho$	-	Density - of solution (1.16 g/cm <sup>3</sup> ) - of crystal (1.69 g/cm <sup>3</sup> ) - of Teflon (2.3 g/cm <sup>3</sup> ) - of cement (1.03 g/cm <sup>3</sup> )
$\tau$	-	$t/t_r$ , Dimensionless time

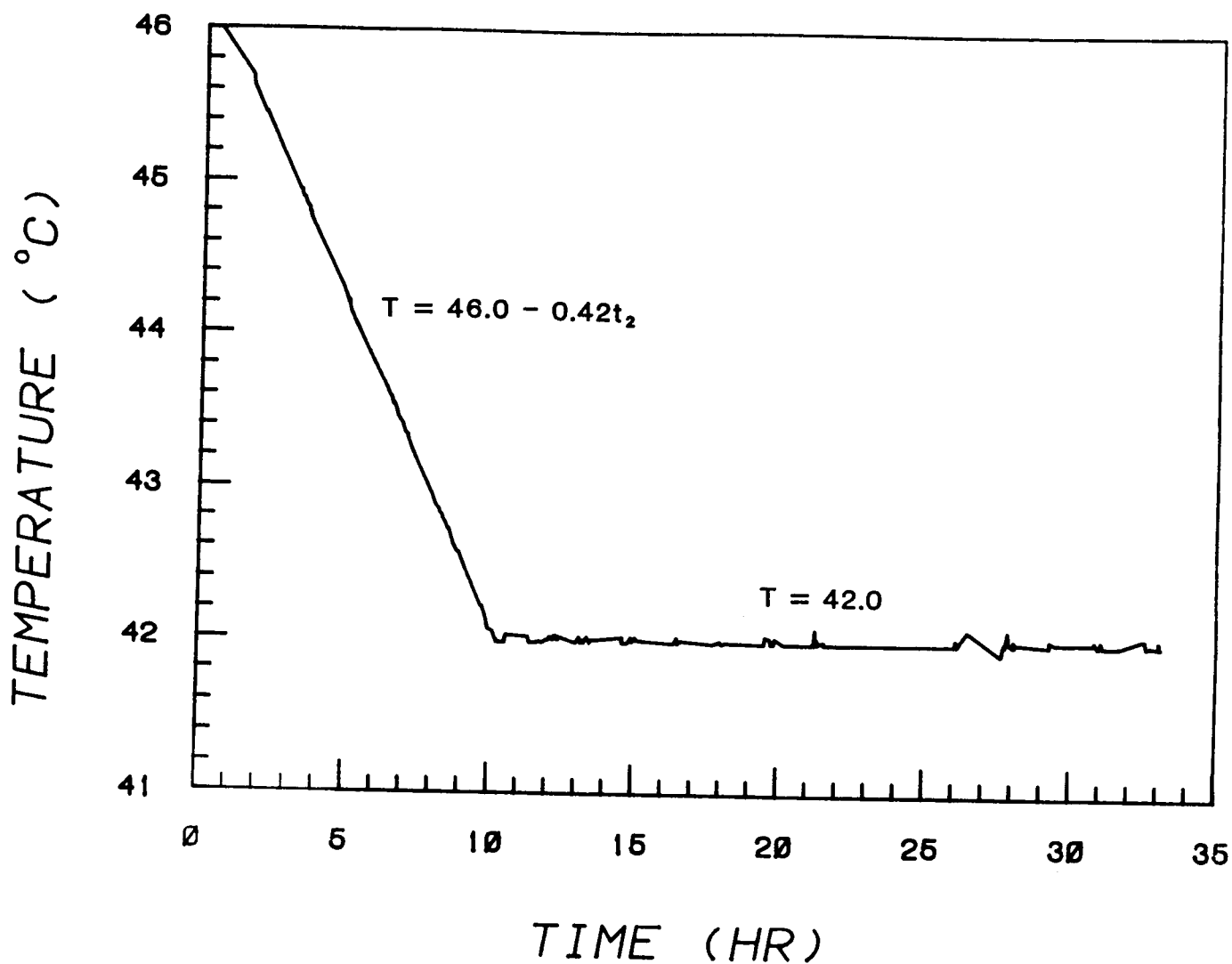


Figure 1. Measured sting temperature vs. time for Cell 3. Wall temperature the same within experimental error.



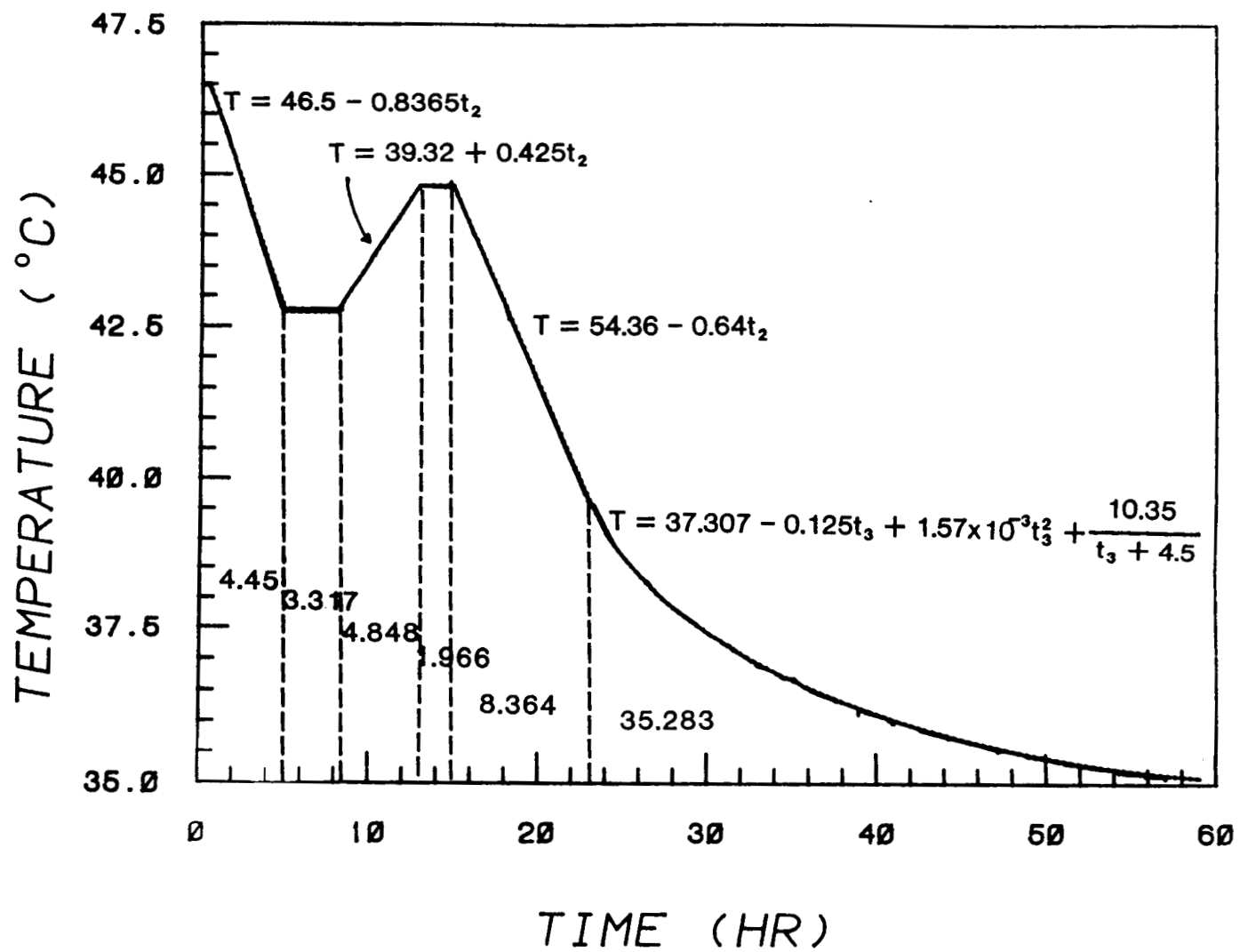


Figure 2. Measured sting temperature vs. time for Cell 2.

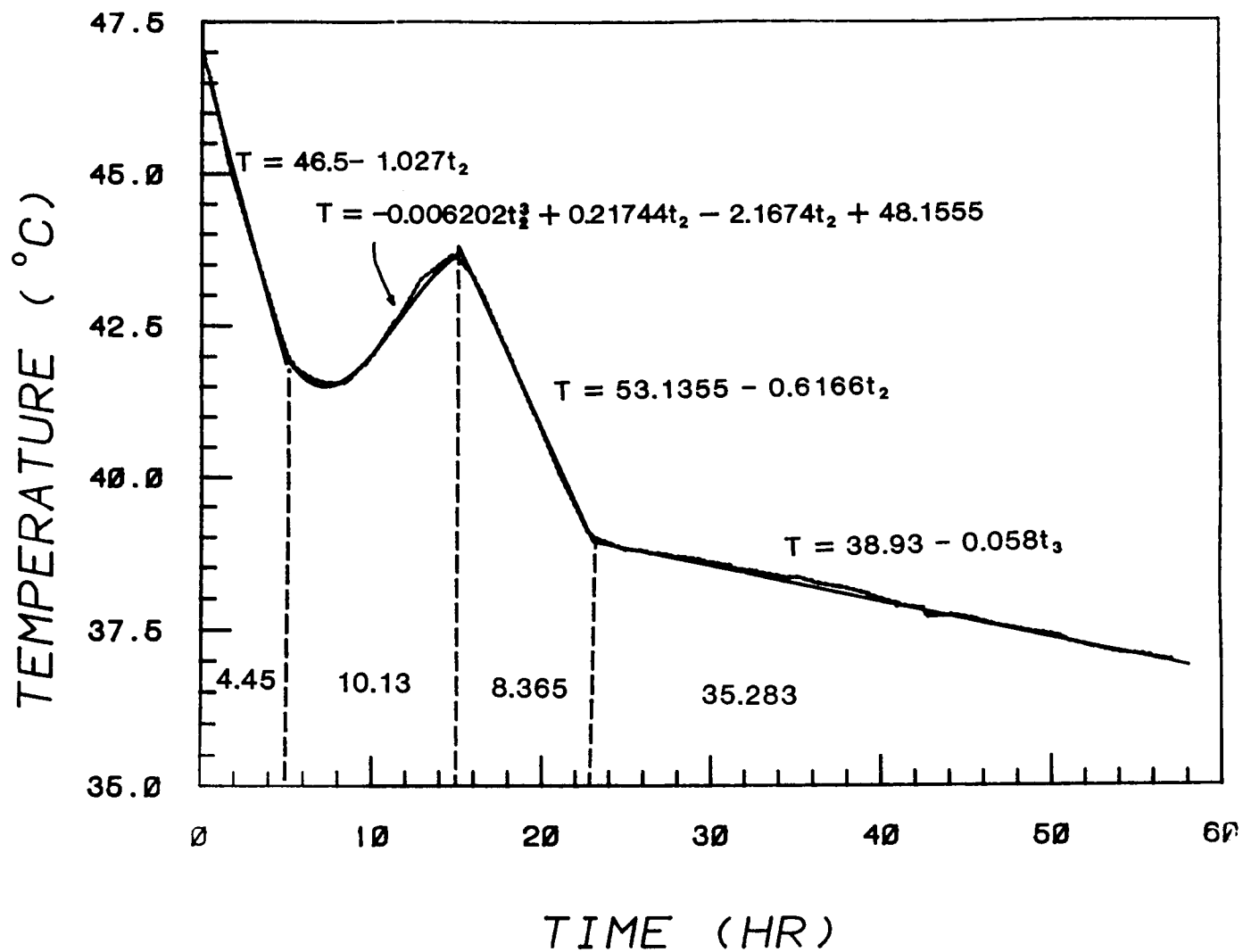


Figure 3. Measured wall temperature vs. time for Cell 2.

ORIGINAL PAGE IS  
OF POOR QUALITY

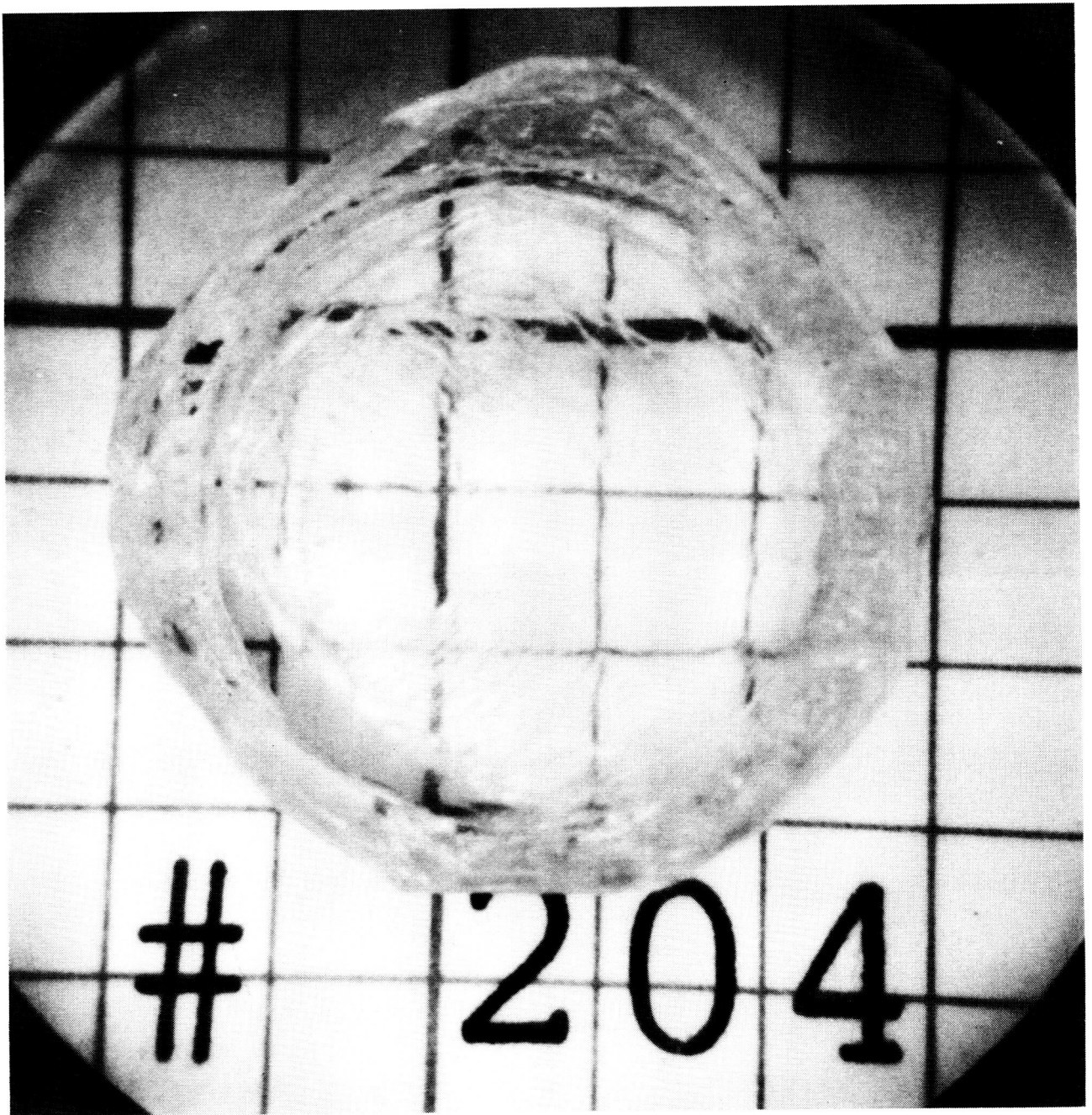


Figure 4. Top view of TGS crystal grown in Cell 3.

ORIGINAL PAGE IS  
OF POOR QUALITY

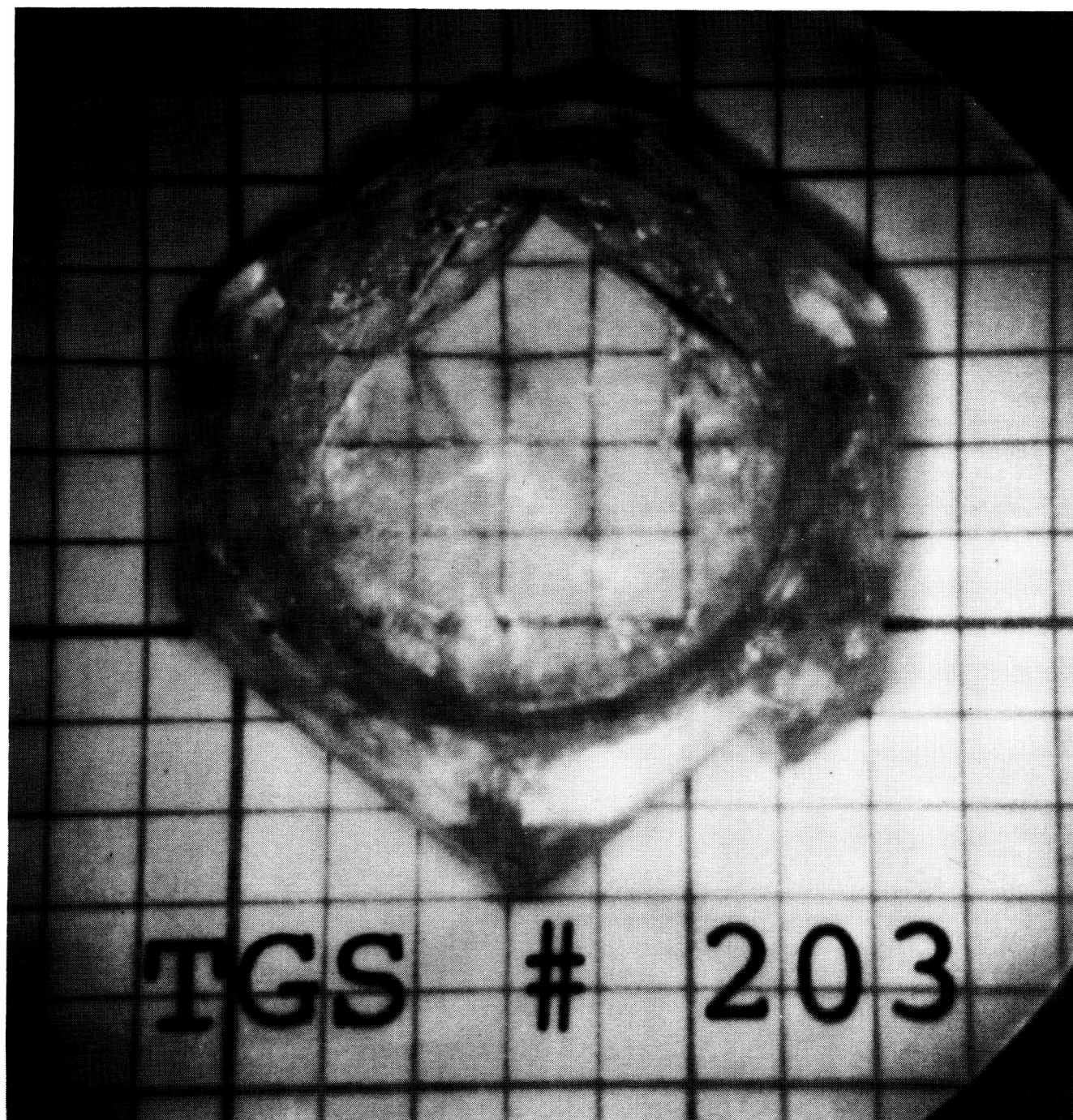


Figure 5. Top view of TGS crystal grown in Cell 2.



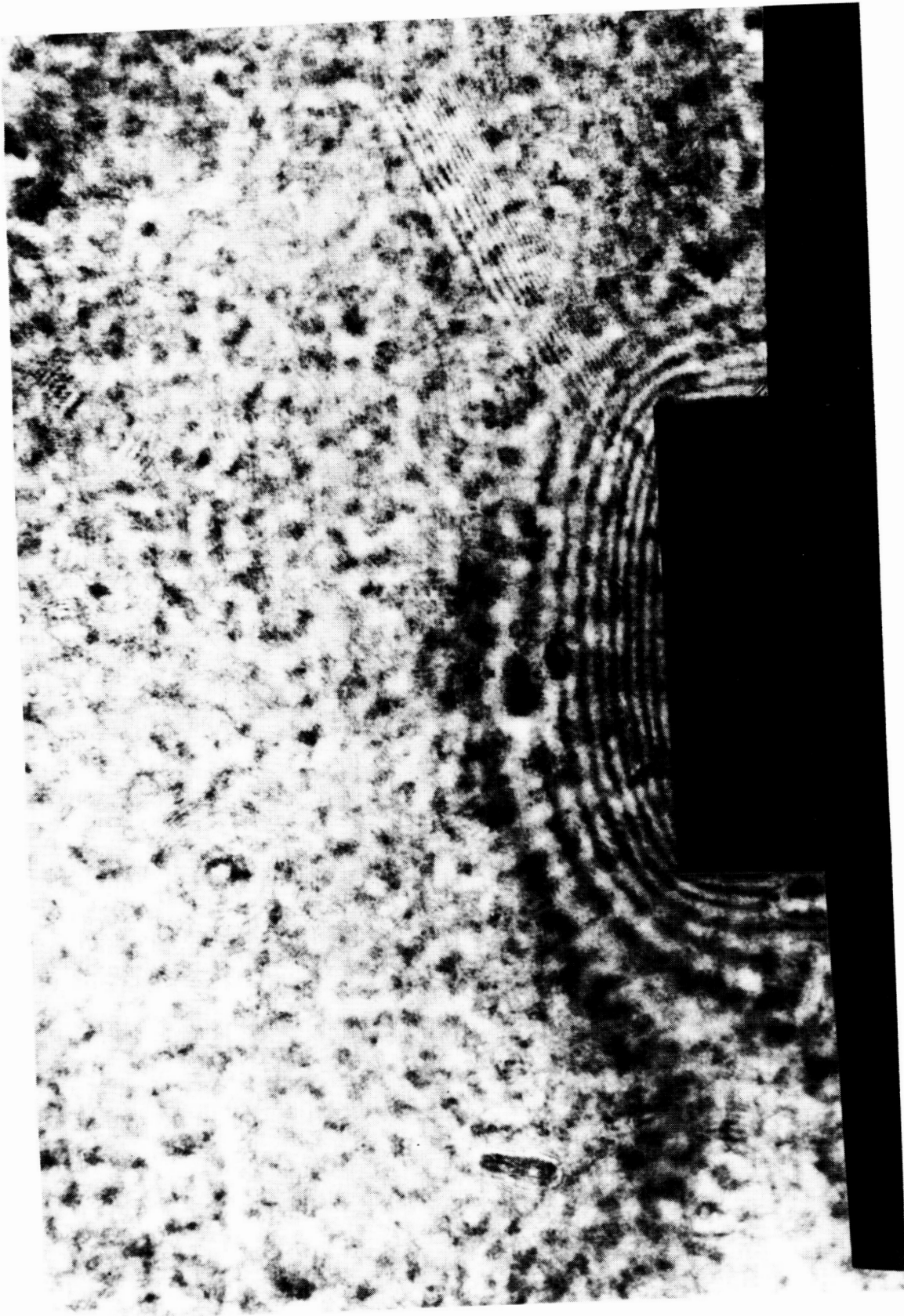


Figure 6. Cell 3 Holographic interferogram of solution near crystal 40.83 minutes after initiation of cap retraction. Object at bottom is mask used to cover image of sting and growing crystal to enhance quantitative comparison with theoretical predictions.

ORIGINAL PAGE IS  
OF POOR QUALITY

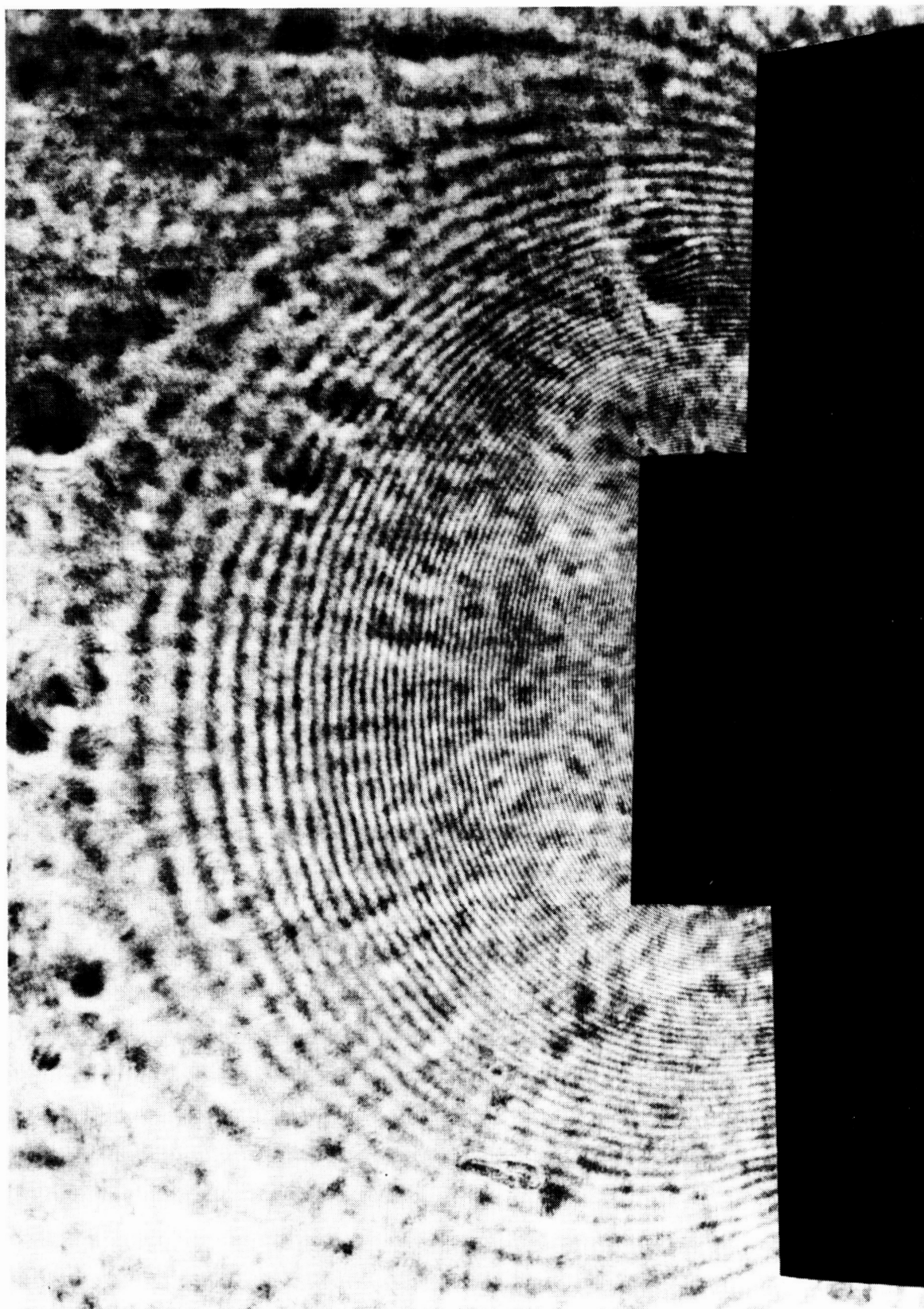


Figure 7. Cell 3 interferogram 16.87 hours after cap withdrawal.

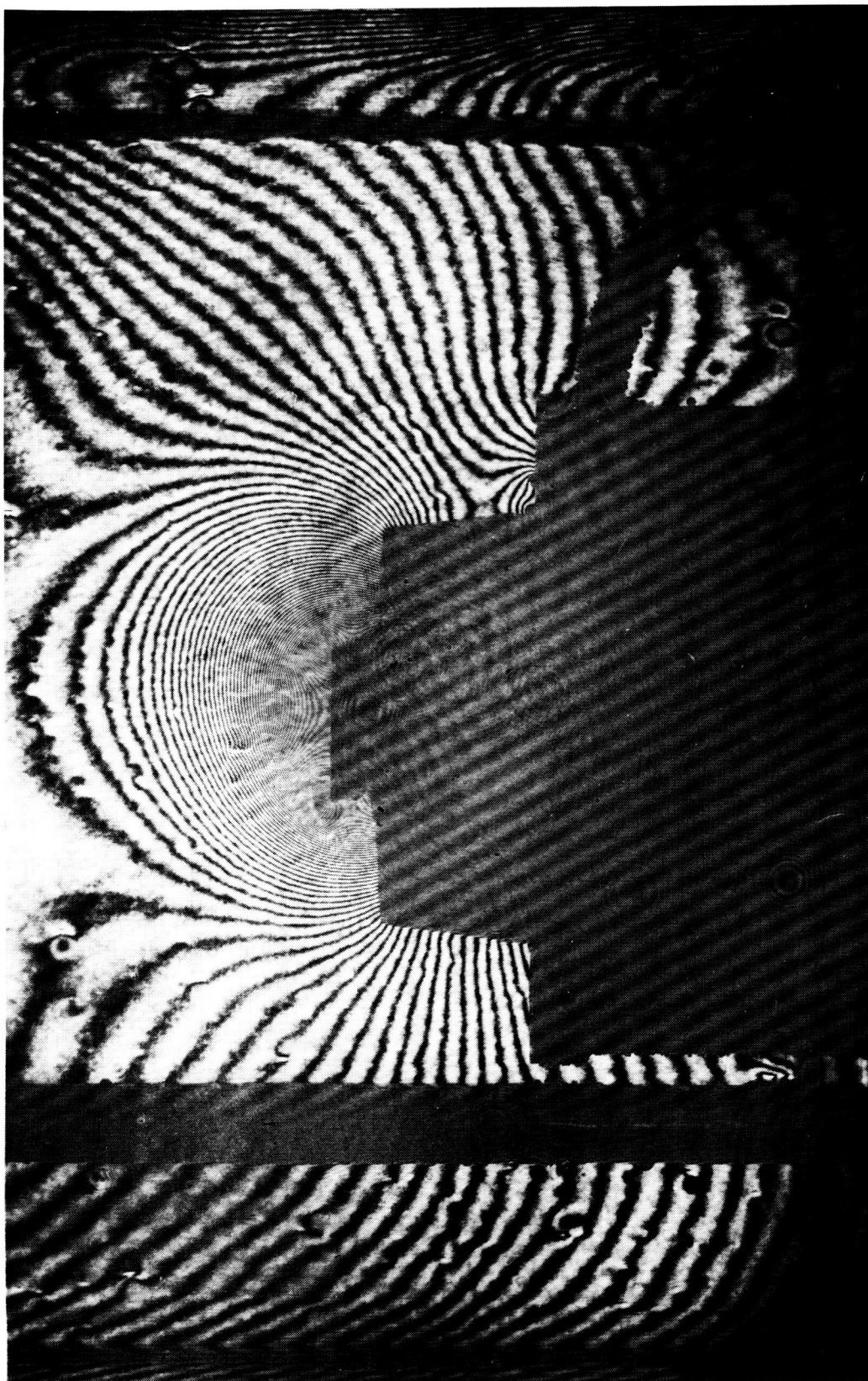


Figure 8. Cell 3 interferogram 24.33 hours after cap retraction. Actual image of sting and crystal are seen in center. Vertical rod to left of sting is thermal sensor. Rod curving down from right side of sting is vacuum line.

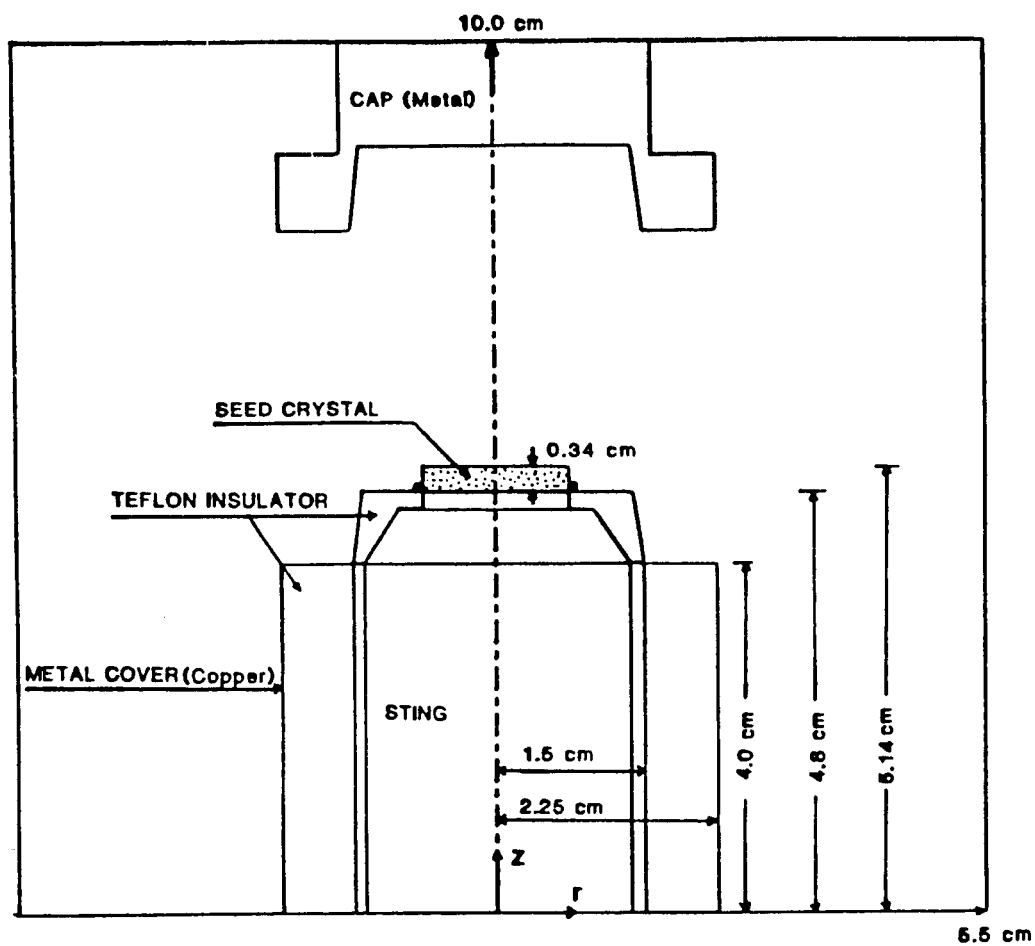


Figure 9. Cell geometry used in computer model.



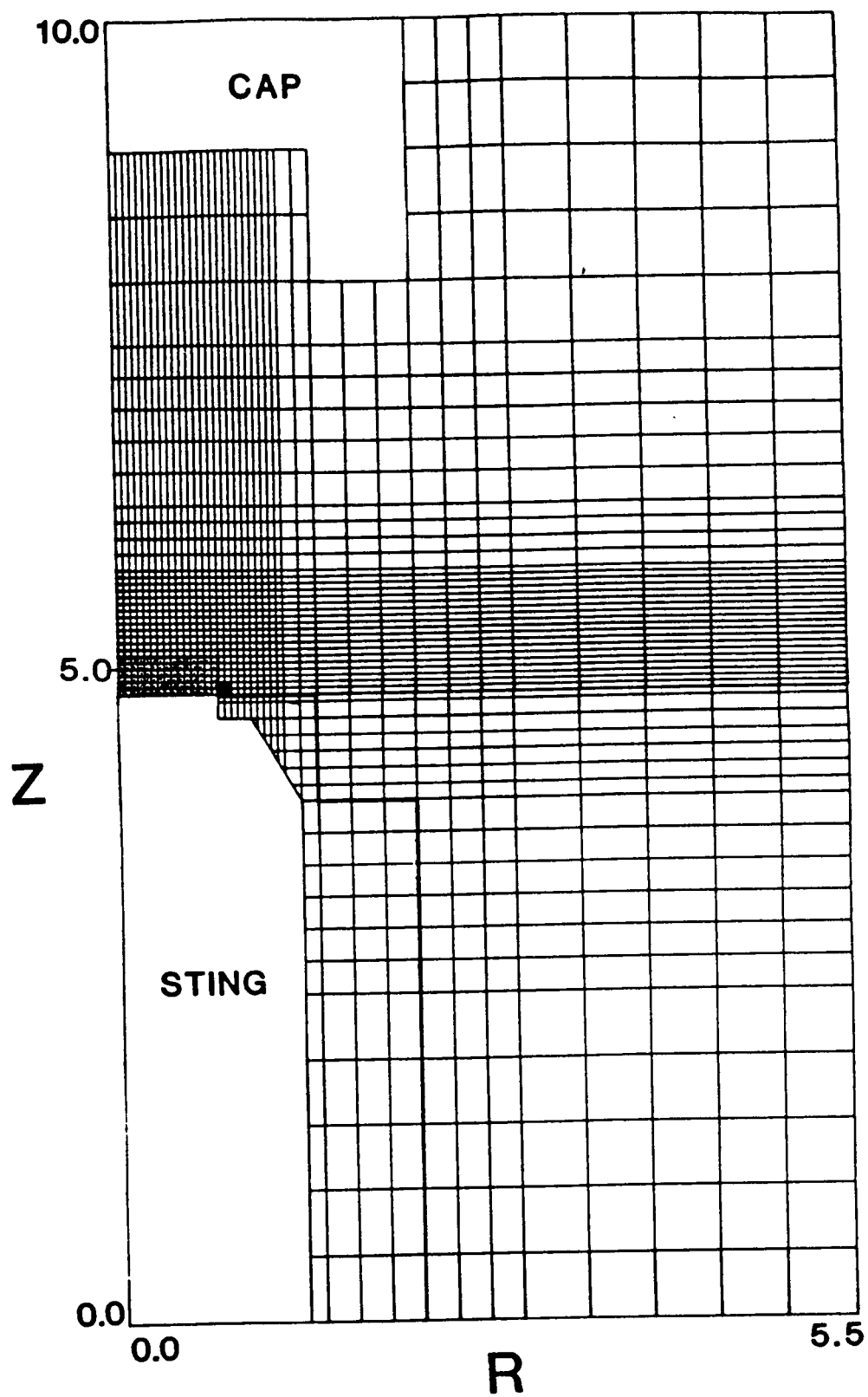


Figure 10. Mesh used for finite difference solution. Numbers are distances in cm.

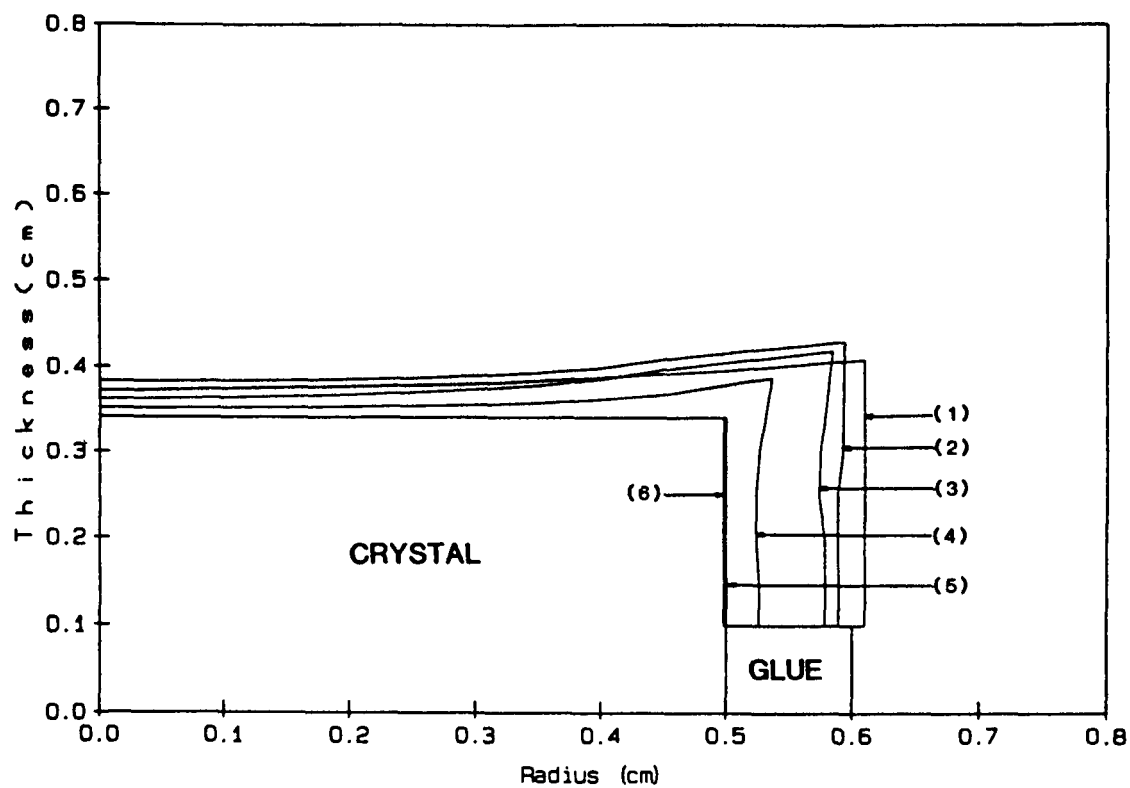


Figure 11. Comparison between the final shape of the crystal grown in Cell 3:

- (1) Averaged from experimental values in Figure 4.
- (2) Calculated using  $D = 3 \times 10^{-5} \text{ cm}^2/\text{s}$ .
- (3) Calculated using  $D = 2 \times 10^{-5} \text{ cm}^2/\text{s}$ .
- (4) Calculated using  $D = 1 \times 10^{-5} \text{ cm}^2/\text{s}$ .

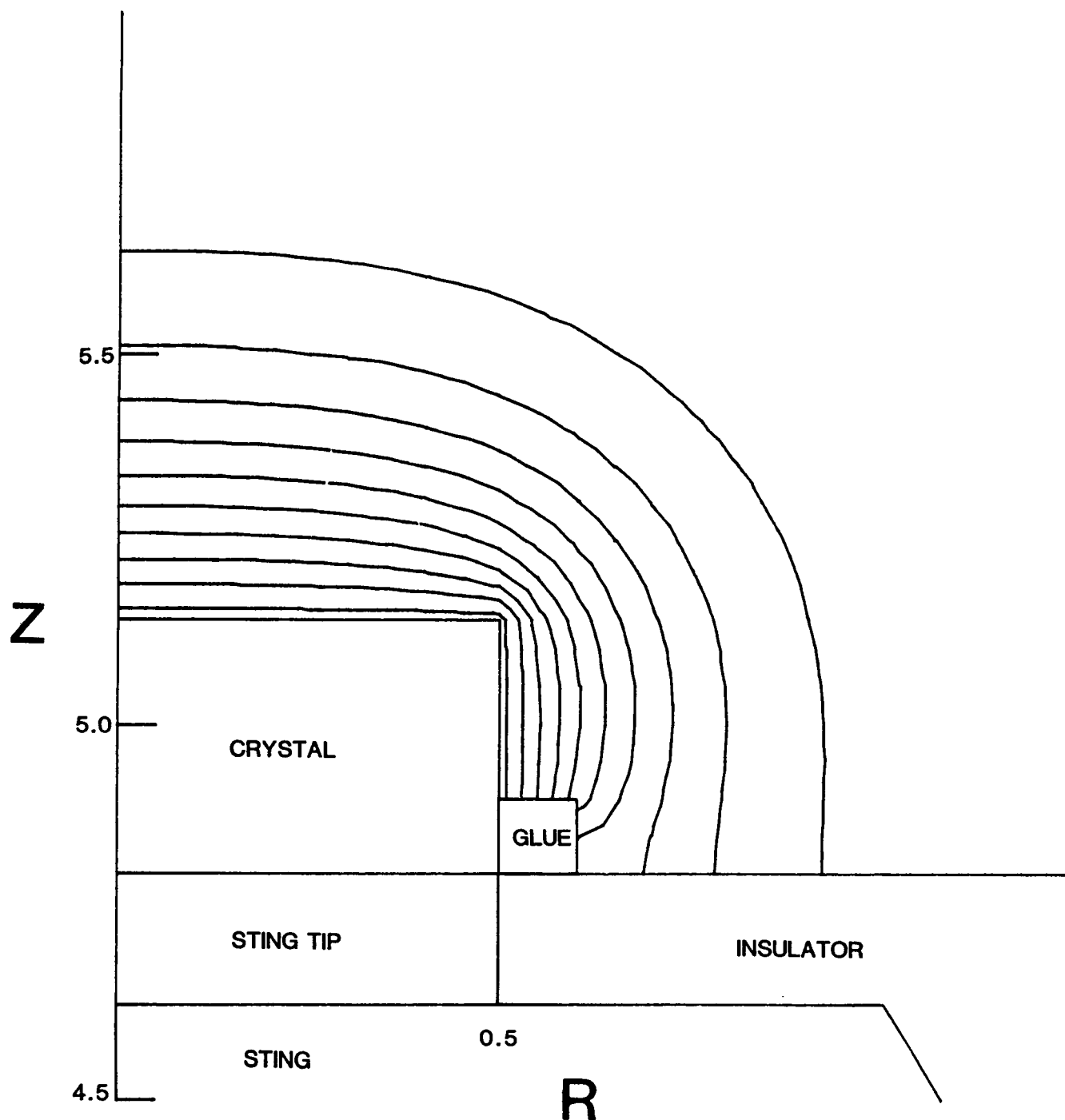


Figure 12. Isoconcentration lines for Cell 3 at end of isothermal dissolution period, 40.83 minutes after cap retraction, calculated using  $D = 2 \times 10^{-5} \text{ cm}^2/\text{s}$ .  $T = 46 \text{ C}$ , concentration at crystal surface =  $1.229 \text{ mmol/cm}^3$ , original concentration of solution =  $1.209 \text{ mmol/cm}^3$ , change in concentration between lines =  $0.002 \text{ mmol/cm}^3$ .

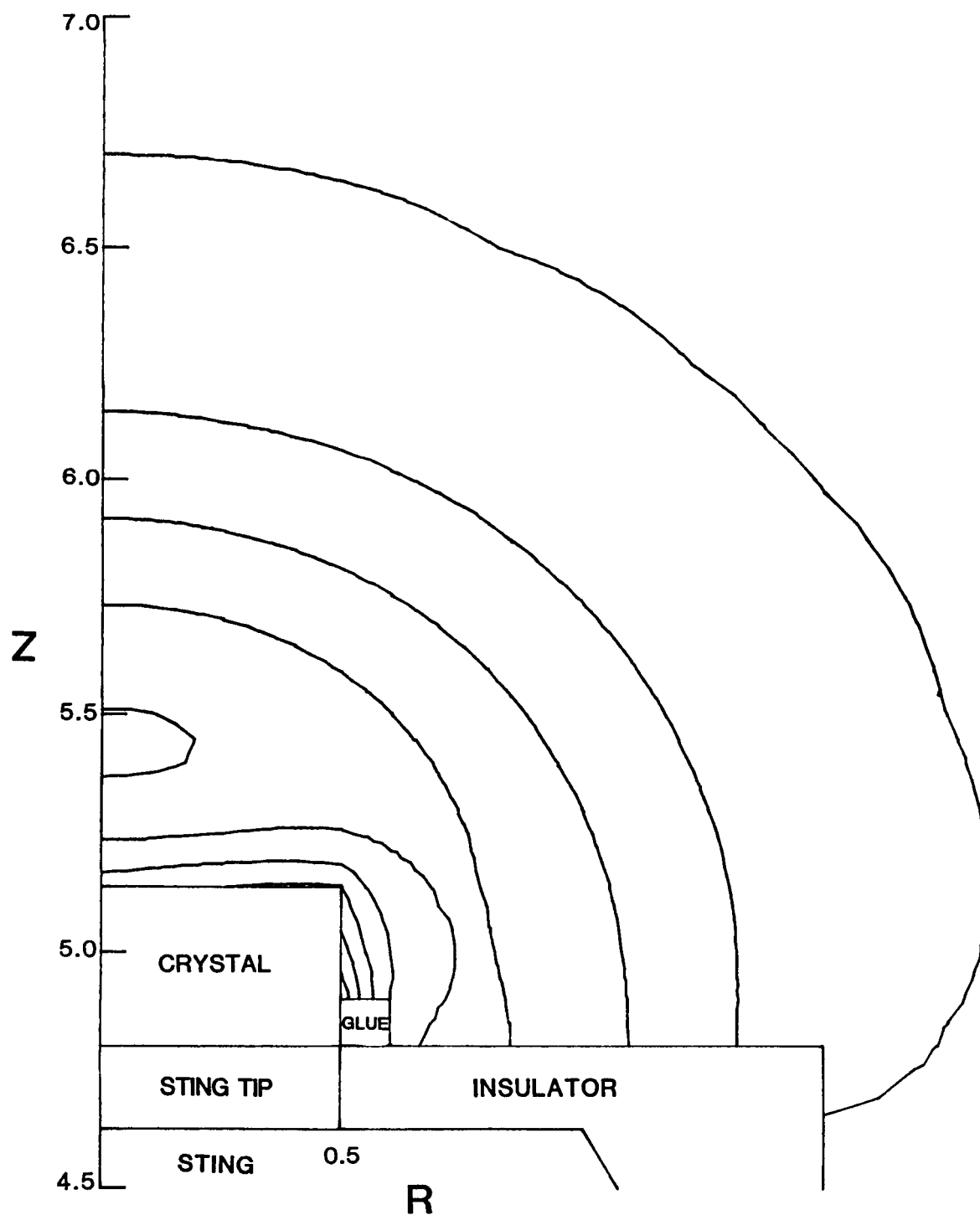


Figure 13. Computed isoconcentration lines for Cell 3 during linear cooldown period, 208.67 minutes after cap retraction.

Change in concentration between lines =  $0.001 \text{ mmol/cm}^3$ .

Maximum concentration at about  $Z = 5.4 \text{ cm}$ ,  $R = 0$ .

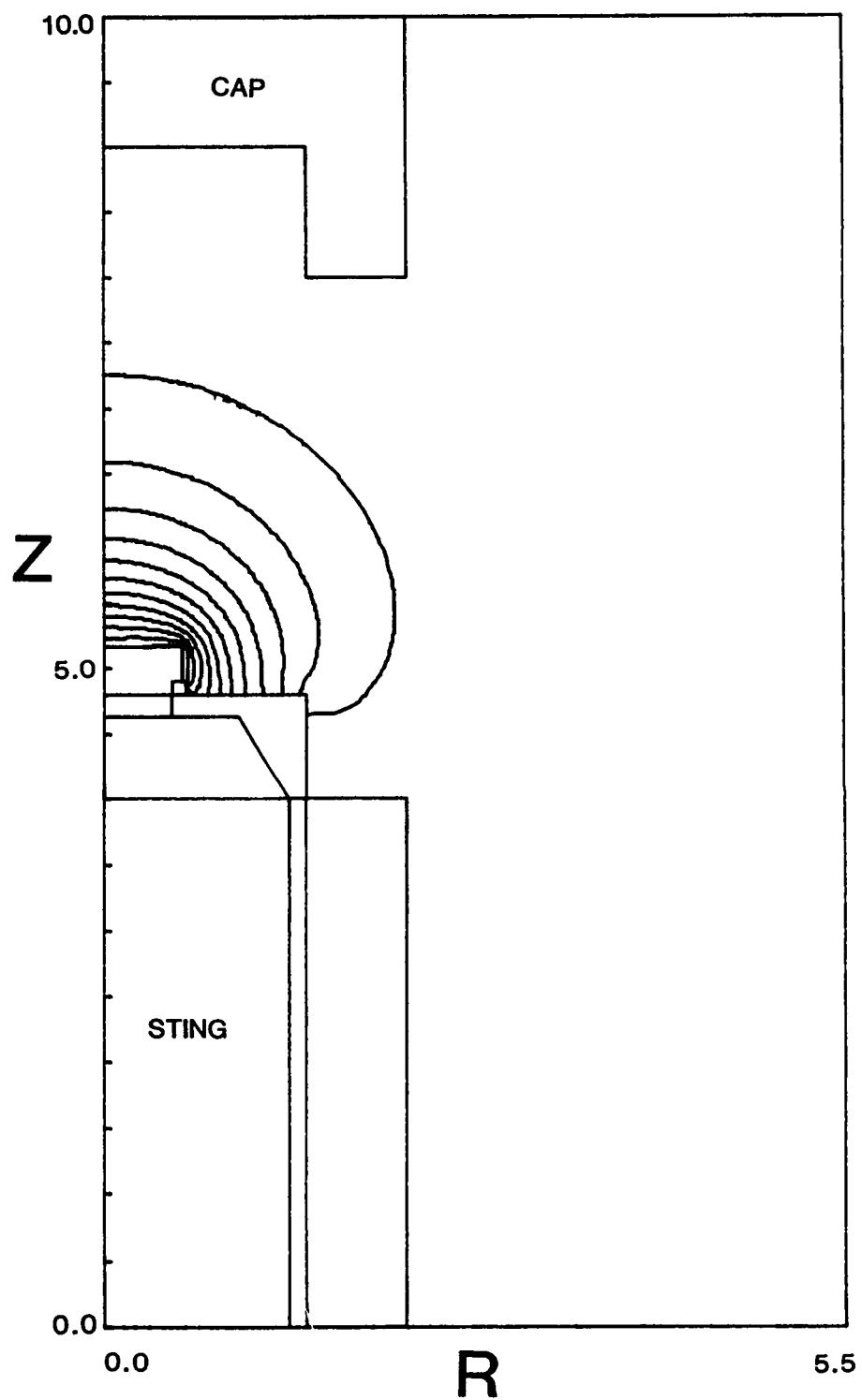


Figure 14. Computed isoconcentration lines for Cell 3 at end of run, 33.97 hours after cap retraction.

Change in concentration between lines =  $0.005 \text{ mmol/cm}^3$ .

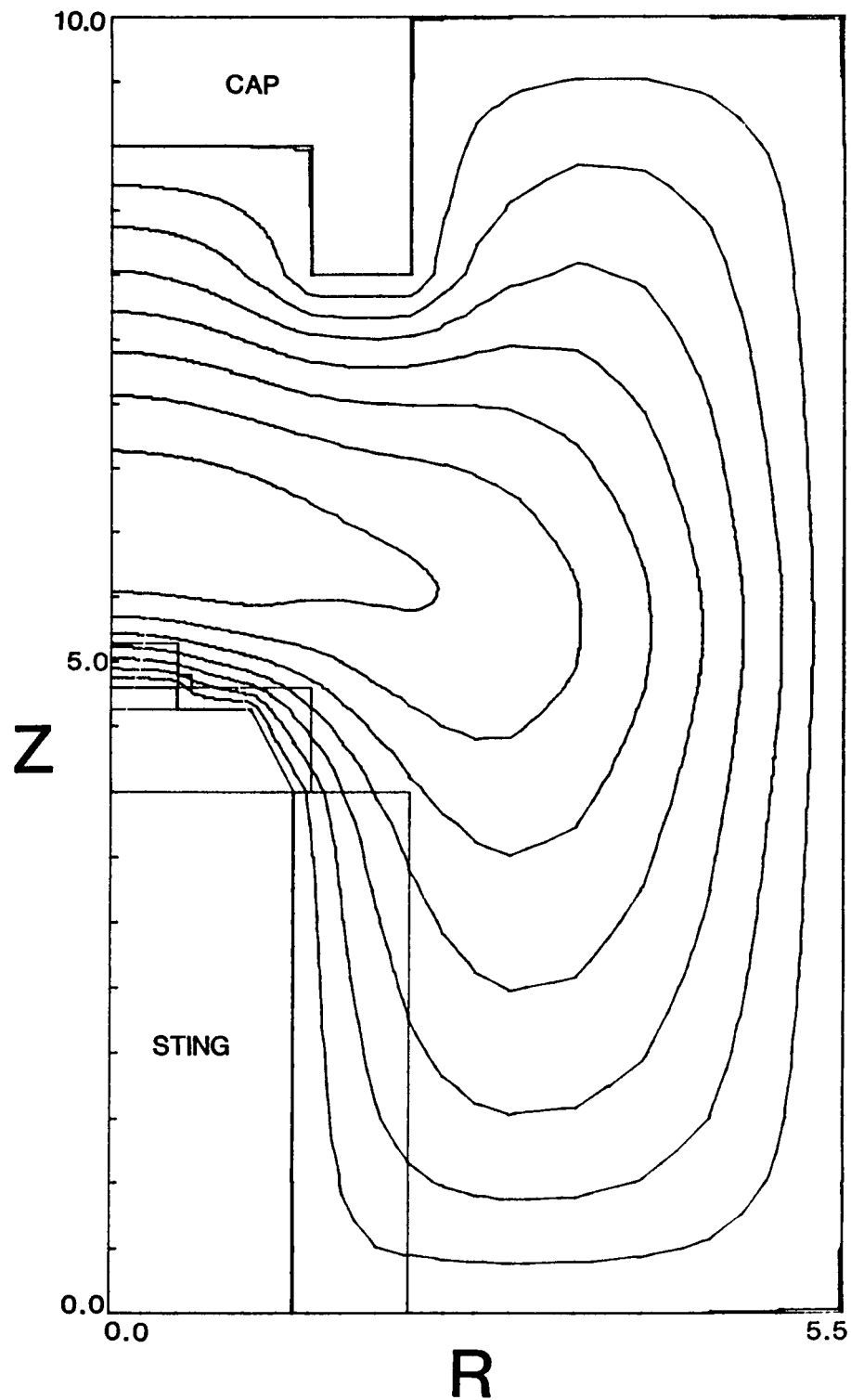


Figure 15. Isotherms for Cell 3 during linear cooldown period, 330.62 minutes after cap retraction. Wall temperature and sting temperature are 43.9 C. Change in temperature between lines = 0.05 C.

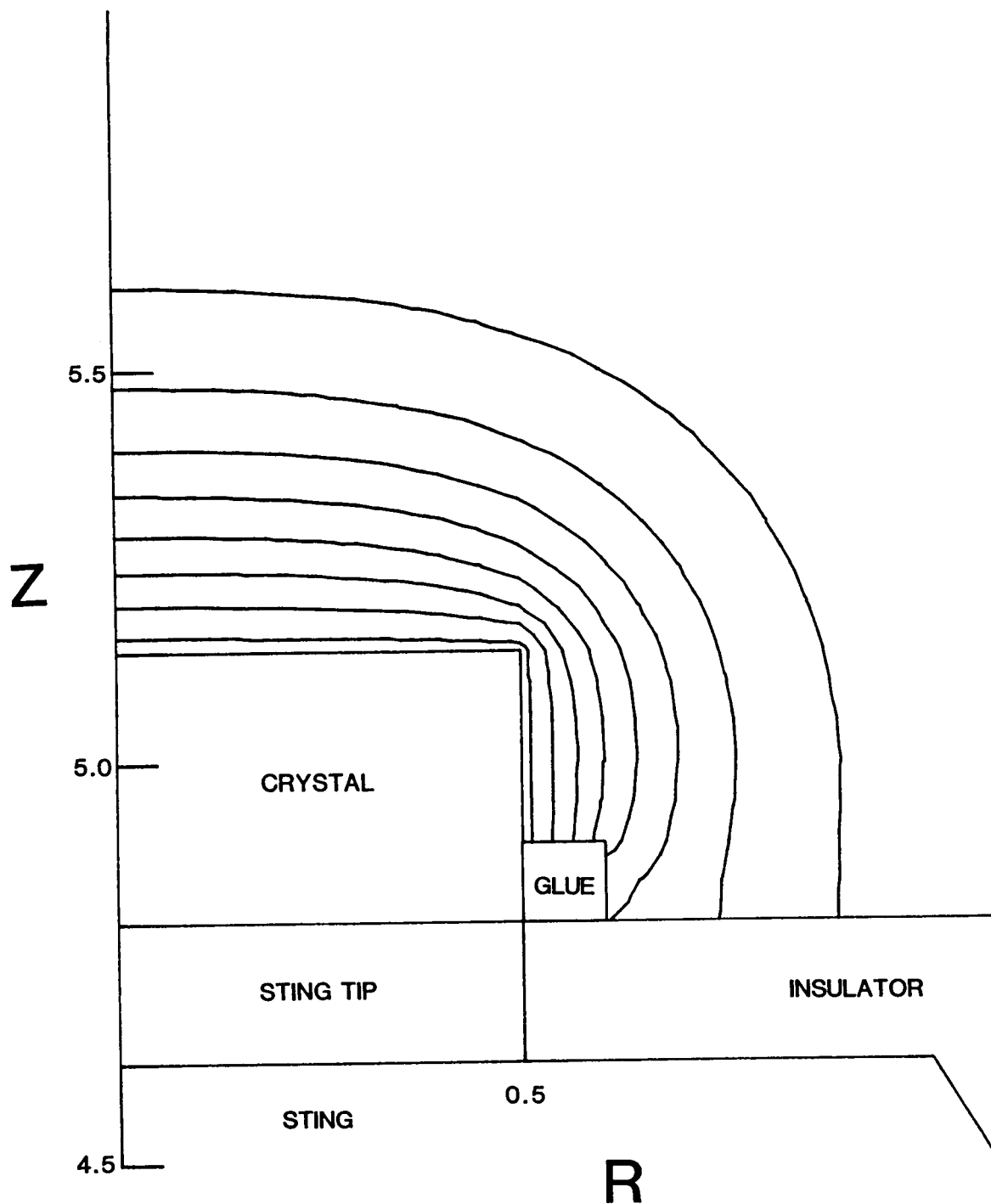


Figure 16. Computed lines of constant refractive index for Cell 3 at end of isothermal dissolution, 40.83 minutes after cap retraction. Refractive index of solution at top crystal surface is 1.38345. Change in refractive index between lines = 0.0001.

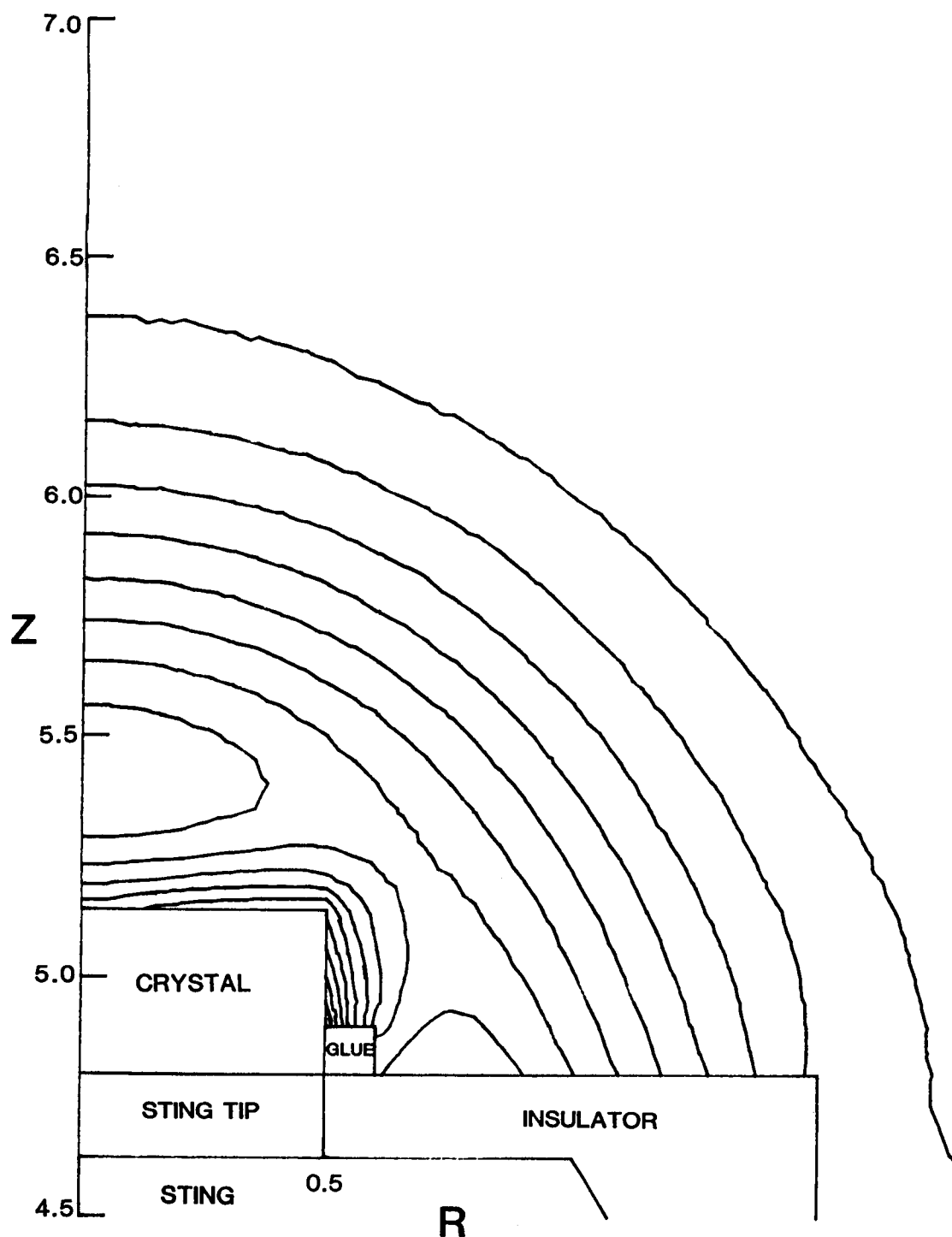


Figure 17. Computed lines of constant refractive index for Cell 3 in the linear cooldown period, 208.67 minures after cap retraction. Refractive index of solution at top crystal surface is 1.38286. Change in refractive index between lines = 0.00002.



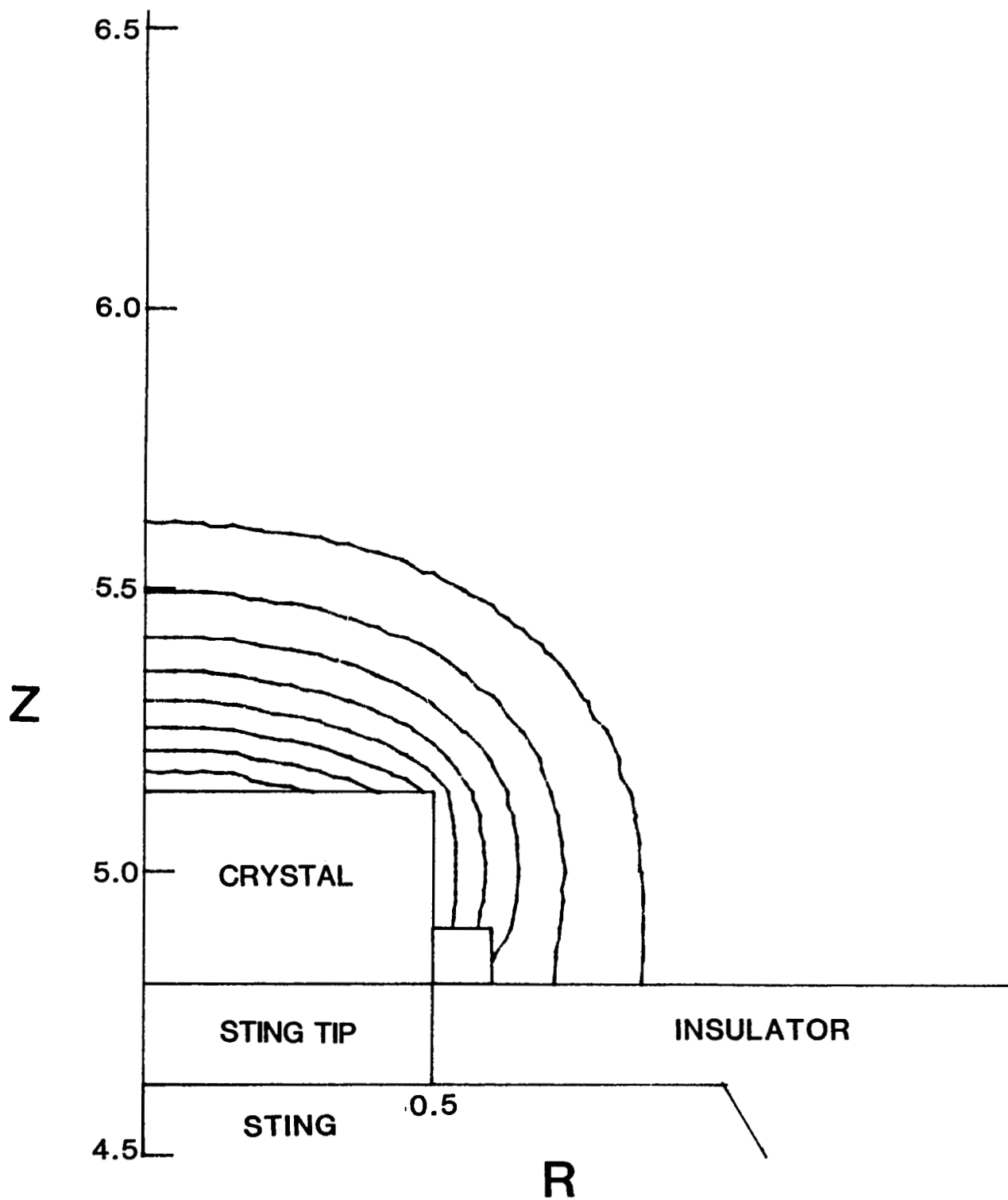


Figure 18. Computed interferogram for Cell 3 at the end of the isothermal dissolution period, 40.83 minutes after cap retraction. Compare with experimental interferogram in Figure 6.

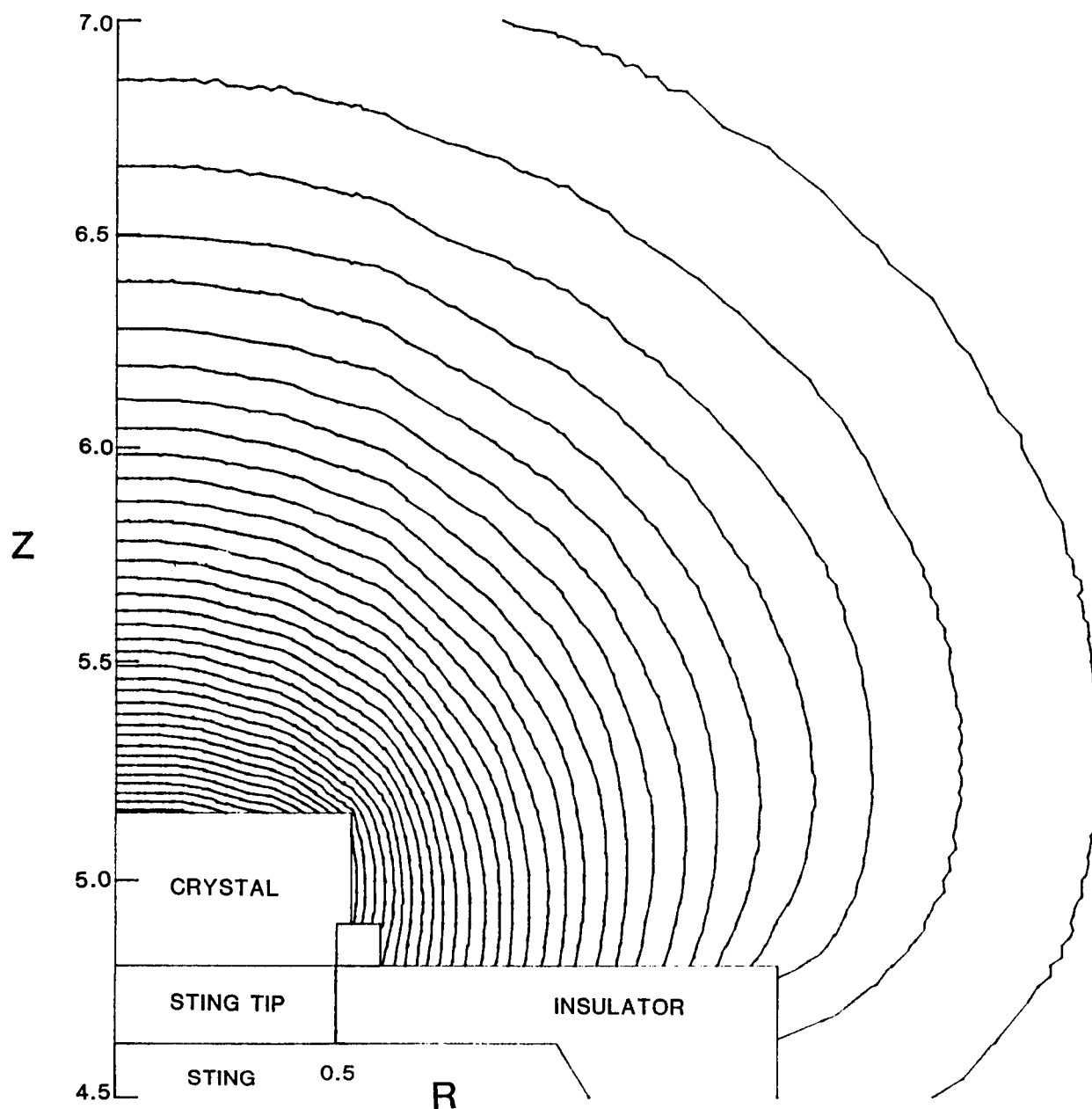


Figure 19. Computed interferogram for Cell 3 in the constant temperature period, 16.87 hours after cap retraction. Every other interference line was deleted for clarity. Compare with experimental interferogram in Figure 7.

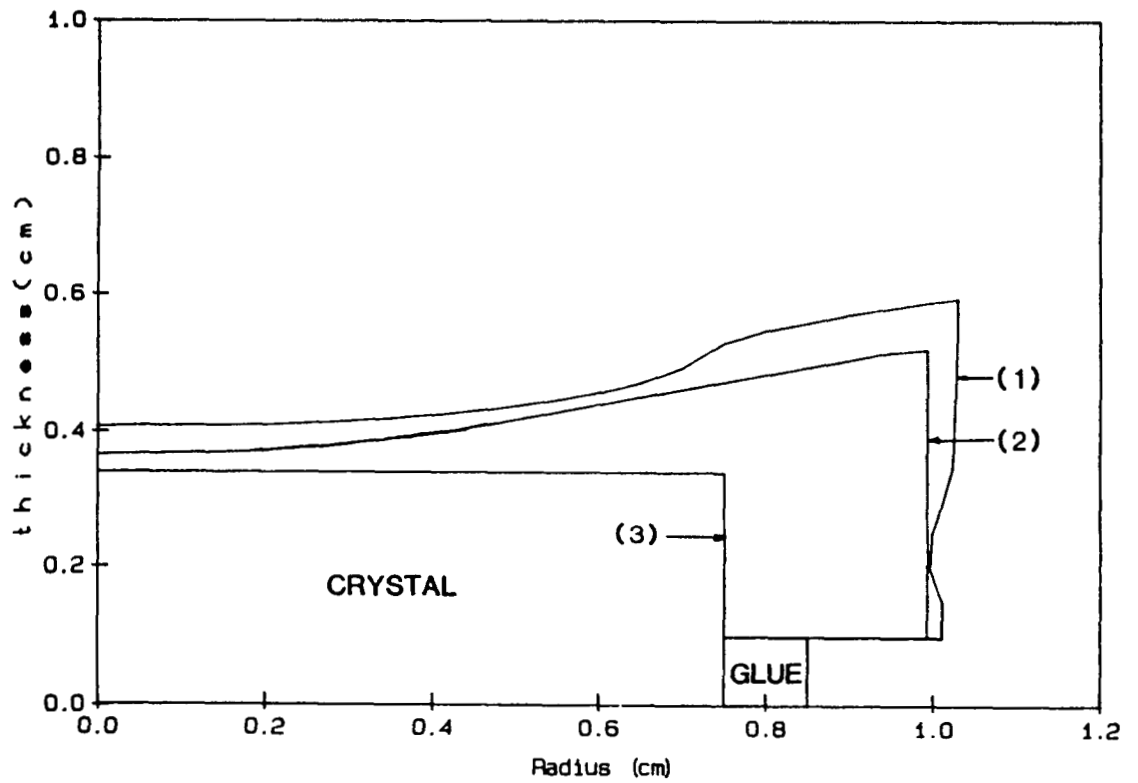


Figure 20. Comparison between experimental and computed crystal shape for Cell 2.

- (1) Calculated using  $D = 2 \times 10^{-5} \text{ cm}^2/\text{s}$ .
- (2) Averaged from experimental measurements.
- (3) Original seed crystal.

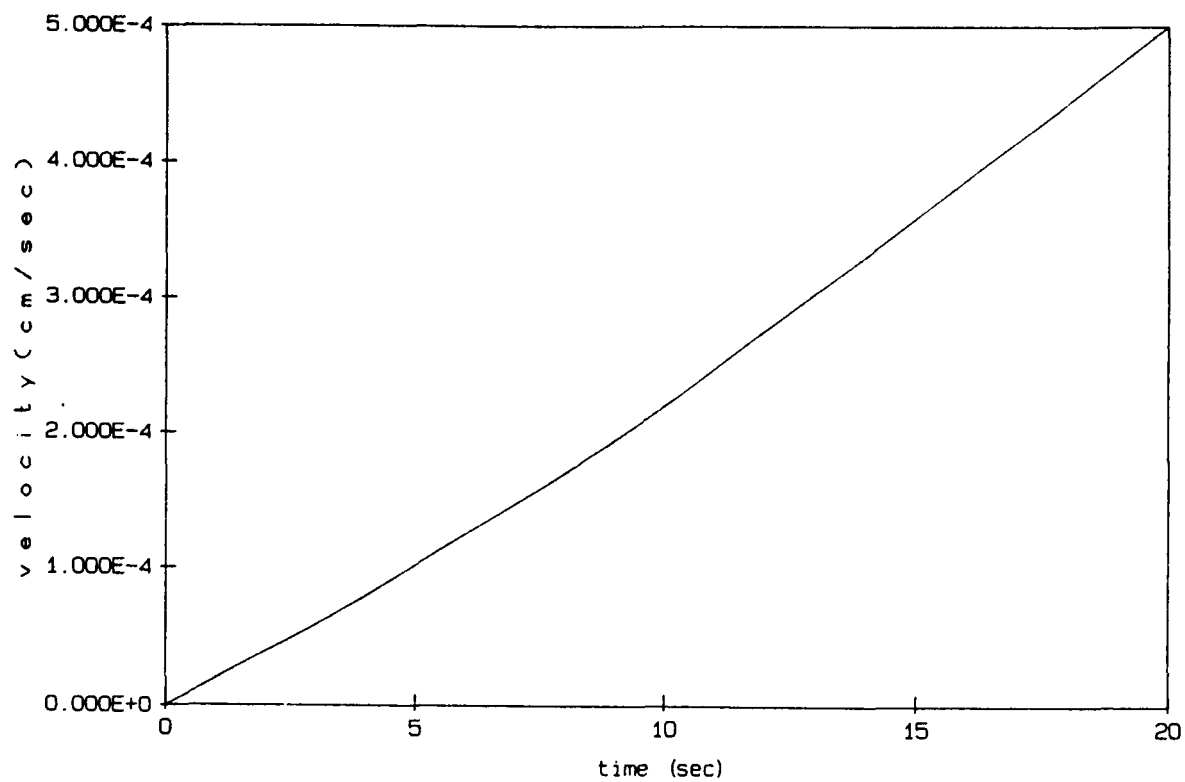


Figure 21. Maximum fluid velocity vs. time after turning  $10^{-4}$  g acceleration ( $Gr = 14$ ) on in Cell 2 after 46 hours of diffusion without convection.

# **A Comparative Study of the Influence of Buoyancy Driven Fluid Flow on GaAs Crystal Growth\***

by J.A. Kafalas and A.H. Bellows

## **ABSTRACT**

This study consists of a systematic investigation of the effect of gravity-driven fluid flow on GaAs crystal growth, and will include GaAs crystal growth in the microgravity environment aboard the Space Shuttle. The program involves a controlled comparative study of crystal growth under a variety of earth-based conditions with variable orientation and applied magnetic field in addition to the microgravity growth. Earth-based growth will be performed under stabilizing as well as destabilizing temperature gradients. The boules grown in space and on earth will be fully characterized to correlate the degree of convection with the distribution of impurities. Both macro- and micro-segregation will be determined.

The space growth experiment will be flown in a self-contained payload container through NASA's Get Away Special program. The advantages of using the GAS program are simplicity of manifesting the payload aboard the orbiter, frequent flight opportunities, quick turnaround necessary for iterative experiments, and low cost. The payload with its large alkaline battery power source will include two redundant experimental systems including separate well insulated growth furnaces. Each sequentially scheduled growth experiment will require approximately 8 hours to complete, and collected data will include micro acceleration, temperature, and furnace power. The use of the specially designed growth ampoule and furnace system for both space- and earth-based growth experiments will lend validity to the comparative studies and simplify the numerical modeling.

## **1. INTRODUCTION**

During the last decade, GaAs has become one of the most important electronic materials. GaAs exhibits an intrinsic electron mobility greater than  $9000 \text{ cm}^2/\text{V-s}$  making it a desirable material for very high speed signal processing devices, and its direct energy gap makes it a useful material for light emitting devices. Recently, undoped semi-insulating GaAs substrates of good quality have become available due to improvements in Liquid Encapsulated Czochralski (LEC) growth technology. The availability of state-of-the-art substrate material

---

\*This work was supported in part by NASA-Lewis Research Center and Wright-Patterson Air Force Base Research Center, under Contract No. NAS3-24644.

has given increased impetus to GaAs integrated circuit technology. Nonetheless, the current GaAs IC yields remain very low. It is not clear to what extent this yield problem should be ascribed to the substrate quality or to the still infant IC processing technology. However, it is clear that in the long run, GaAs IC technology will be substrate-limited unless substrate quality is improved.

While there has been much progress lately in increasing the yield of semi-insulating ingots with attractive transport properties, there has been only moderate success in lowering the dislocation density or enhancing the homogeneity of LEC grown material. Dislocation densities in LEC material are typically  $> 10^4 \text{cm}^{-2}$ . Several groups have shown that the incorporation of an isoelectronic dopant, such as In, into the GaAs lattice can reduce the dislocation density to  $< 10^3 \text{cm}^{-2}$  with no appreciable degradation of the transport properties. Significant reductions in dislocation density have also been achieved through careful tailoring of the thermal environment in the furnace during growth. Even with these very recent improvements, the dislocation density in LEC GaAs remains high relative to Si. In addition, the resistivity and mobility in most GaAs boules varies both radially and axially, and pronounced growth striations are a clear indication of the inhomogeneous distribution of impurities throughout the ingot.

A major cause of these inhomogeneities is the significant degree of temperature fluctuation at the growth interface. In a gravitational field, density gradients in the melt caused by temperature gradients or compositional variations induce appreciable convection currents which produce pronounced turbulence at the growth interface and results in erratic temperature fluctuations. Such temperature instabilities are particularly unfavorable for the growth of III-V compounds such as GaAs and InP in which one of the components is quite volatile. This condition can result in constitutional supercooling and can require a higher temperature gradient for proper crystal growth. In addition, the convection induced temperature fluctuations introduce a fluctuating microscopic growth rate that leads to the inhomogeneous distribution of impurities.

Crystal growth of semiconducting crystals in space has clearly demonstrated that the elimination of convection-driven turbulence at the growth interface can substantially improve crystal quality. Examination of doped crystals of  $\text{InSb}^{(1)}$  and  $\text{Ge}^{(2)}$  grown in the microgravity environment of space yielded no evidence of growth striations. In contrast, impurity striations arising from an inhomogeneous incorporation of impurities during growth are invariably present in earth-based Czochralski grown crystals indicating an inhomogeneous incorporation of impurities during growth. In general, segregation in crystals grown

under microgravity conditions is primarily diffusion-controlled. This mechanism results in a more uniform distribution of impurities or dopants along the axis of the crystal.

Convection currents in the melt can also be suppressed by the application of a magnetic field during growth. The magnetic field can be viewed as increasing the effective kinetic viscosity of the melt by resisting fluid motion through Lenz's Law. Several laboratories, including our own, have been investigating the utility of magnetic field assisted growth in improving the homogeneity of GaAs.<sup>(3-7)</sup> Results at GTE Laboratories,<sup>(3)</sup> illustrated in Figure 1, have shown that, for boules grown in a transverse field  $> 2000$  G, erratic growth striations can be totally eliminated. Moreover, the field-grown GaAs exhibits dislocation densities of  $< 10^3 \text{cm}^{-2}$ . This decrease in dislocation density is probably due to the stabilization of the microscopic growth rate by the magnetic field.

Space-growth and magnetic field growth results demonstrate that convection can profoundly influence the quality and properties of semiconductor crystals. It is important to determine to what degree convection-induced temperature instability at the growth interface affects impurity segregation and development of defects in the crystal. A comparison of the effectiveness of magnetic suppression of convection to the elimination of buoyancy driven flow under microgravity can lead to improved earth-based growth of high quality GaAs under applied magnetic field and optimized temperature gradients. Enhancing the homogeneity and reducing the dislocation density of GaAs are two of the major goals of current research by the GaAs growth community.

## 2. SCOPE OF EXPERIMENT

In this study, a series of experiments has been designed to delineate the role of buoyancy driven fluid flow on the growth of GaAs single crystals under a variety of conditions. The approach chosen for this study is a comparative one in which microgravity growth in space serves as the limiting case of negligible buoyancy driven convection. The microgravity growth experiments are complemented by a series of earth-bound growth experiments that examine the influence of convection on GaAs growth as a function of the orientation of the temperature gradient and the presence or absence of a magnetic field.

The earth-based growth series includes field-free and field-assisted growth. Comparison of the flow-dampening effects of transverse and axial magnetic fields are included in the study. The experiments also include an investigation of the temperature gradient encountered in the three common modes of bulk crystal growth: horizontal Bridgman (HB), verti-

cal Bridgman (VB) and Czochralski (Cz). The various growth modes are illustrated schematically in Figure 2.

The heart of the experimental apparatus to be utilized for the studies is a specially designed furnace and growth ampoule, two of which are mounted in a payload designed for inclusion in one of NASA's Get Away Special payload containers for flight in the cargo bay of the Space Shuttle. The payload is illustrated in Figure 3 and is similar to one successfully operated by GTE Laboratories on STS-41B in February 1984, for studying convective effects in arc lamps.

### 3. EXPERIMENTAL DETAILS

This experiment was designed to be flown in the GAS program because of the unique opportunity it affords for performing sophisticated experiments using the simple, inexpensive, and timely procedures it provides. This program offers the extensive advantages of fast processing, streamlined safety reviews, and flight opportunities on virtually every Shuttle flight.

The payload is 20 inches in diameter, 26 inches high and is suspended from a top plate provided by NASA. The growth furnaces are contained within two 6 inches in diameter, 12 inches long cylinders mounted side by side near the center of the payload. Since no power is available from the orbiter, large battery packs above and below the furnaces supply power for the growth runs. Two isolated microprocessors will respectively control the 2 experiments which will be performed at different times. They will also store in non-volatile EPROM memory 16 channels of data including furnace power, battery voltage, various temperatures, and 3 axes of acceleration.

A diagram of the growth ampoule and furnace is shown in Figure 4. The growth ampoule will contain a pregrown single crystal ingot of GaAs 4 inches long by 1 inch in diameter. The ampoule is fitted with a spring loaded plunger to maintain the geometric integrity of the charge thereby ensuring that there will be no free fluid surfaces in the growth compartment. Under these conditions, Marangoni convection will be eliminated in both earth-based and microgravity experiments. This is a double-walled ampoule especially designed to permit GaAs growth in a spring-loaded system. In this configuration slight pressure-induced distortion of the outer quartz wall will not inhibit piston movement. The growth ampoule will be provided with a means of growth interface demarcation to permit a determination of growth rate as well as the shape of the growth interface. The design will permit



earth-based growth in the three ampoule orientations illustrated in Figure 2, corresponding to the three growth modes. Thus, the growth geometry will be invariant throughout the course of the space and earth-based growth experiments, making possible the comparative study.

The furnace surrounding the growth ampoule will be used in both space and earth-based growth to ensure that the details of the temperature gradient are well controlled. The furnace will accept an axial field solenoid of reasonable size, and it is compatible with the transverse pole gap of the existing electromagnet at GTE Laboratories. Thus, the growth geometry can be held constant during the axial and transverse field-assisted growth series as well. The platinum-wound, Zircar®-insulated furnace is capable of operating at 1200-1300°C at a power level of about 130 watts. The furnace is wound to provide a temperature gradient of about 20°C/in at the growth interface.

In a typical run, the furnace is equilibrated at a temperature that provides melt-back of 3 inches of the pregrown ingot. The remaining 1 inch of unmelted ingot serves as a seed for the regrowth experiment. The furnace is then cooled at a controlled rate to provide a regrowth-rate of about .75 in/hr. Total duration of a run is 8 hours — 2½ hours for warm-up and equilibration, 4 hours for regrowth and 1½ hour for controlled cool-down. Figure 5 is a power consumption vs. time plot of one such experimental run where the solid line represents the steady state power requirement. Area A represents the excess power required for melt-back and area B represents an equivalent decrease in heat input during solidification. The well-behaved power curve at section B indicates a fairly uniform growth rate. For the Space Shuttle portion of this study two sequential runs will be performed in the two independent GAS payload furnaces.

This study is directed primarily toward the determination of the effect of buoyancy driven fluid flow on axial and radial segregation of impurities. The pregrown ingots will all be doped with Se at a concentration range of  $2$  to  $6 \times 10^{17}/\text{cm}^3$ . Selenium was chosen as the dopant because its segregation coefficient is a constant in this concentration range and because it is a shallow donor whose concentration at a particular point can be determined by IR absorption methods.

The regrown ingots will be sectioned as shown in Figure 6. Two axial slices will be taken from each ingot. The remaining portion of the ingot will be diced transversely to provide semi-circular wafers of each portion of the ingot. The axial slices can be profiled to give detailed information on both axial and radial segregation. This can be achieved by both SIMMS and IR absorption methods. Since interface demarcation will be used on half

of the runs, IR microscopy will be used on the appropriate axial slices to determine both micro- and macroscopic growth rates as well as interface shape. The semicircular wafers will be examined to determine the effect of growth parameters on defect density and distribution. Dislocation density and distribution on these wafers will be determined by microscopic examination of wafers etched in molten KOH. The wafers will also be examined by cathodoluminescence techniques to further characterize the nature and distribution of dislocations and other defects.

Several experimental runs have been made with the apparatus described above to optimize the temperature gradient and other growth parameters. Figure 7 is an infra-red micrograph (approximately 200X) taken from an axial slice of one of the regrown boules. This boule was grown in the VB configuration. The photograph clearly shows the initial regrowth boundary with the growth striations in the original LEC grown portion below and the absence of striations in the upper portion regrown in the stabilizing gradient of the VB configuration.

Numerical analysis of the growth furnace and the GaAs crystal growth in various orientations is now in progress. A significant part of this analysis will be performed in collaboration with Prof. R.A. Brown of MIT.

The series of earth-based growth experiments described is now in progress and the microgravity growth runs will proceed when the Space Shuttle flights are resumed.

This comparative study should increase our understanding of the effect of convective flow on crystal growth in general and of GaAs growth in particular. The inhomogeneous impurity distribution and high defect density is a matter of great concern to the GaAs integrated circuits and opto-electronic device industries. We have already shown that magnetic damping of convective flow improves the homogeneity and reduces the defect density of earth-grown GaAs crystals. A direct comparison of the effect of free convective flow to magnetic damping and to the stabilization of the instantaneous growth rate under microgravity should prove valuable.

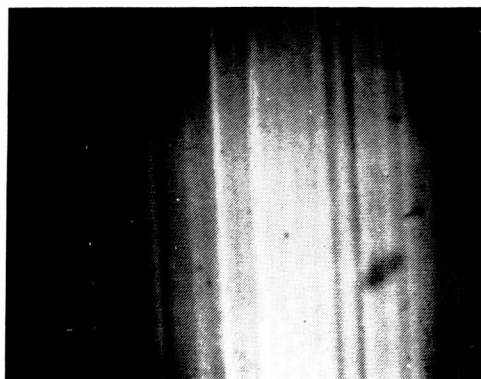
## REFERENCES

1. A.F. Witt, H.C. Gatos, M. Lichtensteiger, M.C. Lavine, and C.J. Herman, J. Electrochem. Soc., 122, 276 (1975).
2. A.F. Witt, H.C. Gatos, M. Lichtensteiger, C.J. Herman, J. Electrochem. Soc., 125, 1832 (1978).
3. J.A. Kafalas in "Gallium Arsenide Technology," David K. Ferry, Editor, pp 70-72, Howard W. Sams & Co. (1985).
4. K. Terashima, T. Katsumata, F. Orito, T. Kikuta and T. Fukuda, Jap. J. Appl. Phys., 22, L325 (1983).
5. K. Terashima and T. Fukuda, J. Cryst. Growth, 63, 423 (1983).
6. T. Fukuda, K. Terashima, T. Katsumata, F. Orito, S. Ozawa, T. Obokata and T. Sato, paper presented at Sixth American Conference on Crystal Growth, Atlantic City, NJ, July 1984.
7. J. Osaka and K. Hoshikawa, paper presented at Third Conference on Semi-Insulating III-V Materials, Kah-nee-tah, Warm Springs, OR, April 1984.

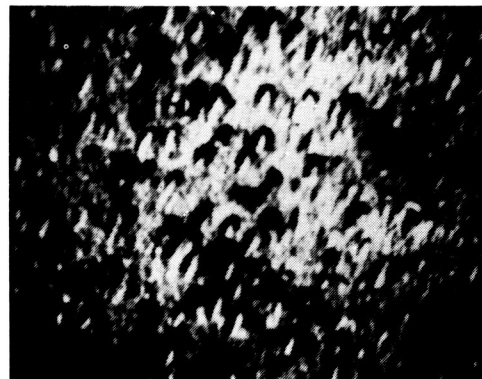
## BIBLIOGRAPHIES

1. "A Comparative Study of the Effect of Bouyancy-Driven Fluid Flow on GaAs Crystal Growth," J.A. Kafalas and A.H. Bellows, 6th Eur. Symp. on Mater. Sci. Under Microgravity, Bordeaux, France (1986).
2. "The Use of Selective Pair Luminescence to Characterize Semi-Insulating GaAs," J.A. Kafalas, E.S. Koteles, S. Zemon and P. Norris, 13th Int. Symp. on GaAs and Related Compd., Las Vegas (1986).
3. "Stability of the EL2 Center in GaAs Under Electron-Hole Recombination Conditions," J.A. Kafalas, M. Levinson and C.D. Coombs, Phys. Rev. B34, p. 4358 (1986).
4. "Configurational Site Symmetries of the EL2 Center in GaAs," J.A. Kafalas and M. Levinson, to be published.
5. "The Comparative Study of the Influence of Convection on Gallium Arsenide Growth," J. Gustafson, A. Bellows and J. Kafalas, Proc. of 2nd Pathways to Space Exp. Workshop, Orlando, FL (June 1986).

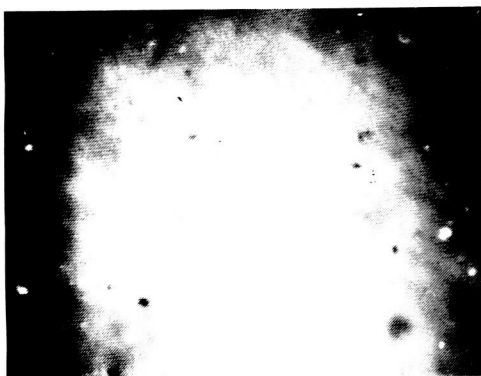
ORIGINAL PAGE IS  
OF POOR QUALITY



Striations at zero field



EDP at zero field



Absence of striations at 2000 G



EPD at 2000 G

Figure 1. Comparison of striations and Etch Pit Densities in "field-off" and "field-on" regions of a crystal.

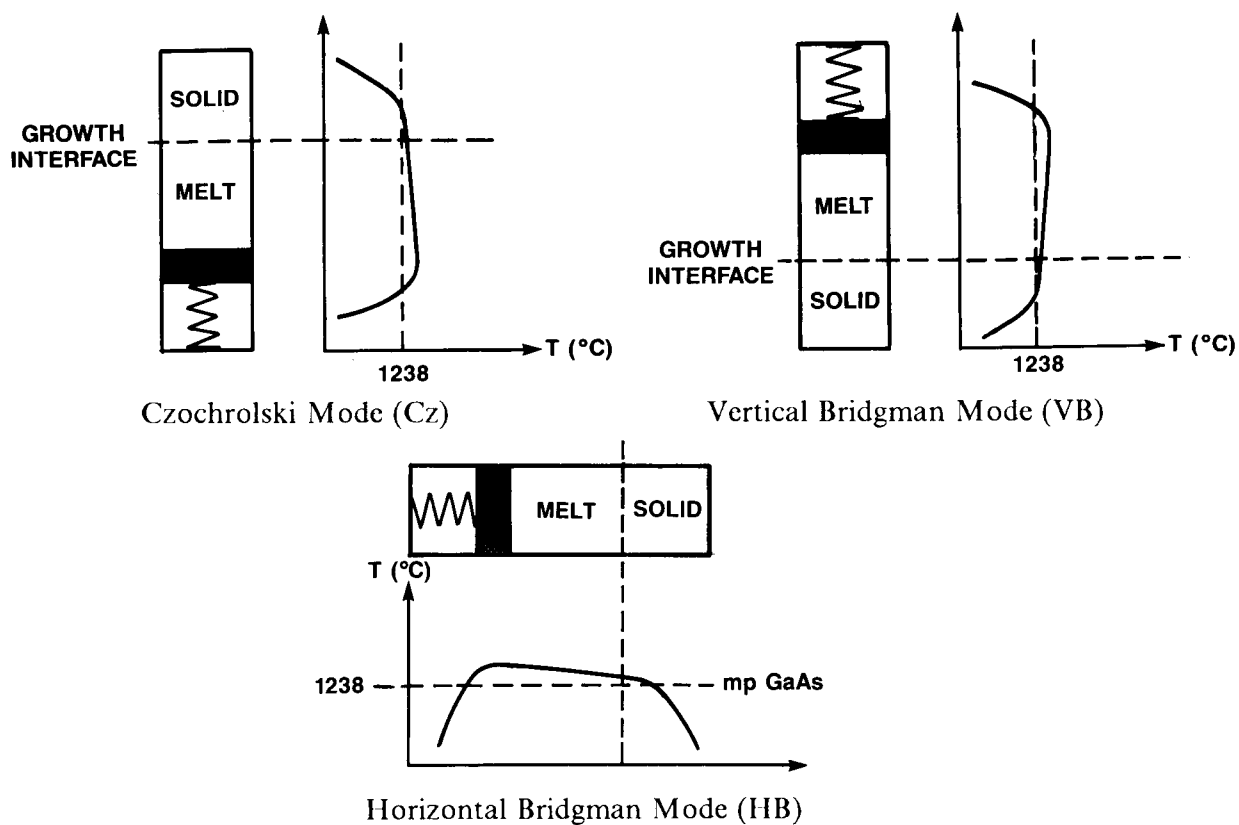


Figure 2. Schematic of the 3 different terrestrial growth orientations with the corresponding temperature gradients.

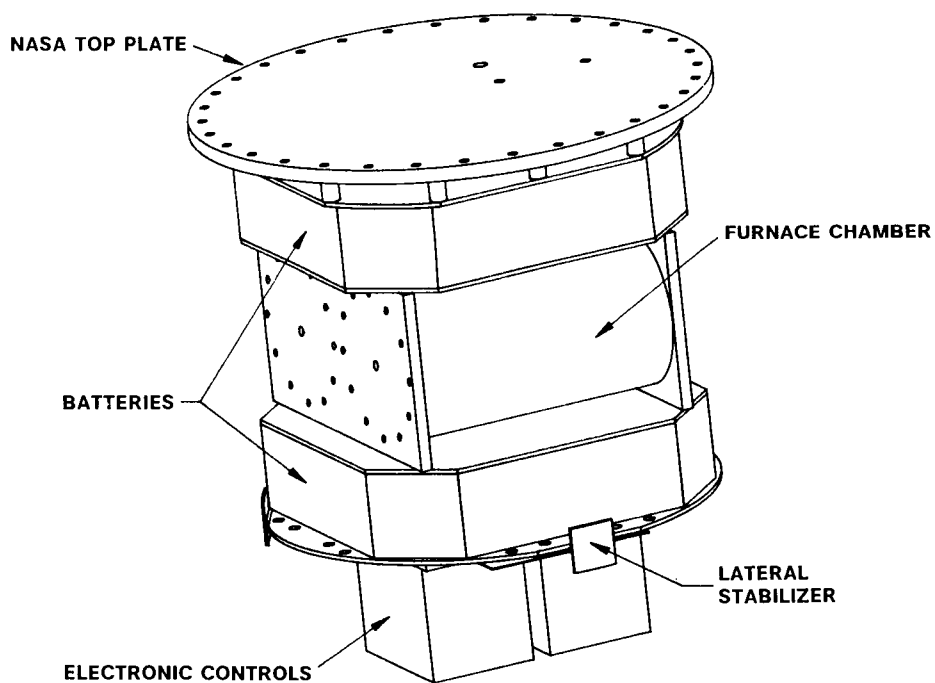


Figure 3. GAS payload for GaAs crystal growth.

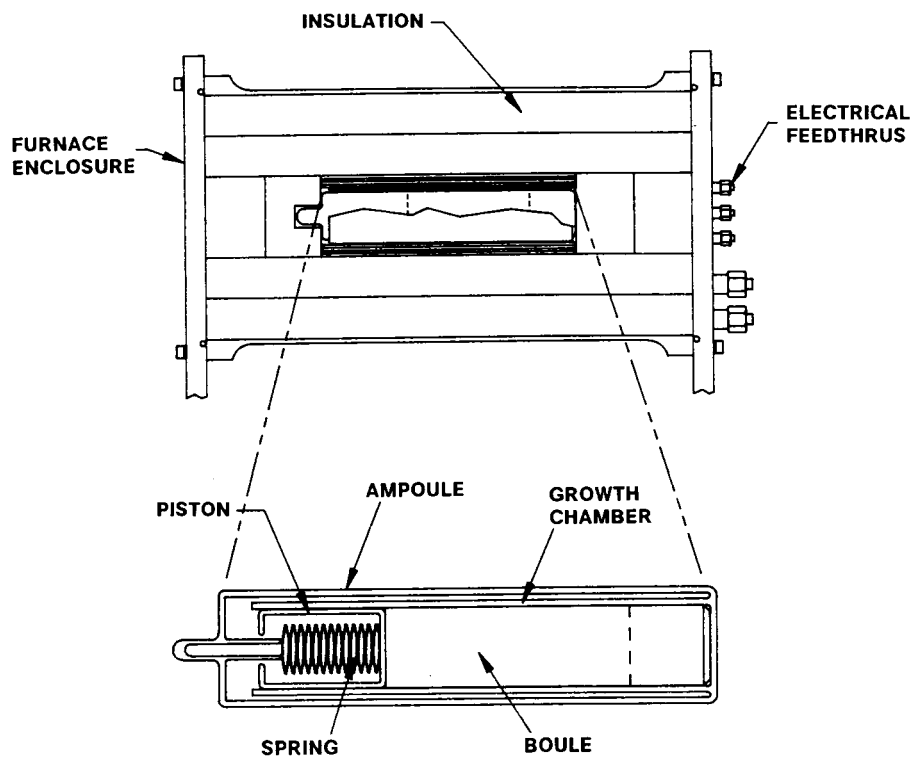


Figure 4. Section view of cylindrical growth furnace and enlarged section of double walled growth ampoule.

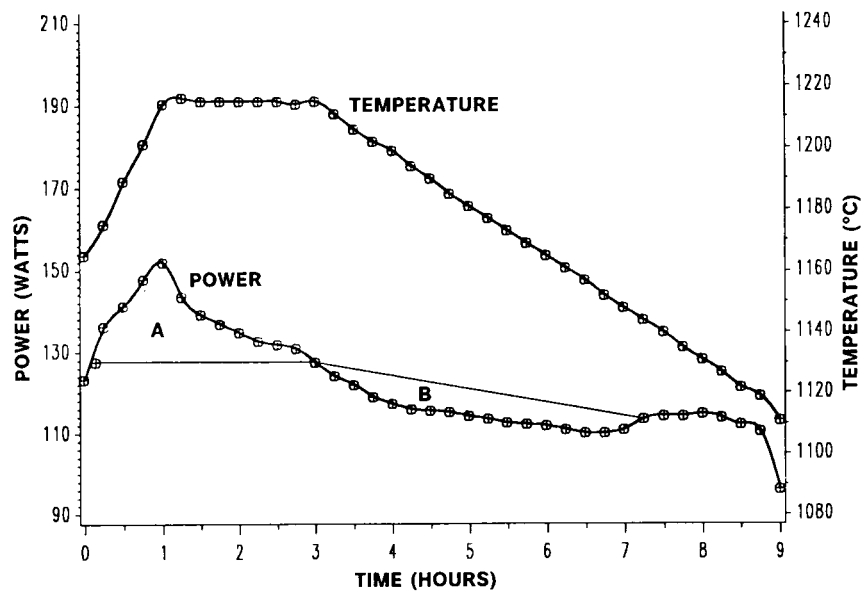


Figure 5. Power vs Time for a typical growth run showing incremental power required to melt boule and equivalent power retrieved during regrowth.

ORIGINAL PAGE IS  
OF POOR QUALITY

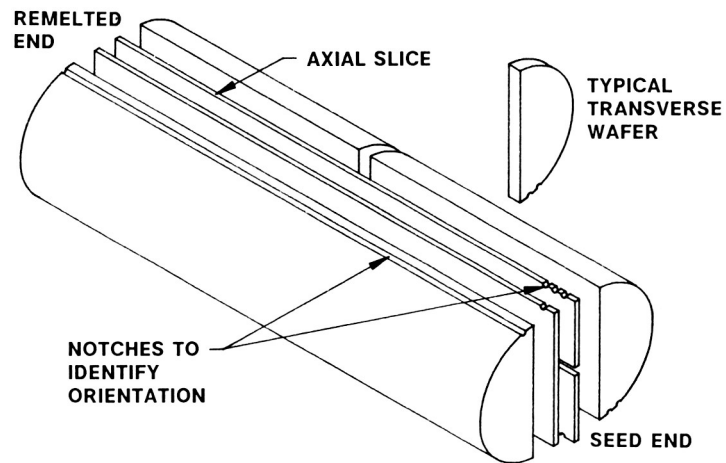


Figure 6. Dicing scheme showing pattern of notches used to permanently indicate orientation of each die.



Figure 7. IR micrograph showing growth striations below the regrowth boundary and evidence of uniform growth above the boundary.

MICROGRAVITY SCIENCE REVIEW

AT

NATIONAL AERONAUTICS & SPACE ADMINISTRATION  
GEORGE C. MARSHALL SPACE FLIGHT CENTER  
MARSHALL SPACE FLIGHT CENTER, ALABAMA 35812

February 10 - 12, 1987

GROWTH OF GaAs CRYSTALS FROM THE MELT IN A  
PARTIALLY CONFINED CONFIGURATION

(Contract No. NAS8-36604)

Submitted by  
Professor Harry C. Gatos  
and  
Dr. Jacek Lagowski  
Department of Materials Science and Engineering  
Massachusetts Institute of Technology  
Cambridge, Massachusetts 02139

**PRECEDING PAGE BLANK NOT FILMED**



### Abstract

Our experimental approach has been directed along two main goals (1) the implementation of a novel approach to melt growth in a partially confined configuration; and (2) the investigation of point defect interactions and electronic characteristics as related to thermal treatment following solidification and stoichiometry. Significant progress has been made along both fronts. Crystal growth of GaAs in triangular ampuls has already been carried out successfully and consistent with our model. In fact, pronounced surface tension phenomena which cannot be observed in ordinary confinement systems have been identified and should permit the assessment of Maragoni effects prior to space processing. Regarding thermal treatment, we have discovered that the rate of cooling from elevated temperatures is primarily responsible for a whole class of defect interactions affecting the electronic characteristics of GaAs and that stoichiometry plays a critical role in the quality of GaAs.

## INTRODUCTION - MOTIVATION

The advantages of near-zero gravity conditions in materials processing in general and solidification (crystal growth) in particular have been demonstrated, at least qualitatively, in a limited number of rather primitive experiments. Valid questions, however, have been raised and remain unanswered regarding the consequences of total confinement of the melt prior to solidification (i.e., stresses resulting from volume expansion during solidification, contamination of the melt surface, and others). Total confinement could also have obscured the study of the effects of surface-driven convection (Marangoni effect) which continue to be a fundamental issue regarding materials processing in space.

An additional issue became critically evident following the analysis of the results of experiments carried out in space. The effects of near-zero gravity conditions can be quantitatively assessed only if reliable approaches and techniques are available for characterization of the system in question on earth and following processing in space. Furthermore, it is imperative that ground research addresses the study and control of all experimental parameters and conditions which could possibly interfere with the identification and assessment of the zero gravity effects and/or lead to artifacts attributable to space processing.

It was with the above questions in mind that we entered into our present program. We also gave critical consideration to the choice of the material. We chose a material which would permit the optimization of the scientific benefits resulting from the elimination of convective interference. In addition, we considered it important to address the potential technological impact that these scientific benefits might have.

## THE MATERIAL

We have chosen GaAs to grow in single crystal form from the melt:

The defect structure of this semiconductor presents immense challenges regarding the nature and origin of defects, their interactions, and their effects on the critical electronic properties. The understanding of the effects of stoichiometric variations, commonly present in GaAs, is severely interfered with by gravity-induced convection during solidification. In turn, convective effects on classical segregation kinetics are usually obscured by stoichiometry variations. The defect structure and segregation kinetics influenced by thermal convection are at the same time substantively affected by Fermi statistics.

GaAs, because of its high electron mobility and direct energy gap, is the most important semiconductor for a broad spectrum of applications in optoelectronic and ultra high speed energy circuits. Next to silicon, GaAs is developing to be the most widely used semiconductor. In fact, GaAs technology is now entering the early stages of exploiting the great potential of this material. Future progress will depend on achieving crystals with reproducibly controlled defect structure to meet the increasing needs of device processing.

## BACKGROUND

The following major reasons precluded the consideration of a total confinement configuration (use of a cylindrical ampul confining the melt to be solidified) for the growth of semiconductor crystals: (1) The observation of a network of ridges at the surfaces of the InSb crystals grown under total confinement in the Skylab mission (Fig. 1). The presence of such ridges interferes with the study of certain aspects of the growth process. (2) Volume expansion upon solidification in the case of semiconductors leads to stresses

which interfere severely with the study of the defect structure by controllable growth conditions (thermal gradients, growth rates, cooling rates, and others). (3) The study of surface tension effects cannot be addressed if the entire surface of the melt is in contact with the confining walls of the container. (4) We have discovered in our ground-based research that stoichiometric variations are caused by thermal convection and lead to impurity segregation which is totally unrelated to the accepted classical segregation kinetics. For example, in the case of Ge and Si impurities, convective currents (stoichiometric fluctuations) lead to fluctuation in the occupation of the Ga and As sites rather than in the overall concentration of these elements in the crystal (Fig. 2). Thus, control of stoichiometry is imperative in the study of GaAs crystal growth; precise stoichiometry control can be achieved by controlling the As partial vapor pressure over the melt during solidification. Such control is obviously impossible in a total confinement configuration.

#### THE EXPERIMENTAL APPROACH

The experimental approach has been directed along two main goals: (a) the implementation and study of a novel configuration for crystal growth under partial confinement, and (b) the investigation of native defects interactions and the key electronic characteristics (carrier concentration and carrier mobility) as related to the thermal cycle following solidification and to stoichiometry .

##### Partially Confined Configuration

The novel partially confined configuration conceived for the growth of GaAs crystals from the melt in space is shown schematically in Fig. 3. The melt resulting from a cylindrical charge is confined in a triangular prism. In the absence of gravity the surface energy of the melt is minimized

by acquiring a cylindrical shape. The key features of this new configuration are as follows:

1. The melt is only partially confined, i.e., the contact area between the walls of the container and the melt is minimized.
2. Large free surface of the melt and the large empty space assure efficient control of the melt composition through the melt interaction with arsenic vapor.
3. Large empty space in the container is beneficial for accommodation of the volume expansion (vll%) taking place upon solidification of GaAs.

The growth ampul is made of quartz or pyrolytic boron nitride. Upon proper surface preparation, both of these materials exhibit highly desired non-wetting characteristics. Utilization of quartz leads to Si contamination; however, this process can be effectively suppressed by oxygen added into the growth ampul.

A Horizontal Bridgman (HB) apparatus constructed for the growth of GaAs in standard boats (Figures 4 and 5) has been adapted for our ground-based experiments with the partially-confined configuration. The apparatus has three temperature zones for achieving the desired temperatures and temperature gradients. The low temperature zone which determines the partial pressure of As over the melt is controlled by a heat pipe which leads to excellent temperature control. It should be pointed out that in this HB apparatus the viewing port to facilitate seeding has been eliminated to minimize thermal symmetry and thus minimize gradient-driven convection in the melt.

#### Defect Interactions Related to the Rate of Cooling

We have designed and constructed experimental facilities for the fast cooling of GaAs crystals from very high temperatures (about 1200°C) and also for annealing GaAs crystals at lower temperatures (in the vicinity of 800°C). In both instances the As vapor pressure over the crystal is being controlled

and maintained under near equilibrium conditions to avoid thermal etching during heat treatment or other adverse effects.

Facilities for cutting, polishing and etching of GaAs are available in our laboratory. In addition, a wide spectrum of characterization facilities has been developed for the characterization of GaAs crystals on a micro- and macro-scale. These facilities include Hall effect measurements (over a wide range of temperatures), deep level transient spectroscopy (DLTS), photo-DLTS, infrared absorption, photoluminescence, and electron beam induced current (EBIC) spectroscopy.

## RESULTS

We have carried out a series of preliminary experiments using triangular prismatic containers of BN with the side of the triangular cross section being 3 mm long. They were positioned vertically on a strip heater to minimize the effect of gravity on the lateral filling of the containers. Low melting point metal alloy wires (Pb-In-Sn) were inserted into the cavity. The wires were heated from the bottom (free ends). In all instances, upon solidification, the triangular cavity was not completely filled.

In the light of the above preliminary experiments we proceeded with the construction of triangular quartz prisms in which a cylindrical charge of GaAs with a cross-section diameter of 4 mm could be inserted (Fig. 6). Growth experiments were carried out in the HB apparatus by traversing the prismatic container through the appropriate thermal gradients.

The results of the first trial experiments are very gratifying. As shown in segments of Fig. 6, even in the Horizontal Bridgman configuration the GaAs melt does not fill the entire cavity, provided the internal surfaces of the

prismatic container are properly prepared. As a result, an equilibrium As pressure is maintained over the melt.

These crystals exhibit excellent electronic characteristics (as good as we have achieved in our HB apparatus using conventional boats). In addition, however, striking surface tension phenomena were revealed. These phenomena are of an oscillatory nature. The observed oscillations had three different spacings: about 1 mm, 100  $\mu\text{m}$ , and 10  $\mu\text{m}$  (Figures 7 and 8 ).

Analysis of these oscillations was carried out by chemical etching and photoluminescence. Some results are shown in Figures 9 through 12 . It is seen that the surface morphology oscillations are clearly reflected in the chemical (etching) and electronic (photoluminescence) characteristics of the material. These results are quite recent, and their analysis is still not complete. It appears, however, that they are most likely surface tension driven from variations in surface tension which may originate in variations in melt composition and/or thermal gradients. Very preliminary and qualitative modeling shows that even small changes in surface tension can lead to substantive changes in the contact angle and thus to a cross section area of the melt. In fact, in Table I we present the results of estimated changes in surface tension which can lead to oscillation of the type observed in the crystals. (see also Figures 13, 14, and 15).

In the near future we plan to continue our growth experiments with emphasis on the effect of stoichiometry on the melt as controlled by the As partial pressure. Since the As ambient minimizes contamination of the melt surface, it is expected that small variations in the stoichiometry of the melt should result in substantive variations in surface tension. In addition, we intend to introduce contaminants (e.g., oxygen) in the gas phase to study the effects of such contaminants on surface tension phenomena. We are hopeful that we will

be able to attain experimentally an assessment of the effects of surface tension variations.

In parallel with the growth experiments we pursued the investigation of the cooling cycle on the final properties of GaAs crystals. In accord with our previous results we found that the cooling cycle has a profound effect on the key properties of GaAs such as resistivity, carrier concentration, carrier mobility, excess carrier lifetime, deep level traps, compensation, thermal stability, macro- and microscopic uniformity, and dislocation density.

We also found that cooling-related processes may obscure the identification of solidification-related phenomena, and they could be mistaken for segregation-related growth velocity effects.

In our experimental approach we compare crystals grown under different solidification rates with those solidified at the same rates but subjected to a different cooling rate. We concluded that the cooling rate is a far more relevant parameter than the solidification rate.

We also utilized growth in magnetic fields to identify properties affected by solidification (some results are shown in Fig. 16).

A dramatic illustration of the importance of a cooling cycle is provided by ITC GaAs, a new type of GaAs with inverted thermal conversion, which is obtained by fast cooling of a GaAs crystal from 1200°C (Fig. 17 ). A detailed discussion of this material discovered in our laboratory in the course of this study appeared in a recent publication (Appl. Phys. Letters 49, 892 (1986)).



## SUMMARY

Our novel partially confined configuration for the growth of GaAs single crystals in space has been extensively tested on the ground. Even on the ground growth proceeds with a substantial fraction of free surface. We expect that in space our configuration will approach levitation conditions with perfectly controlled ambient. In the light of the results to date we will be able to study crystal growth parameters without interference, not only from gravity driven convection, but also from confining walls. Furthermore, it will be possible to investigate in semiconductor growth the effects of surface driven variations.

Table I

INHOMOGENEITIES IN GaAs GROWN  
UNDER PARTIAL CONFINEMENT

	Inhomogeneities		Estimated Surface Tension Fluctuations	
	Magnitude $\delta R/R$	Spacing	Magnitude $\delta \gamma/\gamma$	Period
Macroscopic <sup>(a)</sup>	5%	1 mm	5%	10 min
Intermediate <sup>(b)</sup>	<0.3%	50-100 $\mu\text{m}$	<1%	0.5-1 min
Microscopic <sup>(c)</sup>	--	10-20 $\mu\text{m}$	--	4-15 s

(a) Seen as changes in crystal diameter, R.

(b) Seen in photoluminescence and differential etching.

(c) Seen in differential etching.

## FIGURE CAPTIONS

- Figure 2. Electron concentration and ionized impurity microprofiles of Si-doped melt-grown GaAs. (a) and (b) correspond to different segments of the same crystal.  $n$  is the net free electron concentration,  $N_A$  is the concentration of Si in As sites, and  $N_D$  is the concentration of Si in Ga sites.  $N_A + N_D$  is total Si concentration. Note that variations in  $n$  are not necessarily related to variations in  $N_A + N_D$ .
- Figure 3. Schematic representation of the partially-confined configuration in Horizontal Bridgman mode including the corresponding temperature profiles.
- Figure 4. Horizontal Bridgman growth apparatus and thermal profile (top). The quartz ampul contains the As source, 1; a breakable seal, 2; and seal breaking weight, 3; the quartz diffusion barrier, 4; a quartz boat, 5; the GaAs seed crystal, 6; and polycrystalline GaAs, 7.
- Figure 6. Top segment quartz triangular prisms containing GaAs cylindrical charge; sandblasting the internal surfaces causes the upper prism to be opaque.  
Middle segment Portion of the GaAs crystal after growth; the cylindrical seed and the grown crystal are clearly delineated.  
Bottom segment Cross section of crystal grown in the triangular prism container. On the left-hand side it is apparent that the melt wetted the container; on the right-hand side growth took place under clean conditions.
- Figure 7. Oscillations on as-grown crystal (spacing about 1 mm).
- Figure 8. Schematic representation of oscillations on crystals.
- Figure 10. Oscillations revealed by profilometer scanning.
- Figure 11. Oscillations revealed by profilometer scanning.
- Figure 12. Photoluminescence scanning revealing oscillations in crystals grown in partially confined configuration.

- Figure 13. Representation of contact angle of melt with quartz container.
- Figure 14. Representation of various contact angles of melt with quartz container.
- Figure 15. Illustration of surface tension changes and its effects.
- Figure 16. Compensation ratio (carrier mobility) in crystal grown with magnetic field turned on periodically. The as-grown crystal exhibits no effects of the magnetic field. Upon annealing at 850°C the effects of the magnetic field become quite evident. Another manifestation of the dominant role of defect structure in GaAs.
- Figure 17. Low-temperature (4.2 K) optical absorption spectra of n-type melt-grown GaAs in the spectral range of photoionization and intracenter transitions of the occupied EL2 donor. (a) As-grown crystal, (b) ITC crystal, i.e., after annealing at 1200° C for 16 h and quenching. Note elimination of EL2 absorption.

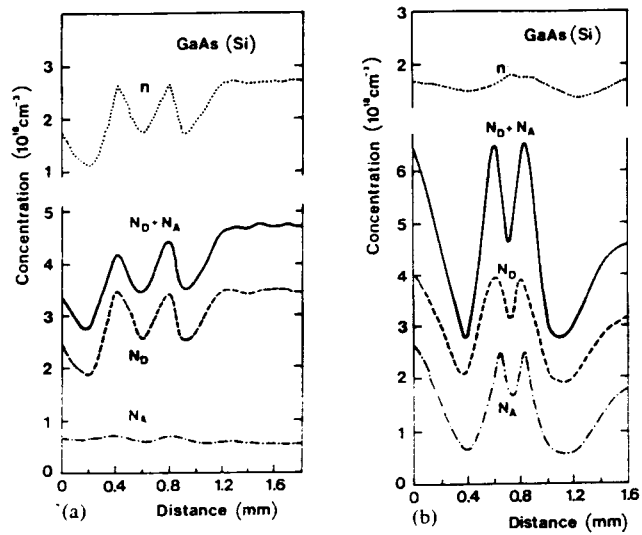


Figure 2.

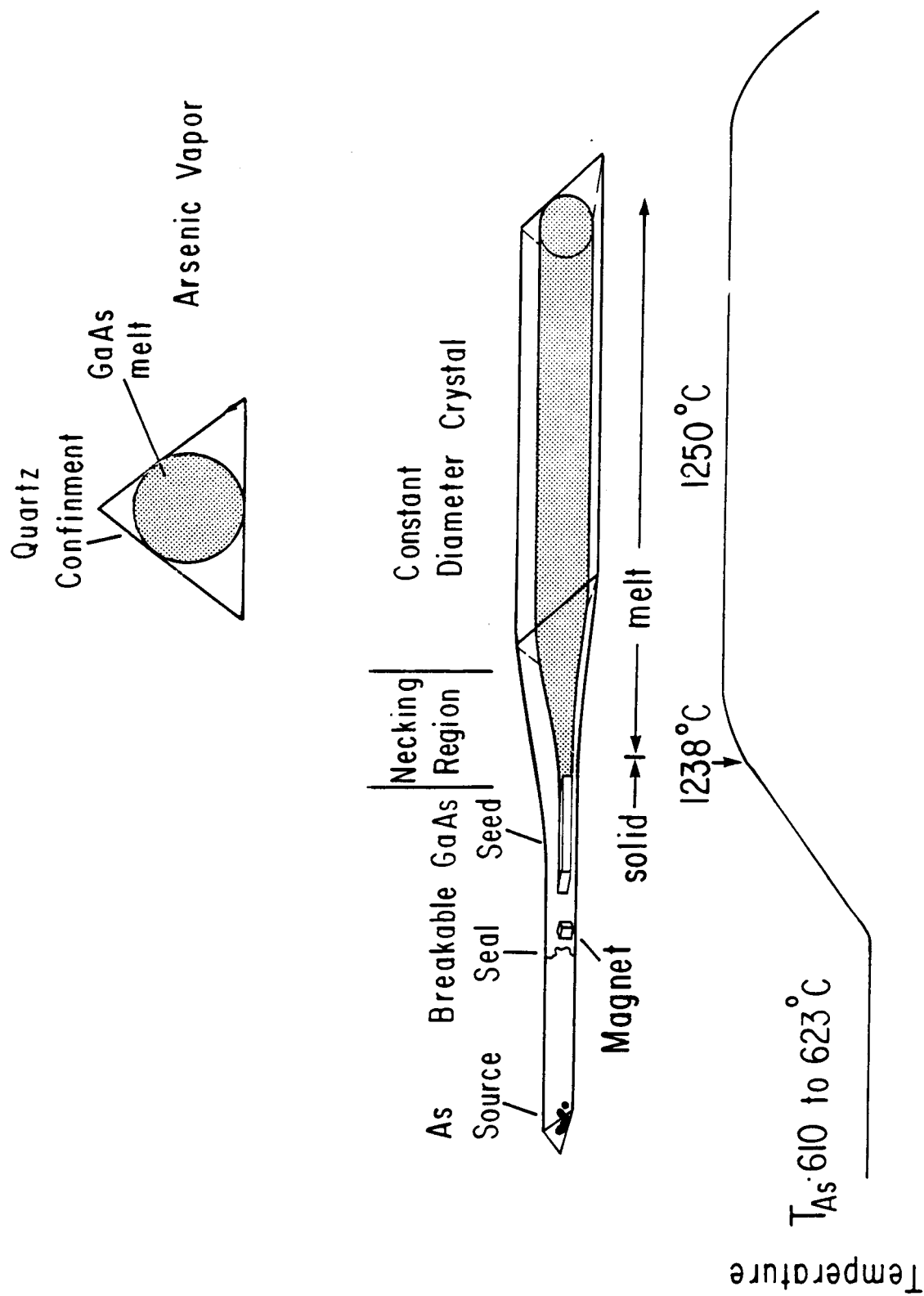


Figure 3.

ORIGINAL PAGE IS  
OF POOR QUALITY

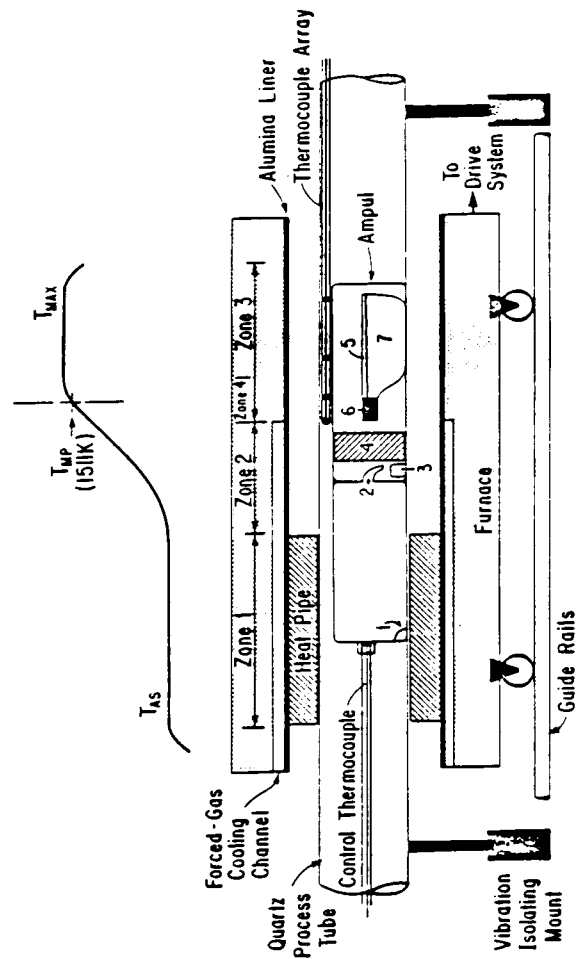


Figure 4.

ORIGINAL PAGE  
BLACK AND WHITE PHOTOGRAPH

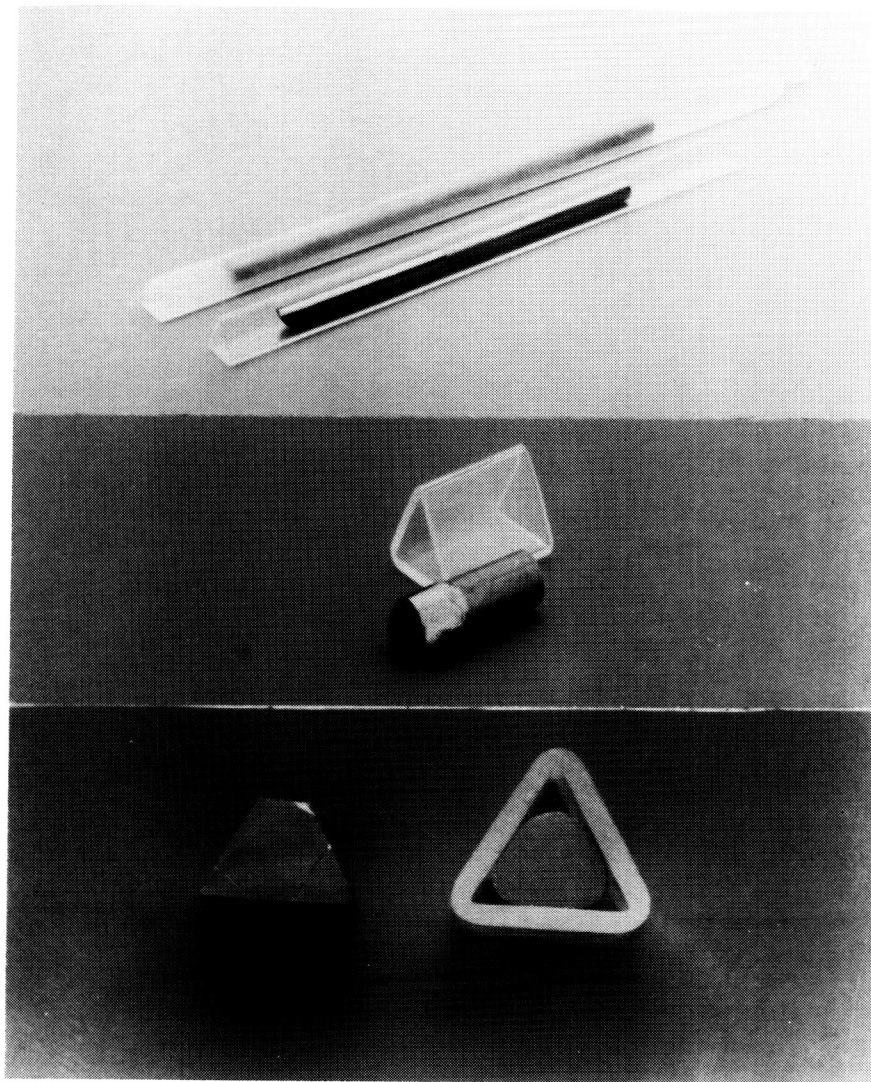


Figure 6.



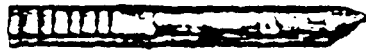


Figure 7.

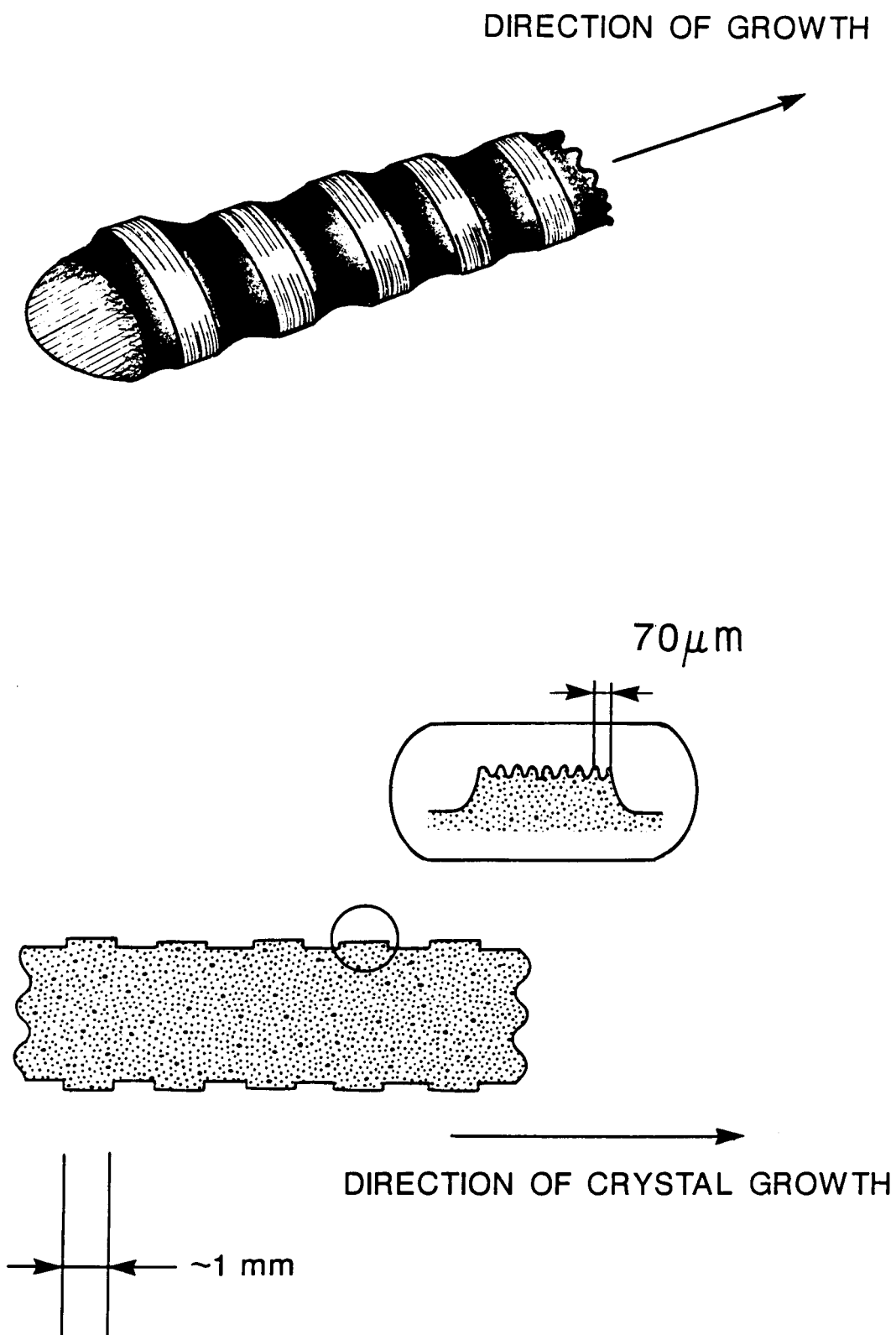


Figure 8.

ORIGINAL PAGE 11  
OF 14 IN PLASTIC

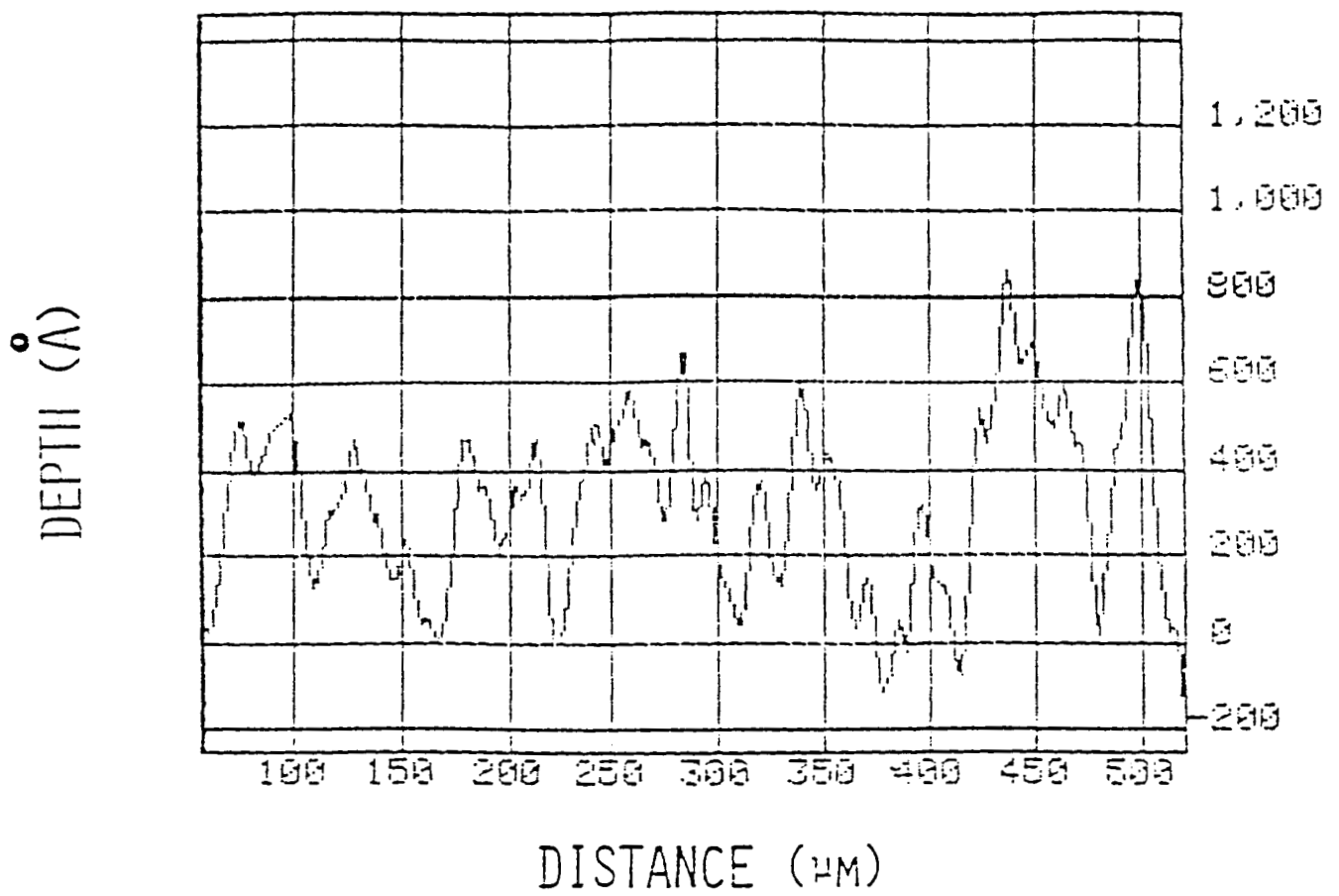


Figure 10.

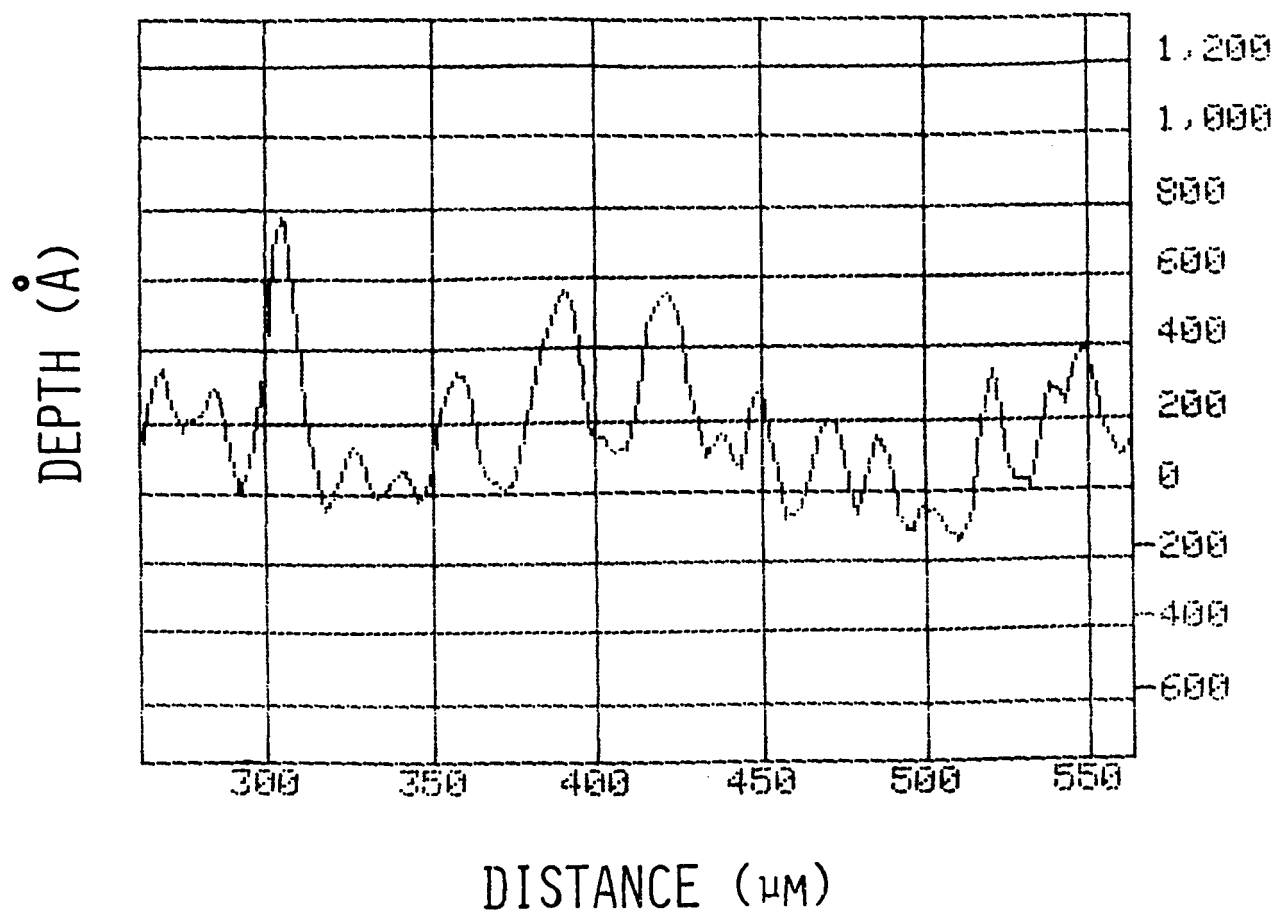


Figure 11.

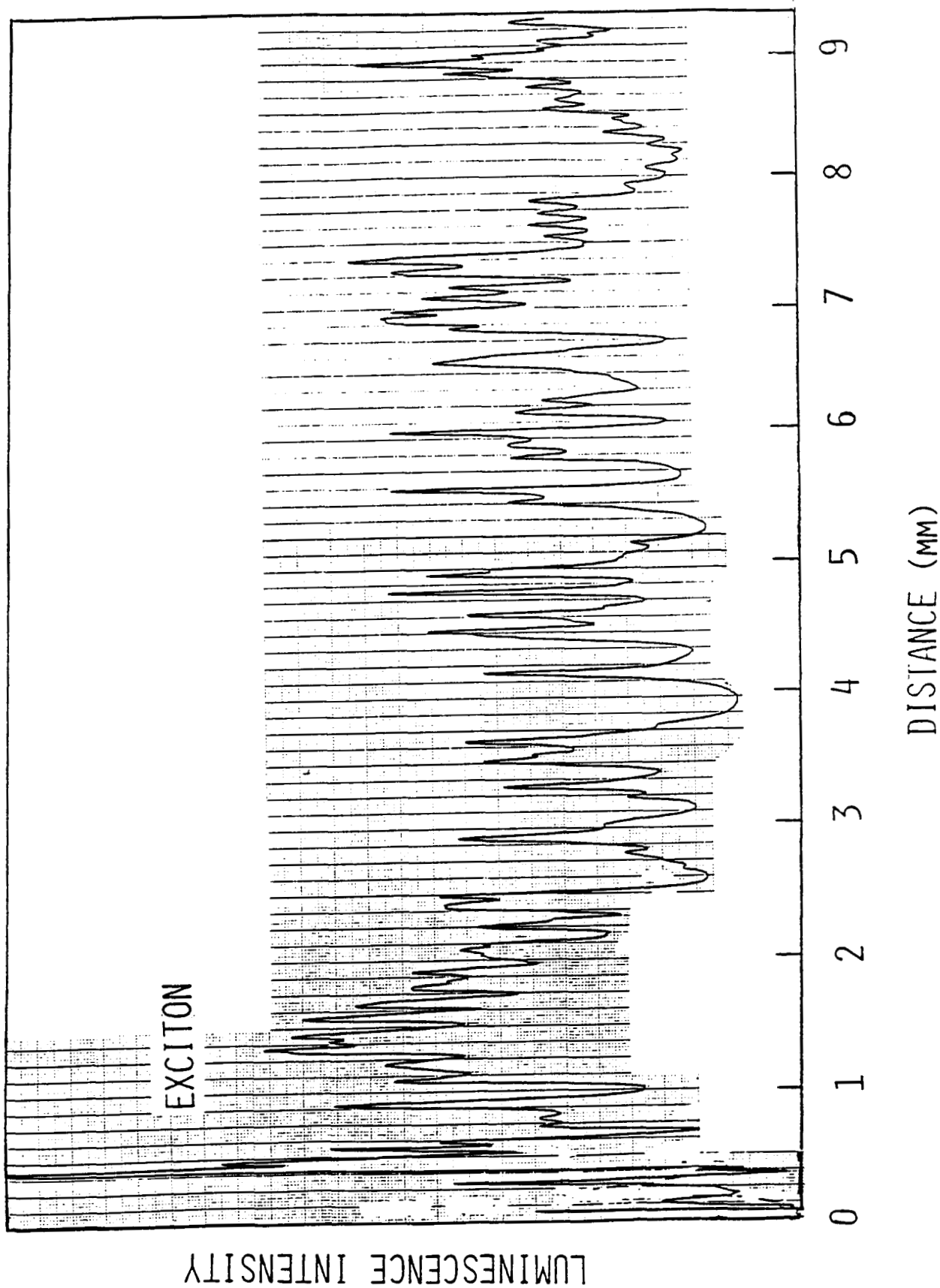


Figure 12.

L/A - LIQUID/AMBIENT

S/L - SOLID/LIQUID

S/A - SOLID/AMBIENT

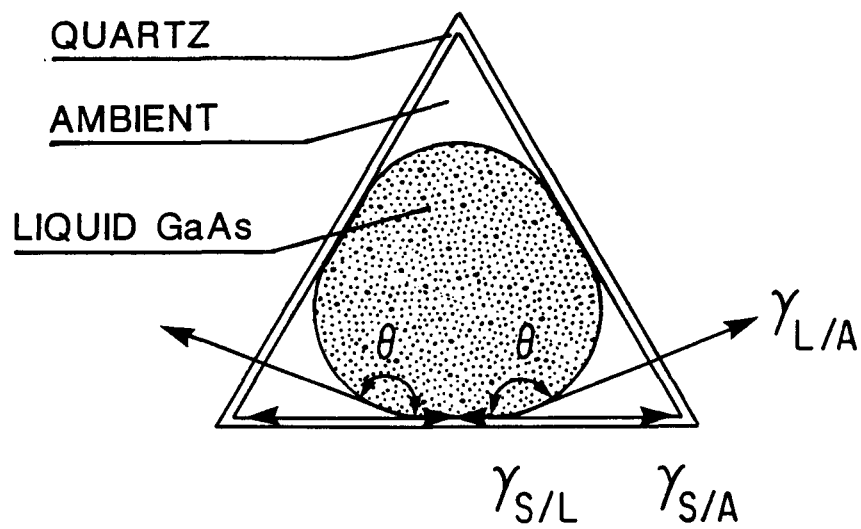
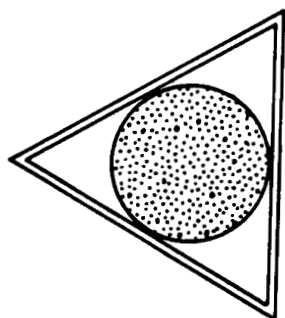
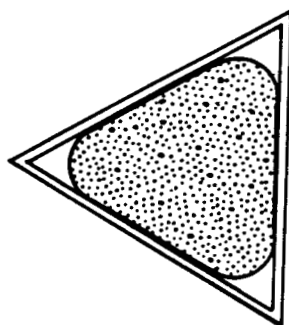


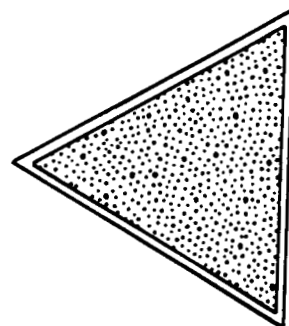
Figure 13.



(a)



(b)



(c)



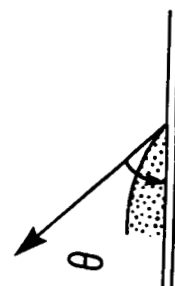
$$\gamma_{L/A} \gg \gamma_{S/A} - \gamma_{S/L}$$

$$\theta \sim 180^\circ$$



$$\gamma_{L/A} > \gamma_{S/A} - \gamma_{S/L}$$

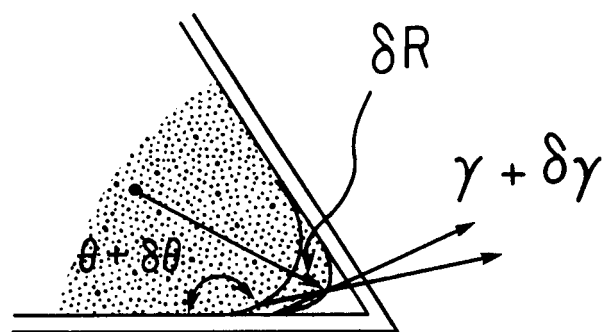
$$\theta > 90^\circ$$



$$\gamma_{L/A} < \gamma_{S/A} - \gamma_{S/L}$$

$$\theta < 90^\circ$$

Figure 14.



A small change in  $\gamma$  will change the contact angle,  $\theta$  and the cross section of the liquid column

$$\frac{\delta R}{R} \simeq - \frac{\delta \gamma}{\gamma} \cos \theta$$

Figure 15.



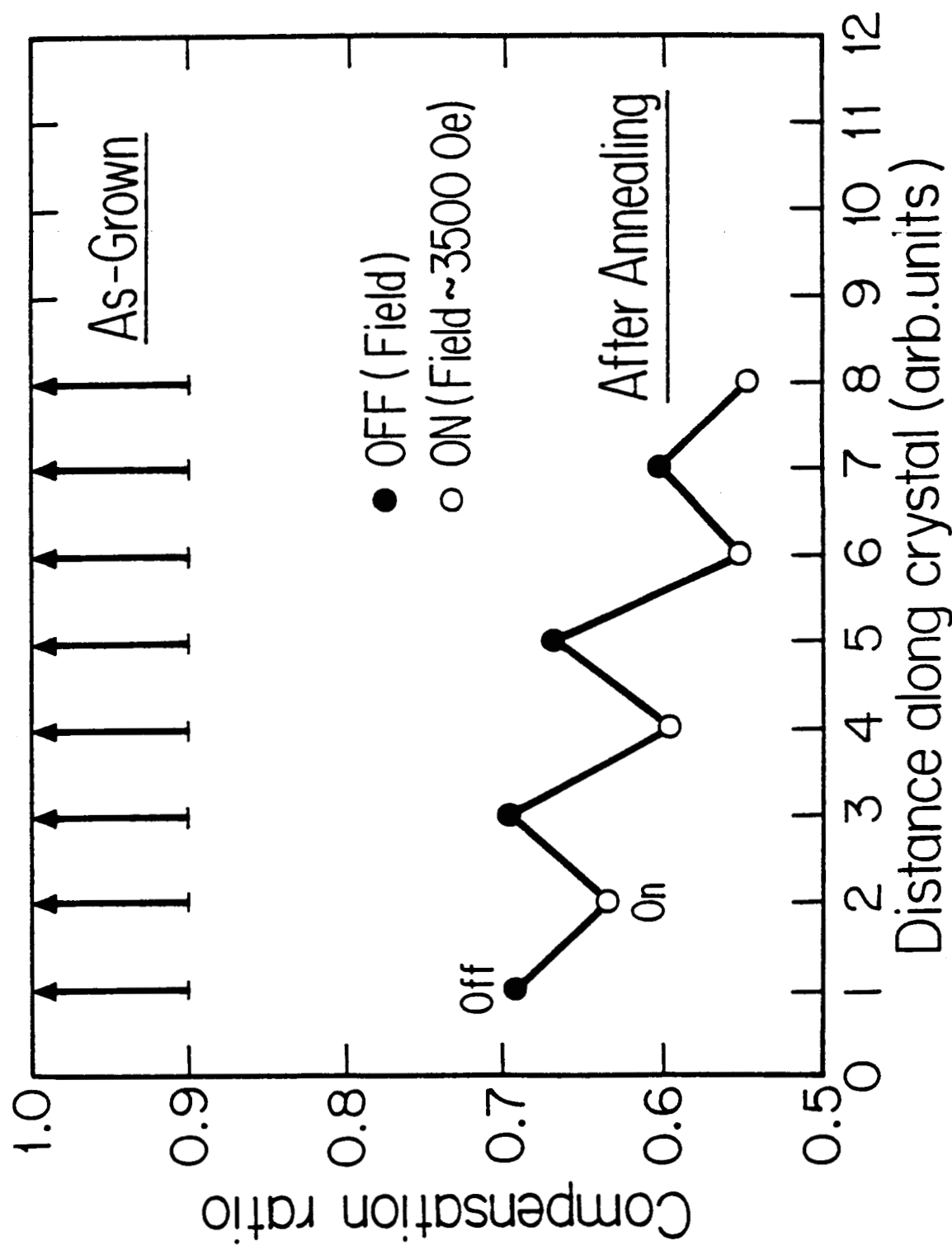


Figure 16.

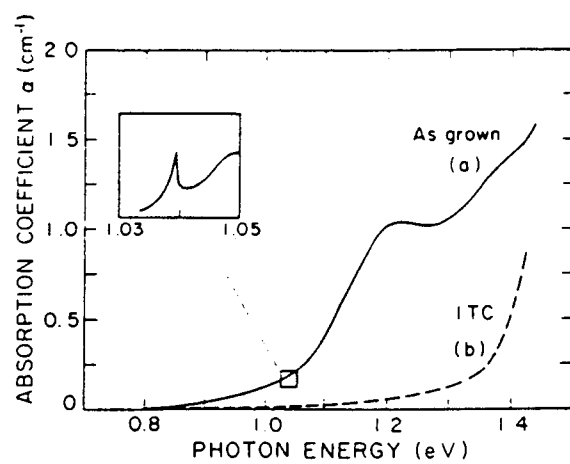


Figure 17.

## Growth of Solid Solution Single Crystals

S. L. Lehoczky and F. R. Szofran

Space Science Laboratory  
NASA Marshall Space Flight Center  
Huntsville, AL 35802ABSTRACT

Based on the thermophysical properties of  $\text{Hg}_{1-x}\text{Cd}_x\text{Te}$  alloys, the reasons are discussed for the failure of conventional Bridgman-Stockbarger growth methods to produce high quality homogeneous crystals in the presence of Earth's gravity. The deleterious effects are considered which arise from the dependence of the thermophysical properties on temperature and composition and from the large amount of heat carried by the fused silica ampules. An improved growth method that we have developed to optimize heat flow conditions is described and experimental results are presented. The problems associated with growth in a gravitational environment are discussed. The anticipated advantages of growth in microgravity are given and the implications of the requirements for spaceflight experiments are summarized.

PRECEDING PAGE BLANK NOT FILMED

## Growth of Solid Solution Single Crystals

S. L. Lehoczky and F. R. Szofran

Space Science Laboratory  
NASA Marshall Space Flight Center  
Huntsville, AL 35802

### Introduction

The technological utility[1] and the scientific interest[2-7] in  $\text{Hg}_{1-x}\text{Cd}_x\text{Te}$  have been well documented. Likewise, the difficulty in growing bulk, compositionally homogeneous material by directional solidification is widely recognized[2,5-9]. In this paper, we discuss the reasons that Bridgman and related directional solidification methods normally fail in the presence of Earth's gravity and show that in such a gravitational environment it is nearly impossible to grow crystals that are both radially and axially homogeneous for significant crystal lengths. Because the HgTe-rich component rejected during solidification is more dense, the vertical Bridgman-Stockbarger growth process would appear to be both gravitationally and thermally stable against convection, but this is not generally true. Due to the peculiar relationships between the thermal conductivities of the melt, solid, and ampule, it is practically impossible to completely avoid radial temperature gradients in the growth region[2]. Thus, in spite of the stabilizing influence of the solutal density gradient, significant thermosolutally driven fluid flow occurs in a narrow region near the interface[10]. It is expected that under reduced gravity conditions,  $g \lesssim 10^{-5} g_0$ , such flows can be significantly suppressed to yield a corresponding reduction in the associated radial composition gradients in the solidified crystals.

In general, the presence of radial temperature gradients near the growth region will cause a curvature in the solid-liquid interface which need be neither an isothermal nor an isoconcentrational surface. Furthermore, the growth of high quality crystals usually requires a slightly convex growth interface as viewed from the melt[11]. Under the influence of stable growth conditions, such interface geometries readily lead to lateral alloy segregation because of the tendency of the more dense HgTe-rich liquid to settle at the portions of the surface having the lowest gravitational potential. Because the alloy solidus temperature decreases with increased HgTe content, the interface temperature will be lowered in this region, causing the interface curvature to increase. Although lateral diffusion will tend to drive the interfacial melt compositions to some equilibrium values, most of ground-based melt-growth experiments show large radial compositional variations that are probably

a direct consequence of such an interfacial fluid flow phenomenon[3,5-9,12]. Although growth at very slow rates, under the influence of reduced stabilizing composition gradients and thus non-steady flow conditions, yielded radially more homogeneous ingots[8], no ingots could be obtained by the Bridgman-Stockbarger method that were simultaneously axially homogeneous for any length. In this paper, we discuss a method that we have developed and used to obtain various desired interface shapes in  $\text{Hg}_{1-x}\text{Cd}_x\text{Te}$  and other II-VI solid solution alloys. It is expected that the method, when combined with reduced stratification effects will yield crystals with improved compositional uniformities and reduced line defect densities. Finally, the properties of  $\text{Hg}_{1-x}\text{Cd}_x\text{Te}$  and other similar alloy semiconductors impose some specific requirements on spaceflight hardware and experiment design. These will be discussed, also.

### Conventional Approach to Vertical Bridgman Growth

The conventional Bridgman-Stockbarger method usually uses a wide adiabatic zone between the hot and cold zones of the growth apparatus[11]. This method yields the desired flat isothermal surfaces for situations where the thermal properties of the solid and melt, particularly the thermal conductivity, are the same or where the thermal effects of the ampule can be neglected. Unfortunately, neither of these conditions apply for  $\text{Hg}_{1-x}\text{Cd}_x\text{Te}$ . The thermal diffusivity varies substantially with both composition<sup>x</sup> and temperature[13] and the thermal conductivity of the requisite fused silica ampule is comparable to that of the material[14]. An example of the effect of different thermal conductivities is shown in Fig. 1. Because of the generally higher thermal conductivity in the melt than in the solid, the use of a wide adiabatic zone will produce isothermal surfaces near the interface that are bowed downward into the solid, as shown. Although the interface under this condition will be neither an isothermal nor an isocompositional surface, it will be bowed in the same direction as the isotherms near it. This will lead to the collection of HgTe-rich liquid at the low region of the interface and thus the HgTe-rich centers in radial slices that are generally although not universally[2,15] reported for Bridgman grown  $\text{Hg}_{1-x}\text{Cd}_x\text{Te}$ . This effect has been discussed elsewhere[2].

### An Improved Bridgman Growth Method

During this investigation, we have developed a method for the vertical growth of  $\text{Hg}_{1-x}\text{Cd}_x\text{Te}$  and similar alloys that minimizes the problems with the conventional method outlined above[2,3]. This method depends on the careful control of the radiation heat transfer near the growth interface. This is achieved by using a thin (~4 mm) thermal barrier between the hot and cold zones of the growth apparatus and by the judicious choice of the growth temperatures[2]. Each zone is provided with an isothermal furnace liner (heat pipe) to assure isothermality of the zone. A detailed description of the heat transfer during growth has been given in ref. [2]. There it is shown that the interface can evolve during growth from concave (viewed from the melt) to convex and back to

concave by selection of a proper set of growth parameters. This type of evolution is shown in Fig. 2.

We believe that this method, when used in a microgravity environment, will yield single crystalline material which is simultaneously homogeneous in both the axial and radial directions. The relative simplicity of the method makes it the choice for evaluating the potential benefits of growing  $\text{Hg}_{1-x}\text{Cd}_x\text{Te}$  and similar materials in microgravity.

### Results and Discussion

Over the past several years, we have performed a detailed evaluation of the effects of growth parameters on the axial and radial compositional uniformity in directionally solidified  $\text{Hg}_{1-x}\text{Cd}_x\text{Te}$  and other similar pseudobinary alloys. To obtain a measure of the relative importance of the various heat and mass transfer processes involved, detailed radial and axial composition profiles have been obtained for many ingots. The axial compositional profiles for a series of  $x=0.2$  and  $0.4$  ingots have been deduced from precision density measurements [9,16] and have been described previously. One example is shown in Fig. 3. Additional profiles, including some for  $x=0.6$  ingots, have been measured more recently. All profiles that did not suggest interface breakdown could be fit well by a set of one dimensional diffusion equations [3,8,9,17-19]. Furthermore, the best values ( $4.5 \times 10^{-5}$  to  $6.0 \times 10^{-5} \text{ cm}^2/\text{s}$ ) for the effective diffusion coefficient,  $D$ , did not show any significant growth rate or other growth parameter dependence. Most of the samples grown were 5 mm in diameter and we suspect the effective diffusion coefficient would vary with diameter. Nonetheless, these results suggest that the expected convective flows resulting from curvature in the growth interface and horizontal temperature gradients did not penetrate the entire melt column.

In some ingots, the axial composition profile showed evidence of interfacial breakdown. This was manifested by a sudden increase in Cd content near the last-to-freeze end of the ingot. Because of the strong correlation between this effect and the temperature gradient to growth rate ratio, doubtless the observed effect is due to interfacial breakdown. Either the interface becomes dendritic and convection currents cause the CdTe-rich dendrites to break off and rise to the top of the melt or small, CdTe-rich particles are homogeneously nucleated slightly above the interface and then rise. The latter is possible because the variation in thermophysical properties with composition and temperature permit a condition where the melt is constitutionally supercooled slightly above the interface but not at the interface. For example, the thermal conductivity increases sharply just above the interface [2]; this reduces the temperature gradient away from the interface more rapidly than if the thermal conductivity in the melt were constant.

Extensive infrared transmission edge and x-ray energy dispersion measurements were used to assess the magnitude of radial segregation [3,8,9,12]. The segregation showed a definite growth rate,  $R$ ,

dependence, with the most pronounced effect occurring for the slowest growth rates. This effect is illustrated by the results for two  $x=0.2$  ingots L6 and L7. The radial compositional data for several slices from each ingot are shown in Fig. 4. Both ingots were grown under identical conditions except for the growth rate. L6 was grown at a rate of 2.68 cm/day and had total radial compositional variations of about 0.05 in  $x$  over most of its length. L7 was grown at a rate of 0.59 cm/day and had total variations of less than 0.0025 in  $x$  between 3 and 10 cm from the first-to-freeze end[8]. Similar growth rate dependences have been observed for higher alloy compositions, also.

Several years ago we proposed that the vertical extent of the convective region above the crystal growth interface must be small compared to the effective diffusion length,  $\sim 2D/R$ [12], because of the good fit of the axial compositional variations to a one-dimensional diffusion model as discussed above. A more recent investigation of the similar Ge-Si alloy system by Rouzaud, et al., yielded similar conclusions[20]. Rouzaud, et al. have also shown that these observations are in accord with the results of Hart's[10] stability analysis of saline solutions having stabilizing compositional gradients and horizontal thermal gradients. For our growth conditions the thermal and solutal Rayleigh numbers for the melt near the interface are estimated to be about  $10^4$  and  $10^6$ , respectively. A stability analysis of Hart's type thus implies flow characteristics that may straddle the critical stability curve depending on the choice of the exact growth conditions. In agreement with the conclusions suggested by the experimental results[12], such an analysis also suggests that the extent of the flow region should be about a factor of 10 smaller than the estimated size of the effective diffusion lengths involved. This type of analysis also suggests that for  $g$ -values less than  $10^{-5} g_0$ , the residual flow velocities can be made to be more than a factor of 10 smaller than the proposed interface translation rates ( $\sim 0.4 \mu\text{m/s}$ ).

Coriell and Sekerka[21] have shown that under steady conditions, the radial variation in composition is given by

$$\delta C = C_0 ((k-1)/k) (R/D) \delta z \quad (1)$$

and that  $\delta z$ , the vertical bowing of the interface, is determined by the thermal conditions alone.  $C_0$  is the overall melt composition and  $k$  is the interface segregation coefficient. Assuming the same  $\delta z$ , Eqn.(1) yields a change in  $\delta C$  from ingot L6 to L7 that is about a factor of 5 smaller than the measured value. We thus conclude that the difference in radial segregation between L6 and L7 is probably due to a transition to a time dependent flow regime as  $R$  is reduced and not to the steady state condition considered above. It is worth noting that the temperature distribution at the interface during  $\text{Hg}_{1-x}\text{Cd}_x\text{Te}$  growth is growth rate dependent because of the composition and temperature dependence of the thermophysical properties so that  $\delta z$  is expected to depend on growth rate. Recent numerical simulation of the complete heat flow problem[22] suggests, however, that this effect is probably less significant than

previously assumed[2].

#### Advantages of a Low-Gravity Environment

Frequently, the desirable surface geometry for crystal growth is planar or nearly so. Usually, however, the optimum interface shapes tend to be those that bow slightly into the melt[23] because these shapes are expected to produce ingots with better crystal perfection. While such shapes are difficult to achieve for  $\text{Hg}_{1-x}\text{Cd}_x\text{Te}$ , it can be done with judiciously chosen thermal boundary conditions[3,15]. Nonetheless, such an interface is highly susceptible to interface runaway and usually leads to CdTe enrichment in the center for the same reasons that an interface that is bowed into the solid produces slices with HgTe-rich centers[3,5-9,12].

In microgravity it is expected that the highly desired slightly convex growth surfaces will be easier to maintain because of the reduced tendency for stratification of the denser (HgTe-rich) fluid component. At the same time, the near-elimination of radial temperature gradient driven convection is expected to provide for a better control of the lateral compositional distribution in the melts. We thus expect that by growing under the influence of low-gravity conditions ( $g \lesssim 10^{-5} g_0$ ), crystals with significantly improved crystallinity and compositional homogeneity can be prepared as compared to the best crystals that can be produced on earth. It is also reasonable to expect that careful characterization of both the space- and ground-grown materials will lead to better insights into the peculiarities of the various growth mechanisms that will permit improvements in earth-based processing of  $\text{Hg}_{1-x}\text{Cd}_x\text{Te}$  and other compound semiconductor alloy systems.

It has been suggested[24], that CdTe,  $\text{Hg}_{1-x}\text{Cd}_x\text{Te}$ , etc. probably possess extremely small yield strengths near their growth temperatures. If this is the case, the high dislocation density ( $\sim 10^5 \text{ cm}^{-2}$ ) usually seen in these crystals could be due to stresses induced by the samples own weight, that is, self-induced stresses. Although it is not a major goal of the present experimentation, an effort will be made to assess the validity of this hypothesis.

#### Flight Experiment Implementation

Throughout this report we have emphasized the importance of careful control of the thermal environment near the growth interface. Thus, to assure the incorporation of these capabilities into the flight hardware, a prototype crystal growth system has been developed in our laboratory by B. R. Aldrich and a flight-qualified version is now in the process of construction. The prototype, shown in Fig. 5, has been used to grow crystals of several semiconducting materials including  $\text{Hg}_{0.8}\text{Cd}_{0.2}\text{Te}$  and doped Ge. Precise thermal field and interface shape control has been demonstrated. The growth system includes five active thermal control points and two passive control features. This degree of control is necessary to compensate for the lack of heat pipes and yet provide the



necessary temperature profile to obtain the desired interface geometries. Heat pipes are used in ground-based studies and are planned for a future flight furnace.

The restrictions imposed by constitutional supercooling and the wide separation between the liquidus and solidus of the HgTe-CdTe phase diagram limit the maximum allowable growth rate to 0.6 to 1.0  $\mu\text{m/s}$  for reasonable values ( $\sim 100$  to  $150^\circ\text{C}$ ) of the applied axial temperature gradient. We have selected 0.4  $\mu\text{m/s}$  for the initial growth rate to allow for a likely decrease in the effective "diffusion rate" because of the reduced flow contribution. Several growth rate changes are being planned for the first flight experiment. A careful analysis of the resulting transient in compositional distributions will be used to establish interface geometries for given growth conditions and to ascertain the effects of growth rate on the radial and axial compositional variations under nearly diffusion limited conditions.

#### Acknowledgements

We thank Dr. Robert J. Naumann for many helpful discussions. The work is supported by the National Aeronautics and Space Administration Microgravity Science Division.

## References

1. R. K. Willardson and A. C. Beer, eds., Semiconductors and Semimetals, 18, Academic Press (1981).
2. F. R. Szofran and S. L. Lehoczky, J. Crystal Growth, 70, 349 (1984).
3. F. R. Szofran, D. Chandra, J.-C. Wang, E. K. Cothran, and S. L. Lehoczky, J. Crystal Growth, 70, 343 (1984).
4. S. L. Lehoczky, C. J. Summers, F. R. Szofran, and B. G. Martin, in: Materials Processing in the Reduced Gravity Environment of Space, North-Holland, Amsterdam (1982). G. E. Rindone, ed.
5. P. Capper, J. J. G. Gosney, C. L. Jones, and M. J. T. Quelch, J. Crystal Growth, 63, 154 (1983).
6. C. L. Jones, P. Capper, B. W. Straughan, and A. W. Vere, J. Crystal Growth, 63, 145 (1983).
7. P. Capper, C. L. Jones, E. J. Pearce, and M. J. T. Quelch, J. Crystal Growth, 62, 487 (1983).
8. S. L. Lehoczky and F. R. Szofran, NASA CR-161949 (1981).
9. S. L. Lehoczky, F. R. Szofran, and B. G. Martin, NASA CR-161598 (1980).
10. J. E. Hart, J. Fluid Mech., 49, 279 (1971).
11. T.-W. Fu and W. R. Wilcox, J. Crystal Growth, 48, 416 (1980).
12. S. L. Lehoczky and F. R. Szofran, in: Materials Processing in the Reduced Gravity Environment of Space, North-Holland, Amsterdam (1982). G. E. Rindone, ed.
13. L. R. Holland and R. E. Taylor, J. Vacuum Sci. Technol., A1, 1615 (1983).
14. R. J. Naumann and S. L. Lehoczky, J. Crystal Growth, 61, 707 (1983).
15. B. E. Bartlett, P. Capper, J. E. Harris, and M. J. T. Quelch, J. Crystal Growth, 46, 623 (1979).
16. H. A. Bowman and R. M. Schoonover, J. Res. Natl. Bur. Std., 71C, 179 (1967).

17. V. G. Smith, W. A. Tiller, and J. W. Rutter, *Can. J. Phys.*, 33, 723 (1955).
18. J. C. Clayton, NASA CR-162049 (1982).
19. J. C. Clayton, M. C. Davidson, D. C. Gillies, and S. L. Lehoczky, *J. Crystal Growth*, 60, 374 (1982).
20. A. Rouzaud, D. Camel, and J. J. Favier, *J. Crystal Growth*, 73, 149 (1985).
21. S. R. Coriell and R. F. Sekerka, *J. Crystal Growth*, 46, 479 (1979).
22. Y. M. Dakhoul, Computational Analysis of Crystal Growth, Continuum, Inc. (January 1987). Final Report Contract No. NAS8-36483 and to be published.
23. C. E. Chang and W. R. Wilcox, *J. Crystal Growth*, 21, 135 (1974).
24. M. Brown, private communication.

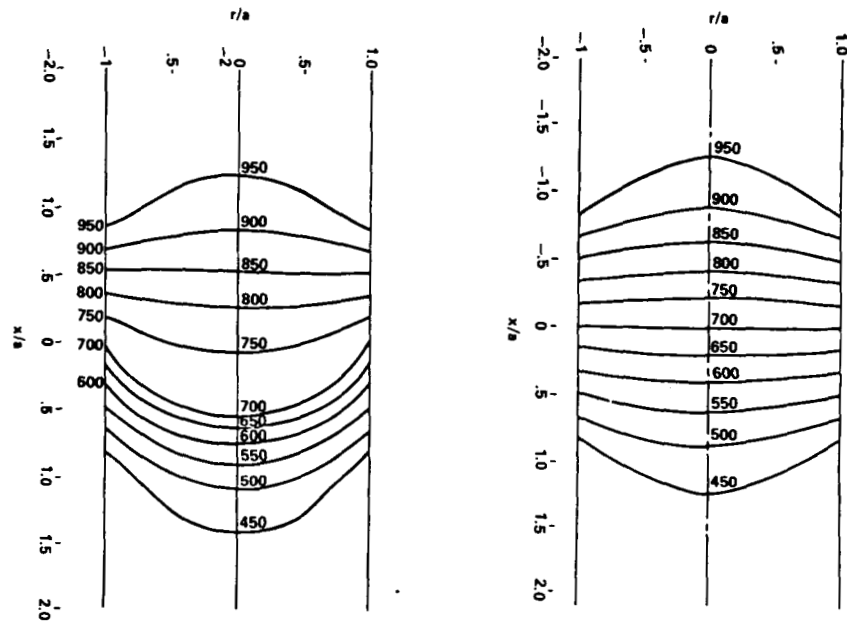


Figure 1. Effect of higher melt thermal conductivity on isotherms. Upper and lower zone temperatures of 1000 and 400, respectively, are used with a  $2x/a$  thick adiabatic zone centered at 0. Notice how the melting point isotherm of 700 changes from the right-hand, equal thermal conductivity case to the left-hand case where the thermal conductivity in the melt is seven times that in the solid.

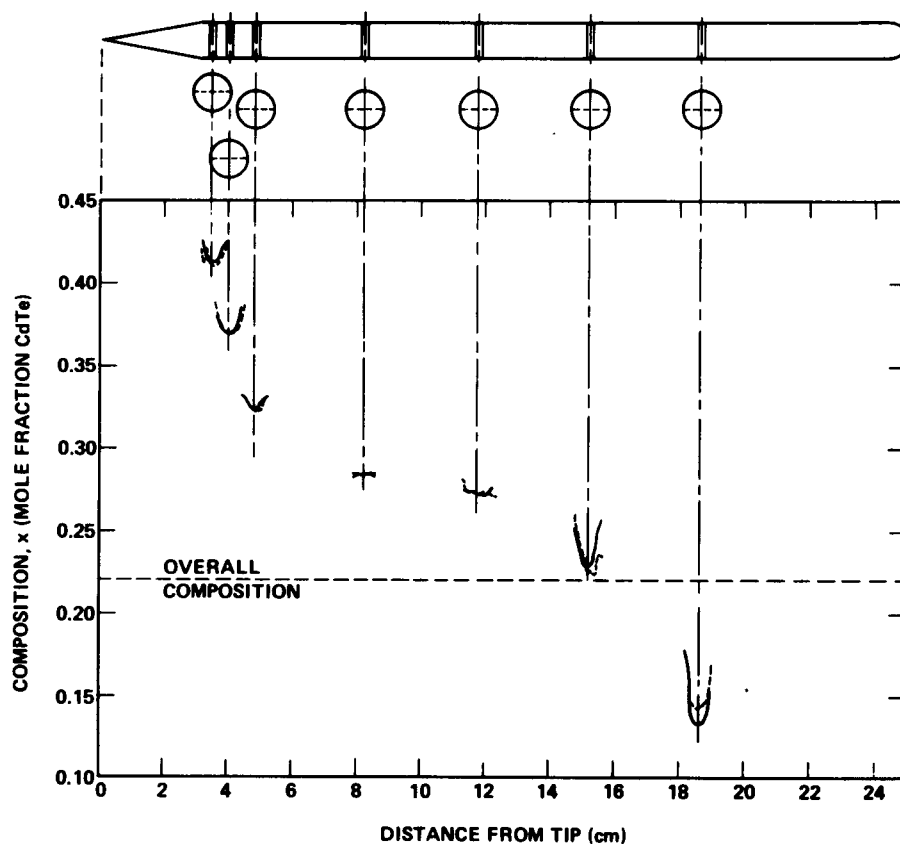


Figure 2. Radial compositional variations from seven slices from a 1-cm diameter ingot grown according to the improved Bridgman method suggested in this paper. The two curves for each slice show the composition on the same scale as the horizontal axis. These curves show the evolution of the interface during growth from concave to flat or slightly convex and back to concave.

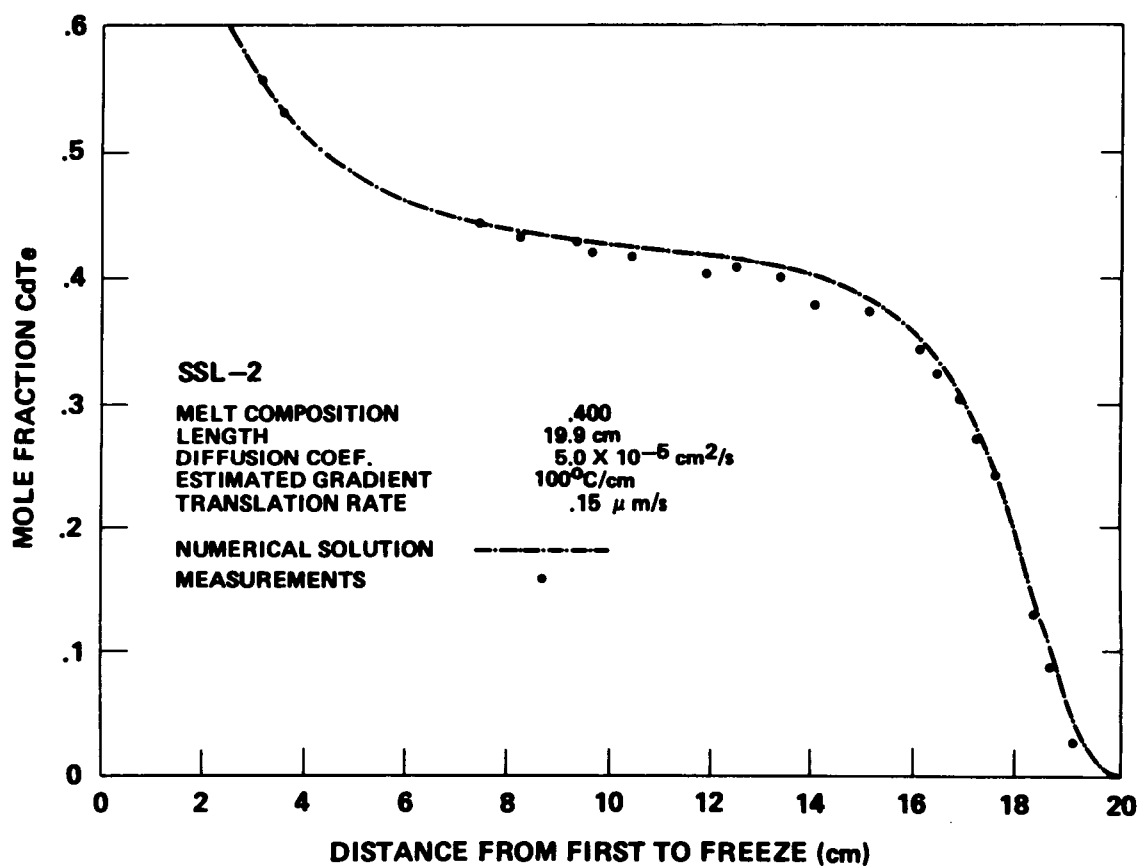


Figure 3. The fit of a one-dimensional diffusion model to axial compositional data for a slowly-grown ingot.

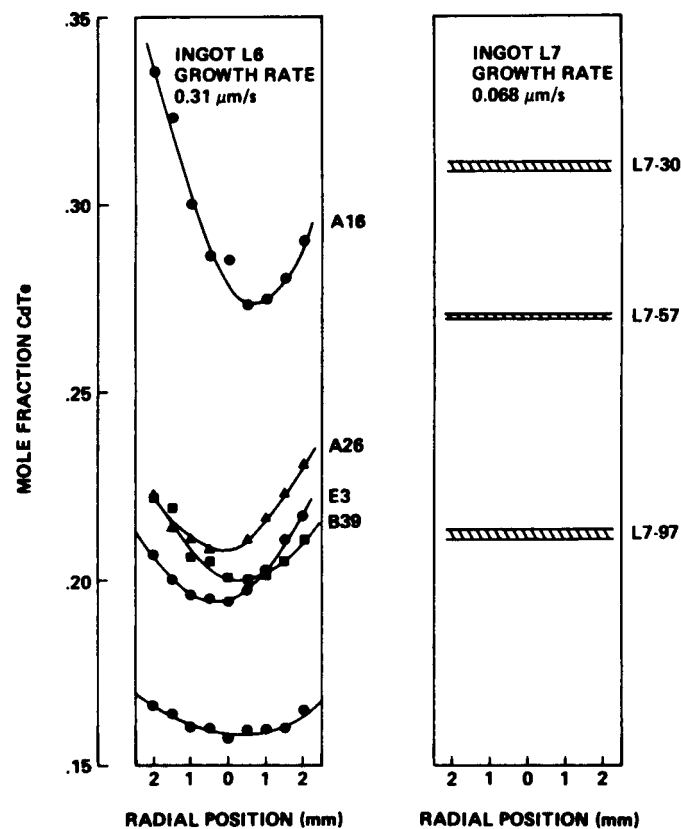
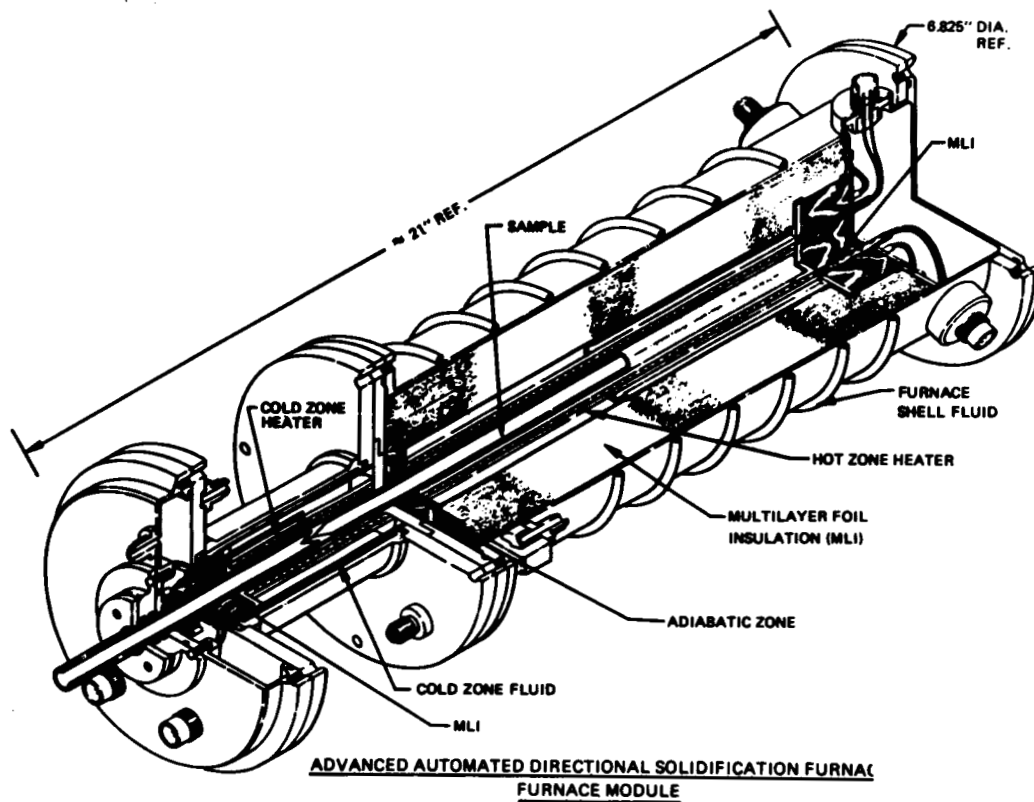


Figure 4. Comparison of two  $x=0.202$  ingots grown under identical conditions except that the growth rates were different as indicated in the figure. For ingot L6 the curves connect measurements for five slices. For ingot L7 the bands indicate the spread of compositions for each of three slices.



JA-10,842-85

Figure 5. Cutaway drawing of the AADSF laboratory version.

ORIGINAL PAGE IS  
OF POOR QUALITY



MICROGRAVITY SCIENCE  
AT  
LANGLEY RESEARCH CENTER

Archibald L. Fripp, William J. Debnam Jr., Glenn A. Woodell  
and Ivan O. Clark  
NASA Langley Research Center  
Hampton, Virginia 23665

Roger K. Crouch  
NASA Headquarters  
Washington D.C. 20546

Fredrick M. Carlson  
Clarkson University  
Potsdam, New York 13676

and

Richard T. Simchick  
PRC Kentron, Inc.  
Hampton, Virginia 23666

## INTRODUCTION

The Microgravity Science effort at the Langley Research Center is centered on the growth of the compound semiconductor alloy, lead tin telluride. Lead tin telluride is a substitutional alloy of lead telluride and tin telluride that is miscible over the entire compositional range. The semiconductor properties of this material are dependent on the ratio of the two components and consequently, the uniformity of an array of devices is dependent on good compositional control<sup>1</sup>.

This material was chosen for microgravity research because of a number of reasons. Lead tin telluride is not only a useful semiconductor material which has been used for construction of infrared detectors and tunable diode lasers but it also has a similar phase diagram to other compound semiconductors of interest such as mercury cadmium telluride and mercury zinc telluride. Lead tin telluride is very interesting from a purely scientific point of view in that it is both solutially and thermally unstable but, in a one dimensional analysis with growth axis parallel to the gravity vector, only one instability works, per orientation, at a time. This double convective instability can not be made stable by balancing thermal and solutal expansion in a high temperature gradient<sup>2</sup>. Lead tin telluride is amenable to study for it is easily compounded, it has a relatively low vapor pressure, it is single phase and there is existing, though limited, literature on its growth and properties.

The Langley effort consists of both ground based and flight research. This paper will concentrate on the flight effort with

reference to the ground based effort only when necessary for clarity.

## MATERIALS PROPERTIES

The composition of lead tin telluride chosen for flight experiments is 20% SnTe and 80% PbTe. At this composition the segregation coefficient is 0.7 and the material will begin to solidify at 904°C. The steady state temperature, if steady state could be reached, is 894°C.

The properties of lead tin telluride that make it interesting for space processing are its coefficients of thermal and solutal expansion of the liquid phase. These coefficients are of course functions of both temperature and composition but values at the melting point of  $\text{Pb}_{0.8}\text{Sn}_{0.2}\text{Te}$  are  $118 \times 10^{-4}/^{\circ}\text{C}$  and  $-0.23/\text{mole fraction SnTe}$ . These are relatively large values and hence will produce a large driving force for convection in a gravity field. Note that the expansion is in opposite directions at the melt-solid interface such that even in a one dimensional analysis there can be no stable orientation.

A more complete listing of materials properties can be found in reference 3.

## SCIENCE REQUIREMENTS

The solute distribution in a directionally solidified crystal is quantitatively given by equations of Smith et al<sup>4</sup> and Tiller et al<sup>5</sup> if the only mixing in the liquid is through diffusion. If the liquid is mixed with fluid velocities that greatly exceed the interface velocity, e.s. strong convection, then the solute distribution is given by the normal freeze equation<sup>6</sup>. Solidification configurations in which both diffusion and other mixing forces are needed to describe the model are amenable to analytical solutions only in a few special cases<sup>7</sup>. Figure 1. shows the calculated solute distribution for 20% SnTe for the two extreme cases. This figure shows that between an initial and a final transient the crystal composition is constant if the fluid motion is governed only by diffusion where as there are no regions of constant composition in the growth where the liquid is totally mixed. Figure 2. shows the compositional profile of an Earth based growth. This result, which matches growth from a highly mixed liquid, is always obtained for ground based growth.

The desired growth mode is of course one in which convection is zero so compositional steady state can be reached. However fluid dynamic calculations<sup>8</sup> have shown that finite convection exists in the physical configuration used in crystal growth experiments even at  $1 \times 10^{-8}$  Earth gravity if there is a density gradient orthogonal to the gravity vector. It has also been calculated<sup>7</sup> that due to the residual atmosphere the minimum gravity level expected on the Space Shuttle is on the order of

$1 \times 10^{-3}$  Earth gravity even at the center of mass of the craft. From this brief discussion, fluid motion can be expected in the Microgravity experiments and the experimental objectives become ways of determining how much convection exists under what driving forces and what is the effect of the convection.

An ideal microgravity crystal growth experiment would require control of the interface shape and position<sup>10,11</sup> growth rate (not just ampoule translation rate), axial and radial temperature gradients and the residual body force vector. The desired analysis procedures would include not only the normal post growth procedures but also in situ measurements of fluid velocities and interface position and shape. Not all of these controls and measurements will not be available for either MEA or AADSF experiments but progress is being made to at least incorporate the measurements in the Earth based growth of lead tin telluride at Langley. The interface movement with respect to ampoule position in the furnace and axial temperature gradients have been measured as a function of furnace profiles<sup>12</sup>. X and gamma rays have been used to measure thermocouple movement in the furnace as well as the interface position and shape<sup>13</sup>. An electrochemical technique of titrating trace amounts of oxygen through a solid electrolyte into the ampoule and then measuring its time of travel between electrodes is being used to measure the fluid motion<sup>14</sup>.

## FLIGHT EXPERIMENTS

A flight opportunity has been made available in the MEA furnace and additional flight opportunities are anticipated in both the MEA and the AADSF. Each of these experiments will be described separately below.

### MEA

The Materials Experiment Assembly ( MEA ) is a stationary, i.e. no ampoule translation, furnace with either one (isothermal model ) or three ( gradient model ) temperature zones and a water cooled block at one end. A helium quench is available if desired. Each zone in the gradient model can be independently controlled and the maximum temperature is approximately 1000°C.

Furnace characterization is important for any crystal growth experiment but it is especially vital for a stationary furnace such as MEA in which a temperature gradient is to be translated through the furnace at a constant rate. To this end an instrumented inert ( $\text{SiO}_2$ ) cartridge with thermal properties similar to lead tin telluride was constructed and ground based tests were conducted in the flight furnace. The maximum temperature gradient, at the solidus temperature, that could be maintained over the length of the cartridge was 20°C/cm hence the growth rate needed to be kept below 3.5mm/hr to prevent interfacial breakdown<sup>15</sup>. The growth rate was derived by carefully profiling the furnace at various zone settings and then

determining both the zone temperatures and the time between these settings which would translate a 900°C isotherm through the cartridge at a constant 3.5mm/hr after the cooling water was turned on to initiate growth. Figure 3. shows the chosen furnace temperature profile for the three zones and Figure 4. shows the translation of the desired isotherm through the  $\text{SiO}_2$  sample in ground based tests.

The flight sample was a quenched polycrystalline boule that was compounded from the elements. A quenched sample was chosen because even though such sample exhibits large microsegregation the macrosegregation is lower than a ground based directionally solidified sample hence diffusion alone could homogenize the melted sample. The ampoule was 2mm thick fused silica with a 6mm fused silica plug sealed in each end. The MEA instrumentation allowed for two monitoring thermocouples which were placed in grooves on the ampoule. The ampoule was then placed in a stainless steel sheath for insertion into the furnace.

The experiment was performed on Shuttle Flight STS 61A in October 1985. The MEA furnace was returned to MSFC and it was opened to retrieve and return samples to the investigators on December 4, 1985. The ampoule was removed from the metal sheath at MSFC and then taken back to Langley for analysis.

The primary concerns in analysis are the axial composition distribution and the observation of voids, if any, in the crystal. The axial composition will indicate the extent of deviation from planar, diffusion controlled, growth. Voids have occurred in Earth grown samples when the growth direction was parallel with the gravity vector.

The crystal was examined for voids using gamma radiation before the ampoule was opened. No voids were observed. The ampoule was opened by cutting the quartz with a wire saw.

In order to examine the axial composition the crystal had to be cut along its axis and polished. The first and, to date, only cut position was chosen to not only bisect the crystal through the center axis of the ampoule but also to bisect a small mound on the free surface of the crystal.

The composition of the crystal was measured with a wavelength dispersive electron microprobe. Axial data is shown in figure 5. The continuous curve is the calculated values of SnTe concentration if the liquid was continuously and totally mixed during solidification. As can be seen, the data is a reasonable match to the mixed curve in the region between 2mm and approximately 38mm. The first 2mm follows the anticipated thermal supercooling curve that is explained in a previous paper<sup>14</sup>. The extent of apparent mixing shown in the next 34mm was not expected. Although apparent mixing can result from a number of factors such as a non-planar interface, time variations in growth rate, a very slow growth rate where the diffusion barrier extends the length of the ampoule and, of course, convective driving

forces it is probable that the main contributor was convection even though the gravity level was on the order of  $1 \times 10^{-4}$  Earth gravity.

Post flight analysis of the furnace, performed by MSFC engineers, determined that the cooling water loop did not function as planned. This is a primary concern because the programmed time evolution of the sample temperature, hence growth rate, was determined with the cooling water operational. Knowledge of the growth rate is vital to the thorough analysis of the experiment.

The furnace was to start its electrical cool down shortly before the start of the coolant flow. The advent of the coolant would produce a  $40^{\circ}\text{C}$  drop in temperature at the base of the melt to start the solidification process. The furnace was programmed to provide a steady growth rate from that time. The lack of a coolant, of course, changes the growth rate. Additional calibration runs are being conducted to determine the actual growth rates that occurred under flight conditions. However, a certain amount of speculation can be made based on the available data.

One possible explanation for shape of the composition vs distance at 38mm is as follows. Due to lack of cooling water crystal growth began three hours later (see the  $904^{\circ}\text{C}$  isotherm in figure 6) than expected but the furnace still went into a power down mode as programmed. Figure 6 shows that the number two thermocouple (T2 in Fig. 6) was reading approximately  $35^{\circ}\text{C}$  above the melt point when the center furnace (TM in Fig. 6) turned off. Hence there was a rapid increase in growth rate when the interface was in the vicinity of T2. Figure 7. shows an initial and a final transient curve for diffusion controlled growth with a growth rate of 35mm/hr superimposed on the data. The hypothesis is that the increased growth rate due to the furnace shut down was sufficient to overcome the fluid velocity due to convection and a transition from convection controlled growth to diffusion controlled growth occurred. The variation in composition after this point may be due to interface breakdown which would be expected to occur in diffusion controlled growth and the G/R ratio of the higher growth rate.

The observation of a transition from convection controlled growth to diffusion controlled growth would be very significant to microgravity science if it can be verified. The first step toward verification is to calibrate the MEA furnace for the actual flight conditions and the second step is to perform the growth in space with different growth rates.

#### AADSF

The advanced automated directional solidification furnace (AADSF) represents a significant improvement over the MEA. The most obvious improvement is an ampoule translation mechanism; the

lack of which has produced the greatest uncertainty in the MEA experiment. The second most important improvement is an insulated zone between the hot and cold zones which along with a higher temperature capability ( $>1150^{\circ}\text{C}$ ) will produce axial temperature gradients of  $100^{\circ}\text{C}/\text{cm}$  or greater.

The precise tests that will run in the AADSF will be influenced by the evolving analysis of the MEA sample and the results of the continued ground based work. However the best idea at present is to conduct a series of crystal growth experiments in which the growth rate is varied between runs. The slowest growth rate of interest would be that designed for the MEA flight,  $3.5\text{mm}/\text{hr}$ . Higher growth rates would be matched to calculated fluid velocities<sup>9</sup> but limited by the need to preserve interface stability as calculated for the furnace temperature gradient. The lead tin telluride fluid velocity will decrease with decreasing body force levels but it is expected to be finite on the Space Shuttle regardless of operational mode. Hence the attainment of compositional steady state will be controlled by both the configuration of convection cells ( a low velocity cell near the interface will form a barrier to a high velocity, counter rotating cell that is higher in the ampoule ) and the relative velocity of the fluid and the interface.

#### CONTINUED GROUND BASED RESEARCH

Even though flight opportunities are absolutely necessary for continued development of Microgravity Science there is also a strong need for continued ground based research. Crystal growth has to be continuously developed from an art and turned more into a science. The Microgravity Science program has been a leader in this effort especially in getting crystal growers to think in terms of fluid mechanics.

The field of fluid mechanics applied to crystal growth has a great potential for near term payoff. Progress is being made through this laboratory and elsewhere<sup>9,11,17</sup> but the solutions of the fluid dynamic equations as applied to physical growth systems are still in an embryonic state. More and continued research is needed not only in the calculations but also in confirming measurements of both heat and fluid flow.

Another area that needs additional attention is the effect of interface shape on crystal growth. The interface shape of a crystal being grown by directional solidification is controlled by a combination of heat flow patterns and the thermophysical properties of the material and the extent of convection in the liquid. The interface shape, in turn, can have a pronounced effect on the diffusion and convection patterns of the rejected solute as well as defect density and dopant concentration in the final crystal. That is, interface shape and dopant/solute convection are interactive in that one affects the other.

Interface demarcation with Peltier pulsing has shown a two dimensional image of the three dimensional interface<sup>10-12</sup>. This technique has produced a wealth of scientific data but it is limited to a select few semiconductor crystals. Chemical etching after growth will show the extent of turbulence and meltback on some crystals when such conditions occur<sup>20</sup>.

A technique using X and gamma radiation to observe the interface during growth has been developed at Langley<sup>13</sup>. This technique has been successfully demonstrated on both germanium and lead-tin-telluride to observe and control the interface position but additional effort is needed to go beyond semi-quantification of the interface shape.

#### SUMMARY

Although space research is still in an embryonic state a combination of Earth based and space flight experiments are being coupled to yield a better understanding of the complex interaction of heat and fluid flow on the dynamics of crystal growth. Continued efforts on the ground as well as additional flight opportunities are needed to continue the drive to fully understand the advantages, both scientifically and economically, of microgravity crystal growth.

## REFERENCES

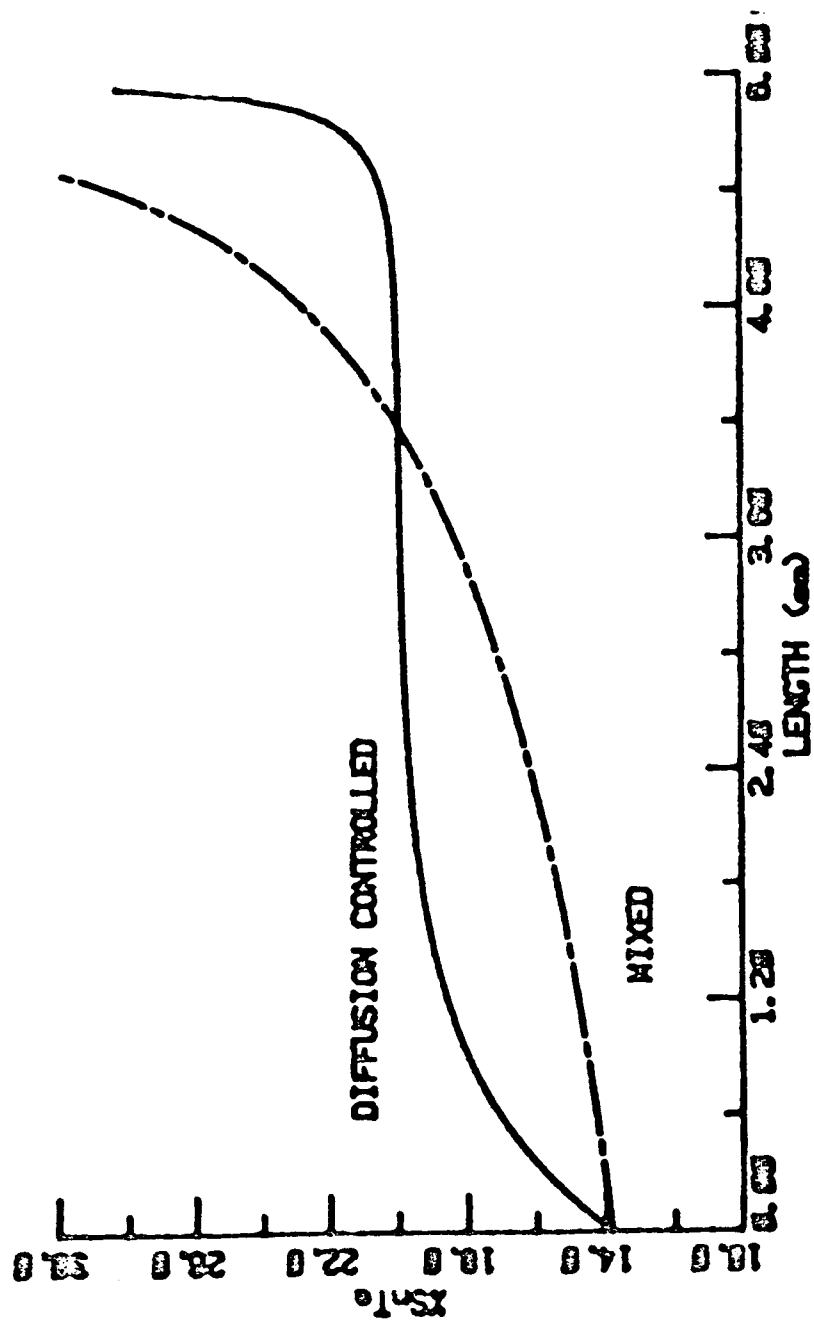
1. Fripp, A. L.; Crouch, R. K.: J. Infrared Phys. 19, 701 (1979).
2. Coriell, S. R.; Cordes, M. R.; Boettinger, W. J.; Sekerka, R. F.: J. Crystal Growth, 49, 13 (1980).
3. Crouch, R. K.; Fripp, A. L.; Debnam, W. J.; Clark, I. O.: NASA Technical Memorandum 85698, September, 1983.
4. Smith, V. G.; Tiller, W. A.; Rutter, J. W.: Canadian J. Phys., 33, 723 (1955).
5. Tiller, W. A.; Jackson, K. A.; Rutter, J. W.; Chalmers, B.: Acta. Met. 1, 428 (1953).
6. Flemings, M. C.: Solidification Processing (McGraw Hill, New York, 1974) p.34.
7. Burton, J. A.; Prim, R. C.; Slichter, W. P.: J. Chem. Phys. 21, 1987 (1953).
8. Carlson, F. M.; Sheu, J.: J. Crystal Growth, Submitted.
9. Alexander, J. I. D.; Lundquist, C. A.: Motions in Fluids Caused by Microgravitational Accelerations and Their Modification by Relative Rotation., paper 87-0312, AIAA Aerospace Sciences Meeting, January 12-17, 1987. Reno, Nevada.
10. Coriell, S. R.; Sekerka, R. F.: J. Crystal Growth, 46, 479 (1979).
11. Carlson, F. M.; Fripp, A. L.; Crouch, R. K.: J. Crystal Growth, 68, 747 (1984).
12. Ejim, T. I.; Jesser, W. A.; Fripp, A. L.: J. Crystal Growth, 69, 509 (1984).
13. Barber, P. G.; Crouch, R. K.; Fripp, A. L.; Debnam, W. J.; Berry, R. F.; Simchick, R.: J. Crystal Growth, 74, 228 (1986).
14. Hurst, J. H.; Anderson, T. J.; Fripp, A. L.: The Seventh American Conference on Crystal Growth, July 12-17, 1987. Monterey, California, Submitted.
15. Mullins, W. W.; Sekerka, R. F.: J. Appl. Phys., 35, 444 (1964).
16. Fripp, A. L.; Crouch, R. K.; Debnam, W. J.; Clark, I. O.; Wagner, J. B.: J. Crystal Growth, 73, 304 (1985).



17. Chang, C. J.; Brown, R. A.: J. Crystal Growth, 63, 343 (1984).
18. Murgai, H. C.; Gatos, H. C.; Witt, A. F. : J. Electrochem. Soc., 123, 224 (1976).
19. Lichtensteiger, M.; Witt, A. F.; Gatos, H. C.: J. Electrochem. Soc., 118, 1013 (1971).
20. Barber, P. G.; Crouch, R. K.: J. Electrochem. Soc., 131, 2803 (1984).

## FIGURE CAPTIONS

- Figure 1. Calculated curves of solute distribution in directional solidified  $\text{Pb}_{.8}\text{Sn}_{.2}\text{Te}$  for both diffusion and convection controlled growth. The length and growth rate are chosen to be compatible to the MEA experiment.
- Figure 2. Microprobe data of composition vs distance for a typical Earth grown crystal of  $\text{Pb}_{.8}\text{Sn}_{.2}\text{Te}$ . The solid curve is from the normal freeze equation.
- Figure 3. Temperature control settings for the three zone MEA furnace. TH refers to the zone furthest away from the cooling block. TM refers to the center zone and TC is for the zone adjacent to the cooling block.
- Figure 4. Position of the  $900^{\circ}\text{C}$  isotherm as a function of time. Measurement was made on the ground but in the flight furnace. The sample was an instrumented  $\text{SiO}_2$  cylinder the size of the flight cartridge.
- Figure 5. Microprobe data of composition vs distance. Each scan is parallel to the ampoule center line but are separated by 3.7mm. The solid curve is calculated from the normal freeze equation.
- Figure 6. Temperature data for the MAE A2 flight. Curves marked TH, TM and TC are furnace thermocouple data from the zones as described in Figure 3. The data marked T1 and T2 are from thermocouples attached to the ampoule.
- Figure 7. The data is the same as figure 5. The solid curves are the initial and final transients if the growth changed from convection controlled to diffusion controlled growth.



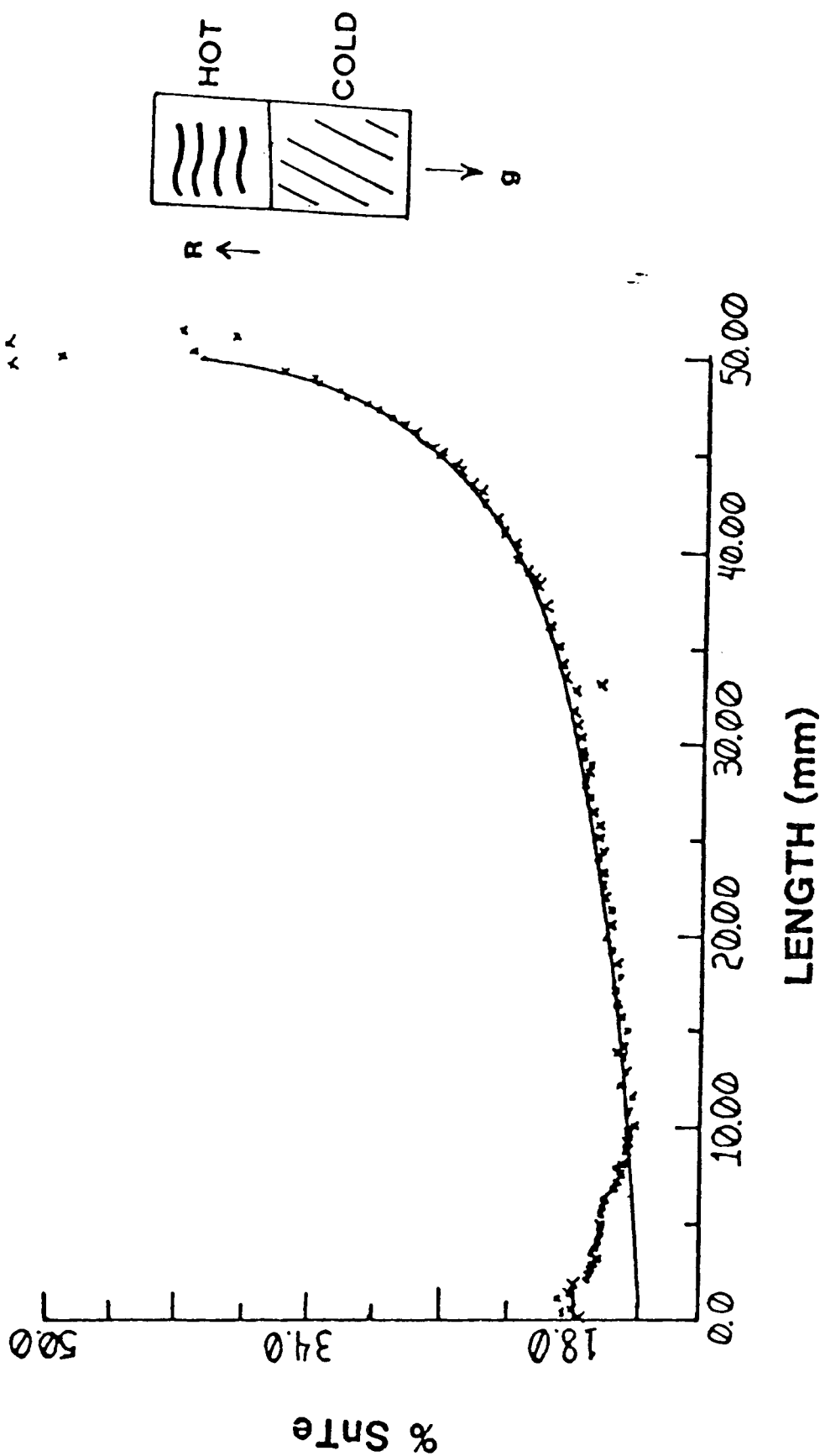
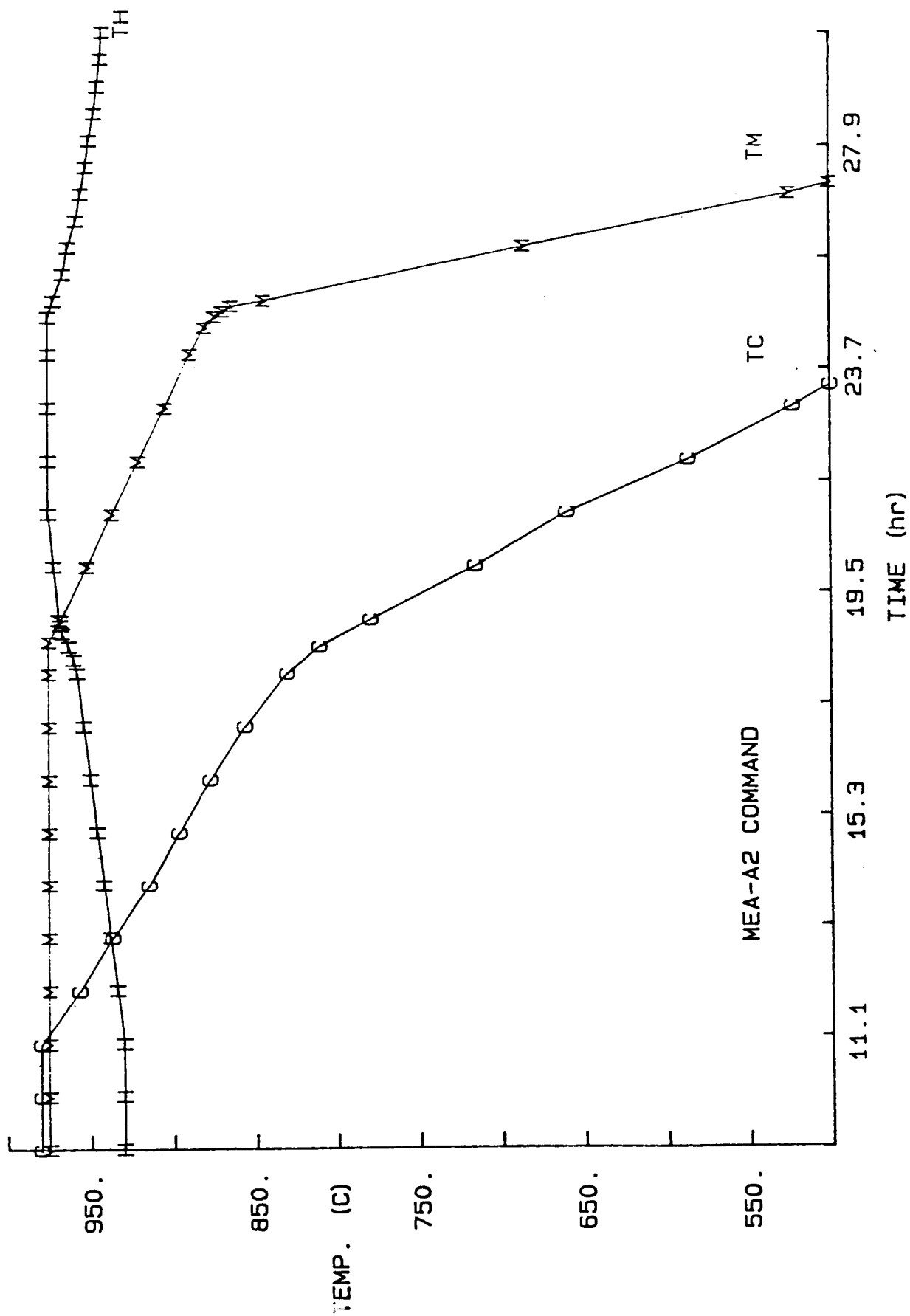
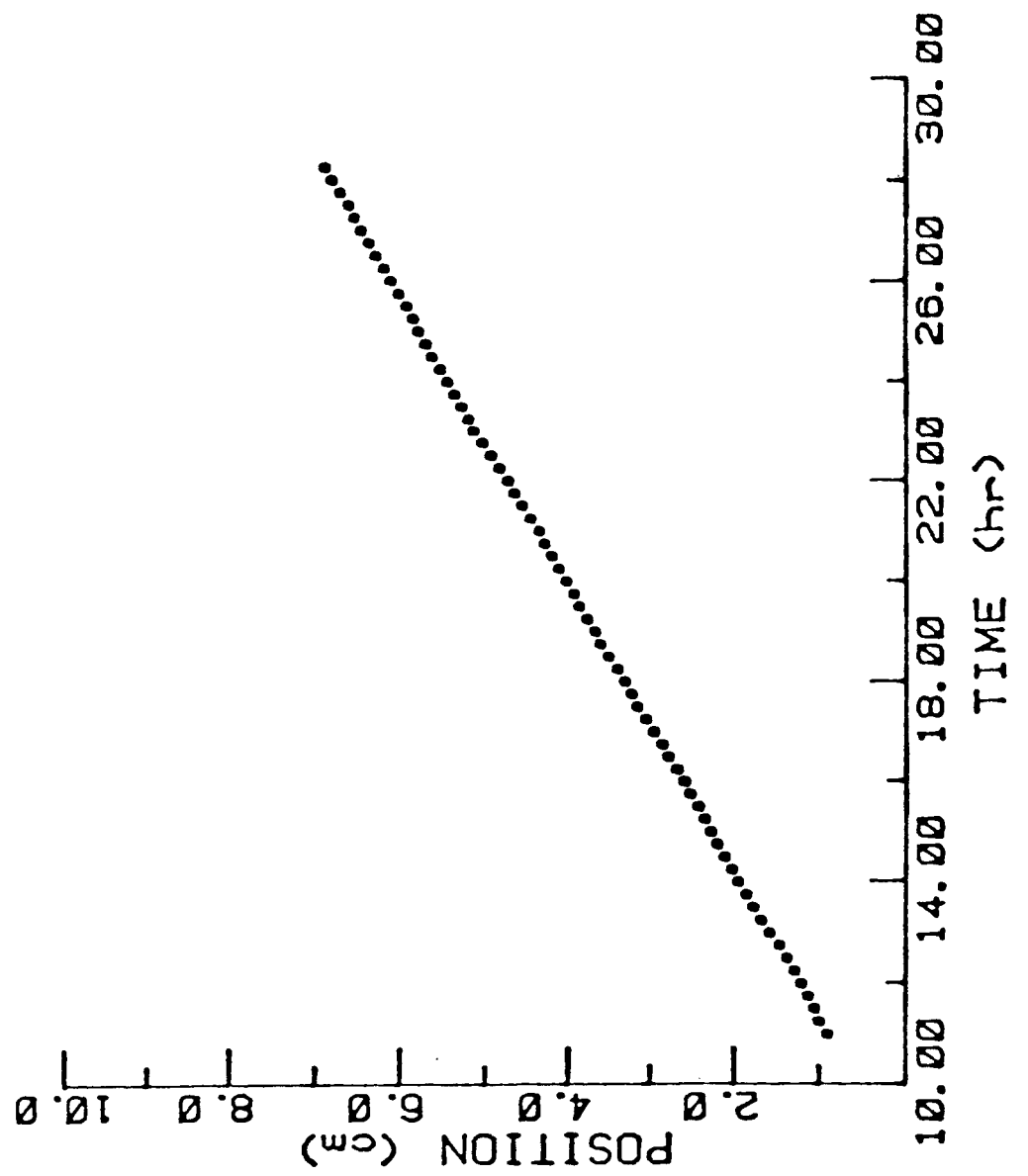
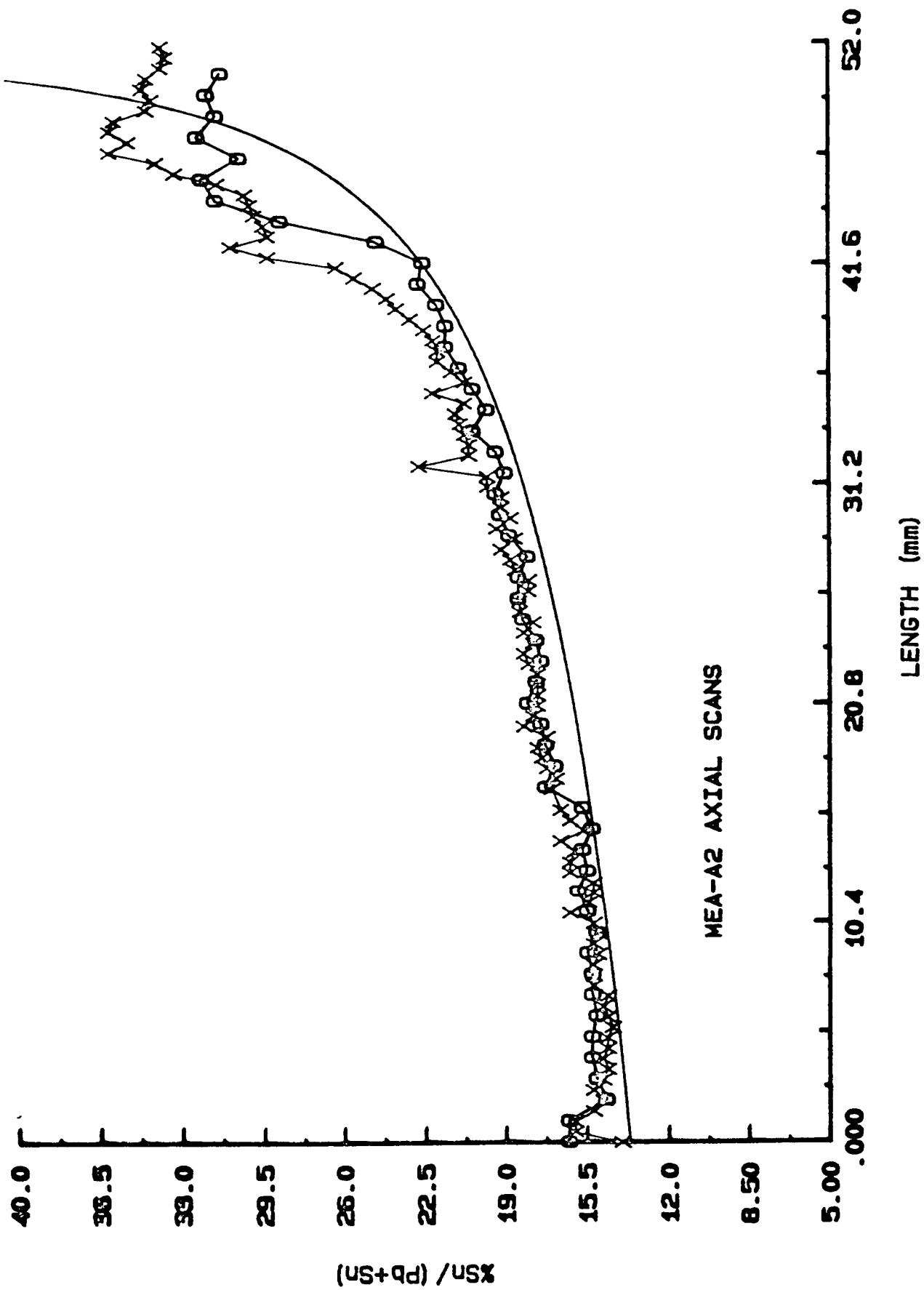
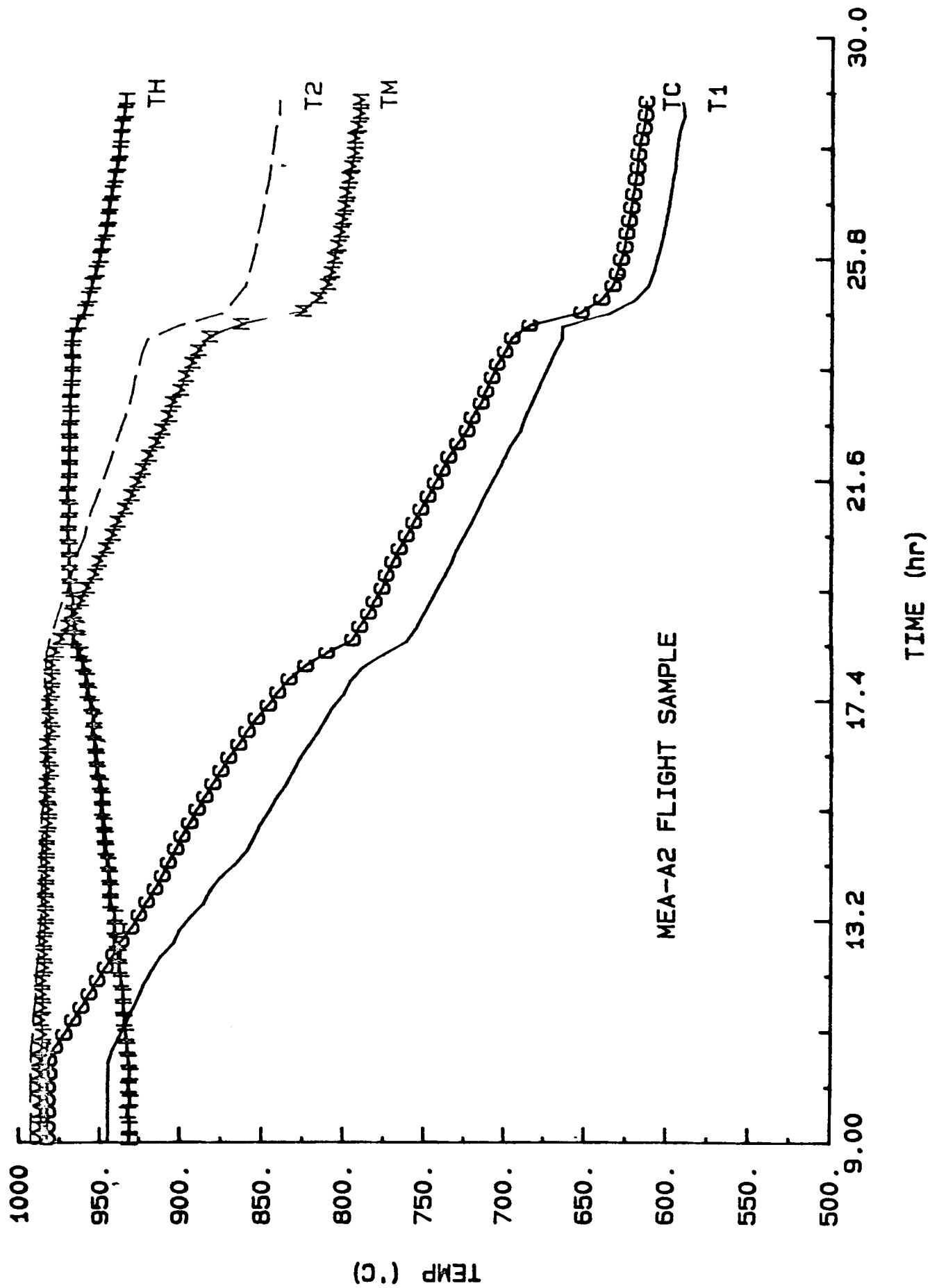


Fig 2

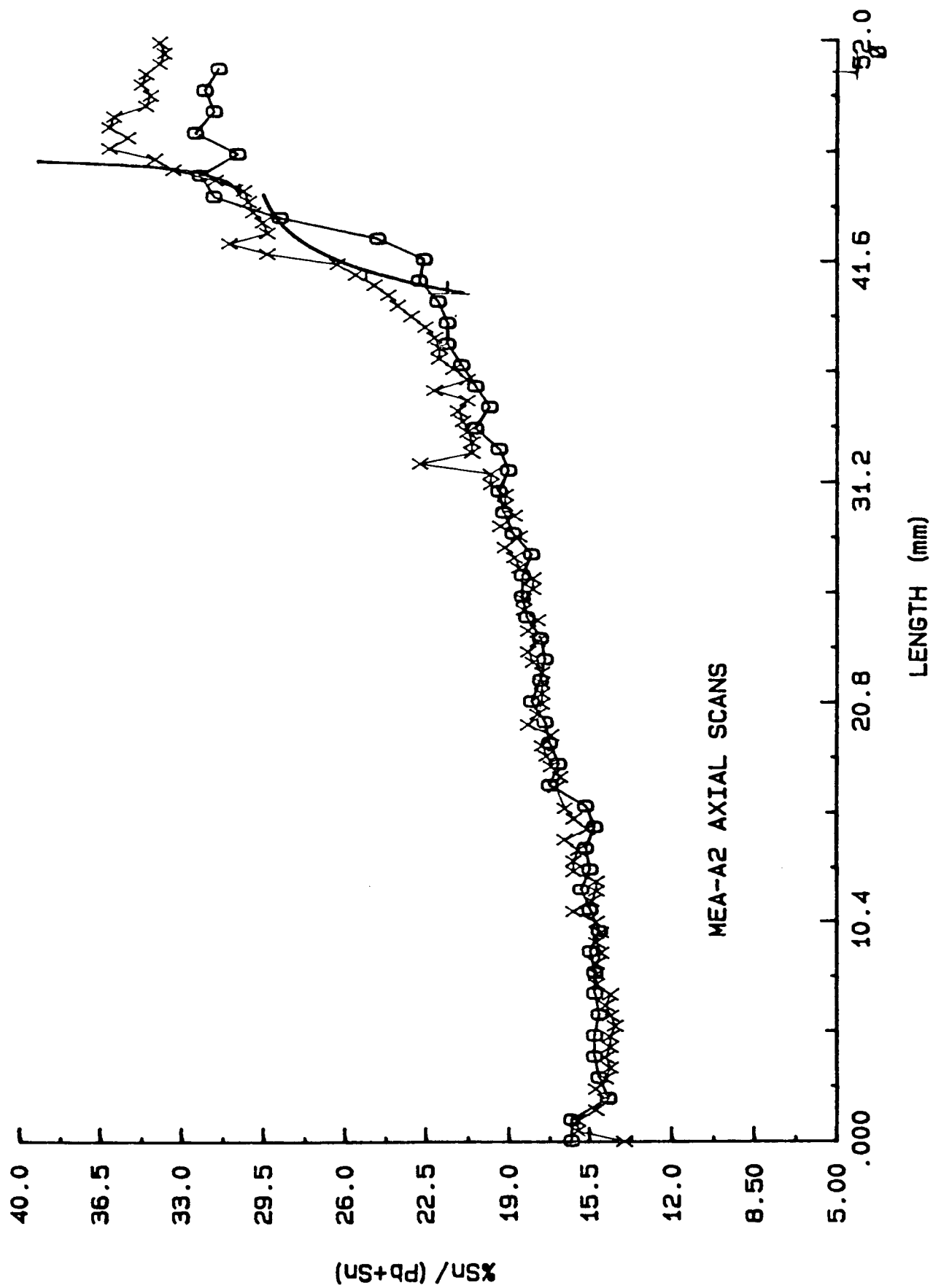












## **METALS AND ALLOYS**

**PRECEDING PAGE BLANK NOT FILMED**

ISOTHERMAL DENDRITIC GROWTH - A LOW GRAVITY EXPERIMENT

M. E. Glicksman, R. C. Hahn, T. A. Lograsso,  
E. R. Rubinstein and M. E. Selleck

Materials Engineering Department  
Rensselaer Polytechnic Institute  
Troy, N.Y. 12180-3590

and

E. Winsa

NASA Lewis Research Center  
Cleveland, Ohio 44135

Submitted to NASA Headquarters Code E-N as a publication  
as a part of the Flight Experiment Science Review, March  
9, 1987. Lewis Research Center, Cleveland, Ohio 44135

PRECEDING PAGE BLANK NOT FILMED

## ABSTRACT

The growth of dendrites in pure melts and alloys is controlled by diffusion-limited transport of heat and/or solute. The presence of temperature or concentration gradients within a molten phase subject to gravitational forces generally promotes convection, which in turn, modifies the diffusion processes. In the case of dendritic growth, where convective flows are three-dimensional and complex, the normally isotropic diffusional transport mechanisms are rendered anisotropic. The introduction of anisotropic transport mechanisms alter the fundamental crystal growth behavior. Ground based studies of a pure material, succinonitrile, have shown that kinetic and morphological characteristics of dendritic growth can be strongly affected by convective flows. Experimentally measured growth velocities and dendrite tip radii at undercoolings greater than 1.0 K agree well with values predicted by theoretical models of dendritic growth based on diffusional transport mechanisms. At undercoolings less than 1.0 K, the experimental data deviates from the predicted values and is the result of convective flows disturbing the otherwise spatially isotropic diffusion field. The vigor of melt convection is controlled by several parameters often expressed as a lumped dimensionless group, the Grashof number  $Gr = g\beta\Delta T\ell^3/\nu^2$ , where  $g$  is the acceleration due to gravity;  $\beta$  is the volumetric expansion coefficient;  $\Delta T$  is the undercooling;  $\nu$  is the kinematic viscosity; and  $\ell$  is the relevant length scale, e.g., the characteristic diffusion distance.

Dendritic growth, by its nature, does not permit independent manipulation of the controlling length scale,  $\ell$ , which is determined by materials properties (e.g. diffusion coefficient or thermal diffusivity) and the undercooling or supersaturation. The reduction of  $g$  through orbital free fall is often the only practical way to lower  $Gr$  sufficiently to permit careful observation of the morphological and kinetic characteristics of isothermal dendritic growth. Estimates have been made as to how low gravitational accelerations would have to be reduced in order to observe "convection free" dendritic growth at undercoolings from 0.1 to 1.0 K. The purpose of the proposed microgravity isothermal dendritic growth experiment (IDGE) is to test dendritic growth theory at low undercoolings where growth kinetics are normally overwhelmed at  $1g$ . A microgravity experiment would allow convection to be reduced to a level which would permit observations in the range of undercoolings 0.1 to 1.0 K where both tip radius and growth velocity can be measured with high accuracy and then compared with values predicted by transport/stability theory. Previously conducted ground-based studies and the current approach to performing these studies in low earth orbit will be described.

## INTRODUCTION

Dendritic growth is the most common form of crystal growth in metallic alloys and other systems forming centrosymmetric, simple crystal structures. Dendrites are complex branched forms that grow in specific crystallographic directions and evolve into elaborate 3-dimensional structures. The characteristic branching, see Figure 1, establishes the typical length scales for the microsegregation of chemical species rejected at the growing solid-liquid interfaces. The patterns of chemical segregation have a profound influence on the electrical, mechanical, and corrosion characteristics of the cast material.

Dendritic crystal growth occurs in metals and alloys in the presence of either constitutional supercooling in the case of alloys or thermal supercooling in the case of pure materials. Latent heat or solute is released as the dendrite advances, which changes the local density of the surrounding liquid. Gravitational forces, if present, cause complex, three-dimensional convective flows. These convective flows alter the thermal fields governing dendritic growth, affecting both the growth rate and tip radius of the dendrite [1]. Figure 2 shows the effect of various growth orientations with respect to the gravity

ORIGINAL PAGE IS  
OF POOR QUALITY

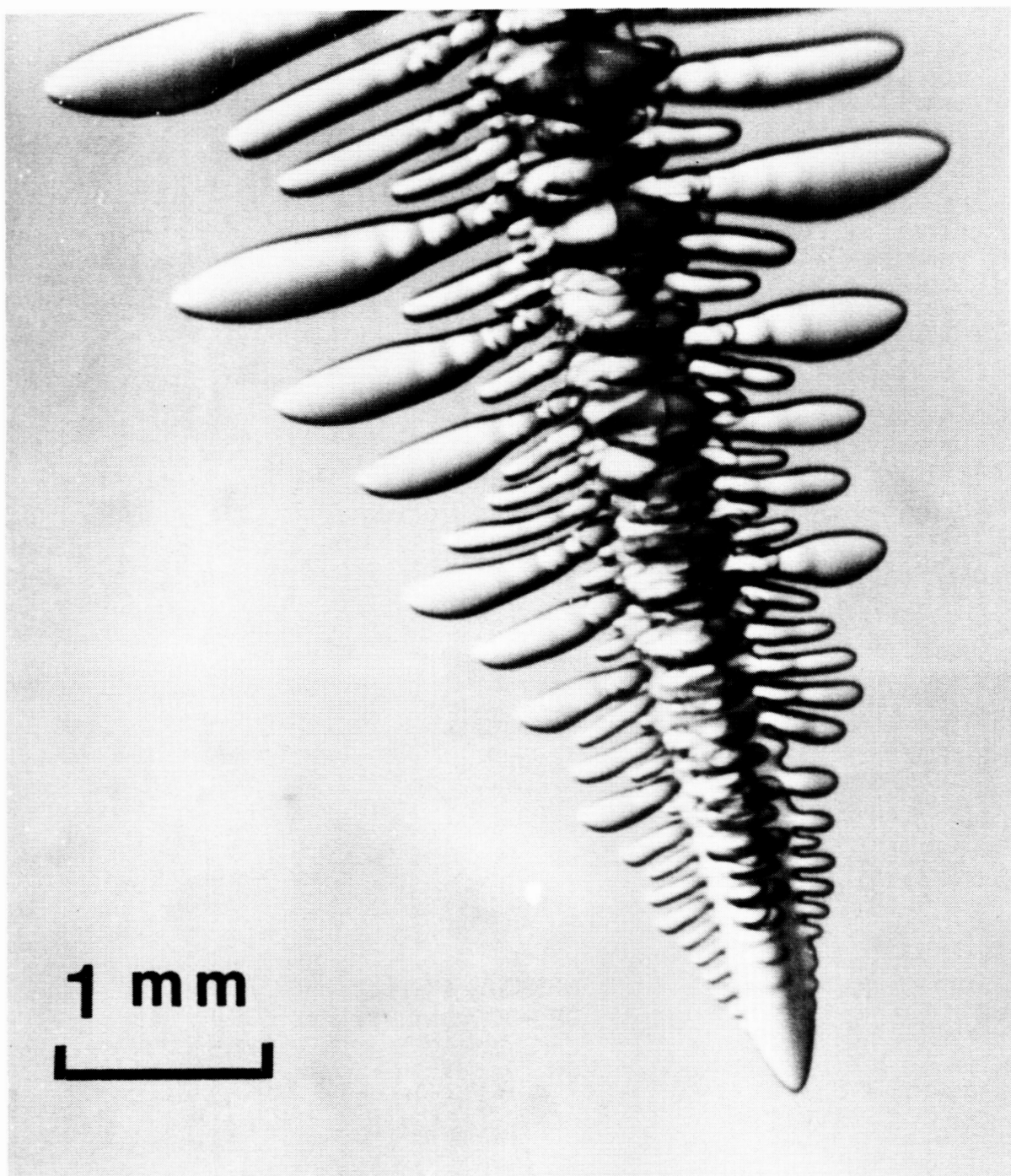


Figure 1 Dendritic crystal growing in succinonitrile.

ORIGINAL PAGE  
BLACK AND WHITE PHOTOGRAPH

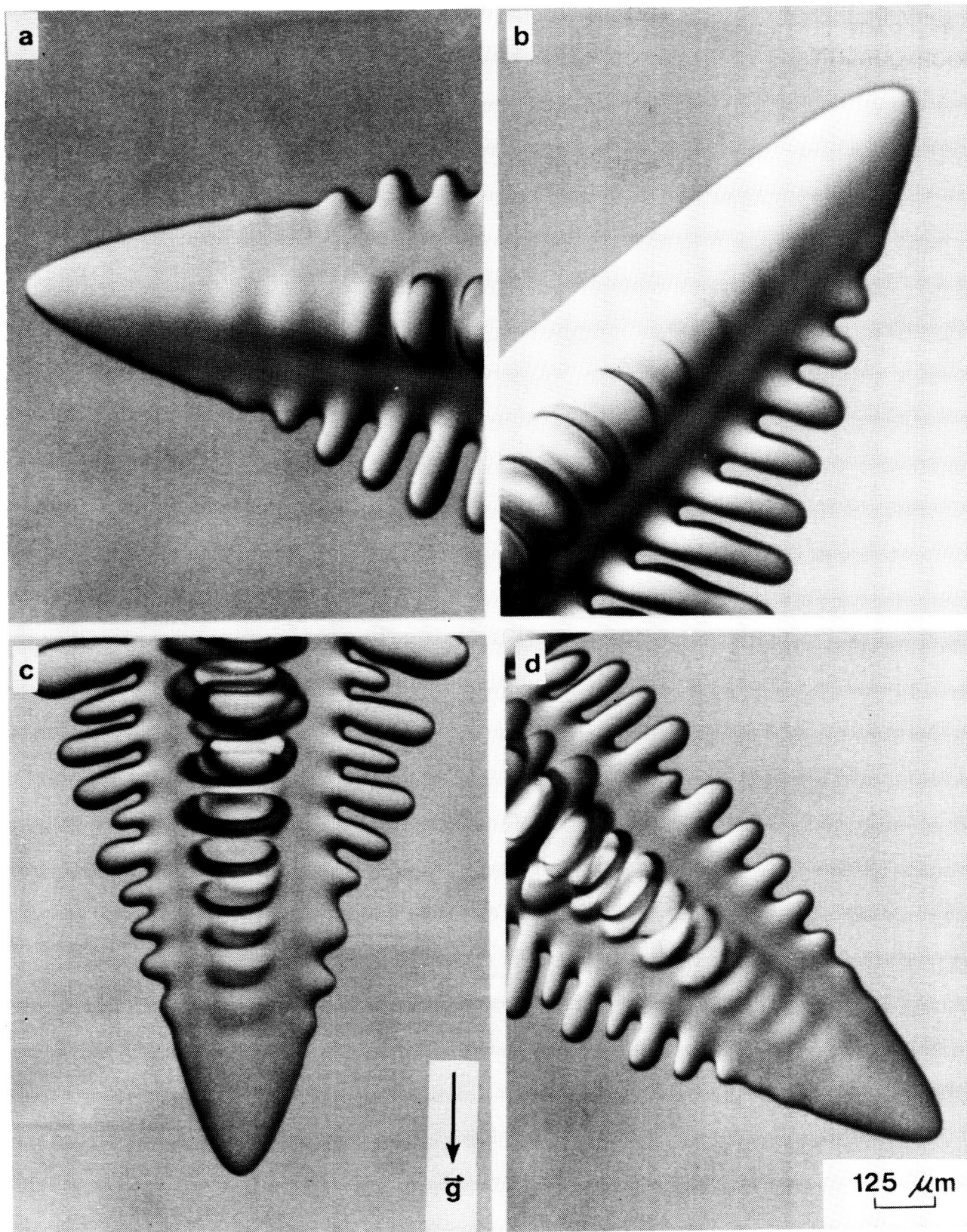


Figure 2 Succinonitrile dendrites show in true growth orientation with respect to gravity: (a) perpendicular to gravity, side branching is suppressed on top; (b) as growth angle is increased side branch is further suppressed on top; (c) parallel to gravity side branches are symmetrical; (d) a slight increase in growth angle results in little noticeable asymmetry.



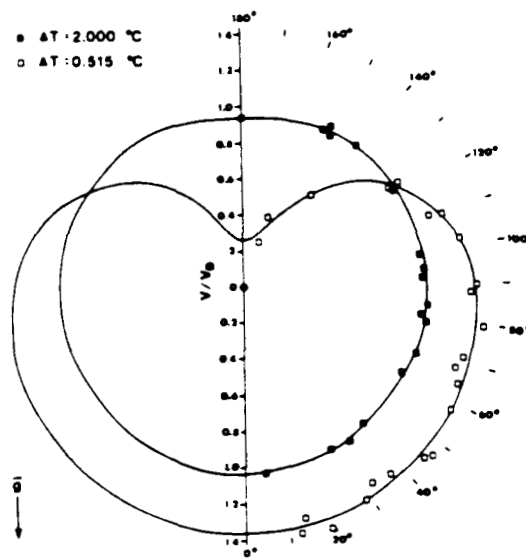


Figure 3 Growth velocity as a function of growth angle with respect to gravity at 2.0 K and 0.515 K undercooling.

vector at 1g on the morphology and the sidebranch structure of a dendrite. A corresponding spatial anisotropy in the growth rate is shown in Figure 3. Convective effects have their greatest influence at small undercoolings and, therefore, it would be desirable to quantify the diffusion-limited kinetics of dendritic growth at these undercoolings in the absence of convection, in order to comprehend the influence of convection on the dendritic growth process. Small undercoolings are also advantageous from an experimental point of view since the growth velocities are low and tip radii are large, allowing accurate measurements of both. Determination of both of these quantities is necessary to test dendritic growth theory adequately. It is the intent of the isothermal dendritic growth experiment (IDGE) to test dendritic growth theory in low earth orbit where convection will be reduced to a level that will permit observations of diffusion controlled growth in the range of undercoolings from 0.1 K to 1.0 K.



## DENDRITIC GROWTH THEORY

Over the past 30 years, numerous theories have been developed describing steady-state dendritic growth [2,3]. Experimental evidence [3] has shown that these theories correctly describe one or more aspects of dendritic growth but none were capable of a complete description of the growth kinetics. The comparison of experimental data to the various models indicate that two of these theories, the Ivantsov model [4] and the Langer and Muller-Krumbhaar stability criterion [5,6,7] when used in combination, adequately predict the kinetics of dendritic growth.

Ivantsov modeled steady-state dendritic growth using heat transport theory, by assuming that a paraboloid of revolution described the shape of the dendrite devoid of sidebranches. Ivantsov also neglected any capillarity effects and molecular attachment kinetics. The solution to the diffusion equation yields an expression for the dimensionless undercooling of the form:

$$\Delta\theta = Pe \exp(Pe) E_1(Pe), \quad (1)$$

where  $\Delta\theta = (T_m - T_\infty)/(L/C_p)$  is the dimensionless undercooling;  $T_m$  is the melting temperature;  $T_\infty$  is the temperature of the melt far from the interface;  $L$  is the latent heat of fusion;  $C_p$  is the heat capacity;  $Pe = VR/2\alpha$  is the Peclet number;  $V$  is the growth velocity;  $R$  is the dendrite tip radius;  $\alpha$  is the thermal diffusivity and  $E_1$  is the first exponential integral. This solution, however, does not yield a unique value of growth velocity and tip radius at each undercooling, but provides a set of values of the form  $VR = \text{constant}$ . A morphological stability criterion is invoked to obtain the steady-state operating tip radius and growth rate at a given undercooling.

Langer and Muller-Krumbhaar (LM-K) have applied linear stability theory to a paraboloidal solid-liquid interface and derived an expression for the stability of a dendritic surface which is marginally stable at the tip and unstable at all other points. A stability criterion was formulated, in the limit of vanishing surface tension, and can be expressed as:

$$\sigma^* = 2\alpha d_0 / VR^2 \approx 0.025, \quad (2)$$

where  $d_0 = T_m \gamma C_p / L$  is the capillary length, and  $\gamma$  is the solid-liquid surface energy. The LM-K criterion predicts an independent continuum of operating tip radii and growth rates which can then be combined with the Ivantsov model,  $VR = 2\alpha Pe$ . These two equations can be solved yielding a unique growth velocity and tip radius at each undercooling, simultaneously satisfying stability and energy transport. Experimental data for succinonitrile [1,2] agree well with the predicted growth velocities at undercoolings greater than approximately 1.2 K, as shown in Figure 4. At smaller undercoolings, convective flows

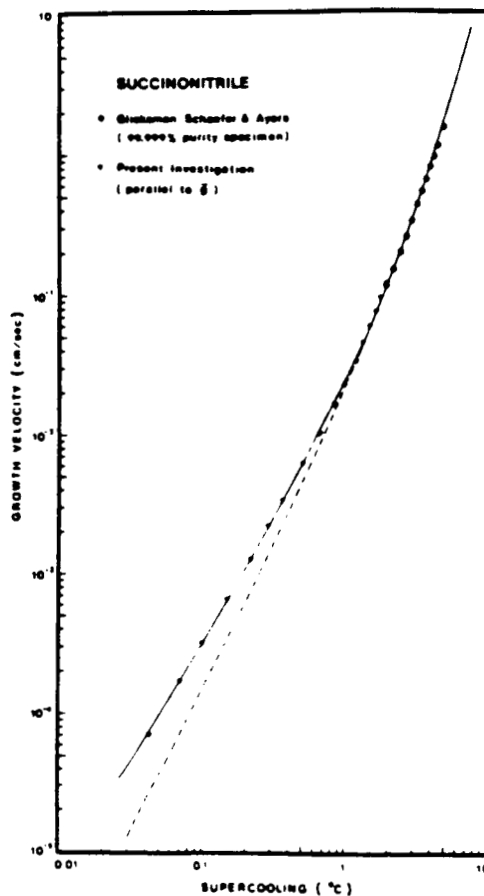


Figure 4 Growth velocity as a function of undercooling. Calculated values are shown as a dashed line.

begin to disrupt the spatially isotropic diffusive transport of heat and both growth velocity and tip radii begin to deviate appreciably from those predicted from theory [2]. A microgravity dendritic growth experiment is planned in an effort to extend the range of agreement between theory and experiment to lower undercoolings where, at 1g, the growth kinetics are overwhelmed by convection.

A new "mechanism" for the velocity selection in dendritic growth has been advanced in recent years [8-11]. This mechanism has been called "microscopic solvability" and has been applied to dendritic growth and viscous fingering. This new approach is based on the premise that a finite surface tension and crystalline anisotropy introduces a solvability condition, not considered in the LM-K theory, which determines the operating growth velocity. The incorporation of finite surface tension and anisotropy into the equations which govern dendritic growth yields a discrete set of solutions for small undercoolings, each having a unique velocity. The final operating state of the dendrite is then determined by stability analysis around a chosen steady-state shape such that the solution with the largest velocity is the most stable. For small undercoolings, this analysis also yields an explicit relationship between the growth velocity and the degree of crystalline

anisotropy,  $\alpha$ , of the form [12]:

$$v \approx \alpha^{7/4} . \quad (3)$$

In addition, the model is able to predict stable sidebranch formation when finite thermal noise about the steady-state solution is introduced. At present, it is unclear whether this model is consistent with available experimental data. Since the analysis has been carried out for small undercoolings, it has been suggested [12] that a check on the validity of this analysis must be performed in a "convection free" environment. The results from the proposed microgravity experiment may assist in the evaluation of this analysis.

### ESTIMATE OF REQUIRED MICROGRAVITY LEVELS

The reduced microgravity environment in the low earth orbit flown by the Space Transportation System (STS) can still give rise to convection which could adversely affect dendritic growth. The measured gravitational environment can be divided into two regimes, a low frequency range (DC to  $10^{-3}$  Hz) and a high frequency range ( $10^{-3}$  to 10 Hz). The DC component [13] arises from orbital friction and drag forces and is typically  $10^{-8}$  g to  $10^{-4}$  g in magnitude. AC accelerations arise from a variety of sources, both intrinsic to the orbit and within the STS orbiter itself, which range in amplitude from  $10^{-6}$  g to  $10^{-1}$  g [13]. Prior to conducting a microgravity experiment such as the IDGE, it was necessary to determine if the typical gravitational spectrum encountered will affect dendritic growth. An order-of-magnitude estimate of the upper limit of allowable gravitational accelerations can be calculated using a scaling analysis developed by Langbein [14]. According to the analysis, the allowable acceleration level can be estimated as:

$$a_0 = \frac{\rho \delta T}{\Delta \rho \nabla T_0} [\omega^2 + (v/L^2)^2]^{1/2} [\omega^2 + (\alpha/L^2)^2]^{1/2} \quad (4)$$

where  $\rho$  is the density,  $\Delta \rho = \beta \Delta T$  the density change induced in the melt with temperature;  $\nabla T_0$ , in this case, is the undercooling;  $\delta T$  is the allowable temperature deviation of the interface due to convection;  $\omega$  is the circular frequency of the acceleration;  $v$  is the kinematic viscosity; and  $L$  is the length scale over which convection occurs. It is possible to calculate the frequency and amplitude of acceleration required to induce convection sufficient to modify the growth kinetics by substituting appropriate values into the analysis and by assuming that 1% change in temperature,  $\delta T$ , will not affect the measured growth parameters within experimental error. The results of these calculations are shown in Figure 5 as a function of undercooling. At high undercoolings, the growth kinetics are relatively insensitive to convection whereas

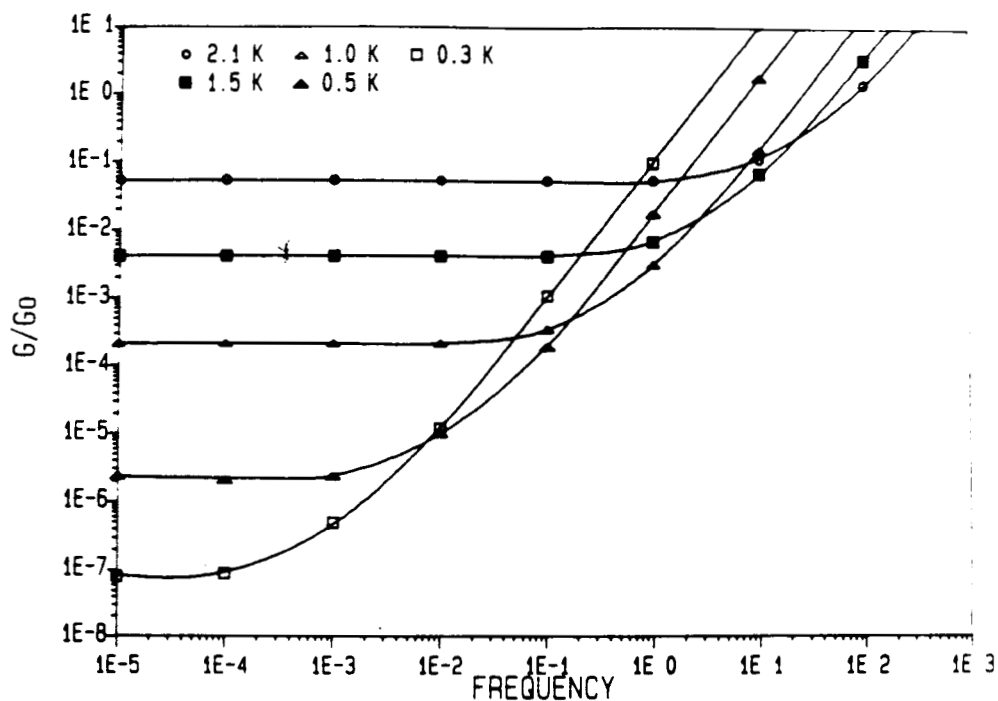


Figure 5 Acceleration limit for the onset of convection at various undercoolings. Any combination of frequency and "G" levels below the calculated curves are sufficient to induce convection which measurably modifies growth kinetics.

at low undercoolings the opposite is true. Furthermore, as the frequency increases, the level of allowable accelerations increases rapidly, indicating that dendritic growth is insensitive to gravitational fluctuations of short duration. It can therefore be assumed that the "typical" STS gravitational environment will probably provide an adequate low-gravity spectrum to study nearly convection-free dendritic growth.

#### EXPERIMENT PROFILE

The flight experiment planned will be divided into two phases, 1) "warmup" and 2) data acquisition cycles. The "warmup" phase consists of raising the temperature of the thermostat from approximately 30 °C to the operating range of 58 °C to 62 °C during which all systems are checked and initialized. Data acquisition cycles will be determined as an offset from this melting point. Data acquisition cycles are started after the succinonitrile is

fully molten. The thermostat In addition, a check of the melting point of the sample (succinonitrile, a cubic test material) is conducted allowing the temperature sensors to be calibrated to the actual melting point. This is an essential step in the initialization process since all subsequent undercoolings set and measured during the temperature is then lowered to the desired undercooling while crystal growth is suppressed by an inhibit heater until thermal equilibrium is attained throughout the sample. The inhibit heater is then turned off and dendritic growth is allowed to occur. Photographs will be taken after each millimeter of dendritic growth. The sample is then reheated above the melting point until it becomes fully molten and the cycle is repeated at a new undercooling. A total of ten undercoolings, ranging from 0.1 K to 1.0 K in increments of 0.1 K, will each be examined twice during the course of the STS mission.

## **IDGE EXPERIMENTAL APPARATUS**

The actual flight version of the experimental apparatus is still in the initial development stage at NASA Lewis Research Center and Rensselaer Polytechnic Institute. The isothermal dendrite growth experiment will be mounted on the Material Science Laboratory (MSL) in the shuttle cargo bay and will be essentially autonomous, except for a limited number of preprogrammed computer commands. The apparatus consists of four major subsystems: 1) a temperature controlled thermostatic bath, 2) a photographic data collection system, 3) a start detection system to initiate data collection and 4) a crystal growth chamber. The delicate laboratory growth chamber, Figure 6a, is being redesigned for the flight experiment. The current development of a growth chamber for flight aboard STS, Figure 6b, has focused on the following two aspects: A) examination of the effect of the design of the growth chamber on the crystal growth processes and the resultant dendrite orientation and B) identification of suitable construction materials which are chemically compatible with succinonitrile, such that any impurity-induced melting point changes do not exceed 10 mK. The present discussion will describe the dendrite orientation testing. A more detailed description of the other components and their performance requirements can be found elsewhere [15].

## **DENDRITE ORIENTATION TESTS**

The purpose of these tests is to identify the growth chamber design most favorable for growth of an oriented single crystal, resulting in a single dendrite growing coaxially from the capillary tip (see Figure 6b). If this can be achieved, the photographic system can be aligned such that the focal planes would be coincident with the

ORIGINAL PAGE IS  
OF POOR QUALITY

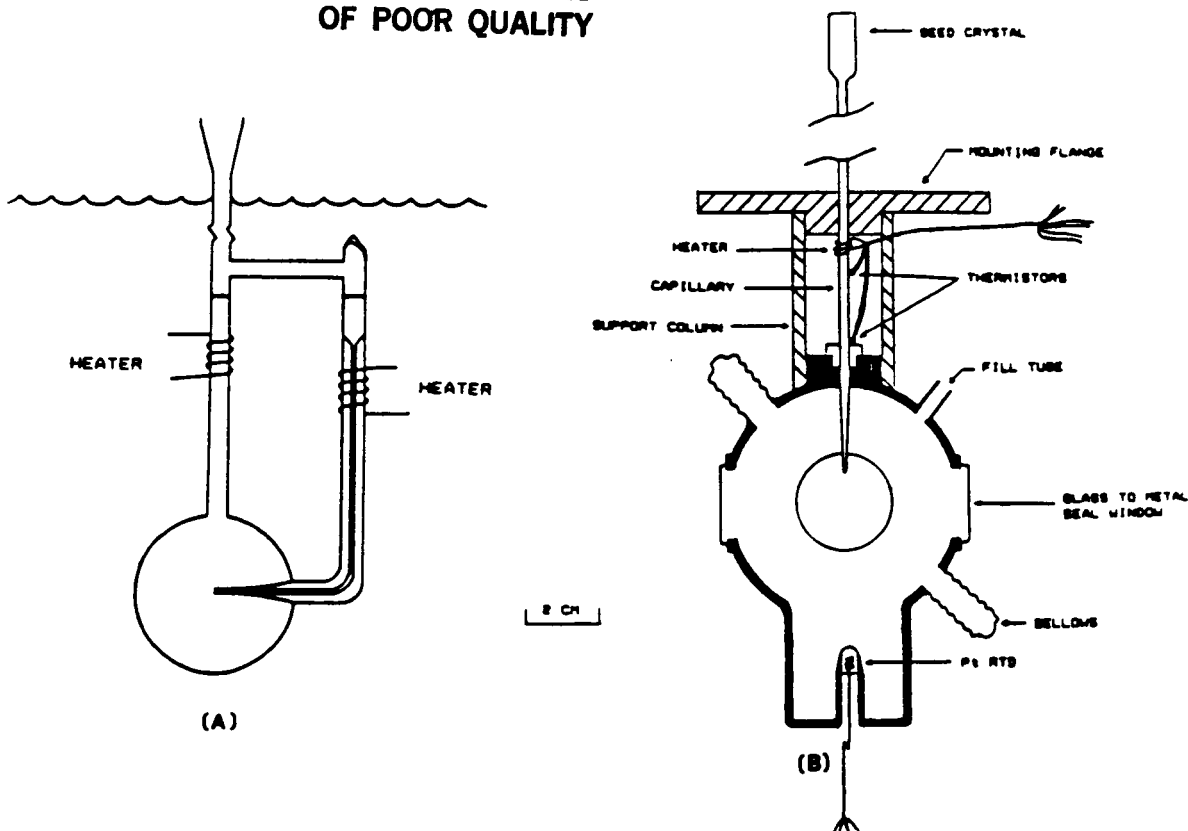


Figure 6 (a) The laboratory growth chamber used in ground based studies. (b) The current design of the flight growth chamber.

dendrite, providing clear sharp images of the dendrite during the entire course of its growth. The kinetic and morphological measurements can be measured directly from the negative with small, if any, corrections needed to obtain the true velocity and true shape of the dendrite. Two common techniques to obtain an oriented single crystal are either to furnish the growth chamber with a seed of the proper orientation or to provide a "crystal selector", such as a constriction or helix, in the capillary tube. It is uncertain, however, whether the seed crystal orientation can be maintained when the solid is propagated down the capillary.

Numerous laboratory growth chambers of varying designs have been constructed in order to examine the effect of design on the orientation of the resultant dendrite. The procedure used in conducting these tests is similar to the flight experiment procedure discussed previously. Crystallization is initiated when the inhibit heater is turned off and the solid grows as a thin film along the inside wall of the capillary tube. The advancing solid-liquid interface is not planar, but

appears to be cellular at low undercoolings ( $< 0.5$  K) and dendritic at larger undercoolings ( $> 0.5$  K). The solid film emerges from the capillary tip and breaks down into dendrites which grow outward into the melt. The first series of tests examined the influence of the capillary tip material, and its size and shape on the orientation of the resultant dendrite. The results of these experiments indicate that these factors have little influence over the orientation of the emerging dendrite; however, size and shape of the tip do affect the manner and number of dendrites growing from the tip. In almost all cases a single crystal, the orientation of which varied randomly from test to test, emerged from the tip, even though a seed crystal was not used. This is clearly illustrated in Figure 7 where the observed growth angle with respect to vertical is plotted against the number of the observation. The mean value of growth angle for these observations is approximately  $25^\circ$ , which corresponds to the mean value expected for a completely random distribution. This behavior may be attributed to one of the following: 1) the starting solid was multicrystalline, but crystal selection occurred in the capillary prior to the emergence of the dendrite, 2) the starting solid was a single crystal but growth down the capillary was multicrystalline with

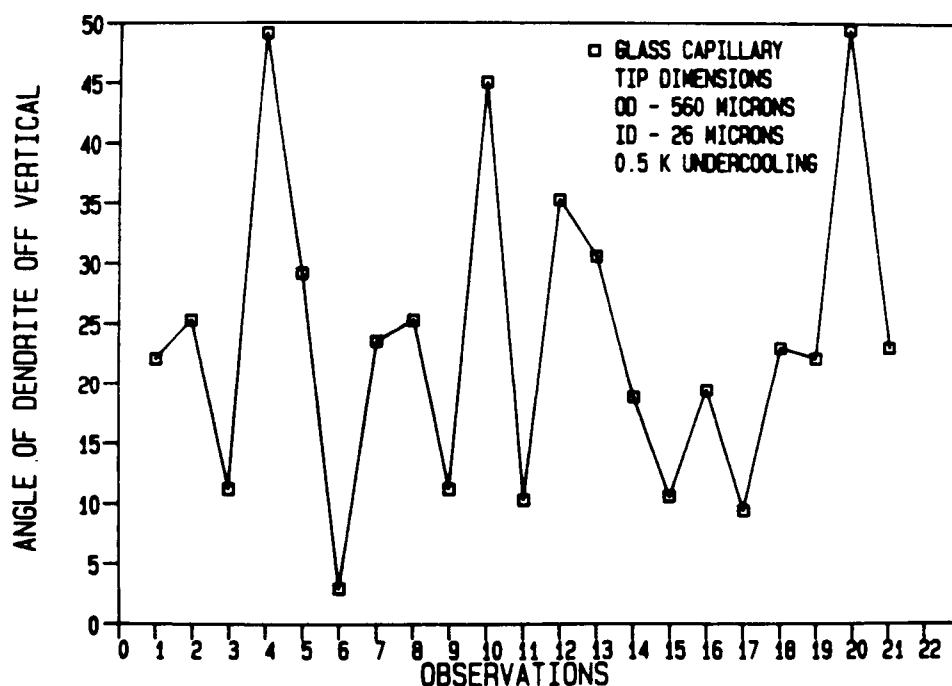


Figure 7 Observed dendrite growth angle with respect to the capillary axis as a function of the number of the test.

crystal selection occurring in the capillary, or 3) the starting solid and growth down the capillary were single crystalline but the original single crystal was destroyed between tests and replaced inadvertently by a another single crystal of differing orientation. It is believed that the first and third possibilities could be easily resolved by seeding and careful procedural control to ensure the integrity of the seed crystal. If growth down the capillary is multicrystalline, however, it may be impossible to achieve an oriented dendrite without some mechanism to repeatedly select a crystal with the proper orientation. Furthermore, this issue raises the question of the need for a seed crystal of the proper orientation if, in fact, it is not possible to propagate that seed into a undercooled melt. Further testing will attempt to identify the necessary conditions, if any, where growth of a single crystal from a undercooled melt is possible.

#### **SUMMARY**

The IDGE is an active crystal growth experiment designed to test dendritic growth theory at low undercoolings where convection prohibits such studies at 1g. The experiment will be essentially autonomous, though limited in-flight interaction through a computer interface is planned. One of the key components of the apparatus will be a crystal growth chamber capable of achieving oriented single crystal dendritic growth. Recent work indicates that "seeding" the chamber with a crystal of the proper orientation will not, in and of itself, be sufficient to meet this requirement. Additional flight hardware and software required for the STS flight experiment are currently being developed at Nasa Lewis Research Center and at Rensselaer Polytechnic Institute.

#### **ACKNOWLEDGMENT**

This work is being conducted with the support of the Materials Processing in Space Program, National Aeronautics and Space Administration under NAG 3-333 with liaison through the Lewis Research Center.

#### **REFERENCES**

1. M. E. Glicksman and S. C. Huang, Adv. Space Res., Vol 1, 25 (1981).
2. S. C. Huang and M. E. Glicksman, Acta Met, Vol 29, 701 (1981).
3. M. E. Glicksman, R. J. Schaefer and J. D. Ayers, Met Trans A, Vol. 7A, 1747 (1976).



4. G. P. Ivantsov, Dokl. Akad. Nauk, USSR, Vol 58, 567 (1947).
5. J. S. Langer and H. Muller-Krumbhaar, Acta Met, Vol 26, 1681 (1978).
6. J. S. Langer and H. Muller-Krumbhaar, Acta Met, Vol 26, 1689 (1978).
7. J. S. Langer and H. Muller-Krumbhaar, Acta Met, Vol 26, 1697 (1978).
8. D. Kessler, J. Koplik and H. Levine, Phys. Rev., Vol. A30, 3161 (1984).
9. E. Ben-Jacob, N. Goldenfeld, G. Kotliar and J. Langer, Phys. Rev. Lett., Vol. 53, 2110 (1984).
10. J. S. Langer, Phys. Rev., Vol. A33, 475 (1986)
11. D. Kessler, J. Koplik and H. Levine, Proceedings of NATO A.R.W., "Patterns, Defects and Microstructures in Non-Equilibrium Systems", (1986) To be published.
12. N. Goldenfeld, Proceedings of the NATO ASI, "Physiochemical Hydrodynamics: Interfacial Phenomena" (1986) To be published.
13. Final Report - Low Acceleration Characterization of Space Station Environment, Revision A, SP85-MSFL-2928, Prepared by Advanced Programs Department, Space Programs Division, Teledyne Brown Engineering, Huntsville, Alabama (1985).
14. D. Langbein, "Allowable G-levels for Microgravity Payloads", To be published in ESA Journal.
15. M. E. Glicksman, E. Winsa, R. C. Hahn, T. A. Lograsso, E. R. Rubinstein and M. E. Selleck, "Solidification Under Microgravity Conditions - Dendritic Growth", To be published in AAS Journal.

## ISOTHERMAL SOLIDIFICATION IN A BINARY ALLOY MELT

Principal Investigator : V.Laxmanan, Department of Metallurgy & Materials Science, Case Western Reserve University, Cleveland, Ohio 44106.  
Concurrently, Visiting Scientist, NASA Lewis Research Center, Mail Stop 105-1, Cleveland, Ohio 44135.

## ABSTRACT

A space shuttle experiment employing the General Purpose (Rocket) Furnace (GPF) in its isothermal mode of operation is manifested on MSL-3, circa 1989. The central aim of this experiment (first in a series of proposed experiments) is to investigate the effect of reduced gravity levels on the segregation behavior in a slowly, and isothermally, cooled sample (cooling rate 0.003 K/sec, thermal gradients  $< 0.05$  K/mm, the top is slightly hotter than the bottom) of a binary Pb-15 wt% Sn alloy. This experiment would thus be able to simulate, in a small laboratory sample, about 20 mm dia 60 mm high and weighing about 150 grams, some aspects of the segregation phenomena occurring in large industrial ingots. Ground-based experiments conducted in the single-cavity simulator of the GPF, located at the Marshall Space Flight Center (MSFC), in support of the microgravity experiment are described in detail. The results of the MSFC experiments are compared with other related experiments conducted at Case Western Reserve University (CWRU), wherein the isothermal constraints were relaxed.

The isothermally processed samples indicate a small and gradual increase in fraction eutectic, and a corresponding increase in tin content, from the bottom to the top of the ingot. At a given height from the ingot bottom, we also observe a radial variation of eutectic fraction, or tin content. The radial variations are minimal near the ingot bottom, but there are large radial variations in the top half. The microgravity experiment would most likely indicate a smaller variation in fraction eutectic from the bottom to the top. Also, the large radial variations near the top would be much less pronounced, if not totally absent. In the CWRU experiments, we have been able to simulate more severe segregation, including segregation defects known as freckles. Follow up experiments employing the GPF without the isothermal constraints, or other suitably modified space shuttle hardware are suggested.

---

Prepared in conjunction with the presentations to the Schrieffer Committee Review of Space Shuttle experiments at the Lewis Research Center, March 9, 1987.

PRECEDING PAGE BLANK NOT FILMED

## Introduction

When a molten alloy is allowed to freeze a number of important physical factors come into play which together contribute to the formation of a solid phase of non-uniform composition. First, the density of the solid and liquid phases are different, i.e., the fractional density change

$$\beta = (\rho_s - \rho_L) / \rho_s > 0,$$

resulting either in liquid flow towards the freezing regions to feed shrinkage ( $\beta > 0$ ) or flow away from the solid-liquid interface if  $\beta < 0$ . Here  $\rho_s$  is the density of the solid and  $\rho_L$  the density of the liquid. Second, the latent of fusion liberated during solidification must be transported away from the solid-liquid interface, resulting in temperature gradients in the liquid and solid phases. Third, the various alloying elements redistribute themselves differently between the liquid and solid phases, i.e., the partition ratio  $k > 1$  or  $k < 1$ . The remanent liquid is thus either enriched ( $k < 1$ ) or depleted ( $k > 1$ ) in alloying elements, resulting in a continuously changing liquid composition and hence a continuously changing solid composition. There is little that can be done to alter these three factors, which are dictated solely by fundamental physical and chemical laws governing the atomic or molecular arrangements in the solid and liquid states. The final solid formed is thus necessarily inhomogeneous in composition.

In terrestrial solidification processes, the inevitable segregation resulting from the fact that  $k \neq 1$ , and/or  $\beta \neq 0$ , is further aggravated by the complicating effects of gravity-driven fluid flow. Temperature and concentration gradients within the liquid phase give rise to density gradients, which in turn leads to fluid motion within both the fully liquid and partially frozen regions of a freezing ingot. Also, in a gravity field, density differences between the solid and liquid phases can result in settling or floating of detached solid particles or dendrites, and hence segregation, due to this effect. Thus, gravity-driven fluid flow effects can lead to (large) compositional changes, occurring over distances of the order of the dimensions of the ingot. We refer to this as macro-segregation. In the absence of any significant gravitational fluid flow effects, compositional changes would be confined to distances on the order of the local primary or secondary dendrite arm spacings in a freezing ingot. We refer to this as micro-segregation. A more quantitative definition of macro- and microsegregation is given later.

It is now generally accepted [1-5] that gravity-driven fluid flow is the underlying cause for the severe segregation pattern often observed in many industrial solidification processes ("freckles" in superalloys, U, Nb base alloys and other specialty alloys, "A" and "V" segregates in steels, etc). Non-uniformity of composition reflects itself in an undesirable variation in mechanical, chemical, electrical, magnetic or other physical properties of the alloy and thus leads to an inferior performance during service. A great deal of experimental and theoretical effort has been expended over the years to understand the basic mechanisms responsible for the observed segregation behavior, and a number of control strategies have been proposed to minimize segregation defects. There is, however, much that remains to be learned from a fundamental standpoint.

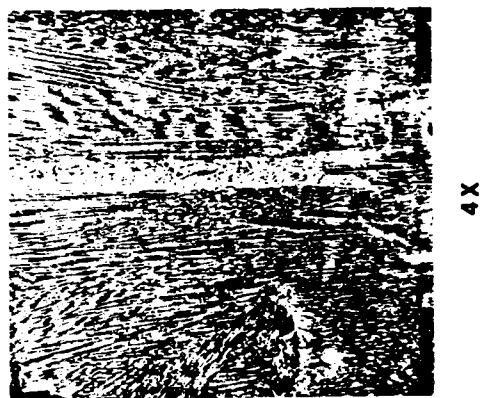
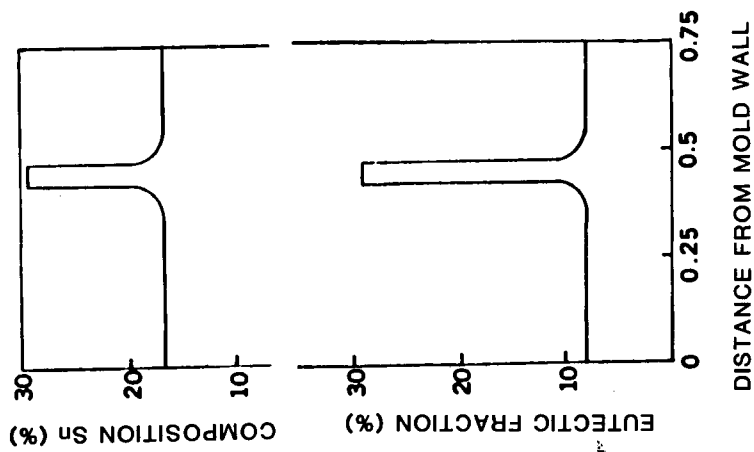


Fig. 1 : Columnar freckle in one of the CWRU experiments; Table 2, experiment no. 4. The tin enriched region is slightly off-center with respect to the ingot axis and extended approximately to the mid-height of the ingot from the top.

The basic mechanisms leading to severe segregation defects such as "freckles"\*, Figure 1, during alloy solidification are also quite similar to the mechanisms believed to be responsible for other natural processes such as atmospheric currents, and, thermo-haline or thermo-solutal convection responsible for ocean currents. In the presence of severe salinity gradients, thermosolutal convective effects can lead to the formation of "salt fingers" in oceans; the oceanographers analog of "freckles." [6] Thus, a fundamental understanding of segregation phenomena during alloy solidification has wider applications.

#### Experimental Approach: Justification for Microgravity

The principal objective of the experiments to be described here is to investigate the effect of reduced gravity levels on macro- and microsegregation in a slowly cooled sample of a model binary Pb-15 wt% Sn alloy. The reduced gravity experiment will be performed aboard the space shuttle. One currently approved microgravity experiment is manifested for flight on the MSL-3, circa 1989, and will employ the General Purpose (Rocket) Furnace (GPF) in its isothermal\*\* mode of operation. A series of three other space shuttle experiments, also employing the GPF, has also been proposed [7]. These are aimed at investigating segregation behavior without the isothermal constraints imposed in the first experiment. Experiments of this type may, however, be satisfactorily performed in other experimental apparatus, such as the ADSF or AADSF\*\* with stationary sample of suitable aspect ratio, or even the IDGA.\*\*

A number of ground-based (1-g) experiments have been carried out in the interim as a precursor to the microgravity experiments. The main purpose of this paper is to describe some of the important ground-based results obtained to date. The 1-g experiments may be divided into two categories. The first set involves tests conducted at the Marshall Space Flight Center (hereafter MSFC tests). These tests employed the single cavity simulator of the GPF. The MSFC tests were all aimed at:

- i) Ensuring complete reproducibility, in earth-based studies, of the thermal conditions to be employed in the microgravity experiment. Thus, these tests were mainly concerned with achieving nearly isothermal conditions, to reflect the constraints imposed for the first space shuttle experiment. This has been accomplished successfully in many tests (12 to date), Table 1. A typical cooling rate in the MSFC test was 0.003 K/sec. Axial thermal gradients in the samples were often less than 0.05 K/mm. The GPF will be programmed to achieve identical thermal conditions in the space shuttle experiment.
- ii) A detailed characterization of the thermal conditions within the solidifying sample using the maximum of six thermocouples which could

---

\* A "freckle" is a long column or extended region of solute enriched or solute depleted material. The term solute is used here to denote the minor species in a binary or multi-component alloy.

\*\* This constraint was imposed by MSFC back in April 1984 when this experiment was first proposed. The "isothermal" experiment was originally scheduled to fly on the D-1 mission, then planned for October/November 1985. IDGA: Isothermal Dendrite Growth Apparatus. AADSF: Advanced Automatic Directional Solidification Furnace.

HEAT NUMBER	CHEMICAL COMPOSITION		SOLIDIFICATION TIME, min	COOLING RATE c/min	TEMPERATURE GRADIENT G, c/cm	LIQUIDUS ISOTHERM VELOCITY $R_L$ , cm/min	FRECKLES
	Pb%	Sn%					
1	85.1	14.9	65	3.23	1.54	2.0830	NO
2	85.1	14.9	150	1.21	16.85	0.0718	NO
3	84.7	15.3	230	0.98	24.70	0.0397	NO
4	84.8	15.2	350	0.55	22.32	0.0246	YES
5	86.0	14.0	520	0.425	34.25	0.0124	YES
6	85.0	15.0	300	0.713	21.10	0.0338	?
7	15.0	85.0	59	2.32	27.56	0.0842	NO
8	15.7	84.3	135	0.89	19.49	0.0354	NO
9	15.6	84.4	170	0.69	16.14	0.0551	NO

CD-86-20012

Table 1 : Summary of important solidification parameters in the samples processed at CWRU.

SAMPLE	COOLING RATE, K/SEC	AVERAGE TEMPERATURE GRADIENT, K/MM	QUENCH TEMPERATURE, °C	COMMENTS
LERC001	0.0030	0.051	164.5	MULTIPLE HEATS
LERC002	0.0030	0.011	169.2	PRELIMINARY CARTRIDGE DESIGN
LERC003	0.0029	0.092	269.0	
LERC004	0.0031	0.078	259.5	
LERC005	0.0030	0.070	164.0	
LERC006	0.0033	0.025	164.5	FINAL PLUNGER DESIGN
LERC008	0.0086	0.028	281.0	
LERC010	0.0036	0.097	285.0	TWO HEATS

\* TEMPERATURE GRADIENT IN SAMPLE WAS REQUIRED TO BE LESS THAN 0.1 K/MM. TEMPERATURE GRADIENT DECREASES AS MORE AND MORE SOLID FORMS.

CD-87-24853

Table 2 : Summary of processing conditions in the single-cavity simulator of the GPF located at MSFC.

be accommodated with the single-cavity GPF simulator. Only two thermocouples are permitted in the microgravity experiment.

- iii) Tracking the evolution of segregation in the sample under 1-g conditions by interrupting the solidification and rapidly quenching the partially frozen alloy, thus preserving the high temperature structure. The samples were quenched from various temperatures within the liquid-solid range prior to complete solidification of the alloy.

The MSFC tests thus represent the most critical and extensive 1-g data base for the microgravity experiment.

The second set of experiments, summarized in Table 2, are the 1-g tests conducted at Case Western Reserve University (hereafter CWRU tests), in an apparatus which was built to mimic the essential thermal characteristics of the GPF. These tests were conducted over a much wider range of thermal gradients and cooling rates. Cooling rates were varied between 30 K/sec and 210 K/sec whereas thermal gradients varied between 0.15 K/mm to 3.5 K/mm. These thermal conditions are well within the capabilities of the GPF, and represent experimental conditions that could be employed in potential future space shuttle experiments, or looking even further, in materials processing experiments in the space station.

Thus, in these ground-based experiments, we have been able to simulate some aspects of the segregation phenomena occurring in large industrial ingots in a relatively small laboratory sample - about 20 mm dia., 60 mm high, and weighing about 150 gram - under carefully controlled conditions. The MSFC tests simulate the solidification behavior in the interior of large, statically cast, industrial ingots wherein solidification occurs over long periods of time, often 2 to 3 days, with negligibly small thermal gradients and cooling rates. Typical solidification time in the MSFC test was about 640 minutes, i.e., the alloy was partially solid for nearly 11 hours. An important outcome of the first microgravity experiment would be a clear demonstration of the relative importance of fluid flow due to shrinkage and gravitational effects. If shrinkage flows are predominant, or at least as important as gravitational effects, a potentially useful strategy for controlling macrosegregation on earth would be to manipulate the alloy composition to achieve negligibly small density differences between the liquid and solid phases ( $\beta \rightarrow 0$ ).

The CWRU tests, on the other hand, simulate the thermal conditions attained in a number of other industrial solidification processes - continuous casting, ESR or VAR ingots, for example. In these tests we have been able to produce more severe segregation, including "freckles", illustrated earlier in Figure 1. Again, the microgravity experiment would help elucidate the fundamental role of gravity in triggering these severe segregation defects. For example, in experiments wherein the thermal (and hence the density) gradient is somewhat steeper, freckles were observed, whereas in others with a smaller thermal gradient only a pronounced compositional change from the top to bottom is observed: see figure 16, later in this paper which summarizes the compositional data for experiments in Table 2. Experiments No. 4, 5, and 6 are particularly noteworthy.

### Unique Features of the GPF-type Experiments: Comparison with DS Experiments

In the binary Pb-15 wt% Sn alloy, solidification begins at the liquidus temperature ( $T_L \sim 290^\circ\text{C}$ ). Liquid becomes enriched in Sn as solidification proceeds and solidification ends at the eutectic temperature ( $T_E = 183^\circ\text{C}$ ) when a fraction  $f_E$  of the original liquid freezes as a two-phase solid. Thus, solidification occurs over a very wide range of temperatures in this alloy, from approximately  $290^\circ\text{C}$  to  $183^\circ\text{C}$ , or over an interval of about  $100^\circ\text{C}$ . Since the maximum ingot dimension, the height, is only about 50 to 60 mm in the GPF experiments, axial thermal gradients considerably less than 2 K/mm will result in the formation of a two-phase region of part liquid and part solid, the so-called mushy zone, throughout the entire ingot.

We define a fully developed mushy zone (FDMZ) as a mushy zone bounded at the top by the liquidus isotherm,  $T_L$ , and at the bottom by the eutectic isotherm,  $T_E$ . A partially developed mushy zone (PDMZ), on the other hand, is one that may be bounded at the top by an isotherm  $T < T_L$  and at the bottom by an isotherm  $T > T_E$ . The mushy zone is almost always completely developed in directional solidification (DS) experiments, wherein the velocity of the tip isotherm,  $R_t$ , is exactly equal to the velocity of the eutectic isotherm,  $R_E$ , both being exactly equal to the withdrawal speed of the sample,  $V$ , Figure 2. In principle, the tip temperature  $T_t$  in a DS experiment is always less than the liquidus temperature  $T_L$ . The dendrite tip undercooling

$$\Delta T = T_L - T_t$$

is a function of the growth

$$R (= R_t = R_E = V),$$

and the externally imposed thermal gradient  $G$ , but is negligibly small compared to the freezing range of the alloy\* under most of the usual conditions of dendritic growth in alloys [8-10]. Also, the mushy zone thickness,  $M$ , remains constant in a typical DS experiment once steady-state conditions have been achieved.

In the GPF-type experiments on the other hand, the mushy zone thickness,  $M$ , is never constant, but changes slowly with time, depending on the thermal gradient and the cooling rate. These experiments are

\* The equilibrium freezing range  $\Delta T_0 = T_L - T_S$  is often used in the theory of dendritic solidification in alloys as the reference temperature for non-dimensionalization [9-12]. Thus,  $\Delta T / \Delta T_0 \ll 1$  under the usual conditions of dendritic growth, typically only about 0.001 or less. The quantity  $T_L - T_E$  is the non-equilibrium freezing range. Non-equilibrium conditions prevail during most common experimental conditions because of relatively small rates of diffusion in the solid phase compared to the liquid [13]. We assume compositional equilibrium is achieved only "locally" at the solid-liquid interface.



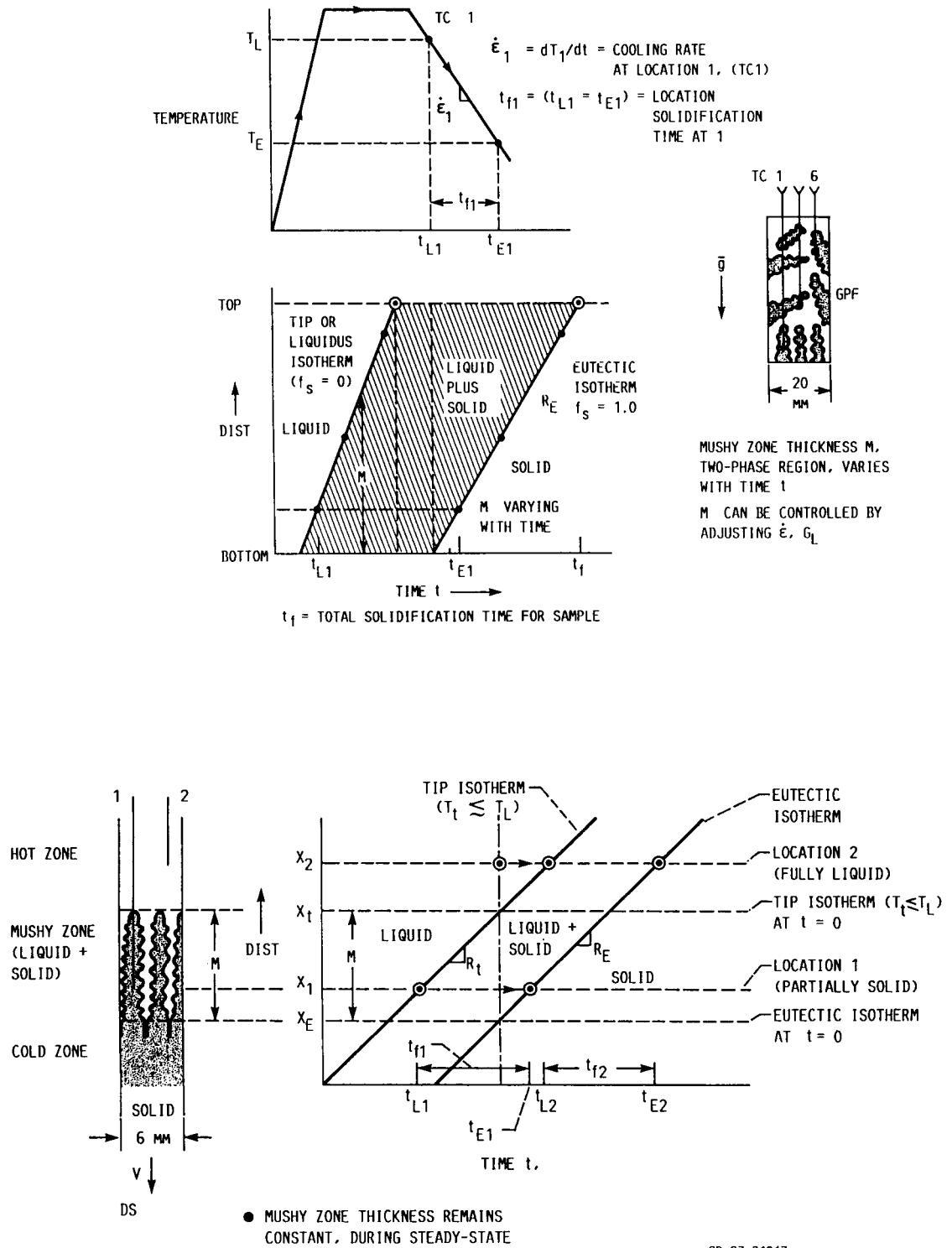


Fig. 2 : Comparison of mushy zone character in GPF-type experiment and directional solidification (DS) experiments.

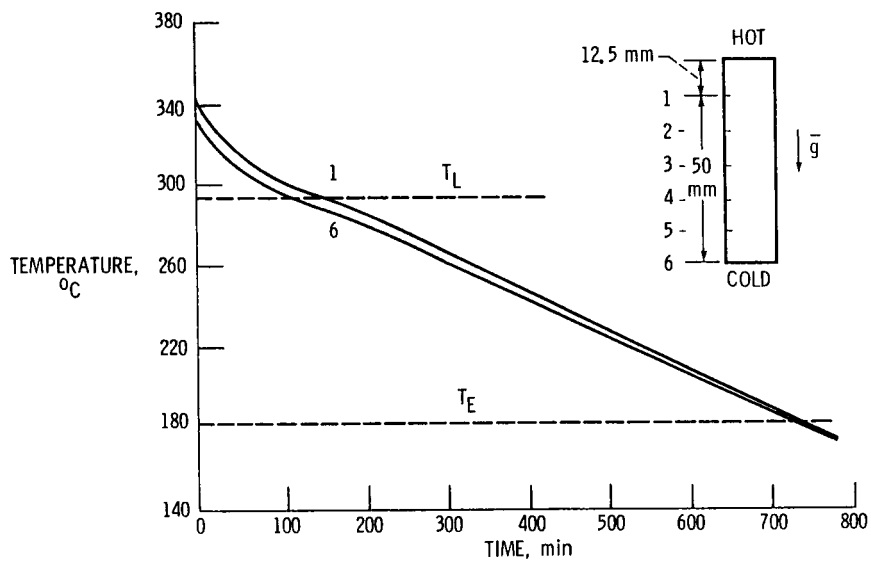


Fig. 3 : Typical temperature-time plot for slowly cooled sample in single-cavity GPF simulator; LeRC 002, Table 1.

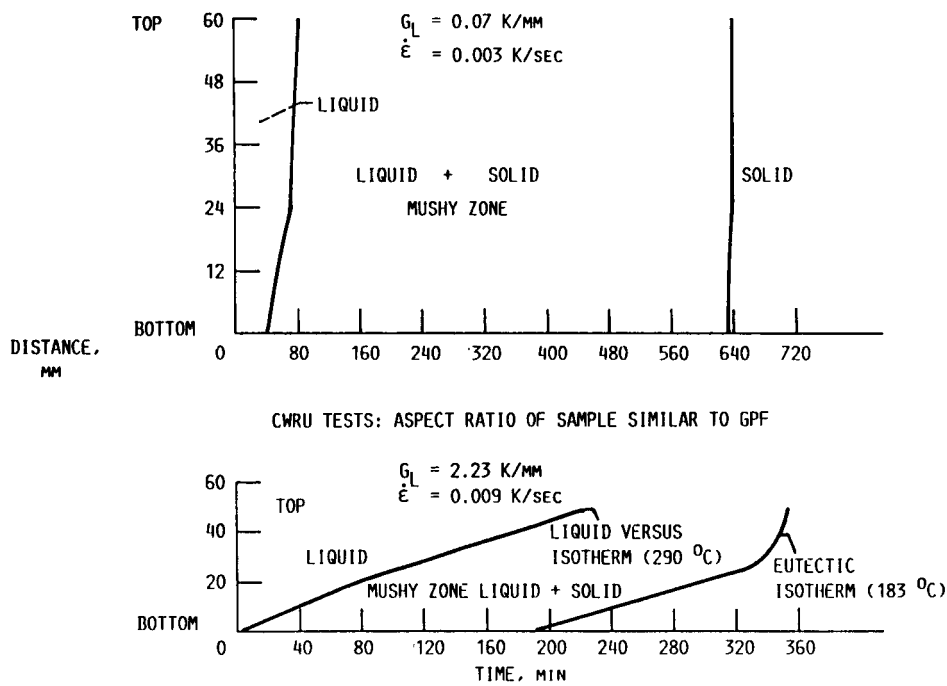


Fig. 4 : Comparison of evolution of mushy zone (two-phase, liquid plus solid, region) in MSFC and CWRU experiments.

therefore uniquely suited to investigate the influence of gravity-driven fluid-flow effects on macro- and microsegregation during dendritic solidification. Moreover, both FDMZ's and PDMZ's can be created, with various bounding temperatures at the top and the bottom, see also Figure 5. The DS experiments do not allow such a flexibility.

Figure 3 plots the experimentally determined temperature-time profile at various locations in one of the MSFC tests. Figure 4 re-plots the same information differently. Here we imagine tracking the position of a given isotherm, say the eutectic or liquidus isotherm, in the sample as a function of time. Note that the ingot is partially solid i.e., mushy, (the dendritic network of solid has no particular directionality because of the nearly isothermal conditions prevailing, see microstructure of a partially quenched sample in Figure 11a) with a fully liquid zone above the mushy zone in the early stages of the experiment. The thickness of the mushy zone increases gradually with time, during the first 90 minutes or so, until the entire sample becomes liquid plus solid. This sequence of events is shown schematically in Figure 5. The sample remains part liquid plus solid during the greater part of the experiment, with the temperature decreasing slowly with time, and is abruptly frozen when the eutectic isotherm sweeps through the ingot. In the calculations in Figure 4, we assume that the liquidus isotherm of the original alloy demarcates the fully liquid region from the liquid plus solid region, i.e., we have implicitly assumed that the bulk liquid composition remains unchanged and is always equal to the initial alloy composition of  $C_0 = 15 \text{ wt\% Sn}$ .

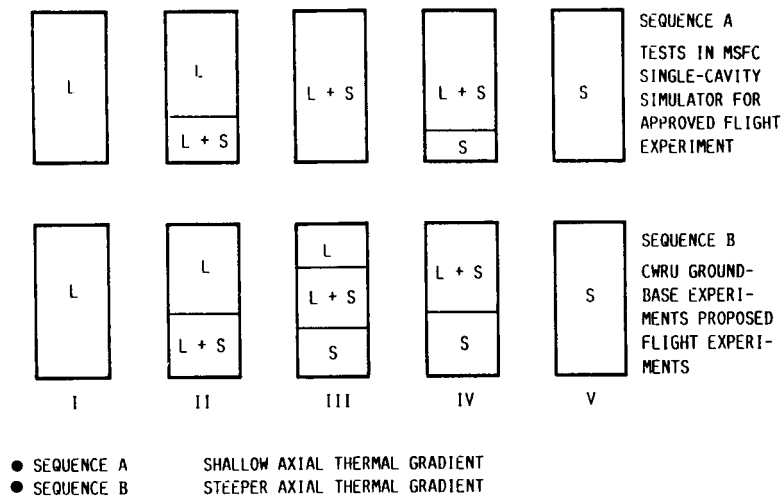
This is a questionable assumption, particularly because of the compositional changes occurring in the interdendritic liquid due to enrichment of Sn during the course of the experiment, and the attendant change in the bulk liquid if there is significant fluid motion. The spatial and temporal variation of the liquid composition is, however, unknown apriori without further detailed calculations and the above approximation is still a useful one to delineate the various phase regions.

A similar solidification sequence was observed in some of the CWRU tests, those with thermal gradients much less than  $2 \text{ K/mm}$ , the significance of which has been discussed earlier. Some of the CWRU tests, however, yielded a slightly different sequence because of the steeper thermal gradients employed. Figures 4b and 6 illustrate, for example, the thermal conditions which lead to the "freckle" noted in Figure 1. In this case, the mushy zone never penetrates the sample completely. A completely solid layer is formed at an early stage in the experiment. However, density gradients in this case are much greater in the corresponding MSFC tests. Figures 4 through 6 compare the solidification sequence in the MSFC and CWRU tests.

In summary, the GPF-type experiments of the type being planned for the proposed and approved space shuttle experiments offer a number of unique and innovative opportunities to critically examine the role of gravity-driven fluid flow effects.

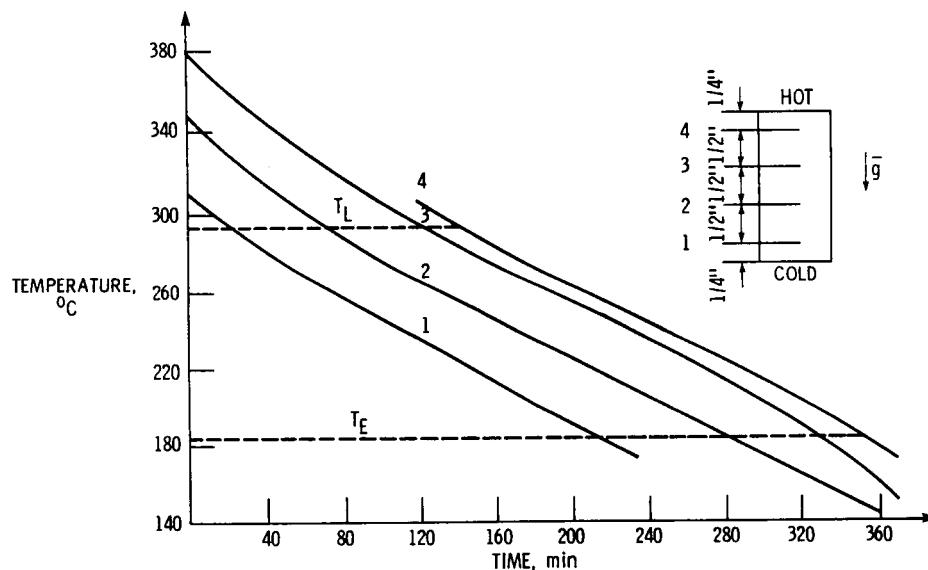
#### Characterization of Macro- and Microsegregation

Consider a small volume element within a freezing alloy, Figure 7. The volume element is fixed in space and the dimensions of the element are supposed to be appropriate to the size scale of the dendrites growing in the melt and the local dendrite arm spacings. At time  $t < 0$  the element is fully liquid. The temperature  $T > T_L$  and the liquid composition within



CD-87-24846

Fig. 5 : Schematic illustration of sequence of solidification in GPF-type experiments. Fully developed mushy zone (FDMZ) is seen in sequence B, stage III. The mushy zone is partially developed in all other stages.



CD-86-20004

Fig. 6 : Temperature-time plot for slowly cooled sample in one of the CWRU experiments leading to the freckle illustrated in fig. 1. The axial thermal gradient is steeper than in the MSFC tests.

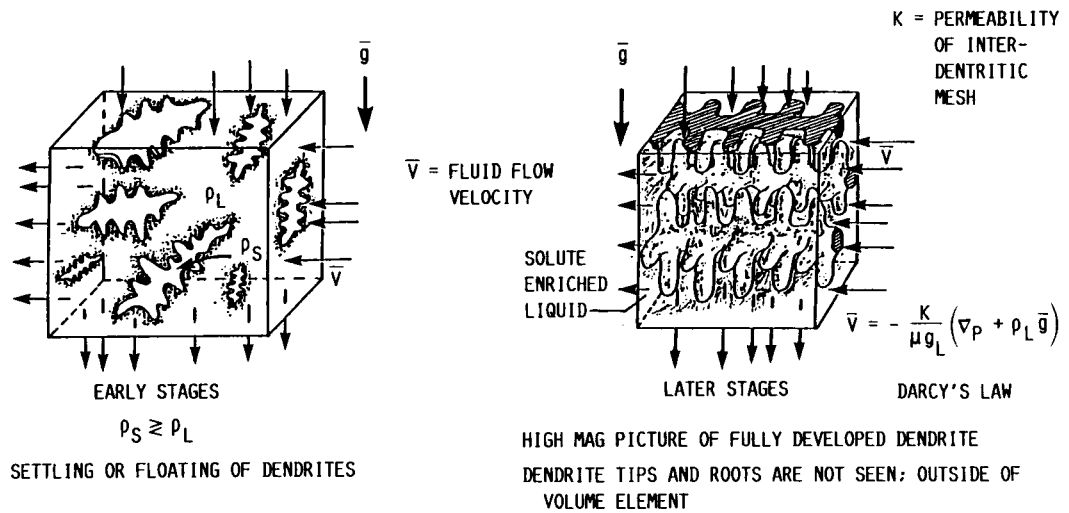


Fig. 7 : Schematic illustration of small volume element undergoing solidification in an ingot.

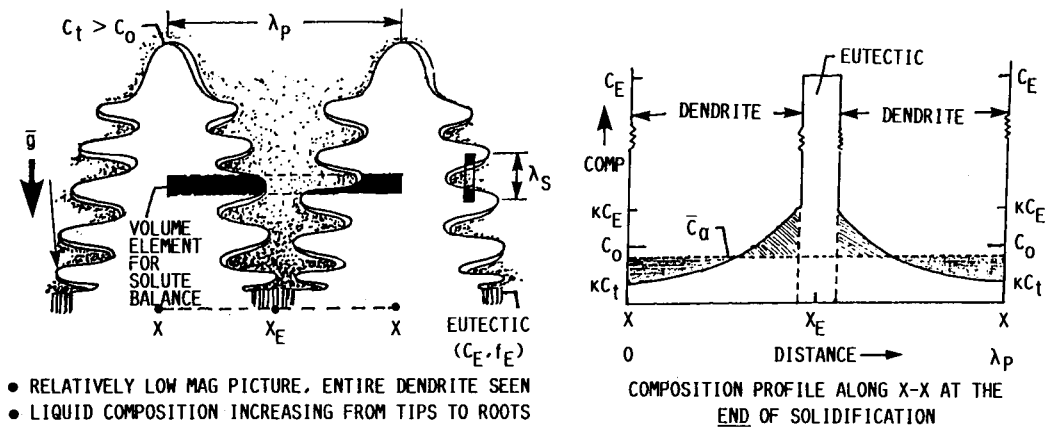


Fig. 8 : Microsegregation, i.e. compositional change, between the center-line of two individual dendrites.

the element is assumed to be uniform and equal to  $C_0$ . At  $t = 0$  the temperature  $T$  has dropped to  $T_t$  and the dendritic array begins to sweep through the element. The first solid (dendrite tip) to form has a composition  $kC_t$ . Here  $T_t$  is the dendrite tip temperature and  $C_t$  is the liquid composition in equilibrium with the tips:  $T_s < T_t < T_L$  and  $C_0 < C_t < C_0/k$ . The exact values of  $C_t$  and  $T_t$  depend on the dendrite tip growth rate  $R_t$ , the thermal gradient  $G_L$  in the liquid and the alloy composition [9-12]. As solidification proceeds fraction liquid within the element decreases and correspondingly the liquid composition increases ( $k < 1$ ). Let  $C_L$  be the liquid composition within the element at time  $t$  when the liquid fraction remaining in the element is  $f_L$ . This is the situation depicted in Figure 7.

When the liquid composition within the element has increased to  $C_E$ , the eutectic composition, two-phase or eutectic solidification begins. Let  $\bar{C}_\alpha$  denote the average composition of the dendritic solid within the element at this time, Figure 8, and let  $f_E$  denote the fraction of liquid remaining in the element just prior to the beginning of eutectic solidification. The volume element is completely frozen when the fraction liquid  $f_E$  freezes at the eutectic temperature,  $T_E$ .

The average composition of the dendrite,  $\bar{C}_\alpha$ , will be some unknown value between  $kC_t$  and  $kC_E$ , but must obviously be less than  $C_0$ , Figure 8. Let  $\bar{C}_{\alpha\beta}$  denote the average composition of the two-phase or eutectic solid formed within the element, and,  $\bar{C}_s$  the average composition of the finally solidified alloy, i.e., the average composition of the dendrite plus average composition of the two-phase solid:

$$\bar{C}_s = \bar{C}_\alpha f_\alpha + \bar{C}_{\alpha\beta} f_E \quad (1)$$

where  $f_\alpha = 1 - f_E$ .  $\bar{C}_{\alpha\beta}$  depends on the growth rate of the eutectic front,  $R_E$ , and the thermal gradient.  $\bar{C}_{\alpha\beta} = C_E$  only in the ideal case when the liquid is isothermal [14], i.e., when  $G_L/R_E$  is very small.  $\bar{C}_{\alpha\beta} \rightarrow C_0$  for high values of  $G_L/R_E$ . The task at hand is now to calculate theoretically the values of  $\bar{C}_\alpha$ ,  $\bar{C}_{\alpha\beta}$  and  $f_\alpha$  or  $f_E$  in Equation (1) above. A mathematically rigorous calculation, which also allows for fluid-flow effects, is admittedly very difficult to perform. A simple model, based on the work of Flemings, Hunt, and co-workers has recently been proposed by the author [15]. This is discussed later. Equation 1 may however be used to define quantitatively the basic notions of macro- and microsegregation.

In general, the average composition of the final solid formed within the volume element of Figure 7 may be greater than, equal to or less than the initial alloy composition  $C_0$ . If, perchance,  $\bar{C}_s$  is exactly equal to  $C_0$ , we say that there is NO macrosegregation within this element. If the same situation exists within every single random volume element in the

casting or ingot\* it is easy to visualize that there will be no "macroscale" variations in the average composition of the solid as we sample various portions of the ingot. The entire ingot will appear to be homogeneous in composition.

We may verify this for example by measuring the chemical composition by atomic absorption spectrometry, X-ray analysis, or wet chemistry tests, by taking small random drillings from various locations. Such chemical measurements are reported later. Or we may measure composition variations non-destructively by traversing a rather coarse or diffuse electron beam across various regions. The fraction eutectic  $f_E$  may also be used as a measure of the various in the average composition of the final solid. This offers another convenient non-destructive method of quantifying macrosegregation in the sample. A comparison of the results obtained from these various techniques is presented in Figure 9.

Note that even if  $\bar{C}_S = C_0$ , there are still compositional variations but these are strictly on a "microscopic" scale - the scale of the dendrite arm spacings. This is microsegregation, Figure 8. These microscopic variations can be detected by traversing small regions of the sample with a finely focused electron beam (microprobe analysis). Ideally we should be able to show that the average composition between any two dendrites or a group of dendrites is exactly equal to  $C_0$ , IF there is NO macrosegregation. Unfortunately, electron microprobe analysis do not yield accurate quantitative measurements of alloy composition; only relative variations can be detected.

How do we ensure conservation of solute if  $\bar{C}_S$  within a random volume element is greater than or equal to  $C_0$ ? This is simply a matter of faith. There have been no analytical calculations, or numerical models, reported in the literature which rigorously demonstrate global conservation of solute after duly accounting for ALL important effects, in particular fluid-flow effects. We simply ASSUME solute conservation: i.e., regions in the casting wherein  $\bar{C}_S > C_0$  are exactly matched by regions wherein  $\bar{C}_S < C_0$ . It is easy to demonstrate, with some useful simplifications, that when fluid flow effects are included,  $\bar{C}_S$  is equal to  $C_0$  only in the special case when  $k = 1$  [15].

$$\bar{C}_S = C_0 \left[ \frac{k}{k'} + (1 - \frac{k}{k'}) g_E^{k'} \right] \quad (2)$$

$$\text{where } k' = 1 - \frac{(1-k)}{(1-\beta)(1+\xi)} \quad (3)$$

$\xi = v \cdot \Delta T / \epsilon$  is the fluid flow parameter, assumed to be constant throughout solidification.  $v$  is the fluid flow velocity within the element,  $\nabla T$  is the thermal gradient and  $\epsilon$  is the cooling rate.  $g_E$  is the volume fraction eutectic in the element.  $g_E = f_E$  if  $\beta = 0$ . Equations (2) and (3) are derived in reference 15. For  $\beta = 0$  and  $\beta = 0$ , equations (2) and (3) indicate that  $\bar{C}_S$  is always equal to  $C_0$ , that there is NO macrosegregation and ONLY microsegregation within the volume element of Figure 7.

\* The casting may also be a "microcasting" such as a rapidly solidified powder particle or melt spun ribbon [15].

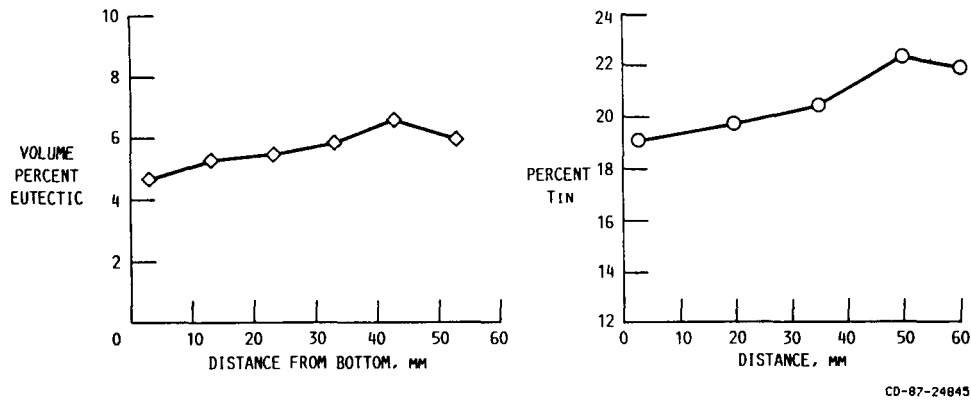


Fig. 9 : Comparison of fraction eutectic measurement and tin content measurements for slow cooled MSFC test. Tin content was obtained from a coarse beam raster, in a microprobe. The probe averages the composition across several dendrite and eutectic regions, such as shown in the quantimet image field micrograph of fig. 11.

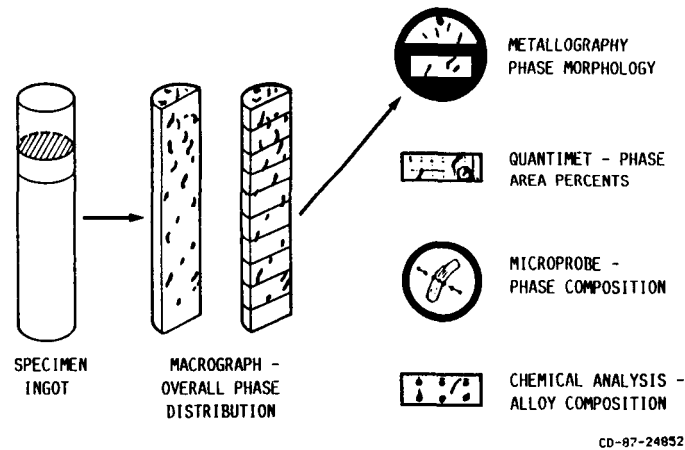


Fig. 10 : Sequence of analysis of GPF samples after isothermal or non-isothermal processing.



Thus, fluid flow and shrinkage effects are the underlying cause of macrosegregation in terrestrial solidification processes. Carefully controlled microgravity experiments would help verify the simple analytical calculation presented here. This must of course be coupled with a more rigorous numerical calculation. The crux of the matter quite simply is the evaluation of the spatial and temporal variation of the fluid flow parameter  $\xi$  or the "effective" partition ratio,  $k'$  as defined by Equation (3). Spatial variations of  $\bar{C}_s$  in the final ingot arise, simply speaking, from the spatial variation of  $k'$  during solidification.

To summarize, macro- and microsegregation in an alloy may be quantified by detailed measurements of  $\bar{C}_\alpha$ ,  $\bar{C}_s$ ,  $f_\alpha$ , or  $f_E$ . Other related morphological characteristics of interest are i) the tip composition,  $C_t$  or  $kC_t$ , i.e., the composition at the centerline of the dendrite in the finally solidified alloy, ii) the primary and secondary dendrite arm spacings,  $\lambda_p$  and  $\lambda_s$  respectively, iii) the cell or dendrite length, i.e., the mushy zone thickness,  $M$ . Variation in dendrite arm spacings in the ingot are of particular interest since this suggests variation in the permeability of the dendritic network to fluid flow during solidification. A careful measurement of dendrite arm spacings in 1-g control tests is also important because dendrite arm spacings in reduced gravity experiments have often been reported to be higher than in the 1-g experiments [16-19].

### Experimental Results

The isothermally processed samples from the MSFC tests and the samples processed at CWRU have all been subjected to a rigorous regimen of post-mortem metallographic analyses, Figure 10. These include detailed microstructural characterization, viz. primary and secondary dendrite arm spacing measurements using optical metallography techniques, quantimet measurements of area fraction eutectic (two-phase material) in the sample, microprobe measurements to delineate microsegregation across individual dendrites, and a coarse beam raster to arrive at a qualitative measure of macrosegregation. Finally, a more detailed macrosegregation characterization was performed by actual chemical composition measurements of small drillings from various random locations. Such destructive chemical measurements have been kept to a minimum. Indeed, one of our objectives in this program has been to establish that non-destructive techniques such as fraction eutectic measurements with a quantimet offer a very reliable alternative.

The quantimet provides very accurate measurements of the area fractions of the dendrite and eutectic phases at any given location. The accuracy of the quantimet measurements depends on the ability of this instrument to detect various shades of grey. In a carefully prepared sample, the dendrite and eutectic phases etch differently; the dendrite phase often appears much much darker than the eutectic phase. Figure 11 illustrates a typical microstructure, or image field, used in the quantimet measurements. Each image field is a rectangular box approximately 650 microns by 400 microns. Typically about 800 such image field measurements can be obtained in a single transverse cross-section of the sample. The average of these 800 or so quantimet measurements gives the area fraction eutectic at say a given distance from the bottom of the ingot.

ORIGINAL PAGE IS  
OF POOR QUALITY

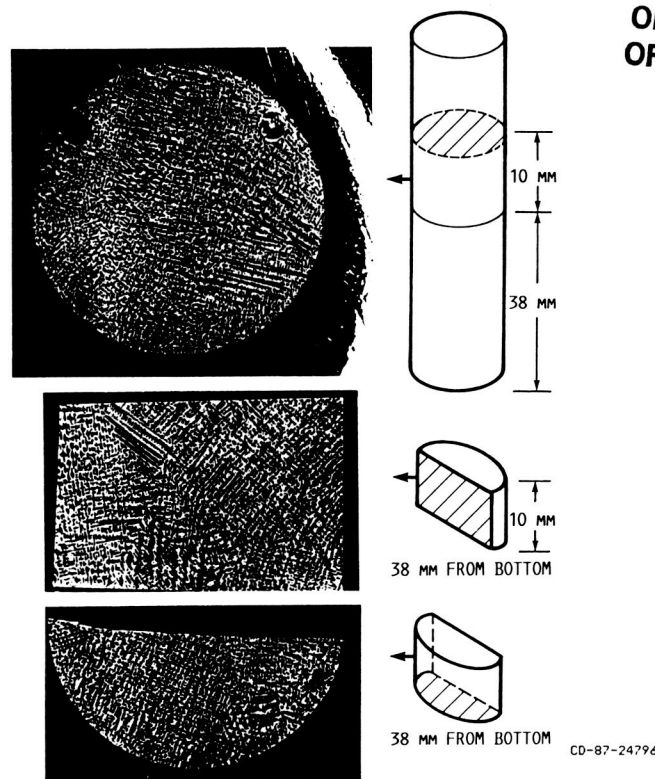
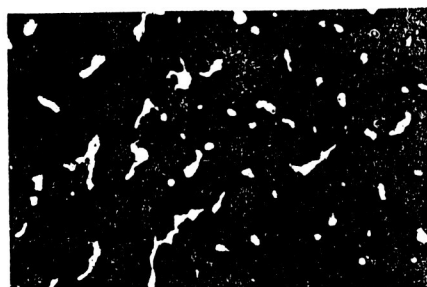


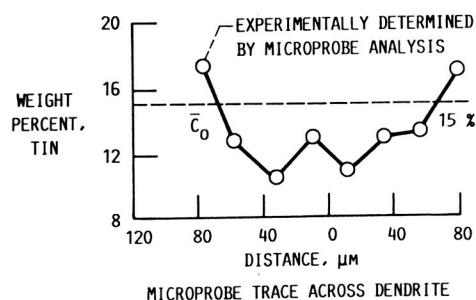
Fig. 11a : Low magnification photomicrographs illustrating dendritic growth in a partially frozen and quenched sample of Pb-15 wt% Sn alloy.



TYPICAL QUANTIMET IMAGE  
FIELD FOR FRACTION  
EUTECTIC MEASUREMENT -  
LIGHT AREAS ARE EUTECTIC



HIGHER MAG PICTURE OF EUTECTIC  
DENDRITE REGION THICKNESS  
~270  $\mu\text{m}$



CD-87-24797

Fig. 11b : Image field for fraction eutectic measurement and a higher magnification picture of dendrite and eutectic regions. Note the sharp boundary between the dendrite and eutectic regions. Also indicated is the microsegregation profile across the dendrite region.

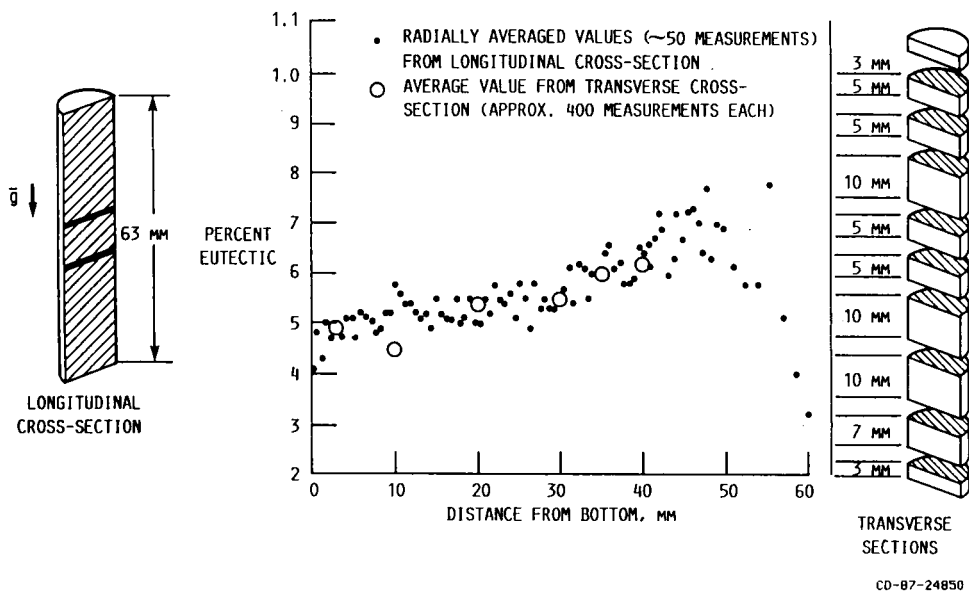


Fig. 12 : Fraction eutectic measurements in slow cooled sample, processed isothermally in the GPF single cavity simulator. Thermal conditions in this experiment are identical to those to be employed in the microgravity experiment.

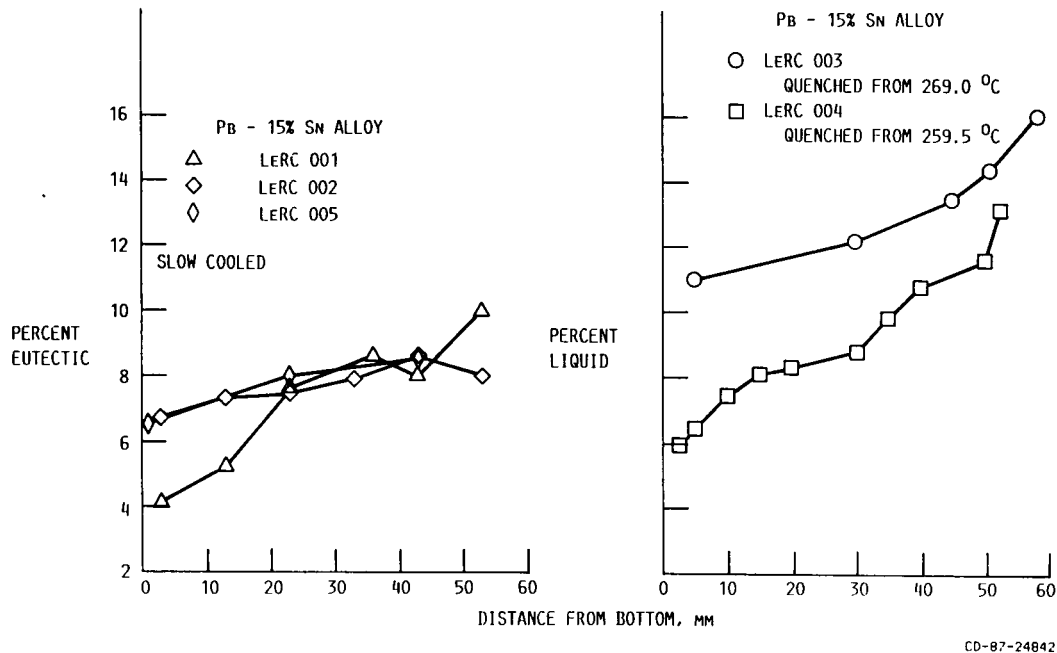


Fig. 13 : Summary of fraction eutectic and fraction liquid in isothermally processed samples; MSFC tests, table 1.

(The full circular cross-section yields about 800 or more measurements, the semi-circular sections yield up to 450 measurements, a complete longitudinal cross-section yields over 1250 measurements).

Figure 12 provides an example of our fraction eutectic measurements for one of the MSFC test samples. Each data point here (solid dots) represents an average of about 50 measurements made in a longitudinal cross-section. This thus gives us a radially averaged measurement. The large open circles here are measurements made in a transverse (semi-circular) cross-section. Each one of these open circles now represents an average of about 450 measurements, which accounts for both radial and circumferential variations at that height. Both sets of measurements indicate the same trend: the fraction eutectic increases gradually from the bottom to the top of the ingot. This suggests an enrichment of the remanent liquid with Sn and a gradual floating of the lighter Sn-enriched liquid to the top of the ingot during the unusually long solidification time (640 minutes or about 11 hours) experienced by this slowly cooled ingot. This is also confirmed by the coarse beam microprobe measurements, Figure 12b.

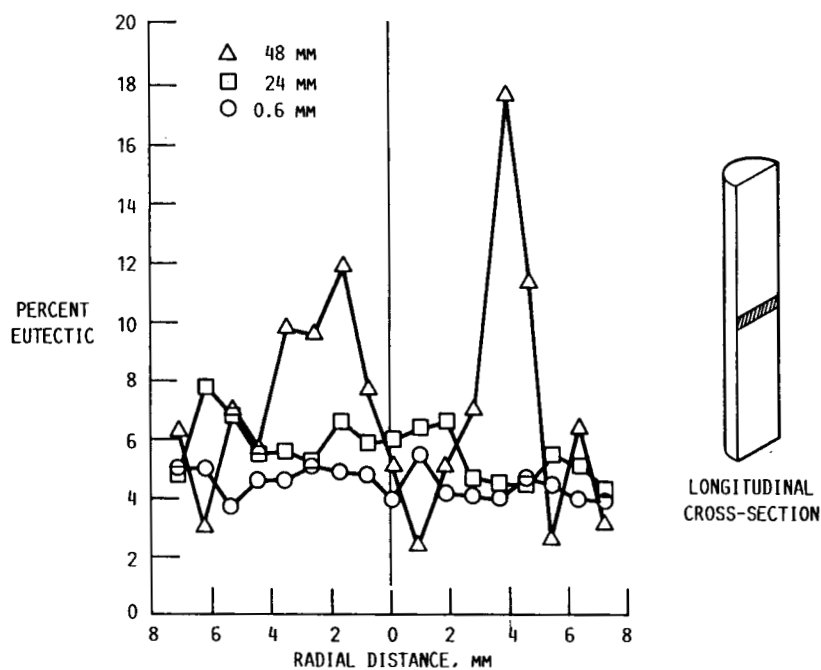
Figure 13 summarizes the results obtained from the various MSFC tests. In some of these tests solidification was interrupted by rapidly quenching the sample prior to complete solidification. In this case the quantimet measurements give the fraction of liquid remaining in the sample at various locations just prior to the initiation of the quench. The quenched liquid has a very fine structure and again etches differently in a carefully prepared sample.

Figure 14 plots the radial segregation pattern at various fixed distances from the ingot bottom; i.e., the variation in fraction eutectic with distance measured from the axis of the ingot. We are simply re-plotting here the measurements taken in the longitudinal cross-section of Figure 12. Each data point in Figure 14 represents the very "local" measurement, at that point. Note that radial variations of fraction eutectic are quite small near the bottom of the ingot, but large radial variations are observed in the top half of the ingot. This radial segregation pattern is somewhat reminiscent of the segregation profiles observed in many earth-growth semi-conductor crystals (PbSnTe, HgCdTe, Ga-doped Ge, for example) wherein the solidification morphology is much more simple [23] - a planar interface as opposed to the intricate dendritic pattern here.

Figure 15 summarizes our secondary dendrite arm spacing measurements. The numbers within the parenthesis represent the number of measurements taken in each of the samples to arrive at the average value reported here. Figure 16 is an example of the composition measurements in the CWRU tests. A more detailed report of the MSFC and CWRU test results is under preparation [20, 21].

### Modeling of Segregation Behavior

In this section some preliminary semi-analytical calculations are described which were aimed at pinpointing some of the important elements of a satisfactory theoretical model for segregation behavior. A full numerical simulation, which includes fluid-flow effects, is also being developed to describe more completely the rather complex and interesting radial and longitudinal segregation pattern observed in the isothermally processed samples.



CD-87-24849

Fig. 14 : Radial segregation pattern in isothermally processed sample.

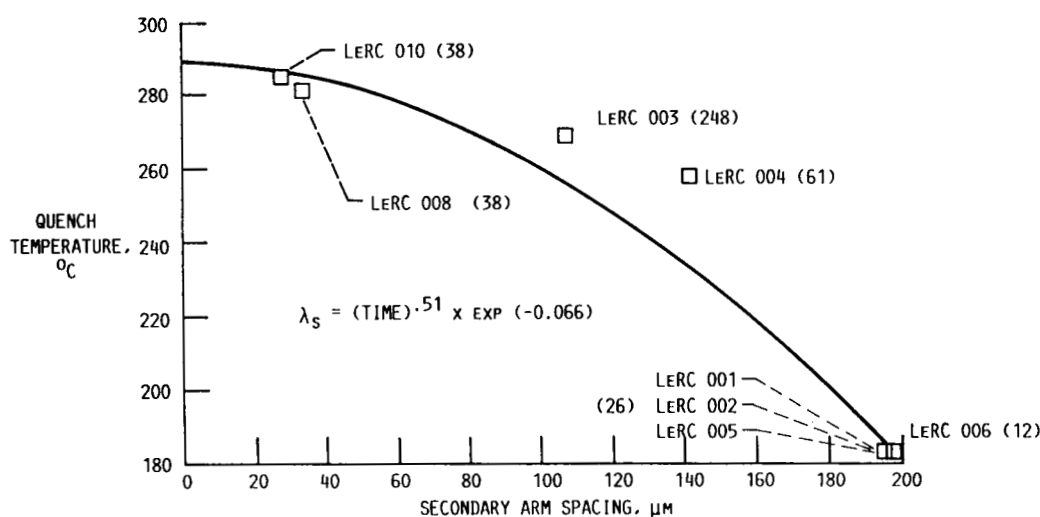


Fig. 15 : Summary of secondary dendrite arm spacing measurements in isothermally processed samples. Numbers in parantheses indicate the number of measurements per sample. Note that the secondary dendrite spacing is quite fine in samples wherein solidification was interrupted at high temperature. These interrupted tests show that in the completely solidified sample, the spacing increases from about 20 microns at the early stages of solidification to the final value of about 200 microns. This phenomenon is called coarsening.

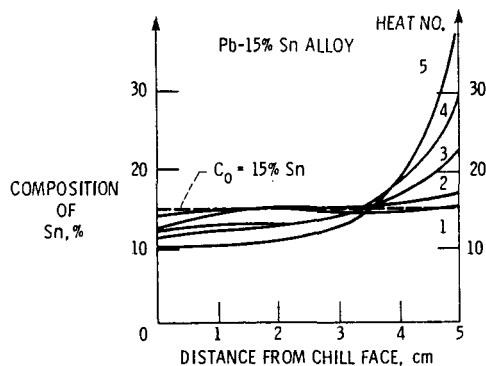


Fig. 16 : Summary of composition measurements (using a diffuse microprobe beam as in fig. 9) in the slow cooled samples processed at CWRU.

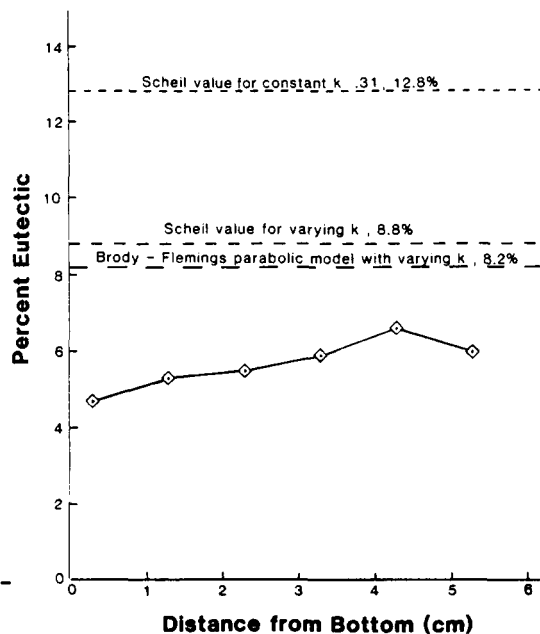


Fig. 17 : Comparison of fraction eutectic measurements with the predictions of various models for segregation. The models predict the maximum eutectic fraction in a randomly located volume element. Fluid flow is neglected.

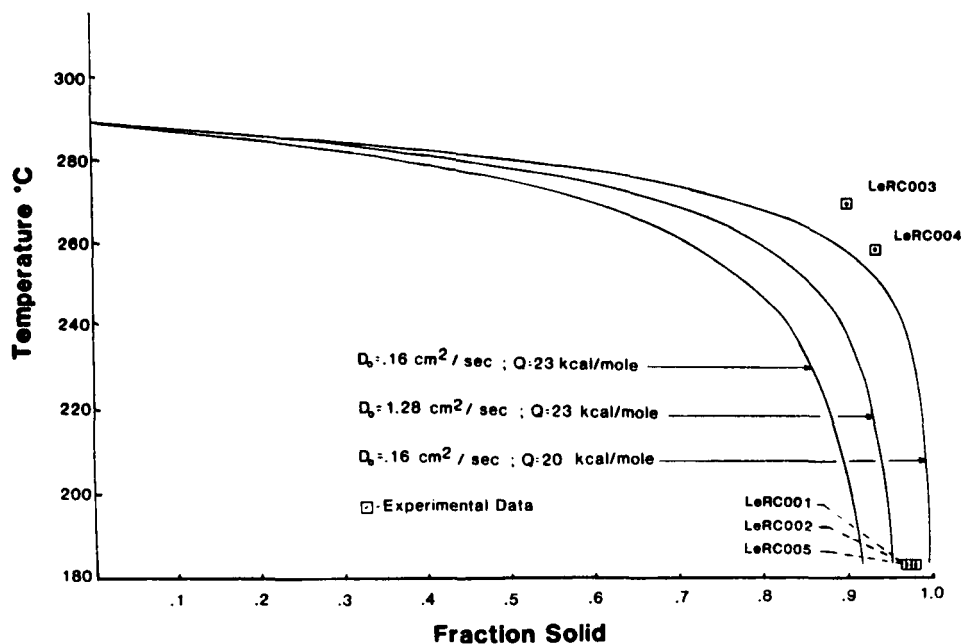


Fig. 18 : Theoretical plots of fraction solid versus temperature for various theoretical models. The amount of solid formed at the eutectic temperature is the fraction eutectic predicted in the finally solidified alloy. A high diffusion coefficient of tin in the solid implies tin content in the dendrite and hence smaller amounts of eutectic in the final solid.

The analytical calculation is simply aimed at determining the maximum amount of eutectic that would be formed in the sample, within a random volume element such as considered in Figure 7. We completely neglect fluid-flow effects as a first step, i.e., the fluid-flow parameter is taken to be small compared to unity and we set  $\beta = 0$ . The differential solute balance (see Table 3) may be readily integrated with these approximations if we also assume the partition ratio  $k$  to be constant. The integrated result is actually the same as the familiar Scheil equation [22]. However, in this case, the Scheil equation gives the "local" variation in composition within a small volume element, rather than the variation of composition from one end of the ingot to the other, as in semiconductor crystal growth [23, 24]. (In electronic crystal growth applications, the solid morphology is planar and the entire ingot is taken as the volume element in the differential balance; see also Flemings in reference 25. Here the volume element for the differential solute balance is of the order of the dendrite arm spacings). For the Pb-15 wt% Sn alloy with  $k = 0.31$ , this yields a fraction eutectic of about 12.8%. This is much higher than the maximum, radially averaged, value determined in these experiments and is represented by the horizontal line in Figure 17.

The partition ratio  $k$  is however not a constant and varies from about 0.50 close to the liquidus temperature to about 0.31 close to the eutectic temperature. Allowing for a varying  $k$  and performing a numerical integration of the Scheil balance yields a much lower fraction eutectic, 8.8 % compared to 12.8% with constant  $k$ .

Next we allowed for some diffusion of the rejected solute into the solid, i.e., we consider a two-sided model for segregation. Two such models were proposed by Brody and Flemings [26] and this was subsequently modified by Clyne and Kurz [27]. "Back-diffusion" or diffusion in the solid is characterized by the dimensionless parameter  $\alpha = D_s t_f / \lambda_s^2$ , where  $D_s$  is the diffusion coefficient of Sn in the solid and  $t_f$  is the "local" solidification time. Clyne and Kurz defined another dimensionless parameter  $\alpha'$  which is a function of  $\alpha$ . A large value of  $\alpha$  or  $\alpha'$  implies a significant contribution from diffusion in the solid. Diffusion of solute into the solid will increase the average solute content of the dendrite ( $C_\alpha$ ) and hence reduce the amount of eutectic formed. We again performed a numerical integration of the differential solute balance and allowed for i) varying  $k$  with temperature and composition, ii) variation in dendrite arm spacing with time during solidification, which we deduced from our interrupted quench tests, Figure 15, iii) variation in diffusion coefficient with temperature. The results of these calculations are shown in Figures 17 and 18. The maximum value of  $f_E$  predicted is now only about 8.2% which is much closer to the maximum value (radially averaged) of about 6% in our experiments.

Again, these preliminary semi-analytical calculations only point out the important ingredients of a more complete analysis which must necessarily include fluid-flow effects. Only such a calculation will be able to re-capture the details of both the longitudinal and radial segregation pattern reported here.

Table 3: SUMMARY OF VARIOUS THEORETICAL MODELS FOR SEGREGATION BEHAVIOR IN BINARY ALLOYS

MODEL	Reference Number	Assumptions	Differential Solute Balance	Integrated Solute Redistribution Equation	Comments
Gulliver (1913)	29	<ul style="list-style-type: none"> <li>No concentration gradients in liquid (Complete mixing assumption)</li> </ul>	$\frac{df_L}{f_L} = - \frac{dC_L}{C_L(1-k)}$	$C_S^* = kC_0(1-f_s)^{k-1}$ Scheil Equation	<ul style="list-style-type: none"> <li>Entire ingot is the volume element for solute balance when applied to predict segregation during semicon ductor crystal growth; Model predicts variations from end to end of ingot in this case, ref. 24</li> </ul>
Hayes & Chipman (1938)	30	<ul style="list-style-type: none"> <li>No diffusion of rejected solute into solid during freezing; one-sided model</li> </ul>			
Scheil (1942)	22	<ul style="list-style-type: none"> <li>Planar interface</li> </ul>			<ul style="list-style-type: none"> <li><math>\bar{C}_S = C_0</math> for all values of <math>k</math></li> </ul>
Brody & Flemings (1966) (BF)	26	<ul style="list-style-type: none"> <li>No concentration gradients in liquid</li> <li>Some diffusion of rejected solute into solid during freezing; two-sided model</li> <li>Linear rate of thickening of dendrite arms</li> <li>Same as above, but parabolic rate of thickening of dendrite arms</li> </ul>	$\frac{df_L}{f_L + \alpha k} = - \frac{dC_L}{C_L(1-k)}$ $\frac{df_L}{f_L(1 - 2\alpha k) + 2\alpha k} = \frac{dC_L}{C_L(1-k)}$	$C_S^* = kC_0 \left[ 1 - \frac{f_s}{1-\alpha k} \right]^{k-1}$ Linear model  $C_S^* = kC_0 \times \frac{k-1}{\{1-(1-2\alpha k)f_s\}^{1-2\alpha k}}$	<ul style="list-style-type: none"> <li>For <math>\alpha=0</math> or <math>\alpha'=0</math> BF or CK models reduce to Scheil equation, although applied for dendritic growth</li> <li>Volume element during dendritic growth has a length equal to <math>\lambda_p</math> or <math>\lambda_s</math>, fig. 8, not entire ingot length as when Scheil equation is used for crystal growth (plane front solidification)</li> </ul>



Table 3: SUMMARY OF VARIOUS THEORETICAL MODELS FOR SEGREGATION BEHAVIOR IN BINARY ALLOYS (Cont.)

MODEL	Reference Number	Assumptions	Differential Solute Balance	Integrated Solute Redistribution Equation	Comments
Clyne & Kurz (1981)	27	Same as for Brody & Flemings parabolic model except $\alpha$ is replaced by $\alpha'$		$\alpha' = \alpha [1 - \exp(-\frac{1}{\alpha})] - \frac{1}{2} \exp(-\frac{1}{2\alpha})$	<ul style="list-style-type: none"> <li>For both BF and CK models, <math>\bar{C}_S = C_0</math> only for special values of <math>\alpha</math> (or <math>\alpha'</math>). These models thus violate conservation of solute within the volume element. Note, solute cannot enter or leave volume element by any means, see FN model below.</li> </ul>
Flemings and Nereo (1967) (FN)	33	<ul style="list-style-type: none"> <li>No concentration gradients in liquid (although there is a temperature gradient across volume element, fig. 7)</li> </ul>			<ul style="list-style-type: none"> <li><math>\bar{C}_S \neq C_0</math> in general.</li> <li><math>\bar{C}_S = C_0</math> for <math>k'=1</math> i.e. <math>k=1</math> and/or <math>\beta=0, \xi=0</math></li> <li>Since solute can enter or leave volume element because of fluid flow, it is <u>assumed</u> that there is <u>global</u> conservation of solute</li> </ul>
Mehrabian, Keane and Flemings (1970) (MKF)	2	<ul style="list-style-type: none"> <li>No diffusion of re-jected solute into solid; one-sided model</li> <li>Solute can enter or leave volume element because of fluid flow</li> <li>Fluid flow is mainly due to shrinkage for FN</li> </ul>	$\frac{\partial g_L}{g_L} = - \frac{\partial C_L}{C_L (1-k')}$ $k' = 1 - \frac{(1-k)}{(1-\beta)(1+\xi)}$	<ul style="list-style-type: none"> <li><math>C_S^* = k' C_0 (1-f_s)^{k'-1}</math> if <math>\xi, \beta, k</math> constant</li> <li>Only numerical integration possible when <math>\xi \neq 0</math>, i.e. <math>\bar{V} \neq 0</math></li> </ul>	

Table 3: SUMMARY OF VARIOUS THEORETICAL MODELS FOR SEGREGATION BEHAVIOR IN BINARY ALLOYS (Cont.)

MODEL	Reference Number	Assumptions	Differential Solute Balance	Integrated Solute Redistribution Equation	Comments
		<ul style="list-style-type: none"> <li>MKF model includes both shrinkage and gravity-induced flow. Darcy's law used to model flow.</li> </ul>	$\xi = \bar{V} \cdot vT/\epsilon = \frac{\bar{V} \cdot vC_L}{\partial C_L / \partial t}$		
Poirier (1983)	5	<ul style="list-style-type: none"> <li>Same as for FN and MKF except that there is a concentration gradient in the liquid</li> <li>Unidirectional solidification only considered</li> </ul>	$\frac{\partial g_L}{\beta_E g_E \left( \frac{1}{1-\alpha} \right)} = \frac{(1-\alpha) \partial C_L}{\frac{\alpha \rho_L}{m_\rho} - (1-k) C_L}$ $\beta_E = \frac{\rho_s E - \rho_s}{\rho_s} = \frac{D_L G_L^2 m_\rho}{\rho_s \epsilon \tau m_L}$ $\alpha = \frac{D_L G_L^2 m_\rho}{\rho_s \epsilon \tau m_L}$ $\tau = D_L / D_{eff} = \text{tortuosity}$ $m_\rho = \partial \rho_L / \partial T$	<ul style="list-style-type: none"> <li>Only numerical integration possible in general</li> </ul>	<ul style="list-style-type: none"> <li><math>\bar{C}_s \neq C_0</math> in general as for FN or MKF.</li> <li>Global conservation of solute assumed.</li> </ul>

Table 3: SUMMARY OF VARIOUS THEORETICAL MODELS FOR SEGREGATION BEHAVIOR IN BINARY ALLOYS (Cont.)

MODEL	Reference Number	Assumptions	Differential Solute Balance	Integrated Solute Redistribution Equation	Comments
Flemings (1964)	31	<ul style="list-style-type: none"> <li>Solute can enter or leave volume element but only because of diffusion. There is a concentration gradient in the liquid, in a direction perpendicular to the growth direction of array</li> </ul>	$\frac{df_L}{f_L} = \frac{dC_L}{C_L(1-k) - s\Delta C_0}$ $s = \frac{a k}{k-1} \quad a = \frac{D_L G_L}{m_L R C_0}$	$C_s^* = C_0 [s + k(1-s)f_L^{k-1}]$	<ul style="list-style-type: none"> <li>Assumption of exponential decay ahead of tips can be relaxed</li> <li>It may be shown that solute conservation is obeyed, i.e. <math>\bar{C}_s = C_0</math> for all values of <math>s</math></li> </ul>
Bower, Brody and Flemings (1966) (BBF)	32	<ul style="list-style-type: none"> <li>There is no concentration gradient lateral to growth direction of array, i.e. liquid within volume element, fig. 8, is uniform in composition.</li> <li>Concentration gradient in interdendritic liquid is constant. Exponential decay in bulk liquid ahead of tips</li> </ul>	$s = - \frac{D_L G_{CI}}{R \Delta C_0}$ $G_{CI} = G_L / m_L$	$\bar{C}_s = C_0 [s(1-f_L) + (1-s)(1-f_L^k)]$	<ul style="list-style-type: none"> <li>For <math>f_L \rightarrow 0</math>  <math>\bar{C}_s \rightarrow C_0</math> i.e.  <math>\bar{C}_s \rightarrow C_0</math></li> <li>First solid to form in volume element has composition <math>kC_t &gt; kC_0</math>, i.e. dendrite tips are undercooled</li> </ul>
Solari & Biloni (1980)	34	This model attempts to combine the BBF model and the BF model. The dendrite tip composition is calculated from the Burden & Hunt analysis rather than the BBF analysis.			Solute conservation within the volume element is again violated.

Table 3: SUMMARY OF VARIOUS THEORETICAL MODELS FOR SEGREGATION BEHAVIOR IN BINARY ALLOYS (Cont.)

MODELS	Reference Number	Assumptions	Differential Solute Balance	Integrated Solute Redistribution Equation	Comments
Laxmanan (1985/87)	9-11, 15, 28	<ul style="list-style-type: none"> <li>Same as for BBF model except that isoconcentrates are non-planar in the immediate vicinity of tips</li> <li>Multi-dimensional diffusion near tips treated approximately by two models.</li> <li><math>\lambda = \phi/2p</math> Diffusion field in vicinity of tips is given by Ivantsov solution in the ideal case when <math>G_L = 0</math>, i.e. dendrite surface is isothermal</li> <li><math>\lambda = 1/16</math> Diffusion field in vicinity of tips given by a generalization of the Zener treatment, in the ideal case of <math>G_L = 0</math>, instead of Ivantsov.</li> </ul>	$\frac{df_L}{f_L} = \frac{dC_L}{C_L(1-k) - q\Delta C_0}$ <ul style="list-style-type: none"> <li><math>s = \frac{ak}{k-1}</math></li> <li><math>a = \frac{D_L G_L}{m_L R C_0}</math></li> <li><math>G_{CI} \neq G_L/m_L</math></li> <li><math>\frac{\Delta C}{\Delta C_0} = \frac{2p\lambda k}{b} \left[ 1 + \frac{s}{k} \tilde{N}_g(p) \right]</math></li> <li><math>\tilde{N}_g(p) = (1-2p\lambda)/2p\lambda</math></li> <li><math>b = 1-2p\lambda(1-k)</math></li> </ul>	<ul style="list-style-type: none"> <li><math>C_s^* = C_0 \{q+k(1-q)f_L^{k-1}\}</math></li> <li><math>\bar{C}_\alpha = C_0 [q(1-f_L) + (1-q)(1-f_L^k)]</math></li> <li>Note for <math>f_L \rightarrow 0</math>, <math>\bar{C}_\alpha \rightarrow C_0</math> for all values of <math>q</math></li> <li>For <math>q \rightarrow 0</math>, i.e. for <math>G_{CI} \rightarrow 0</math> model reduces to Scheil equation</li> </ul>	<ul style="list-style-type: none"> <li>Model satisfies solute conservation since <math>\bar{C}_\alpha \rightarrow C_0</math> for <math>f_L \rightarrow 0</math> i.e.</li> <li><math>\bar{C}_s \rightarrow C_0</math> for <math>f_L \rightarrow 0</math></li> <li>When <math>G_{CI} = G_L/m_L</math>, <math>q=s</math>, i.e. model reduces to BBF</li> <li><math>q = \Delta C/\Delta C_0</math> is in general greater than <math>s</math>.</li> <li>Unknown Peclet number <math>p</math>, i.e. tip radius is determined either from minimum tip undercooling assumption or from the marginal stability hypothesis, ref. 9.</li> <li>First solid to form in volume element has composition <math>kC_t &gt; kC_0</math>, i.e. <math>\Delta T &gt; 0</math>.</li> </ul>

### Future Plans: Summary and Conclusions

1. A rather intricate longitudinal and radial segregation pattern has been observed in the isothermally processed samples. These results suggest significant gravity-driven fluid-flow effects. The microgravity experiment should indicate a much less pronounced variation of fraction eutectic. A numerical simulation of the 1-g data and the anticipated microgravity results is being planned.
2. The isothermally processed MSFC samples have been subjected to a rigorous regimen of detailed post-mortem metallographic analyses. Several thousand measurements per sample have already been performed (more are under way), and several important morphological details have been measured. In particular the detailed characterization of the primary and dendrite arm spacings in the samples is a pre-requisite to satisfactory numerical modeling of fluid-flow effects. These measurements were also carried out in anticipation of reportedly larger values of the dendrite arm spacings in other reduced gravity experiments, particularly those performed in the KC-135 flights, compared to the corresponding 1-g spacings.
3. Thermal conditions to be employed for the microgravity experiment have been shown to be reproducible in several repeat tests (12 to date). The majority of these tests were conducted with the axis of the sample oriented in the direction of the gravity vector. The single-cavity simulator of the GPF at MSFC is mounted on trunions and allows for many different orientations. It would be extremely desirable to perform additional tests in the single-cavity simulator with at least 3 or 4 different angular orientations with respect to gravity vector; 30, 45, 90, 180. These tests were intentionally deferred thus far since our goal was to first develop a satisfactory engineering design of the spring-loaded specimen cartridge. The additional tests mentioned here would indicate the role of gravitational convection in establishing the (very reproducible) thermal profiles obtained thus far in the MSFC experiments. The final programming of the GPF for the microgravity experiment must take into account the outcome of these additional tests. (The springs loaded plunger has been included to eliminate the complicating effects of Marangoni convection associated with a free liquid/gas interface).
4. Ground-based results already in hand (CWRU tests) indicate a rich variety of experiments that could be gainfully performed in follow-up shuttle experiments. These follow-up experiments should be performed without the isothermal constraints of the first experiment, in the GPF, or other suitably modified shuttle hardware: for example, the Automatic Advanced Directional Solidification Furnace (AADSf) with a stationary sample of appropriate aspect ratio, or even the Isothermal Dendrite Growth Apparatus (IDGA). Both pieces of hardware are currently under development.
5. Finally, the currently approved and other proposed shuttle experiments in this series have been planned in a manner that would allow both a more fundamental understanding of the role of gravity during solidification as well as yield information of great value from an engineering standpoint.

# NOMENCLATURE

R	Dendrite tip growth rate	$\lambda$	Solutal lambda, Zener number, $\Omega^0/2p$
$T_L$	Liquidus temperature, alloy melt	$\lambda = \phi 2p$	"Point" effect from Ivantsov
$T_S$	Solidus temperature	$\lambda = 1/16$	"Point" effect from generalized Zener
$T_t$	Dendrite tip temperature	s	Chalmers number, $D_L G_L / R \Delta T_0$ ; $D_L G_i / R \Delta T_0$
$\Delta T$	Tip "undercooling", $(T_L - T_t)$	q	Dimensionless parameter $- D_L G_{CI} / R \Delta C_0$
$C_0$	Initial alloy composition	$f_E, g_E$	Fraction eutectic or two phase
$C_t$	Liquid composition at tip	$\xi$	Fluid Flow parameter
$C_t^0$	Liquid composition at tip, isothermal case	$k'$	Effective partition ratio
$\Delta C$	Solute buildup at tip, $(C_t - C_0)$	$\bar{C}_s$	Average composition of solid when $g_s = 1$
$G_C$	Concentration gradient at tip, non-isothermal case	$\bar{C}_\alpha$	Average composition of dendrite
$G_i$	Interdendritic thermal gradient, in liquid	$C_E$	Eutectic composition
$G_L$	Thermal gradient in liquid, at tip	$\lambda_p$	Primary dendrite arm spacing
$G_{CI}$	Concentration gradient in interdendritic liquid	$\lambda_s$	Secondary dendrite arm spacing
$m_L$	Slope of equilibrium liquidus line	M	Mushy zone thickness
k	Partition ratio, assumed constant. May or may not be equilibrium value.	$C_s^*$	Solid composition at interface
$\Delta C_0$	Solute buildup for plane front, steady state: $C_0(1-k)/k$	$C_L^*$	Liquid composition, at interface
$\Delta T_0$	Undercooling at planar interface, steady-state, $(T_L - T_s) = -m_L \Delta C_0$	$\rho_{SE}$	Density of two-phase, eutectic solid
$D_L$	Diffusivity of solute in liquid	$\beta, \beta_E$	Fractional density change
$\Omega$	Supersaturation at tip, non-isothermal case, $\Delta C / C_t(1-k)$	$\alpha, \alpha'$	Dimensionless groups, determine diffusion in solid.
$\Omega^0$	Supersaturation at tip, isothermal case, $\Delta D^0 / C_t^0(1-k) = 2p\lambda$ in general		
$\Delta C / \Delta C_0$	Dimensionless solute buildup at tip		
p	Solute Peclet number, $Rr_t / 2D_L$		
$r_t$	Tip radius of dendrite		
$\phi$	Ivantsov function, solute case, $pe^{PE_1(p)}$		

### Acknowledgements

The author is grateful for financial support provided by NASA under the "Microgravity Science and Applications Program" during the course of this work. Sincere thanks are also due to Dr. Hugh Gray for his encouragement and support, to Messrs. E. Winsa, A. Studer, and L. Wang for their enthusiastic and active involvement in almost every phase of this work. Finally, my sincere thanks to Mrs. Marge Benko for her help in the preparation of this manuscript.

### References

1. M.C.Flemings, Scand. J. Metallurgy, 5, 1-15 (1976).
2. R.Mehrabian, M.Keane and M.C.Flemings, Met.Trans., 1, 1209, 1970.
3. S.M.Copley, A.F.Giamei, S.M.Johnson and M.F.Hornbecker, Met.Trans., 1, 2193 (1970).
4. A.Sample and A.Hellawell, Met.Trans B, 13B, 495 (1982).
5. D.Poirier, in U.S.-Japan Co-operative Science Program Seminar on Solidification Processing, June 26-29, 1983, Dedham, Mass. Proc.Eds. G.Ohira and M.C.Flemings.
6. T.L.Bergman and A.Ungan, Int.J.Heat & Mass Transfer, 11, 1695 (1986), also, T.L.Bergman, F.P.Incorpera and R.Visankta, J.of Heat Transfer, Trans. ASME, 108, 206 (1986).
7. V.Laxmanan, Science Requirements Document for STS-experiment on "Isothermal Solidification in a Binary Alloy Melt," October 1984.
8. H.Esaka and W.Kurz, J.Cryst.Growth, 72, 578 (1985).
9. V.Laxmanan, J.Cryst. Growth 75, 573 (1986).
10. V.Laxmanan, J.Cryst. Growth, 77 (1987) in press.
11. V.Laxmanan, Acta Met 33, 1023, 1037, 1475 (1985).
12. R.Trivedi, J.Cryst.Growth, 49, 219 (1980).
13. M.C.Flemings, in Solidification Processing, McGraw Hill pp 31-36, (1974).
14. M.C.Flemings, in ref.13, pp 110-112.
15. V.Laxmanan, in Processing and Properties of Structural Metals via Rapid Solidification Processing, to be published by ASM, Metals Park, Ohio. Eds. F.H.Froes and D.J.Savage (in press).
16. M.H.McCay, J.E.Lee and P.A.Curreri, Met.Trans A, 17A, 2301 (1986).
17. M.H.Johnston, P.A.Curreri, R.A.Parr and W.S.Alter, Met.Trans A, 16A, 1683 (1985).
18. R.A.Parr and M.H.Johnston, Met.Trans A, 9A, 1825 (1978).
19. M.H.Johnston and C.S.Griner, Met.Trans A, 8A, 77 (1977).
20. L.Wang, "Gravitational Macrosegregation in Pb-Sn Alloys", M.S. Thesis, Dept. of Metallurgy and Materials Science, Case Western Reserve University, 1985.
21. A.Studer, "Macrosegregation in Isothermally Processed Pb-Sn Alloys", M.S. Thesis, Dept. Of Metallurgy & Materials Science, Case Western Reserve University, thesis in progress.
22. E. Scheil, Z.Metallkunde, 34, 70 (1942).
23. S.L.Lehoczky and F.R.Szofran in Materials Processing in the Reduced Gravity Environment, MRS Symp Proc. Ed.G.E.Rindone, p 409 (1982).
24. R.K.Crouch, A.L.Fripp, W.J.Debnam, I.O.Clark and F.M.Carlson, in ref. 23, p 611.
25. M.C.Flemings, in ref. 13, pp 77-83, 141-146, (1974).
26. H.D.Brody and M.C.Flemings, Trans. AIME, 236, 615 (1966).
27. T.W.Clyne and W.Kurz, Met.Trans A, 12A, 965 (1981).

28. V.Laxmanan, "Analysis of Microsegregation During Cellular and Dendritic Solidification", in preparation.
29. G.H.Gulliver, J.Inst.Metals, 9, 120-157 (1913).
30. A.Hayes and J.Chipman, Trans AIME, Proc. of Detroit Meeting, Oct. 1938, p 85.
31. M.C.Flemings, Trans AFS, 72, 353, (1964).
32. T.F.Bower, H.D.Brody and M.C.Flemings, Trans. AIME, 236, 624 (1966).
33. M.C. Flemings and G.E. Nereo, Trans AIME 239(1967) 1449, 242 (1968) 41,50.
34. M.Solari and H.Biloni, J.Cryst. Growth, 49, 451, (1980).



## CASTING AND SOLIDIFICATION TECHNOLOGY (CAST)

Directional Solidification Phenomena  
in a  
Metal Model at Reduced Gravity

M. H. McCay  
University of Tennessee Space Institute  
Tullahoma, Tennessee

The CAST experiment will study the phenomena that occur during directional solidification of an alloy, e.g., constitutional supercooling, freckling, and dendrite coarsening. The reduced gravity environment of space will permit the individual phenomena to be examined with minimum complication from buoyancy driven flows.

Constitutional Supercooling

In recent years a series of Space Processing Applications Rocket (SPAR) and KC-135 aircraft experiments have been flown to study the effects of gravity on the solidification of first, a metal-model ( $28 \text{ NH}_4\text{Cl-H}_2\text{O}$ )<sup>1,2</sup> and then metal alloys (Sn-15Pb, Sn-3Bi, Al-4.5Cu, MAR-M246 and PWA 1480)<sup>3-6</sup>. In the first metal-model experiment (bi-directional solidification) four  $[110]$  dendrite arrays nucleated and grew outward from the container walls filling the entire crucible. No crystallites appeared ahead of the interface, implying that in the absence of gravity, the forces were not present that would cause dendrite fragmentation and movement in the liquid. The second (unidirectional solidification) experiment also began  $[110]$  growth at the cooled wall, but several  $[100]$  crystallites appeared and grew ahead of the interface. In each instance the low-gravity arrays grew significantly slower than one-g ground runs. In the two metal-model experiments, the growth rates were the same ( $R$ , cm/min) but the temperature gradients differed by a factor of 7 ( $70^\circ \text{ C/cm}$  for flight one

and  $10^{\circ}\text{C}/\text{cm}$  for flight two). This gives constitutionally super-cooled regions of 0.5 cm and 3.8 cm, respectively. Based on theories of the columnar to equiaxed transition in castings 7-9, several interpretations can be made from these results, the principal two being that gravity driven fluid flow is responsible for the melting off of dendrite arms and their transport into the melt, or a non-convection related constitutional supercooling phenomena encourages nucleation ahead of the interface. Rather than distinguishing between the two possibilities as was intended, the SPAR experiments were inconclusive.

A third explanation was the occurrence of residual flows from the de-spin of the sounding rocket. If these were still present when the second experiment began freezing, they could account for crystallites moving into the fluid. This hypothesis was tested in KC-135 and F104 low gravity aircraft experiments<sup>10,11</sup> using shadowgraph, interferometry and Schlieren techniques. These optical techniques enabled the experimenters to observe both the depletion layer adjacent to the growth interface and the presence of convection plumes. The flight profile of the KC-135 causes a sample to experience one to two g's before entering a 20 sec. period of low gravity. During unidirectional solidification studies growth plumes were established during the initial high g and flow rates on the order of 1cm/min were seen prior to inception of the low ( $.01\text{ g}$ ) gravity period. These plumes dampened and began to diffuse 10 seconds after entry into low gravity, indicating that the predicted <sup>12</sup> damping times for these experimental cases must have been inaccurate. Further thermal data from F104 flights supports the concept that damping times in these materials are rapid. It, therefore, is implausible that the nuclei were carried ahead of the interface by residual flows.

Experiments with metal systems on SPAR produced similar results.<sup>3,4</sup> The Sn - 15Pb alloy solidified with large equiaxed grains in contrast to the more columnar plus small equiaxed grains obtained from one-g and centrifuge solidification. The Sn - 3Bi alloy also solidified initially with large grains on SPAR, but the final region surrounding the shrinkage cavity froze with small equiaxed grains. It is not known if these small grains formed due to constitutional supercooling nucleation, a gravity independent flow as a result of the shrinkage cavity, or gravity driven convection due to the sounding rocket leaving the low-gravity conditions. The controversy remains concerning the formation of grains ahead of an interface.

The investigators feel that this controversy can be resolved by a more thorough study of solidification in microgravity. The extended times available on Spacelab will allow experiment conditions that cover a range of growth rates, temperature gradients and, hence, constitutionally supercooled regions without the confusing presence of gravity driven fluid flow. The solute and thermal fields associated with the dendrite growth front will be measured and compared to a theoretical (computational) model.

### Freckling

The ammonium chloride-water system is used to study the occurrence of thermo-solutal convection and pluming as it would occur in metal systems such as steel castings,<sup>13,14</sup> the superalloys<sup>15</sup> or others,<sup>16,17</sup> since it has a density inversion at the interface due to rejection of water-rich solute. This phenomena is often called freckling and tends to limit the range of

compositions for many alloys processed on earth since it causes localized segregation and small equiaxed grains in the final casting. The plumes contain cooler liquid with a different composition from the surrounding region and as they traverse through the dendrite forest creating a channel, they carry crystalline fragments which appear as trails of equiaxed grains in the final ingot. The region of the freckles, therefore, has a different composition (and melting point) and crystalline morphology from the remainder of the ingot.

Freckling was first studied systematically in the metal-model  $\text{NH}_4\text{Cl-H}_2\text{O}$ <sup>15</sup> and found to depend on thermal diffusivity, density inversion, solute diffusivity and viscosity. Several investigators<sup>15,16</sup> have attempted to define criteria for the width and stability of the inverted layer. One criteria is based on thermal properties and the other on concentration effects. Since neither criteria includes both the effect of latent heat and segregation simultaneously, they grossly underestimate the solidification conditions (growth rate and temperature gradient) that are necessary to eliminate freckling. The presence of latent heat increases the size of the segregation generated inverted layer at a critical growth rate. This is not apparent from the earlier two criteria. Consideration of the combined effects decreases the growth rate for stability in 28  $\text{NH}_4\text{Cl-H}_2\text{O}$  by two orders of magnitude.<sup>18</sup>

In the proposed flight experiment, the size and characteristics of the layer as a function of growth conditions will be measured using holography and compared with present theories. For the minimum temperature gradient ( $2^\circ\text{C/cm}$ ) the layer will decrease with increasing growth rate until a critical  $R$  is reached upon which the layer will increase due to latent heat effects. For the maximum temperature gradient ( $28^\circ\text{C/cm}$ ), the layer will decrease

monotonically with increasing R since the critical R will never be reached due to FES limitations.

Freckling has generally been thought to begin within the mushy zone below the dendrite tips. A recent study, <sup>17</sup> however, also on  $\text{NH}_4\text{Cl-H}_2\text{O}$ , suggests that the channels for freckling originate at the dendrite front and spread. Since optical techniques such as Schlieren and interferometry easily delineate the plumes, the FES system is a powerful tool for studying this phenomena. The size of the inverted layer can be as large as 1cm under the proposed experiment's low temperature gradient and growth conditions. In ground based experiments the layer becomes unstable long before it reaches its maximum size with the result that events within the layer are difficult to study. During the IML flight the layer can reach a large enough size that its characteristics, such as internal pluming, can be resolved.

#### Dendrite Coarsening

Dendrite coarsening is a phenomena that occurs on the micro-scale and is primarily responsible for final dendrite arm spacings by causing the dissolution and shrinkage of smaller arms and the growth of larger arms. It is a function of local solidification time, and temperature and concentration gradients.

The SPAR experiments <sup>1-4</sup> and KC-135 flights <sup>5,6</sup> have shown a gravity-related coarsening effect on the secondary dendrite arms. Each alloy system showed greater arm spacings for the low-gravity solidification. In the instance of KC-135 flights, the arm spacings increased in low-g, decreased in

high-g and then increased again when the next low-g parabola was flown. Theories on dendrite structure<sup>19,20</sup> suggest that by changing the surrounding concentration field and effective diffusion length, the perturbation frequency and, hence, the dendrite arm spacing is affected. In the case of low-gravity, the diffusion length would increase and, therefore, so would the arm spacings.

A more recent KC-135 experiment<sup>5</sup> on the superalloy PWA 1480 has shown the same physical results for the primary arm spacings (e.g. spacing increases as gravity level decreases). Review of current theories<sup>21,22,23</sup> suggests that these spacings are related to temperature gradient and growth rate or concentration gradient. This would drive the material toward smaller arm spacings in reduced gravity which is contrary to the experimental results. This was the first study of low-gravity primary arm spacings, and it suggests that there may be a subtle effect which has not yet been identified.

It is planned that once the solidification process itself has been modelled for the microgravity environment, the coarsening of the dendrite arms will be studied. This will be accomplished using a magnification lens attachment to the FES and is proposed for a subsequent flight.

#### Method and Approach

The study will proceed systematically with a matrix of nine temperature gradients and growth rates that will encompass a range of density inverted layer sizes and constitutionally supercooled regions. Based on earlier KC-135 results, the temperature gradients are expected to be different in low-gravity for the same test parameters, so two non-solidifying control samples will be

run at identical conditions to two of the matrix runs to evaluate those differences. To produce more rapid solidification fronts, two runs will be processed in which the fluid is cooled below its freezing point and solidification initiated by a cold thermal pulse.

Holograms will be taken during each of these growth runs. In this way, various optical techniques can be used through post-flight reconstructions to determine concentration and thermal profiles, observe perturbations in the inverted layer, and distinguish nuclei that form ahead of the interface.

Since  $\text{NH}_4\text{Cl-H}_2\text{O}$  has been extensively used for similar studies, it has been chosen for these experiments. A two component system is required in order to model alloy solidification and investigate freckling phenomena. The present investigators have characterized  $\text{NH}_4\text{Cl-H}_2\text{O}$  optically in addition to accumulating other significant property data. Compared to other available metal models (e.g. succinonitrile with solute),  $\text{NH}_4\text{Cl-H}_2\text{O}$  is the superior medium available.

## REFERENCES

1. M. H. Johnston and C. A. Griner, Met. Trans. A, 8A, 1977, p. 77.
2. M. H. Johnston, C. S. Griner, R. A. Parr and S. J. Robertson, J. of Crystal Growth 50 (1980), p. 831.
3. M. H. Johnston and R. A. Parr, Met Trans 13B (1982), p. 85.
4. M. H. Johnston and R. A. Parr, Proceedings, Materials Research Society, Materials Processing in the Reduced Gravity Environment of Space, G. E. Rindone, Editor, Elsevier Science Publishing Co., Inc., p. 651, (1982).
5. M. H. McCay, J. E. Lee and P. A. Curreri, Met. Trans. 17A, pp. 2301-2302, (1986).
6. M. H. Johnston, P. A. Curreri, R. A. Parr and W. S. Alter, Met. Trans. 16A, pp. 1683-1686, (1985).
7. W. C. Wingard and B. Chalmers, Trans. Am. Soc. Metals, 46, 1954.
8. A. K. Jackson, J. D. Hunt, D. R. Uhlmann and T. P. Steward, III, Trans Met. Soc. AIME, 236, 1966, p. 149.
9. R. D. Doherty, P.D. Cooper, M. H. Bradbury and F. J. Honey, Metallurgical Transactions A, 8A, 1977, p. 397.
10. M. H. Johnston and R. B. Owen, Met. Trans. A, 14A, (1983), p. 2163.
11. R. B. Owen and M. H. Johnston, Optics and Lasers in Engineering, Vol. 2, p. 129, (1981).
12. R. B. Owen and M. H. Johnston, Optics and Lasers in Engineering, 5, p. 95, (1984).
13. R. J. McDonald and J. D. Hunt, Trans AIME 245 (1969), pp. 1993-1997.
14. R. J. McDonald and J. D. Hunt, Met. Trans. 1 (1970), pp. 1787-1788.
15. S. M. Copley, A. F. Giamei, S. M. Johnson and M. F. Hornbecker, Met. Trans. 1 (1970), pp. 2193-2204.
16. R. M. Sharp and A. Hellawell, J. of Crystal Growth 12 (1972), pp. 261-262.
17. A. K. Sample and A. Hellawell, Met. Trans. 15A (1984), pp. 2163-2173.
18. T. D. McCay and M. H. McCay, submitted to Metallurgical Transactions A.
19. M. E. Glicksman, N. B. Singh and M. Chopra, Materials Processing in the Reduced Gravity Environment of Space, Guy E. Rindone, Editor, Elsevier Science Publishing Company, Inc. (1982), p. 461.
20. M. E. Glicksman and P. W. Voorhees, Met. Trans. A 15A (1984), p. 995.



21. J. D. Hunt, "Solidification and Casting of Metals," The Metals Society Book 192, London, 1979, pp. 3-9.
22. W. Kurz and D. J. Fisher, Acta Metall., 1981, Vol. 29, pp. 11-20.
23. K. Somboonsuk, J.T. Mason, and R. Trivedi, Metall. Trans. A., 1984, Vol. 15A, pp. 967-75.

Dendritic Growth and Structure of Undercooled Nickel Base Alloys\*

by

M.C. Flemings and Y. Shiohara  
Massachusetts Institute of TechnologyABSTRACT

The principal objectives of this overall investigation are to (1) study means (including microgravity) for obtaining high undercoolings in levitation melted droplets, and (2) study structures produced upon the solidification of these undercooled specimens.

Thermal measurements are made of the undercooling, and of the rapid recalescence, to develop an understanding of the solidification mechanism. Comparison of results is made with modelling studies. Characterization and metallographic work is done to gain an understanding of the relationship between rapid solidification variables and structures so produced. Undercoolings up to three hundred degrees centigrade have been obtained on earth, in spite of vigorous convection. The conduct of similar experiments under microgravity is expected to broaden the base of this information, and to extend the understanding of solidification behavior. Performing this experiment in space would permit near elimination of gravitational convection and induction stirring during undercooling and recalescence.

In ground based work to date, solidification of undercooled Ni-25wt%Sn alloy was observed by high-speed cinematography and results compared with optical temperature measurements.<sup>(1)</sup> Samples studied were rectangular in cross section, and were encased in glass. Cinematographic measurements were carried out on samples undercooled from 68 to 146K. These undercoolings compare with a temperature range of 199K from the equilibrium liquidus to the extrapolated equilibrium solidus. At all undercoolings studied, the high-speed photography revealed that solidification during the period of recalescence took place with a dendrite-like front moving across the sample surface. Spacings of the apparent "dendrites" were on the order of millimeters. The growth front moved at measured velocities ranging from 0.07 meters per second at 68K undercooling to 0.74 meters per second at 146K undercooling. These velocities agree well with results of calculations according to the model for dendrite growth of Lipton, Kurz, and Trivedi. It is concluded that the coarse structure observed comprises an array of very much finer, solute-controlled dendrites.

Also in ground based work, high-speed optical temperature measurements were made of the solidification behavior of levitated metal samples within a transparent glass medium.<sup>(2)</sup> Two undercooled Ni-Sn alloys were examined, one a hypoeutectic alloy and the other of eutectic composition. Measurements were carried out on samples at undercoolings up to 330K. Recalescence times for the 9 mm diameter samples studied decreased with increasing undercooling from the order of 1.0 second at 50K undercooling to less than  $10^{-3}$  second for undercoolings greater than 200K. Both alloys recalesced smoothly to a maximum recalescence temperature at which the solid was at or near its equilibrium composition and equilibrium weight fraction. For the samples of hypoeutectic alloy that recalesced above the eutectic temperature, a second nucleation event occurred on cooling to the eutectic temperature. For samples which recalesced only to the eutectic temperature, no subsequent nucleation event occurred on cooling to the eutectic temperature. For samples which recalesced only to the eutectic temperature, no subsequent nucleation event was observed on cooling. It is inferred in this latter case that both the  $\alpha$  and  $\beta$  phases were present at the end of recalescence. A solidification model is proposed for growth

---

\* For presentations at the Science Review of Flight Experiments, Microgravity Science and Applications Division of NASA office of Space Science and Applications to be held at the George C. Marshall Space Flight Center, February 10, 1987.

and ripening of the dendrite structure during recalescence.

Microstructures of samples produced in ground based work were determined by optical metallography and by SEM, and microsegregation by electron microprobe measurements.<sup>(3)</sup> A gradual morphology change from dendritic to spherical was found with increasing undercooling, with the structure being fully spherical at about 180K undercooling. Dendrite element spacing was shown to be primarily determined by the ripening which occurred during cooling after recalescence; this cooling took place in the range of 0.2 to 8 seconds, depending on sample size, undercooling and location in the sample. The extent of ripening in all samples must have been very large. For example, the calculated dendrite tip radii in samples undercooled 50 and 200K respectively were 0.2 and 0.017 micron. The radii of the dendrite elements observed were about 5 and 2 microns respectively. Hence the scale of the structure presumably increased about a factor of 25 at 50K undercooling and over 100 at the higher undercooling. Solute distribution and amounts and forms of eutectic were measured. The solidification model referred to above was employed to interpret results obtained.

A series of flight tests has been planned to conduct experiments similar to the ground based experiments described above. The main immediate objectives are to (1) evaluate containerless melting and solidification of nickel base alloys with and without glass coatings, (2) develop techniques for study of recalescence behavior, (3) develop an understanding of undercooling phenomena in a microgravity environment, and (4) develop an understanding of microstructures so produced. A hoped for ultimate objective of this work is to obtain higher undercoolings than are achievable in ground based experiments and to thereby produce and be able to study new structures of scientific and technological interest.

The Space Shuttle Columbia carried an alloy undercooled experiment in its STS 61-C mission in January 1986. A sample of Ni-32.5wt%Sn eutectic was melted and solidified under microgravity conditions. Because of unanticipated problems with the equipment, (clogging of cooling water lines), this undercooling experiment on the shuttle was cut short. Undercooling achieved was probably less than 30K. Interesting features observed on the solidified specimen included an apparent surface nucleation site, curved dendrites with non-orthogonal secondary dendrite arms, and dendrite fragments with extremely fine dendrite arm spacing (<0.5 micron) on the surface.

Additional experiments are projected for later flights to obtain higher undercoolings and improved data acquisitions, and to study the eutectic as well as the hypoeutectic Ni-Sn alloy. In addition, an experiment is planned with a different alloy which freezes over a much narrower solidification range than the Ni-25%Sn alloy. This could be Fe-Ni, Ni-Cu, or very dilute Ni-Sn.

### Part I Dendrite Tip Velocity

The experimental apparatus used in this work consists of a high frequency levitation melter, an optical temperature measuring system with an overall response time of less than 6 microseconds, a data storage and manipulation system, and a high speed camera system with operating speeds up to 500 frames per second. For much of the work, metal samples were 9 mm in diameter, levitation melted within a glass slag. For portions of the work involving high speed photography, the glass slag was contained within a quartz tube of rectangular cross section, in order to obtain a sample with flat surfaces for better focusing of the camera as shown in Figure 1. The bulk of work conducted was on Ni-25% Sn alloy, a hypoeutectic alloy. Limited work was also conducted on the eutectic alloy Ni-32.5% Sn.

Undercoolings obtained in the work were up to 320 K. Temperature was measured before, during and after recalescence, and in a number of runs high speed motion photography was carried out during recalescence.

Figure 2 shows a series of eight photographs, taken 2 milliseconds apart, of recalescence of

a nickel-25wt% tin alloy which had been undercooled 131 K. The camera sees "dendrites" growing on the surface of the metal because of the temperature difference behind the growth front. The dendrites are significantly hotter than the bulk liquid into which they are growing. They appear darker on this negative photograph. Figure 3 is a drawing of the progression of the dendrites shown photographically in Figure 2, and Figure 4 is a plot of interface position vs. time of the growing dendrites. Curves a through c represent growing dendrite tips while curve e, progressing at a much slower rate, represents the thickening rate of one of the dendrites. A summary of data from a series of runs of growth velocity vs. undercooling is shown in Figure 5, and Figure 6 shows these same data (the black points) on another plot. Figure 6 also contains data points on dendrite tip velocity obtained from thermal measurement, as will be described in Part II below. Finally, it compares these data to three important dendrite growth models, that of Lipton, Kurtz and Trivedi (LKT),<sup>5)</sup> of Boettinger and Coriell (BC),<sup>6)</sup> and that of Lipton, Glicksman and Kurtz (LGK),<sup>7)</sup>.

Note that the agreement of our experiment with these theories is quite good. The most recent, and most precise, is the LKT model, although it differs little from the BC model for the range of parameters in this work. Figure 7 plots the various undercoolings at the dendrite tip vs. total undercooling, and this plot is helpful in understanding how the growth proceeds. For example, consider dendritic growth at a total bulk undercooling of 200 K. The dendrite tip is growing at a temperature of only about 6 K above the bulk liquid temperature; this is the amount of the thermal undercooling  $\Delta T_\alpha$ . The bulk of the undercooling, approximately 160 K, results from buildup of solute at the dendrite tip,  $\Delta T_D$ , and the remainder of the undercooling, approximately 35 K, is accounted for by depression of the liquidus temperature from the curvature effect,  $\Delta T_r$ . Figure 7 shows that for bulk undercoolings even to temperatures well below the equilibrium solidus, dendrite growth is controlled primarily by solute diffusion. It also shows that the dendrite tip temperature is not greatly different from the bulk liquid temperature. Hence the "dendrites" that we see by cinematography must, in fact, represent an isotherm somewhat back from the dendrite tip where recalescence has occurred to a point that there is a visible temperature difference.

Another result of the theory is plotted in Figure 8; that is, dendrite tip radius vs. bulk undercooling. This calculated radius is quite small, since it is controlled primarily by solute diffusion. It ranges from approximately 0.2 microns at 50 K undercooling to approximately 17 nanometers at 200 K undercooling. Yet the "dendrites" that we see by high speed cinematography are very much larger than this. These measured tip radii are also plotted in Figure 8, and it is seen that they are about three orders of magnitude larger than the calculated radii. The suggestion is clear - that what we see is a growth front morphology determined by thermal diffusion, whereas the actual growing dendrites themselves must be very much smaller, controlled primarily by solute diffusion.

Our schematic model of a growing dendrite to account for these observations is shown in Figure 9. The growth front proceeds into the bulk undercooled metal with a large thermally controlled, dendrite-like morphology, as sketched. Within these large dendrite features are growing very much smaller solute controlled dendrites, whose tip radius and growth behavior is described by analyses such as that of LKT. Recalescence behind the dendrite tip occurs very rapidly so that recalescence is substantially complete not far behind each growing tip. Some isotherm such as that sketched as  $T_R$  is then the isotherm observed cinematographically.

## Part II Recalescence Behavior

As indicated earlier, recalescence behavior was measured optically. The temperature measurement system consisted of a two-color pyrometer (Capintec Ratioscope III), a pair of matched amplifier circuits, and a digital storage oscilloscope (Nicolet, model 2090-III). The two silicon photocells of the pyrometer operate at narrow near-infrared wavelength bands centered at 0.81 and 0.95 microns. The response time of the temperature measurement system was less than 6 microseconds. A computer (Hewlett Packard, model 85) was interfaced to the oscilloscope for calculations.

Figure 10 shows two typical recalescence curves. There is first a period of "rapid recalescence," followed by a period of "slow recalescence." In the sample undercooled only 125 K there is finally seen a period of temperature decrease, due to heat extraction to the surroundings.

The time for the period of "rapid recalescence" ranges from fractions of milliseconds at high undercoolings to some seconds at low undercoolings (Fig. 11). With the model for dendritic growth described earlier in mind, we can use these thermal data to obtain a separate and confirming estimation of dendrite tip velocity. Assuming rapid recalescence progresses so quickly that it is nearly complete just behind the growing dendrite tip, then the time for rapid recalescence must represent the time for dendrites to sweep across the sample surface. Hence, dendrite tip velocity is given by something like the sample diameter divided by recalescence time. The thermally determined points for dendrite tip velocity in Figure 6 were calculated in this way.

The period of "slow recalescence" seen is dramatically slower than the period of rapid recalescence. It is so dramatically different that it leads one to suspect immediately a different mechanism is involved. Figure 12 shows recalescence of one sample plotted in a different way, as residual undercooling vs. time on a log scale. Note that the portion of this curve to the far right (portion representing the period of slow recalescence) plots as a straight line with a slope of  $-1/3$ . This result, and other results including metallography to be discussed later, is strongly suggestive that the period of slow recalescence is controlled by ripening of the dendritic structure which first forms.

The maximum recalescence temperature measured for a number of runs is plotted in Figure 13 vs. initial bulk undercooling. For undercoolings greater than about 100-120 K the data correspond closely to the assumption that, at the maximum recalescence temperature the liquid and solid phases are present at their equilibrium compositions and amounts. This result, at first surprising, is to be expected as a result of the extremely fine structures that form, and assuming ripening is occurring to a significant extent. Experimental results deviate significantly from the calculated results (based on simple adiabatic recalescence) at lower undercoolings. This, we believe, is due to the fact that recalescence at the lower undercoolings is not adiabatic, and significant heat extraction to the surrounding is occurring during the later stages of recalescence.

Thermal curves of samples following recalescence show the typical types of cooling curves observed in usual castings and ingots. That is, for the hypoeutectic alloy, when recalescence occurs above the eutectic temperature, the cooling curves show first formation of the primary phase alpha during cooling to the eutectic, and then nucleation and growth of the eutectic at the eutectic temperature, Figure 14.

Figure 15 summarizes our model for the solidification of these melts in terms of the "paths" of the liquid and solid compositions during recalescence. Consider a sample undercooled to a temperature  $T_N$ . Solute buildup in front of the dendrite tip results in a surface liquid composition given by the point A. The solid composition is then A' given according to the equilibrium partition ratio. Both A and A' are depressed from the equilibrium liquidus and solidus by  $\Delta T_r$ , the depression of the equilibrium curves from the radius of curvature effect. Recalescence behind the dendrite tip is then limited by solute diffusion within the interdendritic regions and liquid and solid compositions at the interface move upwards during the period of rapid recalescence to the temperature  $T_R$ . Thereafter they rise more slowly to the equilibrium liquidus and solidus (assuming adiabatic recalescence). Finally, the temperatures fall due to heat extraction to the surroundings and the remaining solidification is as in usual castings and ingots.

### Part III. Structure and Microsegregation

Microstructure of undercooled nickel-25wt% alloy was found to exhibit a morphology transition from a typical dendritic structure at low undercoolings to a spherical, non-dendritic structure at high undercoolings, as can be seen in Figure 16. We believe the morphology changes seen with increasing undercooling result directly from the increasing ripening that occurs at the higher undercoolings. Many microstructural observations tend to qualitatively support this view. The existence of ripening can be seen in a simple way by examining microstructures at different locations within a given sample. Figure 17 shows a series of microstructures at different locations within a 9 mm diameter sample of the hypoeutectic alloy undercooled 324 K. Dendrite element spacing varies significantly from surface to center as a result of ripening, and experimental results agree well with simple calculations.

The explanation of the results obtained is that although cooling rate is essentially the same at

center and surface, the large amount of eutectic present results in a "local solidification time" that is much longer at the center than at the surface of the sample. The local solidification time is the sum of the time for solidification of the primary phase and for solidification of the eutectic. The time for eutectic solidification is the time for the eutectic solidification front to reach the given radial location; therefore, the local solidification time is dependent on the location. For the calculated results shown in Figure 17, the usual relationship of dendrite arm spacing and local solidification time, which is based on the ripening kinetics, was applied.

Quantitative measurement of solute concentration in the dendrites was made using electron microprobe analysis (EMPA). Typical profiles across dendrite arms are shown in Figures 18 and 19. Figure 18 shows a profile obtained from a region near the center of a sample undercooled 62K. The solute concentration increases radially outwards in the dendrite arm. Figure 19 is a profile obtained from a typical highly undercooled sample. This specimen, undercooled 324K, shows negligible segregation of solute in the spherical "dendrite element." The solute concentration in the spherical elements was about 19wt%Sn, and the composition of the second phases was 40wt%Sn. These are the compositions of the two phases at equilibrium at the eutectic temperature.

Minimum measured solute concentrations for a number of samples are plotted versus initial undercoolings in Figure 20 with calculated curves. The calculated curve #1 is based on a simple model assuming complete equilibrium of liquid and solid at the maximum recalescence temperature. Curve #2 makes this assumption and also assumes that liquid forming from remelting during recalescence is trapped with the growing dendrite arms.

The volume fraction of lamellar eutectic structure was observed to decrease with increasing undercooling, as may be seen qualitatively from the photographs of Figure 16. The measurements of volume fraction of lamellar eutectic structure were made by point counting. Figure 21 shows measurements of volume fraction of lamellar eutectic structure compared with calculated curves. Curve #1 and #2 are calculated on the same bases as the similarly numbered curves in Figure 21, referred to above.

The microstructure of the eutectic alloy is significantly affected by undercooling. In general, the microstructure of an undercooled eutectic sample consists of two distinguishable regions: normal lamellar eutectic and anomalous eutectic. Figure 22 shows structures for three Ni-32.5wt%Sn eutectic alloy samples with different initial undercoolings. At low undercoolings, the structure is largely lamellar eutectic (Fig 22[a]). At intermediate undercoolings, the structure is composed of the two regions (Fig. 22 [b]). In samples with high undercoolings (Fig. 22 [c]), lamellar eutectic can be observed only at high magnification. Figure 23 shows that the volume fraction of lamellar eutectic decreases with increasing initial undercooling.

#### Part IV Flight Experiment Performed

The Space Shuttle Columbia carried an Alloy Undercooling Experiment on its STS 61-C mission in January, 1986. The experiment was performed in the electromagnetic levitator (EML). A sample of Ni-32.5wt%Sn eutectic was melted and solidified under microgravity conditions. Because of unanticipated problems with the equipment, (clogging of cooling water lines), this undercooling experiment on the shuttle was cut short. The data of the temperature - time trace of the sample during heating, melting and solidification are shown in Figure 24. The data were obtained at a rate of 125 measurements per second using a pyrometer. The large amount of noise is due to insufficient isolation of the measurement circuit. The severe noise which occurred at the time of power cut-off is due to the operation of a motion picture camera. The noise caused difficulty in estimating the level of undercooling attained. This result with others including solidification time measurement indicate that the specimen undercooling was probably less than 30K.

Metallographic examination of the specimen revealed an apparent nucleation site, shown in Figure 25(a). At low magnification, it can be seen that a large curved dendrite proceeds from this site. No other such obvious nucleation site was found on the surface of the specimen. A higher magnification photograph of the dendrite is shown in Figure 25(b). The secondary arms are not orthogonal to the primary branch. This curved dendrites (bending) is thought to be caused by thermal stress due to nonuniform heat flow and/or mechanical stresses due to convection

(Marangoni effect). Curved dendrites have not been observed on any samples in ground based experiments of this study.

Because the specimen attained only a small undercooling, the microstructure consists primarily of lamellar eutectic. Several patches of anomalous eutectic structure were also found, as shown in Figure 26. The fraction of anomalous eutectic in the cross-section of the flight specimen was measured at less than 10 percent, corresponding to initial undercooling of less than 30K (Figure 23). One type of feature, which was discovered, does not at first, seem consistent with the fact that the initial undercooling of the specimen was small. A number of dendritic fragments, such as that shown in Figure 27, were observed on the surface. The secondary arm spacing of this dendrite is less than 1 micron. The explanation of this observation must be that the fine spacing is due to decanting of the remaining liquid from the surface due to shrinkage during solidification, so that little coarsening occurred.

## Part V Projected Space Experiments and Objectives

### Objectives and rationale for the flight experiments

On earth, we have achieved up to 320 K initial undercooling for Ni-25wt%Sn and Ni-32.5wt%Sn alloys. We hope to achieve higher undercoolings under microgravity conditions, since the higher power would not be needed to maintain levitation during cooling, and no gravitational convection due to difference of densities take place. A goal would be to attain the "hypercooling" regime, where complete solidification would be achieved during recalescence. Amounts of "hypercooling" (which is an undercooling below the liquidus equal to the sum of equilibrium freezing temperature range and latent heat of fusion divided by specific heat) are about 500K for Ni-25wt%Sn and about 450K for Ni-1wt%Sn alloy.

If we can achieve these high undercoolings in space, the exciting opportunity would be made available to obtain, examine, and test new structures and phases in specimens much thicker than usual "splat-cooled" or other earth based rapidly solidified specimens. We would expect to obtain fully homogeneous, non-dendritic structures, and in some cases metastable phases.

On earth, rapid solidification can be attained and also practically used by rapid quenching such as melt spinning and gas atomization processes. In these processes, rapid solidification rate is gained by heat extraction to the surroundings, therefore, the obtainable materials are usually limited in size, generally less than 100 microns. In the proposed experiments herein, we could obtain rapidly solidified materials in relatively large sizes of 1 centimeter in diameter, since the heat to be extracted for solidification would be extracted before the onset of solidification, provided "hypercooling" is achieved.

Space experiments now projected are to obtain higher undercoolings and improved data acquisition. An experiment is also planned with a different alloy which freezes over a much narrower solidification range than Ni-25wt%Sn. Lower undercooling would be required for the alloy closer to achieve "hypercooling". The alloy could be Fe-Ni, Ni-Cu, or very dilute Ni-Sn. The planned (proposed) shuttle experimental conditions are given in detail in Table 1.

Current ground based research work is providing the background for understanding solidification behavior and structures at high undercoolings. This work permits us to develop and predict parameters for space experiments, and to develop improved techniques for these space experiments.

### REFERENCES

1. Y. Wu, T.J. Piccone, Y. Shiohara and M.C. Flemings, accepted for publication in Met. Trans. A (1987)
2. T.J. Piccone, Y. Wu, Y. Shiohara and M.C. Flemings, accepted for publication in Met. Trans. A (1987)
3. Y. Wu, T.J. Piccone, Y. Shiohara and M.C. Flemings, to be submitted for publication
4. T.J. Piccone, F.H. Harf, Y. Wu, Y. Shiohara, M.C. Flemings and E.A. Winsa, proceedings of MRS Fall Meeting Symposium (1986)

5. J. Lipton, W. Kurz and R. Trivedi, to be published in Acta. Met.
6. W.J. Boettinger and S. Coriell, proceedings of NATO Workshop on "Rapid Solidification Technologies", Castle of Theuren, FRG, (March 1985)
7. J. Lipton, M.E. Glicksman and W. Kurz, Mat. Sci. Eng., 65 (1984), 570



Table 1 Experimental conditions for projected space experiments

**MATERIALS:**

<u>Alloy</u>	Ni-25wt%Sn	$T_L - T_s = 200 \text{ K}$	$T_L = 1507 \text{ K}$
	Ni-1wt% Sn	$= 8 \text{ K}$	$= 1740 \text{ K}$
	Ni-5wt% Sn	$= 65 \text{ K}$	$= 1699 \text{ K}$
	Fe-25wt%Ni	$= 16 \text{ K}$	$= 1722 \text{ K}$
	Ni-10wt%Cu	$= 11 \text{ K}$	$= 1706 \text{ K}$

Glass

with and without glass coatings  
 Ferro-brand EG-0222 silicate glass  
 Pyrex-brand 7740 borosilicate glass

Size

Metal: 7 - 10 mm (in diameter)  
 Glass coating thickness: 0.3- 1.0 mm

**HEATING:**

High frequency induction heating.

**ATMOSPHERE:**

Inert gas (Ar, or He), Vacuum, and/or He-H<sub>2</sub> gas  
 "To avoid oxidation of the metal samples by direct exposure of the metal surface to the ambient atmosphere"

**DATA ACQUISITION:**

(a) **Pyrometric temperature measurements**

- i) 125 data points/second for entire heating and cooling cycle,
- ii) 2000 or more data points/second for approximately 30-40 seconds after power cut-off,
- iii) Assured accuracy by use of a proper lens and two- or three-color pyrometer,
- iv) Maximum noise should be under  $\pm 5 \text{ K}$ ,
- v) After calibration and smoothing, precision should be within  $\pm 5 \text{ K}$ .

(b) **Cinematography**

In each cycle, the surface of the spherical specimen should be observed and cinematography will be made:

- i) For 30-40 seconds at 16 frames/second after power cut-off, A much faster frame speed would be desirable.
- ii) with 0.1 mm resolution or better at the specimen surface,
- iii) with depth of field (in focus) larger than 2 mm in diameter for a sphere, and preferably larger than 5 mm.

ORIGINAL PAGE IS  
OF POOR QUALITY

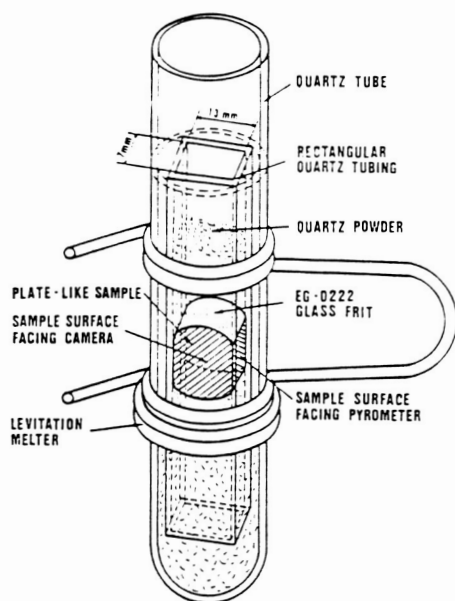


Figure 1. Sample assembly used for photographic measurements of growth behavior.

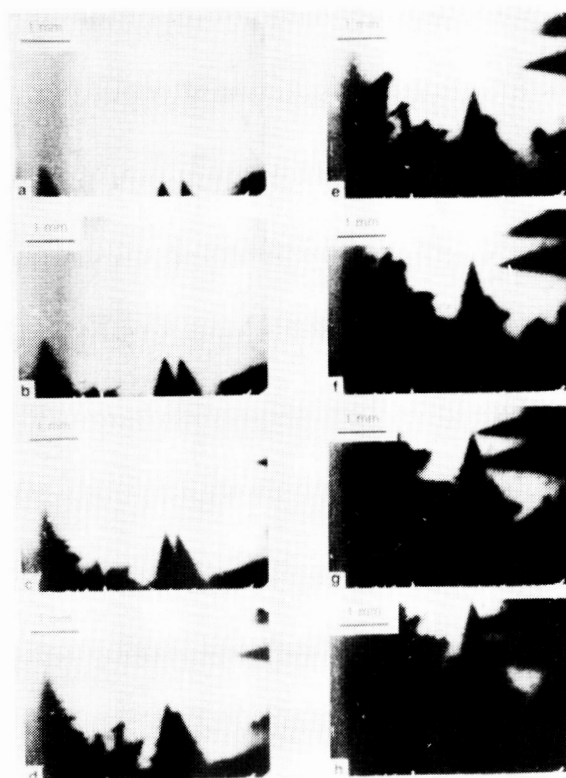


Figure 2. Eight photographs, taken 2 milliseconds apart, of recalescence of a Ni-25wt% Sn hypo-eutectic alloy sample undercooled by 131 K.

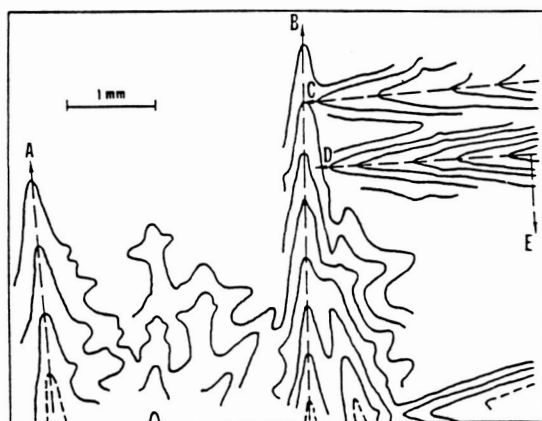


Figure 3. Drawings of the advancing solid-liquid interface of a Ni-25wt%Sn hypoeutectic alloy sample during recalescence. Undercooling is 131 K. The time interval between lines is milliseconds. Drawings were traced from photographic negatives.

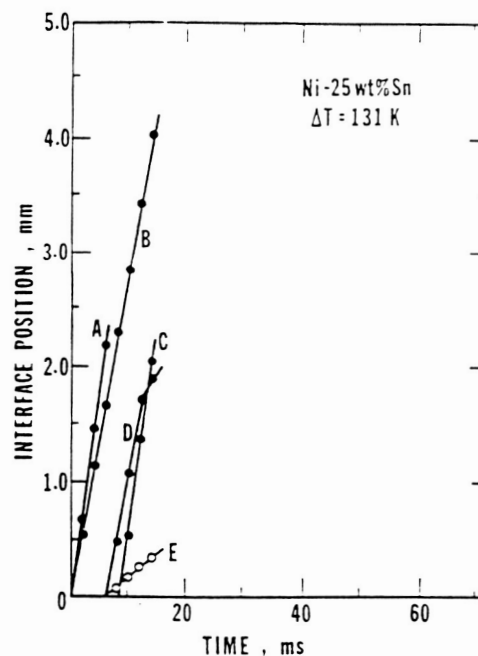


Figure 4. Movement of several parts of an advancing solid-liquid interface versus time for a Ni-25wt%Sn hypoeutectic alloy sample undercooled by 131 K. A, B, C, D, and E correspond to dendrites and directions shown in Figure 3.

C-6

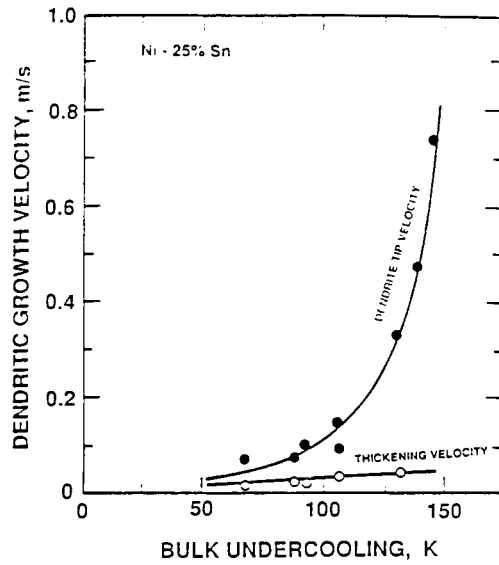


Figure 5. Dendrite tip velocity and dendrite thickening velocity versus initial undercooling for Ni-25wt%Sn alloy samples, measured by high-speed cinematography.

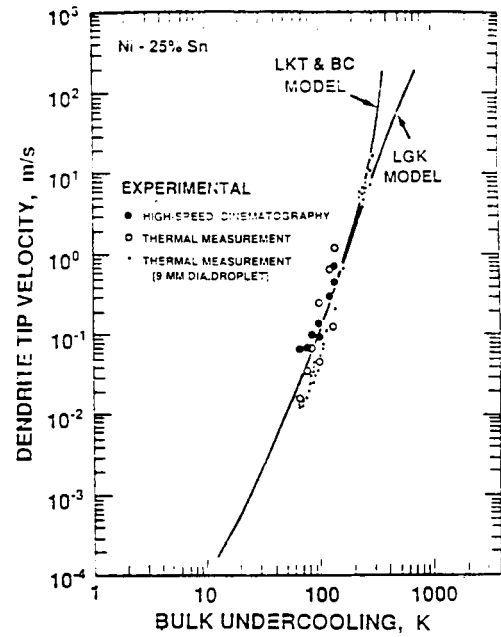


Figure 6. Dendrite tip velocity vs. bulk undercooling for Ni-25wt%Sn alloy. Experimental results and calculated curves based on the models developed by Lipton, Kurz, and Trivedi and Boettinger and Coriell (LKT-BC) and Lipton, Glicksman, and Kurz (LGK).

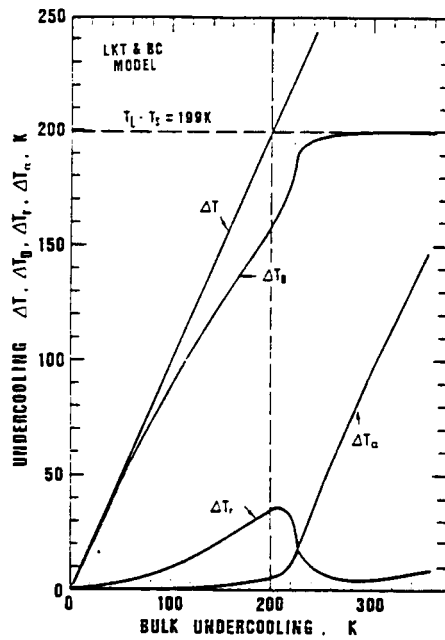


Figure 7. Results of calculations of solute undercooling ( $\Delta T_D$ ), capillarity undercooling ( $\Delta T_C$ ), and thermal undercooling ( $\Delta T_A$ ) as functions of bulk undercooling, using the Lipton, Kurz, and Trivedi model.

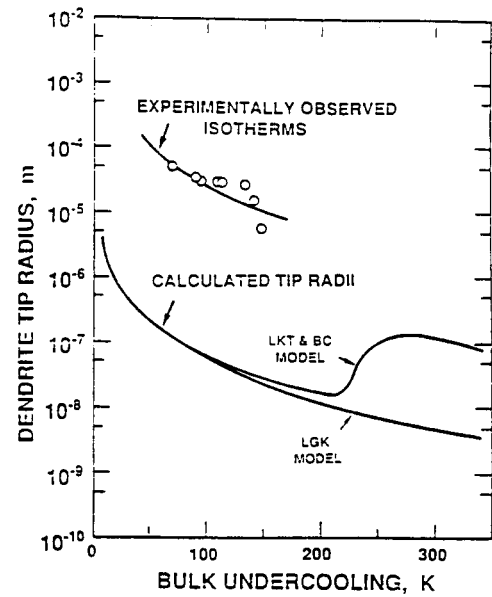


Figure 8. Measured coarse "dendrite" tip radius and calculated dendrite tip radius vs. bulk undercooling for Ni-25wt%Sn alloy.

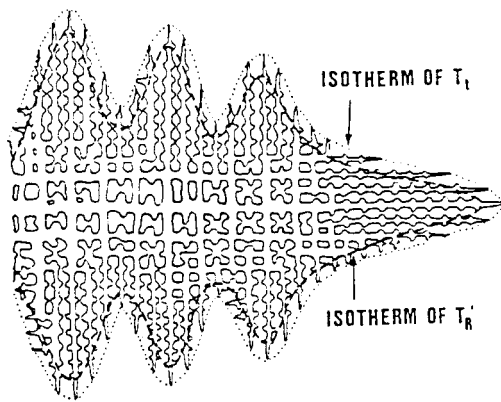


Figure 9. Schematic diagram of coarse "dendrites" growing into undercooled melt.

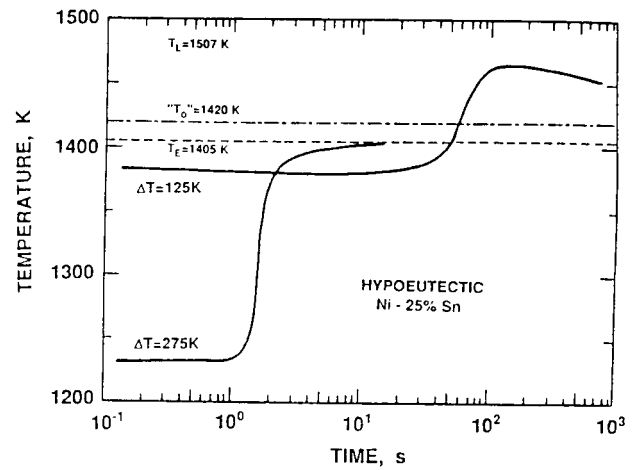


Figure 10. Recalescence behavior of two samples of hypoeutectic alloy. Time scale is logarithmic.

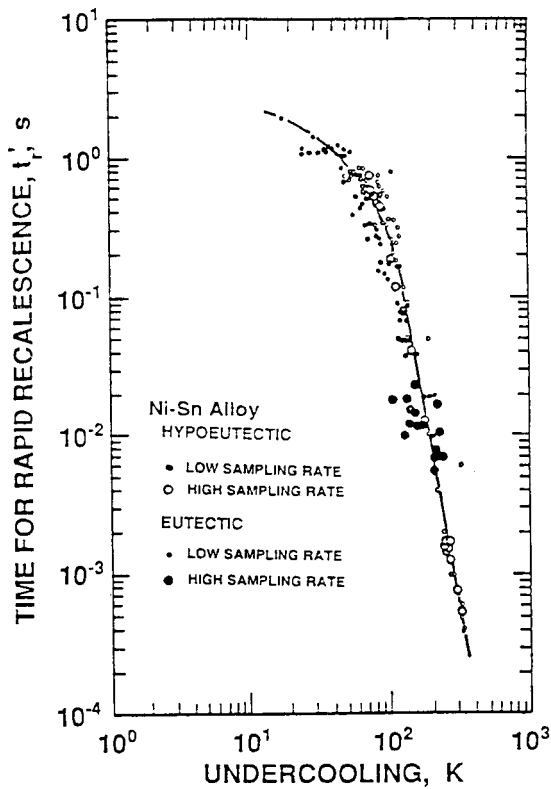


Figure 11. Recalescence time versus undercooling.

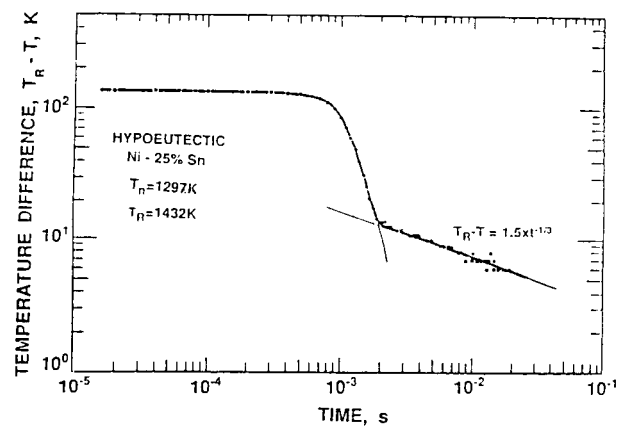


Figure 12. Recalescence behavior, hypoeutectic alloy, plotted on log-log scale to show linear behavior in temperature range of slow recalescence.

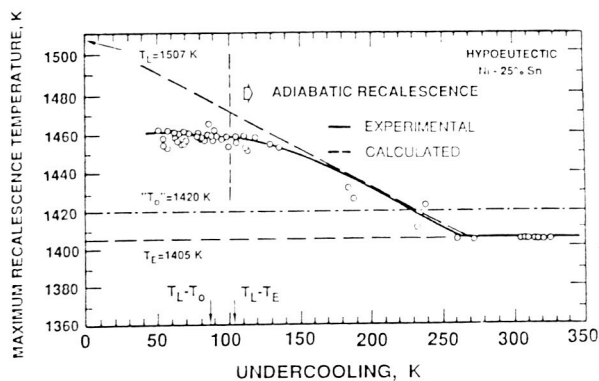


Figure 13. Maximum recalescence temperature,  $T_R$ , versus undercooling, hypoeutectic alloy.

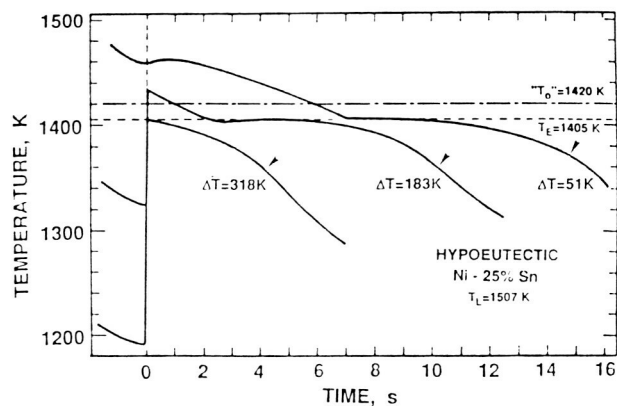


Figure 14. Recalescence and cooling curves for three samples of hypoeutectic alloy, low sampling rate.

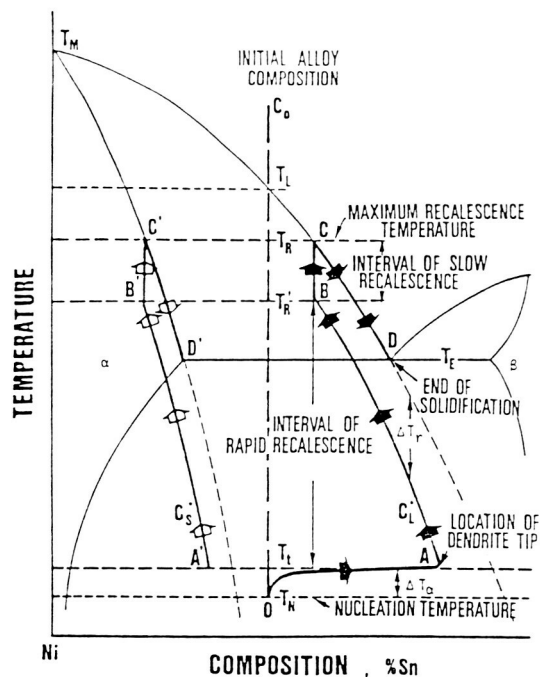


Figure 15. Schematic "solidification path" of undercooled Ni-25wt%Sn alloy. ABCD is the path of the liquid composition at the liquid-solid interface. A'B'C'D' is the path of the solid composition at the liquid-solid interface. Path OA describes the change in solute concentration in front of the advancing dendrite tip. The temperature difference between the two "paths" and the phase diagram extensions are exaggerated.

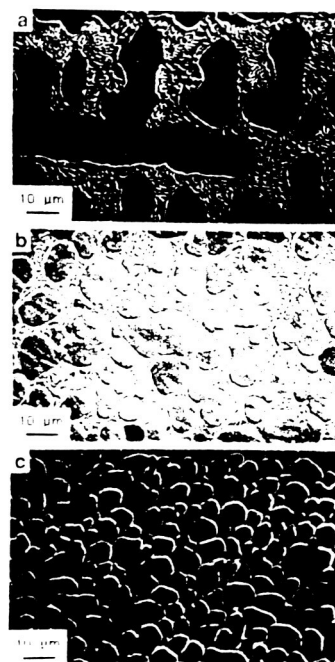


Figure 16. Cross-sectional microstructures of three Ni-25wt%Sn hypoeutectic alloy samples with different initial undercoolings. (a) 112K; (b) 183K; and (c) 324K.

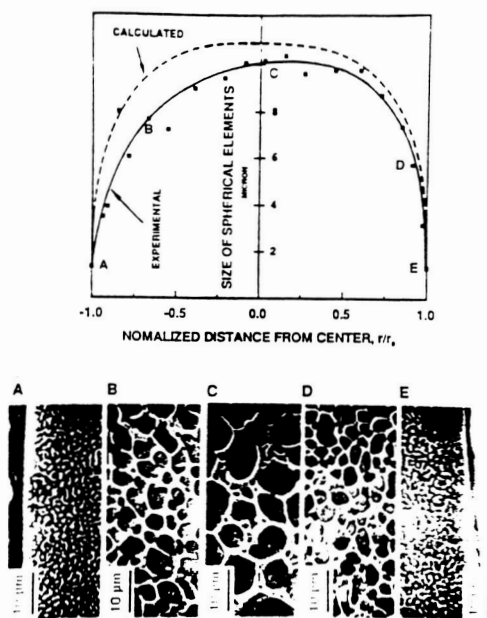


Figure 17. Dependence of diameter of spherical elements on position in a Ni-25wt%Sn hypoeutectic alloy sample undercooled by 324 K. The five photographs correspond to the five data points labeled in the plot.

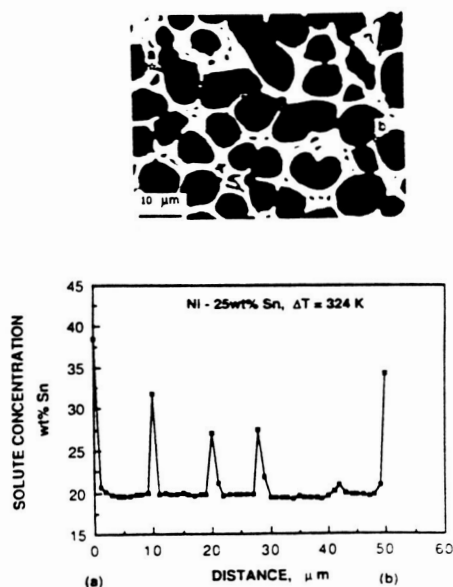


Figure 19. Composition profile across five spherical dendrite elements, measured by electron microprobe, in a Ni-25wt%Sn alloy sample undercooled by 324K. Note that the contrast difference observed here was not the result of a composition difference.

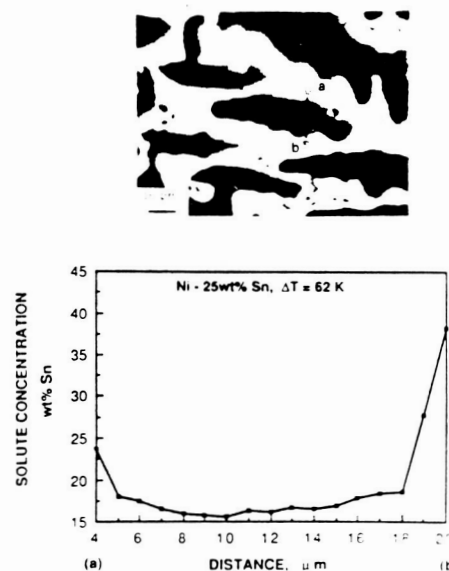


Figure 18. Composition profile across one dendrite arm, measured by electron microprobe, in a Ni-25wt%Sn alloy sample undercooled by 62K. Note that the solute-poor core revealed qualitatively by the contrast difference was confirmed by the quantitative measurement.

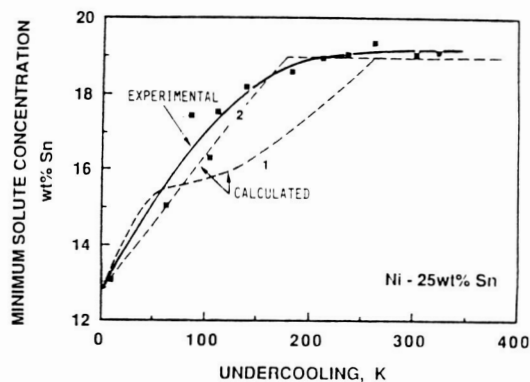


Figure 20. Comparison of experimental results of minimum solute concentration versus undercooling with calculations for Ni-25wt%Sn alloy.

ORIGINAL PAGE IS  
OF POOR QUALITY

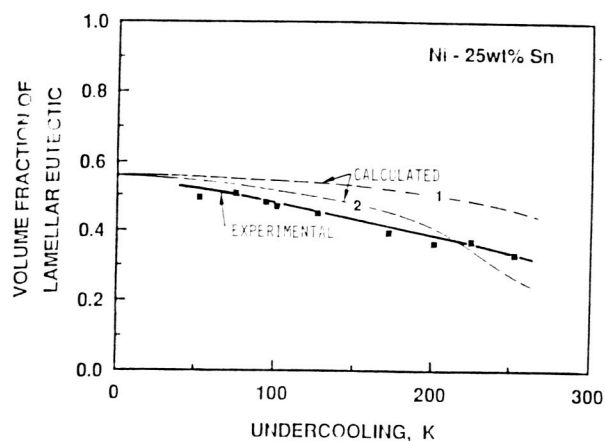


Figure 21. Comparison of experimental results of volume fraction of lamellar eutectic structure versus undercooling with calculations for Ni-25wt%Sn alloy.

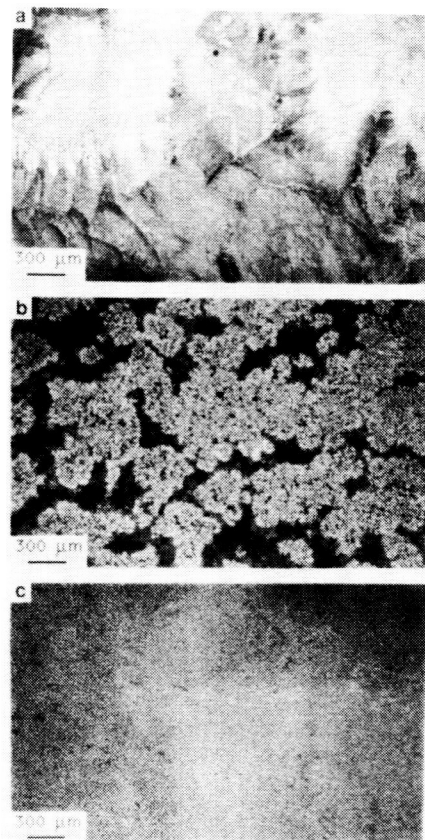


Figure 22. Cross-sectional Microstructures, taken by optical microscopy at low magnification, for three Ni-32.5wt%Sn eutectic alloy samples with different undercoolings, showing the dendrite-like appearance of the anomalous eutectic regions. Undercoolings: (a) 31K; (b) 113K; and (c) 225K.

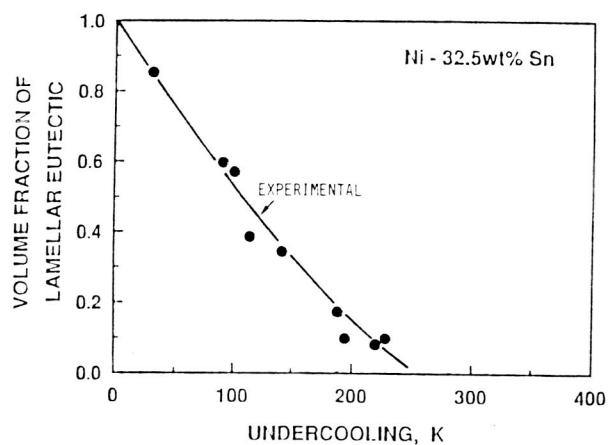


Figure 23. Plot of volume fraction of lamellar eutectic structure versus undercooling for Ni-32.5wt%Sn alloy.

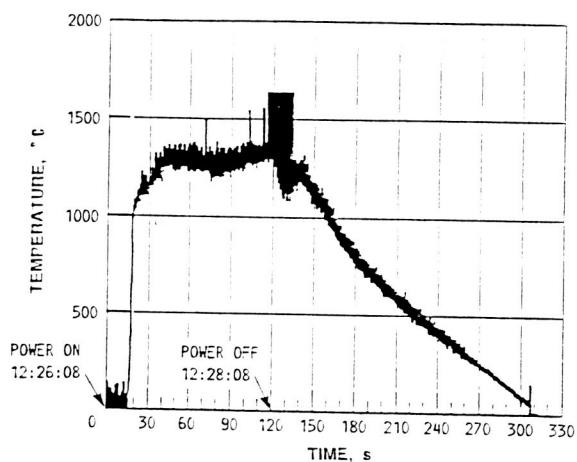


Figure 24. Time-temperature trace of flight specimen during processing, obtained using a pyrometer at 125 measurements per second.

ORIGINAL PAGE  
BLACK AND WHITE PHOTOGRAPH

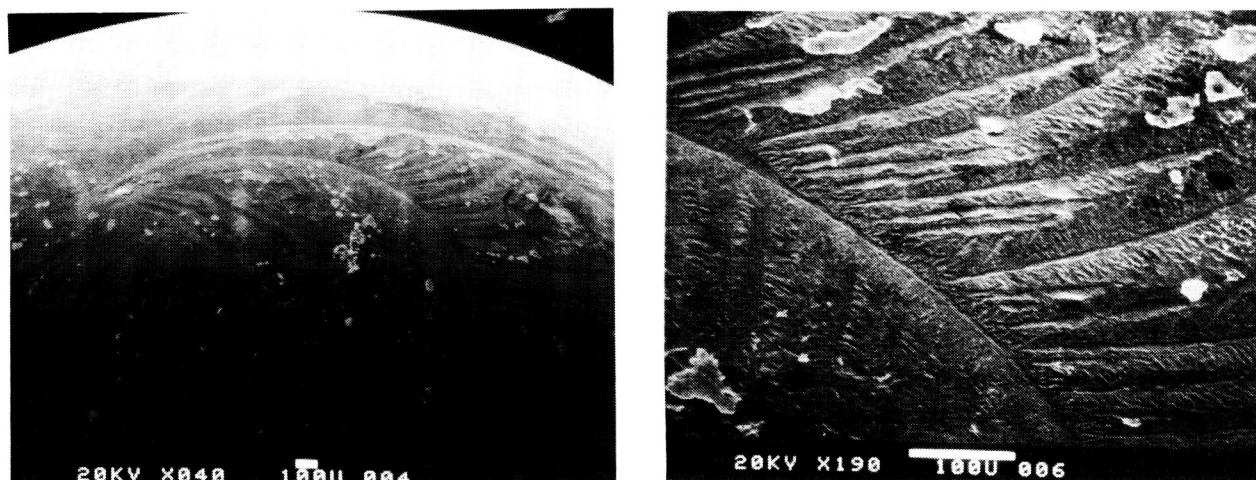


Figure 25. Surface microstructures of flight specimen, showing (a) apparent nucleation site and large curved dendrite, and (b) non-orthogonal secondary dendrite arms.

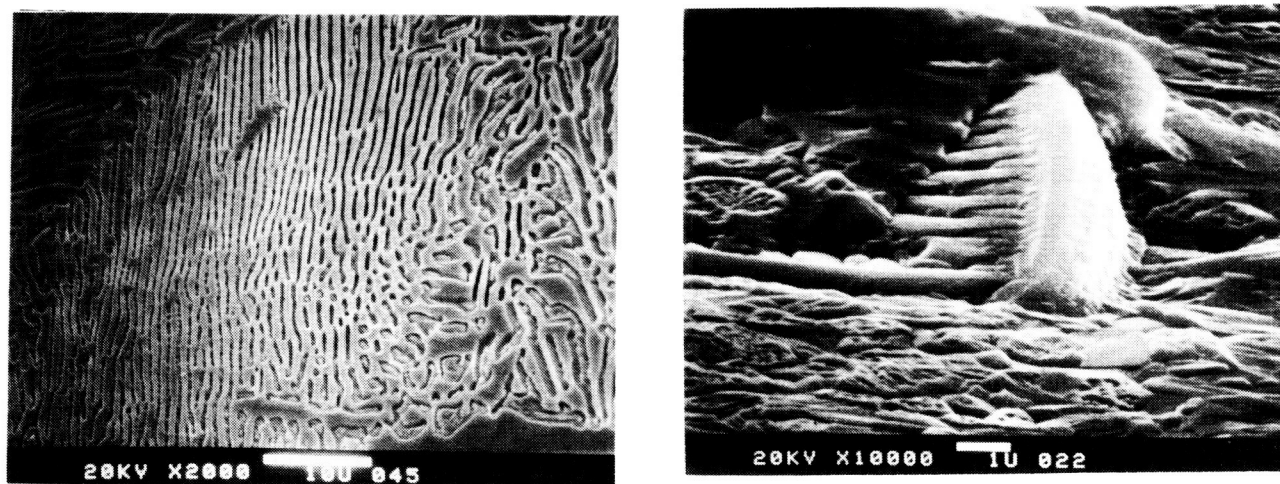


Figure 26. Cross-sectional microstructure of flight specimen, showing lamellar eutectic (left) and anomalous eutectic (right).

Figure 27. Fine dendrite fragment on flight specimen surface.

ORIGINAL PAGE  
BLACK AND WHITE PHOTOGRAPH



THE INFLUENCES OF CONVECTION ON DIRECTIONAL SOLIDIFICATION  
OF EUTECTIC Bi/MnBi

David J. Larson, Jr.  
Grumman Corporate Research Center  
Bethpage, NY 11714-3580

ABSTRACT- Eutectic alloys of Bi-Mn were directionally solidified using the Bridgman-Stockbarger technique to determine the influences of gravitationally-driven thermo-solutal convection on the Bi-MnBi rod eutectic. Experiments were conducted that varied the level of convection by varying the growth parameters (solidification velocity or applied temperature gradient) and growth orientation (relative to the terrestrial gravitational vector), by microgravity damping, by applied magnetic field damping, and by imposing forced convection. Peltier interface demarcation and in-situ thermocouple measurements were used to monitor interface velocity and thermal gradient and to evaluate interface planarity.

Rod diameter, in the regular faceted/non-faceted MnBi/Bi eutectic, was found to vary with solidification velocity. At high solidification velocities the rods appear circular in cross-section, but as the velocity is slowed the cross-section becomes more faceted changing to chevrons, then to hexagonal segments and finally to a platelet structure at very low velocities. Inter-rod spacing and mean rod diameter were found to vary as the inverse square root of the solidification velocity, as expected. Interface undercooling was found to vary as the square root of the solidification velocity, also as predicted by theory. Inter-rod spacing and mean rod diameter were not found to be influenced by the applied thermal gradient, in contradiction to suggestions that all eutectics with faceting at the interface should show a temperature gradient dependence.

Forced convection at the interface was found to have little effect within the cooperative growth regime, however, increased mixing substantially coarsened the low velocity platelet structure and promoted radial segregation. Damping of the natural thermal convection, using transverse applied magnetic fields or microgravity significantly increased interfacial undercooling and decreased both the mean rod diameter and the inter-rod spacing. Magnetic field damping and microgravity damping were found to be equally effective at damping the natural thermal convection. Magnetic field damping was ineffective at damping thermo-solutal convection during off-eutectic solidification, whereas microgravity damping was shown to be effective under similar growth conditions.

## 1. INTRODUCTION

Morphological control as a means of optimizing mechanical and physical properties has gained increased acceptance over the past several decades. Eutectic solidification reactions are attractive in this respect because substantial microstructural refinement (to sub-micron dimensions) and alignment can be achieved directly, by controlling the solidification parameters. Eutectic reactions are also of interest and importance because many of the most significant commercial materials, such as cast irons, solders, brazements, and Al-Si castable alloys, solidify via this reaction. Controlling the morphologies and microstructures of this class of alloys is thus highly significant.

This work reports on a study of the Bi/MnBi eutectic solidification

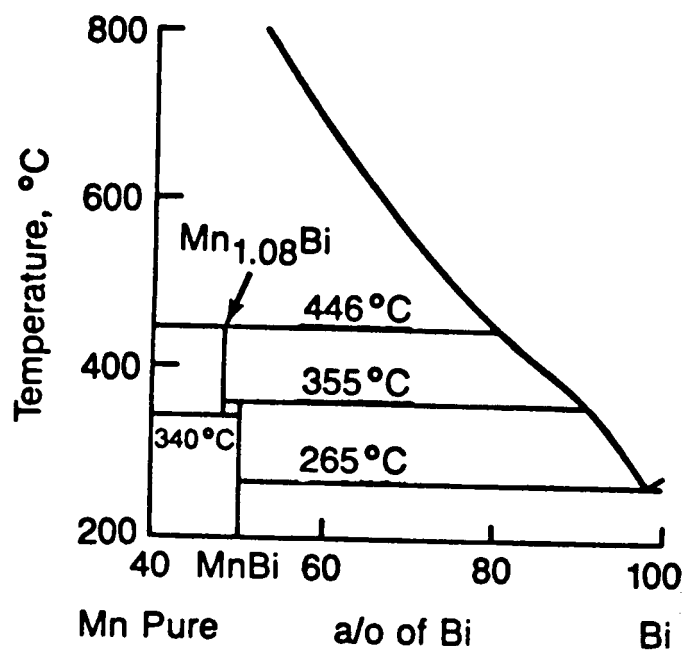


Figure 1a. BI-MnBI region of the BI-Mn phase diagram<sup>(1)</sup>.

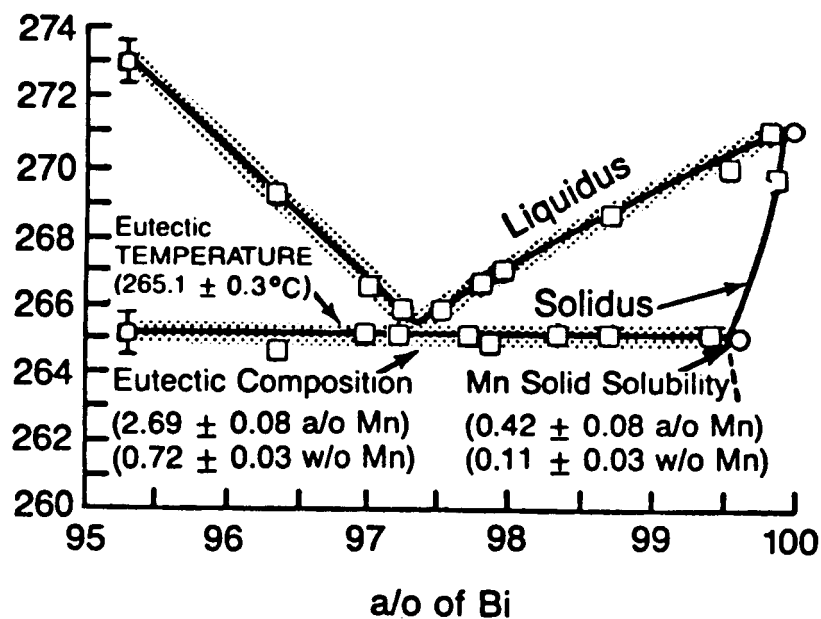


Figure 1b. BI/MnBI eutectic region of the BI-Mn phase diagram<sup>(2)</sup>.

reactions using the Bridgman-Stockbarger directional solidification technique as a means of controlling solidification parameters. The Bi-Mn phase diagram (1) is shown in figure 1a, and the eutectic Bi/MnBi phase diagram segment (2) is shown in figure 1b. It is clear from the phase diagram that this is a highly asymmetric eutectic solidification reaction. The low volume fraction phase, MnBi, would be expected to be arrayed as a fiber within a matrix of terminal solid solution Bi. The MnBi phase might be expected to have a tendency to facet as it is a non-cubic intermetallic. Directional solidification of this rod eutectic results in the simultaneous growth of the MnBi faceted rod and Bi matrix phases in a regular array coupled by the diffusion field in the liquid ahead of the solidification interface.

The dependence of the inter-rod spacing,  $\lambda$ , and the rod diameter,  $d$ , on velocity is described by the well known Jackson-Hunt (3) theory for eutectics growing under diffusion controlled, plane-front, solidification conditions. This theory is well established for eutectic systems without faceting at the solidification interface. The relationship predicts that  $\lambda$  and  $d$  vary as the inverse square root of the solidification velocity and that interface undercooling,  $\Delta T$ , varies as the square root of solidification velocity. The optimum growth velocity, undercooling, and wavelength is described as growth in extremum and, stated simply, demands that at a given solidification velocity the structure will grow at a minimum undercooling. Alternatively, a structure growing at a given undercooling will grow at a maximum velocity. The Bridgman-Stockbarger technique imposes a solidification velocity on the solidification interface, and thus growth occurs with minimum undercooling.

The Jackson-Hunt (3) theory was appended by Verhoeven et al (4) to

include the influence of forced convection. It was concluded that the diffusional field ahead of the solidification interface was so tightly coupled to the interface that it was unlikely to be influenced by macroscopic fluid flow. Early experiments using microgravity as a means of damping convection suggested that, counter to theory, the damping of gravitationally driven convection refined both the inter-rod spacing and the mean rod diameter (5). Subsequent experiments in microgravity confirmed this finding and suggested that interface undercooling was increased under damped conditions (6-8). The present study was undertaken to better understand the origins of these discrepancies.

## 2. EXPERIMENTAL TECHNIQUE

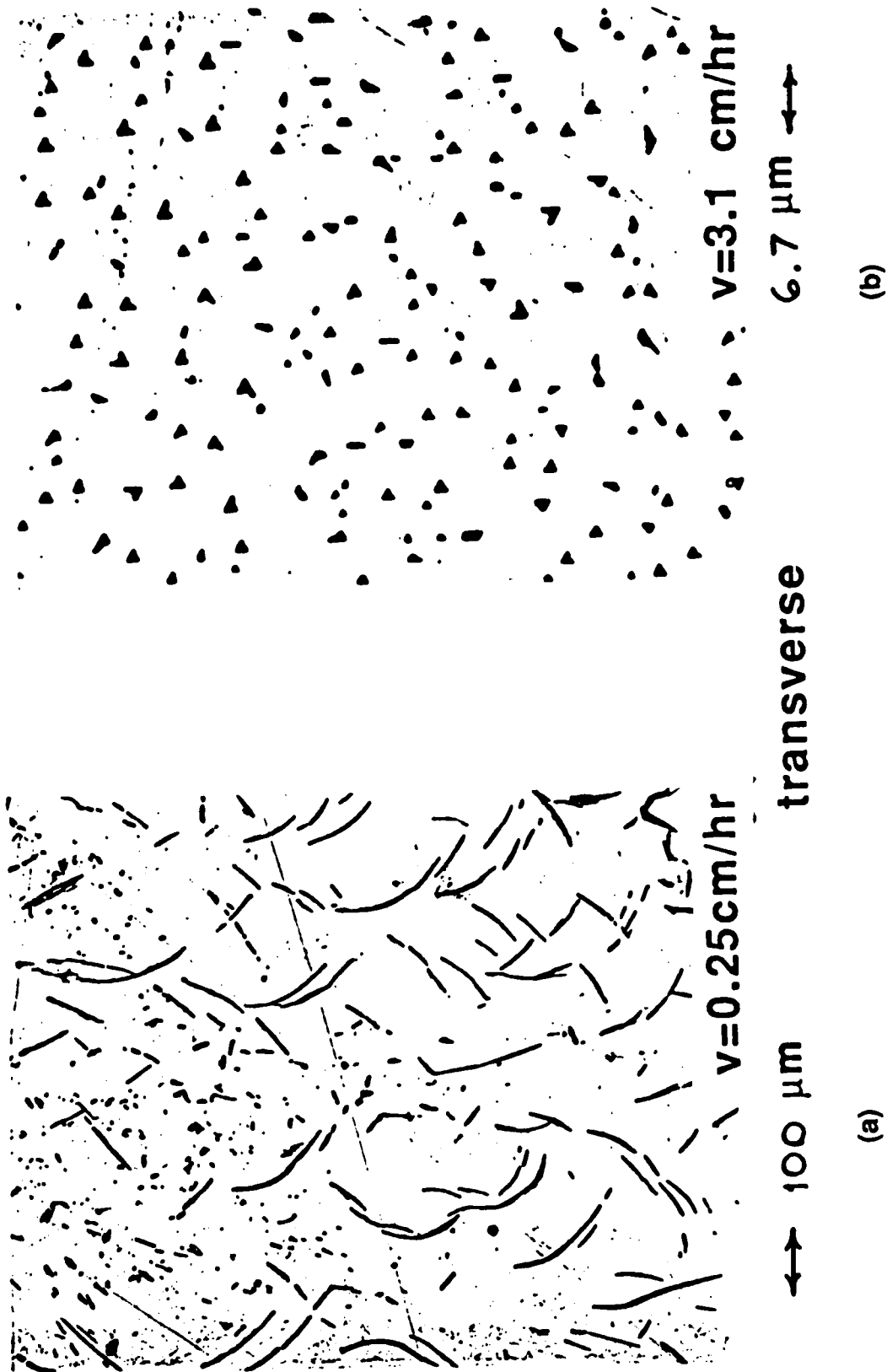
Experiments were conducted over a wide range of solidification velocities (0.5 to 50 cm/h) and thermal gradients (5 to 125 °C/cm). Growth orientation relative to the terrestrial gravity vector was varied, some experiments conducted vertically upwards (thermally stabilized) and some vertically downwards (thermally destabilized). It was assumed that for compositions on the eutectic that there was no solutal component to the gravitationally-driven convection. Additional experiments were conducted in the suborbital microgravity environment on sounding rockets flying Keplerian trajectories, and another was conducted in the microgravity orbital environment of the space shuttle. Applied transverse magnetic fields were also used to damp the natural thermal convection. Lastly, forced convection was imposed on the solidification interface by conducting spin-up/spin-down experiments while directional solidification was taking place. Peltier interface demarcation was used to monitor the solidification velocity and the interface shape and

in-situ ultrafine thermocouples were used to monitor the cooling rate and thermal gradient within the samples. Sample velocity,  $V$ , and thermal gradient,  $G$ , in the liquid ahead of the interface were used as experiment parameters, as previously noted, whereas radial thermal gradients were minimized by using a thermal model of the Bridgman-Stockbarger process and Peltier interface demarcation to adjust the growth conditions until a near-planar interface was achieved. Our experimental techniques have been previously described (9,10).

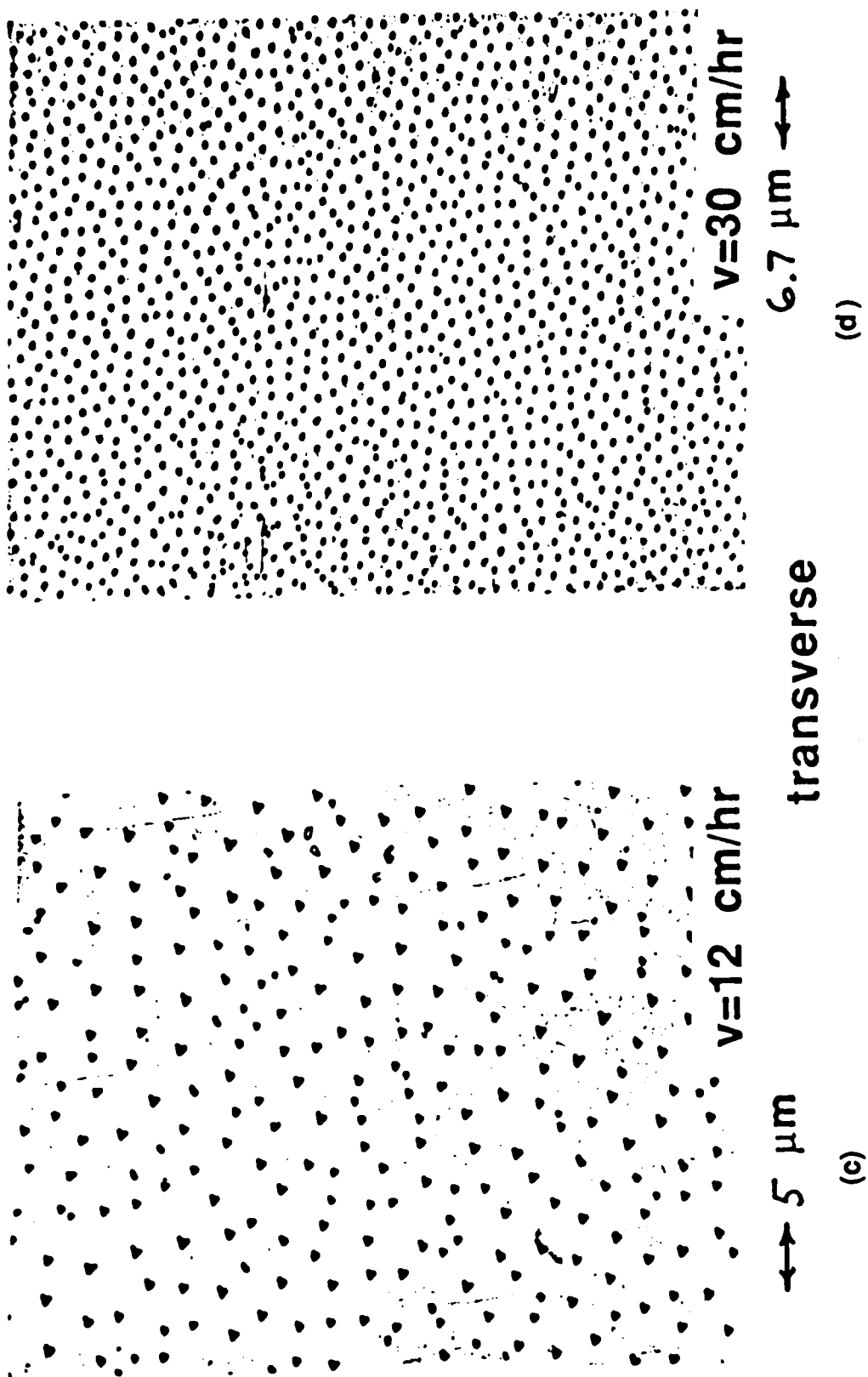
### 3. EXPERIMENTAL RESULTS AND DISCUSSION

The solidification morphology of the dispersed MnBi rods was found to be a regular array of high aspect ratio fibers whose growth axis coincided with the 'c' direction of the equilibrium MnBi phase, which is hexagonal. The rod-cross-section was found to vary in morphology as a function of solidification velocity and to coincide with the basal plane of the hexagonal cell. Typical examples of the rod cross-sections as a function of solidification velocity are shown in figures 2a-d. At the highest solidification velocities, Fig. 2d, the rods become chevron-like and then appear as degenerate hexagonal segments that confirm that the growth planes that define the shape are the hexagonal prismatic planes. For velocities in excess of 2 cm/hr the structure is properly described as a regular faceted (MnBi)/non-faceted (Bi) eutectic, and the growth is cooperative.

At velocities below 0.75 cm/hr, Fig. 2a, the morphology has changed to a platelet structure reminiscent of graphite in cast iron. The reason for this is evident when the relative stability of rods and lamellae are considered,



Figures 2. Typical Bi/MnBi microstructures photographed normal to the solidification direction as a function of solidification velocity. (a)  $V = 0.25\text{ cm/hr}$ , (b)  $V = 6.7\text{ cm/hr}$ .



Figures 2. Typical Bi/MnBi microstructures photographed normal to the solidification direction as a function of solidification velocity. (c)  $V = 12.0$  cm/hr, (d)  $V = 30.0$  cm/hr.



following arguments presented by Jackson-Hunt (3). They calculate, for a system with isotropic interfacial free energies, that the minimum undercooling for growth of rods is lower than for lamellae when a critical surface energy ratio is less than unity. Substituting our experimental data into their equation results in the ratio approaching unity (0.996) when the morphological transition that we note takes place. At velocities greater than 0.75cm/hr, the rod structure will grow with the smaller undercooling and thus will grow ahead of, and ultimately eliminate the lamellar structure which grows with larger undercooling, and vice versa.

The sensitivity of the platelet and rod regimes to convection was tested by conducting spin-up/spin-down tests in the course of the Bridgman-Stockbarger directional solidification. This imposed forced convection at the solidification interface. Figure 3 shows the results of this study(9). It is clear that the platelet regime is extremely sensitive to the increased convection, whereas the rod regime is relatively insensitive. The reason for the platelet sensitivity to convection is probably due to a non-isothermal interface which is sensitive to the fluid flow and to changes in the thermal gradient ahead of the solidification interface. The insensitivity of the rod growth is probably due to its coupled nature and to a moderately high level of laminar convection which exists in the melt even without the forced convection. This natural convection has already affected the solidification conditions, particularly the interface undercooling, and further mixing has little effect. This will be discussed further after the damping experiments are described.

The eutectic mean rod diameter and mean inter-rod spacing and standard

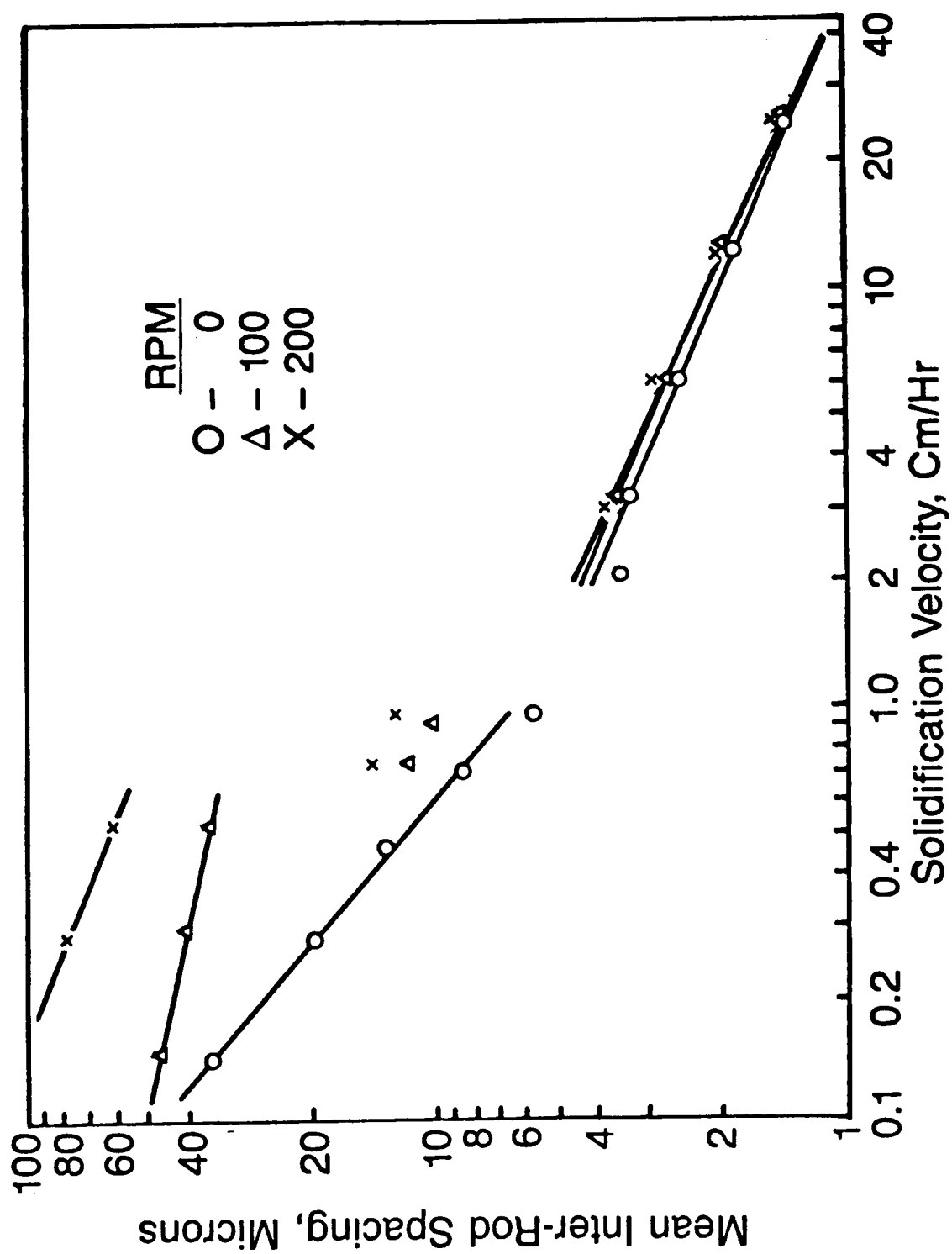


Figure 3. Mean Bi/MnBi inter-rod spacing as a function of solidification velocity, with forced convection imposed on the solidification interface.

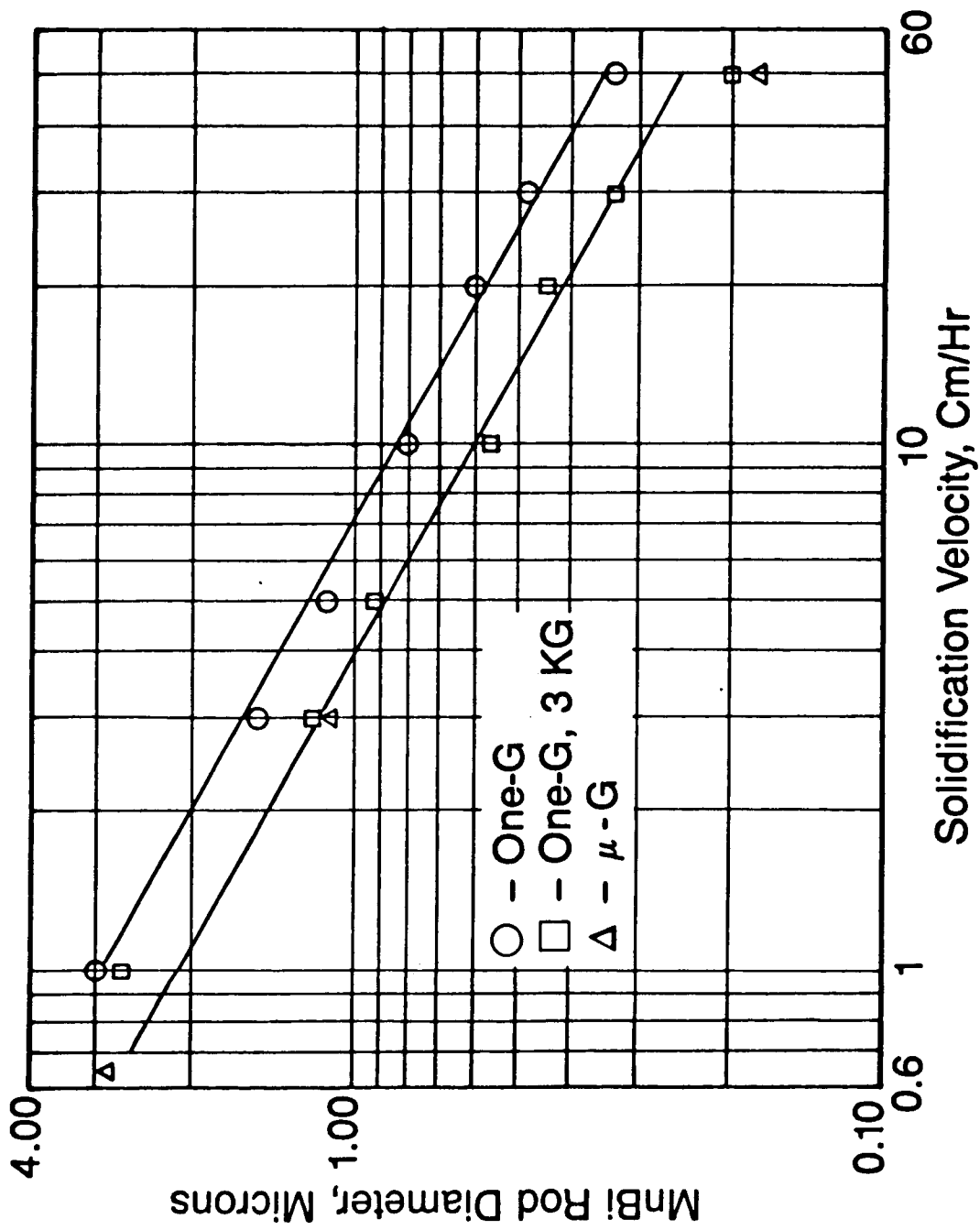


Figure 4b. Mean MnBi rod diameter as a function of solidification velocity, with and without convection damping imposed on the sample.

deviations were determined from metallographic sections taken normal to the solidification direction using a Leitz Texture Analyzer System (TAS). Data for the mean rod diameter and inter-rod spacing versus solidification velocity are present in Figures 4a and 4b, respectively. Data for samples processed in one-g, without damping, are shown as circles. The line fitting these data is drawn with the anticipated  $V^{-1/2}$  dependence and serves to confirm this dependence for both the mean rod diameter and the inter-rod spacing. Samples grown at differing growth orientations relative to the gravity vector could not be distinguished and as a consequence only a single curve is presented.

Figures 4a and 4b also show the mean rod diameter and the mean inter-rod spacings for samples processed in one-g using applied magnetic field damping (squares) and samples processed in orbit using microgravity damping (triangles). It may be seen that the microgravity damped and applied magnetic field damped results are statistically distinct from the one-g undamped results. It is apparent that the reduction of the level of convection has served to decrease both the inter-rod spacing and the mean rod diameter significantly. It is clear, too, that magnetic field damping and microgravity damping are equally effective at damping the gravitationally-driven thermal convection present in the eutectic melts

The reason for the structural refinement is not so apparent, and as a consequence a series of experiments were conducted to investigate whether the applied thermal gradient in the melt ahead of the solidification interface was responsible for refinement. This concept stemmed from suggestions (10,11) that the presence of faceting at the eutectic solidification interface should invariably lead to non-isothermal interfaces that should show a

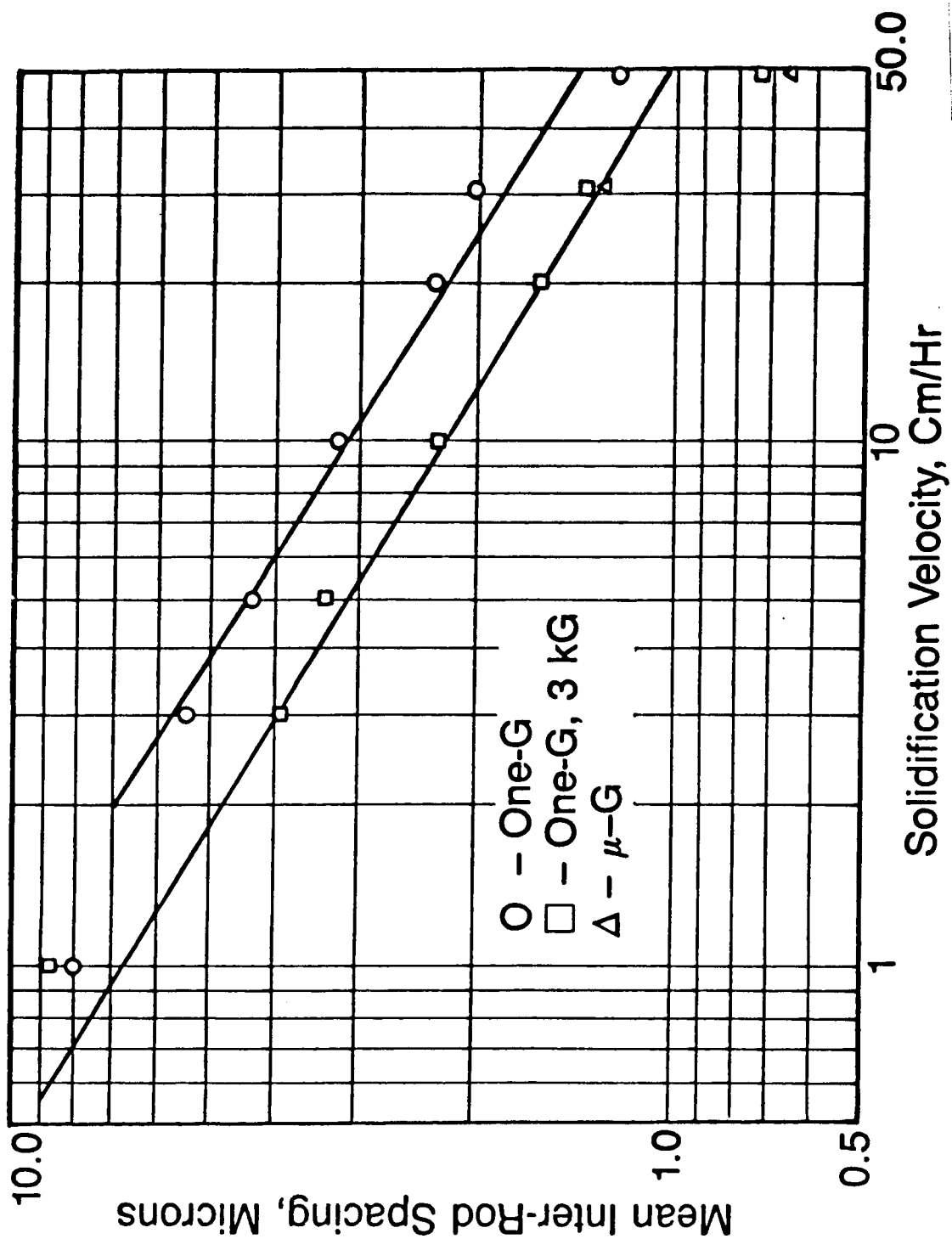


Figure 4a. Mean Bi/MnBi Inter-rod spacing as a function of solidification velocity, with and without convection damping imposed on the sample.

gradient sensitivity. The non-isothermal interface was a natural consequence of the faceted phases' inability to respond quickly to a perturbation, and thus, the diffusional coupling at the solidification interface was disturbed. This resulted in one phase leading or lagging (non-isothermal) and the establishment of a solutal boundary layer of the same order as those encountered during off-eutectic solidification or during solid solution crystal growth. The latter condition introduces the possibility of convection sensitivity, though this line of reasoning was not pursued.

Another reason for suspecting that the applied thermal gradient was the origin of the structural refinement was experimental evidence which showed that thermal gradients ahead of the solidification interface increased from approximately 100 °C/cm in one-g to about 120 °C/cm under damped conditions (12,7,8). Since it was reported that increased thermal gradients decreased rod diameter and inter-rod spacing <sup>(10)</sup>, it was logical to assume that the thermal gradient was the gravitationally dependent (flow dependent) cause for the effect.

Figure 5 shows the results of the present investigation <sup>(13)</sup>. The thermal gradient was varied from approximately 5°C/cm to 120°C/cm and a least squares fit to the data confirms the  $V^{-1/2}$  dependence predicted, but does not support a dependence of the spacing on temperature gradient. If  $G^n$  was that the thermal gradient dependent function, the exponent determined from the structural data by linear regression analysis was 0.027. This is within the experimental error and it may be concluded that no such dependence exists for the Bi/MnBi rod eutectic.

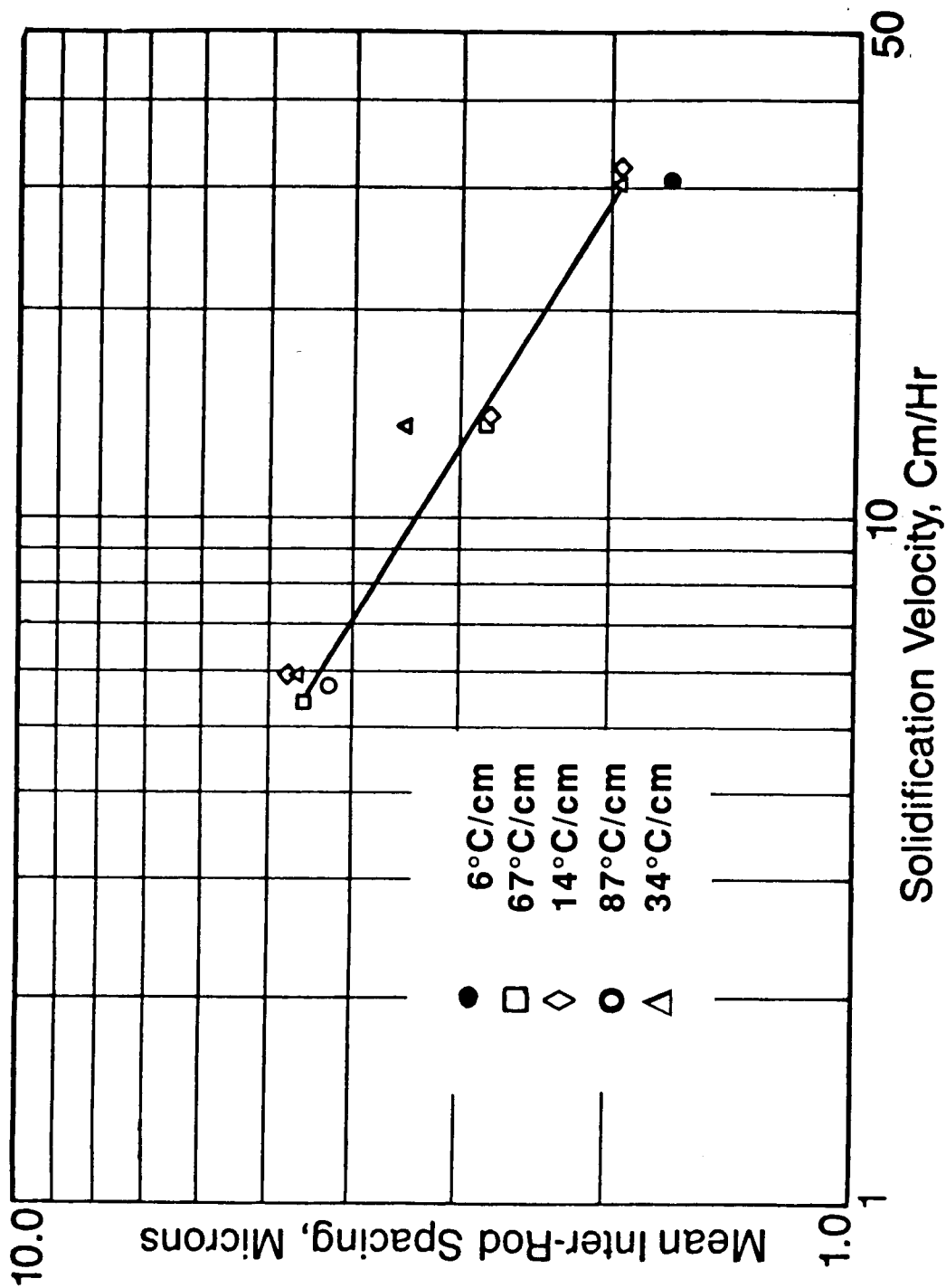


Figure 5. Mean Bi/MnBi Inter-rod spacing as a function of solidification velocity showing the dependence on applied thermal gradient.

The reason for the absence of the thermal gradient dependence in this case is due to two factors, which were confirmed by Peltier interface demarcation experiments. Figure 6 shows the results of these experiments (14, 15). The photomicrograph shown was taken from a polished section of the sample cut parallel to the growth direction. The polarity of the current pulse applied was negative, causing cooling at the solidification interface. The interface was thus 'instantaneously advanced' resulting in a refinement of the structure. However, what should be noted is that the structure has had no difficulty adjusting to this severe perturbation and so the primary hypothesis for suspecting a non-isothermal interface must be rejected. In addition, the interface immediately preceding the band of pro-eutectic single phase Bi is seen to be very nearly planar. Considering the thermal conductivities of the respective phases, the interface must grow very nearly isothermally.

Evaluation of thermal data demonstrated that in one-g the sample experienced a small but reproducible interface undercooling; however, the damped samples experienced a much greater degree of undercooling. This was unexpected, and the data are shown in Figure 7. These data may be fit with the expected  $V^{1/2}$  functionality (3), and they raise the possibility that the undercooling is the origin of the structural refinement. This hypothesis suggests that since the Bi/MnBi eutectic is highly asymmetric the extrapolated liquidus and solidus lines defining the undercooled phase relations might be significantly different from the phase relations prescribed by the equilibrium phase diagram. In the case of a eutectic alloy of Bi-Mn, undercooling of approximately 6°C (the maximum noted), would reduce the expected volume fraction of the dispersed MnBi phase by an amount comparable to that measured



# PELTIER INTERFACE DEMARCATION

negative polarity



growth direction ↓

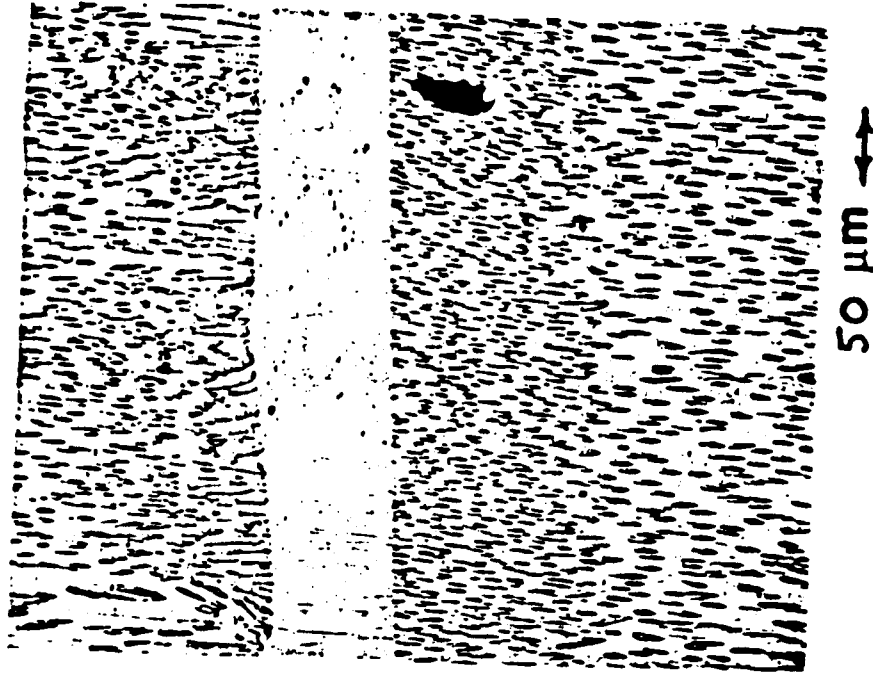


Figure 6. Photomicrograph of a longitudinal section of a Bi/MnBi sample directionally solidified showing a Peltier interface demarcation. The refinement of the Bi/MnBi structure during the pulse should be noted.

Eutectic Bi-Mn

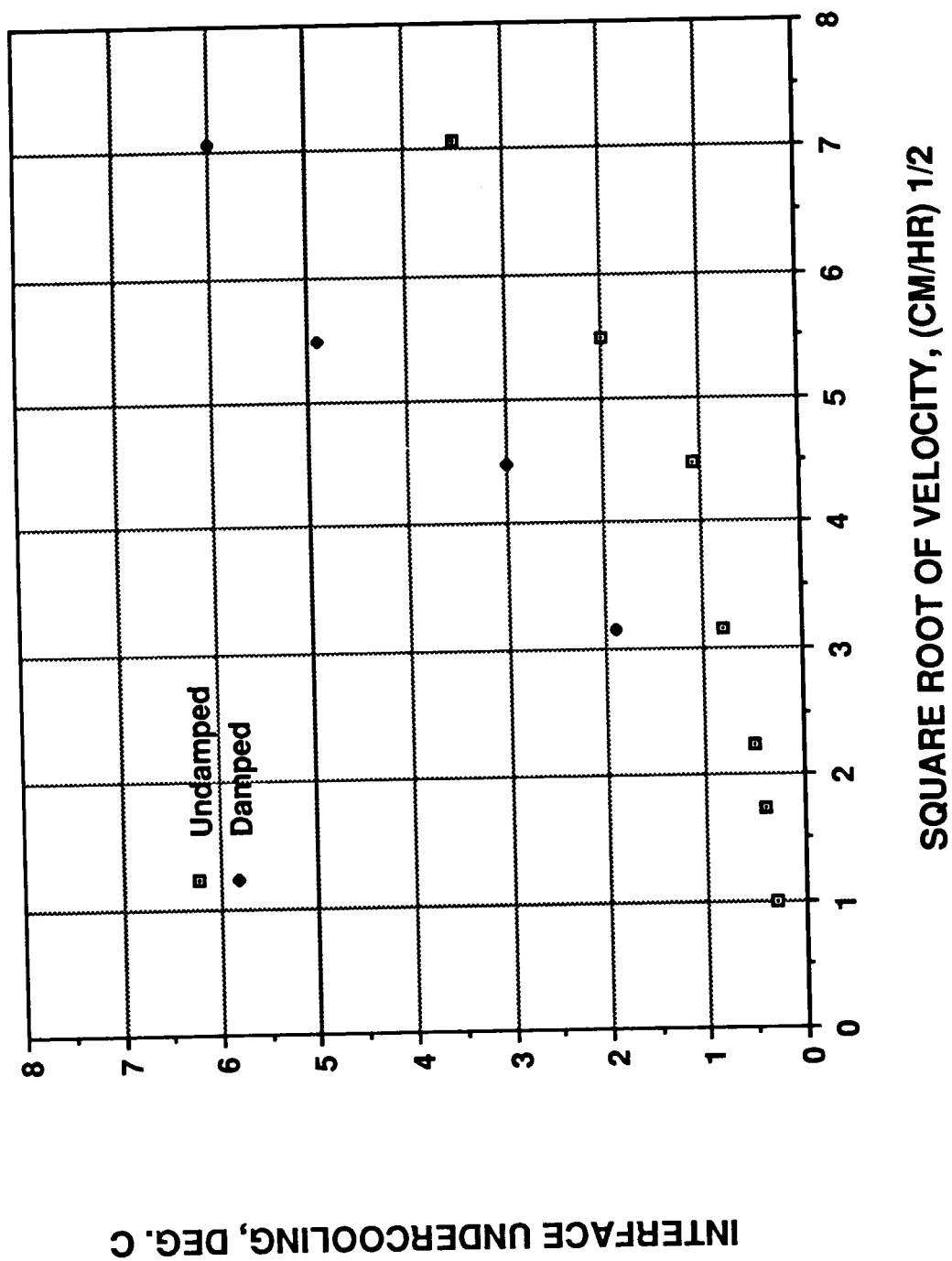


Figure 7. Interface undercooling as a function of the square root of the solidification velocity, for samples solidified with and without convection damping.

within the damped sample undercooled 6°C. Figure 8 shows the result of volume fraction calculations based on the measured rod and inter-rod dimensions of both the undamped and damped samples. It is clear that there is a strong velocity dependence, however, there is no statistically significant difference between the curves. This is critically important to note since the damped and undamped cases experienced significantly different undercooling conditions. The evidence suggests that even though the phase diagram is asymmetric, this factor is not the cause of the structural refinement. Actually, in one microgravity processed sample, the terminal solid solubility of Mn in Bi was noted to be almost twice what the equilibrium solubility was determined to be, 0.21 wt.% Mn. This is consistent with an extended solubility due to the undercooling. It has been reported that compositional adjustments within the Bi/MnBi eutectic are made by varying the inter-rod spacing and maintaining the rod diameter essentially constant during a constant velocity test. This would suggest that a decreased volume fraction of MnBi would be accommodated by maintaining the rod diameter constant and increasing the inter-rod spacing. This is entirely inconsistent with our experimental finding.

Recently, a new theory has been proposed by Magnin and Kurz <sup>(16)</sup> that purports to describe the solidification behavior of faceted/non-faceted eutectics. This theory is really an extension of the Jackson-Hunt <sup>(3)</sup> theory, incorporating and adjusting the Fisher-Kurz <sup>(11)</sup> theory. Figure 9 is a plot using this theory and shows the undercooling versus inter-rod spacing for an envelope of curves, each for a constant velocity and showing the anticipated gradient dependence. It is clear that although a gradient dependence is predicted, it occurs at very low velocities, below that of the present work. Figure 10 shows how these parameters would change at constant velocity if the

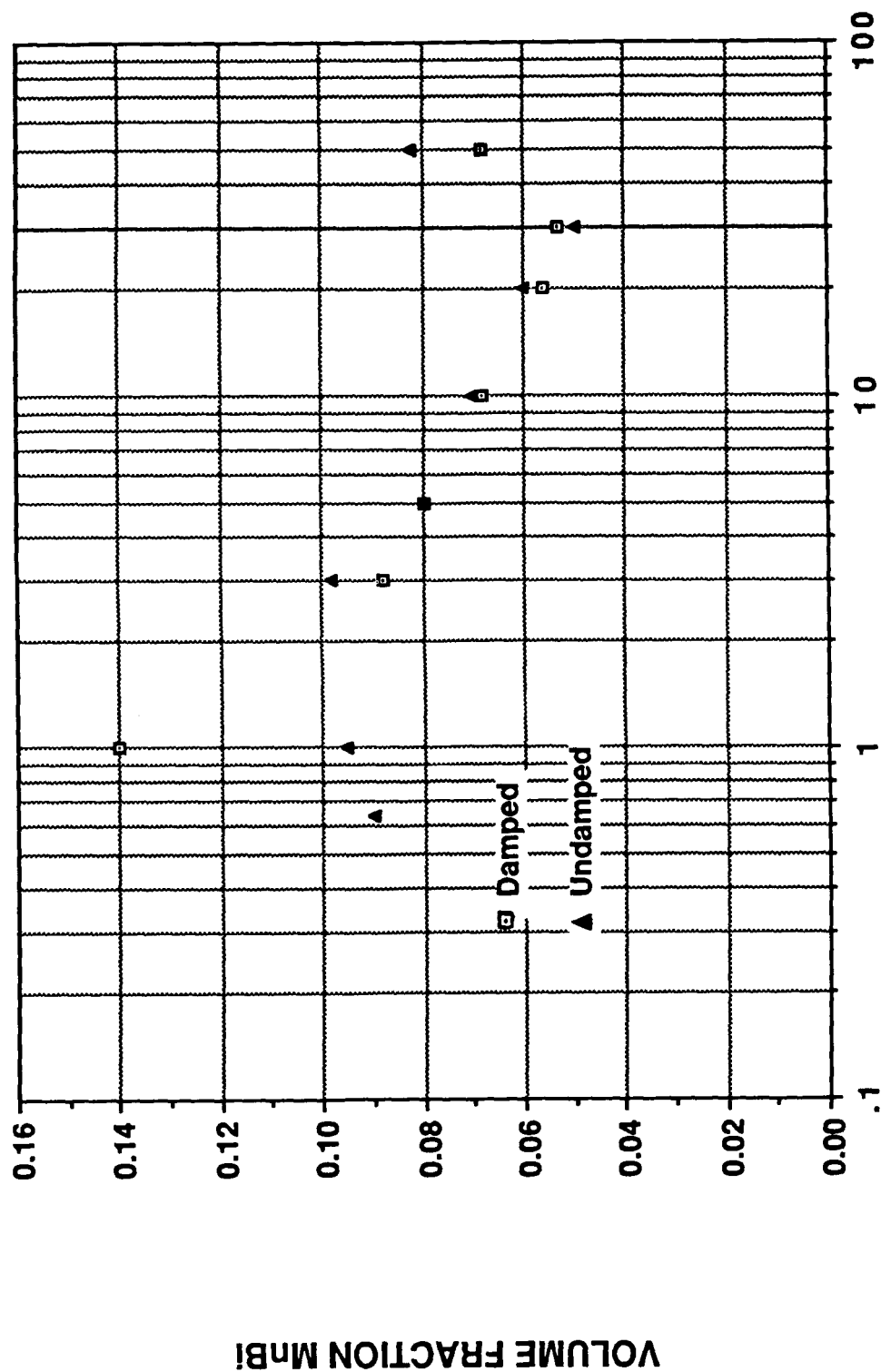


Figure 8. Volume fraction of the dispersed MnBi phase as a function of the solidification velocity, for samples solidified with and without convection damping.

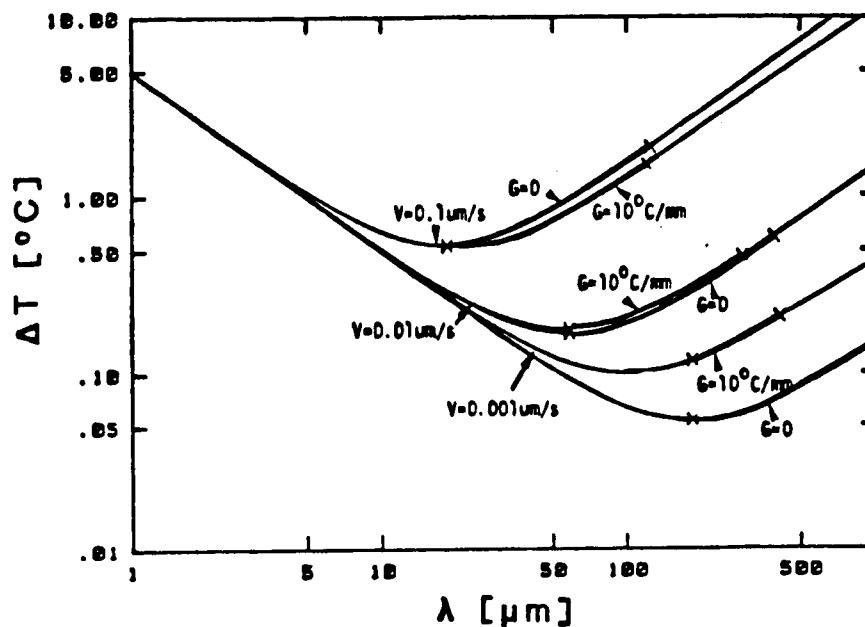


Figure 9. Interface undercooling as a function of eutectic spacing<sup>(16)</sup>, showing the sensitivity to solidification velocity and to the applied thermal gradient.

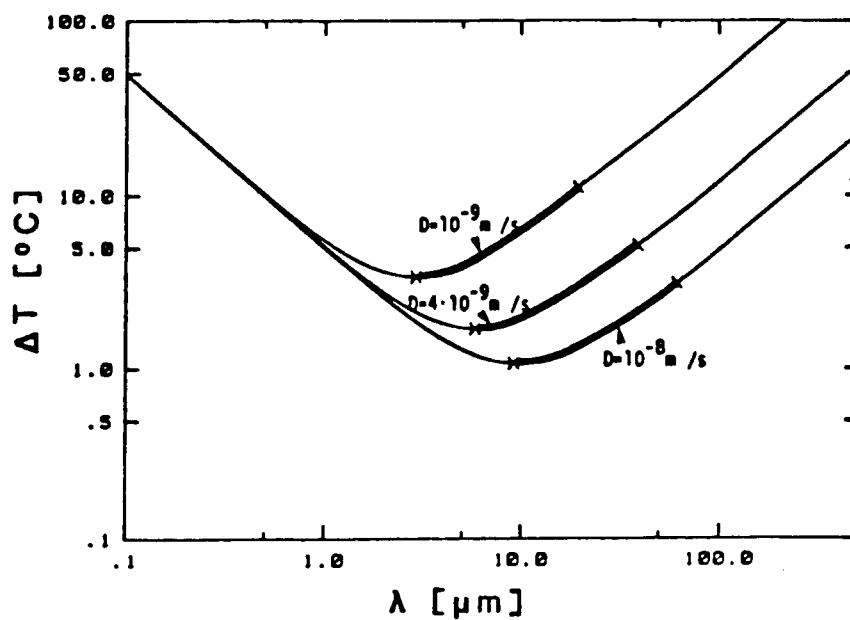


Figure 10. Interface undercooling versus eutectic spacing<sup>(16)</sup> showing the sensitivity to a varying inter-diffusion coefficient, at constant velocity.

interdiffusion coefficient within the liquid were varied. It is clear from their results that the interdiffusion coefficient has much greater potential impact on undercooling and/or microstructure than any other.

If we take our data and consider the three invariant relationships predicted by the Jackson-Hunt (3) theory, that is

$$\lambda^2 V = K_1 \quad (1a)$$

$$\Delta T \lambda = K_2 \quad (1b)$$

$$\Delta T^2 / V = K_2^2 / K_1 \quad (1c)$$

We find that although the data may fit the correct functional dependencies, the constants do not cross-correlate. This indicates that at least one of the terms that we are considering a constant may, in fact, be varying. Evaluation of the various possibilities indicates that the inter-diffusion coefficient is a most likely candidate, and should be considered to be a mass transport coefficient that may have a convective contribution incorporated within it. As convection is damped, the transport coefficient decreases. The alternative possibility is that the interdiffusion coefficient in the liquid is sensitive to the temperature depression associated with the interfacial undercooling and decreases as a function of interface temperature. The calculated interdiffusional coefficient for our damped samples is illustrated in Figure 11 and the corresponding adjustments to Figures 9 and 10, using our data, are presented as Figure 12. This plot successfully incorporates all of our relevant data and offers a concise summary of these complex interaction parameters.

#### 4. SUMMARY

Data have been presented which demonstrate that the presence of

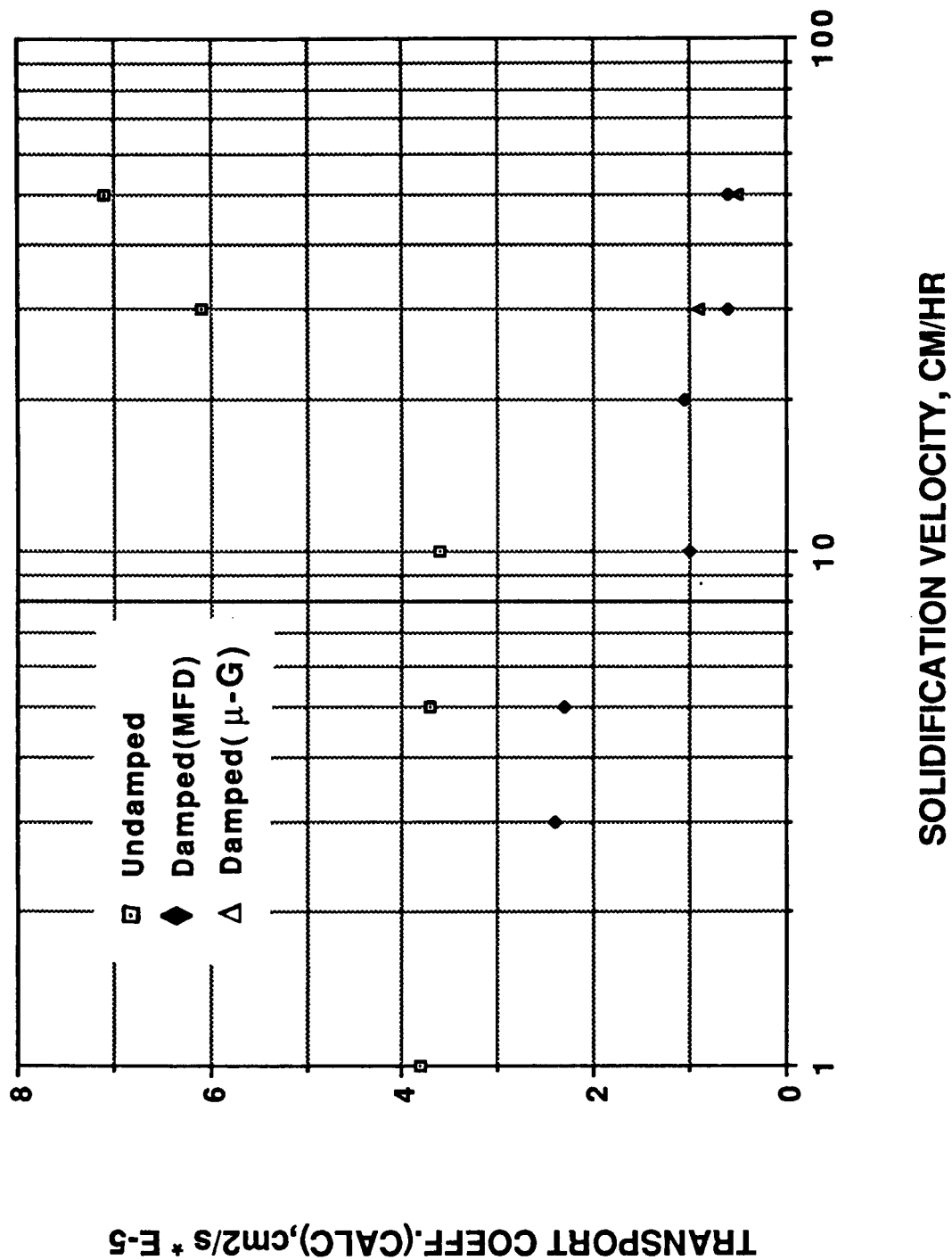


Figure 11. Calculated mass transport coefficient <sup>(3)</sup> as a function of solidification velocity for samples solidified with and without convection damping, eutectic Bi/MnBi.

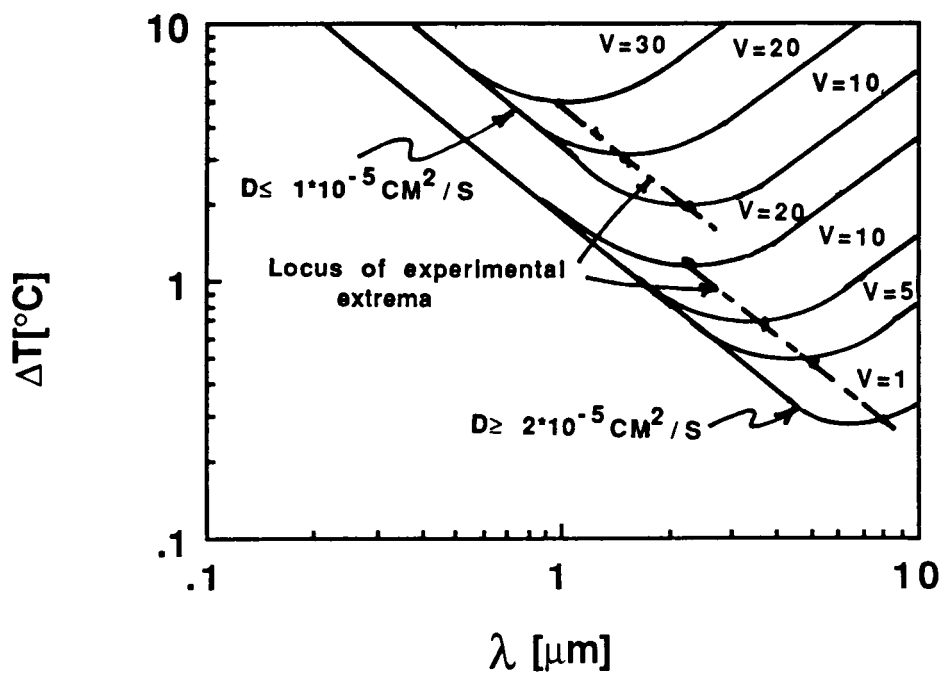


Figure 12. Interface undercooling as a function of the mean inter-rod spacing for eutectic Bi/MnBi showing the sensitivity to solidification velocity and convection damping.



convection during the directional solidification of faceted/non-faceted eutectic Bi/MnBi serves to significantly increase the mean rod-diameter and inter-rod spacing and to substantially decrease the interface undercooling. Alternatively, damping the natural, gravitationally-driven, convection normally encountered during directional solidification terrestrially, either by using applied magnetic field damping or microgravity damping, serves to decrease the spatial dimensions of the eutectic structure and to significantly increase the interfacial undercooling. The Jackson-Hunt and Magnin-Kurz theories have been used to explain these results. Microgravity damping and applied magnetic field damping of the natural thermal convection were both shown to be effective.

#### 5. REFERENCES

1. T. Chen and W. Stutius, IEEE Trans. Magn., Vol. 10, p. 581, (1974).
2. R.G. Pirich, G. Busch, W. Poit, and D.J. Larson, Jr., Met. Trans. A., Vol. 11A, p.193, (1980).
3. K.A. Jackson and J.D. Hunt, Trans. Met. Soc. AIME, Vol. 236, p.1129, (1966).
4. J.D. Verhoeven and R.M. Homer, Met. Trans., Vol.1, p.3437, (1970).
5. D.J. Larson, Jr., Grumman Research Dept. Report, RE-532, (1976).
6. J.L. DeCarlo and R.G. Pirich, Met. Trans. A, Vol. 15A, p. 2155, (1984).
7. R.G. Pirich and D.J. Larson, Jr., Grumman Research and Development Center Report, RE-602, (1980).
8. R.G. Pirich, Grumman Research and Development Center Report, RE-642, (1982).
9. G.F. Eisa, W.R. Wilcox, and G. Busch, Jour. Crystal Growth, Vol. 78, p.159, (1986).
10. B. Toloui and A. Hellawell, ACTA Met., Vol. 24, p. 565, (1976).
11. D.J. Fisher, "Aspects of Faceted/Non-faceted Eutectic Growth", Thesis No. 301, Ecole Polytechnique Federale de Lausanne, Switzerland, (1978).

12. D.J. Larson, Jr. and B.S. Dressler, Grumman Corporate Research Center Report, RM-837, (1986).
13. P.S. Ravishankar, W.R. Wilcox, and D.J. Larson, Jr., Acta Met., Vol. 28, p. 1583, (1980).
14. R.P. Silberstein, D.J. Larson, Jr., and B.S. Dressler, Met. Trans. A, Vol. 15A, p.2147, (1984).
15. R.P). Silberstein and D.J. Larson, Jr., M.R.S., Mat. Res. Soc. Symp. Proc., Vol. 87, p. 129, (1987).
16. P. Magnin, "Competetive Stable/Metastable Solidification of Fe-C-X Eutectic Alloys", Thesis No. 560, Ecole Polytechnique Federale de

## Pb-Zn Liquid Metal Diffusion

R.B. Pond, Sr. \*

J.M. Winter, Jr. \*\*

(Contract No. NAS8-35610)

The Lead-Zinc binary equilibrium system has indicated for a long time the limitations placed on Pb-Zn alloys due to the extended solubility gap in the liquid state. The two separate melts existing above the monotectic temperature have such greatly different densities that they quickly segregate into two layers by gravitational forces. Such a phenomenon has denied us alloys of Pb-Zn lying between the limits of 0.9% and 99.5% Pb.

With the capabilities afforded by micro-gravity processing it should be possible to generate the entire spectrum of Pb-Zn alloys. Since virtually no gravity driven segregation is expected in space processing any alloy composition could be generated by putting the desired ratio of Zn and of Pb into a container, heating above the consolute temperature for that alloy (under micro-gravity conditions), holding at temperature for a sufficient period of time to allow homogenization by diffusion and then solidifying the alloy by lowering the temperature. The question is "how long will the homogenization effort take?" or "what are the diffusion constants for liquid Pb and liquid Zinc?"

There are three generally accepted methods for determining the extent of diffusion in liquid metals. They are incoherent scattering of slow neutrons, NMR relaxation spectroscopy, and radioactive tracer methods. The most direct method is found in the use of radioactive tracers.(1) This is the method used by Ukanwa in a Skylab experiment.(2)

The current investigation concerns the Lead-Zinc system. Ground based studies of this system were carried out under a previous contract (NAS8-33046) to examine the possibility of obtaining a couple which, after diffusion, could be examined continuously along the diffusion axis by quantitative metallography to determine the extent of diffusion.

\* R.B. Pond, Sr. is Professor of Metallurgy, The Johns Hopkins University, and Chairman of the Board of Directors of Marvalaud, Inc.

\*\* J.M. Winter, Jr. is President of Marvalaud, Inc.

In this ground based study, a method was developed to generate the Pb-Zn diffusion couple. This "liquid shear cell" design was utilized in manufacturing the specimens for the current study. Wire type specimens of high purity zinc and high purity lead were inserted in the graphite shear cell (see Fig. 1). The graphite part A was rotated relative to part B after the cell with its load was elevated in temperature to just above the melting point of Zn (and therefore above the melting point of Pb). This developed a diffusion couple in which diffusion began immediately. However, the couple was solidified from the Zn end immediately after the shear operation so that an almost planar liquid solid interface will be maintained. The resulting solid diffusion couple from cavity 1 has a small  $L_1$  and  $L_2$  region as illustrated in Fig. 2. The couple from cavity 2 was discarded since gravity convection upset the phase configuration after the shearing operation. The specimens were manufactured in the multi-cavity liquid shear cell illustrated in Fig. 3. Flight specimen No. 10 in Fig. 3-A illustrates the characteristic shape of the couple interface in specimens produced in this shear cell.

The specimens were analyzed by x-ray florescence in the scanning electron microscope along their length to provide exact information on the chemical composition gradient (see Fig. 2).

The dimensions of the specimens are 0.185 inches diameter by .600 inches long. The couple interface was situated at the midposition of the length. Each specimen was contained within a metallurgical grade graphite crucible having a pressed fit graphite cap and a wall thickness of 0.102 inches. This graphite assembly is 0.468 inches diameter by 0.660 inches long and will fit into the GPRF-Cartridge (Drawing 95M19100-2, June 1975) supplied by Marshall Space Flight Center. The graphite assembly was baked out before the specimen was loaded into it.

After the specimen in its graphite holder was inserted into the stainless steel cartridge, it was TIG welded under vacuum to provide a flight worthy sample. A sheathed Type K thermocouple was welded to the cartridge to provide a means of monitoring the temperature of the assembly during flight. This assembly is illustrated in Fig. 4.

Two diffusion experiments were run simultaneously in the multipurpose furnace each in its own isothermal cavity. Two flight samples, two flight backup samples, and two flight space samples were generated for this study. One couple was required to be held at a temperature of  $440^{\circ}\text{C}$  (minus  $10^{\circ}\text{C}$ , plus  $1^{\circ}\text{C}$ ) which is just above the eutectic temperature (and also above the melting point of zinc) for 40 minutes and then quenched to at least  $315^{\circ}\text{C}$  within three minutes. The other couple was required to be held at a

temperature of  $820^{\circ}\text{C}$  ( $\pm 10^{\circ}\text{C}$ ) for 40 minutes and then quenched to at least  $315^{\circ}\text{C}$  within 8 minutes.

Since the success of the investigation depended on the temperature, it is appropriate to examine the origins of the values. In the previous ground based studies, diffusion couples having the diffusion direction parallel with gravity direction and zinc (the lighter material) on top were maintained at temperature for specific times after which they were rotated 90 degrees and solidified. Second phase material was precipitated from the melt; its volume depending upon the position along the axis and the diffusion time. The gravity segregation was presumed to be primarily radial, and identification of the micro-constituents and measurement of the segregated volume by quantitative metallography allowed an approximation of the extent of diffusion. A summary of some of this data is presented in Fig. 5. This approximation limited the diffusion time to 40 minutes due to the short length of the couple. After this time period, the specimen would begin to level in composition.

Two soaktemperatures were selected to allow examination of diffusion rates in the case where only a single liquid phase was involved at all times during the diffusion as well as in the case where four phases and three interfaces result from the diffusion and during the diffusion cycle. If the specimen was uniformly cooled, then in the solid state at least five interfaces should be present as can be seen from Fig. 6.

In order to discuss the solidification process, the following symbols are used:

$L_1$  = zinc rich Pb-Zn liquid  
 $L_2$  = lead rich Pb-Zn liquid  
 $T_M$  = temperature of monotectic reaction  
 $L_M$  = liquid of the monotectic composition  
 $L_{2M}$  = liquid  $L_2$  at the monotectic temperature (98% Pb)  
 $T_E$  = temperature of eutectic reaction  
 $L_{2E}$  = liquid of the eutectic composition

We can now trace the following steps in the solidification process:

- (a) As  $T_2$  decreases to  $T_M$ ,  $L_2$  precipitates  $L_1$  and  $L_1$  precipitates  $L_2$ .
- (b) Just above  $T_M$  exists primary  $L_{1M}$  and primary  $L_{2M}$ .
- (c) Just below  $T_M$  exists a layer containing in monotectic form solid (monotectic) Zn and  $L_{2M}$

derived from  $L_1^M$ , and a layer of primary  $L_2^M$  containing small islands of monotectic Zn.

- (d) Between  $T_M$  and  $T_E$ , post monotectic zinc crystallizes from  $L_2$ .
- (e) Just above  $T_E$  exists a layer of monotectic Zn containing droplets of  $L_2^E$  with post monotectic primary zinc and a layer of  $L_2^E$  containing crystals of post monotectic primary zinc.
- (f) Below  $T_E$  exists a layer of monotectic zinc containing islands of eutectic with post monotectic Zn and a layer of eutectic of Pb and Zn containing crystals of post monotectic Zn.

X-ray florescence can be used to identify the micro-constituents at various positions along the diffusion path and then quantitative metallography used to establish the chemical gradient. This allows a Fick type of analysis to produce the diffusion constants.

Specimens 9 and 10 were run in a MEA capsule on a shuttle flight the first week in November, 1985. It is our understanding that due to a frozen exit valve on the gas cooling system, Specimen 9, which had diffused at  $820^\circ\text{C}$  for forty minutes, was not quench cooled and therefore stayed at the elevated temperature for over 60 minutes resulting in a degree of leveling as can be seen in Fig. 7. X-ray florescence analysis and quantative metallography analysis show the composition at the tip of the couple to be 46% lead.

For some unknown reason, Specimen 10 did not achieve the melting temperature of zinc much less the specified  $440^\circ\text{C}$ , and therefore a liquid metal diffusion system never developed. This can be seen in Fig. 8 wherein the zinc can be observed to have never melted. X-ray florescence analysis of this specimen has justified the fact that the zinc never melted as the Zn contains far less than 1% Pb.

This experiment is expected to be rescheduled utilizing the backup specimens already prepared and submitted.

#### REFERENCES

1. N.H. Nachtrieb, "Diffusion in Liquid Metals," Chapt. 12, Liquid Metals: Chemistry and Physics, Ed. by Sylvan Z. Beer, Marcell Dekker, Inc. New York, 1972.
2. A.O. Ukanwa, "Radioactive Tracer Diffusion," Proceedings of Third Space Processing Symposium - Skylab Results 1974 - NASA.

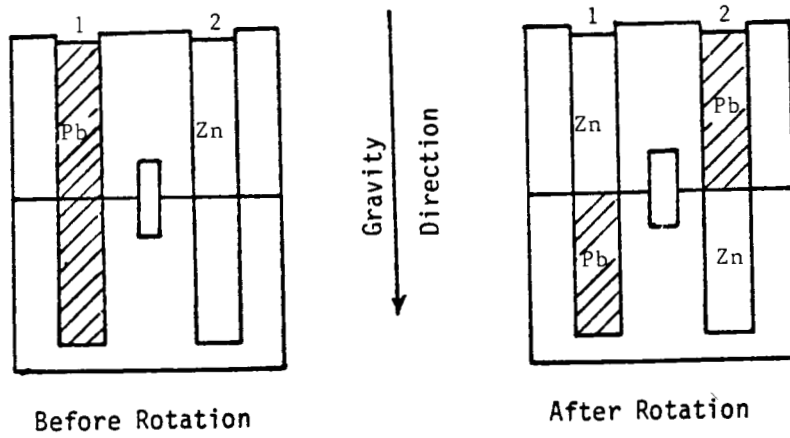


Figure 1 Liquid Shear Cell

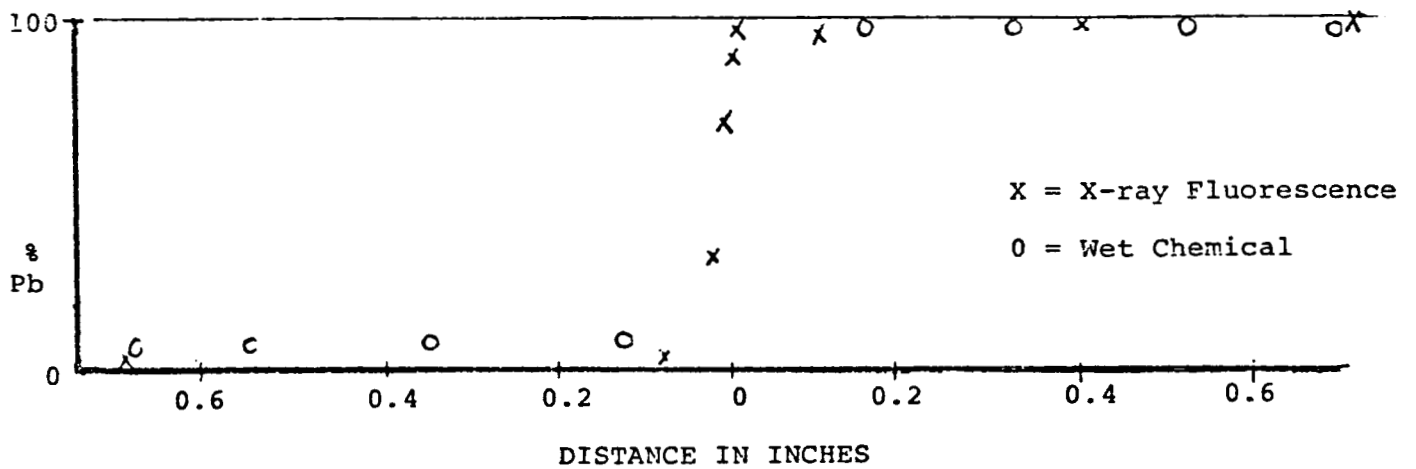


FIGURE 2



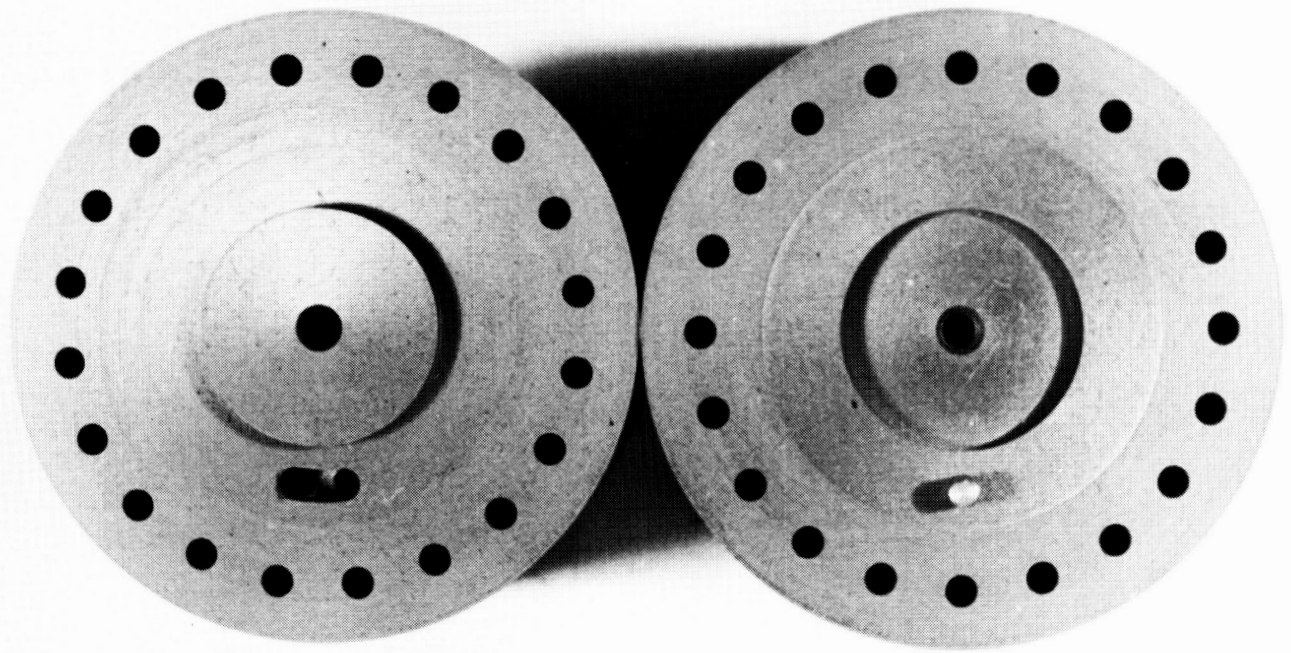
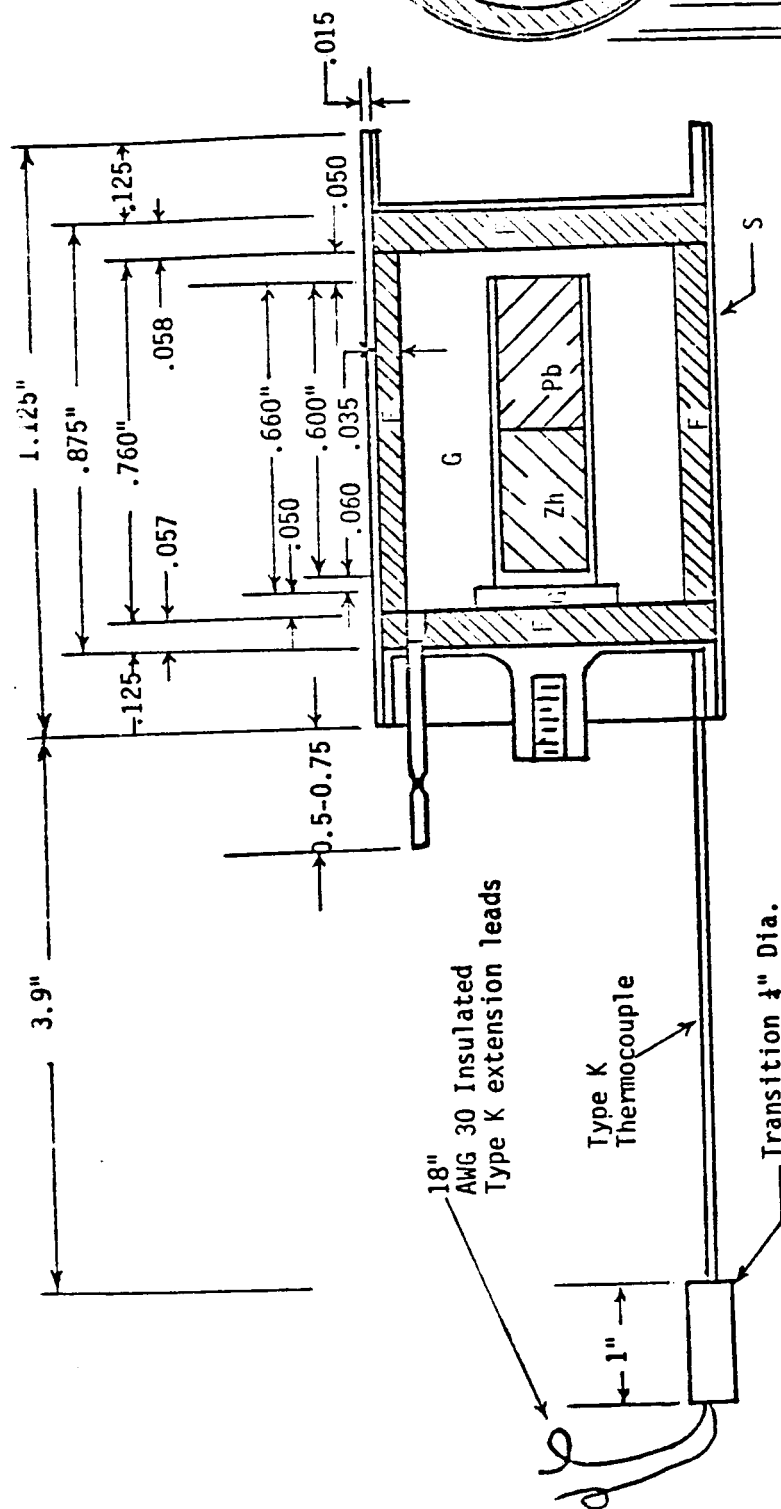


Figure 3 Graphite Shear Cell



Figure 3-A Pb-Zn Interface  
Flight Specimen No. 10 15X



#### NOTES

Inconel sheathed, ungrounded thermocouple  
brazed to end plate.

Sample weights in grams:

No.	9	--	2.495	--	Flight
	10	--	2.530	--	Flight
	11	--	2.514	--	Flight Back-up
	12	--	2.498	--	Flight Back-up
	13	--	2.496	--	Flight Spare
	14	--	2.507	--	Flight Spare

Materials  
F - Fiberfrax  
G - Graphite  
S - Stainless steel cartridge  
(Drawing 95M19100-MSFC)

Marvalaud, Inc.  
Specimen-Crucible-Cartridge-Assembly  
MEA - A - 2 - Exp. 83-01  
Module 1 and 2  
4-1-84

Figure 4. Sketch of Specimen-Crucible-Cartridge Assembly.

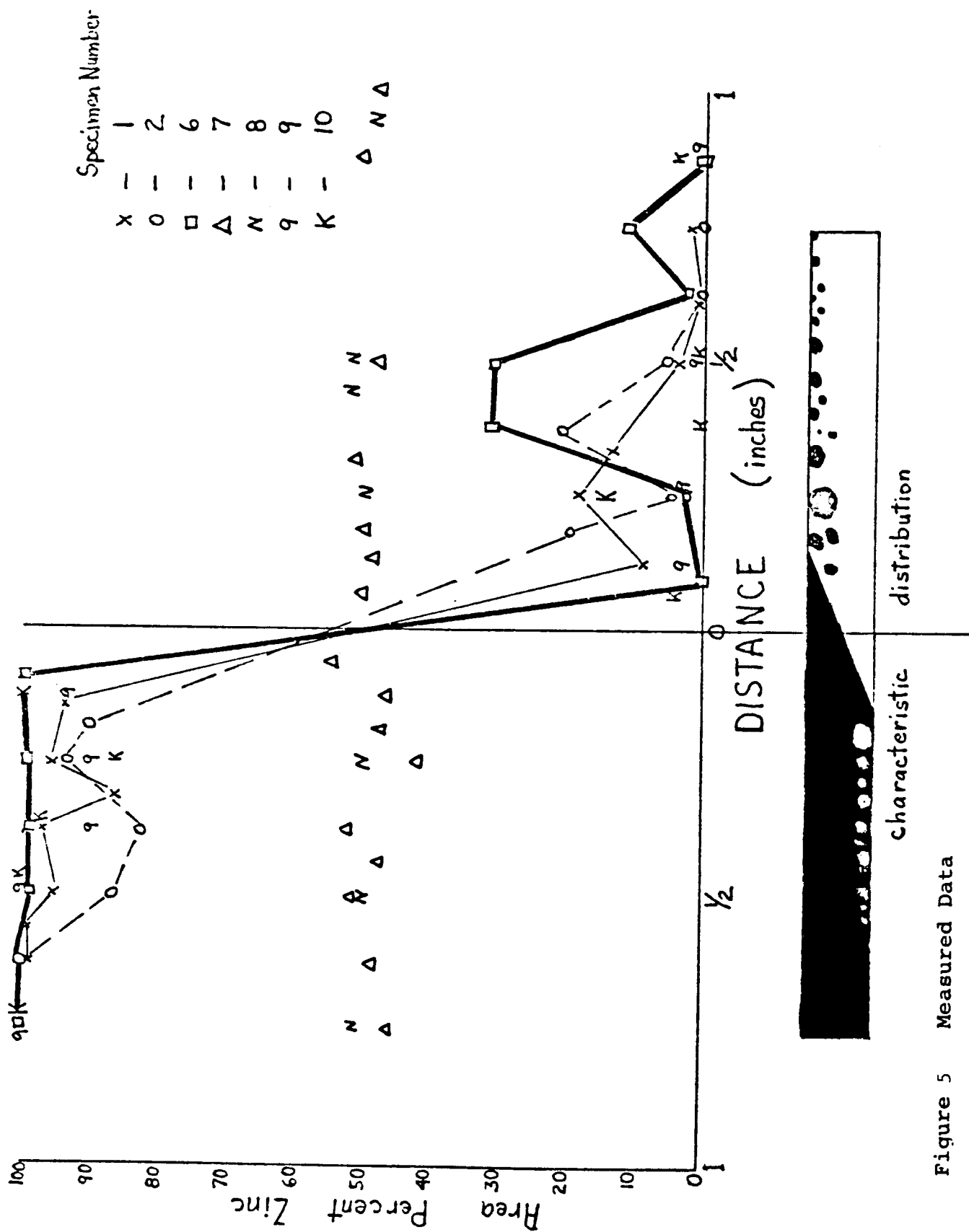
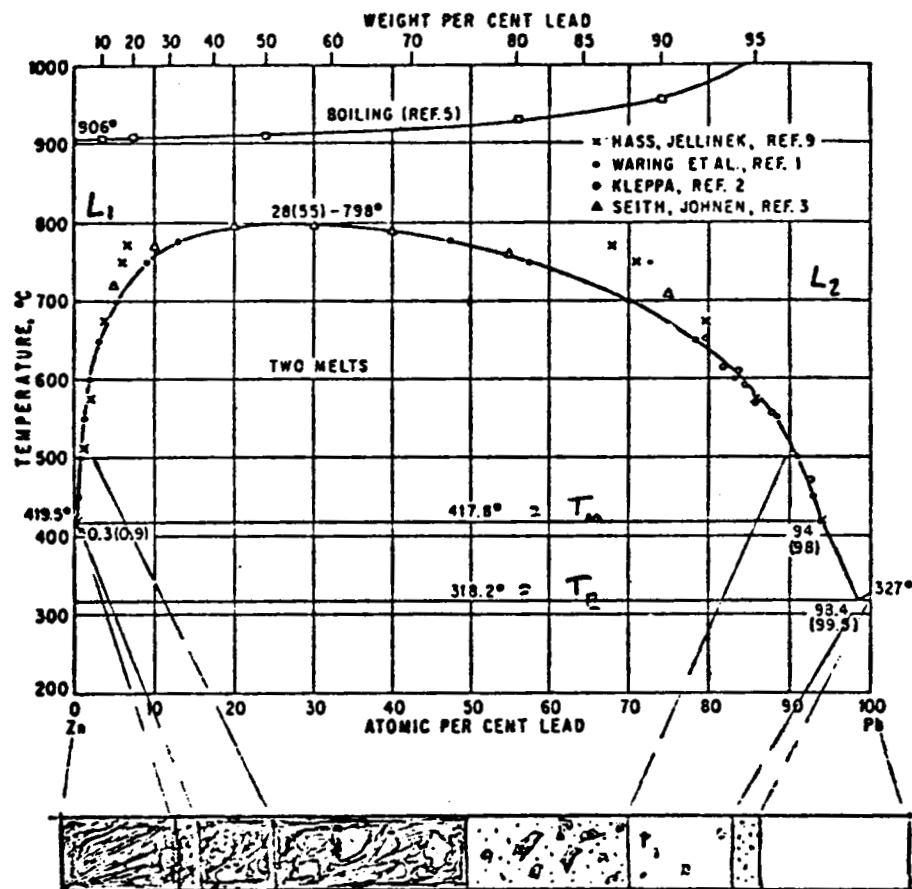


Figure 5 Measured Data

ORIGINAL PAGE IS  
OF POOR QUALITY



ROOM TEMPERATURE PROFILE

FIGURE 6

ORIGINAL PAGE  
BLACK AND WHITE PHOTOGRAPH

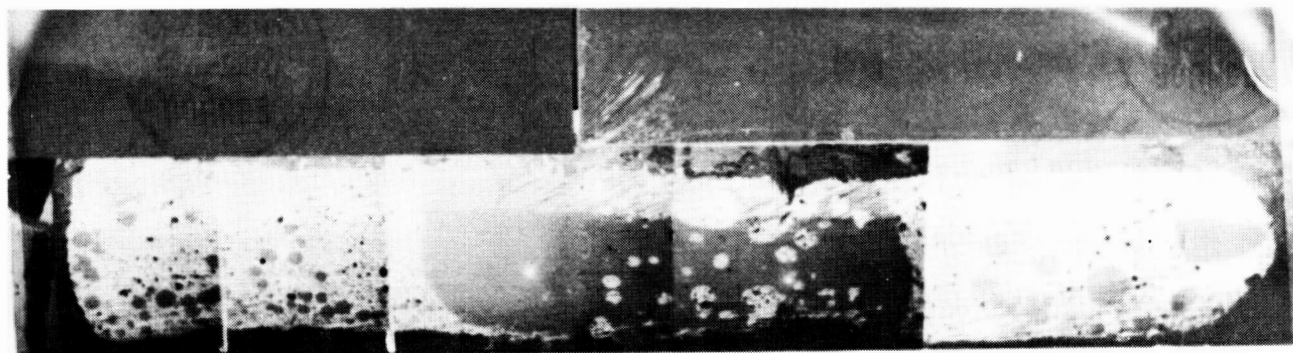


Figure 7 Micrographs of Flight Specimen No. 9

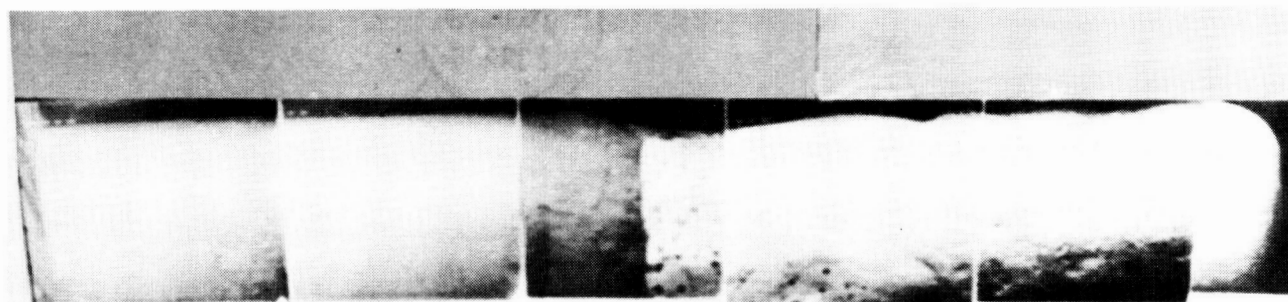


Figure 8 Micrographs of Flight Specimen No. 10



## Report Documentation Page

1. Report No. NASA TM-4069 Vol. 1	2. Government Accession No.	3. Recipient's Catalog No.	
4. Title and Subtitle Microgravity Science and Applications Flight Programs, January-March 1987, Selected Papers		5. Report Date October 1988	
		6. Performing Organization Code EN	
7. Author(s)		8. Performing Organization Report No.	
		10. Work Unit No.	
9. Performing Organization Name and Address NASA Office of Space Science and Applications Microgravity Science and Applications Division		11. Contract or Grant No.	
		13. Type of Report and Period Covered Technical Memorandum	
12. Sponsoring Agency Name and Address National Aeronautics and Space Administration Washington, DC 20546		14. Sponsoring Agency Code	
15. Supplementary Notes			
16. Abstract  This report is a compilation of selected papers written by the flight program principal investigators. The Microgravity Science and Applications Flight Program was reviewed by a panel of eight chaired by Professor J. Robert Schrieffer in 1987. Dr. Schrieffer and his committee reviewed the flight program and made recommendations to the Director of the Microgravity Science and Applications Division as to the quality of the science contained in the program and improvements that could be made in some of the research efforts.			
17. Key Words (Suggested by Author(s)) electronic materials combustion science microgravity science and applications		18. Distribution Statement  Unclassified - Unlimited  Subject Category 29	
19. Security Classif. (of this report) Unclassified	20. Security Classif. (of this page) Unclassified	21. No. of pages 532	22. Price A23